AD-A263 541

COMMISSION OF THE
EUROPEAN COMMUNITIES

EUROPEAN
MATERIALS
RESEARCH
SOCIETY

SYMPOSIA PROCEEDINGS 36

CdTe and Related Cd Rich Alloys

R. Triboulet
W.R. Wilcox
O. Oda
editors

CdTe AND RELATED Cd RICH ALLOYS

Accession For		
NTIS GRA&I		☑
DTIC TAB		☐
Unannounced		☐
Justification		
By		
Distribution/		
Availability Codes		
Dist	Avail and/or Special	
A-1		

DTIC QUALITY INSPECTED 4

EUROPEAN MATERIALS RESEARCH SOCIETY SYMPOSIA PROCEEDINGS

Volume 1: Ceramic Materials Research (ed. R.J. Brook)
Volume 2: Photon, Beam and Plasma Assisted Processing (eds. I.W. Boyd and E.F. Krimmel)
Volume 3: Deep Implants (eds. G.G. Bentini, A. Golanski and S. Kalbitzer)
Volume 4: Metastable Alloys: Preparation and Properties (eds. K. Samwer, M. von Allmen, J. Bøttiger and B. Stritzker)
Volume 5: Superconducting and Low-Temperature Particle Detectors (eds. G. Waysand and G. Chardin)
Volumes 6A, 6B: High T_c Superconductors (eds. P.F. Bongers, C. Schlenker and B. Stritzker)
Volume 7: Solid State Ionics (eds. M. Balkanski and C. Julien)
Volume 8: Rare-Earth Permanent Magnets (ed. I.R. Harris)
Volume 9: Defects in Silicon (eds. C.A.J. Ammerlaan, A. Chantre and P. Wagner)
Volumes 10A, 10B: Silicon Molecular Beam Epitaxy (eds. E. Kasper and E.H.C. Parker)
Volume 11: Acoustic, Thermal Wave and Optical Characterization of Materials (eds. G.M. Crean, M. Locatelli and J. McGilp)
Volume 12: Beam Processing and Laser Chemistry (eds. I.W. Boyd and E. Rimini)
Volume 13: Interfaces in Biomaterials Sciences (eds. D. Muster and G. Hastings)
Volumes 14A, 14B: High T_c Superconductor Materials (eds. H.-U. Habermeier, E. Kaldis and J. Schoenes)
Volume 15: Metal Matrix Composites (eds. G. Chadwick and L. Froyen)
Volume 16: Magnetic Thin Films, Multilayers and Superlattices (eds. A. Fert, G. Güntherodt, B. Heinrich, E.E. Marinero and M. Maurer)
Volume 17: Metallurgical Coatings and Materials Surface Modifications (eds. H. Hintermann and J. Spitz)
Volume 18: Surface Processing and Laser Assisted Chemistry (eds. I.W. Boyd, E. Fogarassy and M. Stuke)
Volume 19: Materials for Optoelectronic Devices, OEICs and Photonics (eds. H. Schlötterer, M. Quillec, P.D. Greene and M. Bertolotti)
Volume 20: SiC, Natural and Synthetic Diamond and Related Materials (eds. A.A. Gippius, R. Helbig and J.P.F. Sellschop)
Volume 21: Analytical Techniques for the Characterization of Compound Semiconductors (eds. G. Bastard and H. Oppolzer)
Volume 22: Micronic Integrated Sensors (ed. J.L. Robert)
Volume 23: High Energy and High Dose Ion Implantation (eds. S.U. Campisano, J. Gyulai, P.L.F. Hemment and J.A. Kilner)
Volume 24: Laser Surface Processing and Characterization (ed. I.W. Boyd)
Volume 25: Nuclear Methods in Semiconductor Physics (eds. G. Langouche, J.C. Soares and J.P. Stoquert)
Volume 26: Clays and Hydrosilicate Gels in Nuclear Fields (ed. A. Meunier)
Volume 27: Chemistry of Cements for Nuclear Applications (eds. P. Barret and F.P. Glasser)
Volume 28: Nuclear Materials for Fission Reactors (eds. Hj. Matzke and G. Schumacher)
Volume 29: Modifications Induced by Irradiation in Glasses (ed. P. Mazzoldi)
Volume 30: Polyconjugated Materials (ed. G. Zerbi)
Volume 31: SiGe Based Technologies (eds. E. Kasper, Y. Shiraki and T.P. Pearsall)
Volume 32: Materials Surface Processing (eds. M. Stuke, E.E. Marinero and I. Nishiyama)
Volume 33: Chemistry for Electronic Materials (eds. Y. Pauleau, G. Wahl, K.F. Jensen and T. Hirai)
Volume 34: Semiconductor Materials Analysis and Fabrication Process Control (eds. G. Crean, R. Stuck and J. Woollam)
Volume 35: Synthetic Materials for Non-Linear Optics and Electronics (eds. C. Taliani, Z.V. Vardeny and Y. Maruyama)
Volume 36: CdTe and Related Cd Rich Alloys (ed. R. Triboulet, W.R. Wilcox and O. Oda)
Volume 37: Single Chamber Processing (eds. Y.I. Nissim and A. Katz)

CdTe AND RELATED Cd RICH ALLOYS

PROCEEDINGS OF SYMPOSIUM F ON
NEW ASPECTS ON THE GROWTH, CHARACTERIZATION
AND APPLICATIONS OF CdTe AND RELATED Cd RICH ALLOYS
OF THE 1992 E-MRS SPRING CONFERENCE

STRASBOURG, FRANCE, JUNE 2–5, 1992

Edited by

R. TRIBOULET
CNRS, Lab. de Physique des Solides de Bellevue, Meudon, France

W.R. WILCOX
Clarkson University, Potsdam, NY, USA

O. ODA
Nikko Kyodo Co., Ltd, Saitama, Japan

1993
NORTH-HOLLAND
AMSTERDAM – LONDON – NEW YORK – TOKYO

93 4 20 155

©1993 ELSEVIER SEQUIOIA S.A. All rights reserved.

No part of this publication may be reproduced, stored in a retrieval system, or transmitted, in any form or by any means, electronic, mechanical, photocopying, recording or otherwise, without the prior written permission of the copyright owner, Elsevier Sequoia S.A., P.O. Box 564, 1001 Lausanne, Switzerland.

Special regulations for readers in the U.S.A. - This publication has been registered with the Copyright Clearance Center Inc. (CCC), Salem, Massachusetts. Information can be obtained from the CCC about conditions under which photocopies of parts of this publication may be made in the U.S.A. All other copyright questions, including photocopying outside of the U.S.A., should be referred to the copyright owner, Elsevier Science Publishers B.V., unless otherwise specified.

No responsibility is assumed by the Publisher for any injury and/or damage to persons or property as a matter of products liability, negligence or otherwise, or from any use or operation of any methods, products, instructions or ideas contained in the material herein.

Printed on acid-free paper

ISBN: 0 444 89910 3

Published by:
North-Holland
Elsevier Science Publishers B.V.
Sara Burgerhartstraat 25
P.O. Box 211
1000 AE Amsterdam
The Netherlands

Reprinted from:
MATERIALS SCIENCE AND ENGINEERING B16 (1-3)

The manuscripts for the Proceedings were received by the Publisher:
mid July – September 1992

Printed in The Netherlands

Contents

Foreword . . . ix

Organizers and Sponsors . . . xi

Mechanical properties of CdTe . . . 1
R. Balasubramanian and W. R. Wilcox (Potsdam, NY, USA)

Basic problems of vertical Bridgman growth of CdTe . . . 8
P. Rudolph and M. Mühlberg (Berlin, Germany)

Defects and electrical properties of doped and undoped CdTe single crystals from tellurium-rich solutions . . . 17
E. Weigel, G. Müller-Vogt, B. Steinbach, W. Wendl (Karlsruhe, Germany), W. Stadler, D. M. Hofmann and B. K. Meyer (Munich, Germany)

Floating-zone melting of CdTe . . . 23
W.-M. Chang, W. R. Wilcox and L. Regel (Potsdam, NY, USA)

Bridgman growth and assessment of CdTe and CdZnTe using the accelerated crucible rotation technique . . . 29
P. Capper, J. E. Harris, E. O'Keefe, C. L. Jones, C. K. Ard, P. Mackett and D. Dutton (Southampton, UK)

$Cd_{1-x}Zn_xTe$ substrates for $Hg_{1-x}Cd_xTe$ liquid-phase epitaxy . . . 40
M. Bruder, H. Figgemeier, R. Schmitt and H. Maier (Heilbronn, Germany)

Horizontal Bridgman growth of large high quality $Cd_{1-x}Zn_xTe$ crystals . . . 44
P. Brunet, A. Katty, D. Schneider, A. Tromson-Carli and R. Triboulet (Meudon, France)

Computer simulation of CdTe crystal growth and application . . . 48
Ch. Steer, M. Hage-Ali, J. M. Koebel and P. Siffert (Strasbourg, France)

Heteroepitaxy of CdTe on GaAs and silicon substrates . . . 51
J. P. Faurie, R. Sporken, Y. P. Chen, M. D. Lange and S. Sivananthan (Chicago, IL, USA)

CdTe rotation growth on silicon substrates by metallo-organic chemical vapour deposition . . . 57
H. Ebe and H. Takigawa (Atsugi, Japan)

Growth and structure of $CdTe/Cd_{1-x}Mn_xTe$ multiple quantum wells showing excitonic 2S states . . . 60
J. H. C. Hogg, J. E. Nicholls, S. R. Jackson, W. E. Hagston, D. E. Ashenford, B. Lunn (Hull, UK) and S. Ali (Homs, Syria)

Laser growth of CdTe epitaxial film on CdTe substrate . . . 64
C. Coutal, J. C. Roustan, A. Azema, A. Gilabert, P. Gaucherel (Nice, France) and R. Triboulet (Meudon, France)

Growth of CdTe single crystals by vapour condensation on the surface of polycrystalline source material . . . 68
A. Szczerbakow and Z. Gołacki (Warsaw, Poland)

Structural and electronic properties of CdTe-based heterostructures . . . 71
N. Magnea, A. Tardot, H. Mariette and N. Pelekanos (Grenoble, France)

Short period CdTe–ZnTe and CdTe–MnTe superlattices . . . 79
W. Faschinger, F. Hauzenberger, P. Juza, H. Sitter, A. Pesek, H. Zajicek and K. Lischka (Linz, Austria)

Spectroscopy of donors and donor-bound excitons in $CdTe/Cd_{1-x}Zn_xTe$ multiple quantum wells . . . 83
R. T. Cox, A. Mandray, S. Huant (Grenoble, France), F. Bassani (Saint Martin D'Hères, France), K. Saminadayar (Grenoble, France) and S. Tatarenko (Saint Martin D'Hères, France)

Piezoreflectivity investigation of CdTe/(Cd,Zn)Te heterostructures . . . 87
J. Calatayud, J. Allègre, P. Lefebvre and H. Mathieu (Montpellier, France)

© 1993 - Elsevier Sequoia. All rights reserved

Piezomodulated reflectivity on CdMnTe/CdTe quantum well structures as a new standard characterization method 92
E. Kurtz, K. Schmitt, D. Hommel, A. Waag, R. N. Bicknell-Tassius and G. Landwehr (Würzburg, Germany)

Structural defects in bulk and epitaxial CdTe 96
K. Durose, A. Turnbull and P. Brown (Durham, UK)

RHEED studies of MBE growth mechanisms of CdTe and CdMnTe 103
A. Waag, Th. Behr, Th. Litz, B. Kuhn-Heinrich, D. Hommel and G. Landwehr (Würzburg, Germany)

Properties of dry-etched CdTe–epitaxial layer surfaces and microstructures 108
M. Neswal, K. H. Greßlehner, K. Lischka, P. Bauer, A. Brandstötter and K. Lübke (Linz, Austria)

Qualification of a new defect revealing etch for CdTe using cathodoluminescence microscopy 113
C. C. R. Watson, K. Durose, A. J. Banister (Durham, UK), E. O'Keefe and S. K. Bains (Southampton, UK)

In situ reflectance anisotropy studies of the growth of CdTe and other compounds by MOCVD 118
V. Sallet, R. Druilhe, J. E. Bouree, R. Triboulet (Meudon, France), O. Acher (Bruyeres-le-Chatel, France), V. Yakovlev and B. Drevillon (Palaiseau, France)

Specific behaviour of CdTe ion implantation damage 123
G. Leo (Orsay, France), A. V. Drigo (Padua, Italy) and A. Traverse (Orsay, France)

Structural properties of defects in $Cd_{1-x}Zn_xTe$ 128
D. M. Hofmann, W. Stadler, K. Oettinger, B. K. Meyer (Garching, Germany), P. Omling (Lund, Sweden), M. Salk, K. W. Benz (Freiburg, Germany), E. Weigel and G. Müller-Vogt (Karlsruhe, Germany)

Positron trapping at native vacancies in CdTe crystals: In doping effect 134
C. Corbel, L. Baroux, F. M. Kiessling, C. Gély-Sykes (Gif-sur-Yvette, France) and R. Triboulet (Meudon, France)

New method for the determination of V_{Cd} concentrations in p-CdTe 139
H. Zimmermann, R. Boyn, P. Rudolph, J. Bollmann, A. Klimakow (Berlin, Germany) and R. Krause (Halle, Germany)

Effect of the $\{h11\}$ orientations and polarities of GaAs substrates on CdTe buffer layer structural properties 145
A. Tromson-Carli, G. Patriarche, R. Druilhe, A. Lusson, Y. Marfaing, R. Triboulet (Meudon, France), P. D. Brown and A. W. Brinkman (Durham, UK)

Scanning tunneling microscope investigation of the effects of CdTe substrate preparation on molecular beam epitaxially grown *n*-CdTe layers. 151
M. Ehinger, M. Wenzel, T. Litz and G. Landwehr (Würzburg, Germany)

X-Ray photoelectron diffraction from the CdTe(111)A polar surface 155
G. Granozzi, G. A. Rizzi, A. M. Capobianco, R. Bertoncello, M. Casarin and E. Tondello (Padua, Italy)

Ion channelling Rutherford backscattering spectrometry structural characterization of CdS/CdTe heterostructures 160
A. Guerrieri (Mesagne, Italy), A. V. Drigo, F. Romanato (Padua, Italy), N. Lovergine and A. M. Mancini (Lecce, Italy)

Complete characterization of epitaxial CdTe on GaAs from the lattice geometrical point of view 165
P. Möck (Berlin, Germany)

Relation between dislocation density, bulk electrical properties and ohmic contacts of CdTe 168
I. Hähnert and M. Wienecke (Berlin, Germany)

Effect of large-scale potential relief on the electronic transport in doped and compensated CdTe: the role of impurity correlations. 172
N. V. Agrinskaya (St. Petersburg, Russian Federation)

Efficient n-type doping of CdTe epitaxial layers grown by photo-assisted molecular beam epitaxy with the use of chlorine 178
D. Hommel, S. Scholl, T. A. Kuhn, W. Ossau, A. Wagg, G. Landwehr (Würzburg, Germany) and G. Bilger (Stuttgart, Germany)

Effect of thermal annealing on the microstructure of CdTe and $Cd_{1-x}Zn_xTe$ crystals 182
J. Shen, D. K. Aidun, L. Regel and W. R. Wilcox (Potsdam, NY, USA)

Diffusion of gallium in cadmium telluride 186
G. W. Blackmore (Malvern, UK), E. D. Jones (Coventry, UK), J. B. Mullin (Malvern, UK) and N. M. Stewart (Ipswich, UK)

Depth non-uniformities in thin CdTe layers grown by MBE on InSb substrates 191
D. E. Ashenford, P. Devine, J. H. C. Hogg, B. Lunn and C. G. Scott (Hull, UK)

Chemical diffusion of Hg in CdTe 195
J. H. C. Hogg, A. Bairstow, G. W. Matthews, D. Shaw and J. D. Stedman (Hull, UK)

Effect of interdiffusion on dislocation generation in epitaxial layers on CdTe, (Cd,Zn)Te and Cd(Te,Se) substrates 199
I. Utke, L. Parthier and M. Schenk (Berlin, Germany)

Carbon and silicon in travelling heater method grown semi-insulating CdTe 202
L. Chibani, M. Hage-Ali, J. P. Stoquert, J. M. Koebel and P. Siffert (Strasbourg, France)

Donor activation efficiency and doping profile quality in In-doped CdTe and CdZnTe quantum structures 207
F. Bassani, S. Tatarenko (Saint Martin D'Hères, France), K. Saminadayar (Grenoble, France) and C. Grattepain (Meudon, France)

Implantation-enhanced interdiffusion in CdTe/ZnTe quantum wells 211
A. Hamoudi, E. Ligeon (Grenoble, France), J. Cibert, L. S. Dang (Saint Martin D'Hères, France) and J. L. Pautrat (Grenoble, France)

Native defect equilibrium in semi-insulating CdTe(Cl) 215
P. Höschl, R. Grill, J. Franc, P. Moravec and E. Belas (Prague, Czechoslovakia)

Native point defects in CdTe and its stability region 219
M. Wienecke, H. Berger and M. Schenk (Berlin, Germany)

Deep levels in semi-insulating CdTe 223
P. Moravec, M. Hage-Ali, L. Chibani and P. Siffert (Strasbourg, France)

Overview of CdTe-based semimagnetic semiconductors 228
J. P. Lascaray (Montpellier, France)

Comparative reflectivity study of coupled and uncoupled CdTe/CdMnTe asymmetric double quantum wells 235
I. Lawrence, G. Feuillet, H. Tuffigo (Grenoble, France), C. Bodin, J. Cibert, P. Peyla and A. Wasiela (Saint Martin D'Hères, France)

Time-resolved light-induced Faraday rotation in $Zn_{1-x}Mn_xTe$ and $Cd_{1-x}Mn_xTe$ 239
S. Hugonnard-Bruyere, J. Frey, R. Frey and C. Flytzanis (Palaiseau, France)

Determination of the iron acceptor level in CdTe 243
B. K. Meyer (Garching, Germany), H. Linke, P. Omling (Lund, Sweden), M. Salk and K.-W. Benz (Freiburg, Germany)

Fourier transform IR spectroscopy of CdTe:Fe 246
M. C. Carmo and M. J. Soares (Aveiro, Portugal)

Thin films of CdTe produced using stacked elemental layer processing for use in CdTe/CdS solar cells 250
R. W. Miles, M. T. Bhatti, K. M. Hynes, A. E. Baumann and R. Hill (Newcastle-upon-Tyne, UK)

Potentiality of photorefractive CdTe 257
J. Y. Moisan, P. Gravey, G. Picoli, N. Wolffer and V. Vieux (Lannion, France)

Deep centres for optical processing in CdTe 262
E. Rzepka, Y. Marfaing, M. Cuniot and R. Triboulet (Meudon, France)

Time-resolved build-up and decay of photorefractive and free-carrier gratings in CdTe:V 268
K. Jarasiunas, P. Delaye, G. Roosen (Orsay, France) and J. C. Launay (Saint Médard en Jalles, France)

Optical, photoelectrical, deep level and photorefractive characterization of CdTe:V 273
J. P. Zielinger, M. Tapiero, Z. Guellil (Strasbourg, France), G. Roosen, P. Delaye (Orsay, France), J. C. Launay and V. Mazoyer (Talence, France)

Compact visible microgun-pumped CdTe–$Cd_{1-x}Mn_xTe$ laser 279
J. Cibert, C. Bodin, L. S. Dang (Saint Martin D'Hères, France), G. Feuillet, P. H. Jouneau, E. Molva, R. Accomo and G. Labrunie (Grenoble, France)

High quality CdTe and its application to radiation detectors 283
M. Ohmori, Y. Iwase and R. Ohno (Saitama, Japan)

Gamma- and X-ray detectors manufactured from $Cd_{1-x}Zn_xTe$ grown by a high pressure Bridgman method 291
J. F. Butler, F. P. Doty, B. Apotovsky (San Diego, CA, USA), J. Lajzerowicz and L. Verger (Grenoble, France)

Compensation of trapping losses in CdTe detectors 296
M. Richter, P. Siffert and M. Hage-Ali (Strasbourg, France)

The electronic bistability in doped semiconductors with polar optical scattering: the reversible switching effect in CdTe:Cl at room temperature 302
N. V. Agrinskaya and V. I. Kozub (St. Petersburg, Russian Federation)

Power switching with CdTe:Cl 304
J. Lajzerowicz, L. Verger, F. Mathy and M. Cuzin (Grenoble, France)

Picosecond diffraction kinetics of transient gratings in CdTe and CdZnTe 309
N. Gouaichault-Brugel, L. Nardo, M. Pugnet and J. Collet (Toulouse, France)

Author Index 313

Subject Index 315

Foreword

Symposia provide a valuable forum for stimulating interest and activity in the latest developments in an emerging field of research or scientific breakthrough. This has been the case for the Symposium F on *New aspects on the growth, characterization and applications of CdTe and Cd-rich related alloys* that was held at the Conseil de l'Europe of Strasbourg on June 2–5, 1992 in the frame of the EMRS Spring Meeting 1992 dedicated to Electronic Materials. The research reported at this Symposium F has resulted in this volume, which contains 12 invited and 51 contributed papers.

Some 100 scientists attended. They were mainly from France (30), Germany (26), UK (9), USA (8), and Russian Federation (5), although the meeting was fortunate in attracting researchers of eight other countries.

This four-day Symposium has provided the opportunity to take stock of the researches devoted to CdTe and related Cd-rich alloys (roughly in the band gap energy range 1–2 eV) during the last decade, since the encyclopedic and famous work of De Nobel (1960), the Strasbourg conferences of 1972 and 1977, both dedicated to CdTe, and the excellent monography of K. Zanio (1977).

CdTe exhibits numerous attractive features. It has a band gap of 1.5 eV, just in the middle of the solar spectrum, making it an ideal material for photovoltaic conversion. It also has a high average atomic number of 50, very convenient for nuclear detection. A high electro-optic coefficient is another feature (5.5 for CdTe:V to compare with 1.2 for GaAs:Cr or 1.34 for InP:Fe) allowing high performance electro-optic modulators and photorefractive devices. It can present both types of conductivity (n and p), which makes diode technology and field effect transistors possible, and it has a semi-insulating state as well. CdTe-based semimagnetics, owing to the large solubility of some magnetic ions like Mn or Te in a II–VI matrix, display extremely exciting properties making the material attractive for basic studies and potential applications. This is also true for heterostructures where the band gap engineering concept opens up a tremendous field of possibilities.

Because of these attractive properties, there has been a never-failing interest in CdTe for about thirty years. The history of CdTe has been marked by the different applications to which it has given rise, from the first solar cells of the sixties, reactivated industrially for about five years, to the nuclear tomography, the industrial production of substrates for the MCT epitaxial growth (expressed by an annual world production of several tons of material), the electro-optic modulators and now the photorefractive devices.

At the same time, CdTe has been an ideal tool for fundamental studies dealing with *e.g.*: self-compensation; crystal growth in micro or macro gravity, owing to its extreme sensitivity to all growth parameters; study of its structural defects; semimagnetic physics; quantum well superlattices (more recently where it appears either as a barrier in CdTe/(Cd, Hg)Te/CdTe structures or wells in (CdA)Te/CdTe/(Cd, A)Te structures with A being typically Zn or Mn); thermodynamics of defects owing to its large stoichiometry departure whose extension is still much debated; the significant influence of native defects on its electronic properties.

The true revival of CdTe owing to the possibilities of the "new" techniques of epitaxial growth at low temperatures (like MBE or MOCVD (heterostructures, superlattices, band gap engineering concept)), the fantastic progress of the growth and characterization techniques leading to a better knowledge and control of its

properties, and the emergence of new application fields, have been at the centre of this international conference.

The good health of CdTe is particularly shown through the richness of the device sessions: classical devices, like nuclear detectors and solar cells are improved while new applications appear in the field of photorefractivity, non linear optics, optical switching, and light emission with new quantum well structures. Owing to the emergence of new applications and the possibilities of the epitaxial growth techniques at low temperature, the research devoted to CdTe, this "old" material, is enjoying a new boom. CdTe remains a topical material. It is hoped that further meetings will stimulate additional interest and support for this very interesting and important compound.

R. TRIBOULET
W. R. WILCOX
O. ODA
Chairmen

Organizers and Sponsors

International Organizing Committee

R. Triboulet, Chairman (France)
W. R. Wilcox, Co-chairman (USA)
O. Oda, Co-chairman (Japan)
J. B. Mullin (UK)
P. Rudolph (Germany)
J. L. Pautrat (France)
P. Hoschl (Czechoslovakia)
M. Hage-Ali (France)
N. V. Agrinskaya (Russian Federation)
G. Muller Vogt (Germany)

Acknowledgments

The organizing committee wish to acknowledge and thank the following organizations for their generosity in the support of the Symposium:

Centre National de la Recherche Scientifique (CNRS)
Centre National d'Etudes des Télécommunications (CNET)
Direction des Recherches, Etudes et Techniques (DRET)
European Materials Research Society (EMRS)
European Research Office of the US Army (ERO)
Eurorad II-VI
Johnson Matthey
Nippon Mining Co., Ltd.
Osaka Asahi Co., Ltd.
Sumitomo Metal Mining Co., Ltd.
Union Minière, Business Unit Hoboken

Sponsors

This Conference was held under the auspices of:

The Council of Europe
The Commission of the European Communities

It is our pleasure to acknowledge with gratitude the financial assistance provided by

Banque Populaire (France)
Brasserie de Kronenbourg (France)
Centre de Recherches Nucléaires (France)
Centre National de la Recherche Scientifique (France)
Elsevier Science Publishers B.V. (The Netherlands)
Office du Tourisme de la Ville de Strasbourg (France)
The Commission of the European Communities
The Council of Europe
The European Parliament
Ville de Strasbourg (France)

and with respect to

Symposium C: STREM Chemicals, Inc. (France)
Symposium E: XEROX Corporation (USA)
PERKIN ELMER SA (France)
Symposium F: JOHNSON MATTHEY SA (France)

International Standard Serial Number 0921-5107

© 1993—Elsevier Sequoia. All rights reserved 0921-5107/93/$6.00
No part of this publication may be reproduced, stored in a retrieval system or transmitted in any form or by any means, electronic, mechanical, photocopying, recording or otherwise, without the prior written permission of the publisher, Elsevier Sequoia SA, PO Box 564, 1001 Lausanne 1, Switzerland.
Submission of an article for publication implies the transfer of the copyright from the author(s) to the publisher and entails the author(s) irrevocable and exclusive authorization of the publisher to collect any sums or considerations for copying or reproduction payable by third parties.
Upon acceptance of an article by the journal, the author(s) will be asked to transfer copyright of the article to the publisher. This transfer will ensure the widest possible dissemination of information.
For Material Subject to US Copyright Law
Special regulations for readers in the USA
This journal has been registered with the Copyright Clearance Center, Inc., 21 Congress Street, Salem, MA 01970, USA. Consent is given for copying of articles for personal use, or for the personal use of specific clients. This consent is given on the condition that the copier pays through the Center the per-copy fee stated in the code on the first page of each article for copying beyond that permitted by Sections 107 or 108 of the US Copyright Law. If no code appears in an article, the author has not given broad consent to copy and permission to copy must be obtained directly from the author. All articles published prior to 1982 may be copied for a per-copy fee of US $2.50, also payable through the Center. This consent does not extend to other kinds of copying, such as for general distribution, resale, advertising and promotion purposes or for creating new collective works. Special written permission must be obtained from the publisher for such copying.

No responsibility is assumed by the Publisher for any injury and/or damage to persons or property as a matter of products liability, negligence or otherwise, or from any use or operation of any methods, products, instructions or ideas contained in the material herein.

Printed in The Netherlands

Mechanical properties of CdTe

R. Balasubramanian* and W. R. Wilcox

Center for Crystal Growth in Space and Department of Chemical Engineering, Clarkson University, Potsdam, NY 13699 (USA)

Abstract

Thermal and mechanical stresses are thought to play an important part in the formation and multiplication of dislocations during the directional solidification of CdTe. To evaluate the effects of stress on crystal quality, it is necessary to know the mechanical properties of CdTe at all temperatures that a growing ingot would experience. In this context, we have determined the stress-strain behavior and the critical resolved shear stress (CRSS) of CdTe from 300 to 1353 K. Single crystal CdTe specimens, oriented along the ⟨132⟩ axis, were uniaxially compressed at a strain rate of 10^{-4} s^{-1} at different temperatures. B_2O_3 was used as an encapsulant to prevent evaporation of CdTe at temperatures of 773 K or above. The CRSS decreased rapidly with increasing temperature up to 400 K, was nearly constant between 400 and 800 K, and decreased again beyond 800 K. The CRSS ranged from 5 MPa at 300 K to about 0.2 MPa at 1353 K. The shear modulus ranged from approximately 100 MPa at 300 K to 30 MPa at 1353 K. B_2O_3 did not appear to affect the onset of plastic deformation. The apparent shear modulus values were lower with the use of B_2O_3. In a related work, we studied *in situ* the effect of applied stress on tensile specimens of Si, Si-doped GaAs and CdTe crystals by synchrotron X-ray topography. Results indicate that defects, believed to be dislocations, began to move and multiply in Si-doped GaAs and Si crystals at stresses that were approximately 0.3 to 0.6 times the CRSS calculated from an engineering stress-strain diagram. Dislocation motion could not be observed in CdTe due to the poor resolution of the topographs of CdTe samples.

1. Introduction

CdTe is a binary II-VI semiconducting compound with a growing number of industrial applications [1-3]. A number of techniques have been tried to grow large, good quality single crystals of CdTe, but these efforts have met only limited success [1, 2]. One of the problems in bulk-grown CdTe is a high dislocation density [2, 4-6]. Dislocations are thought to propagate and multiply when the stress exceeds the critical resolved shear stress (CRSS) [4, 5, 7].

The thermal stress in a growth system can be modelled fairly accurately if the physical constants of the material and the growth parameters are known. A simplified thermal stress analysis for CdTe ingots grown by the Bridgman technique was reported by Huang *et al.* [4]. For the formulation of a detailed model, data on the physical properties of CdTe at high temperatures are required.

The mechanical behavior of CdTe was studied in the past at temperatures near room temperature or below [8-10]. Maeda *et al.* [8] report that the resolved yield stress for CdTe ranged from around 20 MPa at 200 K to about 5 MPa at room temperature. Similar results for the yield stress were obtained by Lubenets and Formenko [9]. Carlsson and Ahlquist [11] investigated the effect of light on the mechanical properties of CdTe at room temperature. They found that the yield stress of low resistivity CdTe samples increased by 70% as a result of illumination of test specimens.

Gutmanas *et al.* [10] reported the CRSS of CdTe to be 5 MPa at 100 K, and 2 MPa at 500 K. Hall and Vander Sande [12] were the first to conduct experiments to obtain data on the mechanical properties of CdTe at temperatures greater than half the melting point. From their stress-strain curves, the yield stress of CdTe from 300 to 773 K varied from approximately 9 to 2 MPa.

It is only in recent years that studies on the stress-strain behavior of CdTe were conducted at temperatures above 773 K by Imhoff and co-workers [5, 13] and Rai *et al.* [6]. We are not aware of a previous attempt to measure the mechanical properties of CdTe single crystals at temperatures close to its melting point of 1366 K. In this paper we report the results of compression tests on single crystal CdTe from room temperature to 1353 K.

We also studied *in situ* the effect of applied stress on tensile samples of CdTe, Si-doped GaAs and Si single crystals by synchrotron X-ray topography.

*Present address: Johnson Matthey Electronics, East 15128 Euclid Av., Spokane, WA 99216, USA.

0921-5107/93/$6.00 © 1993 - Elsevier Sequoia. All rights reserved

2. Experimental procedure

2.1. Compression tests

Uniaxial compression testing of single crystals is the most widely used method to determine the stress–strain behavior and CRSS of semiconductor materials [5]. This is due to the brittle nature of semiconductors at room temperature that makes machining of tensile specimens difficult (*e.g* "dog-bone" shaped). Here the test technique consisted of uniaxial compression of accurately oriented parallelepiped specimens at a constant strain rate and temperature. The details are described elsewhere [14]. The strain rate was maintained at 10^{-4} s^{-1} in all experiments. The specimens used in our work had ⟨132⟩ compression axes. The sample dimensions were 5 mm × 3 mm × 3 mm with a maximum tolerance of 1 mm in each dimension. A schematic diagram of the test specimen used in this work is shown in Fig. 1.

The compression tests were conducted in the apparatus shown in Fig. 2. A typical experiment was as follows. The specimens for the test were "mined" from ingots grown by a vertical Bridgman method. The CdTe used in our experiments had an etch pit density of 10^4–10^5 cm^{-2}. The oriented grains were subsequently cut to the desired size and compression axis (⟨132⟩). The samples were polished in steps using 5, 0.05 and 0.03 μm alumina suspensions, and chemically polished in a 2% Br–methanol solution.

For experiments carried out at a temperature of 773 K and above, B_2O_3 powder was poured to cover the sample. The apparatus was sealed with the heater and the thermocouple in place. The apparatus was evacuated by a mechanical pump and back-filled a number of times with N_2. Subsequently, a continuous flow of N_2 was established in the chamber containing the test sample. The sample was heated at a rate of approximately 10 K min^{-1} to the desired temperature. The movable piston was brought very slowly into contact with the sample placed vertically; this contact was indicated by the change in load on the load cell indicator. The load–compression data were recorded at constant intervals till the sample had been plastically deformed to approximately 60% of the original length.

The load–compression data were transformed to shear stress–shear strain curves, assuming single glide on a {111}⟨110⟩ slip system [12, 13]. The CRSS was assumed to be the value of the resolved shear stress at the intersection of the linearly extrapolated line of the apparent stage I plastic deformation curve [15] with the initial linear part of the stress–strain curve (elastic regime). The slope of the initial, linear part of the stress–strain curve was recorded as the shear modulus.

2.2. X-ray topography studies

Tensile specimens of Si, Si-doped GaAs and CdTe single crystals were stressed in an apparatus constructed for *in situ* observation of single crystal samples by white beam X-ray topography. X-rays at the National Institute of Standards and Technology (NIST) beamline X-23A3 of the National Synchrotron Light Source (NSLS), Upton, NY, were used in the topography work. The tensile specimens were in the shape of a dog-bone and had a ⟨112⟩ tensile axis. This orientation allowed us to obtain (220) diffraction images of a tensile sample while it was being stressed. A schematic diagram of the sample used in the X-ray topography experiments is shown in Fig. 3.

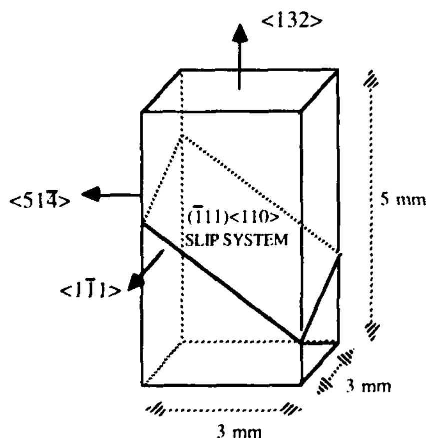

Fig. 1. Compression test specimen.

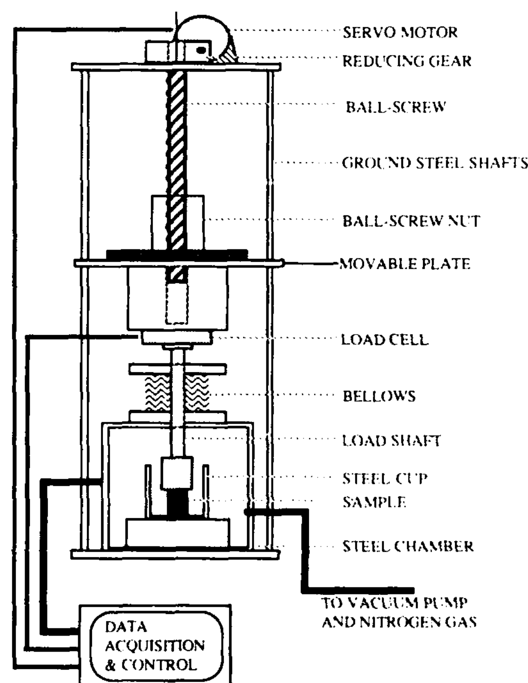

Fig. 2. Compression test apparatus.

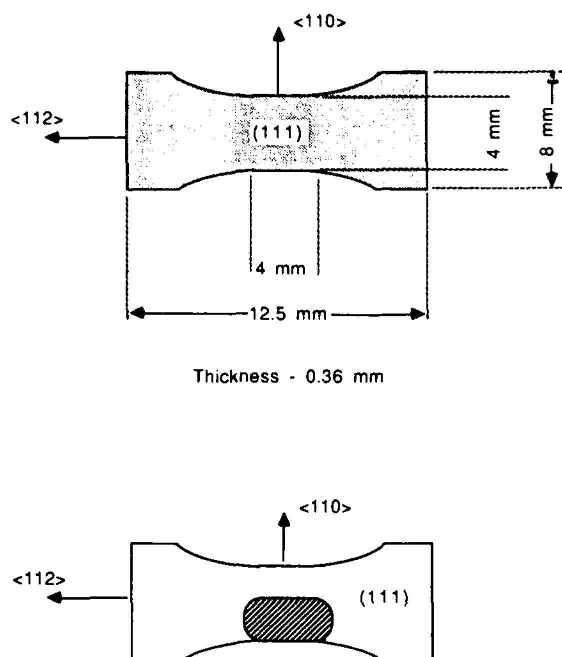

Fig. 3. Top: tensile specimen used in the synchrotron work. Bottom: approximate section of the sample seen in the topographs in Figs. 7–9.

A brief description of the experimental procedure follows. Tensile samples were mounted on the experimental apparatus on the topography rig at Beamline X-23A3 of the NSLS. A diffraction topograph of the sample was recorded on photographic film prior to the start of heating the sample. Subsequently, the diffraction image was observed continuously on a television monitor during heating and stressing of the tensile sample. In this work, the experimental temperatures were 1023–1173 K for Si, 673–873 K for Si-doped GaAs and 373–673 K for CdTe. Topographs were recorded on film at regular intervals. Details on the apparatus and the experimental procedure are given elsewhere [14].

3. Results and discussion

3.1. Results of compression tests on CdTe

Several of our stress–strain curves for CdTe single crystals from 300 to 1353 K are shown in Fig. 4. CRSS *vs.* temperature data are shown in Fig. 5. For comparison with published work, we include the CRSS data reported by Imhoff [5] and Rai *et al.* [6] in Fig. 5. Shear modulus *vs.* temperature data are shown in Fig. 6. The error bars shown in Figs. 5 and 6 are 95% confidence limits obtained from a statistical analysis of the data.

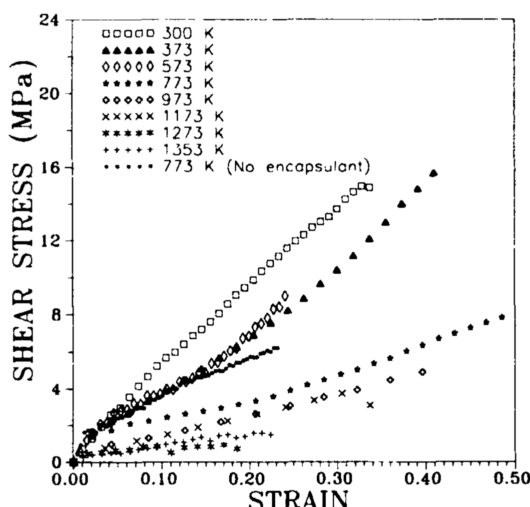

Fig. 4. Stress–strain behavior at different temperatures with ⟨132⟩ compression axis.

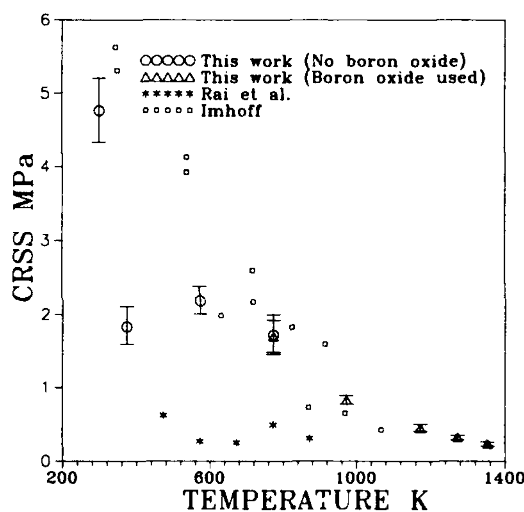

Fig. 5. CRSS of CdTe from 300 to 1353 K. For comparison, data of Imhoff [5] and Rai *et al.* [6] are included.

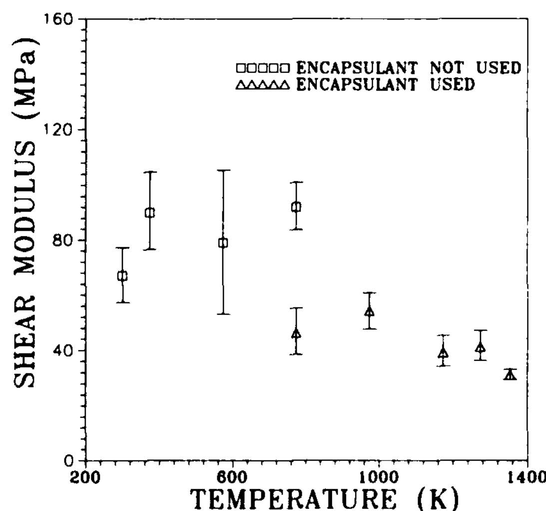

Fig. 6. Shear modulus of CdTe from 300 to 1353 K.

3.1.1. Stress–strain curves of CdTe

At a strain rate of 10^{-4} s^{-1} and temperature of 300 K, the stress–strain behavior of CdTe was linear to a stress of approximately 4.8 ± 0.5 MPa. The departure from linear stress–strain behavior began at a stress beyond 4.8 ± 0.5 MPa. This led to a linear work hardening regime followed by brittle fracture at a strain of 20%–30%. As the temperature was increased to 373 K, a departure from linear stress–strain behavior occurred at a stress of around 1.75 ± 0.25 MPa. The initial slope of the work hardening region also was lower, probably indicating facile slip due to the increase in temperature. At a strain of approximately 30%, the slope of the stress–strain curve (work hardening rate) increased. This might be indicative of stage II plastic deformation [15]. Stage III behavior [15], indicated by another change in the slope of the stress–strain curve, was not seen in any of the stress–strain curves recorded in this work.

At 573 K, the departure from linear stress–strain behavior occurred at a stress of 2.2 ± 0.25 MPa. At 773 K, the value for departure from linear stress–strain behavior was 1.7 ± 0.25 MPa. The stress–strain curve at 773 K showed three distinct regimes, identified in terms of the differences in their slopes, *i.e.* an elastic region followed by stage I and then stage II plastic deformation. At 773 K, the initial slope of the work hardening region was much smaller than those at lower temperatures.

The stage I plastic deformation regime of the stress–strain curve extended over a 15% strain range at 773 K. At 973 K, stage I plastic deformation behavior extended to only a few per cent strain before the slope of the stress–strain curve changed. At temperatures above 973 K, the three stages of the stress–strain curve seen at lower temperatures were absent. A nearly linear work hardening regime followed the elastic portion of the stress–strain curve. The stress–strain behavior seen at temperatures in the region $1173 \leqslant T \leqslant 1353$ K might indicate the onset of stage II plastic deformation immediately following the elastic regime. The yield stress measured from the stress–strain curves in the region $773 \leqslant T \leqslant 1353$ K decreased continuously with increasing temperature.

3.1.2. Shear modulus

A graph of the shear modulus *vs.* temperature obtained from the present work is shown in Fig. 6. The shear modulus of CdTe ranged from an average of 100 MPa at 373 K to 30 MPa at 1353 K. A noticeable difference in the shear modulus values was seen in experiments with and without B_2O_3. In the temperature range $300 \leqslant T \leqslant 773$ K, where B_2O_3 was not used, the shear modulus values ranged from 100 to 70 MPa. In comparison, the average shear modulus in experiments with B_2O_3 ranged from 50 MPa at 773 K to 30 MPa at 1353 K. It appears that B_2O_3 encapsulation was probably responsible for lower values at temperatures of 773 K or more. Imhoff [5], Rai *et al.* [6], and Hall and Vander Sande [12] did not report shear modulus data.

3.1.3. Critical resolved shear stress

Figure 5 shows the CRSS *vs.* temperature from 300 to 1373 K. Three distinct regions can be seen. The average CRSS was 4.8 MPa at 300 K and rapidly dropped to a value of 1.8 MPa at 373 K. As the temperature was increased further, the CRSS remained nearly constant up to a temperature of 773 K. Beyond 773 K, the CRSS decreased again with increasing temperature. Comparison of CRSS values measured in this work with those in the literature indicates both parallels as well as differences. Rai *et al.* [6] reported CRSS values considerably lower than those reported by Imhoff *et al.* [13] as well as those measured in our work. The values of CRSS reported by Rai *et al.* [6] are almost constant in the temperature regime 473 K (about 0.5 MPa) to 873 K (about 0.25 MPa). In comparison, our values of the CRSS ranged from an average of 1.8 MPa at 473 K to 0.9 MPa at 873 K.

There is good agreement of our CRSS data with those reported by Imhoff [5] in the region $773 \leqslant T \leqslant 1100$ K. In the temperature range $373 \leqslant T \leqslant 873$ K, the values of CRSS reported by Imhoff [5] were consistently higher than ours. Differences in our stress–strain behavior of CdTe from that reported in literature [5, 12] could be attributed to the differences in the strain rates, dislocation density and also differences in the machines used.

3.1.4. Effect of the encapsulant on the stress–strain behavior of CdTe

The average CRSS value measured from experiments where B_2O_3 was used was 1.72 MPa. In experiments without B_2O_3 the average value of the CRSS was 1.70 MPa. Thus, in contrast to the results reported by Imhoff [5], in our work B_2O_3 did not affect the CRSS of CdTe single crystals in a compression test. The apparent shear modulus was, however, affected by the addition of B_2O_3. At 773 K, the average shear modulus in experiments with B_2O_3 was 46 MPa. In comparison, in experiments conducted without B_2O_3 an average shear modulus of 92 MPa was measured.

We attempt an explanation for the results described above. When B_2O_3 was used it is likely that a layer of the encapsulant was initially present between the sample and the piston. Hence, it is possible that the highly viscous B_2O_3 acted as a lubricant and reduced the resistance of the compression specimen to loading. The barrel shape of the specimens after plastic deformation

in our experiments indicated sticking of the samples to the loading device.

3.2. Results of synchrotron experiments

About 30 experiments were conducted on Si, GaAs and CdTe samples in this work. Here we show three topographs of an experiment conducted at 1073 K on an Si tensile specimen. A more complete sequence of topographs can be found in ref. [14].

Figure 7 is a (220) transmission X-ray topograph of an Si tensile sample prior to loading. (This topograph is illustrated as a reference for defect formation in topographs shown in Figs. 8 and 9.) As the sample illustrated in Fig. 7 was slowly stressed, no change in the image contrast was noticed to a stress of 9.5 MPa. At 9.5 MPa white, needle-like structures developed along the edge of the gauge-section of the tensile sample. Upon increasing the stress on the sample, these needle-like structures immediately developed into broader bands that moved along the crystallographic slip direction (Fig. 8). We believe that upon reaching a threshold stress, dislocations started to move, producing the white, needle-like structures in the topographs. As the stress was further increased, multiplication of the dislocations resulted in the formation of broad bands, as seen in the topograph shown in Fig. 8. Further increasing the applied stress resulted in the distortion of the topograph (Fig. 9). It is probable that lattice rotation as a result of plastic deformation of the crystal caused the scattering of the X-ray diffraction image. Similar results were obtained in experiments with other Si and GaAs samples.

The important result from our studies and those reported in the literature [16, 17] is that, in semiconductor crystals, dislocation motion and propagation occur in the pre-yield stage of an engineering stress–strain diagram. In Figs. 10 and 11 we show a

Fig. 7. Topograph of an Si sample at 1023 K with no load.

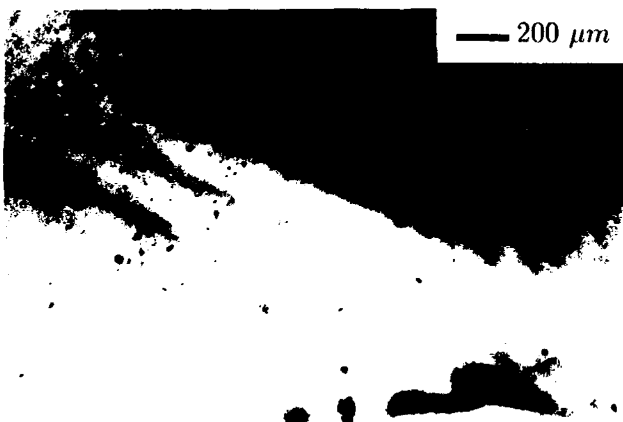

Fig. 8. Topograph of an Si sample when movement of dislocations was observed. A stress of 13.8 MPa was applied to this sample at 1023 K.

Fig. 9. Distortion of the topograph, possibly as a result of lattice rotation in the Si sample.

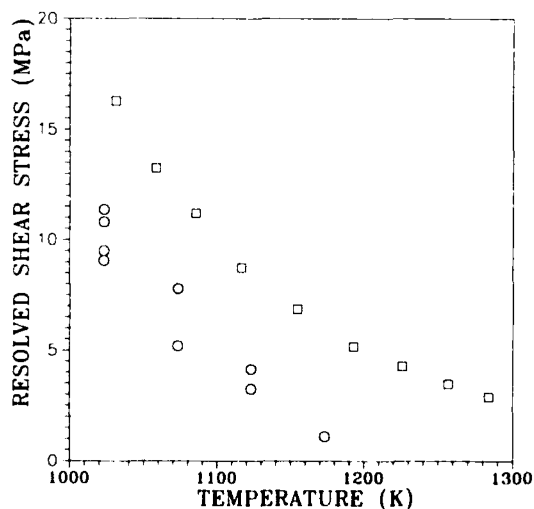

Fig. 10. The stress required to initiate dislocation motion in Si samples as seen by X-ray topography: □, CRSS data for Si (Yonenaga and Sumino [18]); ○, stress required to initiate dislocation movement (this work).

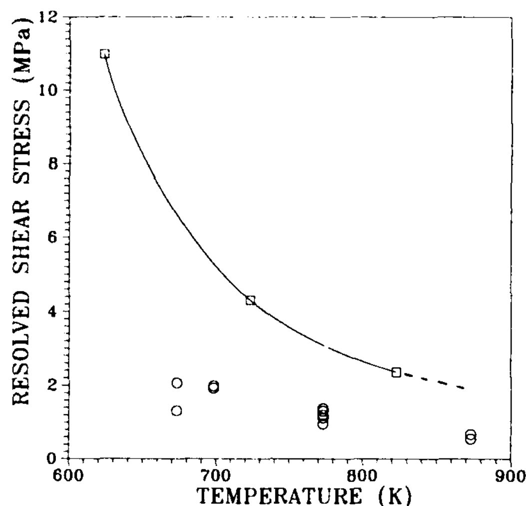

Fig. 11. The stress required to initiate dislocation motion in Si-doped GaAs samples as seen by X-ray topography: □, CRSS data for Si (Swaminathan and Copley [19]); ○, stress required to initiate dislocation movement (this work).

graph of the stress at which dislocation motion was observed in different synchrotron experiments with Si and GaAs samples respectively. The corresponding CRSS values obtained from results of compression tests in the literature are also shown in Figs. 10 and 11.

In the theory of plastic deformation, the CRSS is usually considered to be the stress at which plastic deformation begins [15]. However, our experiments indicate that, in semiconductor crystals, dislocation movement began at stresses much below the CRSS obtained from engineering stress-strain diagrams.

4. Conclusions

The results of the compression tests indicatc that CdTe is mechanically weak at all temperatures and especially near the melting point. Results from the synchrotron experiment suggest that dislocation motion in semiconductor crystals occurs at stresses that are 0.3 to 0.6 times the CRSS. We now attempt an explanation for the difference in the measured values of the CRSS and the stress that was found to cause dislocation motion in the synchrotron experiments.

In uniaxial compression tests, the macroscopic effects of the movement of dislocations (plastic deformation) are measured. For a single crystal sample with a ⟨112⟩ tensile axis, slip is initially restricted to two slip systems. Hence, the initial microscopic motion of dislocations was probably not discernable in an uniaxial compression test. However, as the dislocations started to multiply, and when other slip systems began to take part in the plastic deformation process, the net effect of the microscopic movement of dislocations was observed in the engineering stress-strain tests. Yield was noticed only when the plastic deformation became large enough to cause deviation from linear stress-strain behavior.

While the CRSS value obtained from uniaxial compression or tension tests may give an approximate indication of the initiation of motion of dislocations, it may not be the correct stress to use in modelling crystal growth. In crystal growth, dislocation motion does not in itself present problems. However, during the motion of dislocations, mechanisms for their multiplication exist, such as the Frank-Read source. Hence, stresses that induce motion of dislocations in crystals should be avoided.

Acknowledgments

This work was supported by the Center for Crystal Growth in Space, a NASA Center for the Commercial Development of Space. We would like to thank Dr. Masao Kuriyama, Mr. Ron Dobbyn, Dr Richard Spal and Dr. Gabrielle Long of the National Institute of Standards and Technology for their discussions and the use of beamline X-23A3 of the National Synchrotron Light Source, Brookhaven National Laboratory, Upton, NY.

References

1 B. J. Fitzpatrick, *J. Cryst. Growth, 86* (1986) 106.
2 A. W. Vere, *SPIE Proc., Materials Technologies for IR Detectors, 659* (1986) 10.
3 R. Triboulet and Y. Marfaing, *J. Electrochem. Soc., 120* (1973) 1260.
4 C. E. Huang, D. Elwell and R. S. Feigelson, *J. Cryst. Growth, 69* (1984) 275.
5 D. Imhoff, *Thesis, Diplome D'Ingenieur,* Conservatoire National des Arts et Metiers, Paris, 1989.
6 R. Rai, S. Mahajan, D. J. Michel, H. H. Smith, S. McDevitt and C. J. Johnson, *Mater. Sci. Eng., B10* (1991) 219.
7 E. Dobrocka and J. Sladek, *J. Cryst. Growth, 104* (1990) 419.
8 K. Maeda, K. Nakagawa and S. Takeuchi, *Phys. Status Solidi A, 48* (1978) 587.
9 S. V. Lubenets and L. S. Formenko, *Sov. Phys. Solid State, 31* (1989) 256.
10 E. Y. Gutmanas, N. Travitzky, U. Plitt and P. Haasen, *Scr. Metall., 13* (1979) 293.
11 L. Carlsson and C. N. Ahlquist, *J. Appl. Phys., 43* (1972) 2529.
12 E. L. Hall and J. B. Vander Sande, *J. Am. Ceram. Soc., 61* (1978) 417.
13 D. Imhoff, F. Gelsdorf, B. Pellissier and J. Castaing, *Phys. Status Solidi A, 90* (1985) 537.
14 R. Balasubramanian, *PhD Thesis,* Clarkson University, 1992.

15 T. H. Courtney, *Mechanical Behavior of Materials*, McGraw-Hill, New York, 1990.
16 S. Tohno, S. Shinoyama, A. Katsui and H. Takaoka, *J. Cryst. Growth*, *73* (1985) 190.
17 S. Tohno, S. Shinoyama, A. Katsui and H. Takaoka, *Appl. Phys. Lett.*, *49* (1986) 1204.
18 I. Yonenaga and K. Sumino, *Phys. Status Solidi A*, *50* (1978) 685.
19 V. Swaminathan and S. M. Copley, *J. Am. Ceram. Soc.*, *58* (1975) 482.

Materials Science and Engineering, B16 (1993) 8-16

Basic problems of vertical Bridgman growth of CdTe

Peter Rudolph and Manfred Mühlberg
Humboldt-Universität zu Berlin, FB Physik, Institut für Kristallographie und Materialforschung, Invalidenstrasse 110, O-1040 Berlin (Germany)

Abstract

Many efforts have been made to grow CdTe bulk crystals with a low defect content but improvements are limited. The best ingots with large extended single-crystal regions can be grown by the vertical Bridgman method. However, fundamental studies about the CdTe growth peculiarities are absent. Our investigations are concentrated on the following problems: (i) the influence of the melt structure, from which an associated state is assumed, on the crystalline quality, (ii) the composition instability in conventional ampoules, (iii) the segregation behaviour of the excess component (normally tellurium), (iv) the axial distribution of inclusions and precipitations, (v) the mass transport in modified ampoules with an additional cadmium source, (vi) the correlation between the vacancy and impurity segregation and (vii) the substrate purity as a function of the axial crystal position.

1. Introduction

Recently, there has been an increasing need for single-crystal CdTe and CdTe-rich alloys for several applications: electro-optic modulators, windows, prisms and γ-ray detectors. Furthermore, single-crystalline CdTe slices are used as substrates for different epitaxial deposition processes of (Hg, Cd)Te and (Hg, Zn)Te. This need for substrates is the essential motivation for the increasing efforts in the crystal growth of CdTe and its related compounds. For several years, research activities have been concentrated on the following points of interest: increasing the crystal diameter up to about 75 mm [1, 2] for preparation of greater substrates areas (up to 4 cm × 6 cm); mathematically modelling the temperature field and the influence of convection [3-5]; improving the chemical homogeneity and the electrical properties of the (doped) semiconducting compounds by adjusting a definite cadmium overpressure [6, 7]; alloying with zinc, selenium and manganese with respect to the segregation behaviour and reducing the dislocation density [8-10]. Very little attention has been paid to the melt properties. We have observed that the "thermal history" of the melt state has a strong influence on the crystalline quality of the grown CdTe crystals caused by the associated structure of the II-VI compounds in the molten state (Section 2). Stoichiometry-correlated growth effects will be discussed in Section 3. Furthermore, the segregation phenomena of the excess component caused by composition instabilities in conventional sealed ampoules (inclusion and precipitation distribution) will also be described. An important point of interest is the interaction between the controlled melt composition by exact starting charge scaling using a cadmium source and the optical and electrical properties of the grown crystals. A correlation between intrinsic point defects caused by non-stoichiometric growth conditions (cadmium vacancies) and extrinsic impurities (dopants) is demonstrated in some more recent investigations [11, 12]. In Section 4 we shall discuss first results which show the strong dependence of the total impurity content on the cadmium vacancy concentration (see also ref. 13). Moreover, purification with respect to volatile residual elements can be achieved using a cadmium overpressure during the crystal growth run. Finally, it can be shown that the impurity level of the substrate is a function of the crystal position from which the substrate slice has been taken.

2. The Cd-Te melt state and superheating-supercooling effects

The properties of the liquid phase (melt) are assumed to have a distinct influence on the crystal quality. Some properties characterizing the melt state are summarized in Table 1. In particular, in the case of unseeded Bridgman growth the spontaneous nucleation behaviour will depend on the structure of the molten state. Additionally, the kinetic growth conditions are affected very sensitively by the "form of the growing-in elements", too [14].

0921-5107/93/$6.00

© 1993 - Elsevier Sequoia. All rights reserved

TABLE 1. Some thermodynamical and physical properties of molten CdTe in comparison with GaAs and silicon (where R is the universal gas constant)

Parameter (units)	Value for the following		
	CdTe	GaAs	Si
Melting point T (K)	1365	1511	1683
Vapour pressure at the congruent melting point p (MPa)	0.07	0.1	6.5×10^{-8}
Heat of fusion ΔH (kJ mol^{-1})	58	97	
Entropy of fusion ΔS (J mol^{-1} K^{-1})	41	64	
Type of phase transition mode	Solid semiconductor–Liquid semiconductor	Solid semiconductor–Liquid metal	Solid semiconductor–Liquid metal
Dimensionless radius of liquidus curvature at the congruent melting point $r = \Delta S \beta_i (4R)^{-1}$	62	1735	
Degree of dissociation β_i^L (%)	5	90	
Density ρ^L (g cm^{-3})	5.67	5.71	2.53
Coefficient of thermal expansion α_T^L (K^{-1})	5×10^{-4}	1.78×10^{-4}	1.5×10^{-4}
Thermal conductivity λ^L (W cm^{-1} K^{-1})	1×10^{-2}	1.8×10^{-1}	5.4×10^{-1}
Electrical conductivity σ^L (S cm^{-1})	1×10^{2}	8×10^{3}	1.2×10^{4}
Specific heat c_p^L (J g^{-1} K^{-1})	0.36	0.434	1.0
Dynamic viscosity η (g cm^{-1} s^{-1})	2.3×10^{-2}	2.8×10^{-2}	7×10^{-3}
Prandtl number Pr	0.413	0.068	0.013

Contrary to the III–V compounds the II–VI semiconducting compounds show a hyperbolic shape of the liquidus near to the congruent melting point (Table 1). This liquidus shape indicates a much stronger interaction between unlike particles arising from the considerable ionic contribution to the bond energy. The regular associated solution model is capable of describing the II–VI liquidus shapes in a satisfying manner [15, 16]. The dissociation coefficient in a slowly superheated Cd–Te melt is assumed to be roughly 0.05. On the contrary, in the case of GaAs the melt state is characterized by a degree of dissociation of about 90% (see also Table 1). Consequently, some differences between the crystallization behaviours of III–V and II–VI compounds will be expected. According to experimental investigations of the melt parameters by Glasov *et al.* [17] the melting process of CdTe can be assumed to be a solid semiconductor–liquid semiconductor transition owing to the conservation of a considerable covalent contribution to the cohesive energy in the melt. Because of the spatial character of covalent bonds a three-dimensional arrangement of the associates (tetrahedra) in the slowly superheated melt can be predicted. With increasing melt temperature (superheating) these tetrahedra are reorganized into two-dimensional associates (rings and chains), molecules and separate atoms. Therefore the structure of a slowly superheated melt will be characterized by a great number of these more highly organized particles which should influence the nucleation process and the growth kinetics.

The correlation between superheating and supercooling has been investigated in real Bridgman conditions as a sensitive method for detecting the role of different melt structures. Of course, the general crystal quality was a point of interest and gives information about the "thermal history" of the melt. The results are documented in Fig. 1. At small values of superheating (less than 9 K), no supercooling can be observed in stoichiometric CdTe. At values higher than 9–10 K a distinct supercooling occurs up to 20–30 K. Such behaviour can be explained only by an abrupt structural alteration of the melt state as above discussed. A transition from three-dimensional complex particles to lower dimensions of melt associates can be assumed at this value of $\Delta T = 9$ K. According to Glasov *et al.* [17] an additional transition effect will be expected at a superheating level of about 60 K, obviously as a result of the formation of separate atoms in the melt. In low superheated melts the more highly organized clusters are assumed to reduce the nucleation energy and the result is suppressed supercooling in the tip of the

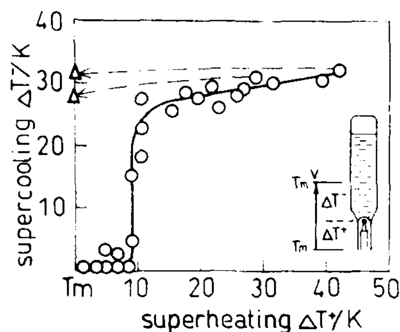

Fig. 1. Influence of the degree of superheating ($\Delta T^+ = T_m + T$) on the degree of supercooling ($\Delta T^- = T_m - T$) for stoichiometric CdTe measured with a thermocouple at the tip of vertical Bridgman ampoules moved with a constant velocity $v = 1$ mm min^{-1}: Δ, supercooling of former high superheated melts subsequently cooled and kept for 5 h at the melting point T_m.

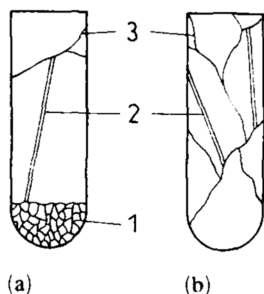

Fig. 2. Typical growth structures of (a) a high ($\Delta T^+ = 27$ K) and (b) a low superheated ($\Delta T^+ = 3$ K) unseeded CdTe crystal: 1, polycrystalline tip region; 2, twin lamella; 3, large grain boundary.

ampoule. In Fig. 1 the open triangles indicate that no structural reorganization will occur during a decrease in the former superheated state of more than 25 K.

The crystal quality of both the tip region and the whole CdTe ingot also depends on the original superheated situation. For a stoichiometric composition a large extended polycrystalline tip can be observed if a superheating of more than 9-10 K is applied (Fig. 2(a)). This polycrystalline first-to-freeze region is followed by a single-crystal part or by a region with only one or two grain boundaries. The dominant growth direction is near to the ⟨112⟩ orientation (Fig. 3). Contrary to this situation, in the case of a small superheating of less than 9-10 K a single-crystal initial growth is often observed (Fig. 2(b)). However, a larger number of grain boundaries and twins is originated during the further growth run. It is assumed that any associated complex will have a strong influence on the growth kinetics and morphological stability owing to the misoriented growth. Our observations are in a good agreement with results of other workers. First Lorenz [19] has observed a supercooling up to 10 K if the

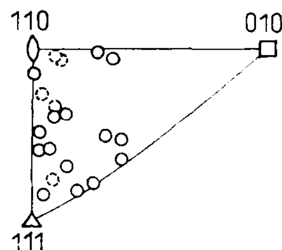

Fig. 3. Stereographic analysis of the "self"-growth orientations of the dominant grains in unseeded CdTe crystals: ○, our results; ◌, results taken from ref. 18.

superheating of the Cd-Te melt was chosen to be higher than 20 K. The influence of superheating ΔT^+ on the crystal quality was also described by Khattak and Schmid [2] in CdTe grown by the heat exchanger method. The higher the melt temperature ($30 \text{ K} \leqslant \Delta T^+ \leqslant 120 \text{ K}$) the smaller is the number of grain boundaries and twins. Lu *et al.* [20] have tried to influence the melt state by a coupled vibration-stirring method. The tendency to initiate a single-crystal tip region was increased by orthogonal vibration of the ampoule with frequencies up to 100 Hz. Such effect may be explained by the acoustic-coupled destruction of associated melt complexes. The observations show that single-crystal growth demands a definite superheating behaviour which is in contradiction to artificial seeding in the tip of the ampoule. Only electrodynamic multizone gradient furnaces should meet all requirements to solve this difficult growth problem in the future.

3. Stoichiometry-correlated growth effects

3.1. Growth without control of the melt composition

Principally, in sealed ampoules without any vapour pressure control the crystal growth of compounds is influenced by variation in the melt composition. First, corresponding to the formula $Cd_{0.5-\delta y}Te_{0.5+\delta y}$, a deviation δy may arise because of weighing errors in the process of the CdTe synthesis. The order of magnitude of such stoichiometry deviation may be simply estimated from

$$N_w = 2\,\partial y\,N_0 \qquad (1)$$

where N_w (cm^{-3}) is the number of tellurium (or cadmium) excess atoms and $N_0 = 1.468 \times 10^{22}$ cm^{-3} is the number of tellurium (or cadmium) atoms in stoichiometric CdTe. Secondly, the melt composition will be influenced by the formation of a gaseous phase over the melt. It is well known from phase relations [21] that a nearly stoichiometric melt of CdTe evaporates incongruently. At 1100°C the different vapour pressures of

Te_2 and cadmium indicate that the vapour phase established over the Cd–Te melt consists of about 96% of cadmium atoms. Therefore the Te_2 partial pressure can be neglected. Using the perfect-gas law the cadmium mass loss from the melt can be calculated [22].

The number of cadmium atoms evaporating into the gaseous phase is equal to the number N_E of additional excess tellurium atoms in the melt. Thus the concentration of excess tellurium atoms in the melt caused by cadmium evaporation becomes

$$N_E = \frac{p_{Cd} N_A}{RT} \frac{V_V}{V_L} \tag{2}$$

with N_A Avogadro's number, and V_V and V_L the volumes of the gaseous phase and the melt respectively. Because of the cylindrical geometry of the ampoule, V_V/V_L reduces to h_V/h_L, the ratio of the melt length to the length of the free volume. At 1100 °C the partial pressure of cadmium is roughly 10^5 Pa [21]. Thus, eqn. (2) can be simplified to

$$N_E = 5.1 \times 10^{18} \frac{h_V}{h_L} \tag{3}$$

The correlation between the number N_E of the tellurium excess atoms in the melt and the h_V/h_L ratio is shown in Fig. 4. Therefore the total deviation from the exact stoichiometry of the melts becomes

$$N_{total} = \pm N_W + N_E \tag{4}$$

where the sign of N_W represents the weighing excess of tellurium or cadmium.

If we assume a completely mixed melt state in conventional vertical ampoules by (natural) convection [23] which were filled with stoichiometrically adjusted

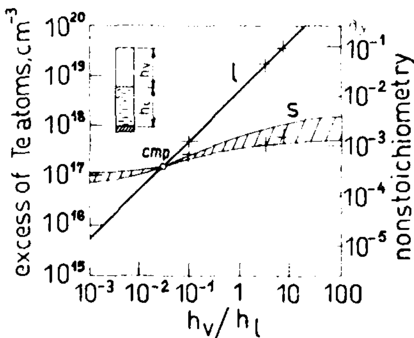

Fig. 4. Estimated tellurium excess in the melt (liquid) and in the first-to-freeze region of CdTe crystals vs. the ratio of the length h_v of the space above the melt and to the length h_l of the liquid column: cmp, congruent melting point composition; +, our experimental results obtained for different h_v/h_l ratios (l) and IR scattering at tellurium precipitates in the tip region (S).

starting material the crystal growth process will always begin from a tellurium-rich melt. Consequently, any segregation phenomena of the tellurium can be expected.

Two different kinds of crystal imperfection will arise by the solidification from tellurium-rich melts.

(i) Inclusions are assumed to originate as a result of morphological instabilities at the growth interface. Tellurium-rich melt droplets will be captured from the boundary layer ahead of the interface. Typical diameters of such inclusions are 1–2 μm, but diameters up to 10–20 μm have also been observed [1, 24–26].

(ii) Precipitates originate during the cooling process from the retrograde slope of the solidus line. The precipitation process is characterized by cadmium vacancy condensation. A diffusion time of less than 1005 is estimated to be needed for nearly complete precipitation at about 700 °C (the cadmium tracer coefficient D is taken from ref. 27). Precipitates observed by transmission electron microscopy have average diameters of about 10–30 nm with distances of roughly 100 nm [28–30]. On the assumption of precipitates and inclusions with a spherical geometry, the total tellurium excess per cubic centimetre in the crystal can be calculated as

$$N_{Te} = \frac{4\pi \rho_{Te} N_A}{3 A_{Te}} \sum_i r_i^3 \rho_i \tag{5}$$

where r_i is the radius and ρ_i the density of the precipitates or inclusions, A_{Te} is the relative atom mass of tellurium, ρ_{Te} is the density of the tellurium mass and the index i represents each class of particle diameters.

The axial distribution of tellurium precipitates and inclusions has been studied by IR extinction analysis and IR transmission microscopy respectively. The precipitate density and diameters have been detected from the energy dependence of the scattering cross-section [31]. The crystals were grown at a growth rate of 1 mm h^{-1} and a temperature gradient of about 8 K cm^{-1} and were cooled to room temperature at a rate of about 20 K h^{-1}. For the above-described analysis the crystals were cut into slices, lapped and chemomechanically polished.

In Fig. 5 the axial distribution of the tellurium excess is shown considering eqn. (5) and with respect to inclusions (full symbols) and precipitates (open symbols). The distribution of inclusions may be explained by the variation in constitutional supercooling rather than by a segregation effect. Radial inhomogeneities were also observed, predominantly at small-angle boundaries and twin lamellae. Nevertheless, some segregation of the tellurium particles takes place and the density is increased in the last-to-freeze region. On the contrary, the precipitation is found to be independent of the

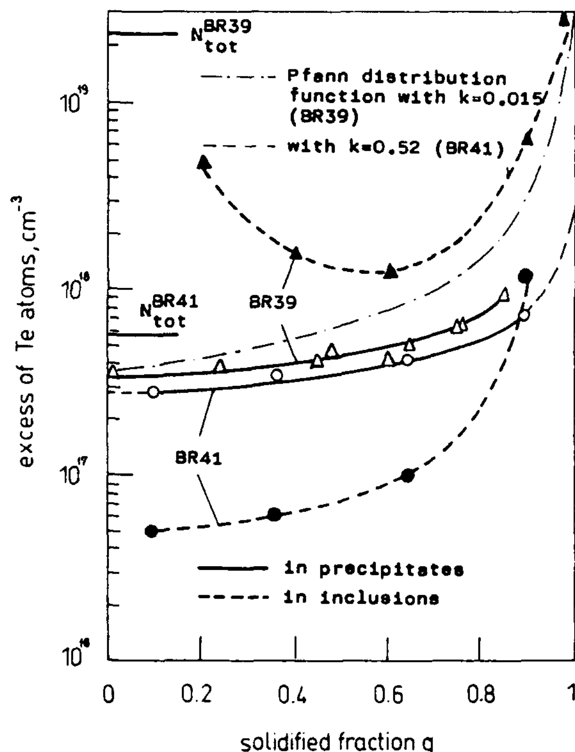

Fig. 5. Axial distribution of the tellurium excess in two vertical CdTe crystals (BR38 and BR41) calculated from eqn. (5): ▲, ●, inclusions analysed by IR transmission microscopy; △, ○, precipitates analysed by IR extinction. N_{tot} is the initial tellurium excess concentration in the melt from eqn. (4).

initial tellurium excess. For example, crystals which differ strongly in their starting melt composition show roughly the same amount of precipitated tellurium (Fig. 5). This is not surprising because the amount of precipitated tellurium depends only on the shape of the solidus line which represents the maximum solubility of tellurium in CdTe at growth temperatures. In crystals grown from the melt with a small deviation from stoichiometry the axial distribution of the precipitated tellurium excess can be simply approximated by Pfann's distribution function with a distribution coefficient k. Near to the congruent melting point the solidus and liquidus lines are assumed to be linear and k shows nearly constant. On the contrary, for melts with a high deviation, such an assumption is not valid, possibly because of the variable values of k which are caused by a steep slope of the solidus line for tellurium concentrations higher than 5×10^{17} cm^{-3}. Summarizing, growth from non-stoichiometric tellurium-rich melt compositions leads to a reduced crystal quality by capturing tellurium in precipitates and inclusions. On the contrary, the analysis of such grown crystals provides additional information about the shape of the T–y phase diagram near to the congruent melting point (Fig. 4).

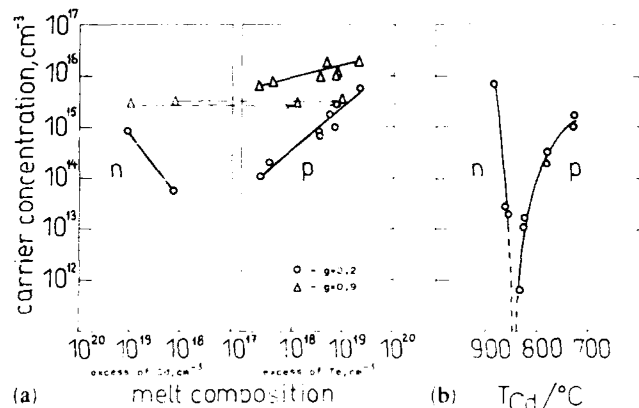

Fig. 6. Variation in the conductivity type and the free-carrier concentration at 300 K using (a) various starting melt compositions and (b) a cadmium extra source at temperature T_{Cd}.

3.2. Growth with a fixed melt composition

Control of the stoichiometry is one of the most important requirements for crystal growth of CdTe with definite properties such as high resistivity, high IR transmission and a small number of tellurium particles. An adjustment of the melt composition can be achieved using a cadmium excess to the stoichiometric composition or by an additional cadmium source which gives a definite overpressure.

Both methods have been analysed. Figure 6(a) shows the correlation between measured free-carrier concentrations [31, 32] and different adjusted material compositions at the tip ($g = 0.2$) and at the end ($g = 0.9$) of several crystals. The conductivity types and the carrier concentrations differ by orders of magnitude in the first-to-freeze region ($g = 0.2$), but the samples all have the same concentration p of about 10^{16} cm^{-3} in the end region. Contrary to the tip region a conversion from p-type to n-type material at $g = 0.9$ has not as yet been observed. We have already shown [33] that in the first-to-freeze region the residual donors and acceptors mostly compensate each other. Thus in this region the resulting carrier concentration is dominated by native point defects very sensitively. Corresponding to Fig. 6 and eqn. (3), nearly stoichiometric material will be obtained using starting material with a cadmium excess δy of about $(2–5) \times 10^{-4}$. Crystals grown under such conditions show high transmission, and inclusions are mainly absent. However, the last-to-freeze region is mostly characterized by residual acceptor impurities owing to segregation coefficients much lower than unity in comparison with any donors with $k \approx 1$ [33]. Therefore the free-carrier concentration at $g = 0.9$ is determined by the sum of residual acceptors which exceed the concentration of the native point defects. Such a scaling method should be only possible in very pure (better than 99.9999%) material.

A finer adjustment of the homogeneity can be achieved using a definite cadmium overpressure. We have located a cadmium reservoir in the top of a specially designed ampoule within a multizone Bridgman furnace (Fig. 7(a)). By variation in the pressure of the cadmium source it was possible to adjust the conductivity type and the carrier concentration in the range 10^{11}–10^{15} cm^{-3} over the whole crystal (see Fig. 6(b)). It can be shown that the conversion temperature from p-type to n-type conductivity is about 810–820°C. This is in good agreement with the p–T phase relation in which the corresponding values are 800 and 850°C. The different values are caused by the uncertainty in the data for the stoichiometric line in the p–T projection [21].

To achieve nearly stoichiometric material a cadmium excess in the melt of about 6×10^{18} cm^{-3} ($\delta y = -2 \times 10^{-4}$) must be used. Therefore in the case of complete mixing of the melt a similar supply of cadmium atoms per cubic centimetre in the vapour phase will be maintained. The calculation was taken from the perfect-gas law (Section 3.1). On the assumption of a (free) volume above the melt of about 120 cm^3 and a vapour pressure of about 10^5 Pa the concentration of cadmium in the gas phase will be about 6×10^{18} cm^{-3}. Taking into account a natural convection of the melt [23] a simple estimation of the mass-balanced growth rate shows critical values of more than 1 mm h^{-1} for steady state conditions. Our crystals were grown with a rate of 1 mm h^{-1} or less.

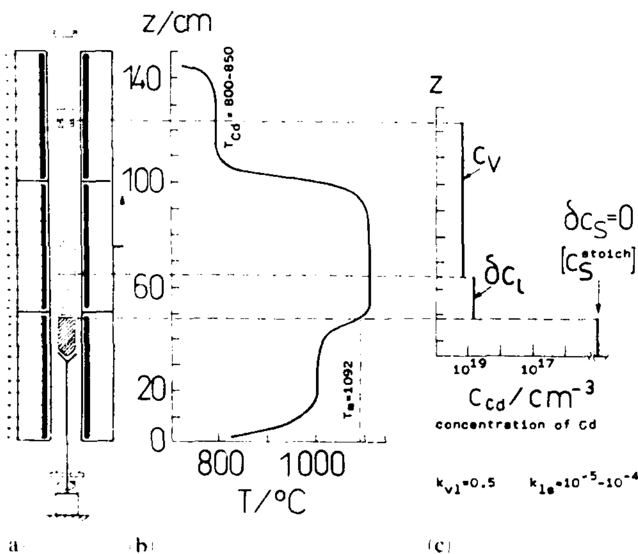

Fig. 7. The vertical Bridgman growth of CdTe single crystals with a controlled cadmium overpressure: (a) furnace and ampoule arrangement; (b) measured axial temperature distribution; (c) estimated relative axial cadmium excess distribution with C_V the concentration of cadmium atoms in the vapour phase, δC_l the excess of cadmium atoms in the melt required for a stoichiometric crystal composition $\delta C_S = 0$, k_{Vl} the coefficient of separation between vapour and melt, and k_{lS} the segregation coefficient between melt and solid.

A time of about 24 h is assumed to guarantee complete saturation of the melt and to avoid any transient effects in the first-to-freeze region. Thermodynamic equilibrium between the cadmium source and the melt surface can be reached by this method and a constant melt composition can be adjusted every time.

CdTe single crystals grown with such controlled cadmium overpressure are characterized by low carrier concentrations which are homogeneously distributed along the growth direction (see Section 4). The tellurium concentration accumulated in precipitates and inclusions is also reduced, resulting in a high IR transmission (2–15 μm) of about 65%.

4. Distribution of residual impurities

The concentration of background impurities has been determined in the raw elements (cadmium and tellurium), in the single-crystal CdTe and in $Hg_{1-x}Cd_xTe$/CdTe liquid-phase epitaxy (LPE) layer/substrate structures [32]. The impurity level in the elements has been distinctly reduced by a triple distillation of cadmium and zone refining of tellurium (40 times) to a value lower than 10^{16} cm^{-3}. The concentrations of sodium, potassium, calcium, silicon, tin, antimony and bismuth are enriched in the CdTe originating from the high temperature procedure in silica ampoules.

Distinct differences between the impurity levels of CdTe crystals grown in the vertical Bridgman method with (VBZ) and without (VB) a cadmium source can be observed. In VB crystals grown from a slightly tellurium-rich melt the axial distribution of the acceptor elements copper, silver and sodium with a distribution coefficient $k<1$ is characterized by pronounced segregation behaviour. On the contrary the distributions of important donors such as chlorine and indium are less marked (Fig. 8(a)). Obviously, the variation in the carrier concentration from the first-to-freeze region ($p \approx 10^{14}$ cm^{-3}) to the end region ($p \leqslant 10^{16}$ cm^{-3}) corresponds to the distribution of the main acceptors. However, a significant discrepancy between the absolute acceptor concentration and the hole concentration can exist because of donor–acceptor compensation effects, neutral complex formations and infiltration of impurities into tellurium inclusions (see Section 3.1). Photoluminescence analysis which is capable of detecting the substitutional impurity concentrations (Cu_{Cd} and Ag_{Cd}) [34] is in good agreement with the corresponding p values. Thus the observed increase in the p-type carrier concentration with increasing normalized crystal position g can be

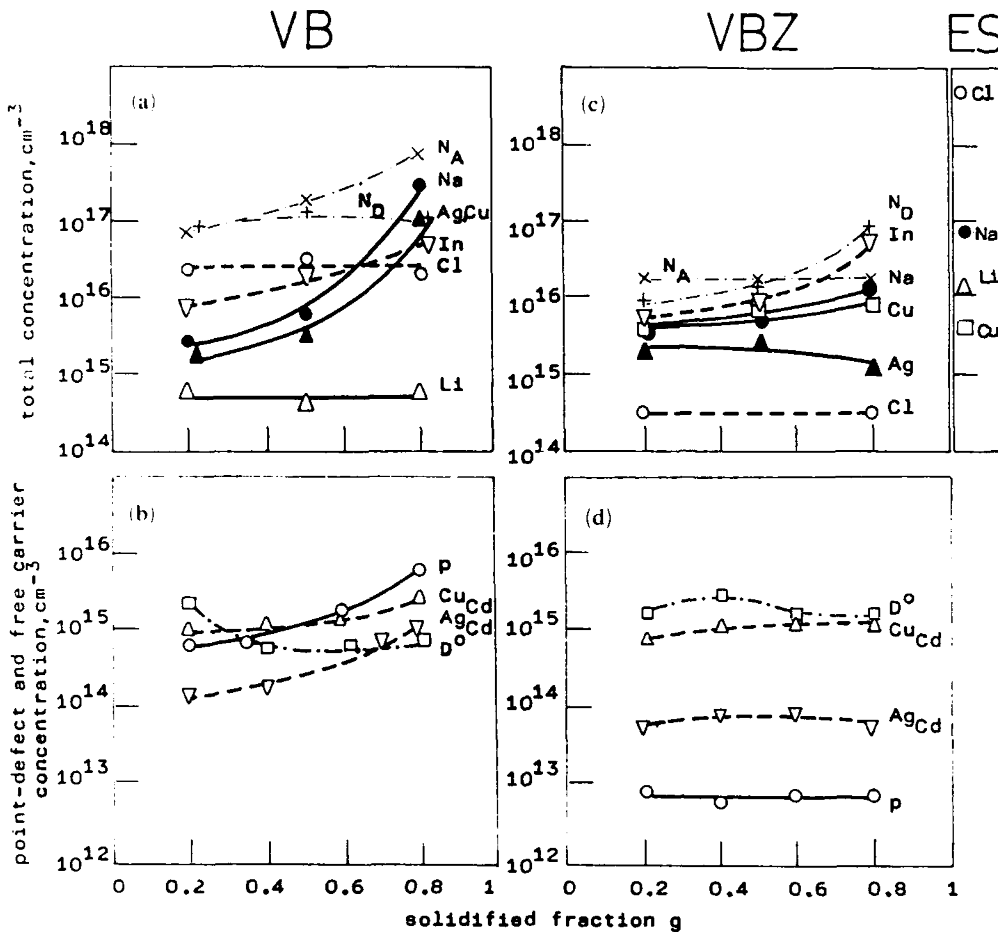

Fig. 8. (a), (c) Total concentrations (determined by spark source mass spectroscopy and atomic adsorption spectrophotometry) for some important residual impurities and the sums of all acceptors (curve N_A) and donors (curve N_D) and, (b), (d), the concentration of substitutional acceptors (curves Cu_{Cd} and Ag_{Cd}) and donors (curve D^0) deduced from photoluminescence analysis [34] and the hole concentration p (curve p) as functions of the axial position g in vertical Bridgman crystals grown without (VB) and with (VBZ) an extra cadmium source (ES).

mainly explained by the distribution of the shallow acceptors which are located at cadmium lattice positions.

In VBZ crystals grown of near-stoichiometric composition the total concentrations are generally lower than in VB crystals (Fig. 8(c)). Some of the volatile impurities (sodium, lithium and chlorine) are enriched in the cadmium reservoir (ES) by an evaporation process from the melt (Fig. 8(c)). The concentrations of silver and copper are also reduced which agrees with the much lower precipitates and inclusion densities in VBZ crystals. Obviously in VB crystals a considerable part of these acceptors are collected in Te inclusions and precipitates. Additionally, the marked decreased cadmium vacancy (V_{Cd}) concentration during the growth with a controlled cadmium overpressure leads to a decreased occupation of cadmium site impurities. The extremely low axial homogeneously distributed free-carrier concentration in VBZ crystals (Fig. 8(d)) shows that the shallow acceptors are strongly compensated by donors. VB crystals always have a high p-type concentration of about 10^{15} cm^{-3} (see Fig. 6(a)) in the last-to-freeze region independent of the melt composition chosen. This observation favours the assumption for the VBZ crystals that the volatile acceptors evaporate and condense at the lower temperature level in the cadmium reservoir. Further investigations are necessary in order to solve this problem which indicates a non-steady state growth process. Consequently, attention has to be paid to the selection of the substrate slices for epitaxial processes. It has been shown [33] that the carrier concentration and the conductivity type of the LPE $Hg_{1-x}Cd_xTe$ layers are influenced by the impurity levels of the substrates taken from different axial positions of conventionally grown VB CdTe ingots. LPE layers grown on substrates selected from the last-to-freeze regions of the VB crystals have

carrier concentrations $p \geq 1 \times 10^{16}$ cm^{-3}. This may be caused by an outdiffusion process from the substrate and should be valid for the fast acceptors such as silver, copper, sodium and potassium. An adjustment of the carrier concentration to values lower than 1×10^{16} cm^{-3} was only possible if the substrates were taken from the first-to-freeze and central regions of the VB CdTe ingots. Additionally, such epitaxial layers can be converted to an n-type conductivity by isothermal annealing. The influence of VBZ substrates on the epitaxial layer quality is a matter for further investigations.

5. Conclusions

We have started some detailed investigations of crystal growth of CdTe from the melt. First, the structure of the melt is shown to have a strong influence on the crystal quality. In the case of unseeded growth conditions a considerable supercooling in the tip region is observed by a high degree of melt superheating (greater than 10 K). There was no supercooling at lower values of superheating. Such behaviour is believed to correlate with the associated structure of the CdTe melt. On the contrary, crystals with a reduced number of grain boundaries can only be obtained if the melt state is superheated by more than 10 K. Secondly, stoichiometry-correlated growth effects have been investigated. In the case of the conventional vertical Bridgman technique in sealed ampoules without any cadmium overpressure the composition of the crystal is influenced by scaling variations of the starting charges and by the length ratio of the melt to the free space over the melt. A slightly tellurium-rich melt will be obtained using nearly stoichiometric material. Hence, a segregation process will be expected. A tellurium-rich state in the liquid and solid phases is the source of two defect types: tellurium inclusions with diameters greater than 1 μm caused by morphological instabilities at the growth interface, and tellurium precipitates with diameters of about 10–30 nm originating from the retrograde slope of the solidus line. For small deviations from the stoichiometry the axial distribution of the precipitates can be simply approximated by a Pfann segregation curve. Two methods have been investigated in order to adjust the melt and the crystal composition: (i) an exact addition of a small quantity of cadmium to the starting material; (ii) use of a cadmium reservoir which gives a cadmium pressure over the melt surface. The second method is assumed to ensure stable thermodynamic conditions during the whole growth process. Crystals grown with such a controlled cadmium overpressure are characterized by a distinctly lower content of precipitates, inclusions and residual impurities. Furthermore, these crystals show a very homogeneous axial and radial distribution of the carrier concentration in comparison with the conventionally grown crystals. Two reasons are discussed for the improved crystal quality: (i) the possible additional purification of the melt during the growth with a cadmium source owing to evaporation of the volatile impurities; (ii) the decreased cadmium vacancy concentration which tends to reduce the cadmium site impurities.

Finally, special attention should be directed to the selection of the CdTe substrate slices for epitaxial processes. The substrate quality is a function of the axial position from which the substrate will be taken. The substrates from the last-to-freeze region of conventionally grown crystals have a high concentration of rapidly diffusing acceptors which infiltrate into the layer during the epitaxial and annealing processes.

Acknowledgments

The authors are indebted to A. Wenzel from Crystal GmbH Berlin for the growth of the VBZ crystals, and to H. Zimmermann, M. Neubert and Dr. M. Wienecke from the Humboldt University for the photoluminescence measurements, IR microscopy and Hall measurements. The investigations have been partially supported by the Volkswagen-Stiftung and the Deutsche Forschungsgemeinschaft Bonn.

References

1 C. J. Johnson, *Proc. Soc. Photo-Opt. Instrum. Eng.*, *1106* (1989) 56.
2 C. P. Khattak and F. Schmid, *Proc. Soc. Photo-Opt. Instrum. Eng.*, *1106* (1989) 47.
3 M. Pfeiffer and M. Mühlberg, *J. Cryst. Growth*, *118* (1992) 269.
4 C. Parfeniuk, F. Weinberg, I. V. Samarasekera, C. Schevzov and L. Li, *J. Cryst. Growth*, *119* (1992) 261.
5 D. H. Kim and R. A. Brown, *J. Cryst. Growth*, *96* (1989) 609.
6 M. Mühlberg, P. Rudolph and A. Wenzel, Trans Tech., Zurich, 1992.
7 W.-B. Song, M.-Y. Yu and W.-H. Wu, *J. Cryst. Growth*, *86* (1988) 127.
8 M. Azoulay, S. Rotter, G. Gafni and M. Roth, *J. Cryst. Growth*, *117* (1992) 276.
9 R. Triboulet, A. Heurtel and J. Rioux, *J. Cryst. Growth*, *101* (1990) 131.
10 A. Tanaka, Y. Masa, S. Seto and T. Kawasaki, *J. Cryst. Growth*, *94* (1989) 166.
11 K. Yokata, H. Nakai, K. Satoh and S. Katayama, *J. Cryst. Growth*, 112 (1991) 723.
12 B. K. Meyer, W. Stadler, D. M. Hofmann, P. Omling, D. Sinerius and K. W. Benz, *J. Cryst. Growth*, *117* (1992) 656.
13 H. Zimmermann, R. Boyn, P. Rudolph, J. Bollmann, A. Klimakow and R. Krause, *Mater. Sci. Eng. B* (1993) 139.

14 S. A. Stroitjeljev, *Kristallochemičeskij Aspect Technologii Poluprovodnikov,* Nauka, Novosibirsk, 1976.
15 A. S. Jordan, *Metall. Trans., 1* (1970) 239.
16 A. Marbeuf, M. Ferah, E. Janik and A. Neurtel, *J. Cryst. Growth, 72* (1985) 126.
17 V. M. Glazov, S. N. Čiževskaja and N. N. Glagoleva, *Židkie Poluprovodniki,* Nauka, Moscow, 1967.
18 R. S. Feigelson and R. K. Route, *Final Rep. CMR-85-3,* 1985 (Stanford University).
19 M. R. Lorenz, *J. Phys. Chem. Solids, 23* (1962) 939.
20 Y.-C. Lu, J.-J. Shian and R. S. Feigelson, *J. Cryst. Growth, 102* (1990) 10.
21 K. Peters, A. Wenzel and P. Rudolph, *Cryst. Res. Technol., 25* (1990) 10.
22 P. Rudolph, M. Neubert and M. Mühlberg, *Proc. 10th Int. Conf. on Cryst. Growth, San Diego, CA, 1992,* in *J. Cryst. Growth* (1993).
23 G. T. Neugebauer and W. R. Wilcox, *J. Cryst. Growth, 89* (1988) 143.
24 J. B. Mullin and B. W. Stragham, *Rev. Phys. Appl., 12* (1988) 267.
25 M. Wada and J. Suzuki, *Jpn. J. Appl. Phys., 27* (1988) L972.
26 S. Sen, W. H. Konkel, S. J. Tighe, L. C. Bland, R. S. Sharma and R. E. Taylor, *J. Cryst. Growth, 86* (1968) 111.
27 P. M. Borsenberger and D. A. Stevenson, *J. Phys. Chem. Solids, 29* (1968) 1277.
28 J. L. Tissot, P. L. Vuillermoz and A. Langier, *Rev. Phys. Appl., 12* (1977) 267.
29 R. S. Rai, S. Mahajan, S. McDevitt and D. J. Johnson, *J. Vac. Sci. Technol. B, 9* (1991) 1892.
30 T. J. Magee, J. Peng and J. Bean, *Phys. Status Solidi A, 27* (1975) 557.
31 U. Becker, P. Rudolph, R. Boyn, M. Wienecke and I. Utke, *Phys. Status Solidi A, 120* (1990) 653.
32 U. Becker, H. Zimmermann, P. Rudolph and R. Boyn, *Phys. Status Solidi A, 112* (1989) 569.
33 P. Rudolph, M. Mühlberg, M. Neubert, T. Boeck, P. Möck, L. Parthier, K. Jacobs and E. Kropp, *J. Cryst. Growth, 118* (1992) 204.
34 H. Zimmermann, R. Boyn, C. Michel and P. Rudolph, *Phys. Status Solidi A, 118* (1990) 225.

Defects and electrical properties of doped and undoped CdTe single crystals from tellurium-rich solutions

E. Weigel, G. Müller-Vogt, B. Steinbach and W. Wendl
Kristall- und Materiallabor der Fakultät für Physik, Universität Karlsruhe, Kaiserstrasse 12, 7500 Karlsruhe (Germany)

W. Stadler, D. M. Hofmann and B. K. Meyer
Physikdepartment E 16, Technische Universität München, 8046 Garching b. München (Germany)

Abstract

CdTe single crystals have been grown using either the Bridgman or the travelling-heater technique. Crystals doped with indium or chlorine were compared with those without any intentional dopant. With high resolution atomic absorption spectroscopy analysis it was possible to measure the effective segregation coefficient of indium down to concentrations of 3×10^{15} In atoms cm^{-3}. Higher amounts of indium resulted in n-type conductivity but, with less indium than 1×10^{15} cm^{-3}, crystals were p type, as is always the case for undoped crystals. Photoluminescence spectra taken from as-grown samples and from samples annealed at 380 °C or 780 °C with subsequent quenching revealed the A centre but require reconsideration of the role of this complex in the compensation models.

1. Introduction

As an interesting material for technical applications (it is used as γ-ray and X-ray detector, as a substrate material for $Hg_{1-x}Cd_xTe$, as material for solar cells and in the optical industry) as well as for purely scientific reasons, CdTe has received much attention in the past [1]. However, in spite of many efforts there are still some gaps in the knowledge of the relationship between on the one hand the parameters of crystal growth and the chemistry and on the other hand the electrical behaviour of the material which can be expressed in the values of concentration, mobility and lifetimes of both holes and electrons. Although there is general agreement on the importance of residual impurities and intrinsic defects and of their interplay [2-6], conclusive correlation to these values is still lacking. Related to these questions is the problem of the self-compensation mechanism, which is even more urgent for the other II-VI compound semiconductors [7].

The aim of our study was to grow single crystals of CdTe with different solution growth techniques under various conditions, *e.g.* growth temperatures, growth velocities and cooling rates. High resolution chemical analysis of intentional and unintentional dopants in the sub-parts per million range and electrical and optical characterization should serve as feedback information for the control and change of our growth parameters.

2. Experimental details

CdTe single crystals were grown either with the Bridgman technique on the tellurium-rich side of the phase diagram [8] or by the travelling-heater method (THM) with a tellurium zone [9, 10]. In the Bridgman case, two values for the starting atomic tellurium-to-cadmium ratio were chosen, namely 55%/45% and 72%/28%, leading to starting temperatures for crystal growth of 1050 °C and 900 °C respectively. Synthesis and growth were carried out in the same quartz ampoules with a graphite coating of the inner walls. Chlorine in the form of $CdCl_2$ and indium in elemental form were used as intentional dopants and were added to the starting materials in Bridgman runs or to the tellurium zone in the THM.

The chemical analysis of the residual impurities and of the dopant concentration was done by atomic absorption spectroscopy (AAS) with a flame in routine operation mode or with a graphite furnace (GFAAS) if better detection limits were necessary.

Electrical characterization of samples was done by conductivity and Hall measurements at around room

0921-5107/93/$6.00 © 1993 - Elsevier Sequoia. All rights reserved

temperature. Contacts for p-type samples were made by electrodeless deposition of gold [11]; contacts were made to n-type samples by a droplet of pure indium. In every case, crystals were lapped and etched in a 5% bromine in methanol solution prior to making contacts.

In addition, photoluminescence (PL) spectra of our crystals at 2 K were recorded using the excitation of the 514 nm line of an argon ion laser with an operating power moderately below 100 mW.

3. Results and discussion

3.1. Chemical analysis of starting materials and crystals

As a basis of reference for the concentration of foreign substances in our crystals, we examined the starting materials cadmium and tellurium from different producers labelled 1–4 in Table 1. Material in every case was specified as purity 99.9999% or better. As expected, the concentration of most elements was beyond detection limits of flame AAS which was in the range of a few atomic parts per million for nearly all elements even when working with amounts of substance exceeding 1 g. The use of the much more sensitive method of GFAAS not only allowed us to lower the detection limits of some elements by up to two orders of magnitude but also reduced substance consumption to 50–100 mg per analysis, which resulted in a much higher local resolution within the samples. Additionally the systematic error connected to specific chemical reactions during some preparation steps for flame AAS could be detected and proved the flame data for iron to be artificially enlarged. The same probably holds for the aluminium values but here the reason may be the non-availability in our laboratory of dust-free conditions which might influence the results because of the normally very high background for aluminium. In summary, our AAS measurements show that the starting materials of highest purity nowadays available seem really to have a total residual content of metal impurities of less than 1 ppm. The measurements on the crystals themselves showed no increase in metal impurity concentration and thus confirmed that growth itself is a further purification step, as the segregation coefficient of most metals is smaller than unity. Impurity take-up of the measured metals from the high purity synthetic quartz ampoules seems to play a minor role in our case. In order to follow some residual impurities quantitatively we have to improve the chemical detection limits for at least one further order of magnitude.

3.2. Chemical analysis of indium-doped crystals

As a well-known doping element leading to n-type conductivity we concentrated on indium as a model dopant to study its segregation behaviour during growth in a quantitative manner and with a high local resolution. We succeeded in following the indium content within a statistical uncertainty of about 20% down to very low concentration ranges only slightly above our present detection limit for this element of 0.07 ppm or 2×10^{15} In atoms cm^{-3}.

TABLE 1. Analysis of foreign elements in starting materials for CdTe using atomic absorption spectroscopy with a flame and with a graphite furnace

	Amount (at.ppm) of the following elements								
	Al	Fe		Ni	Cu	Zn	Ag		In
Flame AAS									
Cd-1			3.2	< 5.0	< 1.8	1.2			
Cd-2			3.8	< 3.4	< 1.2	1			
Cd-3			3.6	< 3.1	< 1.1	< 0.5			< 3
Cd-4			3.9		< 0.7		< 0.2		
Te-1			3.4	< 2.8	< 1.0	< 0.6			
Te-2			4.1	< 3.5	< 1.6	< 0.6	< 0.3		
Te-3			3.7	< 2.2	< 0.8	< 0.4			< 4
Te-4			6.9		< 0.9		< 0.3		
GFAAS									
Cd-1	5.8	< 0.3			< 0.8		< 0.02		< 0.07
Cd-2	9.2	< 1.1			< 0.9		< 0.1	0.6	
Cd-3	6.7	< 1.2	1.9	< 0.2	< 0.9		< 0.1		
Cd-4	2.1	< 0.4					< 0.02		
Te-1	4.7	< 0.3	5.2		< 0.9		< 0.03	0.1	< 0.07
Te-2	6.7	< 1.3			< 1.1		< 0.07		
Te-3	6.7	< 1.1	2.6	< 0.2	< 1.1		< 0.06		
Te-4	6.7	< 0.4							

Figure 1(b) and 1(c) show the indium distribution within Bridgman crystals doped at a level of 0.5 ppm. For comparison a crystal with a concentration roughly an order of magnitude higher is shown in Fig. 1(a). The distribution in every case corresponds exactly to the theory of segregation for directional solidification [12]. So the calculated effective segregation coefficient of 0.2 for Bridgman growth has an accuracy of about ± 15% and shows itself to be independent of concentration. Even for doping amounts as high as 1000 ppm and also for the THM crystals doped with indium we obtained the same k_{eff}. The stated independence of k_{eff} on the indium concentration seems to contradict the results of Yokota *et al.* [13] who believe that they have evidence that the indium segregation coefficient decreases with decreasing indium concentration for the range below about 100 at.ppm In. For higher indium concentrations they found segregation coefficients of between 0.1 and 0.2 well comparable with our values within the given uncertainties. However, one should be aware of the fact that they performed near-stoichiometric growth with a tellurium excess of less than 0.05 at.% whereas in our case the tellurium excess ranged from 5 at.% (Bridgman starting condition) up to 35 at.% (THM). Therefore we believe that with our value of the segregation coefficient we can estimate the actual indium concentration in our crystals even for indium doping levels in the range of 10^{14} cm^{-3}, too small to be detected by AAS, with rather a high confidence.

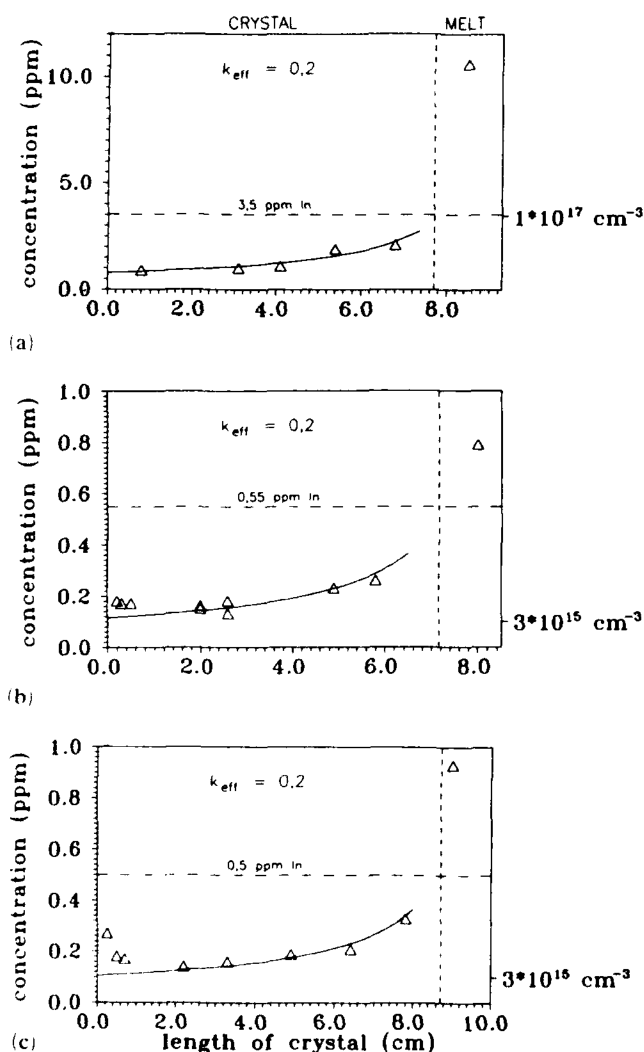

Fig. 1. Indium distribution in crystals of CdTe grown with the vertical Bridgman technique from a tellurium-rich solution: (a) crystal doped with 1×10^{17} In atoms cm^{-3}; (b), (c) examples of two crystals doped with 1.5×10^{16} cm^{-3}.

Looking at the ideal segregation behaviour of indium and at the small scattering of the measuring points we take the higher concentration values at the very top of the crystals which can be seen in Figs. 1(b) and 1(c) to be real. The explanation seems to lie in a high undercooling of the melt necessary for the primary crystallization to set in. Rudolph and coworkers [14] have shown in recent investigations that the undercooling can amount to some 10 K, depending on the overheating of the liquid phase. This is in line with the observations made by many groups that the first region of the grown crystals is always of polycrystalline type.

3.3. Electrical characterization of the crystals

Table 2 shows the electrical parameters of indium-doped Bridgman and THM crystals ordered according to their doping levels together with undoped and chlorine-doped samples. The most pronounced feature is that indium leads to n-type material whereas no intentional doping at all as well as chlorine doping always result in p-type material. Because of the high accuracy of the AAS measurements described in the last section we were able to determine the indium range of the transition between n and p type and have located it to the concentration region $(2-6) \times 10^{15}$ cm^{-3}. Above this region the indium content seems to have no specific influence on the resistivity, being always in the range of 10^3-10^4 Ω cm. Only within the narrow range specified have we succeeded in growing crystals with resistivities exceeding 10^8 Ω cm. The critical indium concentration is comparable with that of the intrinsic defects and therefore is evidence for these defects to play a key role in the whole process. In order to change the intrinsic defect system with the indium content kept constant we treated our samples at different temperatures: annealing for 1 h at 380 °C or 780 °C in an argon atmosphere, followed by rapid quenching to room temperature, had only little effect on the conductivity of crystals with a high indium content, quite in contrast with those with an indium content in the critical range which became p type even at the lower annealing temperature. To demonstrate this point, Fig. 2(a) shows the

TABLE 2. Compilation of the electrical parameters of doped and undoped CdTe single crystals

Crystal and method	In-doping (ppm)	Resistivity (Ohm cm^{-1})	Type	Mobility cm^2 (Vs)$^{-1}$
THM 1	2300	6.00E+03	n	50
Bridgman 1	950	2.00E+03	n	300
THM 2	230	3.00E+03	n	450
Bridgman 2	140	8.00E+02	n	
THM 3	34	8.00E+02	n	390
Bridgman 3	15	4.00E+04	n	
Bridgman 4	3	2.00E+03	n	660
Bridgman 5	0.5	4.00E+03	n	830
Bridgman 6	0.5	6.00E+08	n	900
Bridgman 7	0.1	4.00E+06	p	<20
Bridgman	—	1.00E+04	p	
THM	—	1.00E+04	p	
Bridgman	Cl	>1.00E+08	p	50-80
THM	Cl	>1.00E+09	p	60-90

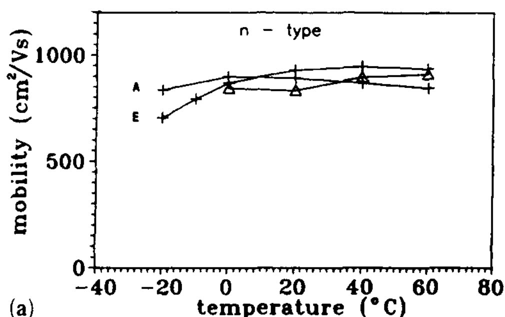

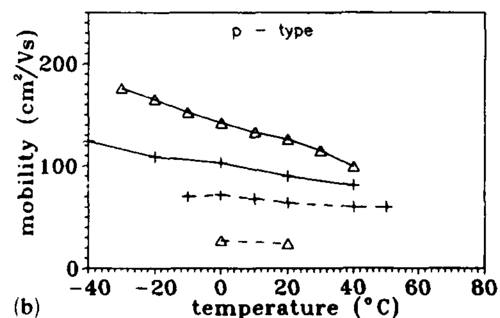

Fig. 2. Hall mobilities of the two crystals from Fig. 1(b) (+) and 1(c) (△) with an average indium concentration of 5×10^{15} cm^{-3} measured in the room-temperature region: (a) as-grown samples (A is a sample from the start of the crystal, and E is a sample from the end portion); (b) after annealing the crystals at 380 °C (– – –) and at 780 °C (——) for 1 h.

Hall mobilities of as-grown crystals with 0.15 at.ppm In (cf. Fig. 1(b) and 1(c)), and Fig. 2(b) the results after annealing at 380 °C and 780 °C. We have to conclude that the temperature treatment increases the number of compensating acceptors in this material. A common candidate often discussed in this context is the A centre consisting of a cadmium vacancy and a neighbouring indium atom. To check this possibility we investigated the PL spectra of our crystals.

3.4. Photoluminescence measurements

Examples of PL spectra for undoped, chlorine-doped and indium-doped samples are presented in Fig. 3. We shall not discuss the fine details of these spectra in this paper but only wish to draw attention to the main features relating to the above-mentioned electrical behaviour. The PL between 1.4 eV and 1.5 eV is related to donor–acceptor recombination lines of residual impurities and of A centre complexes [15]. Heavily indium-doped crystals (Fig. 3(c)) do not show any single lines but are smeared out to only one broad band. However, in the low-level-doped crystals (Fig. 3(d)) the line of the A centre is clearly visible [16]. Another important feature is the deep luminescence around 1.2 eV. This is probably related to intrinsic defects, V_{Cd} being one likely candidate.

The evolution of the spectrum in Fig. 3(d) after annealing shows first a diminishing and then fully disappearing A centre intensity. So this complex is ruled out as a possible candidate to explain our conductivity results. It would be more likely to assume that cadmium vacancies are responsible for the observed effects. It is clearly to be seen that the PL at around 1.2 eV is more pronounced in undoped and chlorine-doped crystals (Fig. 3(a) and 3(b)) which are both p type and that this spectral range shows up clearer in the tempered crystals which also became p type. Of course this needs further confirmation.

4. Conclusions

We have demonstrated for indium that it is possible with GFAAS to follow quantitatively and with high local resolution foreign impurities down to concentration ranges as low as 10^{15} cm^{-3}, comparable with the concentration range of the electrically active intrinsic defects that exist even at low temperatures. With the effective segregation coefficient thus obtained, we can estimate concentrations at least one order of magnitude lower with a high confidence. Regarding new techniques as optical detected magnetic resonance and magnetic circularly polarized emission (MCPE) which can reveal not only the nature but also the fine details of the structure of individual defects, the understanding of the relationship between electrical properties and defect structure should become possible in the near future and provide feedback on the optimization and control of growth parameters and of after-growth treatments which are still a challenge to the crystal grower.

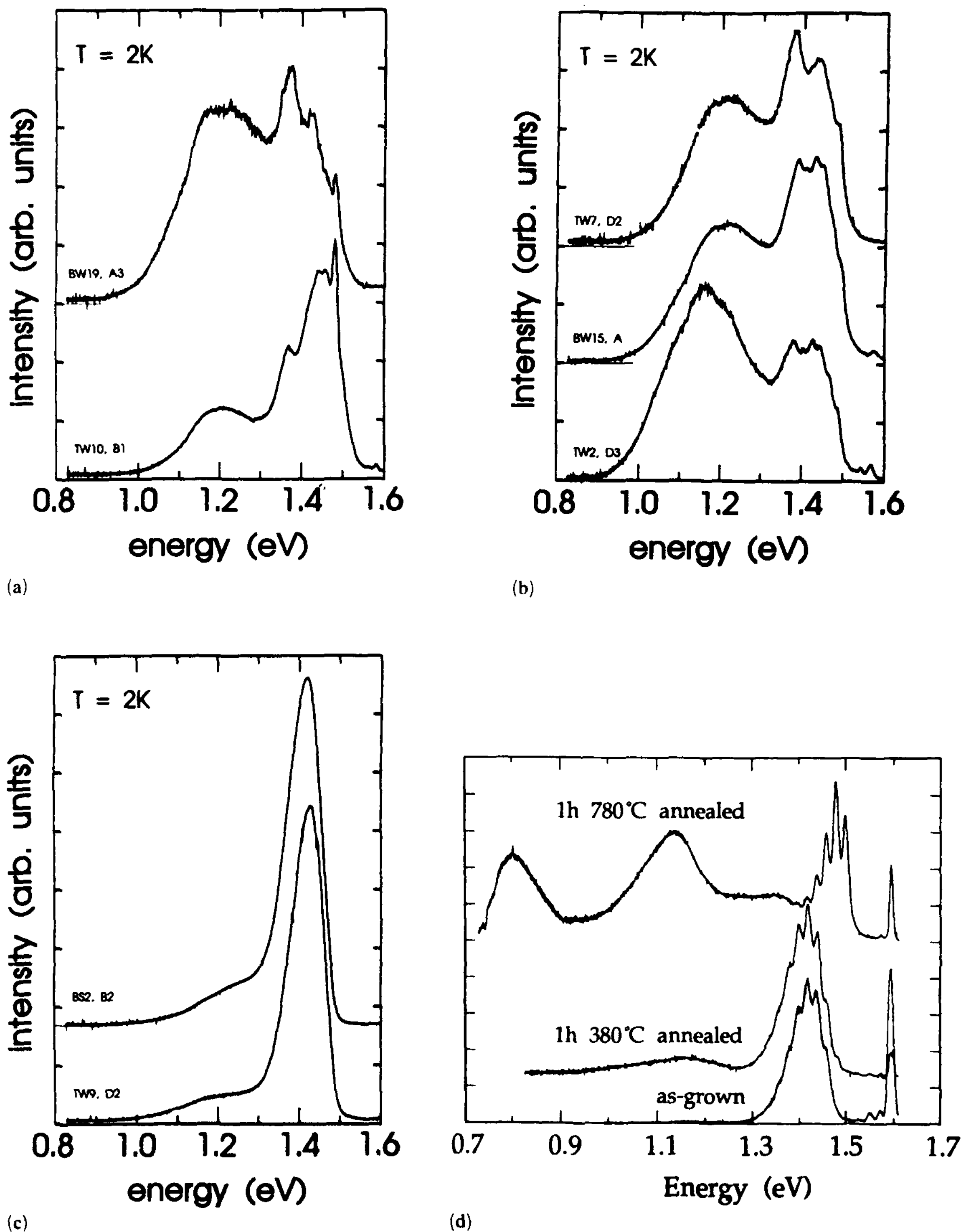

Fig. 3. PL spectra measured at 2 K (labels beginning with B indicate Bridgman crystals and those beginning with T THM runs): (a) undoped THM and Bridgman crystals; (b) three examples of chlorine-doped crystals, two THM and one Bridgman sample; (c) a THM and a Bridgman crystal with an indium level of about 30 ppm or 1×10^{18} cm^{-3}; (d) example of a Bridgman crystal containing 0.2 at.ppm In in its as-grown state and after the tempering steps (cf. Fig. 2) (the zero-phonon lines and neighbouring phonon replicas of the A centre (V_{Cd}–In_{Cd}) [14, 15] are clearly to be seen in the as-grown sample and still after 380 °C annealing but not after 780 °C annealing.

References

1 K. Zanio, *Semicond. Semimet.*, *13* (1978).
2 F. A. Kröger, *Rev. Phys. Appl.*, *12* (1977) 205.
3 P. Siffert, J. Berger, C. Scharager, A. Cornet, R. Stuck, R. O. Bell, H. B. Serreze and F. V. Wald, *IEEE Trans. Nucl. Sci.*, *23* (1976) 159.
4 R. N. Bhargava, *J. Cryst. Growth*, *59* (1982) 15.
5 M. Samimi, B. Bigliari, M. Hage-Ali, J. M. Koebel and P. Siffert, *Phys. Status Solidi A*, *100* (1987) 251.
6 R. E. Kremer and W. B. Leigh, *J. Cryst. Growth*, *86* (1988) 490.
7 J. L. Pautrat, J. M. Francou, N. Magnea, E. Molva and K. Saminadayar, *J. Cryst. Growth*, *72* (1985) 194.
8 P. Höschl, P. Polivka, V. Prosser and A. Sakalas, *Czech. J. Phys. B*,*25* (1975) 585.
9 B. O. Bell, N. Hemmat and F. Wald, *Phys. Status Solidi A*, *1* (1970) 375.
10 R. Triboulet and Y. Marfaing, *J. Cryst. Growth*, *51* (1981) 89.
11 T. C. Anthony, A. L. Fahrenbruch and R. H. Bube, *J. Electron. Mater.*, *11* (1) (1982) 89.
12 W. G. Pfann, *Zone Melting*, Wiley, New York, 1959.
13 K. Yokota, H. Nakai, K. Satoh and S. Katayama, *J. Cryst. Growth*, *112* (1991) 723.
14 M. Mühlberg, P. Rudolph, M. Laasch and E. Treser, *Mater. Sci. Eng.*, *B16* (1993) 8–16.
15 D. M. Hofmann, B. K. Meyer, U. Probst and K. W. Benz, *J. Cryst. Growth*, *101* (1990) 536.
16 B. K. Meyer, W. Stadler, D. M. Hofmann, P. Omling, D. Sinerius and K. W. Benz, *5th Int. Conf. on II–VI Compounds, Okayama, 1991.*

Floating-zone melting of CdTe

Wen-Ming Chang, W. R. Wilcox and L. Regel
Center for Crystal Growth in Space, Clarkson University, Potsdam, NY 13699 (USA)

Abstract

To produce superior crystals of CdTe, floating-zone melting in space has been proposed. Techniques required for floating-zone melting of CdTe have been developed. CdTe has been successfully float zoned using square feed rods and resistance heating. The maximum zone length in a 3.5 mm wide square CdTe rod on Earth was about 5 mm. Evaporation of the CdTe melt was controlled by adding excess cadmium to the growth ampoule combined with heating of the ampoule wall. The temperature of the ampoule wall was the primary factor in determining the deposit-free time. Slow rotation of the growth ampoule was necessary to achieve a complete, symmetric molten zone. The maximum zone travel rate, considered from the heat transfer standpoint only, was experimentally determined to be 6 mm h^{-1}. Most of the resultant cylindrical rods were single crystals with twins. Rods grown at a cooling rate of 40 °C h^{-1} yielded a much lower etch pit density (EPD), ranging from 2.2×10^3 to 8.2×10^2 cm^{-2}, than those grown by quenching, which had EPD values ranging from 5.4×10^4 to 8.7×10^4 cm^{-2}. The pits formed in these rods were randomly distributed, which was different from the cellular structure observed in CdTe produced by the vertical Bridgman technique. A lower EPD was obtained at the periphery of our rods. An approximate radiation model was developed to predict the heater power requirement. For CdTe molten zones, the power requirement predicted by the model differed by 5% to 30% from that measured in the experiments. The model predicts that the power requirement for the zone heater to maintain a static zone varies with the rod radius, R_1 in the range from $R_1^{1.5}$ to $R_1^{1.9}$. This relationship is affected by various factors, such as the ampoule wall temperature and the gap between the rod and the zone heater.

1. Introduction

Sizeable CdTe single crystals with low defect concentrations are desired for the high efficiency of devices. Although much effort has been made, current terrestrial techniques used to grow CdTe still cannot fulfil the device requirements. A possible growth technique to obtain high quality single crystals is floating-zone melting. The floating-zone technique provides containerless processing. Containerless processing significantly reduces undesirable spurious nucleation and contamination from the ampoule, and eliminates any sticking to an ampoule wall. Currently, CdTe is grown commercially by the Bridgman technique. Wilcox *et al.* [1] pointed out that "sticking of the crystal to the ampoule is the major contributor to stress within the crystal in the Bridgman growth technique". In addition, the floating-zone technique requires low energy consumption to maintain the small volume of melt in the zone.

Several advantages arise from conducting floating-zone melting in space. The diameter of the crystal can be enlarged, because supporting the weight of the zone by surface tension is no longer required. Thus, high density, low surface tension materials can be more easily float zoned. Natural convection caused by density gradients will diminish greatly so that turbulence, which can give rise to striations, will be curtailed [2, 3]. Plastic deformation is also reduced in space; the growing crystal of CdTe is not then subjected to its own weight.

Two inherent difficulties associated with floating-zone melting of CdTe are evaporation of the melt and the small size of the molten zone (about 5 mm in diameter and length) owing to the low surface tension and high density of the melt. At the melting point of CdTe, a stoichiometric melt yields 0.8 atm of cadmium vapor pressure and about 0.01 atm of tellurium [4]. The ease with which CdTe fractures also provides a challenging problem in ampoule design. For design of the flight experiment using larger diameter CdTe rods, it is necessary to have some idea of the power requirements.

2. Experiments and results

The ground-based floating-zone apparatus used in this work and the method used to hold the CdTe feed rods have been described elsewhere [5]. Polycrystalline square rods of CdTe donated by II-VI Incorporated were used as feed rods in this work.

0921-5107/93/$6.00

© 1993 - Elsevier Sequoia. All rights reserved

2.1. Zone size

The maximum length L_{max} of a CdTe molten zone in a cylindrical rod for terrestrial experiments can be estimated by Heywang's equation [6, 7] to be about 5.4 mm, using a surface tension of 200 dyn cm^{-1} [8] for molten CdTe at its melting point and a density of 5.65 g cm^{-3} [9]. Heywang's stability plot indicates that the rod diameter must be greater than 7.6 mm to prevent a zone 5.4 mm high from dripping down. However, this is in conflict with heat transfer analyses showing that the rod diameter must be equal to or less than the zone height to form a full zone with nearly planar interfaces (see, for example, refs. 10 and 11). To meet the limits of both zone stability and planar interfaces, the maximum zone size can be obtained by setting the zone diameter equal to its length on Heywang's zone stability curve. In this way, the maximum rod diameter and zone height on earth were estimated to be about 5 mm.

With square CdTe rods 3.89 mm across we experimentally found a maximum zone length of about 4.5 mm; square rods 4.95 mm across gave a maximum zone length of about 5 mm [5].

TABLE 1. Conditions and results of experiments for evaporation of molten CdTe

Experiment no.	Excess cadmium[a] ($mg\ cm^{-3}$)	Hot wall temperature[b] (°C)	Time[c] (h)	Result
1	11.2	850	0.5	Heavy deposit
2	11.6	850	0.5	Moderate deposit
3	12.0	850	1.0	Moderate deposit
4	13.4	850	2	Moderate deposit
5	15.9	850	2	Moderate deposit
6	11.2	900	4	Light deposit
7	13.4	900	4	Light deposit
8	15.0	900	6	Light deposit
9	11.2	950	15	Light deposit
10	11.2	950	16	Light deposit
11	13.4	950	16	Light deposit
12	10.7	1000	—	Furnace burned out

[a]Milligrams of CdTe added to the ampoule per cubic centimeter of free volume inside the ampoule. The volume of the CdTe molten zones was about 0.06 cm^3; *i.e.* the volume of a square CdTe rod of 0.35 cm per side and 0.5 cm long.
[b]Time to observe deposits on the ampoule wall.
[c]The hot wall temperature was the temperature of the furnace used to heat the ampoule and was measured by two type-R thermocouples positioned near the ampoule wall.

2.2. Evaporation control

One of the major obstacles to floating-zone melting of CdTe is the high vapor pressures of cadmium (0.8 atm) and tellurium (0.4 atm) over its stoichiometric melt at the melting point [4]. If condensation can occur elsewhere, these high vapor pressures will cause both cadmium and tellurium to rapidly evaporate from the melt. When this condensation occurs on the ampoule wall above and below the zone heater, the zone length becomes difficult to control for subsequent growth, since the deposit seriously interferes with the heat transfer between the zone heater and the rod. To successfully conduct floating-zone melting of CdTe, evaporation must be eliminated.

According to Kweeder [12], CdTe evaporation can be controlled by heating the wall of the growth ampoule containing the CdTe rod to a high temperature combined with the addition of excess cadmium to the ampoule. (The temperature of the ampoule wall is henceforth called the hot wall temperature.) Therefore, we tested different hot wall temperatures combined with various amounts of excess cadmium added to the ampoule. The hot wall temperature was measured by two type-R thermocouples positioned near the ampoule wall. After the CdTe zone formed, the length of time was recorded at which deposition on the ampoule was observed. Square CdTe rods 3.5 mm across were used in these experiments.

All the experimental conditions and results are listed in Table 1. Since the volume of the molten zone was about the same in each experiment (about 0.06 cm^3, estimated by the volume of a solid square rod 3.5 mm wide and 5 mm long), the amount of excess cadmium added to the ampoule is given here as the amount of excess cadmium divided by the amount of free volume inside the ampoule. No hot wall temperature higher than 1000 °C was tested owing to the maximum service temperature of the top furnace. No experiment with 15.9 mg or more excess cadmium per cubic centimeter of free volume inside the ampoule was performed owing to concern about the possibility of ampoule rupture. From experiments 1, 6 and 9 it was found that, with the same amount of excess cadmium, the time before condensation was elongated by increasing the hot wall temperature. However, when using the same hot wall temperature, the time before condensation was unchanged, even by adding 20% more excess cadmium in experiment 11 than in experiment 10. In addition, with different hot wall temperatures, the deposit-free time was dramatically reduced from 16 to 2 h, even though 42% more cadmium was added in experiment 5 than in experiment 10. The hot wall temperatures used in experiment 5 and 10 were 850 °C and 950 °C respectively. The results showed that evaporation of the CdTe melt can be controlled by the hot wall–excess cadmium technique and that the length of time which the ampoule stayed clear was primarily affected by the hot wall temperature. However, experiments also showed that a higher hot wall temperature required more energy, although it reduced the power

requirement for the zone heater to maintain a molten zone.

The correct explanation for the success of the hot wall–cadmium overpressure technique is uncertain; we speculate as follows. With a high cadmium pressure inside the ampoule, the CdTe melt is no longer stoichiometric, because most of the excess cadmium will go into the molten zone until the vapor reaches equilibrium with the melt; a cadmium-rich melt results. According to the P–T–x phase diagram for CdTe [13], the melting point decreases and the tellurium vapor pressure decreases dramatically as the melt becomes rich in cadmium. In addition, excess cadmium interferes with the mass transfer of tellurium. This has been demonstrated in vapor growth experiments [14]. Therefore, the vapor pressure of tellurium is greatly reduced at potential condensation sites and the driving force $P_{Cd}P_{Te_2}{}^{1/2}$ for nucleation and growth of CdTe is reduced. (Here P_{Cd} is the partial pressure of cadmium and P_{Te_2} is the partial pressure of Te_2.)

2.3. Maximum zone travel rate

A higher zone travel rate is favored for lower energy consumption, but there exists a maximum zone travel rate. For example, Eyer *et al.* [15] experimentally determined the maximum zone travel rate in float-zoning silicon using a double-ellipsoid mirror furnace. In their study, they considered the maximum zone travel rate from the heat transfer point of view as follows. For a constant power supply, as the zone travel rate is increased, the melting interface becomes increasingly convex toward the melt, forming a steep solid cone. Eventually, the cone touches the freezing interface to form a "solid bridge" and there is no longer a complete molten zone. Therefore, they concluded a maximum zone travel to be that which causes a solid bridge.

Several experiments were performed to find the maximum zone travel rate in CdTe floating-zone melting. Since the zone motion was accomplished by moving the ampoule in the present experiments, the zone travel rate described here is referred to as the ampoule translation rate. The maximum zone travel rate in our CdTe floating-zone melting was found experimentally to be 6 mm h^{-1}. However, this maximum zone travel rate was not determined by the formation of a solid bridge, but by the melt running down. Initially, a CdTe molten zone was created in a CdTe rod 3.5 mm square at a hot wall temperature of 950 °C and an ampoule rotation rate of 6 rev min^{-1}. Then, the ampoule was translated downward at a different rate in each experiment. When the ampoule was translated at 6 mm h^{-1}, the CdTe molten zone elongated and the molten CdTe bulged out in the lower portion of the zone. Eventually, the CdTe melt dripped down and two CdTe molten drops were left on the two remaining CdTe rods.

2.4. Crystal growth and characterization

Some 40 experiments were carried out to grow CdTe crystals by floating-zone melting using the ground-based apparatus depicted in ref. 5. The ampoule was translated at rates ranging from 1 to 4 mm h^{-1}, while the ampoule was rotated at rates ranging from 0 to 6 rev min^{-1}.

To create successfully a complete CdTe molten zone, it was necessary to rotate the ampoule to heat the feed rod uniformly. Without rotating the ampoule, the surface of the square rod always melted first at one of the four edges. The molten portion then propagated toward one or two adjacent sides, as shown in Fig. 1(a). Upon further heating, more CdTe melted, some molten CdTe ran down the solid rod below the molten portion, and the remainder of the melt bulged out in the lower region of the molten portion. Subsequently, the molten portion spread out and penetrated into the rod with a thin solid portion left, as shown in Fig. 1(b). Finally, the square CdTe rod melted through and two CdTe molten drops were left on the two remaining rods, as shown in Fig. 1(c). Experiments showed that, when rotating the ampoule at 6 rev min^{-1}, melting usually began simultaneously at the four edges of the rod. Even though sometimes melting did not start at the four edges simultaneously, the other solid edges melted a short time later. Subsequently, a band of molten CdTe formed and a complete, stable zone was still obtained. When rotating the ampoule at a rate lower than 6 rev min^{-1}, a CdTe molten zone was sometimes generated; however, the molten zone was often asymmetric and still often failed to form. When the ampoule was rotated at a rate above 6 rev min^{-1}, melting started at the four edges simultaneously, but the ampoule wobbled slightly; the molten zone always broke about 20 min after it formed. Figure 2 shows three CdTe rods grown by the floating-zone technique at different ampoule rotation rates.

After the growth was completed, the crystals grown were cooled in two manners: one method was to quench, *i.e.* shut down the furnace after finishing growth; the other method was to cool to 300 °C at a rate of 40 °C h^{-1}. However, most of the growth experiments were unsuccessful, owing either to the failure to generate a complete zone or to the melt dripping down during the ampoule translation. Only 14 experiments succeeded in yielding a cylindrical CdTe rod with a length of more than 2 cm. Of the resulting rods, 12 were single crystals with twins.

Rods grown at 40 °C h^{-1} yielded a much lower etch pit density (EPD), ranging from 2.2×10^3 to

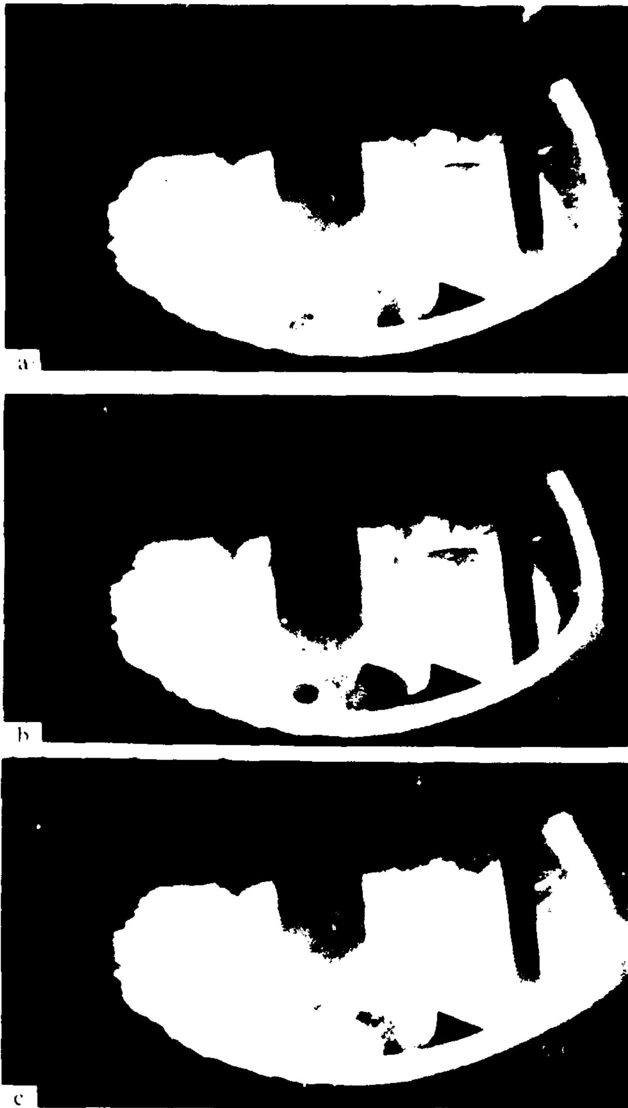

Fig. 1. Photographs showing how zone generation failed when the ampoule was not rotated.

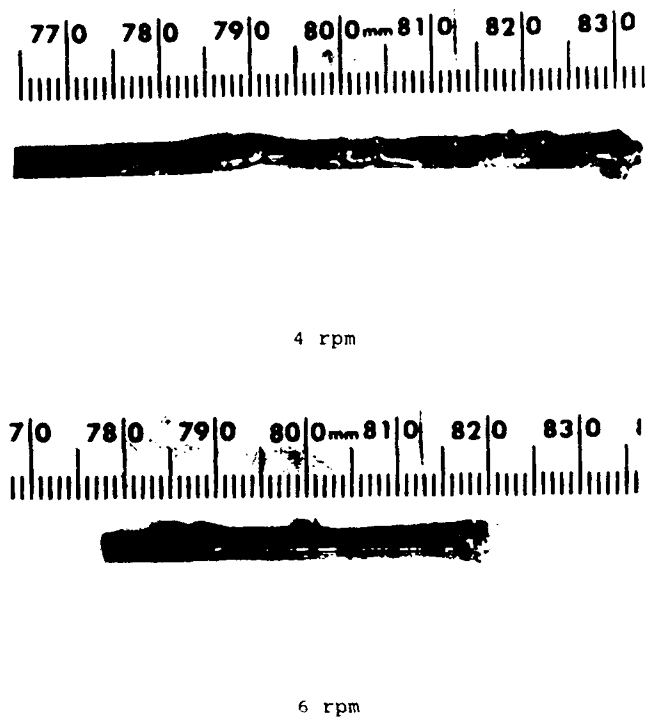

Fig. 2. Photographs of three CdTe rods grown by the floating-zone technique at different rotation rates. The rods were grown at an ampoule translation rate of 2 mm h⁻¹ and with hot wall temperature of 950°C.

8.2×10^2 cm⁻², than those obtained by quenching, which had EPD values ranging from 5.4×10^4 to 8.7×10^4 cm⁻². The pits formed in these rods were randomly distributed, which was different from the cellular structure observed in CdTe produced by the vertical Bridgman technique [17]. A lower EPD was obtained at the periphery of our rods.

The resistivity as grown was 10^6 to 10^8 Ω cm and the crystal grown was n type. The γ-ray response on a wafer 2 mm thick with the highest resistivity (4×10^8 Ω cm) had a very high noise.

3. Power requirement model

To design the floating-zone flight hardware for processing of larger diameter CdTe rods in space, it is necessary to have some idea of the power requirements. The low surface tension and high density of CdTe limit the rod diameter to about 5 mm in terrestrial experiments. Therefore, we performed an approximate heat transfer analysis to predict the power requirement [5]. This model was used to predict the power requirement for the zone heater to maintain a static CdTe molten zone under five different conditions. The power required by the zone heater was also measured by experiments under these five conditions. Table 2 lists the theoretical and experimental results. The power requirement predicted by the model differed by 5% to 30% from that measured in the experiments. This discrepancy might have been caused by violation of the assumptions made in the model. The surface area of the zone is one of the primary factors to determine the power requirement. The surface area of the zone was assumed to be $2\pi R_1 L_0$, where R_1 is the rod radius and L_0 is the zone length. The surface area of the zone, however, was not necessarily $2\pi R_1 L_0$, because square CdTe rods were used in experiments, the zone shape was not actually cylindrical, and the volumetric properties changed upon melting. In addition, the quartz ampoule was assumed to be totally transparent to all radiation, but it actually transmits about 90% radiation with a wavelength shorter than 2.5 μm, though it profoundly absorbs the rest of the radiation [16].

TABLE 2. Experimental and theoretical results for power required by the zone heater to maintain a CdTe molten zone under different operation conditions

Rod radius R_0 (= R_1) (cm)	0.25	0.25	0.25	0.25	0.25
Zone heater radius R_2 (cm)	1.0	1.0	1.0	1.0	1.1
Furnace radius R_4 (cm)	3.0	3.0	3.0	3.0	3.0
Zone heater length L_2 (cm)	1.5	1.5	1.5	1.5	1.2
Furnace length L_4 (cm)	40	40	40	40	40
Furnace temperature T_4 (°C)	970	950	900	850	920
Zone heater insulation thickness X (cm)	1.0	1.0	1.0	1.0	1.5
Power requirement predicted by the model (W)	81	90	114	135	105
Power requirement measured by experiment (W)	86	97	120	173	137

TABLE 3. Relationship between estimated power required by the zone heater and the CdTe rod radius under different conditions

	$T_4 = 950$ °C	$T_4 = 900$ °C	$T_4 = 850$ °C
$R_2 = 4.0R_1$, $\varepsilon_1 = 0.15$	$P \propto R_1^{1.52}$	$P \propto R_1^{1.62}$	$P \propto R_1^{1.67}$
$R_2 = 3.0R_1$, $\varepsilon_1 = 0.15$	$P \propto R_1^{1.66}$	$P \propto R_1^{1.70}$	$P \propto R_1^{1.72}$
$R_2 = 2.4R_1$, $\varepsilon_1 = 0.15$	$P \propto R_1^{1.71}$	$P \propto R_1^{1.71}$	$P \propto R_1^{1.73}$
$R_2 = 4.0R_1$, $\varepsilon_1 = 0.35$	$P \propto R_1^{1.83}$	$P \propto R_1^{1.82}$	$P \propto R_1^{1.82}$
$R_2 = 4.0R_1$, $\varepsilon_1 = 0.55$	$P \propto R_1^{1.87}$	$P \propto R_1^{1.87}$	$P \propto R_1^{1.86}$
$R_2 = 4.0R_1$, $\varepsilon_1 = 0.7$	$P \propto R_1^{1.90}$	$P \propto R_1^{1.89}$	$P \propto R_1^{1.88}$

Here R_1 is the rod radius, R_2 is the inside radius of the zone heater, T_4 is the hot wall temperature, P is the power requirement for the zone heater and ε_1 is emissivity of the solid CdTe.

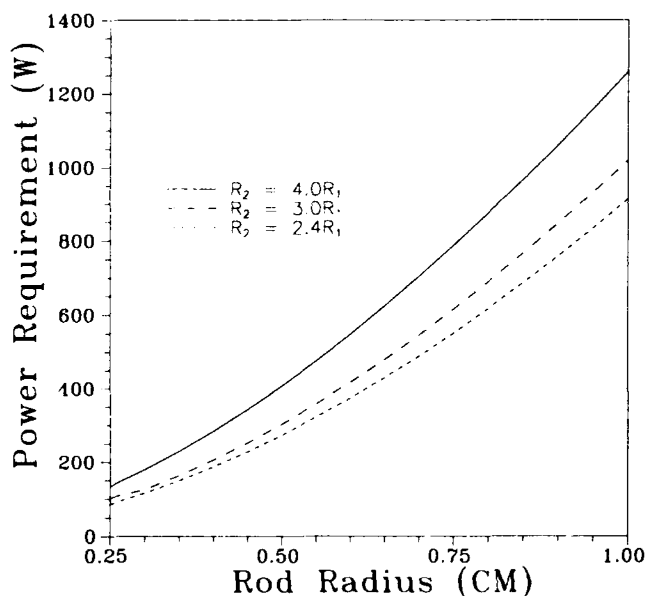

Fig. 3. Estimated power requirement for the zone heater *vs.* the radius of the CdTe rod and gaps between the rod and the zone heater. Here R_1 is the rod radius and R_2 is the inside radius of the zone heater.

The power requirement for the zone heater was also predicted by the model for larger CdTe rods. Figure 3 shows a plot of the power required by the zone heater *vs.* the radius of the CdTe rod for three different gaps between the zone heater and the CdTe rod. The gap between the zone heater and the CdTe is defined as ($R_2 - R_1$), where R_1 is the rod radius and R_2 is the inside radius of the zone heater. The furnace temperature was 900 °C. All the geometric dimensions were proportionally enlarged when the rod radius was increased. For larger rods, the power required by the zone heater depends on many factors, such as the furnace temperature, the gap between the rod and the zone heater, the radiative properties of the materials etc. Table 3 lists the relationship between the power requirement and the rod radius for several different conditions. It shows that the power requirement for the zone heater to maintain a static molten zone falls in the range from $R_1^{1.5}$ to $R_1^{1.9}$.

Acknowledgments

This work was supported by the NASA Center for Commercial Development of Space managed by Battelle-Columbus Laboratories. We are grateful to Alan Markworth and Frank Jelinek for this support and for their encouragement. We express our appreciation to II-VI Incorporated for donating the square CdTe rods used in this work.

References

1 W. R. Wilcox, F. M. Carlson, D. K. Aidun, V. White, W. Rosch, W. M. Chang, R. Shetty, A. Fritz, R. Balasubramanian, G. Rosen, J. Kweeder and C. Wen, *Acta Astronaut.*, 25 (8–9) (1991) 505.

2 D. Schwabe, A. Scharmann, F. Preisser and R. Oeder, *J. Cryst. Growth*, 43 (1978) 305.

3 W. R. Wilcox, *Proc. 29th Aerospace Sciences Meet., Reno, NV, January 1991.*

4 J. B. Mullin and B. W. Straughan, *Rev. Phys. Appliq.*, *12* (1977) 151.
5 W. M. Chang, Ground-based experiments and theory in preparation for floating zone melting of cadmium telluride in space, *PhD dissertation*, Clarkson University, Potsdam, NY, 1992.
6 W. Heywang, *Z. Naturforsch., Teil A*, *11* (1965) 283.
7 H. W. Schadler, in J. J. Gilman (ed.), *The Art and Science of Growing Crystals*, Wiley, New York, 1963.
8 R. Shetty, R. Balasubramanian and W. R. Wilcox, *J. Cryst. Growth*, *100* (1990) 51.
9 V. M. Glazov, S. N. Chizhevskaya and N. N. Glagoleva, *Liquid Semiconductors*, Plenum, New York, 1969.
10 J. L. Duranceau and R. A. Brown, *J. Cryst. Growth*, *75* (1986) 367.
11 B. M. Anisyutin, *J. Appl. Mech. Tech. Phys.*, *29* (1988) 367.
12 J. A. Kweeder, Evaporation control in floating zone refining of cadmium telluride, *MS Thesis*, Clarkson University, Potsdam, NY, 1988.
13 J. B. Mullin and B. W. Straughan, *Rev. Phys. Appl.*, *98* (1976).
14 N. Yellin and S. Szapiro, *J. Cryst. Growth*, *73* (1985) 77.
15 A. Eyer, B. O. Kolbesen and R. Nitsche, *J. Cryst. Growth*, *57* (1982) 145.
16 D. Langbein, *Proc. 6th Euro. Symp. on Material Sciences under Microgravity Conditions, Bordeaux, France, December 1986.*
17 D. F. Weirauch, *J. Electrochem. Soc.*, *132* (1985) 250.

Materials Science and Engineering, B16 (1993) 29-39

Bridgman growth and assessment of CdTe and CdZnTe using the accelerated crucible rotation technique

P. Capper, J. E. Harris, E. O'Keefe, C. L. Jones, C. K. Ard*, P. Mackett and D. Dutton

Philips Infrared Defence Components, PO Box 217, Southampton, Hants SO9 7QG (UK)

Abstract

The Bridgman growth process for CdTe has been extended by applying the accelerated crucible rotation technique (ACRT). Modelling using ACRT has been extended to the 50 mm diameter required to produce grains large enough to yield CdTe (and $Cd_{0.96}Zn_{0.04}Te$) slices suitable for use in liquid phase epitaxy of $Cd_xHg_{1-x}Te$ (CMT) layers. Two regimes are identified: ACRT parameter combinations which give maximum fluid velocities and that which maintains stable Ekman flow. Growth of crystals shows that larger single crystal regions are obtained when the Ekman flow is stable. Effects of changing the ampoule base shape have also been investigated. Techniques have been developed to produce 20 mm × 30 mm substrates oriented close to the (111) direction. Assessment of these samples has included IR transmission, IR microscopy, defect etching, X-ray topography and X-ray diffraction curve width measurements. Chemical analyses have been carried out to determine impurity levels and matrix element distributions. Good quality CMT epitaxial layers, as demonstrated by good surface topography, electrical data and chemical analyses, have been grown onto material produced in this study.

1. Introduction

There has been considerable progress in the epitaxial growth techniques of metallo-organic vapour phase epitaxy (MOVPE) and molecular beam epitaxy (MBE) for $Cd_xHg_{1-x}Te$ (CMT) using non-lattice matched substrates, *e.g.* GaAs. Despite this, substrates based on CdTe are still widely used for liquid phase epitaxy (LPE) growth and for some MOVPE and MBE growth also. Lattice matching by adding small amounts (3%-4%) of Zn and/or Se into CdTe produces higher quality epitaxial layers. Bridgman growth has been used since the earliest days of CdTe development and is still used by the major world suppliers of substrates [1, 2]. In the work reported here, Bridgman growth refers to the vertical configuration, although the horizontal process is also being developed by several groups [1, 3-5].

The major issues in substrate development, as summarized by Johnson [1], include size, purity, stoichiometry, crystallinity, seeding and economics. These are interdependent but, by rating growth techniques in these terms, it is concluded in ref. 1 that both vertical and horizontal Bridgman growth, with overpressure control, are the preferred methods. In these techniques multizone furnaces are needed to control the Cd partial pressure and the thermal flows [1, 6]. We have adopted a different approach based on the addition of the accelerated crucible rotation technique (ACRT) to the simple Bridgman process. The ACRT was originally applied to CdTe by Wald and Bell [7] who used the travelling heater method (THM). Since that early use of ACRT, we have developed the technique for the growth of CMT [8-17].

This paper reports on the application of ACRT to CdTe/CdZnTe growth using ampoule diameters large enough to produce substrate material for LPE growth of CMT, *i.e.* 20 mm × 30 mm in our case. Fluid flows resulting from ACRT were modelled using simulations and estimated from equations developed in ref. 10. Growth of crystals 50 mm in diameter of both CdTe and $Cd_{0.96}Zn_{0.04}Te$ will be described as will the results of changing the ampoule base shape. It will be shown that ACRT increases the volume of single crystal material compared with those of non-ACRT crystals. Techniques for producing substrates oriented close to the (111) direction will be outlined. Assessment methods of the samples have included IR transmission, IR microscopy, defect etching, X-ray topography and diffraction curve measurements and chemical analyses. The properties of our material will be compared with those reported in the literature. The ultimate test of the material is in the LPE growth of CMT, and good

*Present address: II-VI Inc., 375 Saxonburg Blvd., Saxonburg, PA 16056, USA.

0921-5107/93/$6.00

© 1993 - Elsevier Sequoia. All rights reserved

quality layers have been produced on ACRT-grown CdTe and CdZnTe substrates.

2. Accelerated crucible rotation technique

2.1. Application to CMT

In order to improve x uniformity in CMT, a means of stirring melts contained in sealed ampoules was needed. The ACRT of Scheel and co-workers [18–20] was used because it increased the size of crystals and gave stable growth rates [7]. We have shown how the ACRT improves both radial and axial x uniformity in CMT [9, 12]. A secondary benefit of the ACRT was a decrease in the number of major grains [12]. Interface depths in quenched crystals were found to be less for ACRT crystals and increasing the maximum rotation rate Ω_0 produced minimum interface depths for $25 < \Omega_0 < 60$ rev min^{-1} [21]. Quenching studies in flat-based ampoules revealed a flatter interface and single crystal material [13], demonstrating the power of Ekman stirring near the interface. This was confirmed in crystals grown at slow rates in ref. 22. Crystals grown at various rotation rates showed small radial variations for $12 < \Omega_0 < 60$ rev min^{-1} but, outside this range, x variations and crystallinity deteriorated, agreeing with the interface depths [13]. If the trends seen in applying the ACRT to CMT growth are found in the case of CdTe, then larger grains would be expected.

2.2. Modelling

From the paper by Schulz-Dubois [20] three processes are seen to occur on acceleration and/or deceleration. These are as follows.

(a) *Transient couette flow* occurs on rapid deceleration (spin-down), particularly in tall containers. Liquid adjacent to the container walls decelerates faster than does liquid in the bulk, and centrifugal forces drive the inner portions of liquid towards the wall. Horizontal vortices form in counter-rotating pairs.

(b) *Spiral shearing* occurs on both spin-down and spin-up, and is again caused by fluid at the walls changing velocity faster than liquid in the bulk. It is characterized by the thickness d of a layer at the wall where the rotation rate is half its initial value and t_1, the time taken by the central part of the fluid to halve its velocity.

$$d = R(E\Omega_0 t)^{0.5} \approx (\eta t/\rho)^{0.5} \tag{1}$$

$$t_1 = 0.1(E\Omega_0)^{-1} \approx 0.1\rho R^2/\eta \tag{2}$$

where t is the time after container stops rotating (s), R the container radius (cm), Ω_0 the maximum rotation rate (rev min^{-1}), ρ the fluid density (g cm^{-3}), η the dynamic viscosity of the fluid (g cm^{-1} s^{-1}) and E the Ekman number ($\eta/\Omega_0 R^2\sigma$).

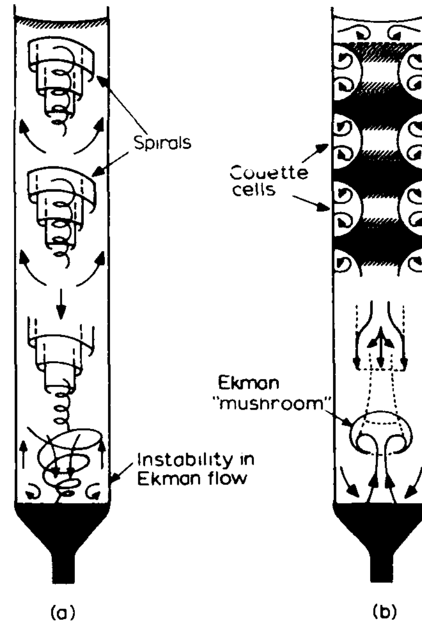

Fig. 1. ACRT simulations in flat-based ampoule for (a) spin-up and (b) spin-down (from ref. 11).

The number of spiral arms is given by

$$N = \Omega_0 \rho R^2/16\pi\eta \tag{3}$$

with separation

$$\Delta r = 4\pi\eta/\rho\Omega_0 r \tag{4}$$

where r is the radius of the point in question.

(c) *Ekman flow* occurs above a solid boundary placed perpendicular to the axis of rotation. During spin-up, fluid is forced to the side walls and returns more slowly through the bulk; the reverse occurs on spin-down.

The Ekman layer thickness is given by

$$d_E = (\eta/\Omega_0\rho)^{0.5} \tag{5}$$

with maximum radial fluid velocity of

$$V = \Omega_0 R \tag{6}$$

and maximum vertical fluid velocity of

$$W = (\eta\Omega_0/\rho)^{0.5} \tag{7}$$

The flow decreases within a time

$$\tau_E = R(\rho/\eta\Omega_0)^{0.5} \tag{8}$$

Figure 1 depicts these flows as seen in water simulation trials [11]. All three flow patterns existed, as predicted, and showed qualitative agreement with the parameters given in eqns. (1)–(8) for liquids with similar properties to CMT melts. The most vigorous stirring arose via Ekman flow at the container base.

Brice *et al.* [10] have reviewed the models developed for ACRT-induced flows. While recognizing that ther-

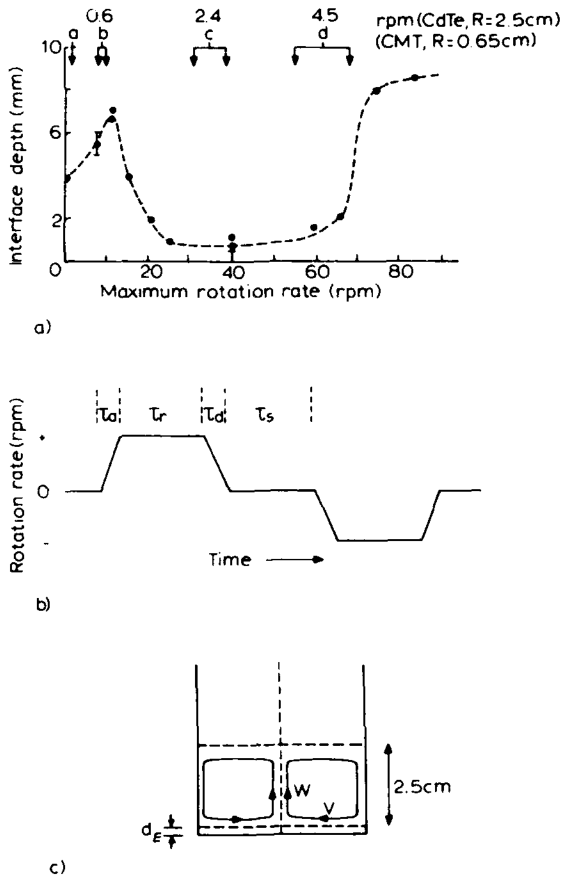

Fig. 2. (a) Interface depth *vs.* ACRT maximum rotation rate for CMT (from ref. 14) and estimates for CdTe from Table 1. (b) ACRT rotation sequence and (c) dimensions and flow velocities in Ekman region during spin-down (referred to in Table 1).

mal and density-driven flows also occur in real systems, they identify three flow regimes as the acceleration and/or deceleration rate increases. (This is equivalent to changes in the maximum rotation rate if the acceleration or deceleration time is kept small, as it usually is.) For small accelerations, axially symmetric fluid flows increase the symmetry of the heat and mass flows. Moderate accelerations produce axial and radial flows at the base (for a height of R to $2R$) which stir fluid in this Ekman region only. Large accelerations give rise to unstable asymmetric flows which can lead to time-dependent mixing. The system is characterized by the dimensionless Reynolds number

$$Re = R^2 \Delta\Omega_c \rho/\eta \quad (9)$$

where $\Delta\Omega_c$ is the step change in rotation rate (rev min^{-1}). Table 1 (from ref. 14) lists the critical Reynolds numbers and corresponding rotation rates for the value of R used in this study (25 mm) and an η/ρ ratio of 0.006 cm^2 s^{-1} which is typical of CdTe melts [23]. These values of Re_c are superimposed onto the interface depth plot for the CMT case (Figure 2(a)). Once Ekman flow is fully established, the interface depth decreases to a minimum. As Re increases further, Ekman flow becomes unstable and the interface depth increases. Clearly, too much melt mixing can be produced by some ACRT conditions, leading to a deterioration in crystal properties.

The ACRT rotation sequence used is depicted in Fig. 2(b) along with the velocities and distances in the Ekman region (spin-down) (Fig. 2(c)). Table 2 lists the relevant parameters and the desired magnitudes of these interrelated variables. Figure 3 shows the dependence of the parameters defined in eqns. (3)–(8) on rotation rate. Rapid acceleration and/or deceleration (in 1–5 s) is easily achieved and the criterion τ_a, $\tau_d \ll \tau_E$ is obtained at any rotation rate. The Ekman layer thickness should be small (less than 0.05 cm),

TABLE 1. Critical Reynolds number and corresponding critical rotation rates for the ACRT in ampoules 25 mm in radius with $\eta/\rho = 0.006$ cm^2 s^{-1}

Event	Re_c	Ω_c (rev min^{-1})
Ekman flow starts[a]	15	0.1
Ekman flow fully developed[b]	70	0.6
Couette flow unstable[c]	270	2.4
Ekman flow unstable[d]	500	4.5

[a]From eqn. (13) of ref. 10.
[b]Corresponds to boundary thickness of about $0.2z_{max}$ (z_{max} is maximum height of Ekman flow).
[c]From eqn. (16) of ref. 10 shown in Fig. 18 of ref. 10).
[d]From Section 2.4 of ref. 10 (shown in Fig. 18 of ref. 10).

TABLE 2. ACRT parameters

Parameter	Figure	Aim
1. Acceleration/deceleration time τ_a, τ_d	2(b)	$\tau_a, \tau_d \ll \tau_E$ (to maximize Ekman flow)
2. Ekman time τ_E	3	$\tau_E \gg \tau_a, \tau_d$
3. Ekman layer thickness d_E	3	$d_E < 0.05$ cm
4. Vertical/horizontal fluid velocities W, V	2(c)	$V\tau_E$, $W\tau_E > R$ (to pass Ekman volume through Ekman layer)
5. Separation of spiral arms Δr	3	$\Delta r < 0.1$–0.01 cm (to enable homogenization via diffusion)
6. Run/stop times τ_r, τ_s	2(b)	$\tau_r, \tau_s \leq \tau_E$ (to maximize use of Ekman flow)
7. Reynolds number Re	2(a)	Re < 500 (for stable Ekman flow)

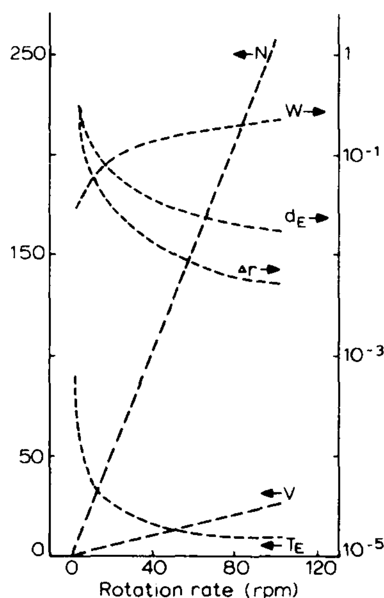

Fig. 3. ACRT parameters for CdTe in ampoules 50 mm in diameter, referring to eqns. (3)–(8).

necessitating rotation rates of more than 20 rev min^{-1}. The horizontal flow velocities are much more than R/τ_E and the vertical flow velocities are approximately R/τ_E for rotation rates up to 100 rev min^{-1}, ensuring that the "Ekman volume" passes through the Ekman layer in each ACRT cycle. A rotation rate of over 50 rev min^{-1} would be required to reduce Δr to the level needed to homogenize the fluid by diffusion. Both these run (at maximum rotation rate) and stop times can be set to τ_E or less, to ensure decaying Ekman flow is not present for significant periods while maintaining high mixing levels.

The above criteria have been met for the growth of CdTe crystals (see Section 3.2). Unfortunately, as can be seen from Fig. 2(a), rotation rates over 5 rev min^{-1} will lead to high Re numbers and consequent unstable Ekman flow. Two quite separate flow regimes can therefore be identified: ACRT parameter combinations which maximize flow (items 1–6 in Table 2) and that which maintains stable Ekman flow (item 7 in Table 2). With $R=25$ mm, combinations of 40 rev min^{-1} with 15 s run and stop times and 4 rev min^{-1} with 50 s run and stop times correspond to the two regimes respectively. Couette flows will occur, on spin-down, for all rotation rates used and should suppress nucleation on ampoule walls.

3. Growth and substrate fabrication

3.1. Overall process

In our Bridgman process, elemental Cd (etched in nitric acid) and cleaved pieces of Te (plus etched Zn for

TABLE 3. Growth conditions of crystals grown

Number	Stoichiometry	Base shape	Rotation parameter (rev min^{-1} s^{-1})
CT50	No excess	Conical	5
CT51	No excess	Conical	5
CT52	No excess	Conical	5
CZT53	No excess	Conical	5
CT55	No excess	Conical	±40/15
CT56	29% Cd excess	Conical	±10/12
CT58	0.5% Cd excess	Flat	±4/50
CT59	0.5% Cd excess	Necked	±4/50
CZT65	No excess	Necked	±4/50
CZT67	1% Te excess	Necked	±4/50
CZT69	1% Te excess	Necked	±4/50

CdZnTe crystals) are loaded into a SiO_2 ampoule which has been coated with a layer of C by pyrolysing propane at 1000 °C. Carbon coating of ampoules prevents charges sticking to ampoule walls [24, 25] and Holland [26] has proposed that it may also reduce isotherm concavity. Melting takes place by slowly ramping the temperature to 820 °C, holding for 24 h to ensure complete reaction, then continuing the ramp to 1150 °C. After holding at this temperature for a few hours, growth takes place by lowering the ampoule at 1 mm h^{-1}. Slow rotation about the vertical axis is used for non-ACRT crystals. Growth took place in the microprocessor-controlled equipment used by Coates *et al.* [15] in ACRT growth of CMT. In addition to the more flexible rotation facility, the rotation parameters, growth rate and temperature are monitored and recorded. The "no-mixing" temperature profile, in which the temperature increases monotonically into the furnace [16], gave shallow temperature gradients which several groups suggest leads to a less stress-induced structure [2, 6, 27, 28].

After cutting away the SiO_2 ampoule above the crystal, the crystal was slid out of the ampoule. Etching in nitric acid removed the excess Cd and abrasion revealed the grain structure and the major twins. Careful maps of this structure acted as a guide in crystal cutting. As the aim was to obtain samples of dimensions 20 mm × 30 mm, crystals were normally cut into 30–35 mm sections prior to slicing parallel to twins. Segments were cut and measured on a Laue camera for orientation. Misorientations from the (111) direction were measured using the technique of Fewster [29]. The crystal segment was transferred to a multibladed cutting machine for slicing using an abrasive slurry, as used for CMT and described by Fynn and Powell [30]. These slices were then examined and areas of 20 mm × 30 mm marked. A diamond wire saw was used to dice the 20 mm × 30 mm samples to

an accuracy of ±0.01 mm. Table 3 summarizes the crystals grown in this study.

3.2. CdTe crystals

Crystals 50 to 53 were grown with a constant 5 rev min^{-1} to act as a base-line to compare with ACRT crystals. Figure 4 shows the grain map for crystal 52. A large grain propagates from the tip to the tail end. Slicing parallel to the twins produced several substrates. Clearly, the precise three-dimensional shape of the largest grain and the disposition of the twins dictates the number of substrates. The other non-ACRT crystals 50 and 51 consisted of small grains and produced no 20 mm × 30 mm substrates.

Crystal 55 was grown with ±40 rev min^{-1} and 15 s run and stop times which should maximize fluid velocities but lead to unstable Ekman flow (see Section 2.2). This crystal consisted of many small grains, suggesting stable Ekman flow is required for large grains. No substrates were obtained.

An intermediate combination of ACRT parameters, *i.e.* ±10 rev min^{-1} and 12 s run and stop times, was used to grow crystal 56. The aim was to confirm whether rotation rates less than 5 rev min^{-1} were necessary for stable Ekman flow, as shown in Fig. 2(a). A weighing error was made which led to this crystal having a 29% Cd excess. This caused polycrystalline growth but, as the excess Cd could not be accommodated in the lattice, it floated on the melt surface and solidified on top of the crystal. The crystal was quenched while the Cd was still molten ($T \approx 400$ °C) and the top of the crystal had the features shown in Fig. 5. (One half has been etched in nitric acid to reveal the features.) These are believed to be spiral sets formed by the ACRT and provide the first direct evidence that such flows exist. The spiral separation is about 0.1 cm at the periphery increasing to about 0.5 cm near to the centre, as predicted from eqn. (4). The number of spiral arms is also in qualitative agreement with eqn. (3).

Crystal 58 was grown using ±4 rev min^{-1} with 50 s run and stop times. This rotation rate should ensure stable Ekman flow while the run and stop times maximize the effect of Ekman mixing. The flat ampoule base ensured that Ekman flow was maximized at the first-to-freeze end. The grain map (Fig. 6) revealed a single grain running the entire length. The central cut shows one dominant grain, albeit with a twin running along the growth axis. Comparing Figs. 4 and 6 suggests that the ACRT increases the single crystal region.

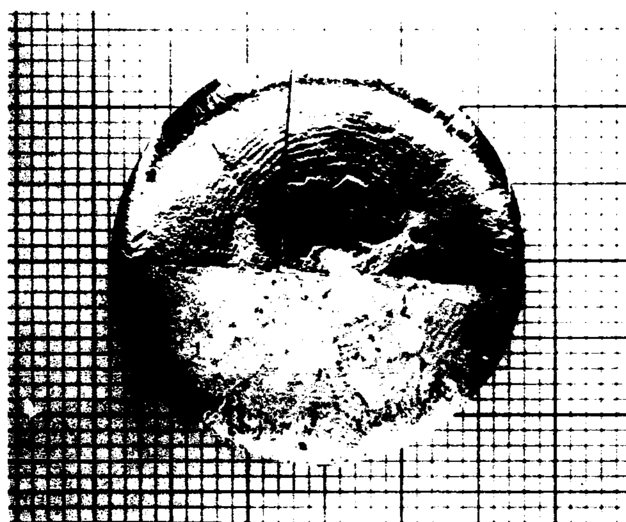

Fig. 5. Spirals frozen-in on CT56.

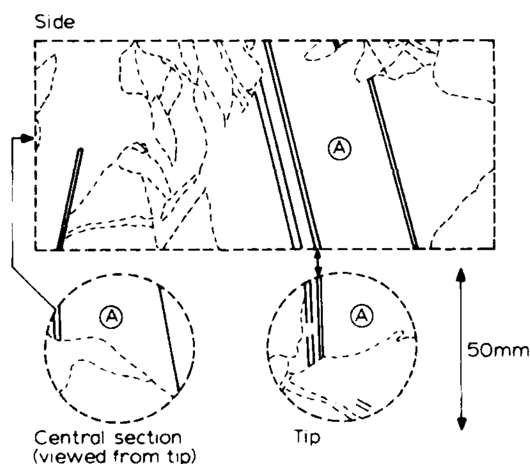

Fig. 4. Grain map of non-ACRT 50 mm crystal showing tip and tail ends after initial cuts, grains and twins (continuous straight lines) around the crystal periphery (side) and in the centre after cut.

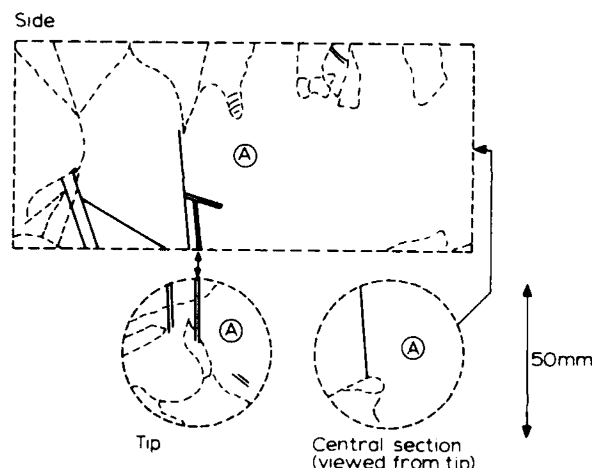

Fig. 6. Grain map of ACRT 50 mm crystal in flat-based ampoule showing tip and tail ends after initial cuts, grains and twins (continuous straight lines) around the crystal periphery (side) and in the centre after cut.

An attempt was made to improve the nucleation conditions at the first-to-freeze end by using a constriction, termed "necked" here. This type of constriction was used by Horowitz *et al.* [31] who grew improved Rb_2MnCl_4 using the ACRT. Other groups have used similar means of restricting grain growth in CdTe [27, 32], while several attempts have been made at (111) seeding [33, 34]. Figure 7 shows the result of using a "necked" ampoule base in our system. The constriction has succeeded in reducing the number of grains propagating through to the full diameter region. At this point Ekman flow dominates and, if stable, should minimize the nucleation of secondary grains. Figure 7 shows that this is partially successful. The grain map of the tip section shows some grains on one side of the crystal but grain A covers some 70% of the area and propagates through to the tail end. The central section cut shows grain A still dominates 70% of the area. Several twins can be seen but, as in crystal 58, they lie roughly parallel to the growth axis. This means that the largest single crystal slices in the (111) direction were potentially some 65 mm × 50 mm in size. As the aim was to produce 30 mm × 20 mm substrates, this crystal was cut in half to maximize their number. Both sections produced 30 mm × 20 mm substrates. In our view, this type of crystal is preferred to ones employing seeding. In the latter case, (111) slices 50 mm in diameter can only yield a single 30 mm × 20 mm substrate. Crystals such as 59 have the potential to yield several (111) slices almost 65 mm × 50 mm in size and many more between this and 30 mm × 20 mm from the sides of the crystal. Several slices produced two 30 mm × 20 mm substrates, which is only achievable, in crystals 50 mm in diameter, if the twins lie nearly parallel to the growth axis. Sliding-boat Te-rich LPE requires regular, rectangular or square substrates so the benefit of the (111) direction lying parallel to the growth axis is clear.

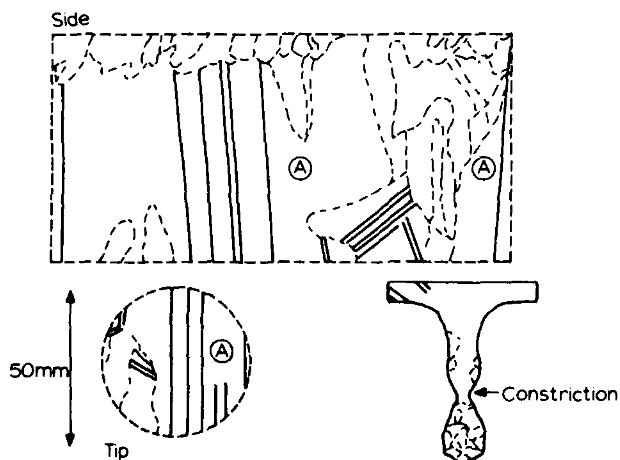

Fig. 7. Grain map of ACRT 50 mm crystal in necked-base ampoule showing tip and tail ends after initial cuts, grains and twins (continuous straight lines) around the crystal periphery (side) and in the centre after cut.

3.3. $Cd_{0.96}Zn_{0.04}Te$ crystals

Crystal 53 was grown with a constant rotation rate of 5 rev min^{-1}, consisted of many small grains with several large cracks and yielded no 30 mm × 20 mm substrates.

Crystal 65 was grown using ± 4 rev min^{-1}, 50 s run and stop times and a "necked" ampoule base. These were the conditions which gave the largest CdTe grains (see Section 3.3). In the case of CdZnTe, however, cracking prevented the cutting of any 30 mm × 20 mm substrates. The grain sizes were, on average, larger than in the non-ACRT crystal.

Suppression of this cracking was achieved by changing the starting stoichiometry and crystal 67, grown under the same ACRT conditions, yielded a number of substrates. The grain size was equivalent to crystal 65. Several slices had grains up to 42 mm × 57 mm in size and a few yielded two 20 mm × 30 mm substrates.

These conditions were repeated to grow crystal 69. Again the grain sizes were equivalent but a fine crack running through the largest grain prevented any substrates being obtained, although smaller pieces were produced for assessment purposes (see Section 4).

4. Assessment

4.1. Polishing

Selected samples were given a mechanical polish on both sides to remove sawing damage. This was followed by a chemical (bromine/ethylene glycol) pad polish to remove mechanical polishing damage, but not the full treatment used prior to LPE growth. Usually, samples with dimensions 20 mm × 30 mm were used but, where partially destructive testing was carried out, samples with small corner grains or edge chips were used.

4.2. IR transmission spectrometry

These measurements were carried out over the range 2–25 μm using a sampling area 3 mm in diameter. Typical values of maximum transmission are given in Table 4. Many of the samples had near maximum transmission, suggesting few electrically active defects or impurities which are known to reduce the percentage transmission [2, 27]. Where lower percentage figures are quoted, they refer to that at 25 μm; the variation is normally linear between the highest figure, measured at 2 μm, and this lowest level. It is necessary to study this aspect, because impurities in substrates may diffuse into LPE layers and affect electrical characteristics.

TABLE 4. Summary of assessment of crystals grown

Property	CdTe		CdZnTe	
	Non-ACRT	ACRT	Non-ACRT	ACRT
IRT (%)	67	67–50	66–50	65–60
Te precipitates				
($<10\ \mu m$)(cm^{-2})	$5–30\times10^2$	$1–30\times10^2$	1×10^4	$2–20\times10^2$
($>10\ \mu m$)	Yes	No	Yes	No
Diffraction curve widths (arc sec)				
(tilt)	17	22	15	17
(strain)	40	26	23	16
EPD (cm^{-2})	9.6×10^4	3.3×10^4	4.2×10^4	5.8×10^4

4.3. IR microscopy

Examination of samples using an IR microscope fitted with a polarizer/analyser attachment reveals Te precipitates (as confirmed by energy-dispersive X-ray assessment) down to 2 μm in size [1]. Table 4 summarizes the densities of small precipitates (less than 10 μm) and the occurrence of larger ones. A few samples were precipitate free but many contained only small precipitates. These small precipitates do not have a major deleterious effect on LPE layer growth [1] but large precipitates can give rise to defects if they lie near to the surface. The non-ACRT crystals had the largest number of large precipitates and occasionally lines of precipitates. The lowest levels of small precipitates, coupled with an absence of large precipitates, occurred in a crystal grown under the preferred ACRT conditions (see Section 3.2). None of the samples were subjected to high temperature Cd annealing which is known to reduce Te precipitates and macro-scale strain [35], and improve transmission [36].

Johnson [1] reports precipitate densities from zero to 1×10^4 cm^{-2} in both CdTe and CdZnTe. Sen *et al.* [6] found their material to have densities of $(2–5)\times10^3$ cm^{-2}. Values ranging from 1×10^2 to 1×10^4 cm^{-2} are given by Wood *et al.* [27], who also note the correlation of small precipitates and low IR transmission. They also report that impurities concentrate at precipitates and are rendered electrically inactive. Care must be taken when Cd annealing is used to reduce precipitates, because this may release impurities (predominantly acceptors [35]) into the material.

4.4. X-ray assessment

A simple Berg–Barrett apparatus was used to assess non-destructively the defects in our material. The equipment is a copy of that described by Fewster [37]. Figures 8 and 9 give examples of topographs for both ACRT- and non-ACRT-grown material. These samples were not suitable for LPE growth because of twins or edge chipping, and are therefore not typical of the best material. Nevertheless, almost the entire sample area in each case was imaged, indicating the material is of good crystalline quality with low strain. Fine cracks can be seen in both the CdZnTe samples, while subgrains and large Te precipitates (black spots) are apparent in the non-ACRT sample. The vertical banding is a consequence of the vertical slit. The technique has proved useful in revealing certain defects, *e.g.* twins, which were not visible after polishing. As such, it can provide a degree of substrate screening prior to LPE growth.

These topographs compare well with those taken with the more difficult Lang technique by Sen *et al.* [6] and double crystal and synchrotron topography by Kennedy *et al.* [33]. Bruder *et al.* [38] have shown an example of a large CdZnTe substrate and noted that strain and subgrains are reduced by slow cooling the material after growth. Low temperature gradients were used by Mühlberg *et al.* [39] to reduce subgrains. Bean *et al.* [40] performed a detailed study using the powerful tool of synchrotron X-ray topography on substrates and LPE layers. They noted that subgrains and large precipitates near to the surface always degrade layer quality.

X-ray peak widths for our topography samples were measured using a high resolution multiple-crystal diffractometer [41]. Values for the strain component are given in Table 4. The lower limit for this arrangement was 14 arc sec. These figures are sensitive to surface preparation and, as mentioned above, these samples were not given the full pre-LPE growth treatment. A better indication of crystal quality is obtained by changing the scan mode (ω–$2\omega'$ in ref. 41) to measure the tilt or mosaic spread. The values shown in Table 4 demonstrate that the ACRT has improved the crystallinity in both CdTe and CdZnTe, and that CdZnTe is better than CdTe, as seen by other groups.

4.5. Defect etching

The samples shown in Figs. 8 and 9 were also subjected to defect etching to reveal etch pit densities

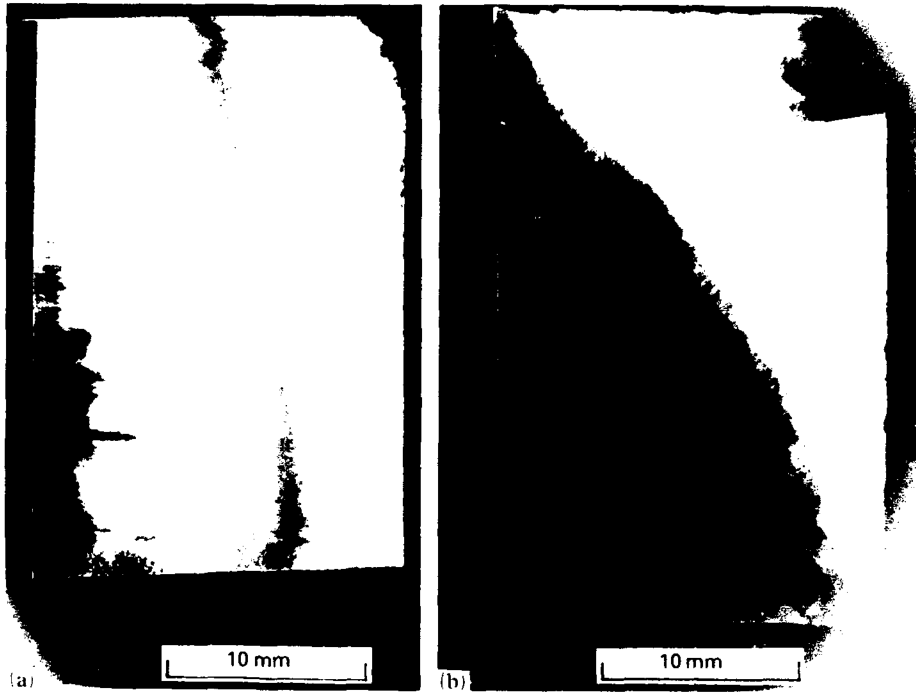

Fig. 8. X-ray topographs of (a) non-ACRT CdTe and (b) ACRT CdTe.

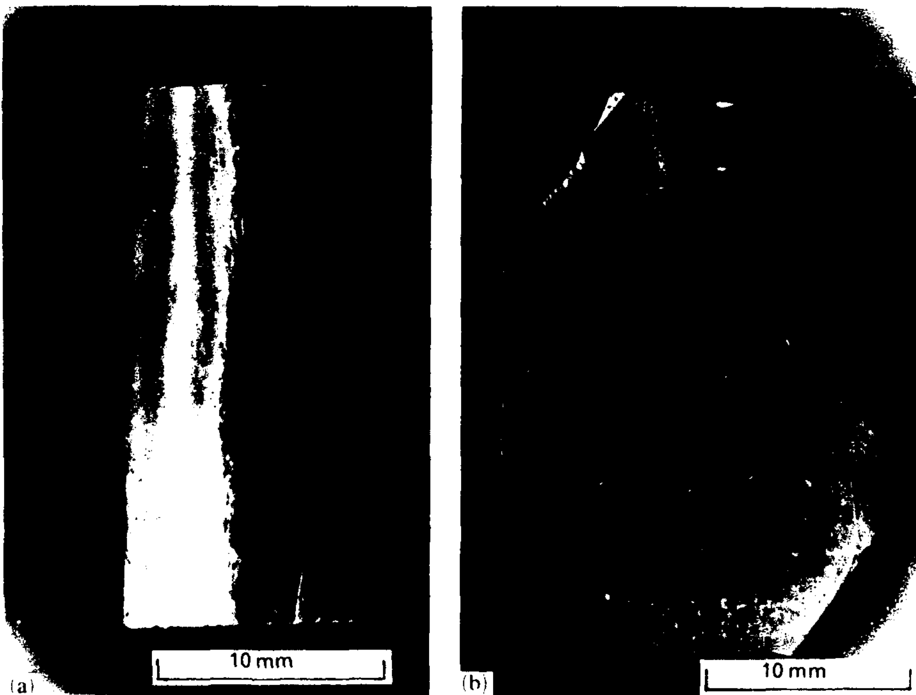

Fig. 9. X-ray topographs of (a) non-ACRT CdZnTe and (b) ACRT CdZnTe.

(EPDs). A variation on the Nakagawa etch technique [42], consisting of 30 s at room temperature in $HF:H_2O_2:H_2O = 1:2:2$ followed by a water rinse was used. Counting the etch pits gave the values shown in Table 4. The lowest figure was seen in the crystal which also had the lowest density of small Te precipitates.

These figures may be compared with the lowest given by Johnson [1] of 8 and 3×10^4 cm^{-2} for CdTe and CdZnTe respectively. A tentative correlation between EPDs and X-ray peak widths suggested in refs. 1 and 34 is borne out to some extent by our work. The value of 3.3×10^4 cm^{-2} compares well with the

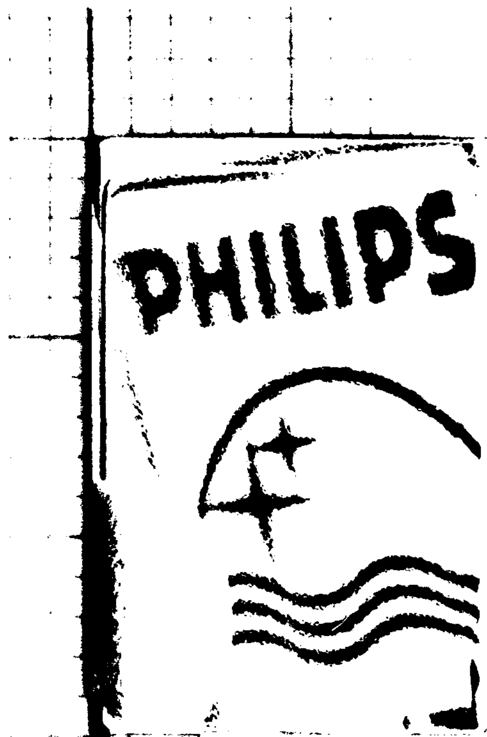

(a)

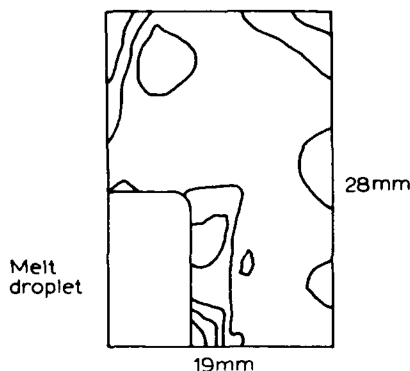

(b)

Fig. 10. (a) CMT layer grown by LPE on ACRT substrate and (b) flatness measurement showing 60% of area within ± 2 μm.

5×10^4 cm^{-2} quoted for CdTe grown by the horizontal Bridgman method [3]. Low EPDs of 2×10^4 cm^{-2} were seen by Sen *et al.* [6] in CdTe, although their CdZnTe showed a higher EPD. A range between 3 and 8×10^4 cm^{-2} was seen by Bruder *et al.* [38] for CdZnTe.

4.6. Liquid phase epitaxial growth

The ultimate aim of the work, and the most important test of the material, is its use in LPE growth of CMT layers. Layers have been grown onto many ACRT-grown substrates by the Te-rich sliding boat technique at 500 °C [43]. Figure 10 shows an example of a layer together with flatness assessment using a scanning laser system. The surface is flat to within ± 2 μm over 60% with the normal fine-scale terracing. The large melt droplet is not typical of more recent layers. Electrical measurements made on as-grown layers revealed carrier concentrations of 2×10^{17} to 4×10^{16} cm^{-3} p type for x between 0.2 and 0.38, as expected for Hg vacancy-controlled material grown at 500 °C [43]. Annealing in Hg (at 200 °C) to remove the vacancies resulted in n type carrier concentrations of $1\text{–}20 \times 10^{14}$ cm^{-3} with mobilities in the range 2×10^4 to 4×10^5 cm^2 V^{-1} s^{-1}, depending on the x value. A lifetime measurement on the sample with the highest mobility gave a value of 1.5 μs for a carrier concentration of 1×10^{14} cm^{-3}, which is within the range found for equivalent bulk material by Pratt *et al.* [44]. These data testify to the high quality of the layers grown on substrates produced in this study.

4.7. Chemical analysis

Work in this section falls into two areas. The first is the measurement of the Zn distribution in the CdZnTe crystals by atomic absorption spectrometry (AAS). In earlier work in CMT growth we found that the ACRT decreased segregation for many impurity elements [45]. Zinc concentrations were measured at three positions (between the 10% and 90% solidified points) of non-ACRT and ACRT crystals. The values were used to estimate the segregation coefficient using Pfann's equation as outlined in ref. 45. The non-ACRT crystal gave a value of 1.18 as compared with 1.25 found by Johnson [1] and 1.16 of Kennedy *et al.* [33]. For the ACRT crystal a value of 1.05 was found, confirming the trend seen in CMT growth. This means that more of the ACRT crystal will have the desired Zn content for lattice matching to the CMT layer.

The second aspect is the purity of substrates and the CMT layers grown on them. Table 5 shows results of laser scan mass spectrometry (LSMS) [46] and secondary ion mass spectrometry (SIMS) analyses. The CdZnTe substrate in this example is free of major impurities, C and O being known surface contaminants. AAS analysis showed levels of Fe of 2×10^{15} cm^{-3} in both the substrate and layer. Both C and O levels increase at the interface but there is no evidence of the interface concentration enhancement (ICE) peaks noted in other reports [47, 48], particularly for Na, K, Li and Si. Levels of impurities in the layer are low, supporting the conclusion from the electrical data that the quality of layers is high.

A recent report by Triboulet *et al.* [49] suggests that IR transmission at room temperature can be used in

TABLE 5. Chemical analyses of CdZnTe substrate grown using the ACRT and LPE layer grown onto such a material

Element	Layer (5–9 μm)	Layer (13–25 μm)	Interface (29–34 μm)	Substrate (50–70 μm)
Li	0.3	0.3	0.3	0.3
C	600	60	600	90
O	30	2	30	1
Na	0.6	1	2	1
Mg	3	3	2	<0.3
Al	0.3	0.3	2	0.6
Si	<0.6	<0.3	<0.6	<0.3
Cl[a]	<2	<0.6	<9	<15
K	0.3	0.3	0.6	0.6
Cu	<3	<2	<	3
I	<3	<2	<6	3
Detection limit (monoisotope)	0.3	0.3	0.6	0.3
(from SIMS)				
Br	<0.4	0.4	0.5	<0.4

[a]Interference from $^{70}Zn^{2+}$. (Results $\times 10^{15}$ cm^{-3}.)

place of chemical analyses to determine rapidly purity levels in substrates. They found a correlation between the percentage transmission at 750 cm^{-1} and $(N_D - N_A)$. Hall measurements showed that full transmission corresponded to a carrier concentration of 5×10^{15} cm^{-3}; a very low doping level. On this basis, our material also contains very few electrically active impurities as the samples studied exhibited near maximum transmission at 750 cm^{-1}.

5. Conclusions

Crystals of both CdTe and $Cd_{0.96}Zn_{0.04}Te$ have been grown by the basic Bridgman process and by the method modified by the ACRT. The aim of this work was to grow crystals with grains large enough to yield substrates suitable for use in LPE growth of CMT layers. Modelling of ACRT has been extended to the 50 mm diameter used in this study and two regimes have been identified: ACRT parameter combinations which maximize fluid stirring and that which maintains stable Ekman flow. Larger single crystal regions are obtained under conditions which maintain stable Ekman flow. A necked ampoule base is shown to enhance grain selection. The overall effect of the ACRT is an increase in size of the largest grain by a factor of between 2 and 5. The largest single crystal (111) areas measured 45–50 mm × 60–65 mm. Substrates of size 20 mm × 30 mm oriented close to the (111) direction have been produced from many of the crystals grown. Samples show high IR transmission, low densities of small Te precipitates and an absence of large precipitates. Defect etching reveals dislocation densities comparable with those reported in the literature. X-ray topographic studies show low strain levels in both CdTe and CdZnTe samples, although some twins were observed, and subgrains in a non-ACRT CdZnTe sample. The ACRT decreases the X-ray line widths in CdTe and CdZnTe material. Chemical analyses show low impurity levels in both the substrate and CMT layer grown onto it. The surface topography of the epitaxial CMT layers is good and the electrical characteristics demonstrate the high quality of layers grown on ACRT material.

Acknowledgments

The authors wish to thank J. C. Brice and P. F. Fewster for their help in ACRT modelling and X-ray techniques respectively. N. L. Andrew also provided technical help with the X-ray diffraction curve width measurements. I. G. Gale and F. Grainger carried out the chemical analyses. Thanks are also due to I. Guilfoy for his help in the development and operation of the FICS 10 grower and W. G. Coates who grew the first few crystals. Special thanks go to J. B. Mullin and M. G. Astles (DRA, Malvern) for their help and encouragement throughout the course of this work.

The work was carried out with the support of the Procurement Executive, Ministry of Defence, sponsored by DRA (ED), Malvern.

References

1 C. J. Johnson, *SPIE, 1106* (1989) 56.

2 O. Oda, K. Hirata, K. Matsumoto and I. Tsuboya, *J. Cryst. Growth, 71* (1985) 273.
3 A. A. Khan, W. P. Allred, B. Dean, S. Hooper, J. E. Hawkey and C. J. Johnson, *J. Electron. Mater., 15* (1986) 181.
4 K. Y. Lay, D. Nichols, S. McDevitt, B. E. Bean and C. J. Johnson, *J. Cryst. Growth, 86* (1988) 118.
5 P. Cheuvart, U. El-Hanani, D. Schneider and R. Triboulet, *J. Cryst. Growth, 101* (1990) 270.
6 S. Sen, W. H. Konkel, S. J. Tighe, L. G. Bland, S. R. Sharma and R. E. Taylor, *J. Cryst. Growth, 86* (1988) 111 (using the specific heat data from J. C. Brice, in J. C. Brice and P. Capper (eds.), *Properties of Mercury Cadmium Telluride*, IEE, London, 1987).
7 F. V. Wald and R. O. Bell, *J. Cryst. Growth, 30* (1975) 29.
8 P. Capper and J. J. G. Gosney, *UK Patent 8115911* (May 1981).
9 P. Capper, J. J. G. Gosney and C. L. Jones, *J. Cryst. Growth, 70* (1984) 356.
10 J. C. Brice, P. Capper, C. L. Jones and J. J. G. Gosney, *Prog. Cryst. Growth Charact., 13* (1986) 197.
11 P. Capper, J. J. G. Gosney, C. L. Jones and E. J. Pearce, *J. Electron. Mater., 15* (1986) 361.
12 P. Capper, J. J. G. Gosney, C. L. Jones and I. Kenworthy, *J. Electron. Mater., 15* (1986) 371.
13 P. Capper, W. G. Coates, C. L. Jones, J. J. Gosney, C. K. Ard and I. Kenworthy, *J. Cryst. Growth, 83* (1987) 69.
14 P. Capper, J. C. Brice, C. L. Jones, W. G. Coates, J. J. G. Gosney, C. K. Ard and I. Kenworthy, *J. Cryst. Growth, 89* (1988) 171.
15 W. G. Coates, P. Capper, C. L. Jones, J. J. G. Gosney, C. K. Ard, I. Kenworthy and A. Clark, *J. Cryst. Growth, 94* (1989) 959.
16 P. Capper, *Prog. Cryst. Growth Charact., 19* (1989) 259.
17 C. L. Jones, P. Capper, J. J. G. Gosney and I. Kenworthy, *J. Cryst. Growth, 69* (1984) 281.
18 H. J. Scheel and E. O. Schulz-Dubois, *J. Cryst. Growth, 8* (1971) 304.
19 H. J. Scheel, *J. Cryst. Growth, 13-14* (1972) 560.
20 E. O. Schulz-Dubois, *J. Cryst. Growth, 12* (1972) 81.
21 P. Capper, J. J. G. Gosney, C. L. Jones and M. J. T. Quelch, *J. Cryst. Growth, 63* (1983) 154.
22 P. Capper, W. G. Coates, C. L. Jones, J. J. G. Gosney, I. Kenworthy and C. K. Ard, *J. Cryst. Growth, 102* (1990) 848.
23 V. M. Glazov, *Liquid Semiconductors*, Plenum, New York, 1964.
24 W. R. Wilcox, F. M. Carlson, D. K. Aidun, V. White, W. Rosch, W. M. Chang, R. Shetty, A. Fritz, R. Balasubramanian, G. Rosen, J. Kweeder and C. Wen, *Proc. 41st Congr. of the International Astronautical Federation, Dresden, IAF-90-357, 1990*, International Astronautical Federation, Paris, 1990.
25 R. Shetty, R. Balasubramanian and W. R. Wilcox, *J. Cryst. Growth, 100* (1990) 51.
26 L. R. Holland, *J. Cryst. Growth, 96* (1989) 577.
27 L. Wood, E. R. Gertner, W. E. Tennant and L. O. Bubulac, *Proc. SPIE, 350* (1983) 30.
28 R. K. Route, M. Wolf and R. S. Feigelson, *J. Cryst. Growth, 70* (1984) 379.
29 P. F. Fewster, *J. Appl. Crystall., 17* (1984) 265.
30 G. W. Fynn and W. J. A. Powell, *The Cutting and Polishing of Electro-optic Materials*, Adam Hilger, Bristol, 1979, p. 17.
31 A. Horowitz, D. Gazit, J. Makovsky and L. Ben-Dor, *J. Cryst. Growth, 61* (1983) 323.
32 W. Hofherr, H. Marguardt, U. Probst, P. Lickinger, D. Linerius and R. Nitsche, paper given at *EW-MOVPE-III, Montpellier, France, 1989.*
33 J. J. Kennedy, P. M. Amirtharaj, P. R. Boyd, S. B. Qadri, R. C. Dobbyn and G. G. Long, *J. Cryst. Growth, 86* (1988) 93.
34 M. Azoulay, A. Raizman, G. Gafni and M. Roth, *J. Cryst. Growth, 101* (1990) 256.
35 C. K. Ard, C. L. Jones and A. Clark, *SPIE, 659* (1986) 123.
36 S. H. Shin, J. Bajaj, L. A. Moudy and D. T. Cheung, *Appl. Phys. Lett., 43* (1983) 68.
37 P. F. Fewster, Analysis of microelectronic materials and devices, in M. Grasserbauer and H. W. Werner (eds.), Wiley, New York, 1991, p. 581.
38 M. Bruder, H.-J. Schwarz, R. Scmitt, H. Maier and M.-O. Möller, *J. Cryst. Growth, 101* (1990) 266.
39 M. Mühlberg, P. Rudolph, C. Genzel, B. Wermke and U. Becker, *J. Cryst. Growth, 101* (1990) 275.
40 B. E. Dean, C. J. Johnson, S. C. McDevitt, G. T. Neugebauer, J. L. Sepich, R. C. Dobbyn, M. Kuriyama, J. Ellsworth, H. R. Vydyanath and J. J. Kennedy, *J. Vac. Sci. Technol. B, 9* (1991) 1840.
41 P. F. Fewster, *J. Appl. Crystall., 22* (1989) 64.
42 K. Nakagawa, K. Maeda and S. Takeuchi, *Appl. Phys. Lett., 34* (1979) 574.
43 J. C. Brice, P. Capper, B. C. Easton, J. L. Page and P. A. C. Whiffin, *Semicond. Sci. Technol., 2* (1987) 710.
44 R. G. Pratt, J. Hewett, P. Capper, C. L. Jones and N. Judd, *J. Appl. Phys., 60* (1986) 2377.
45 P. Capper, I. G. Gale, F. Grainger, J. A. Roberts, C. L. Jones, J. J. G. Gosney, I. Kenworthy, C. K. Ard and W. G. Coates, *J. Cryst. Growth, 92* (1988) 1.
46 F. Grainger and J. A. Roberts, *Semicond. Sci. Technol. 3* (1988) 802.
47 M. G. Astles, H. Hill, G. Blackmore, S. Courtney and N. Shaw, *J. Cryst. Growth, 91* (1988) 1.
48 P. Rudolph, M. Mühlberg, M. Neubert, T. Boeck, P. Möck, L. Parthier, K. Jacobs and E. Kropp, *J. Cryst. Growth, 118* (1992) 204.
49 R. Triboulet, A. Durand, P. Gall, J. Bonnafé, J. P. Fillard and S. K. Krawczyk, *J. Cryst. Growth, 117* (1992) 227.

Materials Science and Engineering, B16 (1993) 40–43

$Cd_{1-y}Zn_yTe$ substrates for $Hg_{1-x}Cd_xTe$ liquid-phase epitaxy

M. Bruder, H. Figgemeier, R. Schmitt and H. Maier

Infrared and Night Vision Devices Subdivision, AEG Aktiengesellschaft, Theresienstrasse 2, W-7100 Heilbronn (Germany)

Abstract

The vertical unseeded Bridgman growth of $Cd_{1-y}Zn_yTe$ (y = 0.04–0.045) is described. Crystals of 65 mm diameter and total mass 2400 g have been obtained. The influence of annealing $Cd_{1-y}Zn_yTe$ substrates has been investigated. The annealing, which reduced remaining strain and tellurium inclusions and precipitates, leads to a very suitable epitaxial layer quality used for the production of two-dimensional IR detector arrays.

1. Introduction

Multielement IR detector arrays require high quality epitaxially grown $Hg_{1-x}Cd_xTe$ layers. Among the various epitaxy methods, liquid-phase epitaxy on lattice-matched $Cd_{1-y}Zn_yTe$ substrates is the appropriate technique to fulfil these requirements. $Cd_{1-y}Zn_yTe$ is transparent in the IR wavelength range, allowing back-side illumination of detector arrays connected to a silicon read-out device by indium bump technology. The zinc content $y = 0.045$ is in order to achieve lattice matching for $Hg_{0.76}Cd_{0.24}Te$ epitaxial layers (epilayers), and $y = 0.04$ for the $Hg_{0.71}Cd_{0.29}Te$ epilayers [1]. As an additional effect, the zinc content increases the stacking fault energy in the lattice, leading to improved mechanical stability of the substrates, while the distribution coefficient of 1.35 [2] leads to a variation in the distribution of only ±0.5% along the total crystal.

For the manufacture of $Cd_{1-y}Zn_yTe$ substrates, different Bridgman methods are employed. The horizontal technique [3] offers the advantage of reduced contact with the growth chamber but requires the establishment of a vapour-controlled system. The vertical Bridgman method [4, 5] allows large crystal volumes and, with the modification of the gradient freeze technique [6], mechanical disturbances in the growth system are reduced. We describe the manufacture of $Cd_{1-y}Zn_yTe$ crystals using the unseeded vertical Bridgman growth method and the characterization of the substrates with respect to the fabrication of high quality IR detector arrays.

2. Experimental details

2.1. *Growth process*

High purity (99.9999%) elements of cadmium, zinc and tellurium are used for synthesis in graphitized sealed quartz tubes. Ampoules with an inner diameter of 65 mm and a mass of 2400 g of reacted $Cd_{1-y}Zn_yTe$ are used for one growth charge. We use a multizone furnace with a temperature of 1140 °C in the melt zone and 900 °C in the post-anneal zone. A temperature gradient of 10 K cm^{-1} is established in an unheated isolated zone between the furnace. In our growth system the ampoule is fixed and the furnace with the gradient moves towards the growth chamber. A growth velocity of 1 mm h^{-1} after a melt homogenization of 24 h is used. After the solidification the crystal is cooled to room temperature with a decreasing rate of 10 K h^{-1}.

2.2. *Substrate preparation*

⟨111⟩-oriented substrates are cut from single-crystal blocks using an inner-diameter saw. Single-crystal areas of 12–25 cm^2 are routinely obtained (Fig. 1). For

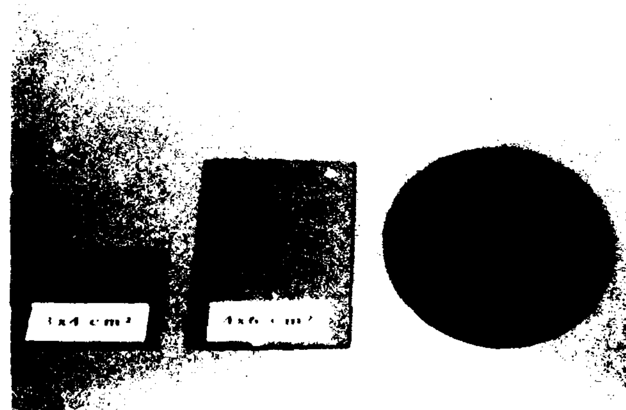

Fig. 1. Single-crystal $Cd_{1-y}Zn_yTe$ slice (diameter, 65 mm) with ⟨111⟩-oriented substrates.

0921-5107/93/$6.00

© 1993 – Elsevier Sequoia. All rights reserved

surface preparation the substrates are lapped, mechanically polished and subsequently etched in a final chemomechanical bromine–methanol step. This treatment leads to scratch-free specular surfaces.

2.3. Liquid-phase epitaxy

The substrates are used for fabrication of $Hg_{1-x}Cd_xTe$ liquid-phase epilayers. The layers are grown from a tellurium-rich solution at a temperature of 470 °C in a vertical dipping system. The growth process is composed of a supercooling of 1 K followed by a ramp cooling rate of 0.2 K min^{-1}. During a growth time of 15 min a layer 10 μm thick is obtained.

3. Results and discussion

3.1. Crystallinity

The evaluation of different growth runs indicates a single-crystal part consisting of 60–80% of the crystal volume. Although the crystals are grown unseeded, 70% of them grow in the ⟨110⟩ direction with a deviation of typically 5°. We found that no seed selection occurs in the tip of the ampoule owing to supercooling of the melt.

After the beginning of the solidification the phase boundary moves to the equilibrium state, while 150 g of the melt has frozen after 1 h. This effect is indicated first by the polycrystalline start of growth and second by an increase in the temperature by 10 K measured with a thermocouple at the tip of the ampoule, resulting from the heat of solidification. After this solidification, fast selection of one grain occurs in the first step of the growth.

3.2. Dislocation density

For the evaluation of the etch pit density distribution in the crystal, the etchant used by Nakagawa *et al.* [7] on the Cd (111) side is the established method for the characterization of $Cd_{1-x}Zn_xTe$ substrates. Independent of the position along the crystal, we found the distribution which is shown in Fig. 2.

The middle part shows good homogeneity with lowest etch pit density values of 2×10^4 cm^{-2}, while the edge shows a sharp increase to values one order of magnitude higher. This area with increasing etch pit density is caused by the wall contact of the growing crystal or by detachment during the cooling phase. Its extension is independent of the grown diameter. This emphasizes the necessity of large-diameter crystals for the fabrication of high quality substrates.

3.3. X-ray topography

To control the lattice perfection of the crystals, the same substrates are submitted to X-ray topography

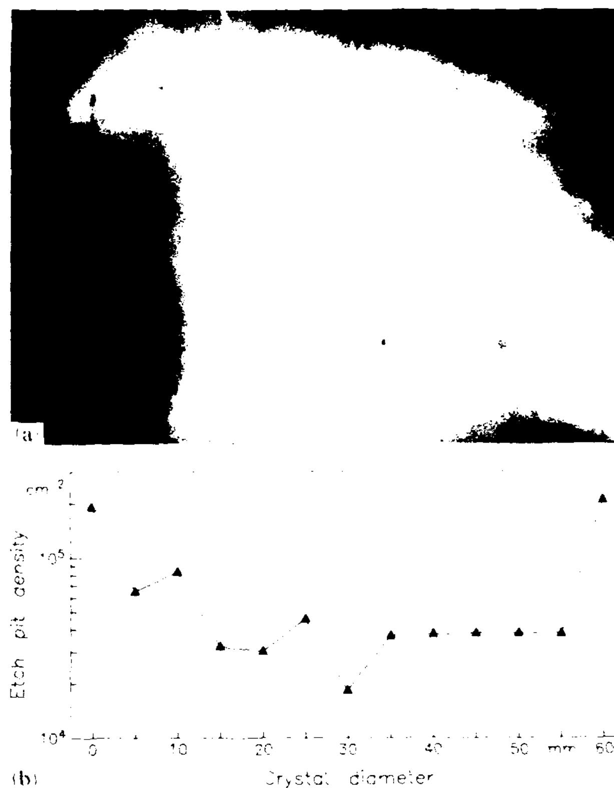

Fig. 2. (a) X-ray reflection topography exposure (substrate dimensions, 30 mm × 20 mm). (b) Etch pit rate distribution vs. crystal diameter.

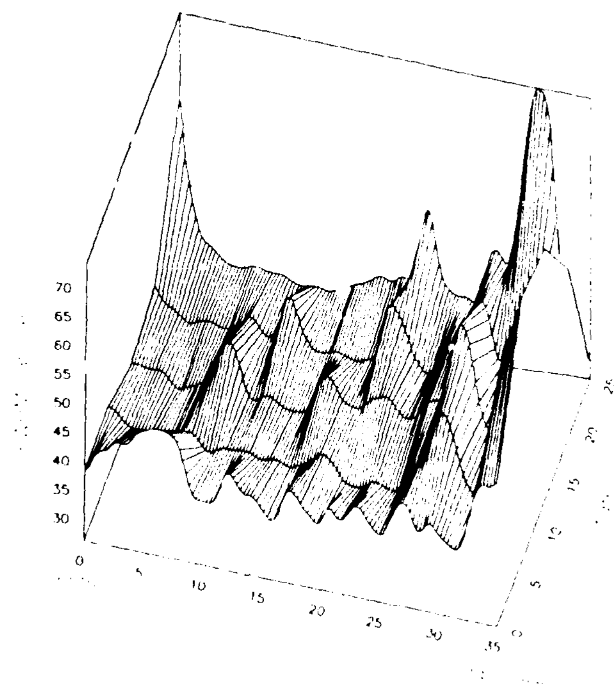

Fig. 3. X-ray rocking curve values of a $Cd_{1-x}Zn_xTe$ substrate vs. the crystal diameter.

measurements. Figure 2 shows reflection topography exposures, which indicate strain and small-angle boundaries in the edge areas.

To study the mosaic structure of the crystal, high resolution diffractometry is employed using a four-crystal Ge ⟨220⟩ monochromator [8], ⟨444⟩ sample reflection and a cross-section of the X-ray beam of 2.5 mm × 0.8 mm. The rocking-curve full width at half-maximum (FWHM) distribution is shown in Fig. 3. In the homogeneous areas we have FWHMs between 30 and 40″, while a value of 25″ corresponds to the resolution of the measurement method with the above conditions.

3.4. IR microscopy

The IR microscopy of substrates shows inclusions in the material with a typical size between 5 and 15 μm and a density of 10^4–5×10^5 cm^{-2}. These inclusions result from temperature fluctuations at the phase boundary, followed by the build-up of small melt droplets in the growing crystal. If such an inclusion cuts the surface, it induces a defect in the grown epilayer.

4. Influence of annealing

Defects as described could propagate into the epilayer and influence the detector performances. Taking the reverse bias maximum dynamic resistivity of the diodes as the criterion, we observe reduced performances on detector elements which are placed on strained areas. Epilayer defects normally lead to total breakdown of detector performance.

To avoid reduced detector yield, effort is made to improve the obtained as-grown substrates. An annealing process near the melting point should heal the remaining strain. On the contrary, under a cadmium overpressure established to prevent material sublimation, tellurium precipitates and inclusions could react with diffused cadmium. Optimized parameters of this developed process are an isothermal temperature of 900 °C, a cadmium vapour pressure of 1.5 atm and an annealing period of 10 days. Figure 4 shows the topography exposure of a heavily strained substrate before

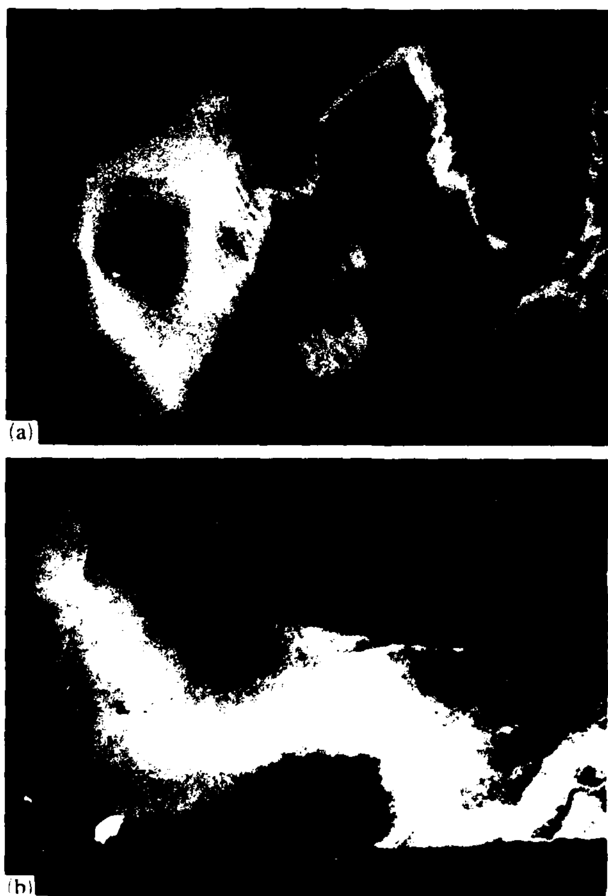

Fig. 4. (a) As-grown heavily strained substrate; (b) same substrate after annealing (substrate dimensions, 30 mm × 20 mm).

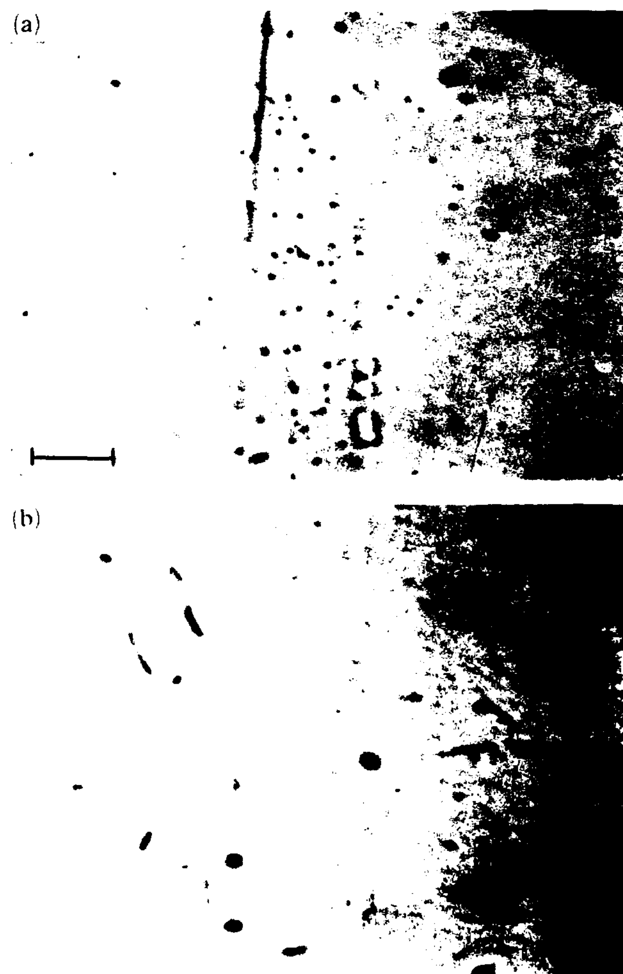

Fig. 5. IR microscopy exposure of same local substrate area: (a) as grown; (b) annealed. The marker represents 100 μm.

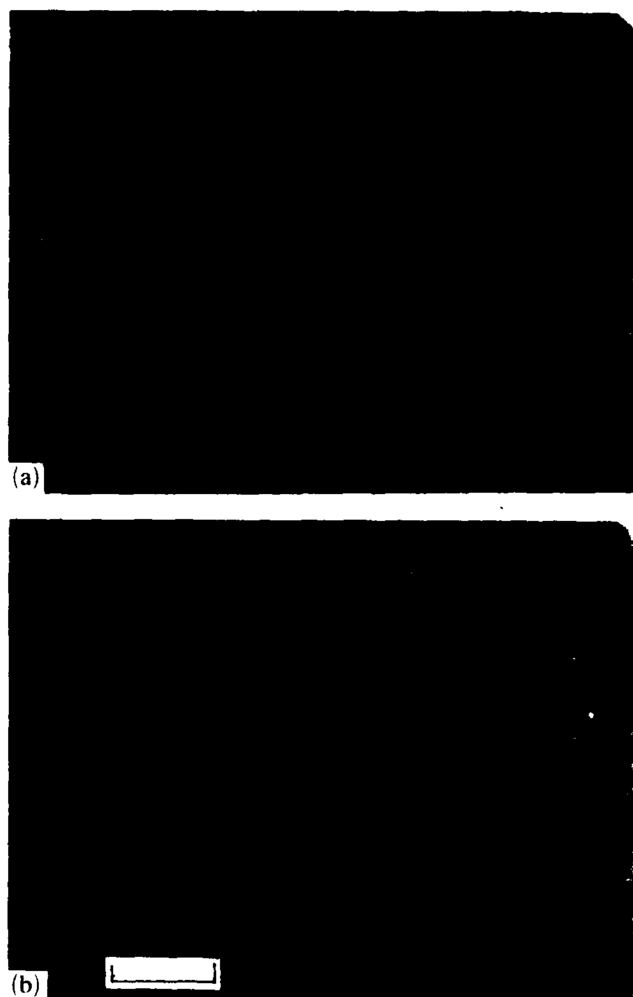

Fig. 6. Etch pit pattern of (a) an as-grown substrate and (b) an annealed substrate. The marker represents 100 μm.

and after annealing. Although a small-angle boundary remains, most strained areas have disappeared. Additional annealing of the sample shows no further improvement.

The influence with respect to precipitates is shown in Fig. 5. Characteristic local areas of the sample are marked by scratches and characterized by IR photography. Most of the inclusions are dissolved; some are gathered into clusters. We found a reduction in the inclusion density by a factor of 10^2 by annealing.

In Fig. 6, the etch pit distribution on the same wafer shows a cellular structure on the as-grown substrate, while the distribution after annealing is homogeneous. The situation is not yet clear as to why the density of the etch pit formation rate does not decrease, confirming the improved mosaic structure of the X-ray topographs.

With substrates treated in this manner, liquid-phase epilayers which show a defect density below 10 cm^{-2} are obtained; this is an important condition for processing multielement IR detector arrays.

5. Conclusion

The vertical Bridgman method is used for fabrication of $Cd_{1-y}Zn_yTe$ substrates, on which $Hg_{1-x}Cd_xTe$ epilayers are grown. The remaining defects in the substrate material are reduced using an anneal process under a cadmium atmosphere. Microscopic defect densities on the epilayers of less than 10 cm^{-2} indicate the high quality of these annealed substrates.

Acknowledgments

The authors would like to thank Mr. M. Regnet, Department of Physics, University of Würzburg, for the measurement and interpretation of the X-ray diffraction rocking curves.

References

1 K. Hirata and O. Oda, *Mater. Lett.*, 5 (1–2) (1986) 42.
2 A. Tanaka, Y. Masa, S. Seto and T. Kawasaki, *J. Cryst. Growth*, *94* (1989) 166.
3 P. Cheuvart, U. El-Hanani, D. Schneider and R. Triboulet, *J. Cryst. Growth*, *101* (1990) 270.
4 M. Bruder, H. J. Schwarz, R. Schmitt and H. Maier, *J. Cryst. Growth*, *101* (1990) 266.
5 M. Mühlberg, P. Rudolph, C. Genzel, B. Wermke and U. Becker, *J. Cryst. Growth*, *101* (1990) 275.
6 A. Tanaka, Y. Masa, S. Seto and T. Kawasaki, *Materials Research Society Symp. Proc.*, Vol. 90, Materials Research Society, Pittsburgh, PA, 1987, p. 111.
7 K. Nakagawa, M. Maeda and S. Takeuchi, *Appl. Phys. Lett.*, *34* (1979) 574.
8 W. J. Bartels, *Philips Tech. Rev.*, *41* (6) (1983–1984) 183.

Materials Science and Engineering, B16 (1993) 44–47

Horizontal Bridgman growth of large high quality $Cd_{1-y}Zn_yTe$ crystals

P. Brunet, A. Katty, D. Schneider, A. Tromson-Carli and R. Triboulet
Laboratoire de Physique des Solides de Bellevue, CNRS, 1 place A. Briand, F-92195 Meudon Cédex (France)

Abstract

High quality $Cd_{0.96}Zn_{0.04}Te$ single crystals, as demonstrated from X-ray diffraction measurements, have been grown by the horizontal Bridgman (HB) method in glassy carbon boats. The relevance of this crucible material has been shown from contact angle measurements with liquid CdTe and $Cd_{1-y}Zn_yTe$. Nevertheless, its thermal conductivity, which is higher than that of silica, is shown to favour a growth interface concavity. The use of [110]-oriented seeds, after determination of the preferential growth axis of CdTe crystals grown by the HB method, has allowed us to control supercooling and to grow single crystals of controlled growth direction. A residual pressure of hydrogen in the growth tube is shown to inhibit any parasitic growth on the $Cd_{1-y}Zn_yTe$ ingot surface and to act on the compensation state of the crystals.

1. Introduction

The need for high performance second-generation $Hg_{1-x}Cd_xTe$-based IR detectors has motivated the research and development of epitaxial $Hg_xCd_{1-x}Te$ detector technology. The quality of the epitaxial layer is critically dependent on the nature and quality of the substrate. At present, $Cd_{1-y}Zn_yTe$ is a leading substrate material for the epitaxial growth of $Hg_{1-x}Cd_xTe$. The addition of zinc not only is used for better lattice matching between the substrate and $Hg_{1-x}Cd_xTe$ layer but also has been shown to reinforce the Cd–Te bond and therefore to decrease the dislocation density of the crystals [1]. Large-diameter single crystals of $Cd_{1-y}Zn_yTe$ with a low defect density and a large volume are thus required. The present lack of high quality large-area bulk $Cd_{1-y}Zn_yTe$ crystals is generally recognized as the main limitation on the development of an efficient HgCdTe detector technology, and as the main reason for the very high price of the substrates.

Most of the commercially available $Cd_{1-y}Zn_yTe$ substrates are cut from boules grown by the vertical Bridgman (VB) method. This VB technique has shown some limits in obtaining high quality crystals [2]. The horizontal Bridgman (HB) method, successfully used for the growth of GaAs, presents several basic advantages over the VB method.

(i) The control of the stoichiometry by a cadmium vapour pressure in contact with both the solid and the liquid is effective in the HB method because of the large free surface.

(ii) There is no ingot confinement if a tapered crucible is used and thus less mechanical stress during growth and cooling.

(iii) Seeding is easier in the HB configuration than in the VB configuration.

(iv) In the HB method the growth interface is not submitted to the weight of the liquid column as in the VB method.

(v) Finally because of its growth axis which is perpendicular to the gravity field, unlike the VB method where the growth axis and gravity field mingle, the HB method has an additional degree of freedom; imposing a transverse gradient allows one to control and to modify the growth interface shape.

The drawbacks of the HB method lie in Marangoni convection due to the large free surface of the liquid in contact with the gaseous phase, resulting in instabilities of the growth surface, and a non-cylindrical shape of the ingots which causes some problems in the technological post-growth operations.

The interest in the HB rather than the VB method has already been discussed in several studies [3–5].

Among the numerous parameters which govern the CdTe Bridgman growth and which have been analysed and discussed in the review by Rudolph [6], we have focused our attention on four main parameters: the nature of the crucible, the control of supercooling, seeding and the nature of the residual atmosphere surrounding the crystal.

2. Experiments

The growth furnace and the growth process used have been described in ref. 4. The liquid temperature (overheating) was fixed at only 5 °C above the melting temperature in order to minimize the convection in the melt and the supercooling as well. The thermal gradi-

0921-5107/93/$6.00
© 1993 – Elsevier Sequoia. All rights reserved

ent was about 2 °C cm^{-1}; the growth rate was in the range 3–6 mm h^{-1} depending on the runs.

2.1. Nature of the boat material

Surface phenomena are crucial in crystal growth; surface tension, the growth angle and the contact angle of the melt on the crucible material have important effects on the quality of the crystals. Glassy carbon is obtained by pyrolysis of organic compounds. This material is extremely stable in temperature and resistant to chemical corrosion. Glassy carbon boats purchased from HTW GmbH (Meitingen, Germany) present an extremely smooth surface aspect and excellent cleanness, as shown from no degassing at 1100 °C. In order to confirm the relevance of this material to CdTe crystal growth, we have performed contact angle measurements of CdTe and $Cd_{1-x}Zn_xTe$ on glassy carbon by the sessile drop method as described in ref. 7. At 1100 °C a wetting angle of 126° has been measured for $Cd_{0.96}Zn_{0.04}Te$ on glassy carbon in comparison with a value of 132° for CdTe on pyrolytic boron nitride [8] which has been considered up to now as the reference.

2.2. Supercooling

From numerous experiments in the VB configuration, we have found supercooling to be one of the most detrimental phenomena in CdTe crystal growth from the melt. At the onset of the growth, the solid–liquid interface jumps up suddenly after travelling for several centimetres, making the first part of the ingots highly polycrystalline.

To avoid this problem, an ingot grown in a classical way by the HB method was then partially remolten. This melt-back process was stopped at about 1.5 cm from the end of the charge in order to keep a "natural seed". The presence of this natural seed suppresses most of the supercooling.

2.3. Seeding

In order to choose the most appropriate crystallographic direction to achieve optimum microstructure and uniformity, seeding has been accomplished by using oriented (Cd, Zn)Te or CdTe crystals.

From a systematic determination of the preferential growth directions of CdTe grains in the HB method using an optical orientation technique as described in ref. 4, we have found that the propagation axis of the crystals is rarely [111] or [100] but is situated in directions close to [110] and [211]. This observation and technological considerations made us choose [110] orientation for our first seed orientation, although it is considered as favouring twinning. In a three-dimensional growth situation such as ours, no orientation can avoid the appearance of twins but experiments using different growth directions are in progress.

2.4. Atmosphere surrounding the crystals

The resistivity of CdTe crystals grown by the Bridgman method has been shown by Yokota *et al.* [9] to vary largely with the residual gas pressure in the ampoules used for preparation. It was proposed that the resistivity increased as the concentration of oxygen incorporated from the atmosphere into CdTe during preparation decreased. The residual gas pressure is quite difficult to control reproducibly from one experiment to another. This is why we have chosen as a more reproducible standard state the presence of a residual hydrogen pressure in the tubes.

3. Results

The crystals grown in glassy carbon crucibles, according to our growth conditions, have been shown always to be of a larger size than those grown in graphitized silica boats. The remelting of the charge has also been shown to have a spectacular effect on the size of the crystals, mainly at the onset of the growth. The ingot generally contains one important grain, up to 40 vol.% of the ingot. The length of the ingot is 25 cm and the section is about 3 cm × 4 cm.

The use of an oriented seed has allowed to keep the selected [110] orientation in the first grain extending over several centimetres. Figure 1 shows the partly

Fig. 1. Photograph of an oriented seed after growth.

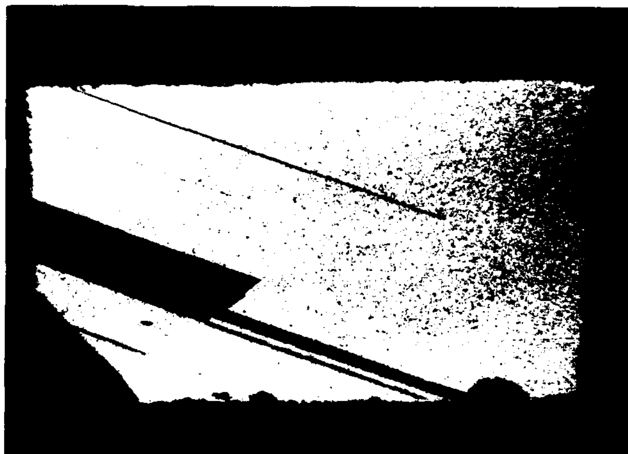

Fig. 2. Photograph of a cross-section of an ingot after 12 cm of growth.

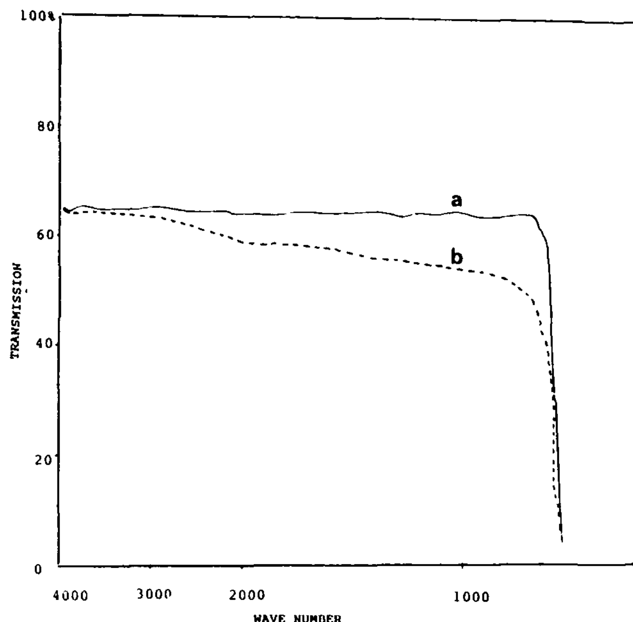

Fig. 3. IR transmission spectra of two (Cd, Zn)Te samples: curve a, growth in a tube sealed under vacuum; curve b, growth in a tube sealed under residual hydrogen pressure.

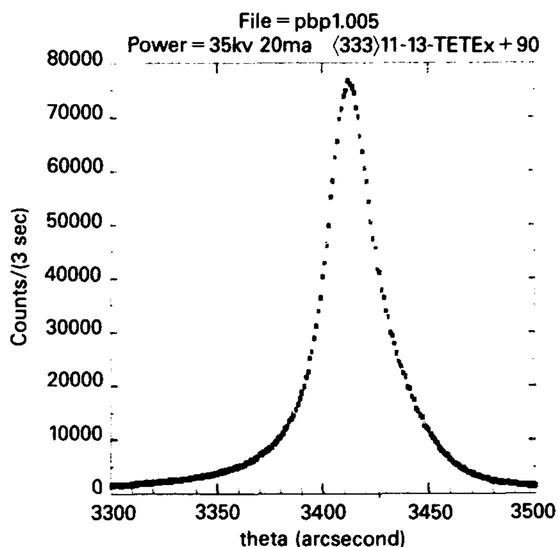

Fig. 4. Typical X-ray double-diffraction rocking curve of a HB-grown crystal measured on a (111) surface using Si(311) as the first crystal.

remolten seed after 2 cm of growth, while Fig. 2 displays a cross-section of the ingot after about 12 cm of growth.

The presence of a residual hydrogen pressure in the tubes has been found to bring about two distinct effects. First, any parasitic growth in the vapour phase on the surface of the ingot, as occurring when the growth is achieved under vacuum, is completely inhibited. The very bright surface of the ingot allows one to see distinctly the growth interface shape which is materialized by periodic transverse lines associated with the density difference between solid and liquid. The interface has been found to present a marked concavity near the boat walls. (The solid–liquid or growth interface is concave seen from the growing crystal.) This probably expresses the fact that the thermal conductivity of glassy carbon (k(1000 °C) = 0.110 W K^{-1} cm^{-1}) is higher than that of the CdTe (k_{sol}(1092 °C) = 0.018 W K^{-1} cm^{-1}). From this point of view, glassy carbon is less favourable than silica which has a thermal conductivity of 0.30 W K^{-1} cm^{-1} but superior to boron nitride (k = 0.25 W K^{-1} cm^{-1}).

The second impact of using a residual hydrogen pressure concerns the electronic properties of the crystals which are slightly affected. Under our classical growth conditions under vacuum, and mainly from the cadmium pressure equilibrium control between liquid and vapour during the growth, and solid and vapour during the cooling step, the crystals are generally semi-insulating. The presence of hydrogen slightly increases the IR absorption as shown in Fig. 3, indicating a modification of the compensation state of the crystals in agreement with the observations of Svob *et al.* [10]. The rocking curve measured by X-ray double diffraction on (111) surfaces using Si(311) as the first crystal shows a single peak structure with a full width at half-maximum (FWHM) lying in the range 20–30″. Figure 4 shows a rocking curve with an FWHM of 28″ from which 8″ can be subtracted. (When the two crystals in an X-ray double-diffraction experiment are not exactly parallel, as in our case, a broadening of the FWHM occurs and can be calculated from the formula $\Delta\theta = (\frac{1}{2}\Delta\lambda/\lambda)(\tan\theta_2 - \tan\theta_1)$, where $\Delta\theta$ is seconds of arc, and θ_1 and θ_2 are the angles of the first crystal and sample respectively.) No mosaic structures are seen

from X-ray topography experiments. Finally the high quality of the material is confirmed by the results on $Hg_{1-x}Cd_xTe$ liquid epitaxy showing excellent epitaxial layers [11].

4. Conclusion

Glassy carbon is shown to be appropriate as a crucible material for the growth of $Cd_{1-y}Zn_yTe$ crystals by the HB method, as already suggested from contact angle measurements. The thermal conductivity of glassy carbon, which is larger than that of silica, appears nevertheless as favouring the concavity of the growth interface at the crucible wall. The detrimental influence of supercooling has been controlled using a small overheating and (110)-oriented seeds after determination of the preferential growth axis of the CdTe crystals which has been found to lie in the range [110]-[211]. A residual pressure of hydrogen in the growth tube is found to inhibit any parasitic growth in the vapour phase on the surface of the ingot, and to act on the compensation state of the crystals.

Finally, the high crystallographic quality of the $Cd_{0.96}Zn_{0.04}Te$ crystals grown by the HB method is demonstrated by X-ray diffraction measurements.

Acknowledgments

This work was supported by Direction des Recherches Etudes et Techniques Contract 89-160.

References

1 K. Guergouri, R. Triboulet, A. Tromson-Carli and Y. Marfaing, *J. Cryst. Growth*, *86* (1988) 61.
2 K. Zanio, *Semicond. Semimet.*, *13* (1978) 12.
3 A. A. Khan, W. P. Allred, B. Dean, S. Hooper, J. E. Hawkey and C. J. Johnson, *J. Electron. Mater.*, *15* (1986) 181.
4 P. Cheuvart, U. El Hanani, D. Schneider and R. Triboulet, *J. Cryst. Growth*, *101* (1990) 270.
5 O. A. Matveev, S. V. Prokof'ev and Y. V. Rud', *Izv. Akad. Nauk SSSR, Neorg. Mater.*, *5* (1969) 1175.
6 P. Rudolph, *Mater. Sci. Eng.*, *B16* (1993) 8-16.
7 A. Katty, P. Dusserre, R. Triboulet and T. Duffar, *J. Cryst. Growth*, *118* (1992) 470.
8 R. Shetty, R. Balasubramanian and W. R. Wilcox, *J. Cryst. Growth*, *100* (1990) 51.
9 K. Yokota, T. Yoshikawa, S. Inano and S. Katayama, *Jpn. J. Appl. Phys.*, *28* (1989) 1556.
10 L. Svob, A. Heurtel and Y. Marfaing, *J. Cryst. Growth*, *86* (1988) 815.
11 B. Schaub, personal communication, 1992.

Materials Science and Engineering, B16 (1993) 48-50

Computer simulation of CdTe crystal growth and application

Ch. Steer, M. Hage-Ali, J. M. Koebel and P. Siffert
CNRS Phase, BP 20, F-67037 Strasbourg Cedex (France)

Abstract

In a step towards intelligent material processing, we studied the effect of the temperature distribution in the growth ampoule on the crystallization process. We constructed a mathematical model to calculate the temperature distribution in the sample, using the temperature profile in the furnace. In the experimental part, this profile was accurately imposed by our modified vertical Bridgman furnace with 12 independent zones. This equipment was applied to pure CdTe, which is known to be a difficult material with which to achieve large single crystal growth. After optimization of the temperature profile and the other growth parameters, we grew several large single crystals.

1. Introduction

Modern control technology together with multi-zone furnaces allow precise control of the temperature profile along the ampoule during crystal growth [1]. However, very little is known about the effect of the temperature profile in the furnace on the crystal growth and the crystalline quality. In this paper, we study the effect of the temperature profile on CdTe crystals in the formation of large single crystals.

Temperature measurements in crystal growth ampoules are nearly impossible. We developed a mathematical model of the heat transfer to calculate the temperature distribution, using a temperature profile of the furnace. With this model we can select those temperature profiles which result in a convex interface shape. For CdTe the temperature range for "good" profiles is very narrow.

To carry out the experimental work, we built a modified vertical Bridgman furnace using 12 independently regulated zones with a precision of 0.1 K. In Section 4 we present some details of crystals and their characterization.

2. Mathematical model of heat transfer

The purpose of the model is to calculate the temperature distribution inside the growth ampoule using the temperature profile of the furnace. Some remarkable analytical approaches were made by Naumann and Lehoczky [2]. Analytical approaches are very difficult owing to the non-linearities during the phase transition at solidification and during radiation heat transfer. Models using the finite element approach do not have this drawback [3]. We used a finite element approach [4] to have full flexibility in choosing a temperature profile. Our model is based on basic heat conduction, considering the conductibility changes with temperature. Convection and radiation are not considered in this article. The basic formulae can be found in ref. 5. We used a direct-solving algorithm in which non-linearities are treated by piecewise linearization and iteration. The thermal parameters used for the calculation are as follows: liquid CdTe, $K = 0.150$ W K^{-1} m^{-1}; solid CdTe, $K = 0.075$ W K^{-1} m^{-1}; quartz, $K = 2.7$ W K^{-1} m^{-1}. With this model, we can calculate the isotherms in the growth ampoule in the absence of convection. The isotherm of the melting point is regarded as the interface shape. The direct verification of the predicted interface shape is very difficult. Some quenching experiments showed a very high crystallization rate of pure, stoichiometric CdTe and the original interface shape could not be determined. However, there is an indirect verification: all the experiments with a predicted convex interface shape resulted in crystals with large, single crystalline areas.

3. Crystal growth equipment

The rapid progress in microelectronics and power electronics has led to new concepts in crystal growth equipment. With a multi-zone furnace, the temperature profile can be imposed by the control electronics. We decided to construct crystal growth equipment with the

0921-5107/93/$6.00
© 1993 - Elsevier Sequoia. All rights reserved

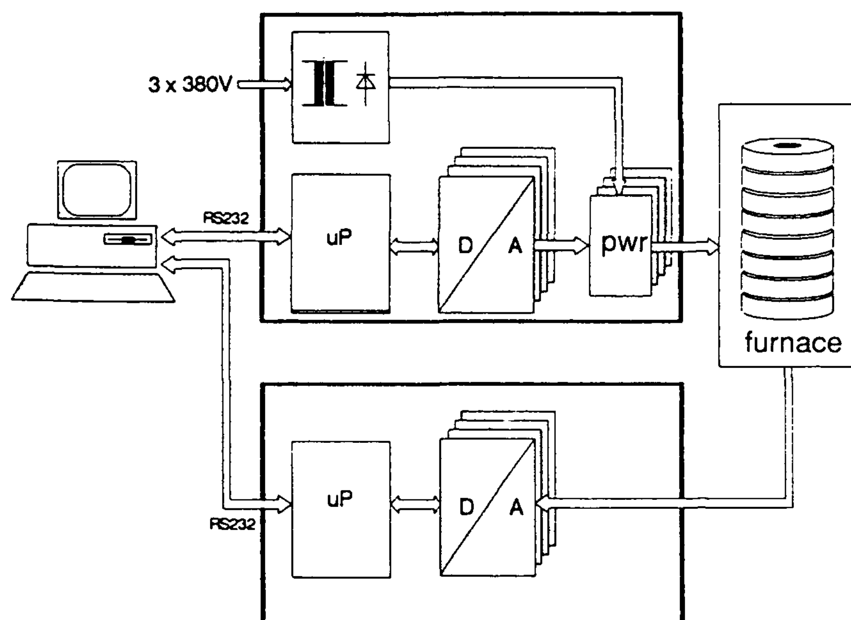

Fig. 1. Diagram of the system.

following characteristics: 0.1 K temperature precision, 12 zones, a digital temperature control algorithm and an automatic growth procedure for exact reproducibility.

The system is comprised of four modules: the furnace, the power control unit, the temperature measurement system and the control computer (as seen in Fig. 1). The furnace was a modified vertical Bridgman furnace with 12 zones. The internal diameter was 40 mm, the zone height 30 mm and the total height 360 mm. The maximum temperature was 1300 °C. The power control unit delivered the heating voltage and current (maximum 30 V and 20 A) to the 12 zones with a total precision of 0.0018 V (14 bits). The temperature measurement system used type S thermocouples to measure the 12 zones with an accuracy of 0.05 K. An IBM PC was used to regulate the furnace temperature and to control the whole growth process. This was done to ensure the exact reproduction of the experimental run.

The equipment has been in operation for 1 year and is stable. It is very useful for research to have the capability of imposing a chosen temperature profile by electronic means without having to make changes to the furnace hardware.

4. Experimental procedure and results

In most experiments we used undoped CdTe. A graphite-coated quartz ampoule ($d = 35$ mm, $l = 200$

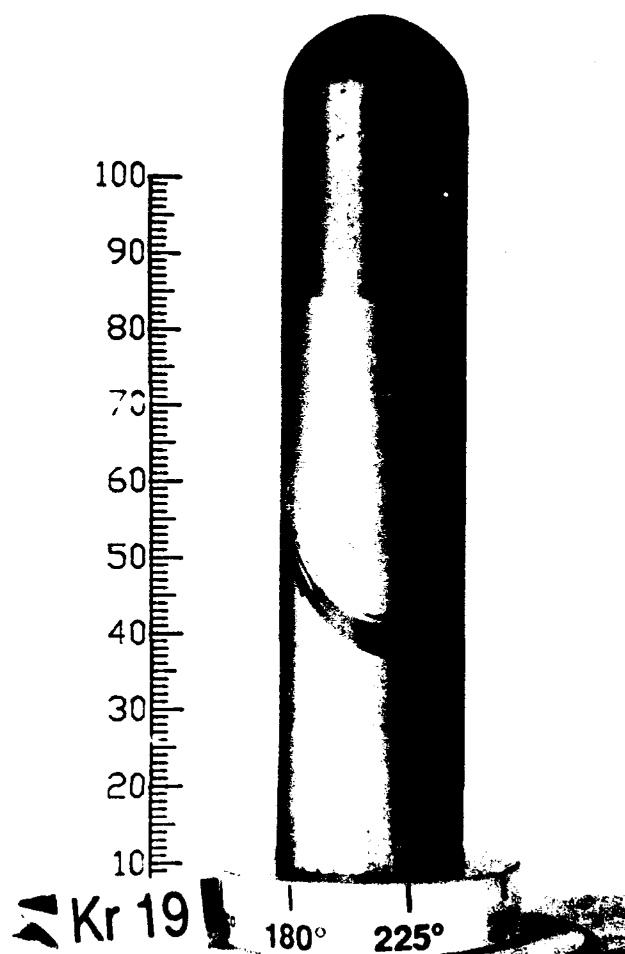

Fig. 2. Typical crystal grown with our equipment.

TABLE 1. Impurity analysis of the crystals (weight-ppm)

Al	Fe	Cu	Ge	Mg	Mn	Se	Ni	Ag	Au	Pb	Sb	Zn
<0.1	<0.1	<0.02	<0.03	<0.5	<0.05	0.8	<0.5	<0.05	<0.05	<1	<0.3	<1

mm) was filled with 99.9999% purity CdTe material, and a slight excess of Te was added to avoid the high vapour pressure of Cd. The ampoule was evacuated and sealed. In the furnace we increased the temperature at a rate of 200 °C h^{-1} up to 1150 °C. This temperature was maintained for several hours to achieve good mixing of the material. Then the temperature profile was imposed and the ampoule lowered at a speed of 2.5 mm h^{-1}. After crystal growth, the temperature was lowered slowly to avoid mechanical stress during cooling. Figure 2 shows a typical crystal grown with our equipment. It started directly as a single crystal, had one grain boundary and continued as a single crystal. Twinning was observed in our crystals. An analysis of some impurities is given in Table 1. The resistivity is about 10^5 to 10^6 Ω cm. The etch pit density is in the range of 3×10^5 cm^{-2}. A thermal stimulated current spectrum is shown in Fig. 3.

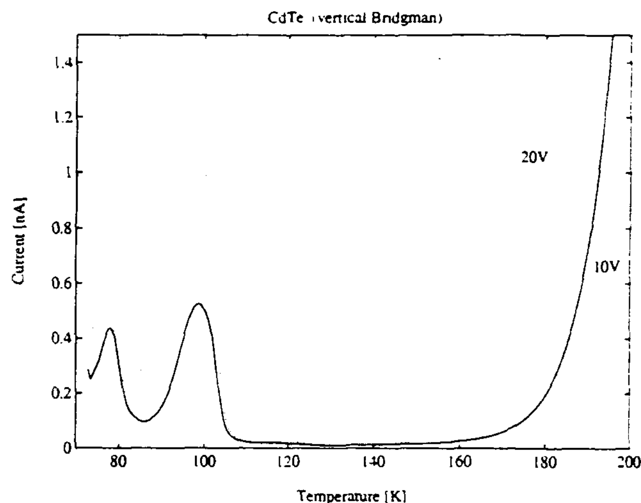

Fig. 3. Plot of current *vs.* temperature for vertical Bridgman grown CdTe.

5. Conclusion and discussion

We developed a mathematical model of the temperature distribution in the growth ampoule, considering heat conduction and conductibility change on phase transition. This model, together with the law of convex interface shape, helped us considerably in understanding and finding the growth conditions for large single crystal growth, a major aim of our work. These crystals were grown by very accurate and versatile furnace equipment.

Of course, there are many questions remaining. We would like to verify directly the predicted interface shape during growth to improve the mathematical model. Quenching experiments are not adequate for stoichiometric CdTe growth. Using a dopant with a high segregation coefficient and plotting the isoconcentrations seems to be a better way. Another interesting study previewed is a comparison between electrodynamical gradient (furnace and ampoule are stationary) and conventionally grown crystals. Other objectives are to reduce twinning and subgrain structures by minimizing the mechanical stress.

Acknowledgments

We thank the Oak Ridge National Laboratory for their SCALE computer code collection, which was modified and used for the finite element calculations.

References

1 M. J. Crochet, F. Dupret, Y. Ruckmans, F. T. Geyling and E. M. Monberg, *J. Cryst. Growth*, 97 (1989) 173.
2 R. J. Naumann and S. L. Lehoczky, *J. Cryst. Growth 61* (1983) 707.
3 L. Y. Chin, *J. Cryst. Growth, 62* (1983) 561.
4 SCALE 4 (Heating 6.1) computer code collection, Oak Ridge National Laboratory, Oak Ridge, TN, 1990.
5 H. S. Carlslaw and J. C. Jaeger, *Conduction of Heat in Solids*, Oxford University Press, 1959, pp. 6.

Heteroepitaxy of CdTe on GaAs and silicon substrates

J. P. Faurie, R. Sporken, Y. P. Chen, M. D. Lange and S. Sivananthan

Microphysics Laboratory, Physics Department, University of Illinois at Chicago, PO Box 4348, Chicago, IL 60680 (USA)

Abstract

CdTe can be grown directly by molecular beam epitaxy on substrates such as GaAs or silicon, which exhibit very large lattice mismatches of 14.6% and 19% respectively. The occurrence of dual epitaxy, which has been previously reported for growth on (100)GaAs, has also been found recently for growth on (211)GaAs. The (133)CdTe-(211)GaAs heterointerface presents a smooth continuation of the tetrahedral bond network from GaAs to CdTe, which is not the case for the (211)CdTe-(211)GaAs interface. Single-domain, twin-free CdTe(111)B films are currently obtained on Si(100) surface where single atomic steps are dominant. The crystalline quality of CdTe/Si films has been dramatically improved as confirmed by X-ray diffraction, photoluminescence and electron microscopy investigations. The narrowest rocking curves obtained for as-grown epilayers are 70 arcsec for (133)CdTe/(211)GaAs, 50 arcsec for a flash-annealed (211)CdTe/(211)GaAs and 140 arcsec for (111)B CdTe/(100)Si. These results confirm that CdTe/GaAs and CdTe/Si composite substrates should be viewed as prime candidates to replace bulk CdTe substrates.

1. Introduction

CdTe is very often viewed as an almost ideal substrate for the epitaxy of $Hg_{1-x}Cd_xTe$ which is obviously very important for IR detector technology. $Cd_{1-x}Zn_xTe$ is another commonly used material because its lattice parameter can be tuned by adjusting the Cd/Zn ratio to obtain a perfect lattice match for any $Hg_{1-x}Cd_xTe$ composition.

Today, these two materials are still widely used as substrates for this purpose, but they have some intrinsic limitations which appear to be difficult to solve. Large-area substrates which exhibit uniform high structural quality are difficult to produce. Furthermore, it has been found recently that the electrical properties of HgCdTe layers grown by molecular beam epitaxy (MBE) on commercially available CdTe and $Cd_{1-x}Zn_xTe$ substrates are controlled by impurities diffusing from the substrate [1]. Because of these limitations and because CdTe and $Cd_{1-x}Zn_xTe$ substrates are very expensive, fragile and difficult to process, GaAs and, more recently, silicon have received much interest not only as substrates for CdTe. The composite CdTe/GaAs or CdTe/Si material can be used as an alternative substrate for $Hg_{1-x}Cd_xTe$ but also in γ-ray and X-ray imaging and spectroscopy, as well as in solar energy conversion and in electro-optical modulation. Compared with CdTe and $Cd_{1-x}Zn_xTe$, GaAs and silicon are much stronger, are available in larger areas with high quality and they are much less expensive than CdTe (at 5×10^{-2} and 2×10^{-3} times the cost per unit area for GaAs and silicon respectively). For IR technology silicon is even more attractive than GaAs because in focal plane array technology the coupling of the silicon substrate with the silicon readout will allow the fabrication of very large arrays, exhibiting long-term thermal cycle reliability because of the absence of thermal expansion mismatch.

CdTe/GaAs and CdTe/Si heteroepitaxial systems have very large lattice mismatches of 14.6% and 19% respectively. The epitaxy requires the formation of heterointerfaces with mixed atomic bonds in order to minimize (and ideally to avoid) electrostatic charge imbalances at the interface. GaAs retains here an advantage over silicon since the ionicity of CdTe is closer to that of GaAs than to that of silicon. GaAs might also have another advantage over silicon as a substrate for CdTe growth by MBE in that the cleaning temperature of 550 °C required for GaAs is much lower than that for silicon, which is 850 °C-900 °C. This causes less outgassing, reducing the likelihood of recontamination of the substrate surface, which is critical for the initiation of the growth. The purpose of this paper is to present the current status of our work on the MBE growth of CdTe on GaAs and on silicon.

2. Experimental details

2.1. GaAs substrate

The growth of CdTe on GaAs(100) has led to a novel epitaxial phenomenon called dual epitaxy with

the occurrence of both the (100)CdTe/(100)GaAs and the (111)B CdTe/(100)GaAs epitaxial orientations. Numerous studies have been carried out to elucidate the origin of the dual epitaxy, resulting in the findings of a number of intriguing aspects of this epitaxial system [2–7].

Recently, we have found that the growth of CdTe on (211)GaAs by MBE also results in dual epitaxy, *i.e.* the occurrence of the (211)CdTe/(211)GaAs and (133)CdTe/(211)GaAs [8]. One of the important observations made by high resolution transmission electron microscopy (HRTEM) is a smooth continuation of the tetrahedral bond network from the GaAs crystal to the CdTe at the (133)CdTe–(211)GaAs interface, which is in striking contrast to the (211)CdTe–(211)GaAs interface for which the tetrahedral bond network is severely distorted because of closely spaced misfit dislocations. Characterization by reflected high energy electron diffraction, X-ray diffraction, transmission electron microscopy (TEM) and photoluminescence has indicated high crystalline quality for both growth orientations, especially for the (133), which may be attributed to the aforementioned difference of interfacial atomic structures.

The analysis of the atomic structure of the (133)CdTe–(211)GaAs interface carried out using HRTEM has shown that the lattice mismatch at the interface is accommodated by a novel mechanism, which occurs with the combination of the 14.6% lattice mismatch between CdTe and GaAs and one wurtzite-type bond sequence of the (211) substrate surface. The geometrical condition for the new mechanism has been summarized as follows [9]. First, consider the growth of one zincblende-type crystal on the surface of another zincblende-type crystal, the surface orientation of which is tilted with respect to a {111} plane by a relatively small angle. If one wurtzite-type bond sequence occurs at the interface, the two crystals will face each other with mutually different crystallographic planes; the two planes are (211) and (133) in the present case. Two surfaces, which are tilted from the {111} plane, are made up of periodic arrangements of {111} terraces. If the unit terrace widths of the two surfaces are nearly equal to each other, the two crystals can form an epitaxial interface without having severe distortions of the tetrahedral bond network and, hence, can accommodate the lattice mismatch between them without introducing closely spaced misfit dislocations. The equality of terrace widths is obtained by the proper combination of the size of the lattice mismatch and the pair of crystallographic planes which form the epitaxial interface. With the geometrical condition summarized above, one finds that the new mechanism can be applied to the growth of other systems of zincblende-type crystals.

At the (133)CdTe–(211)GaAs interface the lattice mismatch is not accommodated by the formation of closely spaced misfit dislocations, in contrast to the (211)CdTe–(211)GaAs interface, but by a new mechanism requiring a lattice mismatch close to 14.6% and a (211) substrate surface as stated before. Therefore, we believe that (133)CdTe/(211)GaAs epitaxy should not be viewed as a twin relation with (211)CdTe [10].

The quality of CdTe which can be grown on GaAs has improved over the years. An important step was made with (111)B CdTe/(100)GaAs when we showed that the severe twinning occurring in the (111) orientation can be eliminated by using a slightly misoriented (100)GaAs face [11]. A misorientation of 2° towards [110] was found to be significantly better than for either of the other orientations tested. A dramatic improvement in crystal perfection has been found for these films compared with those grown on nominal (100)GaAs. On nominal (100)GaAs, X-ray double crystal rocking curve (DCRC) full widths at half-maximum (FWHMs) of CdTe layers were in the 200–300 arcsec range, whereas DCRC FWHMs of 60 arcsec were reported on misoriented (100)GaAs, though not on a routine basis. Such a low value has never been reported for (100)CdTe/(100)GaAs, the homo-orientation being more difficult to control. The effect of the tilt on the suppression of the twins was confirmed later [12] and it has been reported that twin-free layers are obtained on a GaAs surface with gallium steps [13]. X-ray measurements performed on the first CdTe(211)/GaAs(211) and CdTe(331)/GaAs(211) epilayers have shown FWHMs of the order of 160 arcsec and 140 arcsec respectively [8]. These results have been improved on since then. (133)CdTe is now routinely grown with FWHMs of 80 arcsec, the best result being 70 arcsec. For (211)CdTe, FWHMs of 90 arcsec are obtained on a regular basis. However, using a flash technique for annealing on a CdTe(211) layer 11.8 μm thick, an FWHM of 50 arcsec has been measured. To the best of our knowledge, this is the lowest value ever obtained by any growth technique for a CdTe film grown on a GaAs substrate.

2.2. CdTe/Si

Before presenting the development of the growth of CdTe on silicon by MBE, we would like to recall some of the challenges related to this process. First, the very large lattice mismatch (19%) between CdTe and silicon could lead to the idea that epitaxial growth of CdTe on silicon is impossible. It is now well established that epitaxial growth does indeed occur, although the lattice mismatch is expected to create many dislocations at the CdTe–Si interface. Fortunately, this problem is reduced to some extent because the epitaxial relationship is

CdTe(111)/Si(100), which brings the lattice mismatch down to 3.4% along the CdTe[$\bar{2}$11]. Also, it appears that the crystal quality of the CdTe layers has been improved tremendously over the past three years; the FWHM of the X-ray DCRCs is now only 140 arcsec for the best CdTe(111)B/Si(100).

There is also a relatively large thermal mismatch between CdTe and silicon. For practical device applications, one thus should be concerned about the risk of cracking or peeling of the films because of temperature changes either during the fabrication of the film or device, or during its operation. Finally, as a result of the CdTe(111)/Si(100) epitaxial relationship, the CdTe[$\bar{2}$11] axis can be parallel to either the Si[0$\bar{1}$1] or the Si[011] direction. This can generate the formation of domains, rotated 90° apart, whose boundaries are defects which can lead to poor device performance. Therefore, it is important to develop a method to avoid the formation of such domains. We will show that significant progress has been made recently towards this end.

As on other substrates, CdTe(111)B on Si(100) also suffers from the risk of twinning. This problem is not specific to the use of silicon substrates, but it is interesting to investigate the effect of the silicon substrate condition on the formation of twins in the CdTe films. As for now, let it suffice to say that twin-free single-domain films of CdTe(111)B have been grown on Si(100). We will describe the characteristics of the best of these films and show the improvements which were achieved over the last three years. Whenever possible, the reasons for these improvements will be discussed.

3. Results

Direct growth of CdTe on silicon by MBE was reported in 1983 by Lo *et al.* [14] but these layers seemed to consist of a mixture of several crystalline phases. Chou *et al.* [15] used metallo-organic chemical vapor deposition (MOCVD) to grow CdTe directly on silicon. They did not specify the orientation of the layers or whether single crystalline films were obtained. Since 1989, the Microphysics Laboratory of the University of Illinois at Chicago has developed a research program regarding the direct growth of CdTe on Si(100) by MBE. While much work still needs to be done to understand the CdTe–Si interface and to improve further the quality of the CdTe layers, the results are very promising. The best layers are twin-free (within the detection limit of the X-ray DCRC experiment), single-domain, single crystal CdTe(111)B with DCRCs with FWHMs of 140 arcsec. Korenstein *et al.* [16] grew CdTe(111)B on Si(100) by hot-well epitaxy. Using experimental conditions similar to those at the Microphysics Laboratory, they obtained X-ray DCRCs with FWHMs of 315 arcsec.

Some groups tried to overcome the difficulties related to the direct growth of CdTe on silicon by growing an intermediate layer of another material. Examples include (Ca,Ba)F_2 [17], GaAs [18] or ZnTe [19]. Although this method has some short-term advantages, such as the possibility to grow CdTe(211)B or CdTe(100), the presence of such an intermediate layer is not desirable. Recent success with the direct growth of CdTe on silicon fosters the hope that the growth of an intermediate buffer layer can be abandoned.

Figure 1 illustrates the improvement of the crystallinity of the CdTe(111)B/Si(100) layers grown by MBE in the Microphysics Laboratory since 1989. The FWHM of the X-ray DCRCs is taken here as a measure of the structural quality of the layers. From about 1000 arcsec three years ago, the FWHM has been reduced to 140 arcsec for the best layers grown during the second quarter of 1992. Overall, this improvement correlates well with the decrease in the FWHM of the BE peaks in the low temperature photoluminescence spectra. At 12 K, the FWHM is now as

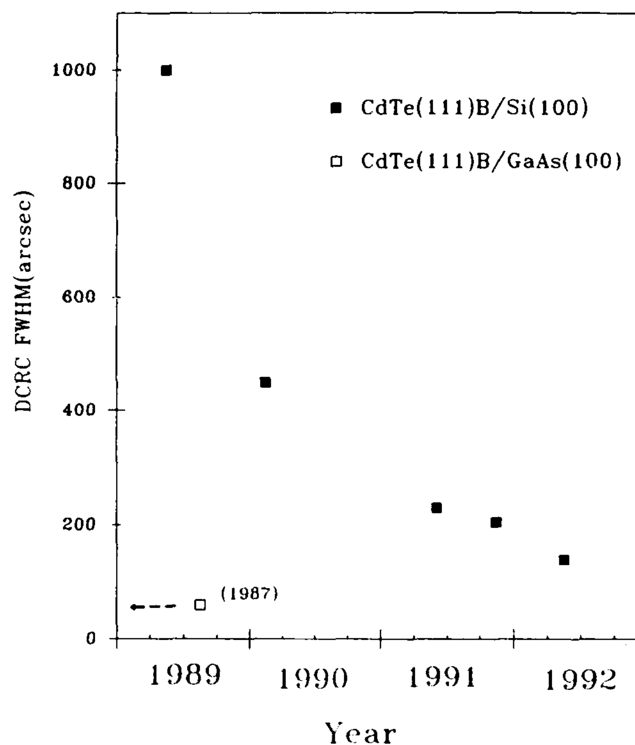

Fig. 1. Full width at half-maximum of the X-ray double-crystal rocking curves on CdTe(111)B/Si(100). Data are for some of the best samples grown in the Microphysics Laboratory since 1989. No distinction is made between substrates with different misorientations. The value for the best CdTe(111)B/GaAs(100) (60 arcsec obtained in 1987) is included for comparison.

low as 1.4 meV, compared with 5.6 meV for some of the earlier samples [19]. The BE peaks from the photoluminescence spectra for such a sample are shown in Fig. 2. The most recent data can be compared with values for CdTe/GaAs for which 60 arcsec and 0.7 meV are the best results reported so far for as-grown layers. Taking into account the fact that the growth for CdTe/GaAs is already much more mature, we consider the results on CdTe/Si as quite competitive.

The improvements in layer quality are due to several reasons. First, the substrate preparation has been improved steadily over the last three years. The chemical cleaning we use before loading the substrates into the MBE system is derived from methods known as Shiraki [20, 21] or RCA clean. The handling of the wafers as well as of the cleaning equipment has been simplified as much as possible, and the timing of the cleaning process was adapted to our needs. *In situ* cleaning done at 850 °C–900 °C has benefited from the use of a new MBE system which was set into operation in September 1989. This system is designed for MBE growth on large-area substrates and one of its interesting features for the growth of CdTe/Si is its newly designed substrate heater for indium-free mounted samples up to 125 mm in diameter.

Further improvements of the crystal quality were achieved when the formation of twins and domains in the CdTe layers was avoided. Cleanliness of the substrates, distribution of steps on the substrate surface and good control of the first stages of growth seem to play key roles in this regard. These issues will be addressed again in a later part of this article.

The surface morphology of the CdTe layers on Si(100) is checked by scanning electron microscopy (SEM). As we pointed out earlier [22], no features are detected on twin-free single-domain films, whereas the domain boundaries are clearly seen in those films where the domains are present. We have not yet completed a study of the effect of repeated temperature changes over a wide range. However, some information can be gathered from the behavior of the CdTe/Si films after low temperature photoluminescence measurements as well as that of $Hg_{1-x}Cd_xTe$/CdTe/Si films after Hall effect measurements. For both experiments, the samples are cooled below 20 K and are allowed to warm up to room temperature at the end of the experiment. For samples up to 10–12 μm thick we do not see cracks or other macroscopic defects caused by this treatment. We are now extending our investigation to thicker samples.

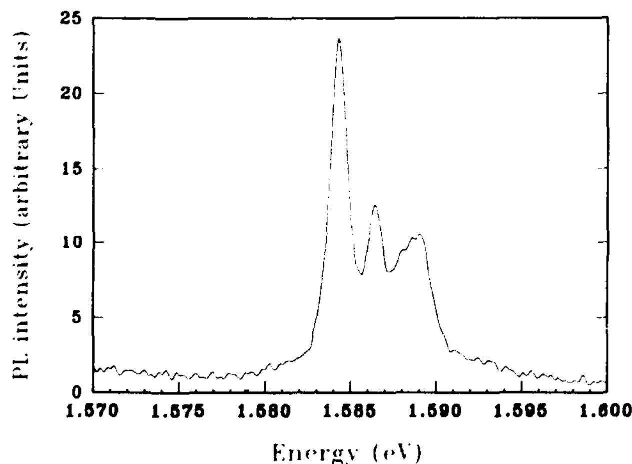

Fig. 2. Photoluminescence spectrum of CdTe(111)B/Si(100) at 12 K excited with a focused argon laser (514.5 nm wavelength) at 1 mW power. The layer is single-domain CdTe(111)B, 11 μm thick.

One of the advantages of silicon substrates is their large size. The MBE equipment of the Microphysics Laboratory can handle substrates with diameters up to 125 mm. We have investigated the uniformity of the MBE-grown layers over such large areas and results have been presented elsewhere [23]. Some of the thickness uniformity data are summarized in Table 1. Shown are the standard deviation of the CdTe layer thickness as well as its maximum variation relative to the average thickness for diamond wafers with diameters of 2, 3 and 5 in.

4. Discussion

We have mentioned repeatedly that to grow CdTe layers for practical purposes it is essential to develop a technique which consistently produces twin-free single-domain films. A first attempt to grow single-domain films involved the use of vicinal Si(100) surfaces with a relatively large tilt (6°–8°) [22]. On such substrates, the CdTe layers were always of the single-domain type and the substrate tilt also seemed to help in avoiding the twinning, at least over large parts of the samples. Concurrently with this obvious improvement of the layer quality, the photoluminescence linewidth decreased to 3 meV. Surprisingly, however, the FWHM

TABLE 1. Thickness uniformity for CdTe(111)B/Si(100) grown by MBE for various substrate diameters

Diameter	5 in (%)	3 in (%)	2 in (%)
$\frac{\sigma d}{\bar{d}}$	2.3	0.6	0.3
$\frac{d_{max} - d_{min}}{\bar{d}}$	6.5		1.0

of the X-ray DCRCs was always larger than for layers grown on nominal Si(100)—usually above 600 arcsec. Although we do not know the effect of these large FWHMs on the quality of $Hg_{1-x}Cd_xTe$ subsequently grown, this fact prompted us to investigate the effect of other tilt angles. This study is still in progress and results will be published in a separate paper. At any rate, it is clear that a small tilt (a few degrees or even less) away from (100) is sufficient to grow single-domain films. Also, the best CdTe layers grown on Si(100) so far were obtained on such slightly misoriented substrates. This may also explain why single-domain films are obtained on some nominal Si(100) substrates, because these substrates usually have a small accidental tilt. In that case, high preheating temperatures would not be necessary for the growth of single-domain CdTe layers on some nominal Si(100) substrates, contrary to our initial assumption [24]. This fact has now been verified experimentally.

In a recent paper [25], we have proposed a model for some of the mechanisms which take place at the beginning of the CdTe–Si(100) interface formation. In this model, single-domain films grow on Si(100) as a consequence of two processes: (1) the step distribution on the substrate surface changes, resulting in the doubling of steps owing to the interaction of the substrate with the incoming atoms, and (2) there is a preference for the growth of CdTe to start at one of the two types of step edges that are present on Si(100). However, if nucleation of CdTe occurs predominantly on the terraces rather than on one type of step, double-domain films will grow except if all the terraces belong to the same silicon-sublattice. As a result, we suggest that single-domain films of CdTe(111)B can be grown on Si(100) under the following circumstances: either the substrate tilt is large enough so that even on the clean substrate, all terraces belong to the same sublattice or, if the substrate misorientation is small, the growth conditions (including substrate cleanliness) must be such that silicon and tellurium atoms can easily diffuse to the step edges. We mention only tellurium atoms here because we have found by X-ray photoelectron spectroscopy that only tellurium binds to the silicon atoms. Cd–Si bonds are not formed, so cadmium binds to the tellurium atoms which are already on the silicon surface. Obviously, in order to grow good CdTe layers on Si(100) with a large misorientation, the substrate cleaning and initial growth conditions are also critical. However, the conditions to grow single-domain CdTe films are less stringent on these substrates than for Si(100) with a small misorientation.

Based on this discussion, we expect to see a range of domain size ratios between 0 (single-domain film) and 1 (two domains of equal size), depending on the experimental conditions (substrate tilt, cleanliness, substrate temperature, growth rate, etc.). A quantitative relation between these factors is difficult to establish, but qualitatively we note that as the preparation of the substrates and the control of the initial growth conditions improves, the minimum value of the substrate tilt for single-domain growth decreases. Finally, it is interesting to note that, as long as the size of one domain is small compared with the other, the upper part of the film can be single domain even if the growth starts with two domains.

The microscopic mechanism which suppresses the twin formation is more difficult to establish. As for the domains rotated 90°, a slight tilt of the substrate surface away from Si(100) seems to help for the growth of twin-free layers. TEM images obtained recently on such a sample show that the microstructure of the CdTe layer is very similar to that of CdTe(111)B on GaAs. While the lower part of this epilayer (up to 3 or 4 μm) contains many microtwins, the upper portion is twin free. X-ray DCRC analysis may therefore lead to the belief that a substantial fraction of the layer is twinned, because of the large probing depth of this technique, while these defects may be limited to the region closest to the substrate–epilayer interface.

5. Conclusions

MBE growth of CdTe either on GaAs or on silicon substrates has been extensively studied in the last few years. Recently, it has been found that the growth of CdTe on (211)GaAs results in dual epitaxy, *i.e.* (211)CdTe/(211)GaAs and (133)CdTe/(211)GaAs. Both X-ray diffraction and TEM indicate that (133)CdTe epilayers have better structural qualities than those of (211)CdTe epilayers, which may be attributed to the smooth continuation of the tetrahedral bond network at the heterointerface. DCRC FWHMs of 70–80 arcsec are currently obtained for this epitaxial orientation. The analysis by HRTEM has shown that the lattice mismatch at the (133)CdTe–(211)GaAs interface is accommodated by a novel mechanism.

The quality of (111)B CdTe grown on Si(100) has also been significantly improved in the last three years as illustrated by DCRC FWHMs which have decreased from 1000 arcsec down to 140 arcsec for the best film. This improvement has been obtained by a systematic investigation of substrate cleaning, substrate misorientation and growth parameters. Single-domain films, which previously were obtained only on vicinal surfaces with double atomic steps, are currently grown on surfaces where single atomic steps are dominant. The twinning has also been eliminated on the top portion of the CdTe epilayer. We have shown that the

quality of CdTe grown directly on silicon is equivalent to that of CdTe grown on silicon with a buffer layer. These results confirm that CdTe/GaAs and CdTe/Si offer many advantages compared with CdTe bu . substrates.

Acknowledgments

The work was supported by DARPA and monitored by AFCSR through Contract F49620-90-C-009 DEF. One of us (RS) would like to acknowledge support from the Belgian National Fund for Scientific Research. We would like to thank Dr Abad for photoluminescence experiments and Z. Ali for technical assistance.

References

1 S. Sivananthan, P. S. Wijewarnasuriya and J. P Faurie, unpublished.
2 N. Otsuka, L. A. Kolodziejski, R. L. Gunshor, S. Datta, R. N. Bicknell and J. F. Schetzina, *Appl. Phys. Lett.*, *46* (1985) 887.
3 J. P. Faurie, C. Hsu, S. Sivananthan and X. Chu, *Surf. Sci.*, *168* (1986) 473.
4 L. A. Kolodziejski, R. L. Gunshor, N. Otsuka, X. C. Zhang, S. K. Chang and A. V. Nurmikko, *Appl. Phys. Lett.*, *47* (1985) 882.
5 C. Hsu, S. Sivananthan, X. Chu and J. P. Faurie, *Appl. Phys. Lett.*, *48* (1986) 908.
6 R. Srinvasa, M. B. Panish and H. Temkin, *Appl. Phys. Lett.*, *50* (1987) 1441.
7 G. Feuillet, J. Cibert, E. Ligeon, Y. Gobil, K. Smainadayar and S. Tatatrenke, *Mater. Res. Soc. Symp. Proc.*, *148* (1989) 389.
8 M. D. Lange, R. Sporken, K. K. Mahavadi, J. P. Faurie, Y. Nakamura and N. Otsuka, *Appl. Phys. Lett.*, *58* (1991) 1988.
9 Y. Nakamura, N. Otsuka, M. D. Lange, R. Sporken and J. P. Faurie, *Appl. Phys. Lett.*, *60* (1992) 1372.
10 M. D. Lange, R. Sporken, K. K. Mahavadi, J. P. Faurie, Y. Nakamura and N. Otsuka, *Appl. Phys. Lett.*, *59* (1991) 2055.
11 J. L. Reno, P. L. Gourley, G. Monfroy and J. P. Faurie, *Appl. Phys. Lett.*, *53* (1988) 1747.
12 J. Cibert, Y. Gobil, K. Saminadayar, S. Tatarenko, A. Chami, G. Feuillet, Le Si Dang and E. Ligeon, *Appl. Phys. Lett.*, *54* (1989) 828.
13 E. Ligeon, C. Chami, R. Danielou, G. Feuillet, J. Fontenille, K. Saminadayar, A. Pouchet, J. Cibert, Y. Gobil and S. Tatarenko, *J. Appl. Phys.*, 67 (1990) 2428.
14 Y. Lo, R. N. Bicknell, T. H. Myers, J. F. Schetzina and H. Stadelmeier, *J. Appl. Phys.*, *54* (1983) 4238.
15 R. L. Chou, M. S. Lin and K. S. Chou, *Appl. Phys. Lett.*, *48* (1986) 523.
16 R. Korenstein *et al.*, presented at the *1991 US Workshop on Mercury Cadmium Telluride, Dallas, TX, October 1991.*
17 H. Zogg and S. Blunier, *Appl. Phys. Lett.*, *49* (1986) 1531.
18 J. M. Arias, S. H. Shin, M. Zandian, J. G. Pasko and R. E. DeWames, presented at the *1990 US Workshop on the Physics and Chemistry of Mercury Cadmium Telluride and Novel IR Detector Materials, San Francisco, CA, October, 1990.*
19 R. Sporken, S. Sivananthan, K. K. Mahavadi, G. Monfroy, M. Boukerche and J. P. Faurie, *Appl. Phys. Lett.*, *55* (1989) 1879.
20 A. Ishizaki and Y. Shiraki, *J. Electrochem. Soc.*, *133* (1986) 666.
21 W. Kern and D. Puotinen, *R. Chem. Assoc. Rev.*, *31* (1970) 187.
22 R. Sporken, M. D. Lange, J. P. Faurie and J. Petruzzello, *J. Vac. Sci. Technol. B*, *9* (1991) 1651.
23 R. Sporken, M. D. Lange, C. Masset and J. P. Faurie, *Appl. Phys. Lett.*, 57 (1990) 1449.
24 R. Sporken, M. D. Lange, S. Sivananthan and J. P. Faurie, *Appl. Phys. Lett.*, 59 (1991) 81.
25 R. Sporken, Y. P. Chen, S. Sivananthan, M. D. Lange and J. P. Faurie, *J. Vac. Sci. Technol., A*, in press.

CdTe rotation growth on silicon substrates by metallo-organic chemical vapour deposition

H. Ebe and H. Takigawa

Fujitsu Laboratories Ltd, 10-1 Morinosato-Wakamiya, Atsugi 243-01 (Japan)

Abstract

We observed a 30° in-plane rotation slip for (111) CdTe epilayers grown on (111) Si substrates by metallo-organic chemical vapour deposition when we increased the group VI to II ratio. We define this effect as rotation growth. This rotation alignment reduces the lattice mismatch between CdTe and silicon from 19% to 3.4%, thus promising better crystallinity. When the group VI to II ratio is increased, the full width at half-maximum of the X-ray rocking curve is decreased from over 1000″ to 400″ for an epilayer 1 μm thick. The rotation growth mechanism was examined by Auger electron spectroscopy and results show that the tellurium atoms are adsorbed to the silicon surface more readily than are cadmium atoms. We also found that the (111) Si substrate had to be misoriented toward the [$\bar{1}$10] direction to suppress twinning in CdTe rotation growth.

1. Introduction

HgCdTe hetero-epitaxial growth on silicon is a key technology for the development of monolithic IR detectors. As CdTe is the most readily available buffer layer for HgCdTe, several attempts have been made to grow CdTe on silicon by molecular beam epitaxy (MBE) [1-3] or metallo-organic chemical vapour deposition (MOCVD) [4, 5]. Since there is a large lattice mismatch of 19% in CdTe/Si, it is difficult to grow good quality epilayers. To reduce this large lattice mismatch some researchers used GaAs [5], BaF_2 or CaF_2 [2] buffer layers between CdTe and silicon. Of these, CdTe direct growth on silicon is still the most attractive, since a simple growth chamber is available and less contamination is expected.

In this paper we study CdTe direct growth on (111) Si by MOCVD. We observed a 30° in-plane rotation of (111) CdTe epilayers on (111) Si substrates and we found that it reduced lattice mismatch between CdTe and silicon from 19% to 3.4%.

2. Experimental details

CdTe was grown on (111) Si substrates by MOCVD. Dimethylcadmium (DMCd) and diethyltelluride (DETe) were used as the cadmium and tellurium sources. (111) Si substrates were misoriented 3° towards [11$\bar{2}$] or [$\bar{1}$10]. Typical chemical cleaning was employed [6]. After annealing the silicon substrates at 1000 °C in a hydrogen ambient, CdTe was grown at a substrate temperature of 400 °C. The epilayers were about 1 μm thick.

Double crystal X-ray diffraction measurement was used to evaluate crystallinity and crystal direction.

3. Results and discussion

3.1. Rotation growth

(111) CdTe was grown on (111) Si substrates. Figure 1 shows the full width at half-maximum (FWHM) of the (333) X-ray rocking curve *vs.* the group VI to II ratio. When the group VI to II ratio is increased, the FWHM decreases from over 1000″ to 400″. The in-plane CdTe crystal direction was evaluated by X-ray diffraction (Fig. 2) to see why the FWHM decreases [7]. In this measurement, the X-ray direction incident on the CdTe epilayer was fixed to get (422) reflection. Specimens were rotated around the epilayer's [111] axis. The (422) X-ray diffraction intensity profile was then measured. Figure 3 shows the (422) X-ray reflection intensity from the CdTe epilayer with respect to the specimen's rotation angle while the (422) reflection angle from the silicon substrate is defined as zero. In this case, the silicon substrate is misoriented in the [11$\bar{2}$] direction. Open circles represent the profile for CdTe grown with group VI to II ratios of 5 and 15, while full circles represent the CdTe profile with a

0921-5107/93/$6.00

© 1993 - Elsevier Sequoia. All rights reserved

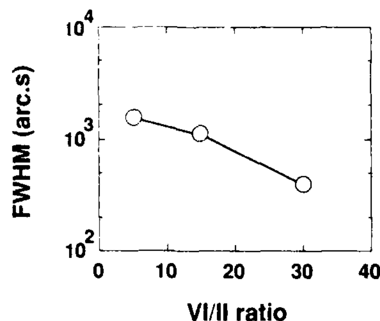

Fig. 1. Full width at half-maximum of the (333) X-ray rocking curve vs. the group VI to II ratio.

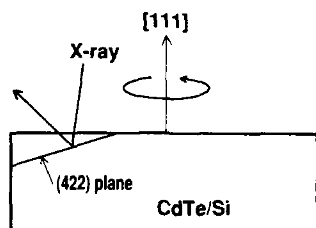

Fig. 2. In-plane crystal direction measurement.

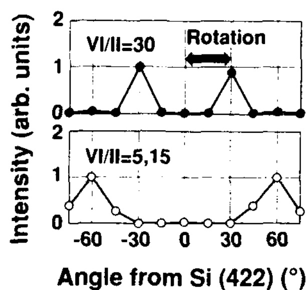

Fig. 3. (422) X-ray reflection intensity from the CdTe epilayer with respect to the specimen's rotation angle while the (422) reflection angle from the silicon substrate is defined as zero.

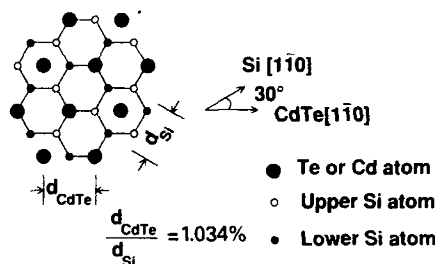

Fig. 4. Top view of 30° rotation slip alignment in the hetero-interface between the CdTe epilayer and the silicon substrate.

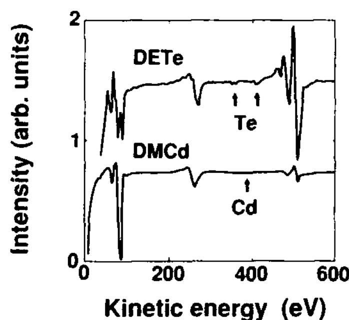

Fig. 5. First growth stage investigation by *ex situ* Auger electron spectroscopy.

group VI to II ratio of 30. For the group ratio of 5 and 15, there is an angle of 60° between the CdTe (422) plane and the direction of the silicon substrate (422) plane. This relationship is similar to the twinning effect which is often observed in zincblende crystals. In contrast, for the group ratio of 30, there is a rotation slip of 30° in the hetero-interface between the CdTe epilayer and the silicon substrate. We define this effect as rotation growth. The two peaks at ±30° indicate twinning in the CdTe epilayers. A method to suppress twinning will be discussed later.

Figure 4 shows the top view of a 30° rotation slip alignment in the hetero-interface between the CdTe epilayer and the silicon substrate. The open circles represent upper silicon atoms and the shaded circles represent lower silicon atoms. To simplify the figure, only one species of tellurium or cadmium atom for CdTe is represented by the large solid circles. In this alignment, the CdTe atom spacing in the [$\bar{1}$10] direction periodically matches the silicon atom spacing in the [11$\bar{2}$] direction. Estimates show that this alignment drastically reduces the actual lattice mismatch from 19% to 3.4%, promising better crystallinity. This effect seems to contribute to the decrease in the FWHM.

Rotation growth seems to originate from the atomic bonding mechanism. The first growth stage was investigated in two samples by *ex situ* Auger electron spectroscopy. Both samples were silicon-exposed for 5 min, one to DETe flow and the other to DMCd. As shown in Fig. 5, a tellurium signal was detected from the sample exposed to DETe. In contrast, no cadmium signal was detected for the sample exposed to DMCd. These results show that tellurium atoms are more readily adsorbed into the silicon than are cadmium atoms. The Auger electron spectroscopy results also suggest that the CdTe growth mode is changed by the group VI to II ratio. When the ratio is small, island growth is dominant because cadmium atoms are adsorbed on top of the CdTe surface in preference to the silicon surface. When the ratio is large, lateral growth is dominant because tellurium atoms are adsorbed on the silicon surface beforehand and then cadmium atoms are readily adsorbed on the tellurium. When the later growth mode is dominant, rotation growth—which we assume is faster in a lateral direction

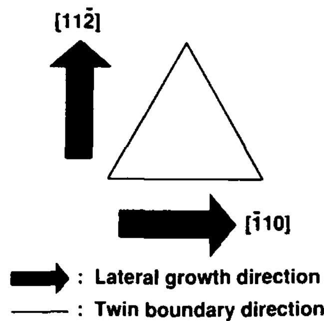

Fig. 6. The relationship between lateral growth direction and twin boundary directions in (111) CdTe.

than normal growth because of lattice matching—dominates at the hetero-interface.

3.2. Twin reduction

As mentioned before, the CdTe crystallinity is improved by the rotation but CdTe exhibits twinning after growth on silicon with a misorientation towards the [11$\bar{2}$] direction. This is because the CdTe epilayer is misoriented towards [$\bar{1}$10], a direction in which CdTe twinning readily occurs. Figure 6 shows the relationship between the (111) CdTe surface misorientation directions and the twin boundary directions. If CdTe grew in a step-flow-like mode, the lateral growth direction matches the misorientation direction. It is difficult to suppress twinning with a surface misorientation towards [$\bar{1}$10], because the lateral growth direction is parallel to one of the twin boundary directions. The CdTe epilayer must be misoriented toward [11$\bar{2}$] to suppress twinning, because all the twin boundaries go across the lateral growth direction. This effect was confirmed experimentally by (111) CdTe MOCVD growth on (111) CdZnTe.

As the [11$\bar{2}$] direction of CdTe is parallel to the [$\bar{1}$10] direction of silicon in rotation growth, the silicon substrate must be misoriented towards [$\bar{1}$10] to suppress twinning. As was predicted, CdTe could be grown on the silicon substrate without twinning by using misorientation toward [$\bar{1}$10].

4. Summarizing remarks

(111) CdTe was grown on a (111) Si substrate by MOCVD.

Increasing the group VI to II ratio rotates the CdTe epilayer 30° in the hetero-interface plane. This rotation reduces lattice mismatch from 19% to 3.4%, promising better crystallinity. When the group VI to II ratio is increased, the FWHM of the X-ray rocking curve decreases from over 1000" to 400" for an epilayer 1 μm thick.

A (111) Si substrate must be misoriented towards [$\bar{1}$10] to suppress twinning in the CdTe rotation growth.

Acknowledgment

We thank Mr. Ishizaki, Dr. Shinohara, Mr. Saito and Mr. Sugiyama for their helpful discussions.

References

1 R. Sporken, M. D. Lange, C. Masset and J. P. Faurie, *Appl. Phys. Lett.*, *57* (14) (1990) 1449.
2 A. N. Tiwari, W. Floeder, S. Blunier, H. Zogg and H. Weibel, *Appl. Phys. Lett.*, *57* (11) (1990) 1108.
3 Y. Lo, R. N. Bicknell, T. H. Myers, J. F. Schetzina and H. H. Stadelmaier, *J. Appl. Phys.*, *54* (7) (1983) 4238.
4 R.-L. Chou and M.-S. Lin, *Appl. Phys. Lett.*, *48* (8) (1986) 523.
5 A. Nouhi, G. Radhakrishnan, J. Katz and K. Koliwad, *Appl. Phys. Lett.*, *52* (24) (1988) 2028.
6 A. Ishizaka and Y. Shiraki, *J. Electrochem. Soc.*, *133* (4) (1986) 666.
7 A. Raizman, M. Oron, G. Cinader and H. Shtrikman, *J. Appl. Phys.*, *67* (3) (1990) 1554.

Materials Science and Engineering, B16 (1993) 60–63

Growth and structure of $CdTe/Cd_{1-x}Mn_xTe$ multiple quantum wells showing excitonic 2S states

J. H. C. Hogg, J. E. Nicholls, S. R. Jackson and W. E. Hagston
Applied Physics Department, University of Hull, Hull HU6 7RX (UK)

D. E. Ashenford and B. Lunn
Engineering Design and Manufacture Department, University of Hull, Hull HU6 7RX (UK)

S. Ali
Physics Department, Albaath University, Homs (Syria)

Abstract

Multiple quantum well structures of CdTe and the dilute magnetic semiconductor $Cd_{1-x}Mn_xTe$ ($x \leq 0.08$) have been grown by molecular beam epitaxy on InSb substrates. High resolution double crystal X-ray diffraction analysis using rocking curve simulations based on the dynamical theory of diffraction shows that these layers are of excellent structural quality and uniformity. The diffraction data indicate the presence of a highly mismatched layer a few monolayers thick at the interface between the InSb substrate and the CdTe buffer layer, which is consistent with previous Raman spectroscopy studies identifying the phase as In_2Te_3. Photoluminescence and photoluminescence excitation spectroscopy measurements indicate that well width fluctuations occur on a monolayer scale. Observation of the 2S state of both light and heavy hole excitons allows the binding energy of both excitons to be deduced—17.1 meV and 19.7 meV respectively—considerably enhanced from their three-dimensional values.

1. Introduction

The work described in this paper is part of a wider study involving the growth and characterization of single and multiple layer structures containing dilute magnetic semiconductor materials. In such structures, the electronic and magnetic systems couple strongly, leading to enhanced optical, electrical and magnetic effects. The present paper concerns the structural and optical investigation of a series of multiple quantum well (MQW) structures based on CdTe and the dilute magnetic semiconductor $Cd_{1-x}Mn_xTe$ grown on (001) InSb substrates by molecular beam epitaxy (MBE). From an analysis of high resolution double crystal X-ray diffractometer data, these structures have been found to contain a highly mismatched layer a few monolayers thick at the InSb–CdTe buffer layer interface, which is identifiable with the In_2Te_3 interfacial layer found at this interface by Raman spectroscopy [1]. The X-ray rocking curve data show extensive short period Pendellösung interference fringes and can be closely matched to simulations based on dynamical diffraction theory.

Photoluminescence and photoluminescence excitation spectroscopy have shown that well width fluctuations are on the monolayer scale. The 2S states of both heavy and light hole excitons have been identified from their large diamagnetic shifts in an applied magnetic field. Their observation has allowed both light and heavy exciton binding energies to be established which are compared with their calculation based on a variational model.

2. Sample growth

The MQW samples were grown using a VG V80H MBE system on (001) InSb which is closely lattice matched (less than 0.05%) to CdTe. The substrate preparation involves a number of cycles of Ar^+ ion cleaning and thermal annealing [2]. CdTe (Hull) and doubly distilled 99.99% Mn (Johnson Matthey) were used as source materials, and the samples were grown at 240°C at a rate of 0.7 μm h^{-1}. The samples consisted of a 15-period MQW stack with nominal growth parameters $L_z = 75$ Å (CdTe), $L_B = 150$ Å ($Cd_{1-x}Mn_xTe$), $x = 0.075$ grown on a CdTe buffer layer 1000 Å thick. All the samples showed excellent structural characteristics, including sample M296 which is the subject of this paper.

0921-5107/93/$6.00

© 1993 – Elsevier Sequoia. All rights reserved

3. X-ray structural analysis

X-ray diffraction data were collected using a double-crystal diffractometer fitted with a (022) channel-cut double-bounce Si beam conditioner. This arrangement, in conjunction with a (111) Si crystal mounted in a dispersive setting on the first axis, which acts as a monochromator, produces a very low background beam at the sample with a small angular width (10 arc sec or less), a wavelength spread of about 0.1 times that of the full width at half-maximum (FWHM) of the Cu Kα_1 profile and reduced Bragg tails. This makes it possible to study fine diffraction details occurring close to strong Bragg reflections.

The 004 Cu Kα_1 rocking curves of this series of MQW samples show, in addition to the main satellite reflections, well-resolved Pendellösung interference fringes which relate to characteristic distances in the structure, enabling these to be accurately determined. The rocking curve of M296 (Fig. 1) shows these features and also a 180″ period modulation of the short period Pendellösung fringes. This modulation corresponds to a real space distance of about 1000 Å and is an artefact which is present in all the samples in the series. This modulation cannot be successfully modelled using either the dynamical or kinematical diffraction theories, even though the CdTe buffer is 1000 Å thick, unless an *ultrathin interfacial* layer of heavily mismatched material is assumed to be present at the InSb–CdTe buffer layer interface. Evidence for the existence of such a layer identified as In_2Te_3, which has an f.c.c. cell with $a_0 = 6.162$ Å, has come from Raman scattering studies of InSb/CdTe heterostructures [1] which suggest that an In_2Te_3 layer up to 20 monolayers thick is formed in the initial stages of CdTe growth on InSb. The lattice parameters of InSb (6.4782 Å) and CdTe (6.4810 Å) differ greatly from that of In_2Te_3, and such an interfacial layer will introduce a phase difference between the wave fields diffracted from the regions of the structure above and below it, because the 004 reflection planes in the In_2Te_3 will be incommensurate. This phase shift, not the scattering from the thin layer itself (which is weak), produces a very significant modulation of the Pendellösung interference fringes. Those fringes arising from the layers above the interfacial layer can be considerably enhanced, depending on the magnitude of the phase shift [3]. This effect has been used by a number of authors to determine the thickness of deliberately grown mismatched layers to monolayer accuracy [4–6]. The phase shift depends on the interfacial layer mismatch, strain state and thickness. For the 004 reflection from (001) InSb/In_2Te_3/CdTe, this phase shift is 29.5° Å^{-1} for In_2Te_3 fully strained to InSb. Since the causal parameter is the phase shift, the resulting Pendellösung fringe modulation is cyclical in units of 2π leading to a corresponding indeterminacy in the interfacial layer thickness equivalent to a phase change of 2π. For fully strained In_2Te_3, the thickness for a phase change of 2π is 12.3 Å.

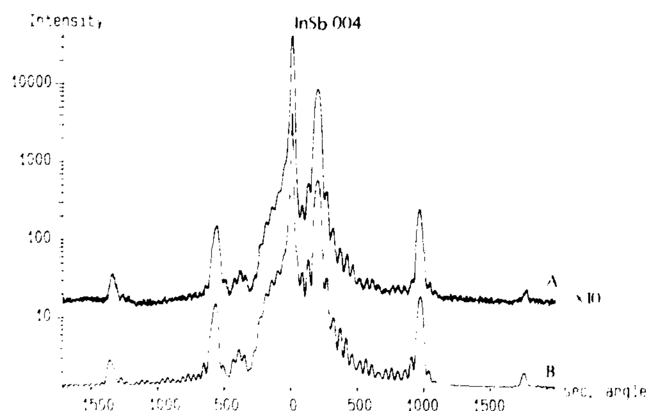

Fig. 1. Results for sample M296. (A) 004 Cu Kα_1 double-crystal X-ray diffraction rocking curve. (B) Dynamical simulation based on the structure InSb|In_2Te_3 14.3 Å|[CdTe 1050 Å]|[MnTe 2 Å]-|(Cd$_{1-x}$Mn$_x$Te 158 Å)(CdTe 75 Å)×15 periods|[Cd$_{1-x}$Mn$_x$Te 158 Å] $x = 0.075$.

For sample M296, simulation of the rocking curve with a fully strained In_2Te_3 layer 2 Å thick included at the substrate–CdTe buffer interface produces a very good fit to the observed 180 arc sec modulation of the Pendellösung fringes. Because of the indeterminacy in the thickness referred to above, acceptable fits also occur for thicknesses which are 2 Å plus integer multiples of 12.3 Å. The simulation in Fig. 1 is based on an In_2Te_3 thickness of 14.3 Å, which is consistent with critical layer thickness considerations, and includes a MnTe layer 2 Å thick to account for the large Mn flux transient which occurs when the Mn cell is first opened. The simulation in Fig. 1 was calculated assuming structural perfection and abrupt interfaces and the very close match to the experimental curve indicates that the samples are close to the ideal. Given the sensitivity of the satellite reflections and the Pendellösung fringe system to layer thickness variations and to interface gradation and roughness which lead to peak broadening and intensity reduction, both increasing with increasing reflection order number, it is apparent that the period cannot vary by more than ±2 Å across the area sampled by the X-ray beam. Interface gradation, which includes the averaged interface roughness occurring on a scale less than the coherence length of the X-ray beam, which is large, is consistent with the estimate of well width fluctuations of plus-or-minus one molecular monolayer (±3.24 Å) determined from photoluminescence studies of the exciton emission lines from this sample, albeit with a

probe size markedly different from the X-ray case since the exciton diameter is calculated to be about 140 Å.

4. Photoluminescence spectroscopy

Photoluminescence (PL) and photoluminescence excitation (PLE) spectroscopy measurements were carried out with the samples at 2 K, excited by either an Ar^+ ion laser or a pyridine dye laser. The emission was dispersed with a 1 m monochromator and detected with a GaAs photomultiplier.

Figure 2 shows the PL of sample M296 excited with 10 mW of 488 nm radiation. The PL emissions are shifted about 25 meV above the band edge of CdTe by confinement of the electrons and holes. The emissions between 7640 and 7660 Å are attributed to the recombination of the 1S state of the heavy hole (e_1h_1) 1S exciton. The broader emission around 7670 Å is shifted about 3 meV to lower energy which, by comparison with bulk CdTe, allows it to be assigned as a donor bound exciton D^0X. The extrinsic nature of this emission was checked by confirming that it saturated at higher laser powers.

The PLE spectrum in Fig. 2 was recorded while monitoring the D^0X emission. The peaks at 7615 and 7652 Å are identified as 1S states of the light (e_1l_1) and heavy (e_1h_1) hole excitons, based on calculation of their energies for partition ratios (the ratio of the valence band to the total band offset) in the range 0.2–0.4 [7–9]. The calculated energies are relatively insensitive to the value of the offset ratio within this range. The

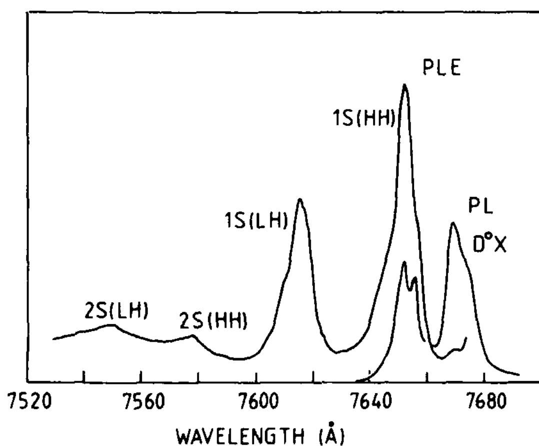

Fig. 2. Photoluminescence (PL) and photoluminescence excitation (PLE) spectra of a $CdTe/Cd_{1-x}Mn_xTe$ MQW (M296) with $L_Z = 75$ Å, $L_B = 150$ Å and $x = 0.075$. The identities of the various peaks are indicated. The structure observed in PL and PLE peaks around 7652 Å is attributed to well width fluctuations.

calculations were carried out assuming pseudomorphic strain of the structure as indicated by the X-ray data. The shoulders observed on each side of the (e_1h_1) 1S PLE peak, and repeated less clearly on the (e_1l_1) 1S peak, are also observed in the PL spectrum but with different intensities. This structure is attributed to well width fluctuations in the MQW stack. The separation between the main peak and the high energy shoulder corresponds almost exactly with that expected for a well width fluctuation of one molecular monolayer. The corresponding separation to the low energy shoulder is equivalent to 0.6 monolayers. The line width and structure observed in these lines indicate that well width fluctuations occur on a monolayer scale. Furthermore, the structure observed on the (e_1h_1) 1S transition is different in PL and in PLE. In particular, the lowest energy peak is stronger in PL. This suggests that migration of excitons takes place, following excitation, to the wider regions of the well. Such migration is unlikely to occur via tunnelling through the relatively thick 150 Å barriers. These considerations, and the observed temperature redistribution of the PL from the low to high energy region, are consistent with intra-well width fluctuations and island growth on a scale comparable with the exciton diameter, calculated as 140 Å (see below).

Of particular interest to the present work is the observation of the two weaker peaks in the PLE spectrum at higher energy which we interpret as the 2S states of the (e_1l_1) and (e_1h_1) excitons. This interpretation is based in part on their diamagnetic behaviour in a magnetic field, applied in the Faraday configuration, and in part on calculations of the binding energies. Application of a field causes both 1S and 2S transitions of Fig. 2 to split into two components. However, the 2S states, unlike their 1S counterparts, move rapidly to higher energy as the field increases. This diamagnetic behaviour is indicative of the larger excitonic radius of the 2S states.

Considerable information can be inferred regarding the exciton binding energies from a knowledge of the 1S–2S energy separations which are observed to be 13.7 meV and 15.8 meV for the (e_1l_1) and (e_1h_1) excitons respectively. We have calculated the exciton binding energies using a variational wavefunction which is the product of the uncorrelated one-particle wavefunctions of the electron and hole (ϕ_e and ϕ_h respectively) and an interaction term ϕ_R which represents the relative motion of the electron and hole, where

$$\phi_R = \phi_{1S} \approx \exp(-r/\lambda)$$

and

$$r^2 = x^2 + y^2 + (1-\beta^2)z^2$$

TABLE 1. Calculated binding energies (BEs) of the 1S and 2S states of the $(e_1 l_1)$ and $(e_1 h_1)$ excitons in a $CdTe/Cd_{1-x}Mn_xTe$ quantum well with $x = 0.075$ for two different partition ratios K

K	$(e_1 l_1)$ $BE_{1S(2S)}$ (meV)	$(e_1 h_1)$ $BE_{1S(2S)}$ (meV)
0.2	11.7 (2.3)	12.8 (2.3)
0.4	12.8 (2.2)	12.8 (2.3)

in which x, y and z are relative coordinates (*e.g.* $x^2 = (x_e - x_h)^2$), and λ and β are variational parameters. An analogous hydrogenic wavefunction was adopted for the 2S state and the variational parameters adjusted to give the maximum binding energy [10]. The calculated binding energies (BEs) for the $(e_1 l_1)$ and $(e_1 h_1)$ excitons in the 1S and 2S states are shown in Table 1 for two different partition ratios.

In the calculations, use of the dielectric constant of CdTe was avoided by expressing the BEs in terms of the three-dimensional Rydberg constant, which for the heavy hole exciton is 10 meV. The equivalent light hole exciton BE was found from the Luttinger effective mass parameters of [11]. The calculated BEs are not very sensitive to the partition ratio K. However, in comparison with the experimentally determined energy differences between the 1S and 2S states, the calculated BEs are clearly underestimated, possibly owing to valence band mixing, which has not been included in these calculations, and interface roughness that is small scale compared with the exciton radius (about 70 Å). Owing to these uncertainties, we have used the ratio of the 1S to 2S BEs from the calculated values to determine the exciton BEs for the 1S and 2S states. For both $(e_1 l_1)$ and $(e_1 h_1)$, this ratio is calculated to have a value close to 5. With this, we determine the 1S BEs for the $(e_1 l_1)$ and $(e_1 h_1)$ excitons to be 17.1 meV and 19.7 meV respectively. Clearly, both light and heavy hole excitons show considerable enhancement of their BEs from their three-dimensional values by confinement. In particular, we notice that for the heavy hole exciton the value is close to that of the LO-photon energy of CdTe, 21.2 meV.

5. Conclusions

We have shown that it is possible to grow MQW structures in the $CdTe/Cd_{1-x}Mn_xTe$ system of excellent quality defined in terms of their structural perfection as determined by high resolution X-ray analysis and by the PL and PLE spectra in which both 1S and 2S states of the light and heavy hole exciton are observed.

References

1 D. R. T. Zahn, K. J. Mackey and R. H. Williams, *Appl. Phys. Lett.*, *50* (12) (1987) 712.
2 D. E. Ashenford, J. H. C. Hogg, D. Johnston, B. Lunn, C. G. Scott and D. Staudte, *J. Cryst. Growth*, *101* (1990) 157.
3 S. Amin and M. A. G. Halliwell, *Inst. Phys. Conf. Ser.*, *117* (9) (1991) 651.
4 L.Tapfer and K. Ploog, *Phys. Rev. B*, *40* (14) (1989) 9802.
5 L. Tapfer, M. Ospelt and H. von Känel, *J. Appl. Phys.*, *67* (3) (1990) 1298.
6 H. Holloway, *J. Appl. Phys.*, *67* (10) (1990) 6229.
7 A. Wasiela, Y. Merle d'Aubigne, J. E. Nicholls, D. E. Ashenford and B. Lunn, *Solid State Commun.*, *76* (1990) 263.
8 W. Heimbrodt, O. Goede, H. E. Gumlich, H. Hoffmann, U. Stutenbaumer, B. Lunn and D. E. Ashenford, *J. Lumin.*, *48–49* (1991) 750.
9 A. Wasiela, P. Peyla, Y. Merle d'Aubigne, J. E. Nicholls, D. E. Ashenford and B. Lunn, *Semicond. Sci. Technol.*, *7* (1992) 571.
10 C. P. Hilton, W. E. Hagston and J. E. Nicholls, *J. Phys. A*, *25* (1992) 2395.
11 Le Si Dang, G. Neu and R. Romestain, *Solid State Commun.* *44* (1988) 1187.

Materials Science and Engineering, B16 (1993) 64–67

Laser growth of CdTe epitaxial film on CdTe substrate

C. Coutal*, J. C. Roustan, A. Azema, A. Gilabert and P. Gaucherel

Laboratoire de Physique de la Matière Condensée, UA CNRS 040, 190 UNSA, 06108 Nice Cedex (France)

R. Triboulet

Laboratoire de Physique des Solides CNRS, 1 Place A. Briand, 92195 Meudon Cedex (France)

Abstract

The growth of CdTe epitaxial film on a CdTe substrate using a laser deposition method has been investigated: the beam of a pulsed ArF excimer laser is focused on a CdTe target and the plume of ejected material is collected onto a (111) Zn-doped CdTe substrate (4%). From the X-ray diffraction measurements and double-diffraction X-ray analysis, the mirror-like film grown is found to be a homoepitaxial layer. Film thicknesses, deduced from optical profilometry, range between 1.9 and 6.5μm. The few differences that appeared between the photoluminescence spectra of the film and the substrate can be explained by a small composition variation and some defects or impurities in the CdTe that lead to new radiative transitions.

1. Introduction

Much progress has been made recently in the epitaxial layer growth technologies and, in particular, molecular beam epitaxy (MBE) [1–3] and metallo-organic chemical vapour deposition (MOCVD) [4, 5] give high quality epitaxial films. Also, laser deposition is less used for II–VI film fabrication [6].

Since their introduction, excimer lasers have quickly found increasing use in material processing applications, mainly because the short wavelength output of lasers results in material removal with few thermal effects. Pulsed ArF excimer lasers used for ablation of CdTe have an efficiency of 0.1 μm per pulse for a fluence of 400 mJ cm^{-2}. The ejected material collected on a substrate leads to the deposition of a film. The properties of excimer laser ablation, such as its few thermal effects and its ability to reproduce the composition of an appropriate target onto a neighbouring substrate, lead us to investigate the possibility of growing CdTe epitaxial films on (111) Zn-doped CdTe substrate (4%). The film thickness is deduced from optical profilometry by measurement of the step between the film and the hidden part of the substrate. X-ray diffraction measurements followed by double-diffraction X-ray analysis demonstrate the homoepitaxy of the CdTe film, with a small angular difference (around 10′). The photoluminescence spectra of the film and substrate exhibit some differences: the intensity level of the impurity transitions is two times higher for the film and the bound excitonic transition is lower for the film than for the substrate.

*Author to whom correspondence should be sent.

2. Experimental set-up

Our experimental set-up includes a 193 nm ArF excimer laser (Lambda Physik LPX 205) and a vacuum chamber in which are mounted the rotating holder which keeps the CdTe target and the sample heated support at a distance of approximately 3 cm from each other. The laser beam is focused through an optical delivery system onto the CdTe target at an angle of incidence of 45°. The source operates with a repetition rate of 5 Hz and a fluence ranging from 0.4 to 1 J cm^{-2}. During the deposition, the substrate temperature is maintained between 230 °C and 270 °C. Moreover, our elaboration cell just allows poor vacuum condition (10^{-3} Torr) to be maintained. With this set-up, a deposition time of 20 min leads to a layer about 4 μm thick. However, the growth rate is not linear because the quartz input window on the beam trajectory is obscured by the evaporated material and this leads to a decrease in the laser beam intensity on the target (Fig. 1).

0921-5107/93/$6.00

© 1993 – Elsevier Sequoia. All rights reserved

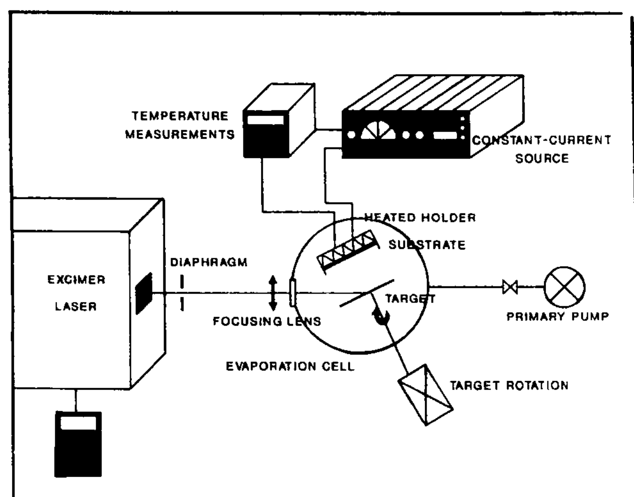

Fig. 1. Experimental set-up.

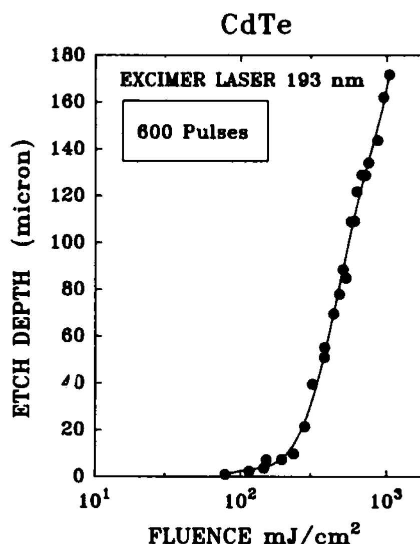

Fig. 2. Etch depth *vs.* laser fluence.

3. Experimental results

3.1. CdTe etching and deposition

A preliminary experiment has been conducted on a CdTe target in order to find the ablation process efficiency. The results are depicted in Fig. 2. Above a fluence threshold of 80 mJ cm^{-2}, the ablation rate increases with the fluence. At 400 mJ cm^{-2} each laser pulse removes a homogeneous CdTe layer the thickness of which is 0.1 μm. This efficiency increases linearly up to 0.3 μm at 1000 mJ cm^{-2}. All the depositions have been carried out in this fluence range which allows us to monitor the film deposition rate. Our first three layers have mirror-like surfaces and their thicknesses are 1.9 μm, 4 μm and 6.2 μm respectively. From optical profilometry, film thicknesses are deduced by the measurement of the step between the film and the hidden part of the substrate. This approach also gives an indication of the surface aspect: neither pinholes nor surface defects appear in our films as is confirmed by optical microscopy.

3.2. Composition analysis

The compositions of the deposited films are compared with the substrate composition using an energy-dispersive X-ray analysis (EDXA) and give the same cadmium and tellurium ratio. There is a slight difference due to the presence of zinc, the concentration of which is less in the film. This will be further confirmed by X-ray, double-diffraction X-ray and photoluminescence results.

3.3. X-ray and double-diffraction X-ray analysis

X-ray diffraction measurements demonstrate the homoepitaxy of the CdTe film but the layer structure has a small angular difference (around 10 min) relative to the substrate. This result is confirmed by double-diffraction X-ray.

Figure 3(b) shows that the (333) rocking curves for the thinner CdTe sample, substrate and film signatures can be obtained simultaneously. The substrate rocking curve is larger than that obtained in the original substrate. This damage is probably due to ejected materials incoming at high speed onto the first atomic layers of the substrate. The rocking curve of the film varies with the probe position, proving inhomogeneous crystalline deposition. The full width at half-maximum (FWHM) is 20 s in the best places (Fig. 3(a)).

3.4. Photoluminescence

Finally, photoluminescence analysis has been carried out to examine the purity of the CdTe epitaxial film. The excitation source is an argon laser, with the experiment conducted at 4 K. The sample probed is the 6 μm thick film.

Figure 4 allows comparison of the substrate photoluminescence measurement and that of the layer. The excitonic transition is detected at 1.6016 eV for the substrate and at 1.601 eV for the film. These results should be compared with the excitonic energy of pure CdTe at 1.596 eV. Moreover, the film luminescence is 10 times lower than that of the substrate.

Low energy transitions due to impurities are about two times higher in the film than in the substrate.

4. Discussion

Double-diffraction X-ray results show that good epitaxial films have been grown by laser deposition.

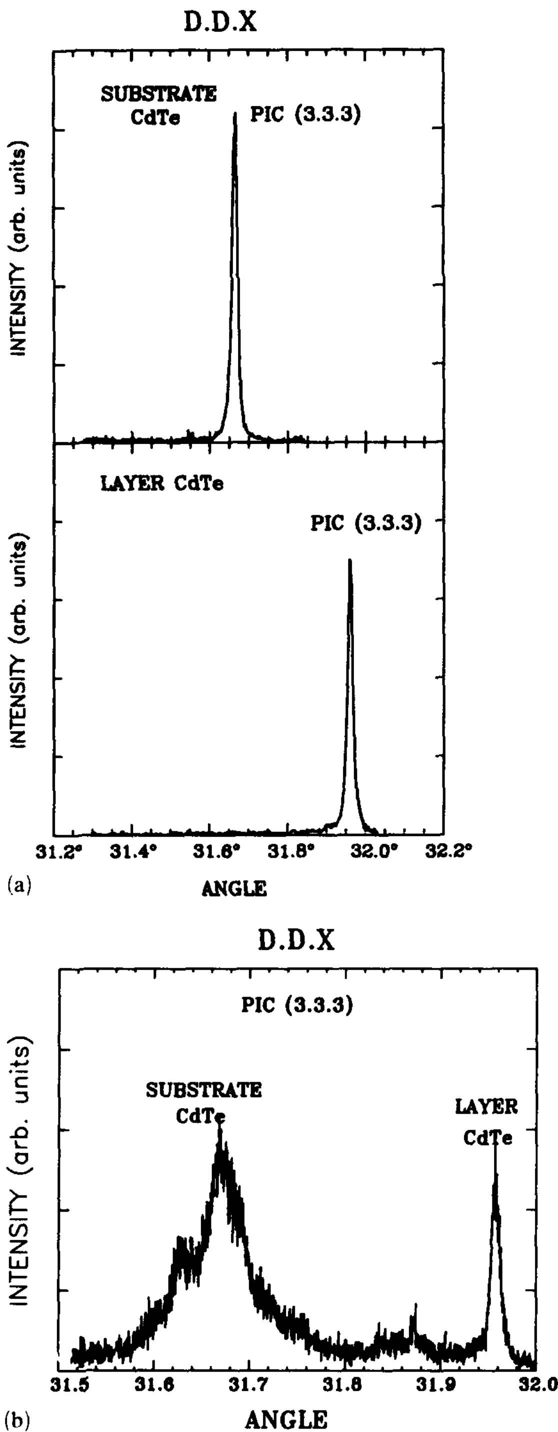

Fig. 3. Double-diffraction X-ray curves: (a) best substrate and film rocking curves; (b) substrate and film rocking curves with the analysis carried out on the edge of the step.

Small angular difference could be explained by a small zinc composition difference between the film and substrate resulting in a strained interface. This zinc composition difference would be responsible for the light energy shift in the luminescence spectra.

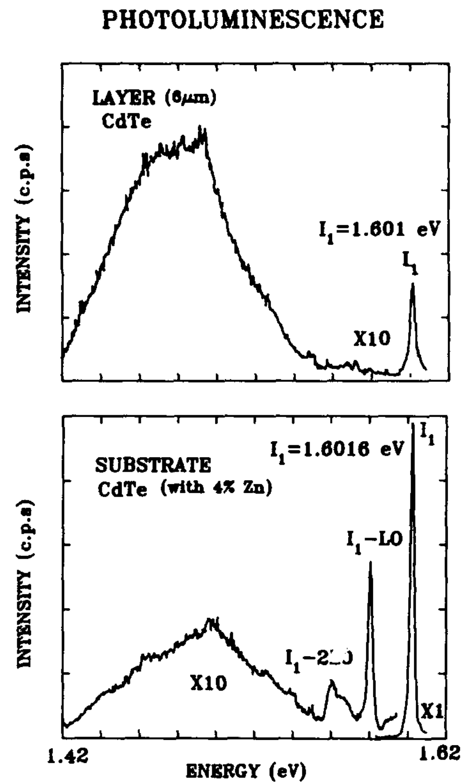

Fig. 4. Photoluminescence spectra.

The lower intensity level of the bound excitonic transition and the higher level for impurity transitions for the film are coherent with our experimental growth conditions and, in particular, the poor vacuum in the elaboration cell during the evaporation process.

5. Conclusions

Even though the growth process and experimental apparatus are very simple, we have demonstrated the ability of ArF excimer lasers to give good epitaxial CdTe films. Double-diffraction X-rays show that the first layers of the substrate surface are lightly damaged by the incoming material; these particles could be slowed down using low pressure neutral gas. Experimental conditions should now be improved and we consider the possibility of carrying out the evaporation in the optimum vacuum conditions.

Preliminary experiments of CdTe films on silicon and GaAs substrates have been undertaken; X-ray analyses exhibit crystalline films, and other structural characterizations are in progress.

Up to now, our film characterizations are only structural investigations and they must be followed by other experiments with the object of giving valuable information on the electric properties of CdTe films.

Acknowledgment

The authors would like to thank Drs Leycuras and Neu for double-diffraction X-ray and photoluminescence analyses.

References

1 R. Sporken, S. Sivananthan, K. K. Mahavadi, G. Monfroy and M. Boukerche, *Appl. Phys. Lett.*, *55* (1989) 1879.
2 M. D. Lange, R. Sporken, K. K. Mahavadi and J. P. Faurie, *Appl. Phys. Lett.*, *58* (1991) 1988.
3 A. N. Tiwari, N. Floeder, S. Blunier, H. Zogg and H. Weibel, *Appl. Phys. Lett.*, *57* (1990) 1108.
4 M. K. Lee, M. Y. Yeh and C. C. Chang, *Appl. Phys. Lett.*, *55* (1989) 1850.
5 S. K. Gandhi, K. K. Parat, H. Ehsani and B. Bhat, *Appl. Phys. Lett.*, *58* (1991) 828.
6 J. J. Dubowski, A. P. Roth, Z. R. Wasilewski and S. J. Rolfe, *Appl. Phys. Lett.*, *59* (1991) 1591.

Materials Science and Engineering, B16 (1993) 68–70

Growth of CdTe single crystals by vapour condensation on the surface of polycrystalline source material

Andrzej Szczerbakow

Infrared Detector Laboratory, "VIGO" Ltd, PO Box 45, ul. Radiowa 3, 00-908 Warszawa 49 (Poland)

Zbigniew Gołacki

Institute of Physics, Polish Academy of Sciences, Al. Lotników 32/46, 02-668 Warszawa (Poland)

Abstract

A method of crystal growth from the vapour phase, which had been worked out for $A^{IV}B^{VI}$ compounds, has been applied to CdTe. Single crystals shaped with (110) and (111) planes of approximately 10 mm size have been obtained. A high level of structure perfection has been confirmed by means of X-ray rocking curve measurements resulting in half-width values down to approximately 15″. The suitability for production of homogeneous CdTe-based $A^{II}B^{VI}$ solid solution crystals is discussed.

Creation of small, well-shaped single crystals on the surface of the source material is a common effect accompanying various sublimation processes but difficulties in controlling the phenomenon to achieve crystals with a satisfactory size are restricting its usefulness. However, growth of large CdS single crystals [1] in a vertical, sealed ampoule and, later on, production of $A^{IV}B^{VI}$ single crystals representing a high level of structure perfection and dimensions of over 10 mm, have been described [2–8]. Positive results for experiments on CdTe have also been reported [9, 10]. Except for experiments on CdS, horizontal growth systems have been applied.

Generally, crystal growth has been performed in ampoules placed in tube furnaces showing no, or only very weak, longitudinal temperature gradients. The application of slightly hotter, border zones [6] has enhanced control of the process by preventing the material from being transported to the end parts of the ampoule.

The existence of radial temperature differences in the furnace chambers has been reported [2, 5], and an active role of these differences in crystal growth has been suggested, but their origin has since been studied [8]. It has been shown that the radial temperature differences may be created as a result of cooling by emission of heat radiation along the furnace axis, and that such a cooling is intensive enough to create the thermodynamic mass driving force required for crystal growth. The effect depends on the geometry of the whole heating system, where one of the most important parameters is the solid angle, under which the cold, far areas are "seen" from the material surface. Possible values for the radial temperature differences have been estimated according to the Stefan–Boltzmann law, with the assumption that heat exchange between a small, spherical body and its environment takes place by radiation only. It has also been shown that the temperature of the body does not depend significantly on its position along the tube radius—this means that the cooling effect remains almost constant in the cross-section of the furnace chamber (except in the case of direct wall contact).

As heat transport by convection outside the ampoule is more intensive than inside, the temperature of the ampoule wall becomes almost equalized with the furnace chamber wall and thus the temperature of the body can be considered not only in relation to the furnace but also to the ampoule. Because the temperature of a crystal is an integrated effect of heat radiation balance and of heat conduction from the ampoule walls via the source material, the coldest parts of the material are those which can be cooled by radiation but have a weak inflow of heat by conduction. This allows explanation of the crystal selection as well as the frequent occurrence of crystals "on the neck" in the early stages of the process.

Although heat radiation study allows definition of the main phenomena influencing the process, the variety of accompanying factors makes it impossible to

0921-5107/93/$6.00

© 1993 - Elsevier Sequoia. All rights reserved

apply purely calculated temperature fields. However, the theoretical interpretation leads to some useful conclusions. For instance, rather short furnaces with a large bore shall be used and the walls of the furnace chamber ought not to be covered with a strongly emitting material.

In order to find a proper temperature profile, one can apply a procedure based on balancing the heat radiation from the hotter, border zones. When heat radiation from the border zones is too weak, condensation in the ampoule end parts is observed. If heat radiation from the border zones is too intensive, the surface of the material becomes hotter than the ampoule walls and the material is transported towards the walls (in the central part of the ampoule) with the creation of a compact, polycrystalline layer. The height of the border zones suitable for crystal growth lies between the cases mentioned above. Difficulties in finding the proper conditions are mainly due to the gas pressures in the ampoule, if lying over approximately 10 Torr—this is probably because the temperature differences inside the ampoule are reduced by heat convection as well as by diluting the transported vapours, if inert gas or a large excess of one of the elements is present.

It should be mentioned that the heat transfer phenomena here do not depend strongly on the properties of the crystallized material in its solid state—even the emissivity does not have a dominant role in the process. Therefore, it has proved possible to use the same furnaces with unchanged temperature profiles for producing various $A^{IV}B^{VI}$ crystals, for example, (Pb,Sn)Te and Pb(Se,S) in the full ranges of compositions with comparable results when based on a temperature of 820 °C in the middle zone [8]. Neither composition gradients nor other signs of macro-segregation have been found, and therefore it has been possible to apply Pb(Se,S) crystals as reference samples in precise lattice constant measurements [11].

Cadmium telluride crystals have been grown in temperature profiles of two types: the first with a constant, longitudinal gradient of 0.1–0.2 °C cm^{-1} at approximately 900 °C in a furnace with bore 40 mm and length 700 mm [9, 10]; and the second showing a temperature "valley" of approximately 10 °C depth on 820 °C [12] (analogous to that used for $A^{IV}B^{VI}$ materials). Crystals grown in the first profile are shown in Fig. 1. The half-width of the X-ray rocking curve measured on as-grown (111) planes varies from 13.9 to 33.8", while the theoretical value is 8.91" [10]. Except for (111) facets (which have been identified as Te-planes), (110) facets are present [9].

The result of CdTe crystallization in the second profile is shown in Fig. 2. The compact block consists of several large grains. The largest facet shown in Fig. 3 has proved to be a (110) plane similar to smooth planes

Fig. 1. CdTe crystals obtained in a weak temperature gradient (millimetre scale seen at the bottom).

Fig. 2. Product of CdTe crystallization in a temperature "valley".

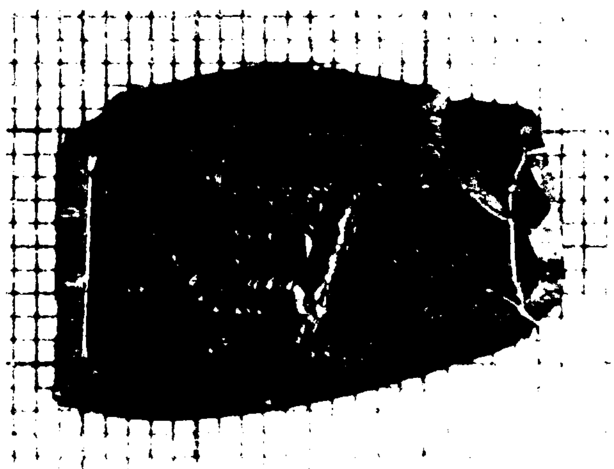

Fig. 3. An as-grown (110) plane.

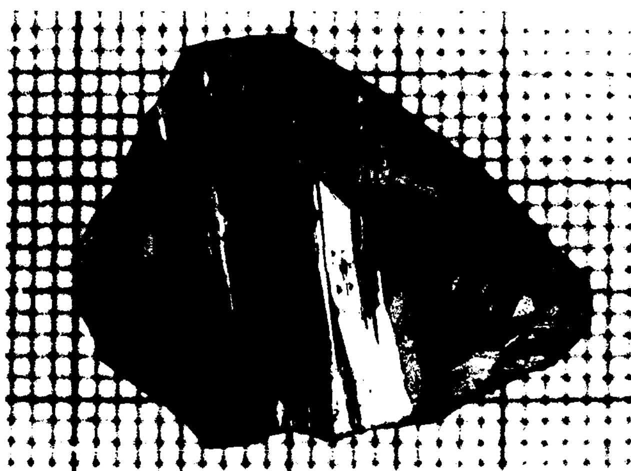

Fig. 4. Pyramid growth on a CdTe crystal.

created by splitting across the block [13]. Small "valleys" in the lower part of the photograph are not due to deep structure defects; however, several parallel lines in the upper part are connected with disoriented areas [13]. Pyramid growth shown in Fig. 4 results probably from vapour transport disturbances due to an excess of one of the elements.

Application of the process to (Cd,Zn)Te and other CdTe-based solid solutions depends on the possibility of composition maintenance. Up to now, this has been confirmed in analogous experiments not only on PbTe–SnTe and PbSe–PbS systems, where the components (as compounds) show rather similar vapour pressures, but also in the growth of homogeneous (Pb,Ge)Te crystals of size 3–5 mm [8]. By means of X-ray diffractometry it has been shown that the crystal compositions are identical with those of the mixtures used as the starting materials [14]. A narrow temperature range of stability for some (Pb,Ge)Te solid solutions has required crystal growth at approximately 680 °C, where the vapour pressure of pure PbTe lies at 0.04 Torr and of GeTe at 3.7 Torr. The vapour pressure difference in the case of the CdTe–ZnTe system is less dramatic—for instance, at 840 °C the vapour pressure of CdTE lies at 4 Torr and of ZnTe at 0.15 Torr. In addition, crystal growth of pure ZnTe at that temperature has been observed.

Preventing segregation is possible even at large vapour pressure differences, when the crystallization proceeds in a sealed ampoule with a low temperature change and with undisturbed vapour circulation. In this case, the condensation stage ought to be considered as being to a large degree reversible to evaporation. Such a quasi-equilibrium interpretation differs principally from the model of unidirectional flow with rapid condensation. The latter model results in the composition of the condensing material being identical with that of the vapour—as appears, for instance, in common liquid distillation.

Contrary to the unidirectional flow processes, the nearly reversible evaporation–condensation procedure tends to reproduce the source composition in the condensing material despite incongruency of particular phase transitions. Here composition change is to be taken as a function of deviation from equilibrium of the system as a whole due to the temperature difference. Maximum enrichment of the condensing material with the more volatile component can be estimated by comparing the partial pressure decrease (as a function of temperature lowering) and the increase (as a function of concentration enlargement). Other phenomena able to influence composition may be considered, but their effect is rather negligible. The "quasi-equilibrium" interpretation is supported not only by crystal growth of pseudo-binary solid solutions just discussed, but also by positive results in the crystal growth of SnTe, despite its strongly incongruent evaporation.

It should be mentioned that the main disadvantage of the method discussed above lies in difficult process control. Some chances of facilitation have appeared in tentative experiments carried out in a vertical system with PbSe as testing material. This can prove preferable in CdTe crystal growth, if confirmed by experiment. In such a case, the growth of $A^{II}B^{VI}$ crystals on the source material in vertical systems may gain new importance.

References

1 E. Kaldis, *J. Cryst. Growth*, 5 (1969) 276.
2 T. C. Harman and J. P. McVittie, *J. Electron. Mater.*, 3 (1974) 843.
3 H. Preier, R. Herkert and H. Pfeiffer, *J. Cryst. Growth*, 22 (1974) 153.
4 I. Kasai, D. R. Daniel, H. Maier and H.-D. Wurzinger, *J. Cryst. Growth*, 23 (1974) 201.
5 H. Maier, D. R. Daniel and H. Preier, *J. Cryst. Growth*, 35 (1976) 121.
6 W. Lo, G. P. Montgomery and D. E. Sweets, *J. Appl. Phys.*, 47 (1976) 267.
7 W. Lo, *J. Electron. Mater.*, 6 (1977) 39.
8 A. Szczerbakow, *J. Cryst. Growth*, 82 (1987) 709.
9 Z. Gołacki, J. Majewski and J. Makowski, *J. Cryst. Growth*, 94 (1989) 559.
10 J. Auleytner, J. Majewski, Z. Furmanik and Z. Gołacki, *Cryst. Res. Technol.*, 25 (1990) 971.
11 H. Berger, H.-H. Niebsch and A. Szczerbakow, *Cryst. Res. Technol.*, 20 (1985) K8.
12 A. Szczerbakow, 1990, unpublished materials.
13 H. Berger, 1990, personal communication.
14 M. Leszczyński, 1989, personal communication.

Structural and electronic properties of CdTe-based heterostructures

N. Magnea and A. Tardot

Laboratoire de Physique des Semiconducteurs, DRFMC, SP2M, Centre d'Etudes Nucléaires de Grenoble, BP 85X, 38041 Grenoble (France)

H. Mariette and N. Pelekanos

Laboratoire de Spectrométrie Physique, CNRS Université J. Fourier, Grenoble (France)

Abstract

This paper reviews the structural and optical properties of $CdTe/Cd_{1-x}Zn_xTe$ strained heterostructures grown by molecular beam epitaxy. Special attention is given to the control of strain and interface roughness and sharpness. It is shown that high quality superlattices are obtained with well width fluctuations on the monolayer scale. The electronic properties are also strain dependent, especially the valence band line-up. Two-dimensional exciton states are the dominant features of the optical spectra of $CdTe/Cd_{1-x}Zn_xTe$ quantum wells. By appropriate quantum well engineering, the exciton-phonon interaction is reduced and large room-temperature absorption observed.

1. Introduction

Recently there have been major developments towards the realization of CdTe-based optoelectronic devices such as $Cd_{1-y}Hg_yTe$ laser diodes [1] compact visible microgun-pumped $CdTe/Cd_{1-z}Mn_zTe$ lasers [2] and photodiffractive devices based on $Cd_{1-x}Zn_xTe$/ZnTe quantum wells (QWs) [3]. The capability of molecular beam epitaxy (MBE) to produce CdTe layers and quantum wells with well-controlled parameters, high structural and interfacial perfection and high purity is at the origin of these realizations. The aim of this paper is to review the structural and electronic properties of MBE-grown $CdTe/Cd_{1-x}Zn_xTe$ heterostructures. It is worth noting that many of the results that are presented here apply equally to CdTe/MnTe and CdTe/HgTe systems.

First we shall describe the optimal growth conditions and demonstrate the importance of strain symmetrization to obtain defect-free superlattices. The sharpness and the roughness of the interfaces are measured from X-ray diffraction, reflection high energy electron diffraction (RHEED) oscillations and exciton linewidth. Interdiffusion is shown to be negligible and the layer thickness fluctuations are on the monolayer (ML) scale. Next we shall describe the electronic band structure, emphasizing the key role of strains in defining the valence band line-up and explaining the optical features. The discussion will also include a short description of the intrinsic Stark effect resulting from the piezoelectric field and the observation of room-temperature exciton absorption in specially engineered quantum wells. In the conclusion we shall review the potential applications which can be expected from CdTe-based heterostructures.

2. Growth

MBE growth is performed on CdTe, $Cd_{0.97}Zn_{0.03}Te$ and $Cd_{0.78}Zn_{0.22}Te$ substrates with (001)-, (111)- and (211)-oriented surfaces. The RHEED oscillation studies show that for the whole range of zinc concentrations the growth proceeds by a two-dimensional (2D) layer-by-layer mode [4]. For Cd(001)-stabilized surfaces the cadmium and tellurium species have a high surface diffusion which provides a wide temperature range (220-320 °C) for growing high quality materials. A cadmium overpressure is also essential to achieve a high efficiency of indium doping [5], to improve the interface flatness and the morphology of the epitaxial layers (epilayers). For the (111) surface, the temperature range for obtaining a 2D growth is narrower and shifted to a higher temperature compared with (001). This is probably due to a decrease in the surface mobilities of cadmium and/or tellurium and hence a higher thermal energy is needed for adatoms to be incorporated in the good site. This reduction in surface migration which favours nucleation on terraces, added to the low value of the stacking-fault energy in II-VI compounds, leads to the formation of twins. To avoid twin formation, we introduce steps, on purpose, by a

0921-5107/93/$6.00

© 1993 – Elsevier Sequoia. All rights reserved

substrate misorientation, so that atoms are preferentially adsorbed at step edges and establish only correct bonds [6]. Then 2D growth by step migration is guaranteed and twin formation prevented. A particular case is the (n11) surfaces with $n > 1$ which can be considered as highly misoriented (111) surfaces towards the (001) direction. They are formed of a periodic array of steps and short terraces; then epilayers grown on these surfaces are effectively free of twinning.

3. Strains

As the CdTe/ZnTe has a large lattice mismatch of 6.4%, the strain is an important parameter to control whether heteroepitaxy has to be carried out. Indeed strain relaxations introduce extended defects which are detrimental to the electronic properties and even in a system with a low mismatch ($\varepsilon \leqslant 0.5\%$) the strain relaxation strongly perturbs the crystal quality. This can be avoided by keeping the CdTe layer thickness below the critical thickness t_c which is defined by the thickness where the elastic energy overcomes the dislocation generation and migration threshold. In the CdTe/ZnTe system, t_c has been shown to vary for the (001) orientation as $\varepsilon^{-3/2}$ with $t_c \approx 4000$ Å for CdTe on $Cd_{0.97}Zn_{0.03}Te$ and $t_c \approx 17$ Å for CdTe on ZnTe [7]. As the material is stiffer along the (111) direction, for (111) growth one expects a critical thickness a factor of 2 lower. The low values of t_c should impose strong limitations on the design of heterostructures, but it is possible to overcome that by growing strained-layer superlattices (SLSs) with an average strain close to zero. This is obtained when the substrate lattice parameter lies in between those of the two components of the superlattice. Then the CdTe layers are in compression and the ternary layers in dilatation. By correctly choosing the layer thicknesses, the coherence between the substrate and the superlattice is maintained whatever the total thickness, provided that the average lattice parameter $\bar{a}_\perp$ of the SLS along the growth axis is equal to the substrate lattice parameter and each layer stays below its own critical thickness. The parameter $\bar{a}_\perp$ is easily calculated by minimizing the total elastic energy with the above condition [8]. Figure 1 shows the X-ray rocking curves of three CdTe/$Cd_{1-x}Zn_xTe$ superlattices grown coherently on $Cd_{0.97}Zn_{0.03}Te$ substrates. The CdTe thickness is kept constant (62 ML) while the zinc concentration increases, $x = 0.08$ for Fig. 1(a), $x = 0.22$ for Fig. 1(b) and $x = 1$ for Fig. 1(c); conversely the thickness of the barriers (63 ML, 11 ML and 2 ML respectively) decreases to maintain coherency for a total thickness of 1 μm. The "zero" order peak, which is due to diffraction by the average lattice parameter, lies very close to the substrate peak and the full width

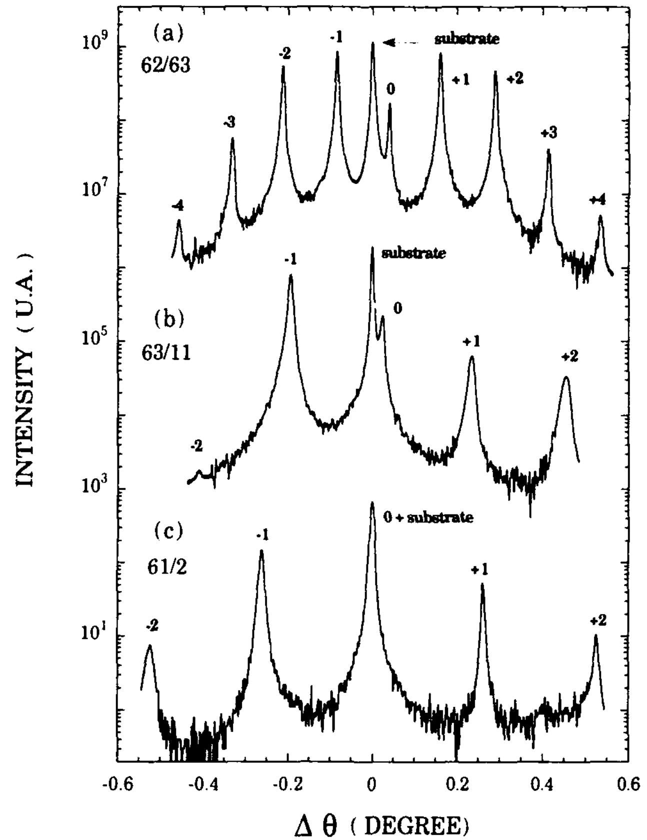

Fig. 1. (004) rocking curves of pseudomorphic CdTe/$Cd_{1-x}Zn_xTe$ SLSs (U.A., arbitrary units): curve (a) $x_{Zn} = 0.08$; (b) $x_{Zn} = 0.22$; (c) $x_{Zn} = 1$. The CdTe layer thickness is kept constant at around 62 ML while the $Cd_{1-x}Zn_xTe$ layer thickness is adjusted to preserve the coherency with the $Cd_{0.97}Zn_{0.03}Te$ substrate.

at half maximum (FWHM) of all the diffraction peaks lies between 20 and 35″. This provides evidence that there is no strain relaxation even in the CdTe/ZnTe SLS, thus demonstrating the importance of strain symmetrization in growing highly mismatched multilayers. Accurate values of thickness, lattice strains and chemical composition of the constituent layers are obtained from kinematical simulations of the SLS rocking curves [8]. Generally the calculations reproduce the X-ray pattern intensities quite well with parameters very close to those deduced from the RHEED oscillation data. As we assume ideally abrupt interfaces in the calculation, this is indicative of a small fluctuation in the average period p ($\Delta p = \pm 1$ ML) and of sharp interfaces along the growth axis.

4. Interfaces

A quantitative evaluation of interface quality is a difficult task. Indeed two kinds of data have to be

measured: interfacial roughness and sharpness. The former reflects the shape of the growth front and "measures" on the atomic scale the size and density of terraces in the interface plane. The latter gives an image of the composition modulation along the growth axis and depends essentially on interdiffusion and segregation phenomena. X-ray diffraction on SLS is used to measure the sharpness and the interdiffusion coefficient [9]. Indeed in a system with a one-dimensional periodic modulation of composition, the intensities of the satellites are proportional to the Fourier component of the direct-space composition profile. Therefore the interdiffusion of CdTe and $Cd_{1-x}Zn_xTe$ is studied on the atomic scale by measuring the variations in satellite intensities as a function of post-growth annealings. Figure 2 shows the variation in the first and second harmonics with annealing time for a CdTe/$Cd_{0.93}Zn_{0.07}Te$ SLS annealed at 360 °C under a cadmium overpressure. Considering an interdiffusion coefficient D_i independent of composition we solve the diffusion equation, calculate the composition profile and then the diffraction pattern and adjust D_i to fit the experimental data. The full lines in Fig. 2 show the calculated variation in I_m by allowing a rectangular starting wave to diffuse. The best fit gives $D_i \approx 1.6 \times 10^{18}$ $cm^2\ s^{-1}$ at 360 °C. In Fig. 3 we show the values of D_i measured at different temperatures between 360 and 420 °C. A least-squares fit of the data yields a temperature-dependent coefficient $D_i = 114\ cm^2\ s^{-1} \exp(-2.2\ eV/kT)$. The good agreement with the high temperature data in ref. 10 also shown in Fig. 3 and the value of the activation energy $E_A = 2.0$ eV indicate that metal vacancies are probably involved in the interdiffusion mechanism. Extrapolation to the growth temperature commonly used ($T_s \approx 280$ °C) gives a value for D_i of about $10^{-22}\ cm^2\ s^{-1}$, showing that the contribution of interdiffusion to interface sharpness is negligible. Nevertheless these data put some limits on the thermal stability of CdTe/$Cd_{1-x}Zn_xTe$ SLSs for subsequent processing and also on the abruptness of the interfaces which can be obtained if higher growth temperatures are needed. First insights into the interfacial roughness are obtained from RHEED oscillations. Indeed the observation of intense RHEED oscillations is characteristic of 2 D layer-by-layer growth, but it is generally difficult to extract any quantitative data about the

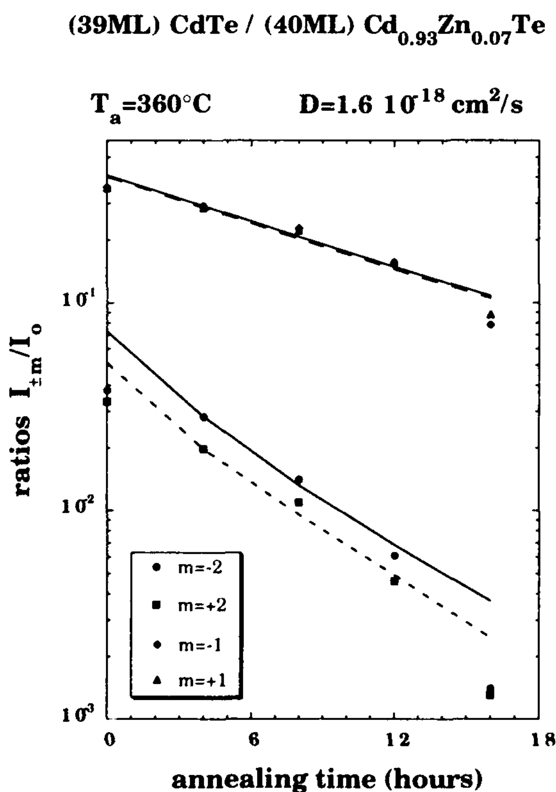

Fig. 2. The Fourier amplitudes of a CdTe/$Cd_{1-x}Zn_xTe$ SLS as a function of annealing time at 360 °C: ●, ■, ◆, ▲, experimental points; ——, curve given by solving the linear diffusion equation assuming that $D = 1.6 \times 10^{18}\ cm^2\ s^{-1}$.

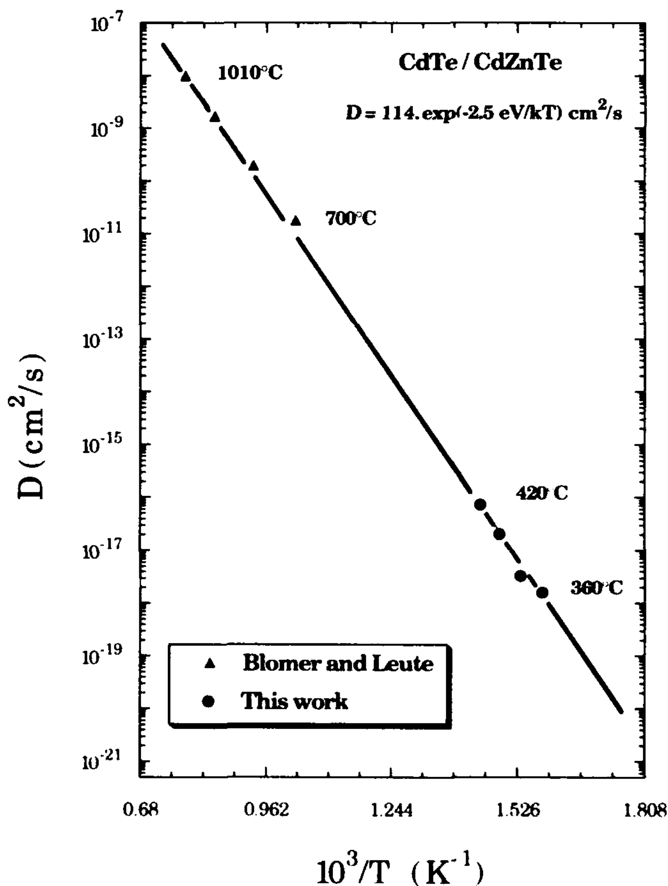

Fig. 3. Arrhenius plot of the interdiffusion data deduced from X-ray measurements and chemical analysis in ref. 10.

density and lateral size of the terraces [11]. A quantitative chemical mapping of the interfaces is given by high resolution transmission electron microscopy. Nevertheless the interface images obtained on cross-sections include information on the roughness and the sharpness which are difficult to separate. Moreover, the contrast between CdTe and $Cd_{1-x}Zn_xTe$ material is too low to obtain quantitative information on the interfaces.

Another microscopic probe is the exciton. Indeed 2 D excitons are sensitive to layer thickness fluctuations with a lateral resolution of the order of the Bohr radius, *i.e.* 60–70 Å in CdTe. Because the recombination energy of the exciton is essentially determined by the well width, the roughness can be estimated from the inhomogeneous broadening of the excitonic recombination lines. Three types of interface morphology have been proposed [12]: (i) smooth with 1 ML terrace areas significantly greater than the exciton Bohr radius (two or three sharp discrete lines are observed); (ii) pseudo-smooth when such areas are much smaller than the exciton which now samples an average potential (a single sharp line without a Stokes shift is observed with a linewidth, reflecting the spatial distribution of interface potentials); (iii) rough if the interface potentials fluctuate spatially for dimensions comparable with or less than the exciton with a depth large enough to induce exciton localization (the recombination line is broad with a Stokes shift). In Fig. 4, we have plotted the 2 K linewidth of the heavy-hole (HH) exciton as a function of QW thickness for barriers with $x = 0.17$. The broadening expected for a 1 ML fluctuation is also plotted. Surprisingly the experimental linewidth remains constant between 1 and 2 meV and lower than that calculated for a monolayer fluctuation except for thick QWs where the linewidth reflects the homogeneous broadening due to the interactions with acoustic phonons, defects etc. No Stokes shift is observed between absorption and emission but the three discrete transitions characteristic of smooth interfaces have never been observed. So we believe that we are rather in the pseudosmooth regime with a growth front distributed on one ML (in agreement with the RHEED oscillation data) with islands of lateral size less than 100 Å but regularly distributed at the interface. The same excitonic linewidths are obtained for high barriers ($x = 0.33$), confirming that the exciton averages the well width fluctuations.

This overview of the structural properties of CdTe/$Cd_{1-x}Zn_xTe$ heterostructures shows that MBE can provide systems with well-controlled parameters. The control of layer thickness, strain state and interface morphology is essential to understand the electronic properties which will be developed in the next two sections.

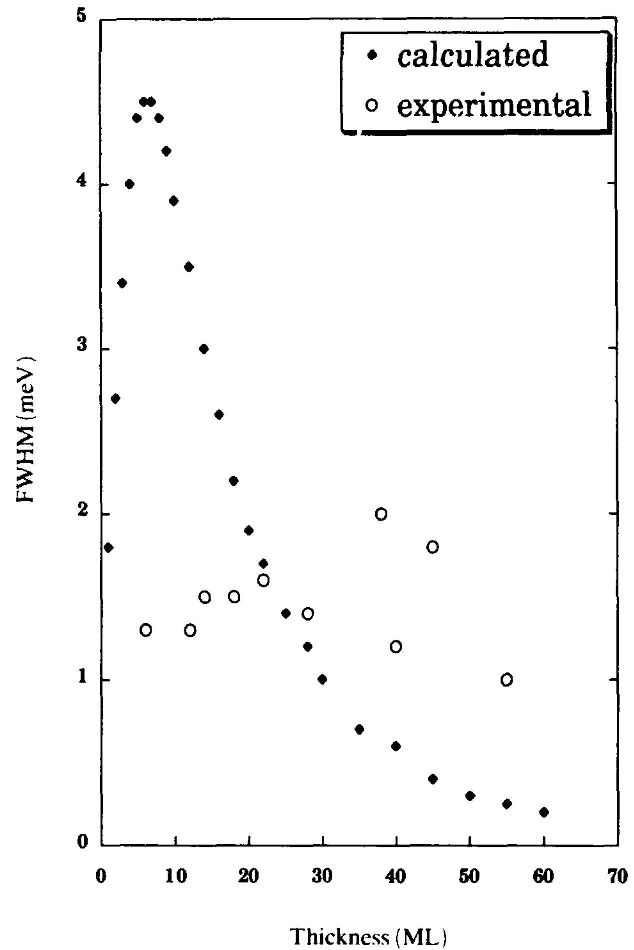

Fig. 4. Plot of the FWHM of the e_1h_1 transitions as a function of CdTe QW thickness: ——, curve calculated by assuming a 1 ML variation.

5. Electronic structure

The understanding of the electronic band structure of strained $CdTe/Cd_{1-x}Zn_xTe$ QWs and SLSs relies on optical spectroscopy and leads to the following description sketched in Fig. 5. The conduction band offset confines the electron in the CdTe QW for the whole composition range. The chemical valence band offset (VBO) is relatively small (about (0.05–0.15) ΔE_g) with some controversy about the true value [13, 14]. The shear part of the biaxial strain lifts the light-hole (LH–HH) degeneracy. One peculiarity of the $CdTe/Cd_{1-x}Zn_xTe$ system is that the LH–HH splitting is approximately half the band gap difference ΔE_g for the whole composition range. As VBO is small, the confining potentials for the holes are essentially determined by the strain. The HHs are confined in the CdTe wells, providing type I e_nh_n transitions, while the LHs are essentially confined to the barriers, producing type

II (spatially separated carriers) $e_n l_n$ transitions. Whether the highest confined level is HH_1 or LH_1 depends on the relative mismatch between the well, the barrier and the substrate. This effect allows one to observe the strain-mediated type I→type II transition [13]. As sketched in Fig. 5(c), a $CdTe/Cd_{0.90}Zn_{0.1}Te$ SLS grown on a CdTe substrate is type II in the sense that the e_1l_1 line is the ground-state transition while the same SLS is type I when grown on a $Cd_{0.92}Zn_{0.08}Te$ substrate (Fig. 5(a)). For low zinc concentration ($x_{Zn} \leqslant 0.2$) the hole localization potential is small ($V_{h,l} \approx 10$–20 meV). This has several consequences.

(i) Ultrafast time-resolved experiments show a dynamic Stark shift resulting from the electric field created by localized electrons in the CdTe wells and by delocalized holes before their capture by the well [15].

(ii) The effect of the electron Coulomb potential on LH confinement increases the wavefunction overlap of the two types of carrier. This increases the oscillator strength of the excitonic transition and makes the type II e_1l_1 transition quasi-direct [14, 16].

(iii) LH states are very sensitive to perturbing potentials. As an example, when 1 ML of ZnTe is introduced in the $Cd_{0.92}Zn_{0.08}Te$ barrier (see Fig. 5(b)) the LH states are pinned by the strain attractive potentials ($V_{lh} \approx 250$ meV). Now the electron–LH overlap and thus the oscillator strength become so small that the e_1l_1 transition is not observed in the spectrum while the e_1h_1 transition is not affected (Fig. 5(b)).

Another important effect of strain is the piezoelectric field which develops for growth on polar surfaces [17]. The strain-induced polarization generates a longitudinal electric field $\boldsymbol{E}_p$ as large as 10^5 V cm^{-1} which deeply affects the electronic band structure and the carrier wavefunction. A review has already been given for (111)-oriented $CdTe/Cd_{1-x}Zn_xTe$ [18]; so we shall just mention the main characteristics of what can be called "intrinsic Stark superlattices". The QW band gap is reduced by the quantum Stark effect (see inset of Fig. 6). Because the electrostatic potential drop increases with increasing layer thickness, the wider the wells, the larger is the red shift. This effect is shown

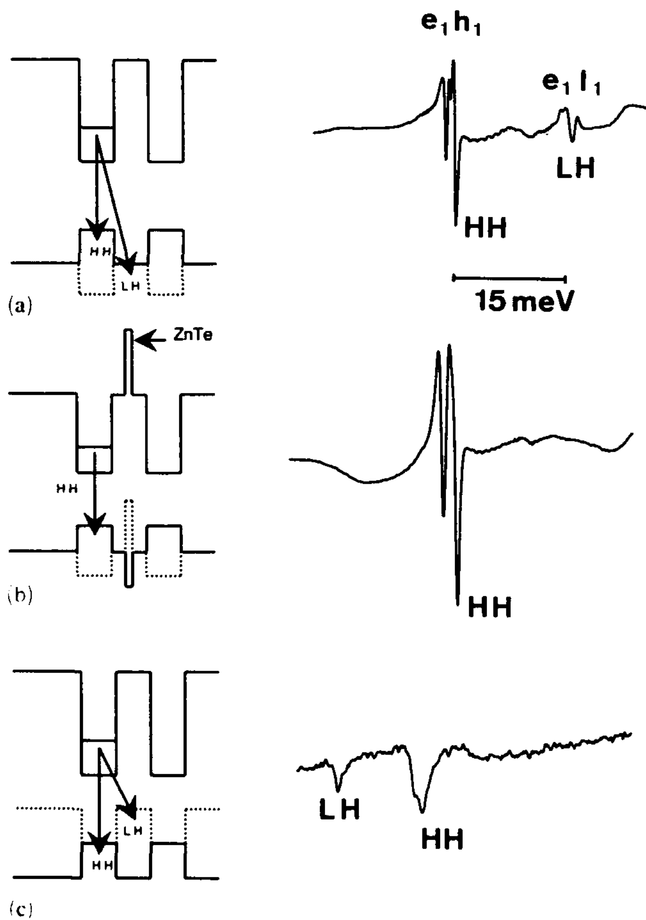

Fig. 5. Band structure of $CdTe/Cd_{1-x}Zn_xTe$ quantum wells for different strain states: (a) $Cd_{0.92}Zn_{0.08}Te$ buffer; (b) $Cd_{0.92}Zn_{0.08}Te$ buffer plus 2 ML of ZnTe in the barrier; (c) CdTe substrate. For each configuration the 1.8 °K reflectivity spectrum shows the HH and LH exciton identified by optical pumping. The HH transition is quite insensitive to the strain state contrary to the LH transition.

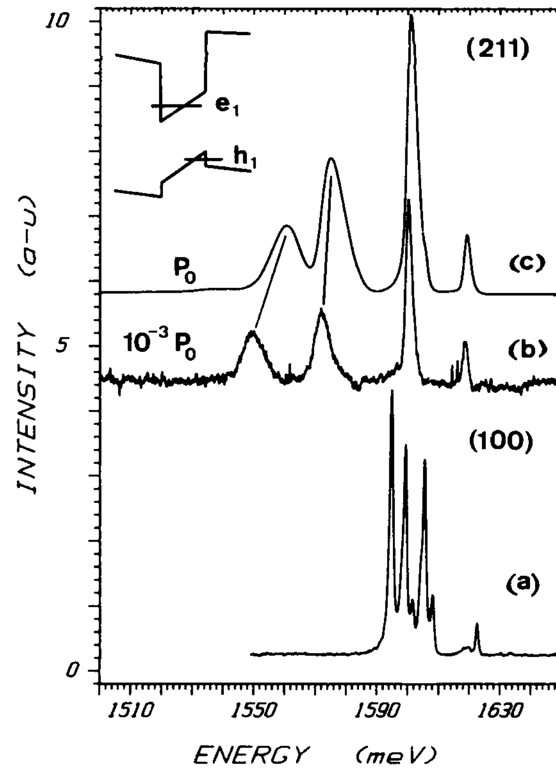

Fig. 6. Plot of 1.8 °K luminescence spectra for a series of CdTe QWs with thicknesses of 120, 80, 40 and 20 Å grown on a $Cd_{0.92}Zn_{0.08}Te$ buffer layer (a-u, arbitrary units): curve (a), (001) surface; curve (b), 211 surface; curve (c), same as curve (b) but with a laser power divided by 10^3.

in Fig. 6 where we compare the low temperature luminescence spectra of four single QWs of various thicknesses grown on (001)- and (211)-oriented $Cd_{0.92}$-$Zn_{0.08}Te$ buffer layers. As the electron and hole confinement potentials are small in these structures, calculations show that the red shift ΔE varies linearly with the QW thickness, which provides a simple way to measure the internal field [18]. The electric field $E_p = 7 \times 10^4$ V cm^{-1} measured for the (211) sample is lower by a factor of 0.7 than that measured on a (111) sample with the same mismatch $\varepsilon \approx 0.5\%$. Indeed the strain-induced polarization generates a pure longitudinal electric field for the (111) growth axis while for the (211) direction a transerve polarization field in the plane of the layers appears. This polarization field does not affect the energy band diagram but leads to birefringence for light propagating along the growth axis [17]. The field E_p measured in the (211) sample corresponds to an interface charge density around 5.5×10^{11} cm^{-2}. If electron-hole pairs are created by optical absorption, the internal field can be screened if the carrier lifetime is long enough. As shown in Fig. 6, when the laser power increases, one observes a blue shift in the photoluminescence transitions proportional to the QW thickness. For an optical density of 1 W cm^{-2} the screening efficiency is around 10% but quickly saturates at higher powers.

6. Exciton states

In high quality heterostructures, the exciton states generally dominate the optical properties. This is especially true in $CdTe/Cd_{1-x}Zn_xTe$ where the exciton binding energy R_y^* is strong owing to the high electron effective mass. In structures with a low zinc concentration and wide well thickness (200 Å or less), R_y^* is comparable with the carrier confinement energy. The electron-hole correlation along the z axis is maintained, while the exciton motion is quantized [19]. This effect has already been extensively discussed [19], so we shall focus on 2 D excitons in highly confined systems and on the importance of confinement to produce room temperature excitonic resonances. The goal is to increase R_y^* and simultaneously to reduce the broadening mechanisms. Figure 7 shows calculations of R_y^* *vs.* the well thickness for two barrier compositions. The calculation is based on variational techniques including the effect of electron Coulomb potential on hole states as well as electron-hole correlations, of significance for QWs with small valence band offset [16]. The maximum value of R_y^* is obtained for barrier composition $x_{Zn} \approx 0.35$ with a well thickness of around 60 Å. To illustrate the effect of confinement on the broadening mechanism, the absorption spectra

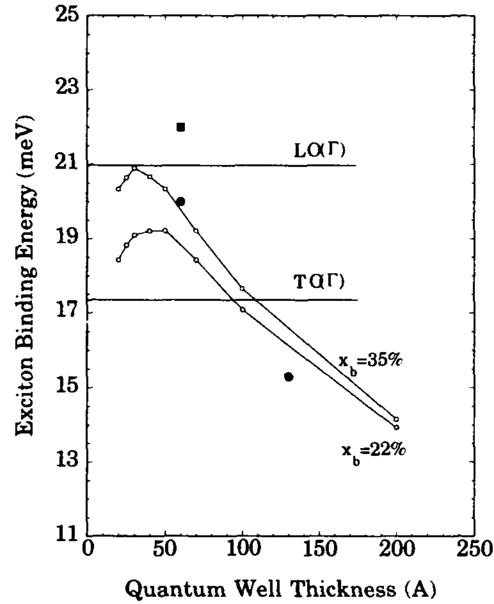

Fig. 7. Plot of the exciton binding energy as a function of QW thickness calculated for two barrier compositions: ●, ■, experimental data deduced from magnetoabsorption. The LO(Γ) and transverse optical (TO) (Γ) phonon energies are indicated.

of four CdTe wells of 60 Å grown on $Cd_{0.78}Zn_{0.22}Te$ substrates have been measured as a function of temperature (Fig. 8). Up to 70 K the spectra are characterized by very sharp transitions with a linewidth of 1-2 meV (inset of Fig. 8) and very large absorption coefficient of 10^6 cm^{-1} $well^{-1}$ at the exciton peak. Above 120 K the line broadens because of exciton-longitudinal optical (LO) phonon scattering. Nevertheless room-temperature absorption is observed with a coefficient of 4×10^4 cm^{-1}. The temperature dependence of the linewidth Γ can be expressed as

$$\Gamma = \Gamma_0 + \Gamma_{ph}\left[\exp\left(-\frac{\hbar\omega_{LO}}{kT}\right) - 1\right]^{-1} \quad (1)$$

where Γ_0 accounts for the inhomogeneous broadening (about 1-2 meV) and Γ_{ph} describes the strength of the LO phonon thermal broadening [20]. Figure 9 shows the plot of the experimental homogeneous broadening $\Gamma - \Gamma_0$ for three CdTe QWs with different values of the exciton binding energy R_y^* obtained by changing the well thickness and/or barrier height. The full curves are fits to eqn. (1) from which it is found that Γ_{ph} is substantially smaller than the bulk value of 30 meV and decreases to 15 meV when $R_y^* \geqslant \hbar\omega_{LO}$. This reduction in Γ_{ph} reflects the larger mean free time for exciton ionization by LO phonons. This has been attributed to the enhancement of the exciton binding energy [20]. Indeed R_y^* increases from a bulk value of 10.6 to 22 meV, close to the LO phonon energy $\hbar\omega_{LO} \pm 21.3$ meV

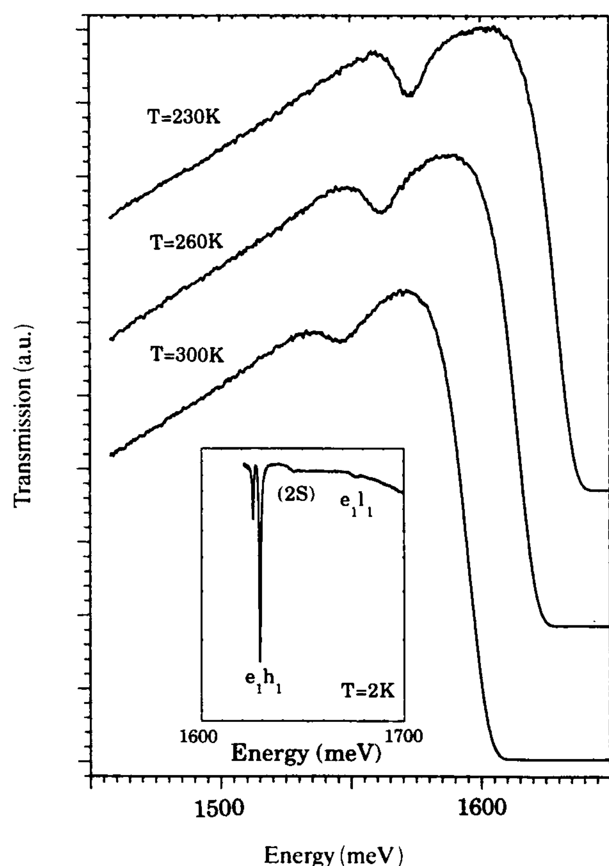

Fig. 8. Temperature-dependent absorption spectra of a sample made up of four 60 Å CdTe wells grown on a $Cd_{0.78}Zn_{0.22}Te$ substrate (a.u., arbitrary units). The inset shows the 1.8 °K absorption spectrum. The line splitting is due to a fluctuation of 1 ML in the first well.

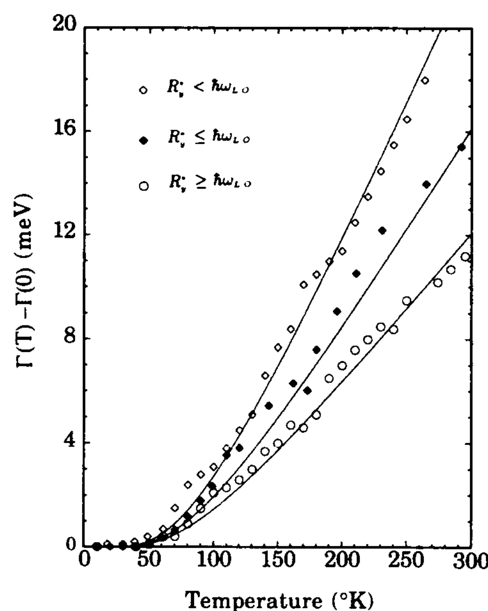

Fig. 9. Homogeneous exciton linewidth as a function of temperature for multiple QWs with various exciton binding energies R_y*: ——, fits of eqn. (1) in the text.

(see Fig. 7), thus decreasing the probability that the collisions between a phonon and an exciton cause the latter to ionize. Simultaneously the oscillator strength is enhanced by the confinement so that room-temperature excitonic resonances are observed even with a very small number of QWs.

7. Conclusion

Certain features of $CdTe/Cd_{1-x}Zn_xTe$ strained heterostructures that we have described are particularly appealing for optoelectronic applications in the near IR. A key point for devices is room-temperature operation. This condition is fulfilled by CdTe(001) QWs grown on zinc-rich substrates with high confinement potentials. Moreover the recent progress made in impurity doping of CdTe opens the way to study near-gap light modulators using these heterostructures. Another important property exhibited by the tellurium-based heterostructures is their strong near-gap photodiffractive coefficient related to the Franz-Keldysh effect. High diffractive yields in two-wave mixing experiments have already been obtained in ZnTe/$Cd_{1-x}Zn_xTe$ quantum wells [3]. With CdTe as the active layer, even higher yields can be expected at around 850 nm. For growth orientation other than (001), the built-in piezoelectric field offers the possibility of optical band gap tuning with large optical nonlinearities. The appropriate combination of all these effects (large excitonic absorption, photorefractive effect and piezoelectric field) in one heterostructure will inevitably lead to very original all-optical switching devices in the spectral range extending from the IR to the visible using mercury and manganese compounds respectively.

Acknowledgments

Special tnanks are due to H. Tuffigo, R. Cox and J. L. Pautrat for fruitful discussions and constant encouragement.

References

1 M. Zandian, J. M. Arias, R. Zucca, R. C. Gil and S. H. Skin, *Appl. Phys. Lett.*, 59 (1991) 1022.

2 E. Molva, J. Cibert, Le Si Dang, C. Bodin and G. Feuillet, Conf. on *Wide Bandgap Semiconductors, Trieste, 1992.*

3 A. Partovi, A. M. Glass, D. H. Olson, G. J. Zydik, K. T. Short, R. D. Feldman and R. F. Austin, *Appl. Phys. Lett.*, 59 (1991) 1832.

4 L. Ulmer, N. Magnea, H. Mariette and P. Gentile, *J. Cryst. Growth, 111* (1991) 711.
5 F. Bassani, S. Tatarenko, K. Saminadayar, J. Bleuse, N. Magnea and J. L. Pautrat, *Appl. Phys. Lett., 58* (1991) 2651.
6 H. P. Zeindl, R. Fuenzalida, J. Messarosch, I. Eisele, H. Oppolzer and V. Huber, *J. Cryst. Growth, 81* (1986) 231.
7 J. Cibert, R. André, C. Deshayes, G. Feuillet, P. H. Jouneau, L. S. Dang, R. Mallard, A. Nahmani, K. Saminadayar and S. Tatarenko, *Superlattices Microstruc., 9* (1991) 271.
8 A. Ponchet, G. Lentz, H. Tuffigo, N. Magnea, H. Mariette and P. Gentile, *J. Appl. Phys., 68* (1990) 6229.
9 R. M. Fleming, D. B. Mc Whan, A. C. Gossard, W. Wiegmann and R. A. Logan, *J. Appl. Phys., 51* (1980) 357.
10 F. Blomer and V. Leute, *Z. Phys. Chem., 85* (1973) 47.
11 J. Z. Hang, P. Dawson, J. H. Neave, K. J. Hugill, I. Galbraith, P. N. Fawcett and B. A. Joyce, *J. Appl. Phys., 68* (1990) 5595.
12 M. Tanaka and H. Sakaki, *J. Cryst. Growth, 81* (1987) 153.
13 H. Tuffigo, N. Magnea, H. Mariette, A. Wasiela and Y. Merle d'Aubigné, *Phys. Rev. B, 43* (1991) 14 629.
14 E. Deleporte, J. M. Berrior, C. Delalande, N. Magnea, H. Mariette, J. Allegre and J. Calatayud, *Phys. Rev. BRC, 45* (1992) 6305.
15 M. K. Jackson, D. Hullin, J. P. Foing, N. Magnea and H. Mariette in A. d'Andrea (ed.), *Proc. Int. Conf. on Optics of Excitons in Confined Systems*, in *Inst. Phys. Conf. Ser., 123* (1991) 203.
16 Ph. Peyla, Y. Merle d'Aubigne, A. Wusiela, R. Romerstouin, H. Mariette, M. D. Sturge, N. Magnea and H. Tuffigo, *Phys. Rev. B, 46* (1992) 1557.
17 D. L. Smitt and C. Mailhiot, *Rev. Mod. Phys., 62* (1990) 173.
18 J. Cibert, R. André, C. Deshayes, L. S. Dang, H. Okumura, S. Tatarenko, G. Feuillet, P. H. Jouneau, R. Mallard and K. Saminadayar, *J. Cryst. Growth, 117* (1992) 424.
19 H. Tuffigo in A. d'Andrea (ed.), *Proc. Int. Conf. on Optics of Excitons in Confined Systems*, in *Inst. Phys. Conf. Ser., 123* (1991) 37.
20 N. T. Pelekanos, J. Ding, M. Hagerott, A. V. Nurmikko, H. Luo, N. Samarth and J. K. Furdyna, *Phys. Rev. B, 45* (1992) 6037.

Short period CdTe–ZnTe and CdTe–MnTe superlattices

W. Faschinger

Institut für Halbleiterphysik, Universität Linz, A-4040 Linz (Austria)

F. Hauzenberger, P. Juza, H. Sitter and A. Pesek

Institut für Experimentalphysik, Universität Linz, A-4040 Linz (Austria)

H. Zajicek and K. Lischka

Forschungsinstitut für Optoelektronik, Universität Linz, A-4040 Linz (Austria)

Abstract

CdTe–ZnTe superlattices (SLs) with a period ranging from 13 to 38 Å have been grown by atomic layer epitaxy (ALE) on (001) GaAs substrates. In a substrate temperature range between 270 °C and 290 °C the growth rate for both CdTe and ZnTe regulated itself to exactly 0.5 monolayers per reaction cycle, allowing the growth of very precisely tailored structures. For lower substrate temperatures the growth rate increased to approximately 0.8 monolayers per cycle, but did not reach 1 monolayer per cycle before ZnTe started to grow polycrystalline. Using the ALE growth parameters for CdTe, SLs of CdTe with metastable cubic MnTe were prepared. The superlattices were characterized by high resolution X-ray diffraction and photoluminescence. The X-ray data show that the SLs exhibit excellent period constancy and smooth interfaces.

1. Introduction

Atomic layer epitaxy (ALE) of semiconductors has recently attracted considerable interest because it has an excellent capability for controlling layer thickness and for growing high quality films at low substrate temperature, so minimizing interdiffusion. This is a consequence of the fact that, provided that the growth parameters are chosen properly, ALE growth is not continuous but occurs in discrete steps (so-called reaction cycles or growth cycles).

Multilayers of II–VI wide-gap compound semiconductors are of current interest for applications in short wavelength optoelectronic devices. Strained layer superlattices (SLs) of CdTe and ZnTe grown by molecular beam epitaxy (MBE) have been extensively studied [1–3]. CdTe and ZnTe are both direct gap semiconductors with band gaps of 1.6 eV and 2.2 eV respectively. By varying the thicknesses of the CdTe and ZnTe layers the band gap can be tailored. If the thickness of each layer is kept below the critical thickness, SLs are perfectly designed as buffer layers, because they are grown without any additional incorporation of misfit dislocations. Furthermore, they may reduce the density of threading dislocations [4].

MnTe crystallizes normally in the hexagonal NiAs structure with a band gap of 1.3 eV [5]. However, it has been shown recently that it can be stabilized in a metastable cubic form by growing it epitaxially on CdTe. In this modification it exhibits a drastically increased direct band gap of 3.2 eV [6]. Because of its high band offset compared with that of CdTe, a blue shift of luminescence peaks of more than 1 eV has been realized in MnTe/CdTe quantum well structures [7]. Very recently, SLs of ZnTe with cubic MnTe have been reported [8]. It was therefore of interest to grow SLs of CdTe with metastable cubic MnTe because large variations in the band gaps from the near IR to the near UV regions (1.6 to 3.2 eV) can be expected. Furthermore, possible two-dimensional magnetic effects are introduced by the narrow MnTe layers.

2. Experimental procedure

The epitaxy was performed in a vertical MBE system equipped with a 30 kV reflected high energy electron diffraction (RHEED) system, seven effusion cell ports, together with fast magnetically coupled shutters for operation in the ALE mode. For ALE growth of ZnTe, CdTe and MnTe, elemental zinc-, cadmium-, manganese- and tellurium-effusion cells were used. As the substrate material we used (100)-oriented semi-insulating GaAs 2° off to the next ⟨110⟩ direction, which was chemically cleaned in a standard H_2SO_4/H_2O_2 etch and preheated to 640 °C before

0921-5107/93/$6.00

© 1993 – Elsevier Sequoia. All rights reserved

growth in order to desorb the oxide layer. A virgin ionization gauge placed near the substrate was calibrated for zinc, cadmium, manganese and tellurium beam intensities by depositing polycrystalline zinc, cadmium, manganese and tellurium films on etched and preheated GaAs substrates at a substrate temperature of −10 °C.

The CdTe/ZnTe SLs were grown on an MBE deposited ZnTe buffer layer about 1 μm thick. In the ALE mode the constituents were deposited by alternating evaporation pulses of 1–2 s duration with 0.2 s dead time between them. The beam flux intensities were adjusted to deposit 2–5 monolayers (MLs) cadmium, 1.6–2.6 ML zinc and 1.3–2 ML tellurium within one evaporation pulse.

In a first set of experiments we examined the growth of ZnTe/CdTe superlattices as a function of substrate temperature ranging from 200 °C to 300 °C. The nominal structure of all SLs was 12 growth cycles ZnTe/12 growth cycles CdTe repeated 30 times. We then grew a series of SLs with constant total thickness (560 nm), a nominal composition of 50% CdTe and 50% ZnTe and a nominal period ranging from 12 growth cycles ZnTe/12 growth cycles CdTe to 4 growth cycles ZnTe/4 growth cycles CdTe at a substrate temperature of 280 °C.

The CdTe/MnTe SLs were grown on CdTe MBE buffer layers 0.2–1 μm thick. The CdTe layers of the SLs were prepared by ALE under the same conditions as determined for the CdTe/ZnTe SLs, whereas the MnTe part of the SLs was grown by MBE under tellurium-rich conditions, since ALE self-regulation is not expected to work for low vapour pressure components such as manganese. RHEED patterns showed a (2×1) reconstruction which was indistinguishable from the pattern occurring during the tellurium pulse of the ALE-grown CdTe, showing that MnTe grew in the metastable cubic structure.

High resolution X-ray diffraction (HRXD) rocking curve measurements were taken around the (004) or (002) peaks to determine the SL period from the spacing of satellites. In the case of one CdTe/ZnTe SL with a period of 20 Å, corresponding to 3 ML ZnTe/3 ML CdTe, we measured four asymmetric ((026), (−335), (335) and (−315)) diffraction reflexes in order to determine the exact composition.

1.7 K photoluminescence (PL) of the CdTe/ZnTe samples was measured at an excitation wavelength of 488 nm on an excitation level of 5 to 20 W cm^{-2}.

3. Results and discussion

The measured SL periods of the sample series grown at different substrate temperatures were all below the value expected for ideal ALE growth with 1 ML per growth cycle even at substrate temperatures as low as 205 °C. At lower temperatures, ZnTe grew polycrystalline, which was concluded from polycrystalline fringes in the RHEED pattern. However, for a substrate temperature between 270 °C and 290 °C the SL periods correspond exactly to a growth rate of 0.5 ML per cycle for both materials. In this temperature range, growth is self-regulating and the SL period does not change if the cadmium, zinc or tellurium flux is varied by a factor of two. This behaviour is in agreement with data reported in the literature: a growth rate of 0.5 ML per growth cycle is reported by Y. Takemura *et al.* [9] for ZnTe and by W. Faschinger and H. Sitter [10] for CdTe. J. Li *et al.* [11] grew ZnTe/CdTe multiquantum wells with a growth rate of about 0.5 ML per growth cycle.

For further investigations of the self-regulating region we grew a series of SLs with different periods but constant total thickness. Figure 1 shows the experimental SL period *vs.* the theoretical SL period calculated with a growth rate of 0.5 ML per growth cycle. The solid line denotes the expected result. As one can see, the agreement between the calculated and measured period thicknesses is excellent, proving the high reproducibility due to self-regulating growth The discrepancy of less than 5% between the theoretical and measured period thicknesses is comparable with the results obtained by G. Lentz *et al.* [12], who grew their ZnTe/$Cd_{0.9}Zn_{0.1}Te$ SLs on (001) $Cd_{0.96}Zn_{0.04}Te$ substrates with phase-locked epitaxy. However, in our case the growth parameters are less critical, as the growth regulates itself.

Figure 2 shows the rocking curves for SLs with a periodicity of 4 ML ZnTe/4 ML CdTe repeated 225 times and 2 ML ZnTe/2 ML CdTe repeated 450

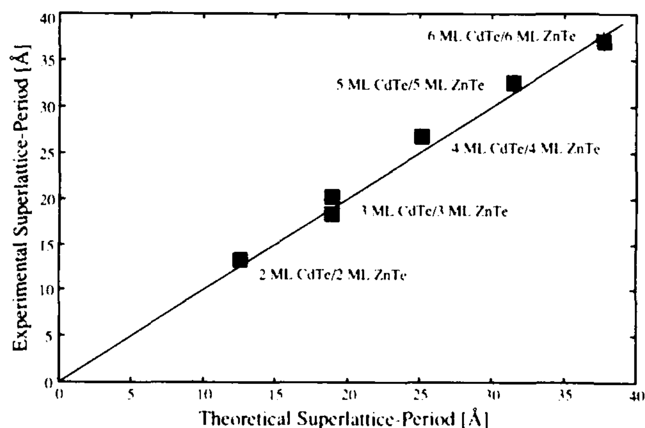

Fig. 1. SL period of the SLs grown at a substrate temperature of 280 °C *vs.* the theoretical SL period for a growth rate of 0.5 ML per growth cycle.

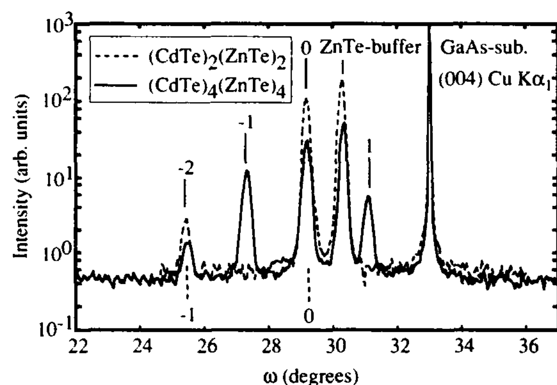

Fig. 2. HRXD spectra around the (004) peak of SLs with the following structures: (a) 4 ML ZnTe/4 ML CdTe (150 repetitions); (b) 2 ML ZnTe/2 ML CdTe (450 repetitions).

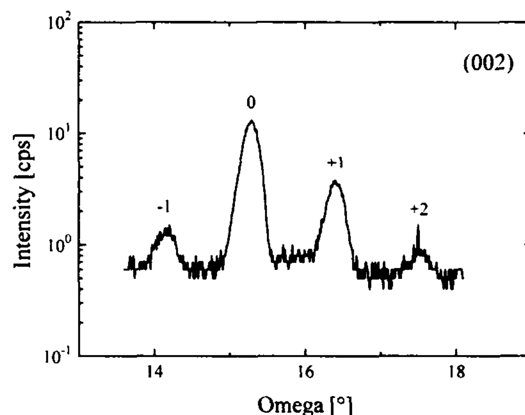

Fig. 3. HRXD spectrum around the (002) peak of a CdTe/MnTe superlattice with 8 ML CdTe and 4.5 ML MnTe (100 repetitions).

times. The fact that the second-order satellite peak of the former and the first-order satellite peak of the latter coincide exactly demonstrates the reliability of the self-regulation. The intensity between satellite peaks reaches almost the background intensity level of 1 count per second. This is a sign of highly perfect periodicity, since periodicity fluctuations should result in a rise of background intensity between the SL peaks [13].

For the 2 ML/2 ML SL, which has to our knowledge the shortest period length published so far, an interface roughness of 1 ML would result in a strong reduction of the satellite peak intensities. The fact that first-order satellites are clearly observed suggests that the interface roughness is below 1 ML. This is in good agreement with results obtained from far IR reflectivity measurements of the same series of samples, where the energy shift of phonons confined in the CdTe layers is evaluated [14].

For the SL with a periodicity of 3 ML CdTe/3 ML ZnTe the thickness of each individual layer is well below the critical thickness [2, 3]. As a consequence, it is reasonable to assume that the SL is of the strained layer type. In this case, the average composition x of the SL can be determined with high accuracy from the position of the zero-order peak of asymmetric reflexes. (Details of this procedure will be published elsewhere [15].) We find an x value of 0.5 ± 0.005, this value corresponding exactly to the one expected for a perfect symmetrical SL. This is a further proof for the accuracy of the self-regulating process.

Figure 3 shows the (200) rocking curve of a CdTe/MnTe SL with a period of 40.5 Å, corresponding to 8 ML CdTe and 4.5 ML MnTe, repeated 100 times. Since the MnTe was grown by MBE without self-regulation, growth with an exact number of MLs was not achieved. To our knowledge this is the first short period SL of CdTe with metastable cubic MnTe published so far. As in the case of CdTe/ZnTe, the peaks are clearly separated and the intensity between the peaks goes down to the background level, demonstrating good period constancy. Compared with CdTe/ZnTe SLs of a similar period, the intensity drop between zero-order and first-order satellite peaks is larger. However, computer simulations of X-ray diffraction showed that this is not due to a decrease in crystalline quality but reflects the differences in atomic scattering factors between zinc and manganese.

Figure 4(a) shows the low temperature PL spectrum of a CdTe/ZnTe SL with an individual layer thickness of 2 ML (full line) and the spectrum of a ZnTe buffer layer grown on the GaAs substrate by conventional MBE (dashed line). We suppose that the SL PL spectrum is a superposition of the PL emission from the SL, the buffer layer and the GaAs substrate. The sharp line at 1.49 eV is most likely a GaAs exciton line. To obtain the SL contribution to the PL emission we subtracted the intensity of the ZnTe buffer layer spectrum from the CdTe/ZnTe SL emission. Since the SL is not transparent at energies above 1.8 eV, the buffer layer PL intensity was set to zero for $h\nu > 1.8$ eV. The result of this procedure is shown in Fig. 4(b). The SL-related PL emission line has a width of about 150 meV. In a similar way, the PL spectra from SLs with individual layer thicknesses of 3–6 ML were obtained. These spectra show a shift of the PL peak energy to smaller values with increasing layer thickness.

The relatively broad and weak SL PL emission stands somehow in contrast to the high degree of crystalline perfection and good interface quality which was observed by HRXD. We assume that threading dislocations, which penetrate from the buffer layer into the SL, are responsible for the broadening of the PL line and also for the broad Bragg reflexes—though they do not affect the interface quality.

Figure 5 shows the PL spectrum of an 8 ML CdTe/4.5 ML MnTe SL with 100 repetitions, which emits

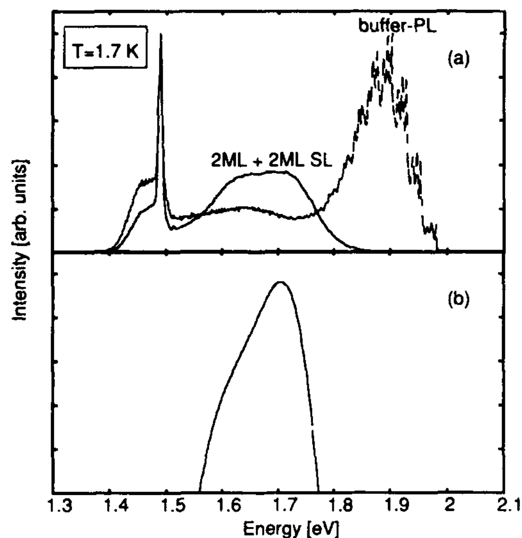

Fig. 4. (a) The 1.7 K PL emission from a 2 ML CdTe/2 ML ZnTe SL (full curve) and from the ZnTe buffer layer (dashed curve). (b) The difference in SL emission and buffer layer emission shown in (a). Since the SL is not transparent for $h\nu > 1.8$ eV, the buffer PL intensity was set to zero in this range.

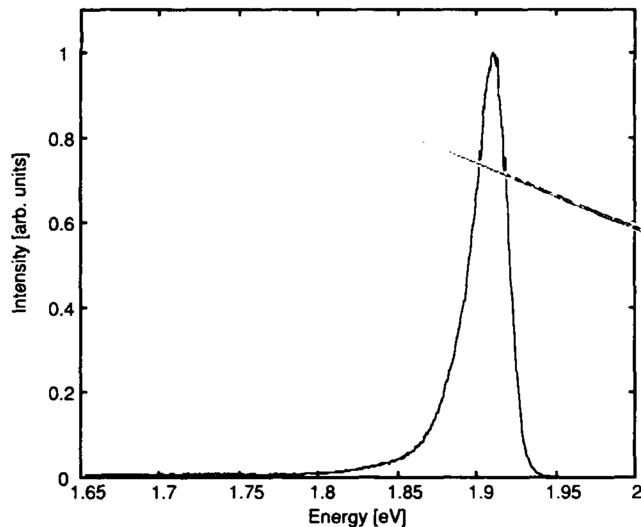

Fig. 5. 1.7 K PL of an 8 ML CdTe/4.5 Ml MnTe SL.

light in a similar spectral range to those of the CdTe/ZnTe samples. In contrast to CdTe/ZnTe, in this case the PL line is very intense and narrow (full width at half-maximum = 25 meV). This fact shows that CdTe/MnTe SLs could be a good alternative to CdTe/ZnTe for light emission between 1.6 and 2.2 eV.

5. Conclusions

ALE has been used to grow CdTe/ZnTe short period SLs on (001) GaAs substrates, and SLs of CdTe with metastable cubic MnTe have been prepared for the first time. We show that the ALE method is well-suited for the fabrication of precisely tailored structures. In a substrate temperature range between 270 °C and 290 °C, ALE of CdTe and ZnTe regulates itself to a growth rate of 0.5 ML per growth cycle, whereas MnTe cannot be grown in a self-regulating way because of the low vapour pressure of manganese. HRXD measurements show that the SL period is constant. Since we are able to observe clear SL satellite Bragg reflexes even for a 2 ML CdTe/2 ML ZnTe SL, we conclude that the interface roughness is less than 1 ML.

Acknowledgments

This work was supported by the "Fonds zur Förderung der wissenschaftlichen Forschung in Österreich" and the "Gesellschaft für Mikroelektronik". We thank O. Fuchs for technical assistance.

References

1 G. Monfroy, S. Sivanathan, X. Chu, J. P. Faurie, R. D. Knox and J. L. Staudenmann, *Appl. Phys. Lett., 49* (1986) 152.
2 J. Cibert, Y. Gobil, Le Si Dang, S. Tatarenko, G. Feuillet, P. H. Jouneau and K. Saminadayar, *Appl. Phys. Lett., 56* (1990) 29.
3 J. Cibert, A. Andre, C. Deshayes, G. Feuillet, P. H. Jouneau, Le Si Dang, R. Mallard, A. Nahmani, K. Saminadyar and S. Tatarenko, *Superlatt. Microstruct.,* 9 (1991) 271.
4 I. Sugiyama, A. Hobbs, O. Ueda, K. Shinohara and H. Takigawa, *Appl. Phys. Lett.,* 57 (1991) 2755.
5 W. D. Johnston and A. E. Sestrich, *J. Inorg. Nucl. Chem., 19* (1961) 229.
6 S. M. Durbin, J. Han, O. Sungi, M. Kobayashi, D. R. Menke, R. L. Gunshor, Q. Fu, N. Pelekanos, A. V. Nurmikko, D. Li, J. Gonsalves and N. Otsuka, *Appl. Phys. Lett., 55* (1989) 2087.
7 J. Han, S. M. Durbin, R. L. Gunshor, M. Kobayashi, D. R. Menke, N. Pelekanos, M. Hagerott, A. V. Nurmikko, Y. Nakamura and N. Otsuka, *J. Cryst. Growth, 111* (1991) 776.
8 P. Klosowski, T. M. Giebultowicz, J. J. Rhyne, N. Samarth, H. Luo and J. K. Furdyna, *J. Appl. Phys., 70* (1991) 6221.
9 Y. Takemura, H. Nakanishi, M. Konagai and K. Takahashi, *Jpn. J. Appl. Phys., 30* (1991) L246.
10 W. Faschinger and H. Sitter, *J. Cryst. Growth,* 99 (1990) 566.
11 J. Li, L. He, W. Shan, X. Cheng and S. Yuan, *J. Cryst. Growth, 111* (1991) 736.
12 G. Lentz, A. Ponchet, N. Magnea and H. Mariette, *Appl. Phys. Lett., 55* (1989) 2733.
13 V. S. Speriosu and T. Vreeland, *J. Appl. Phys., 56* (1984) 2755.
14 T. Fromherz, G. Bauer, M. Helm, F. Hauzenberger, W. Faschinger and H. Sitter, *Phys. Rev. B,* submitted for publication.
15 F. Hauzenberger, W. Faschinger, P. Juza, A. Pesek, K. Lischka and H. Sitter, *Thin Solid Films,* submitted for publication.

Spectroscopy of donors and donor-bound excitons in $CdTe/Cd_{1-x}Zn_xTe$ multiple quantum wells

R. T. Cox*
SPMM/Laboratoire de Physique des Semiconducteurs, CEN-Grenoble, BP 85X, 38041 Grenoble Cedex (France)
A. Mandray and S. Huant
CNRS-MPI High Magnetic Field Laboratory, BP166, 38042 Grenoble Cedex 9 (France)
F. Bassani
Laboratoire de Spectrométrie Physique, CNRS/Université J. Fourier, BP 87X, 38042 Saint Martin D'Hères Cedex (France)
K. Saminadayar
SPMM/Laboratoire de Physique des Semiconducteurs, CEN-Grenoble, BP 85X, 38041 Grenoble Cedex (France)
S. Tatarenko
Laboratoire de Spectrométrie Physique, CNRS/Université J. Fourier, BP 87X, 38042 Saint Martin D'Hères Cedex (France)

Abstract

Optical spectra for D^0X (excitons bound by neutral donors) are identified in emission and absorption spectra of CdTe/$Cd_{1-x}Zn_xTe$ multiple quantum wells that were planar-doped with indium. The effect of quantum confinement on the exciton localization energy is measured as a function of well width. The $1s \rightarrow 2p^+$ transition of neutral donors is studied by far-IR magnetoabsorption spectroscopy and shows no evidence for segregation of the dopant atoms.

1. Introduction

The intrinsic optical properties of CdTe quantum wells with $Cd_{1-x}Zn_xTe$ (CZT) barriers have been studied extensively in recent years (see, for example, the review by Magnea [1]). In this paper, we will describe the optical spectra of CdTe/CZT wells which were doped with the donor impurity indium during their growth by molecular beam epitaxy (MBE). Our study has two main motivations. Firstly, optical spectroscopy of neutral donors (D^0) and of excitons bound to donors (D^0X) can provide useful diagnostic information in doping trials. Secondly, we are interested in the fundamental effects of quantum confinement on the species D^0 and D^0X.

*Author to whom correspondence should be addressed.

2. Experimental details

Indium was introduced into CdTe/CZT microstructures during MBE growth on CZT (3%–4% Zn) substrates at about 220 °C under excess cadmium pressure [2]. The doping was nominally planar with the indium plane placed either at the centres of the CdTe wells or near the well edges. The well widths L_w were in the range 30–250 Å. The optical characterization methods used were (a) luminescence, absorption and photoluminescence excitation spectroscopy in the near-IR (0.7–0.8 $\mu m \approx 1.6$ eV) and (b) Fourier transform absorption spectroscopy in the far-IR (10–400 cm^{-1}) under magnetic fields up to 13 T.

3. Results and discussion

We first discuss the near-IR measurements which concern the bound exciton species D^0X. As reported

0921-5107/93/$6.00

© 1993 - Elsevier Sequoia. All rights reserved

elsewhere [3], we began our study by attempting to dope microstructures consisting of a single quantum well in thick CZT barriers. However, it proved very difficult to adjust accurately the doping on a single plane because of compensation by the large numbers of background acceptor impurities (copper, lithium, etc. in the 10^{15} cm^{-3} range) available in the CZT barriers and substrate. This led us to grow multiple quantum well (MQW) samples of total thickness 0.5 μm or more, with the CZT barrier widths L_b comparable with the well widths L_w, and with doping in each well to give a volume-averaged indium concentration of order 5×10^{16} cm^{-3}. Capacitance–voltage measurements show that these doped MQWs are n-type; this is confirmed by the far-IR spectra (see later) which show absorption due to the internal transitions of D^0.

Figure 1(a) shows luminescence spectra for several doped MQWs. These all give a strong emission line at progressively increasing energy levels with decreasing L_w and lying 3–5 meV below the (heavy hole) free exciton recombination line labelled X. Whereas line X is dominant for undoped samples, it is relatively weak here. We attribute the strong emission lines to the

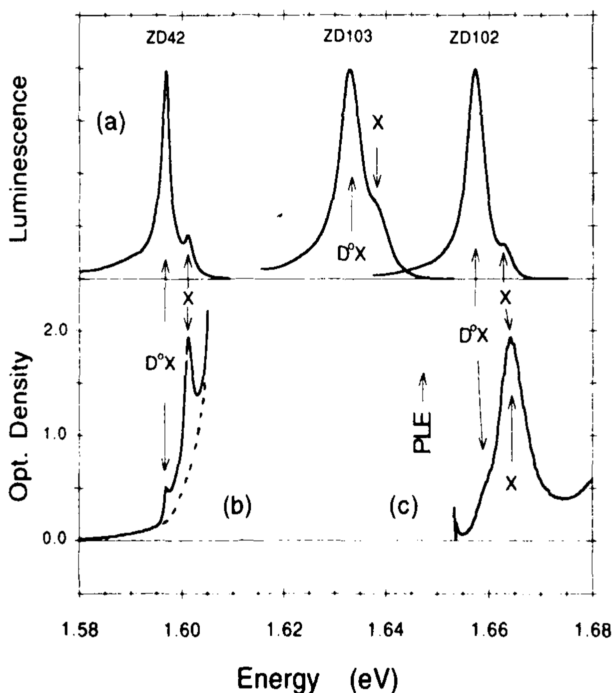

Fig. 1. (a) Normalized luminescence spectra at 2 K for three CdTe/CZT MQWs doped with indium at well centres. Well width L_w is 135 Å for ZD42, 52 Å for ZD103 and 32 Å for ZD102; zinc content in the CZT barriers is 8% for ZD42 and 24% for ZD103 and ZD102. (b) Absolute optical density spectrum ($\log_{10}$(1/transmission)) of sample ZD42 (40 wells = 0.54 μm of CdTe) showing lines X and D^0X on the rising background of the substrate's absorption edge. (c) PLE spectrum (arbitrary units, monitored on low energy wing of D^0X) for sample ZD102, showing Stoke's shift for exciton lines.

recombination of donor-bound excitons D^0X. The energy difference $X-D^0X$ defines the exciton "localization energy" E_{loc}.

Our CZT (3%–4% Zn) substrate material is transparent to about 1.605 meV and for large L_w the confined excitons can be seen in transmission as shown in Fig. 1(b) for sample ZD42 ($L_w = 135$ Å). For this MQW, grown directly on the substrate, the X and D^0X lines are narrow and there is no obvious "Stoke's shift" between the absorption and luminescence peaks.

One expects quantum confinement to compress the wavefunctions of the two electrons and the hole of the D^0X complex and so increase the exciton localization energy with maximum effect at the well centres. Thus, we attribute the sharp low energy edge of the D^0X absorption, giving a marked peak at 1.597 eV in Fig. 1(b), to donors at the well centres. The $X-D^0X$ difference in the absorption spectrum then gives a very accurate value of E_{loc} at the well centre for $L_w = 135$ Å, namely 4.2 meV. In fact, E_{loc} does not appear to depend strongly on the donor position: a sample similar to ZD42 but doped near the well edges gave an absorption onset only about 0.4 meV closer to X. The intensity above the main D^0X peak in Fig. 1(b), extending up towards X, probably corresponds to unresolved excited "rotator" states of D^0X.

For small well widths the X and D^0X lines lie above the substrate absorption edge and their absorption has to be taken from photoluminescence excitation (PLE) spectroscopy. Figure 1(c) shows a PLE spectrum for the narrowest well studied which has $L_w = 32$ Å (10 monolayers, sample ZD102).

In order to maintain high confinement at this small L_w, this sample was grown with relatively high zinc content (24% Zn) CZT barriers 153 Å thick on a relaxed buffer layer of CZT (20% Zn) which matches its average lattice parameter. We think now that it would have been better to match the MQW to a buffer with a different percentage of zinc content, because we get a very large excitonic linewidth (about 5 meV) and a large, energy-dependent Stoke's shift (about 1 meV) between absorption and emission (see Fig. 1(c)). This gives an uncertainty of the order of 1 meV in determining E_{loc}. These effects (and similar effects for sample ZD103 in Fig. 1, also grown on a 20% Zn buffer) have been traced to an unusually high, relaxation-induced defect density found for buffer–alloy compositions in the 20%–25% range [4].

Figure 2 plots the data for E_{loc} and compares these with its value in bulk CdTe [5], redefined to be $E_{loc} = E_T - E(D^0X) = 2.7$ meV where E_T is the transverse exciton energy, which is the appropriate limit for $E(X)$ as L_w approaches infinity.

As seen in Fig. 2, at small L_w the parameter E_{loc} reaches at least twice its bulk value. Comparison with

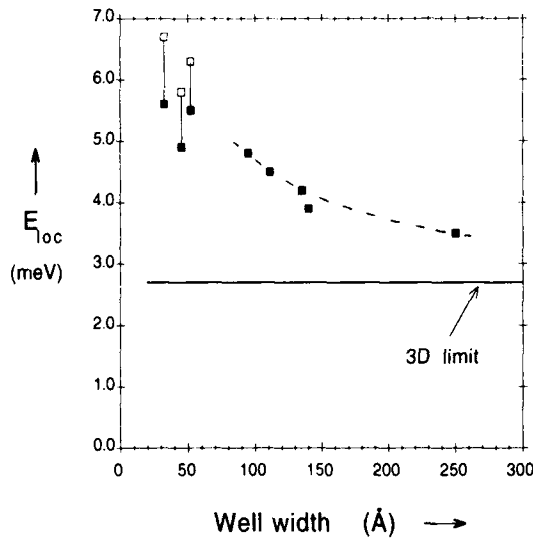

Fig. 2. Measured values of E_{loc} (exciton localization energy in D^0X) at well centres as a function of CdTe well thickness L_w. For the three narrowest wells, grown on high defect density CZT buffers, large Stoke's shifts give the uncertainty ranges indicated (where lower limits are from luminescence data alone and upper values take PLE spectra into consideration). The dashed curve is a guide for the eye only.

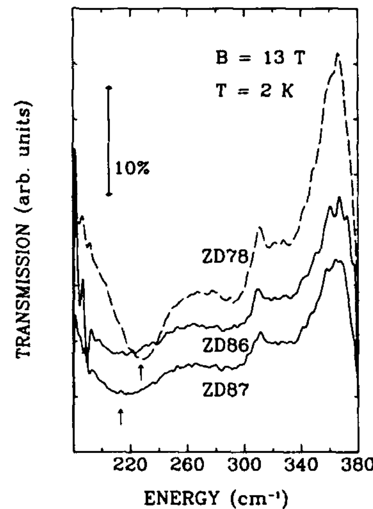

Fig. 3. Far-IR Fourier transform transmission spectra for three CdTe/CZT MQWs in a 13 T magnetic field. The wells have $L_w = 108$ Å; the doping plane is at the well centre for ZD78 and at 10 Å from the lower (upper) edge for ZD86 (ZD87). The transmission dips at 229 cm^{-1} (ZD78) and 215 cm^{-1} (ZD86, ZD87) correspond to the $1s \rightarrow 2p^+$ transition of neutral donors.

limited experimental data for the L_w dependence of the donor ionization energy E_i (from "two-electron D^0X" transitions [6]) suggests that there is no "Haynes' rule" (proportionality of E_{loc} to E_i) for the L_w dependence of E_{loc}: the localization energy increases faster than E_i as L_w decreases from infinity.

We now describe our far-IR transmission measurements in which the $1s \rightarrow 2p^+$ internal transition of neutral donors is observed as a function of the magnetic field. In studies of $GaAs/Ga_{1-x}Al_xAs$ quantum wells it has been shown that the $1s \rightarrow 2p^+$ transition can give valuable information about the effects of confinement on donor states and about impurity redistribution, because its energy depends on the well width and the impurity position in the well [7].

It proved necessary to work in quite a high magnetic field to move the $1s \rightarrow 2p^+$ transition into a transparent region above the reststrahlen band (at relatively low energy in CdTe/CZT). Transmission spectra taken at 13 T and normalized to zero-field spectra are shown in Fig. 3 for three MQW samples with the same well widths, namely $L_w = 108$ Å, but with differing locations of the indium planes. The transmission minima at around 220 cm^{-1} in Fig. 3 can be attributed to the $1s \rightarrow 2p^+$ transition of D^0, confirming that n-type doping has been achieved. The other features in the spectra are not donor related and will not be discussed here.

The $1s \rightarrow 2p^+$ transmission dips in Fig. 3 are displaced to higher energy levels (229 cm^{-1} at 13 T for ZD78) than for bulk CdTe (207 cm^{-1}, see ref. [8]) because quantum confinement has compressed the donor wavefunction, increasing intradonor level spacings. We have made variational calculations of the $1s$–$2p^+$ spacing for these samples using a model [9] suitable for a real MQW structure (finite barrier height, finite barrier width) in a magnetic field. Neglecting electron–phonon interaction and using an effective Rydberg of 12.5 meV and effective electron mass of $0.096m_e$ for CdTe, we calculate a transition energy of 217 cm^{-1} at 13 T for ZD78, in reasonable agreement with the measured value (about 229 cm^{-1}). The discrepancy is most likely because the electron–phonon interaction is neglected, since calculating the transition energy in the bulk with the same assumptions gives an equivalent disagreement.

Figure 3 shows the $1s \rightarrow 2p^+$ transitions lying at lower energy levels for donors near the well edges and gives an insight into the width of the doping profile. Sample ZD86 is doped at nominally 10 Å from the lower interface and ZD87 at the same distance from the upper interface (where "up" means in the growth direction). The two spectra will not be the same if there is unidirectional segregation of the donors (*i.e.* a redistribution of the impurity that is asymmetric with respect to the growth direction) as has been seen in a similar study of donor-doped $GaAs/Ga_xAl_{1-x}As$ MQWs [7]. Segregation would bring some donors towards the middle of the wells in sample ZD86 and thus distort the spectrum towards a higher energy level while donors would be drawn away from the well centres in sample ZD87, distorting the spectrum

towards a lower energy level. Since this is not seen in Fig. 3, we conclude that segregation is not very important here. Moreover, the good resolution between the transmission dips for the centre-doped and edge-doped samples in Fig. 3 suggests that any uniform (*i.e.* bidirectional) donor diffusion is not large on the 40 Å scale.

Because the transitions are close to the optical phonon energy, measurements at a higher magnetic field are needed to determine whether the slightly greater line broadening seen for the edge-doped samples represents a small redistribution effect or arises from other causes. The transmission dip for ZD86 and ZD87 in Fig. 3 is very close to the LO phonon energy (170 cm^{-1}) and the rapidly fluctuating dielectric function can give large line shape distortions such that the dip (215 cm^{-1}) may not represent accurately the true transition energy.

References

1 N. Magnea, *Mater. Sci. Eng., B, 16* (1993) 71-78.
2 F. Bassani, S. Tatarenko, K. Saminadayar and C. Grattepain, *Mater. Sci. Eng., B*, (1992) in press.
F. Bassani, S. Tatarenko, K. Saminadayar, N. Magnea, R. T. Cox, A. Tardot and C. Grattepain, *J. Appl. Phys.*, in press.
3 F. Bassani, K. Saminadayar, S. Tatarenko, K. Kheng, R. T. Cox, N. Magnea and C. Grattepain, *J. Cryst. Growth, 117* (1992) 391.
4 U. Rossner and N. Magnea, to be published.
5 J. Francou, K. Saminadayar and J.-L. Pautrat, *Phys. Rev. B, 41* (1990) 12035.
6 K. Kheng, R. T. Cox, S. Tatarenko, F. Bassani, K. Saminadayar and N. Magnea, *Inst. Phys. Conf. Ser., 123* (1991) 333.
7 S. Huant, R. Stepnlewski, G. Martinez, V. Thierry-Mieg and B. Etienne, *Superlatt. Microstruct., 5* (1989) 331.
8 D. R. Cohn, D. M. Larsen and B. Lax, *Phys. Rev. B, 6* (1972) 1367.
9 J. M. Shi, F. M. Peeters, G. Hai and J. T. Devreese, *Phys. Rev. B, 44* (1991) 5692.

Piezoreflectivity investigation of CdTe/(Cd,Zn)Te heterostructures

J. Calatayud, J. Allègre, P. Lefebvre and H. Mathieu

Groupe d'Etudes des Semiconducteurs, Université Montpellier II, Sciences et Techniques du Languedoc, Place E. Bataillon, 34095 Montpellier Cedex 5 (France)

Abstract

The deformation potentials of CdTe are such that a (001) or (111) in-plane biaxial strain strongly shifts the energies of the light hole states and leaves nearly unchanged the heavy hole states. As a consequence, in strained CdTe-based heterostructures, from piezoreflectivity measurements combined with first-order derivatives of the reflectivity structures, we identify in terms of heavy and light hole excitons all features associated with optically active layers (epilayers, substrates, buffer layers, quantum wells and/or superlattices). This appears of crucial relevance in the CdTe/(Cd,Zn)Te heterostructures (with a zinc composition of less than 0.15) because the lattice mismatch-induced splitting, the electron–hole Coulomb interaction and the valence band offset have the same order of magnitude. This produces a complex situation relating to the electronic states of the valence band. From the analysis of our experimental data via the envelope function formalism, including the specific strain effects, we find (i) new shear deformation potentials of CdTe; (ii) unambiguous identification of the character (heavy or light, type I or II) of excitonic ground states, in CdTe/(Cd,Zn)Te quantum wells and strained-layer superlattices; (iii) an accurate value of the chemical band offset between CdTe and (Cd,Zn)Te; (iv) finally, period dependence of the heavy and light hole exciton binding energies.

1. Introduction

Recent developments in the physics of strained-layer superlattices (SLSs) made it possible to take advantage of lattice mismatch effects as ingredients for a "refined" gap engineering. In particular, not only the energy of the gap, but also its type (I or II) and the symmetry of the involved carriers (light or heavy holes) can now be chosen by adjusting the values of the layer thicknesses and compositions. Of course, correct modelling requires an accurate knowledge of basic material parameters, such as deformation potentials, band offsets, etc. Piezoreflectivity allows us to improve this knowledge and the subsequent band gap engineering.

The principle of piezoreflectivity is the same as for any kind of modulation spectroscopy: when a perturbation is applied to a sample, the band structure and dielectric constant are altered. Consequently, the optical response of the material is in turn modulated. Biaxial piezomodulation has a selective effect on the various components of the spectrum, depending on their symmetry; this allows their identification, as demonstrated in earlier works [1]. The case of CdTe-based quantum wells (QWs) or SLSs is particularly favourable since, for a given value of a biaxial strain applied along the (001) or (111) plane, the energies of heavy holes are almost unchanged, while the energies of light holes are strongly shifted. This is due to the values of the hydrostatic (a_v) and shear (b or d) deformation potentials, which compete to build the stress-induced energy shift of the valence bands. Thus, piezoreflectivity experiments allow an unambiguous assignment of the observed spectral features to light hole or heavy hole excitons.

2. Experimental details

The sample coplanar piezomodulation is carried out by gluing the samples onto a piezoelectric radial transducer, such as lead zirconate titanate (PZT) ceramic, driven by an alternating voltage. Such transducers generate a strain $\Delta l/l \cong 10^{-5}$. The piezomodulated signal is detected with the standard lock-in technique, where the lock-in detector reference is obtained from the a.c. stress driver. The resulting spectrum is then an amplified first derivative of the original spectrum [1].

2.1. A-CdTe epilayers

In Fig. 1 are plotted the direct (R), the wavelength-modulated (WMR) and piezomodulated (PMR) reflectivity spectra of (a) ⟨001⟩-grown and (b) ⟨111⟩-grown CdTe strained epilayers. The spectra reveal two types of features related to heavy and light hole excitons. In both cases, spectra (PMR) show that the light hole exci-

Elsevier Sequoia

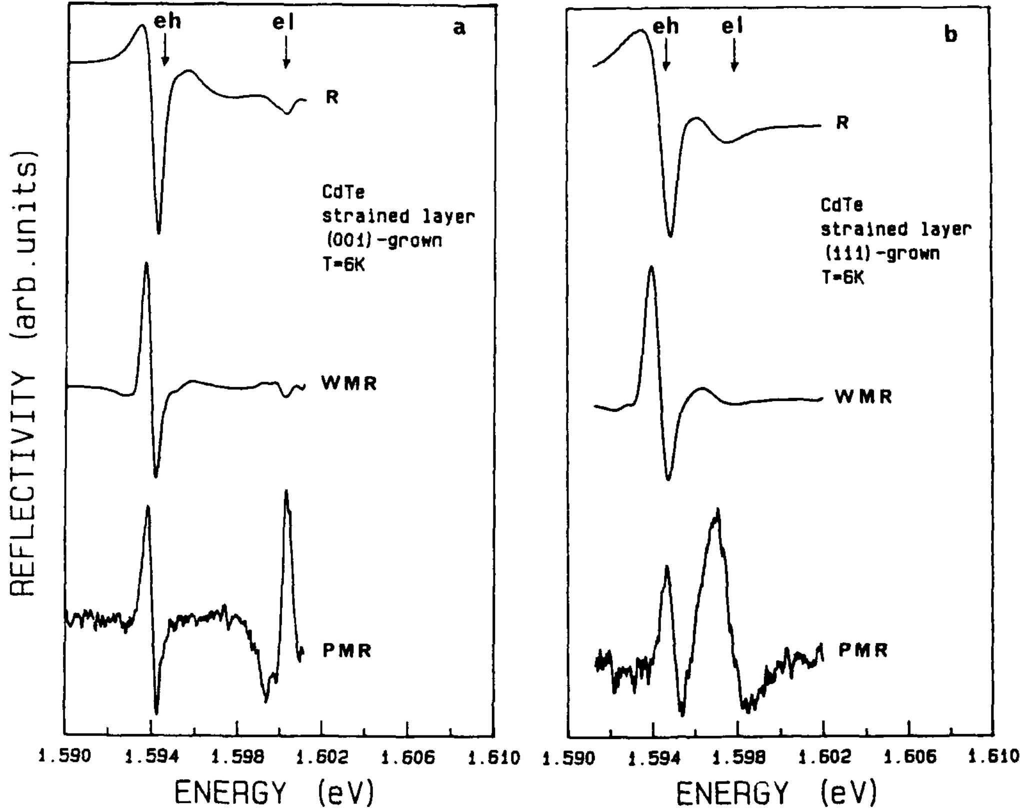

Fig. 1. Direct (R), wavelength-modulated (WMR) and piezomodulated (PMR) reflectivity spectra of (a) ⟨001⟩-grown and (b) ⟨111⟩-grown CdTe epilayers strained by a GaAs substrate.

ton is strongly modulated. The ratio K of the modulation rates of light hole and heavy hole structures is $K_{001} \approx -16$ (for the ⟨001⟩ growth axis) or $K_{111} \approx +30$ (for the ⟨111⟩ growth axis). These coefficients are related to the deformation potentials as follows:

$$\frac{b}{a} = -\frac{2(S_{11}+2S_{12})}{S_{11}-S_{12}} \frac{1-K_{001}}{1+K_{001}}$$

and

$$\frac{d}{a} = -\frac{4\sqrt{3}(S_{11}+2S_{12})}{S_{44}} \frac{1-K_{111}}{1+K_{111}}$$

From the most recent value $a \approx -3.43$ eV [2] of the hydrostatic deformation potential, and with the four K elastic compliance constants given by Greenough and Palmer [3] ($S_{11} \approx 0.416$ kbar^{-1}, $S_{12} \approx -0.171$ kbar^{-1} and $S_{44} \approx 0.483$ kbar^{-1}), we can deduce new shear deformation potentials for CdTe at low temperature: $b \approx -0.98$ eV and $d \approx -3.41$ eV.

2.2. B-CdTe/(Cd, Zn)Te strained quantum wells and superlattices

We have studied a series of CdTe/(Cd,Zn)Te QWs with CdTe layer thicknesses ranging from 50 to 1000 Å, and a series of SLSs consisting of equal thickness layers of CdTe and cadmium-rich (Cd,Zn)Te alloy (%Zn ≈ 10%), with periods ranging from 70 to 400 Å. They were grown in a Riber 32P MBE machine on ⟨001⟩-oriented $Cd_{0.96}Zn_{0.04}Te$ substrates. Reflected high energy electron diffraction (RHEED) provided an *in situ* measurement of the layer thickness with an accuracy of one monolayer. For convenience, we present, in Figs. 2 and 3, experimental data from two particular samples, including both QWs and SLSs.

The main difference between these samples arises from the period of the SLS: sample A (Fig. 2) is a (35 Å)/(35 Å) CdTe/$Cd_{0.91}Zn_{0.09}Te$ SLS, while sample B (Fig. 3) is a (70 Å)/(70 Å) CdTe/$Cd_{0.90}Zn_{0.10}Te$ SLS. Both samples contain an isolated quantum well (IQW) made up by a CdTe layer 210 Å wide. It should be noted that the first superlattice (A) is slightly strained by the $Cd_{0.97}Zn_{0.03}Te$ substrate; in contrast, for sample B, the composition of the $Cd_{0.955}Zn_{0.045}Te$ substrate is close to the average composition of the superlattice. Sample B can therefore be considered as almost free-standing. From a lot of information on direct (R), wavelength-modulated (WMR) and piezomodulated (PMR) reflectivity spectra, we present only the fundamental transitions of the active layers. (QWs and SLSs are carefully studied in refs. 4 and 5.)

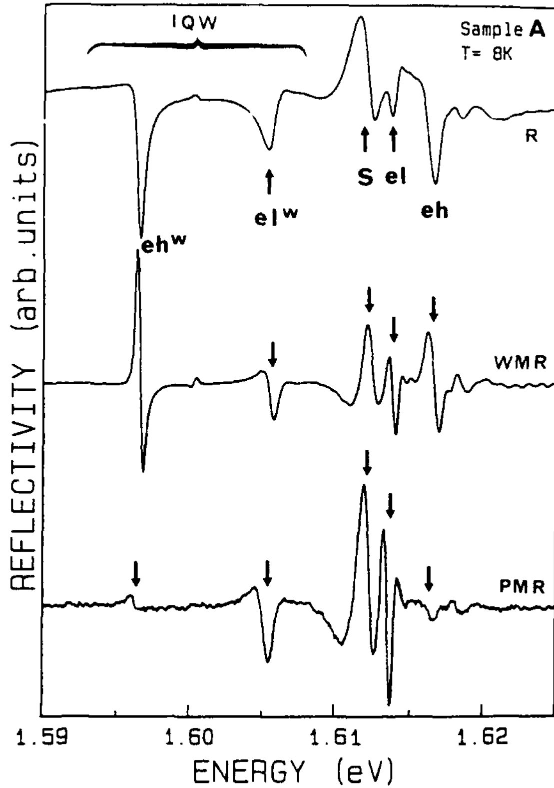

Fig. 2. Standard reflectivity (R), WMR and PMR spectra of sample A. This is a (35 Å)/(35 Å) $CdTe/Cd_{0.91}Zn_{0.09}Te$ SLS containing an isolated quantum well (IQW) made up by a CdTe layer 210 Å wide and slightly strained by a $Cd_{0.97}Zn_{0.03}Te$ substrate.

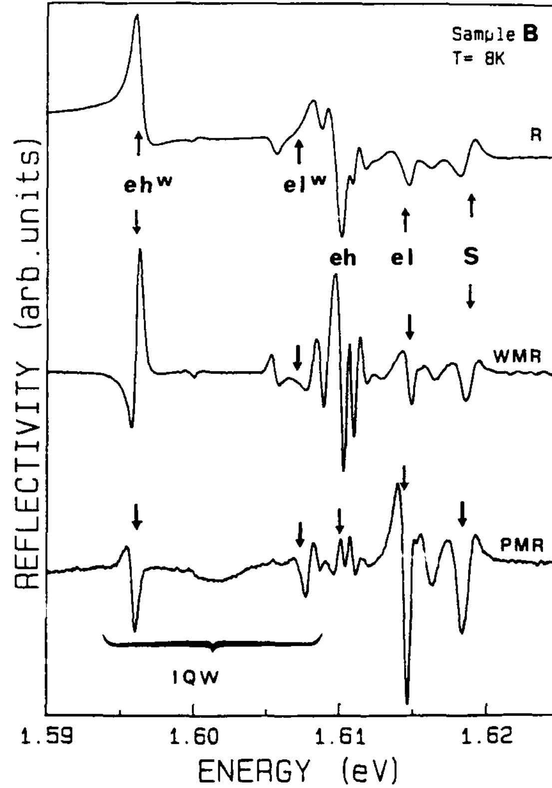

Fig. 3. The analogue of Fig. 2, but for a (70 Å)/(70 Å) CdTe/ $Cd_{0.90}Zn_{0.10}Te$ SLS (sample B). This sample also embeds a CdTe IQW 210 Å wide.

We can identify the features of the substrate (S), of the IQW (eh^{W}, el^{W}) and those of the SLS (eh, el). The fundamental excitonic transition of the IQW 210 Å wide is the exciton line eh^{W} in both cases. This situation is typical of all CdTe QWs grown on (Cd,Zn)Te substrates: the ground exciton state is a type I heavy hole exciton with a binding energy of about 15 meV as predicted by a theoretical calculation; transitions involving light holes are spatially indirect and thus hardly detectable. For the SLSs, the situation is more complex. The fundamental line is the type II (indirect) light hole excitonic transition el in the case of sample A (el < eh, Fig. 2), and the type I (direct) heavy hole exciton eh in the case of sample B (eh < el, Fig. 3). This point is addressed in the next section through a quantitative theoretical analysis of our data.

3. Data analysis and discussion

For each sample, piezoreflectivity allowed us to identify the heavy and light hole confined exciton states. We can now calculate the transition energies within the envelope function formalism, taking account of both the chemical band offset and lattice mismatch effects. The chemical valence band offset Q_V may be written as

$$Q_V = \frac{\Delta E_V}{\Delta E_g}$$

where ΔE_V is the valence band discontinuity in the absence of strain ($\Delta E_V < 0$ for $E_V(\mathrm{CdTe}) > E_V(\mathrm{CdZnTe})$). As this parameter is not well known, we wish to extract a reliable value by fitting our calculated subband-to-subband transitions to our experimental data.

Indeed, the exciton energy eh (el) can be deduced from the subband-to-subband transition EH (EL) by subtracting a quantity which should correspond to the exciton binding energy (EBE). It can be easily shown that an accurate estimation of Q_V is obtained if one takes advantage of the measurement of type II optical transitions in SLSs with rather wide periods, as sketched in Fig. 4, where we show, for a (200 Å)/(200 Å) SLS (sample C), that the EL type II transition is much more sensitive to the value of Q_V than is the EH transition, which is type I. For such a wide period,

the light hole EBE is weak, since the electron and the light hole respectively lie in CdTe and (Cd,Zn)Te layers, with a vanishingly small envelope function overlap. This EBE is slightly higher than 3 meV [6]; in the present case, we have taken a value of 4 meV. Thus, by comparing the experimental el transition energy to EL, we can derive a value Q_V. In order to check the accuracy of this value, we can apply the above method to all our samples. The quality criterion is as follows: if we choose the good value for Q_V, the variation of EH − eh and EL − el *vs.* the period must be the same as for the EBE. We have seen that for wide periods, the heavy hole EBE is equivalent to the heavy hole EBE in a single QW, *e.g.* about 15 meV for a wide QW 210 Å, and the light hole EBE is weak. (This value is the lower limit which can be reached, because of the spatial separation of the carriers. It corresponds to the binding energy of the 2p-like interface exciton (0.25R*), as theoretically predicted, for example, by Matsuura and Shinozuka.) For small periods, the SLS is equivalent to a quasi-alloy, and both light hole and heavy hole excitons recover a three-dimensional binding energy of about 11 meV. Finally, the value $Q_V = -2 \pm 3\%$ provides the average maximum agreement between theory and experiments (note that here 3% corresponds to about 1 meV).

In Fig. 5 we show the values of EH − eh and EL − el for symmetrical SLSs with various periods. First, we note that a value of about 11 meV is effectively obtained for very short periods, which confirms the coherence of our modelling of internal strain effects. Next, the variation of both quantities *vs.* the period is similar to that for EBEs given by recent theoretical calculations [7]. This is particularly crucial in the case of light hole excitons, since another value for Q_V may lead to an inconsistent behaviour of EL − el. We can then conclude that the chemical valence band offset Q_V is small and that the type and character of the fundamental gap of an SLS result from the competition between internal strain effects and the Coulombic interaction. Indeed, the theory shows that, in a free-standing superlattice, the energy of EL is always slightly lower than that of EH. However, since the heavy hole EBE is larger than the light hole EBE, the fundamental gap of the SLS keeps a direct (type I) character (eh < el), as shown in Fig. 6(a). This is the case of sample B presented in Fig. 3. In contrast, sample A (Fig. 2) exhibits a light hole type II ground excitonic transition (el < eh).

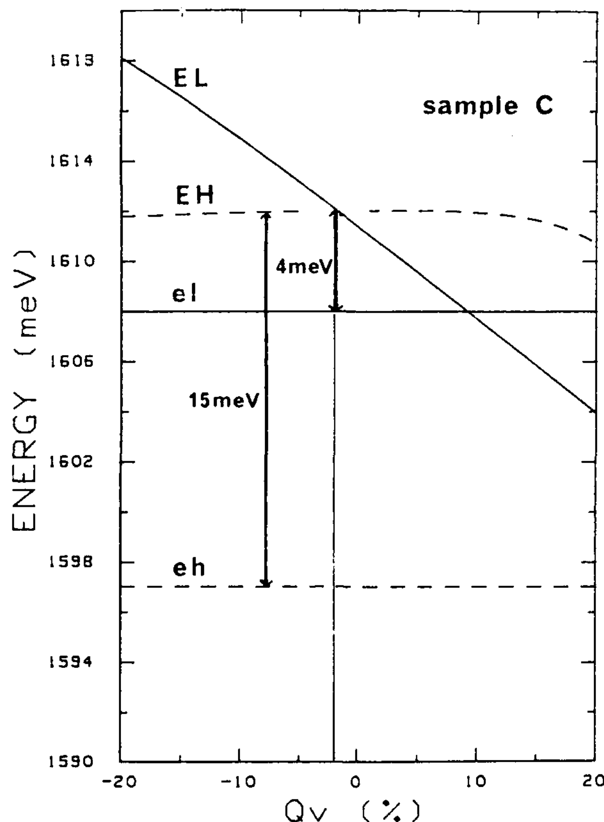

Fig. 4. The dependence of the calculated band-to-band transition energies EH and EL *vs.* the chemical valence band offset ratio Q_V for a (200 Å)/(200 Å) CdTe/$Cd_{0.92}Zn_{0.08}$Te SLS (sample C). The measured excitonic transition energies are also represented by horizontal lines.

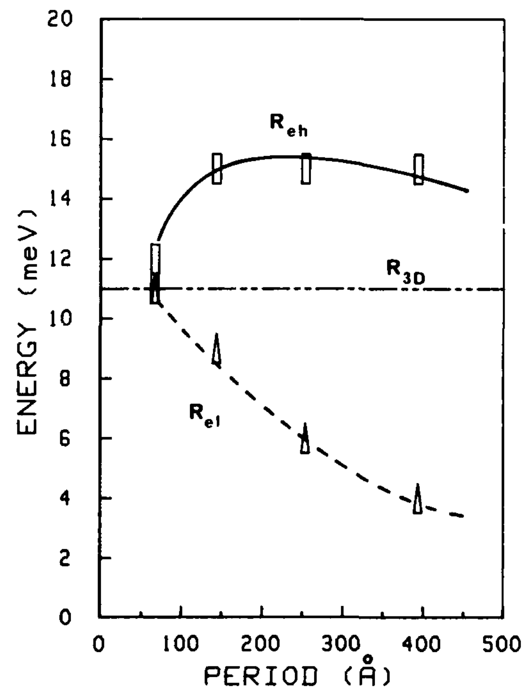

Fig. 5. Plot of the differences EH − eh and EL − el, as deduced from our experiments and calculations, *vs.* the period for several symmetrical SLSs. The variations obtained are those expected, respectively, for the binding energies of a type I heavy hole exciton and a type II light-hole exciton.

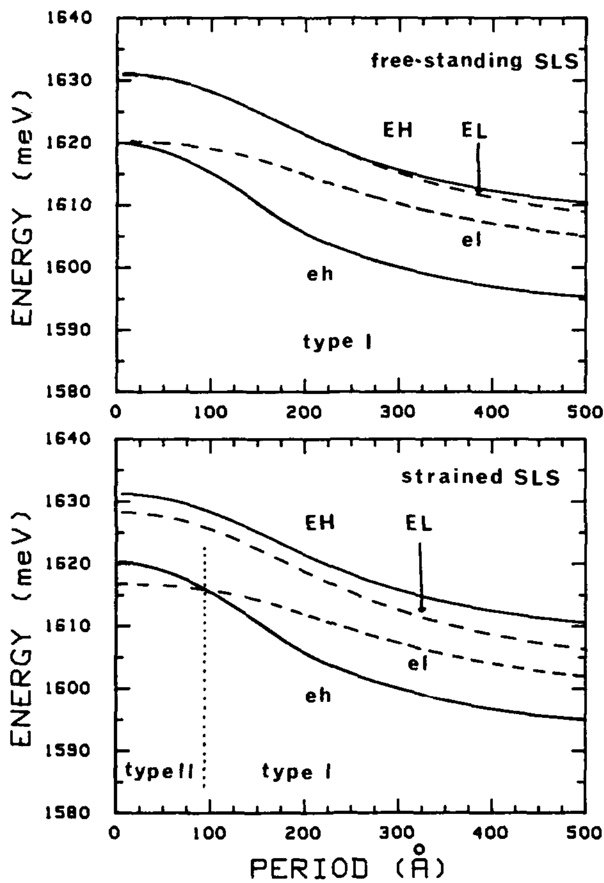

Fig. 6. The calculated energies of the EH (solid line) and EL (dashed line) transitions *vs.* the period for a CdTe/$Cd_{0.91}$-$Zn_{0.09}$Te SLS: (a) in a symmetrical free-standing case (growth on a $Cd_{0.955}Zn_{0.045}$Te substrate); (b) slightly strained by a $Cd_{0.97}Zn_{0.03}$Te substrate. Lines labelled with small letters sketch the energies of the corresponding excitonic transitions obtained by taking account of the binding energy variations derived from the curves in Fig. 5.

This can be explained by two complementary effects: first, due to the weak zinc mole fraction in the substrate the SLS sustains a residual strain which lowers the energy of EL (EL<EH). Secondly, since the period is rather short, the heavy hole and light hole EBEs have values close enough to each other so that this ordering is maintained for excitonic transitions. If the period was larger, this trend would be inverted, as shown in Fig 6(b), which summarizes the two conditions necessary to obtain a light hole type II SLS: (i) a choice of a substrate which leaves CdTe layers less strained than (Cd, Zn)Te layers; (ii) a choice of small periods.

4. Conclusions

By using piezoreflectivity experiments, we have improved the knowledge of CdTe and CdTe/(Cd, Zn)Te strained-layer heterostructures from two points of view. First, quantitative measurements of piezomodulation rates of light hole and heavy hole features provided us with reliable values for the deformation potentials *b* and *d* in CdTe and cadmium-rich (Cd, Zn)Te. Secondly, the assignment by piezomodulation of optical features to light hole or heavy hole excitons, for several samples, was carefully compared with the results of model calculations. This allowed us to extract a value for the chemical valence band offset ratio $Q_V = -2 \pm 3\%$, and the coherent variation of the binding energies of light and heavy hole excitons *vs.* the period of the SLS. Thus, knowing the combined conditions of strain and period which control the type (I or II) of a CdTe–(Cd, Zn)Te SLS, we can now proceed towards refined gap engineering.

Acknowledgments

The authors are grateful to the staff at the joint CNRS-CEA Research Group on II-VI MBE (Grenoble) for providing good quantum wells and superlattices.

References

1 H. Mathieu, J. Allègre and B. Gil, *Phys. Rev. B, 43* (1991) 2218 and references therein.
2 M. Prakash, M. Chandrasekhar, H. R. Chandrasekhar, I. Miotkowski and A. K. Ramdas, *Phys. Rev. B, 42* (1990) 3586.
3 R. D. Greenough and S. B. Palmer, *J. Phys. D, 6* (1973) 587.
4 J. Allègre, J. Calatayud, B. Gil, H. Mathieu, H. Tuffigo, G. Lentz, N. Magnéa and H. Mariette, *Phys. Rev. B, 41* (1990) 8195.
5 H. Tuffigo, N. Magnéa, H. Mariette, A. Wasiela and Y. Merle d'Aubigné, *Phys. Rev. B, 43* (1991) 14629.
6 M. Matsuura and Y. Shinozuka, *Phys. Rev. B, 38* (1988) 9830.
7 P. Peyla, Y. Merle d'Aubigné, A. Wasiela, P. Romestain, H. Mariette, M. D. Sturge, N. Magnéa and H. Tuffigo, *Phys. Rev. B, 46* (1992) 1557.

Materials Science and Engineering, B16 (1993) 92–95

Piezomodulated reflectivity on CdMnTe/CdTe quantum well structures as a new standard characterization method

E. Kurtz*, K. Schmitt, D. Hommel, A. Waag, R. N. Bicknell-Tassius and G. Landwehr
Physikalisches Institut, Universität Würzburg, D-8700 Würzburg (Germany)

Abstract

Piezomodulated reflectivity (PZR) measurements are reported for the first time as a standard characterization method for CdMnTe/CdTe single (SQW) and multiple (MQW) quantum wells grown by molecular beam epitaxy on CdTe substrates 1 mm thick. Previously, modulation spectroscopy studies of II–VI structures required thin substrates which needed special preparation. In this paper we present studies of optical properties of CdMnTe/CdTe SQWs and MWQs using the PZR technique. The samples, mounted on a sinusoidally driven piezoelectric transducer are subjected to an alternating strain. Exploiting "lock-in" techniques, the first derivative of the reflectivity is measured directly. Specific electronic transitions, *e.g.* excitons, are well resolved in the modulated spectrum and can be easily identified. This makes PZR a very sensitive and powerful tool for the characterization of quantum well structures, and a useful complement to other standard techniques such as photoluminescence and excitation spectroscopy.

1. Introduction

In recent years, CdTe and other II–VI compounds have become very popular because of their potential for band gap engineering. Wide gap materials cover a wide range in the visible range up to 3.8 eV (ZnS), while narrow gap II–VI semiconductors can even have negative band gaps (−0.3 eV for HgS). This is of special interest for optoelectronic applications ranging from detectors to diode lasers. Diluted semimagnetic materials, such as CdMnTe have advantages at low temperatures since their band gap can be varied by the manganese content and by the magnetic field as well. Today good quality epilayers, and single (SQW) and multiple (MQW) quantum wells containing II–VI semiconductors can be grown by molecular beam epitaxy (MBE) [1] or metallo-organic chemical vapour deposition (MOCVD) [2].

Characterization of these structures is generally performed either by destructive techniques such as secondary ion mass spectroscopy (SIMS) or optically by means of photoluminescence, photoluminescence excitation (PLE) and modulation techniques [3], such as photomodulated (PMR) and electromodulated (EMR) reflectivity. Piezomodulated reflectivity (PZR) has been successfully employed in the study of bulk materials [4–6] and recently of microstructures [7–10].

The application of uniaxial stress to a sample, as done in PZR, lowers the crystal symmetry but preserves the translational invariance of the crystal. The modulated spectrum consists essentially of the first derivative, related to the energy, of the static reflectivity, and interpretation is straightforward compared with those of other modulation techniques. Many advantages arising from the use of PZR have been accounted for by Lee *et al.* [7].

In this paper, we report on the use of PZR for the characterization of CdMnTe/CdTe SQWs and MQWs. It is shown that this technique is also applicable to samples grown on CdTe substrates 1 mm thick without the need of thinning. This and the fact that optically allowed transitions are well resolved makes PZR a useful complement to other characterization methods.

2. Experimental details

The CdMnTe/CdTe quantum wells used in our study were grown by MBE on (001) CdTe substrates 1 mm thick and of dimensions 5 mm × 10 mm.

To apply external strain to a microstructure, the sample is mounted on a lead–zirconate–titanite transducer using the technique of Gavini and Cardona [5]. To obtain uniform stress at the centre of the sample only its ends are fastened to the transducer with high

*Correspondence should to be sent to Elisabeth Kurtz, Arbeitsgruppe MBE/EPIII, Physikalisches Institut, Universität Würzburg, Am Hubland, D-8700 Würzburg, Germany.

0921-5107/93/$6.00
© 1993 - Elsevier Sequoia. All rights reserved

vacuum grease which is easy to handle and hardens at low temperatures allowing for the relaxation of internal strain owing to cooling. The sample is mechanically modulated along its longer side (*i.e.* its (011) direction) by applying a sinusoidal electric field along the thickness (1.5 mm) of the transducer. Voltages ranging between 600 and 800 V_{pp} are obtained by suitable amplification of the reference taken from a function generator. A frequency of 180 Hz was chosen because of the strong decrease in amplification for higher frequencies. Owing to the high field strength, liquid nitrogen had to be used instead of helium in the bath cryostat. Light from a 100 W Xenophot-halogen lamp was focused to about 1 mm^2 on the sample in a near perpendicular incidence configuration. Warming of the sample can be neglected owing to the fact that it is directly immersed in liquid nitrogen. The reflected light then passes through a grating monochromator (HR640 Jobin Yvon) and is detected by a silicon photodiode.

The signal contains a d.c. component, which is measured by an HP 3468A multimeter, and an a.c. component proportional to the periodic, strain-induced change ΔR in the reflectivity. This a.c. component is detected phase sensitive compared with the modulation reference with an Ithaco 3961B lock-in amplifier. Both signals are recorded simultaneously, processed by computer and divided to obtain the ratio $\Delta R/R$.

3. Results

Two SQWs and three MQWs have been investigated for the present study. The spectra of the SQWs ct302 and ct396 are shown in Figs. 1 and 2, while Figs. 3–5 represent the MQW structures ct310, ct434 and ct530. Interpretation is straightforward. The features at 1.586 eV are attributed to the excitonic transition in the CdTe buffer (substrate). The next higher signatures correspond to heavy and light hole transitions in the

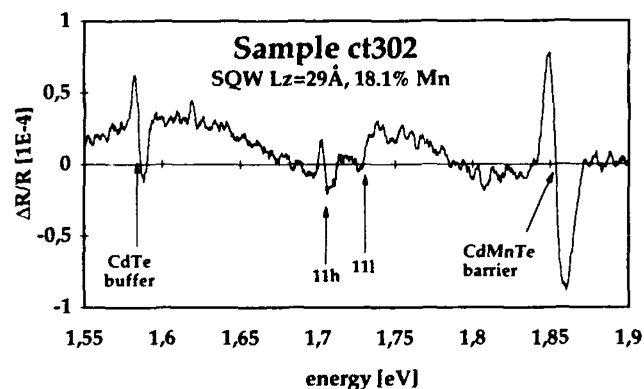

Fig. 1. PZR spectrum of sample ct302 SQW on a substrate 1 mm thick taken at 77 K.

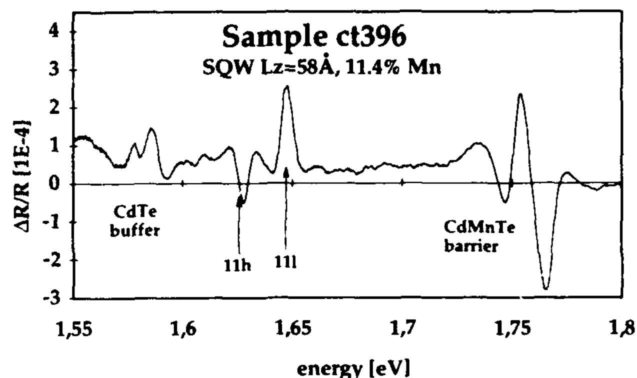

Fig. 2. SQW ct396: thin sample (200 μm) where a relative pre-strain of 10^{-3} was taken into account for the numerical determination of the well width from the heavy and light hole transitions.

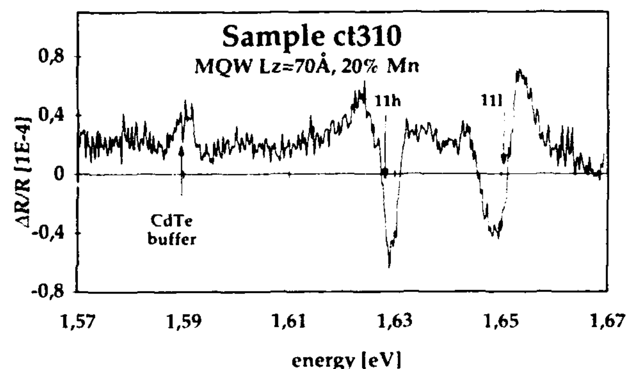

Fig. 3. Sample ct310: MQW on a substrate 1 mm thick. Both manganese content and well width had to be determined numerically from the heavy and light hole features.

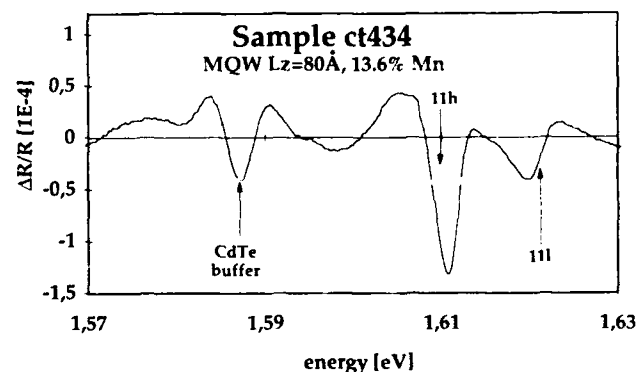

Fig. 4. Sample ct434: MQW with manganese content of 13.6% on a substrate 1 mm thick. The manganese concentration was determined from the reflection spectrum, since the lack of a CdMnTe cap layer resulted only in a very small change of reflection and the transition could not be recognized in the PZR spectrum.

quantum wells. The highest energy feature to be found is the transition in the CdMnTe barrier from which the manganese content x was determined using [11]

$$E_g(Cd_{1-x}Mn_xTe) = (1.586 + 1.501x)\,eV$$

since measurements were performed at liquid nitrogen temperatures. These features could not be seen in the PZR spectra of samples ct310 and ct434, since both lacked a CdMnTe cap layer. In the case of sample ct434, the manganese content could be determined from reflection measurements where the transition was slightly visible while, for sample ct310, both the manganese concentration and well width had to be calculated from the heavy and light hole features.

To obtain the width L_z of the quantum wells from the experimental data, a suitable numerical model equally consistent for both heavy and light hole excitons [12] was used. The splitting is not only caused by strain owing to lattice mismatch between the CdMnTe buffer and the CdTe well but also by differences in confinement and binding energies owing to differences in mass. The energies are calculated from an enhanced two-band model by variational methods using an appropriate envelope function consisting of the product of one particle functions for the electron $\varphi_e(z_e)$ and hole $\varphi_h(z_h)$ and the wave function for the relative motion $\phi_{e,h}(\rho, b)$ with the variational parameter b to account for the two-dimensional diameter of the exciton. The Schroedinger equation of the system is then solved by simultaneously varying three band parameters of the wave function until the resulting exciton energy approaches a minimum. During all the calculations a natural valence band offset of 15% was assumed for the type I CdMnTe/CdTe quantum wells. Further information concerning the general calculation method and the parameters used can be found in ref. 12 and references therein.

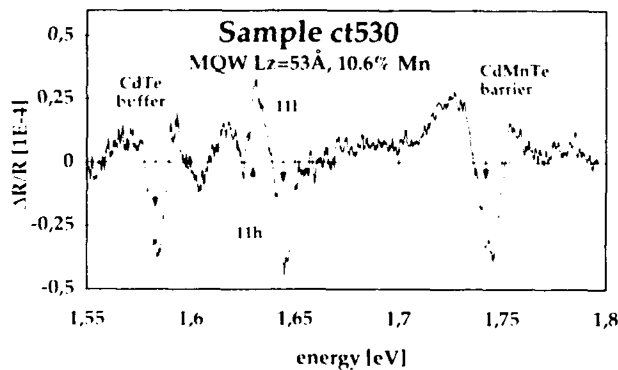

Fig. 5. PZR spectrum of sample ct530 MQW on a substrate 1 mm thick at 77 K.

In the case of the SQWs the thin CdTe layer is embedded in two comparably thick CdMnTe barrier layers. Therefore, the barrier was assumed to be relaxed to its own lattice constant and the well completely strained according to the relative lattice mismatch of $\Delta a/a = (0.0225x)$ [13]. In the MQWs the strain was distributed according to the thickness of the layers. The quantum well thickness L_z was determined using the known manganese concentration, strain distribution in the layers and valence band offset with L_z as the variational parameter for the calculation of the exciton energies. The results for heavy and light hole transitions were fitted to the experimental data giving L_z. In the spectra the calculated energies are marked and labeled accordingly. Owing to the fact that there is a great uncertainty in some of the general parameters used in the calculations, a relative deviation from the actual L_z of approximately $\pm 10\%$ may be considered. In the case of sample ct310 (Fig. 3), both the manganese content and well width had to be determined numerically, since no signal of the barrier could be detected, resulting in a high relative deviation for both values.

Sample ct396 (Fig. 2) is an exception in the way that it was prestrained. Owing to the fact that this

TABLE 1. Major data concerning the samples used in the study, experimental and numerical results

Growth data					Calculated energies			Results	
Sample name	CdTe buffer (μm)	CdMnTe barrier	Number of periods	CdMnTe cover layer (Å)	Natural strain distribution in CdTe well (%)	Heavy hole (eV)	Light hole (eV)	Mn concentration (%)	Quantum well width L_z (Å)
ct302	0.5	1.5 μm	SQW	800	100	1.7072	1.7293	18.1	29
ct396	1.0	1.5 μm	SQW	800	100	1.6260[a]	1.6480[a]	11.4	58
ct310	0.1	300 Å	500	—	75	1.6253	1.6509	20	70
ct434	0.2	75 Å	50	—	50	1.6092	1.6234	13.6	80
ct530	0.5	60 Å	50	1000	50	1.6304	1.6448	10.6	53

[a]These data have been corrected to an additional relative strain of 10^{-3}.

sample is only of dimensions 2 mm × 2 mm and thinned to 200 μm, it could not be fastened in the way described but was fixed completely, leaving no chance for relaxation. Using the known elasticity coefficients and deformation potentials for CdTe [5] $S_{11} = 4.27 \times 10^{-12}$ cm^2 dyn^{-1} and $S_{12} = -1.73 \times 10^{-12}$ cm^2 dyn^{-1}, and $C_3 = 1.1$ eV and $C_1 - C_2 = -4.69$ eV, an additional relative strain of about 10^{-3} was determined from the heavy–light hole splitting of the excitonic transition in the CdTe buffer (substrate). The resulting additional shift of the transitions in the single well of 0.4 meV for the heavy hole and 5.6 meV for the light hole, respectively, had to be considered in the calculation. The numerically determined energies were corrected accordingly. The results and parameters of all the samples are presented in Table 1.

4. Conclusions

Using an appropriate numerical model for the calculation of heavy and light hole transition energies, PZR offers the possibility for the characterization of microstructures directly comparable with the results of photoluminescence excitation. This non-destructive technique is applicable to thick as well as thin samples under the condition that a good coupling between the transducer and sample and a reasonable modulation are guaranteed.

Acknowledgments

Special thanks to Barbara Kuhn-Heinrich and the members of the group of Dr. Ossau for valuable information and the possibility to use the exciton program.

References

1 M. A. Herman and H. Sitter, in M. B. Panish (ed.), *Molecular Beam Epitaxy*, Springer, Berlin, Vol. 7, 1989.
2 J. L. Schmit, *J. Vac. Sci. Technol. A*, *3* (1985) 89.
3 M. Cardona, *Solid State Phys.*, Suppl. 11, Academic Press, New York, 1969, p. 137ff and p. 165ff.
4 W. E. Engeler, H. Fritzsche, M. Garfinkel and J. J. Tiemann, *Phys. Rev. Lett.*, *14* (26) (1965) 1069.
5 A. Gavini and M. Cardona, *Phys. Rev. B*, *1* (2) (1970) 672.
6 D. D. Sell, *Surf. Sci.*, *37* (1973) 896.
7 Y. R. Lee, A. K. Ramdas, F. A. Chambers, J. M. Meese and L. R. Ram-Mohan, *Appl. Phys. Lett.*, *50* (10) (1987) 600.
8 R. L. Harper, R. N. Bicknell, D. K. Blanks, N. C. Giles, J. F. Schetzina, Y. R. Lee and A. K. Ramdas, *J. Appl. Phys.*, *65* (1989) 624.
9 Y. R. Lee, A. K. Ramdas, L. A. Kolodziejski and R. L. Gunshor, *Phys. Rev. B*, *38* (18) (1988-II) 13143.
10 R. G. Alonso, C. Parks, A. K. Ramdas, H. Luo, N. Samarth, J. K. Furdyna and L. R. Ram-Mohan, *Phys. Rev. B*, *45* (3) (1992-I) 1181.
11 Y. R. Lee and A. K. Ramdas, *Solid State Commun.*, *51* (1984) 861.
12 B. Kuhn-Heinrich, W. Ossau, M. Popp, E. Bangert, A. Waag and G. Landwehr, submitted to *Sem. Sci. Technol.*
13 N. Magnea, F. Dalbo, C. Fontaine, A. Million, J. P. Gaillard, L. S. Dang, Y. Merle d'Aubigné and S. Tatarenko, *J. Cryst. Growth*, *81* (1987) 501.

Materials Science and Engineering, B16 (1993) 96–102

Structural defects in bulk and epitaxial CdTe

K. Durose, A. Turnbull and P. Brown*
University of Durham, Department of Physics, South Road, Durham (UK)

Abstract

The advantages of growing bulk CdTe from the vapour are summarized and the structural defects present in material grown using three different vapour methods compared critically. Kawano's growth rate explanation of twin distribution is developed and the effect of growth conditions in anomalous cases is speculated upon. Experimentally observed tilts and rotations in CdTe/GaAs(001) are explained using a dislocation model which indicates a degree of cooperative alignment of certain interfacial dislocation components. The equilibrium distribution of threading dislocations and the prospects for filtering using soft, tensed layers, *e.g.* (HgMn)Te, are discussed.

1. Introduction

The presence of structural defects in both bulk and epitaxial CdTe represents one of the greatest barriers to the utilization of this material in high performance, low cost IR detectors. Although CdTe and (CdZn)Te should be ideal substrates for (CdHg)Te epitaxy, the wafers are expensive because of the difficulties in producing single-grained boules with low defect density. Avoidance of the problem by resorting to foreign substrates, notably GaAs, leads to new defect problems.

Grown-in structural defects in CdTe fall into three categories:

(i) Grain boundaries and twins occur, arising from nucleation and growth phenomena. Twinning is especially prevalent [1] since CdTe has a high ionicity (74%) [2] and hence a low stacking fault energy.

(ii) Dislocations and subgrains are common on account of the low critical resolved shear stress (CRSS) and hence yield stress ($\sigma_y = 25$ kg cm^{-2} at 300 K [3]) of CdTe, which make it susceptible to deformation by thermal stresses during growth.

(iii) Precipitation of excess Cd or Te is prevalent in the bulk material owing to the retrograde solid solubilities of these elements in CdTe [4].

This paper deals with three current topics related to defects in CdTe, namely the relationship of differing bulk vapour growth methods to defect content in bulk CdTe, twin suppression in epitaxy and the effect of interfacial and threading dislocations in CdTe/GaAs.

*Present address: Department of Materials, University of Cambridge, Cambridge, UK.

2. Defects in bulk vapour-grown CdTe

Although the majority of bulk CdTe is grown from the melt, vapour growth is known to offer the significant advantage of growth below the maximum melting point of 1092 °C [5]. Growth at lower temperatures carries the benefits of reduced thermal strain on cooling, higher CRSS at the growth temperature and reduced contamination. Furthermore, control of the vapour composition should enable close stoichiometric control.

A wide variety of vapour growth configurations are available in principle and here the structural defects present in as-grown CdTe boules grown by three of them are compared (see Fig. 1).

The "Durham" method [6] shown in Fig. 1(a) employs an evacuated silica capsule with a conical nucleation tip connected to a Te reservoir by a narrow orifice. As the capsule is drawn upwards through the temperature gradient, transport begins at an ill-defined point and is complete after about 7 days. Polycrystallinity is common although sometimes single crystal boules are obtained, the irreproducibility being due to nucleation at the tip and the inability to control the residual pressure in the tubes. Many of the grains are twin related ($\Sigma = 3, 9, 27$), and broad lamellar twins are common. Te inclusions 5–30 μm in size are invariably associated with grain and twin boundaries, the higher energy boundaries being more heavily decorated [7]. Concentration of dislocations with similar Burgers' vectors into regular arrays was observed by transmission electron microscopy (TEM) [7, 8] and most of the dislocation density was present as subgrain boundaries approximately 100 μm apart. The overall situation is

0921-5107/93/$6.00

© 1993 - Elsevier Sequoia. All rights reserved

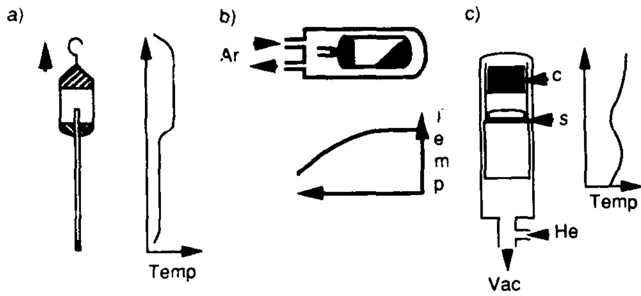

Fig. 1. The three vapour transport configurations compared in this work. (a) "Durham" sealed ampoule method: growth time about 7 days. (b) "Piper–Polich" self-sealing tube in an Ar atmosphere: growth time about 1 day. (c) "ELMA" method using continuous pumping with He back-filling capability.

one in which the grown-in defects have reached a state of equilibrium during the extended growth period and ramped cool down.

In the "Piper–Polich" method [7] (Fig. 1(b)) an open growth tube with a narrow neck is placed in a temperature gradient under Ar at atmospheric pressure. When transport begins the tube self-seals and the crystal grows within 24 h, after which the boule is cooled rapidly by switching off the furnace. The incidence of multiple grains and twinning is similar to that of "Durham" material. However, the dislocations are only loosely organized into arrays of mixed Burgers' vector [7] with a subcell size of about 100 μm and a high intracell dislocation density. Precipitates are small (typically less than 1 μm in size), are coherent with the lattice and are generally scattered throughout the bulk of the material. In "Piper–Polich" boules the short growth time lead to a less equilibrated defect distribution and this appears to be desirable.

The third method examined here has been developed by the "ELMA" research and development association of Moscow. It is illustrated in Fig. 1(c) and utilizes a seed wafer mounted on a sapphire rod. Charge material is supported vertically above it in a hotter region of the furnace. Continuous pumping operates and the chamber can be back-filled with inert gas. The CdTe boule studied here was 50 mm in diameter and about 10 mm deep with a convex growth surface which was identified as (111)A using Laue back reflection and etching in $HF + HNO_3 + CH_3OOH$ (1:1:1) [9]. The etch revealed no large angle grain boundaries and only one small inclined twin lamella was seen. Figures 2(a) and 2(b) show room temperature cathodoluminescence micrographs of a (001)-oriented bromine/methanol etched surface. Figure 2(a) is typical and the black spots due to dislocations are only loosely organized into subgrain boundaries with a minimum separation of about 100 μm. The average dislocation density in the figure is about 10^6 cm^{-2}, somewhat higher than the manufacturer's figure of

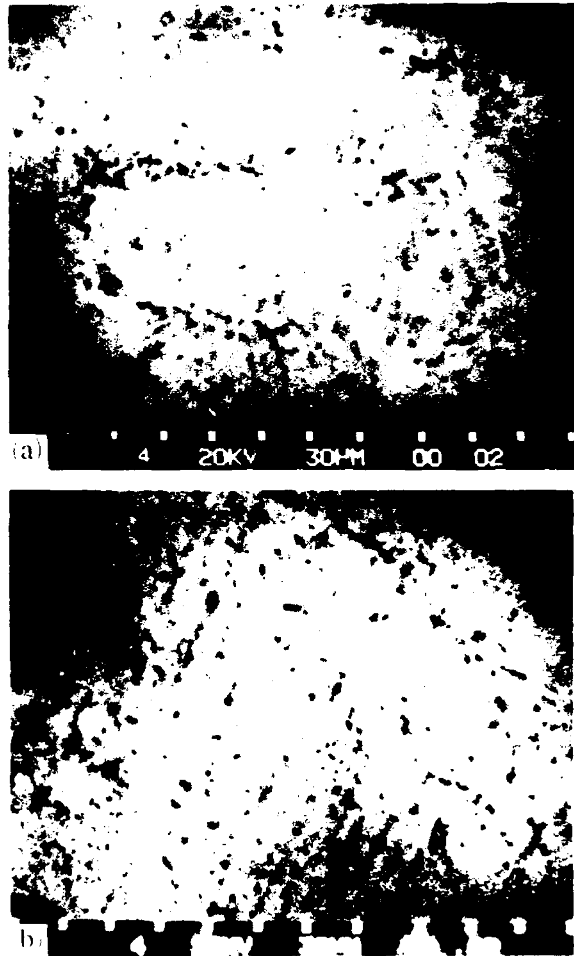

Fig. 2. Room temperature SEM/CL micrographs of a (100) wafer of "ELMA" CdTe: (a) subgrains; (b) slip bands.

5×10^4 cm^{-2}. This is probably because cathodoluminescence has a higher penetration depth than etching and also because no attempt was made to find a good part of the boule. Examination of other parts of the boule revealed slip bands oriented in ⟨110⟩, as shown in Fig. 2(b). These may be a result of thermal stresses caused by sticking to the sapphire block. Also visible in Fig. 2(b) are dark spots with especially high contrast. These are precipitates [10] about 2 μm in size and appear to be randomly distributed throughout the sample. Occasional inclusions up to 10 μm were observed. The use of a seed wafer has yielded single crystal material with a low twin density. Growth would appear to have been relatively rapid, giving distributed rather than associated dislocations and precipitates.

Clearly, the conditions of vapour growth are important in determining the defect content and distribution in CdTe. The use of a seed wafer was efficient in generating single crystal material and further reductions in twin density may be realized if a twin suppressing orientation such as $(\bar{1}\bar{1}\bar{2})$B were used (see Section

3). Precipitation and dislocations are introduced by non-stoichiomery and strain, and their distribution is controlled by the thermal profile of the growth process. It is only through the careful control of these factors that the full benefits of bulk vapour growth will be realized.

3. Twinning in epitaxial CdTe

Twinning in CdTe represents a major problem and is prevalent in almost every form of the material. The relationship between twin and matrix in the sphalerite lattice is highly symmetric and is variously described as a $\Sigma = 3$ coincidence relationship, a $\Theta = 250° 32'$ ⟨110⟩ tilt boundary, a shear in ⟨211⟩ with {111} invariant, or a $\phi = 180°$ ⟨111⟩ twist boundary. Parallel planes in twin and matrix may be identified using one of the four 3×3 matrices which may be written for each ⟨111⟩ twist axis [11-13].

In this paper twinning in homoepitaxial CdTe is examined with reference to the work of Kawano *et al.* [13]. They point out that twinning should only occur during the thickening of an epitaxial layer if the twin orientation grows as fast or faster than the matrix orientation. Many common orientations can be treated by using the fact that $(\bar{1}\bar{1}\bar{1})$B grows faster than (111)A [14] as do planes oriented more closely to $(\bar{1}\bar{1}\bar{1})$B than to (111)A.

Twinning in homoepitaxial {111}CdTe was first assessed by Hails and Brown [15] using scanning electron microscopy (SEM), reflection high energy electron diffraction (RHEED) and cross-sectional TEM (XTEM). Growth on $(\bar{1}\bar{1}\bar{1})$B generates thin lamellar twins throughout the epilayer thickness which have $(\bar{1}\bar{1}\bar{1})$B composition planes, indicating that a growth accident phenomenon causes twin nucleation. Growth in [111]A is disrupted by tetrahedral surface features with fast growing $(\bar{1}\bar{1}\bar{1})$B surfaces. Twinning develops on (111)A but mostly on the inclined $\{\bar{1}\bar{1}\bar{1}\}$B facets since the twin nuclei are not outgrown by (111)A growth.

Twinning on (001) surfaces is known to be anisotropic [16], with the $[1\bar{1}0]$ XTEM projection revealing a higher twin density on $(\bar{1}\bar{1}1)$A and (111)A than does the [110] projection on $(\bar{1}11)$B and $(1\bar{1}1)$B. Use of the twinning matrices allows the indices of the twin planes corresponding to the (001) matrix orientation to be established. The results are summarized in Fig. 3 and show that $\{\bar{1}\bar{1}\bar{1}\}$B planes which intersect [110] support twins with {221}A surfaces, while twinning on the {111}A planes which intersect $[1\bar{1}0]$ give $\{\bar{2}\bar{2}\bar{1}\}$B planes. Since the $\{\bar{2}\bar{2}\bar{1}\}$B planes have close proximity to $\{\bar{1}\bar{1}\bar{1}\}$B, they are expected to grow fast, giving inclined twins which intersect $[1\bar{1}0]$. However, (221)A is slow grow-

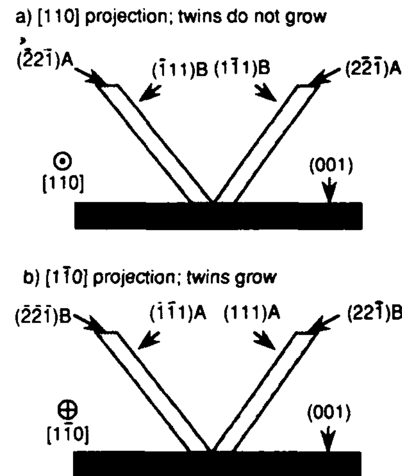

Fig. 3. Anisotropic twinning in CdTe(001): (a) [110] zone axis; (b) $[1\bar{1}0]$ zone axis.

ing so twinning is suppressed on $(\bar{1}11)$B and $(1\bar{1}1)$B planes which intersect [110]. This dispels the notion that twinning is solely a B-face phenomenon. Different material systems and even different samples of the same material show varying degrees of anisotropy. This could be caused by differences in the growth rates in the critical directions in other materials. In the case of a single materials system, anisotropy variation could be caused by growth conditions. Alternative models of anisotropic twinning based on the differential mobility of α and β dislocations [16] and the generation of defects at substrate steps [17] have been advanced.

The growth rate analysis can also be applied to {112} surfaces for which it has been observed that $(\bar{1}\bar{1}\bar{2})$B suppresses twin nucleation but (112)A does not. In these cases, it is expected that the twins will have $(\bar{1}\bar{1}\bar{1})$B and (111)A composition planes. Applying the twinning matrices to {112}A and {112}B gives (552)A and $(\bar{5}\bar{5}\bar{2})$B respectively. However, since both [112] and [552] are oriented symmetrically (at 19.5°) to [111], and similarly for $[\bar{1}\bar{1}\bar{2}]$B and $[\bar{5}\bar{5}\bar{2}]$B, there is no simple basis upon which to allocate relative growth rates. Kawano *et al.* [13] make the assumption that growth in the matrix orientation is fastest for $(\bar{1}\bar{1}\bar{2})$B growth and slowest for (112)A growth to account for the fact that the former suppresses twinning and the latter does not. However, recent XTEM observations of {112}A- and {112}B-oriented metallo-organic vapour phase epitaxy (MOVPE) grown epilayers in this laboratory have shown that twinning is suppressed on (112)A and not on $(\bar{1}\bar{1}\bar{2})$B, the orientations having been confirmed by microdiffraction [18]. It is suggested here that the growth technique or growth conditions used for a particular run may affect the relative growth rates on (111)A and $(\bar{1}\bar{1}\bar{1})$B, hence giving different twinning behaviour.

4. Interfacial and threading dislocations in CdTe(001)/GaAs(001)

4.1. Interfacial dislocation phenomena

Two recent experimental observations of tilts and rotations in CdTe/GaAs deserve further explanation.

(i) The observation that CdTe/GaAs contains subcells about 0.6 mm wide which cause a mosaic spread of 600 arc sec is revealed by triple axis diffractometry. The cell boundaries correlate directly with those in the underlying GaAs in which the misorientations are only about 10 arc sec. Larger tilts of 1°–2° in domains up to 8 mm across have also been observed. Tilts in the CdTe are replicated in any subsequent (CdHg)Te overlayers [19, 20].

(ii) Plan view TEM [21] of near-interface CdTe/GaAs reveals subcells on the scale of a few micrometers, rotated with respect to one another by 1°–4°.

In this work an explanation of these effects based on the properties of interfacial dislocations is advanced. Schwartzman and Sinclair [22] among others has identified the misfit dislocations in as-grown CdTe/GaAs as being predominantly of the 60° type. Such mixed dislocations may be resolved into screw and edge components as shown in Fig. 4. Edge component $\boldsymbol{b}_{e\parallel}$ ($=a/2\sqrt{2}$ in $\langle 110\rangle$) relieves interfacial stress, edge component $\boldsymbol{b}_{e\perp}$ ($=a/2$ in $\langle 100\rangle$) provides a tilt and screw component $\boldsymbol{b}_s$ ($=a/2\sqrt{2}$ in $\langle 110\rangle$) gives an in-plane rotation. The 60° dislocations can lie along either $[\bar{1}\bar{1}0]=\boldsymbol{l}_1$ or $[\bar{1}10]=\boldsymbol{l}_2$ and their Burgers vectors lie in directions pointing either up or down the four other $\langle 110\rangle$ directions comprising the edges of a square-based pyramid on (001). For a layer under compression, *i.e.* CdTe/GaAs, the Burgers vectors must have a $\boldsymbol{b}_{e\parallel}$ component corresponding to an extra half plane in the substrate. If the SF/RH convention is used then the Burgers vectors of the dislocations relieving compressive strain are as follows using the Thompson tetrahedron notation: for $\boldsymbol{l}_1$-DB, AD, CB and AC, and for $\boldsymbol{l}_2$-DB, DA, BC and AC. Although these dislocations are chosen to relieve compressive interfacial strain and hence have defined $\boldsymbol{b}_{e\parallel}$ components there is no such constraint on the $\boldsymbol{b}_s$ and $\boldsymbol{b}_{e\perp}$ components. The number and tilt and/or rotation type of these components present in the eight 60° misfit dislocations is shown in Table 1. Equal numbers of $\boldsymbol{b}_s$ components give rotations clockwise and anticlockwise, and similarly equal numbers of $\boldsymbol{b}_{e\perp}$ components tilt the epilayer up and down. It is therefore feasible to test whether the tilts and rotations arise from a cooperative alignment of interfacial dislocations or whether such components are randomly oriented.

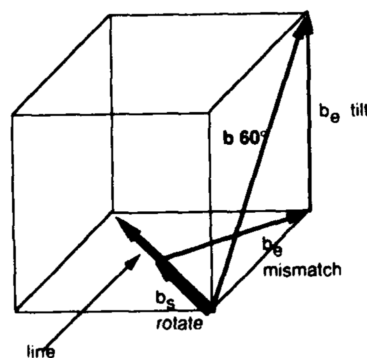

Fig. 4. The components of a 60° dislocation.

4.1.1. Complete cooperative alignment model

If only those dislocations with similar tilt and rotation components exist at the heteriointerface because of alignment phenomena, then the tilts and rotations will be maximized. If ϕ is the tilt angle then

$$\tan\phi \approx \phi \approx \frac{\boldsymbol{b}_{e\perp}}{s}$$

where s is the spacing between dislocations. Hence

$$\phi = \frac{a}{2\times 1.57\times 10^{-9}} \approx 11.8°$$

An analogous calculation for rotation components gives the rotation angle ϕ' as

$$\tan\phi' \approx \phi' \approx \frac{\boldsymbol{b}_s}{\text{spacing}}$$

$$= \frac{a}{2\sqrt{2}\times 1.57\times 10^{-9}} = 8.4°$$

These angles are the maximum possible tilts and rotations and they are independent of domain size.

4.1.2. Random alignment model

If the Burgers vectors are randomly aligned then the components must be treated in the same way as the "random walk" model used in kinetic theory [23]. Using the same treatment for n dislocations, n_+ of

TABLE 1. Summary of the components of 60° dislocation relieving compressive stress

	l_1	l_2	all
Stress relief	4	4	8
Clockwise tilt	2	2	4
Anticlockwise tilt	2	2	4
Rotate anticlockwise	2	2	4
Rotate clockwise	2	2	4

which have a Burgers vector $b_{e\perp}$ pointing up, and defining $x = n_+ b_{e\perp}$ then $P(x)$ the probability of being at x can be shown to be

$$P(x) = \left(\frac{2}{\pi n}\right)^{1/2} \exp\left(\frac{-s'^2}{2n}\right)$$

where s' is the number of steps used to get to x directly. This is a normal distribution with a mean of 0, the standard deviation of steps from the origin being $(2n)^{1/2}$. If the tilting is due to random orientation of the Burgers then it is better than 99% certain to be caused by no more than $3(2n)^{1/2}$ tilt steps. The standard deviation tilt ϕ_{SD} is given by

$$\tan \phi_{SD} \approx \phi \approx b_{e\perp} \frac{(2n)^{1/2}}{d} = b_{e\perp} \left(\frac{2N}{d}\right)^{1/2}$$

where N is the linear dislocation density and d the domain size. This random tilt assessment was first applied to low mismatch III–V systems by Turnbull [24].

For the largest tilt domain reported [19] (8 mm) this gives a maximum tilt of $3\phi_{SD} = 80$ arc sec and for an average domain (0.6 mm) $3\phi_{SD} = 292$ arc sec. For rotations, a 1 μm cell gives a rotation of 1015 arc sec (0.282°). Larger domains give smaller rotations proportional to $1/\sqrt{d}$ for a given mismatch.

4.1.3. Discussion of tilt calculations

The tilt data are summarized in Table 2 and clearly show that the experimentally observed tilts and rotations could not be generated solely by random alignments. Partial but not full alignment of the tilt and rotate components of the interfacial dislocations is implicated. Correlation of the tilt domains in CdTe with those in the substrate could be caused by alignment of the interfacial dislocations with those originating in the substrate. Since the interfacial dislocation density is very high (6.4×10^6 cm^{-1}), such alignments could trigger the partial alignment necessary for the observed effects. Alternatively, the surface steps present on the vicinal surfaces of the substrate subcells could be significant. The rotation domains are on a different scale but need not be related to tilt domains as they could result from island nucleation.

TABLE 2. Summary of tilt and rotation data for CdTe/GaAs

	Tilt		Rotation
Domain size	$d = 8$ mm	$d = 0.6$ μm	$d = 1$ μm
Experiment	1°–2°	600 arc sec	1°–4°
Complete alignment	11.8°		8.4°
Random alignment	80 arc sec	292 arc sec	1015 arc sec or 0.282°

4.2. Threading dislocations

Threading dislocations are defined as those which penetrate the epilayer from the substrate or else which link interfacial segments to the epilayer surface. It has been shown that it is energetically favourable for an interfacial dislocation to be bent upwards to intersect with the surface upon meeting a second interfacial dislocation at right angles. Since the spacing of interfacial dislocations in CdTe/GaAs is 15.7 Å, this helps explain the high near-interface dislocation density encountered in this system and shown in Fig. 5. The long, straight threading dislocations inclined to the substrate have been identified as dislocation dipoles [25] and pure screw [26].

A model of the equilibrium density distribution of threading dislocations has been formulated by Ayers *et al.* [27] for thick mismatched epilayers. It predicts that the dislocation density D varies as thickness h such that

$$D = \frac{|f| \sqrt{2}(1+\nu)(1-2\nu)|\ln\{2\pi|f|/(1-\nu)\}|}{\alpha b h (1-\nu)^3 \{1 - \ln(2b\sqrt{D})\}}$$

where α is a geometric parameter equal to 1 or more and ν is Poisson's ratio and f the misfit. Hence

$$D \approx (\text{const}) \frac{1}{h}$$

Brown *et al.* [26] have recently compared this expression with experimentally determined values for ZnTe/GaAs ($f \approx 7\%$). All the measured dislocation densities were in excess of the maximum equilibrium values calculated using $\alpha = 1$ in Ayers' model, the excess being a factor of 2–5. This indicates that the threading dislocations were not at equilibrium in the MOVPE grown samples examined. The proximity to equilibrium could have implications for dislocation filtering.

For reduction of the dislocation density, selected-area epitaxy is known to be effective for low mismatch systems [28]. However, it is unlikely to be of value for CdTe/GaAs owing to the shortness of the interfacial dislocation segments. Nevertheless, it could be viable at the better matched (CdHg)Te interface, the CdTe being part of a hybrid substrate.

The introduction of a thin layer under tension into CdTe buffers grown on GaAs, *e.g.* ZnTe, provides stress of the correct sign for the filtering of threading dislocations in a compressed layer. This has been successfully demonstrated using subcritical thicknesses of ZnTe [29] which do not introduce further defects

[30]. Strained-layer superlattices have been examined by a number of authors and have met with limited success [16, 31]. An effective procedure has been the introduction of two CdTe/ZnTe superlattices with different barrier-well widths into CdTe/GaAs; however, even this only reduces the dislocation density by a factor of 5 or so.

An alternative approach is to use a single layer of a soft material under tension. The dilute magnetic semiconductor (HgMn)Te is suitable for this since the lattice parameters of HgTe (6.429 Å) and cubic MnTe (6.34 Å) are both smaller than that of CdTe (6.477 Å). The composition $(Hg_{0.9}Mn_{0.1})Te$ has a lattice parameter of about 6.42 Å and might be expected to filter 4×10^5 dislocations cm^{-1} from CdTe. Figure 6 shows a layer of MOVPE grown $(Hg_{0.9}Mn_{0.1})Te$ on a CdTe buffer about 1.5 μm thick. There is a considerable reduction in the dislocation density from about 6×10^4 cm^{-1} just below the interface to about 200 cm^{-1} in the epilayer above it. It is presumed that the low CRSS of the (HgMn)Te layer allows thin interfacial dislocations to be generated easily and that these defects then fail to propagate further into the epilayer. Of course, (CdHg)Te might itself also be considered as a soft tensed epilayer on CdTe and there is evidence that there is a significant improvement of quality in (CdHg)Te. A good example is the reduction of double-crystal X-ray diffraction full widths at half-maximum by a factor of 2 in (CdHg)Te compared with the values observed in hybrid CdTe/GaAs substrates [19]. Further studies of (HgMn)Te as a filtering layer are planned.

5. Conclusions

(i) Vapour growth is an attractive means of producing bulk CdTe, and $(\bar{1}\bar{1}\bar{2})$B seeded growth arrange-

Fig. 5. XTEM of CdTe/GaAs showing threading dislocations.

Fig. 6. Dislocation filtering using (HgMn)Te.

ments with good vapour control and minimal thermal stress could generate excellent material.

(ii) Kawano's growth rate model of twinning in epitaxial layers is successful in most cases. However, specific growth conditions may effect the growth rates on key planes, hence giving "anomalous" twinning behaviour.

(iii) Tilts and rotations in CdTe/GaAs(001) are due to the partial cooperative alignment of interfacial dislocation components.

(iv) Threading dislocations in some MOVPE grown ZnTe/GaAs samples exceed their equilibrium densities and this is likely to be true also for CdTe/GaAs.

(v) (HgMn)Te alloys are a promising dislocation filter for CdTe/GaAs.

Acknowledgments

Thanks are due to all those who supplied material examined in this work including Alex Chernov, Michelle Simmons, Haider Al-Allak and Norman Thompson. Thanks also to Chris Gibson for information services.

References

1 K. Durose and G. J. Russell, *J. Cryst. Growth, 101* (1990) 246.
2 K. Zanio, in R. K. Willardson and A. L. Beer (eds.), *Semiconductors and Semimetals*, Vol. 13, *Cadmium Telluride*, Academic Press, New York, 1978, p. 62.
3 E. Y. Gutmanas and P. Haasen, *Phys. Status Solidi A, 63* (1981) 63.
4 K. Zanio, in R. K. Willardson and A. L. Beer (eds.), *Semiconductors and Semimetals*, Vol. 13, *Cadmium Telluride*, Academic Press, New York, 1978, p. 6.
5 K. Zanio, in R. K. Willardson and A. L. Beer (eds.), *Semiconductors and Semimetals*, Vol. 13, *Cadmium Telluride*, Academic Press, New York, 1978, p. 2.
6 K. Durose, G. J. Russell and J. Woods, *J. Cryst. Growth, 72* (1985) 85.
7 K. Durose and G. J. Russell, *J. Cryst. Growth, 86* (1988) 471.
8 K. Durose, G. J. Russell and J. Woods, *Inst. Phys. Conf. Ser., 76* (6) (1985) 233.
9 P. D. Brown, K. Durose, G. J. Russell and J. Woods, *J. Cryst. Growth, 101* (1989) 211.
10 C. C. R. Watson and K. Durose, Cathodoluminescence microscopy of CdTe, *J. Cryst. Growth*, in the press.
11 C. B. Slawson, *Am. Minerol., 35* (1950) 193.
12 K. F. Hulme and J. B. Mullin, *Solid State Electron., 5* (1962) 211.
13 M. Kawano, N. Oda and T. Sasuki *et al., J. Cryst. Growth, 117* (1992) 171.
14 S. Sivananthan, X. Chu, J. Reno and J. P. Faurie, *J. Appl. Phys., 60* (1986) 1359.
15 J. E. Hails, G. J. Russell, A. W. Brinkman and J. Woods, *J. Appl. Phys., 60* (1986) 2624; *J. Cryst. Growth, 79* (1986) 940.
P. D. Brown, J. E. Hails, G. J. Russell and J. Woods, *Appl. Phys. Lett., 50* (1987) 1144.
16 P. D. Brown, T. Golding and G. J. Russell *et al., Inst. Phys. Conf. Ser., 100* (4) (1989) 357.
17 P. Pirouz, F. Ernst and T. T. Cheng, *Mater. Res. Soc. Symp. Proc., 116* (1988) 57.
18 A. Tromson-Carli *et al., Mater. Sci. Eng., B16* (1993) 145–150.
19 A. M. Kier, A. Graham and S. J. Barnett *et al., J. Cryst. Growth., 101* (1990) 572.
20 A. M. Kier, S. J. Barnett and J. Geiss *et al., EMRS Meeting, 1990.*
21 A. Hobbs, personal communication, 1991.
22 A. F. Schwartzman and R. Sinclair, *J. Electron. Mater., 20* (10) (1992) 805.
23 For a full treatment see, for example, P. W. Atkins, *Physical Chemistry*, 1st edn., Oxford University Press, Oxford, 1978, p. 840.
24 A. Turnbull, *Ph.D. Thesis*, University of Durham, 1992.
25 A. Hobbs, O. Ueda, I. Sugiyama and H. Takigawa, *J. Cryst. Growth, 117* (1992) 475.
26 P. D. Brown, Y. Y. Loginov and P. A. Clifton *et al.*, Dislocations in MOVPE grown ZnTe, *J. Cryst. Growth*, in press.
27 J. E. Ayers, S. K. Ghandhi and L. J. Schowalter, *Mater. Res. Soc. Symp. Proc., 209* (1991) 661.
28 E. A. Fitzgerald and G. P. Watson *et al., J. Appl. Phys., 65* (1989) 2220.
29 P. A. Clifton and P. D. Brown, *Mater. Res. Soc. Symp. Proc., 216* (1991) 135.
30 A. Hobbs, O. Ueda, I. Sugiyama and K. Shinohara, *Inst. Phys. Conf. Ser., 117* (1991) 619.
31 P. D. Brown, H. Kelly and P. A. Clifton *et al., Mater. Res. Soc. Symp. Proc., 216* (1991) 427.
32 I. Sugiyama, A. Hobbs and T. Saito *et al., J. Cryst. Growth, 117* (1992) 161.

Materials Science and Engineering, B16 (1993) 103-107

RHEED studies of MBE growth mechanisms of CdTe and CdMnTe

A. Waag, Th. Behr, Th. Litz, B. Kuhn-Heinrich, D. Hommel and G. Landwehr
Physikalisches Institut der Universität Würzburg, Am Hubland, D-8700 Würzburg (Germany)

Abstract

We report on reflection high energy electron diffraction (RHEED) studies of molecular beam epitaxy (MBE) growth of CdTe and CdMnTe on (100) oriented CdTe substrates. RHEED oscillations were measured for both the growth and desorption of CdTe and CdMnTe as a function of flux and temperature. For the first time, the influence of laser and electron irradiation on the growth rate, as well as desorption, of CdTe is studied in detail using RHEED oscillations. We found a very small effect on the growth rate as well as on the CdTe desorption rate. The growth rate of CdTe was determined for different temperatures and CdTe flux ratios. The obtained experimental results are compared with a kinetic growth model to get information on the underlying growth processes, taking into account the influence of a precursor by including surface diffusion. From the comparison between model and experimental results the sticking coefficients of Cd and Te are determined. The growth rate of CdMnTe increases with Mn flux. This dependence can be used to calibrate the Mn content during growth by comparing the growth rate of CdTe with the growth rate of CdMnTe. The change in growth rate has been correlated with Mn content *via* photoluminescence measurements. In addition, the sticking coefficient of Mn is derived by comparing experimental results with a kinetic growth model. For high manganese content a transition to three-dimensional growth occurs.

1. Introduction

The growth of high quality CdTe and CdTe-based thin film structures by molecular beam epitaxy (MBE) has been demonstrated in the past [1]. One advantage of MBE is the low growth temperature used, far away from equilibrium growth conditions. Under such non-equilibrium conditions, the growth mechanisms can differ drastically from those present for equilibrium CdTe bulk growth, and therefore very different material characteristics can be expected. The mechanisms responsible for the compensation of extrinsic dopants—a problem that is present in all wide gap II–VI semiconductors—can be especially influenced by such non-equilibrium growth methods as MBE or MOCVD.

In addition, very sharp interfaces beween a barrier material and a well material can be grown by MBE, resulting in high quality quantum well structures. CdTe–CdMnTe [2, 3] and CdTe–CdZnTe [4] quantum well structures were grown in the past and their optical properties were investigated in detail. One very interesting feature of such quantum well structures is their high efficiency and very fast recombination time, which was found to be considerably shorter than in comparable GaAs–AlGaAs quantum wells [5].

Though the MBE technology has advanced quite far in the past, little is known about the underlying growth mechanisms.

Here we report on investigations of the growth mechanisms during the MBE growth of CdTe and CdMnTe by reflection high energy electron diffraction (RHEED) intensity oscillation measurements.

2. Experimental details

The epilayer growth was carried out in a four-chamber Riber 2300 MBE system. CdTe(100) substrates were used. The substrate preparation has been described in detail elsewhere [6]. The substrate temperature was measured with a thermocouple in contact with the back of the molybdenum block holding the sample and calibrated using the melting point of indium. For the growth of CdTe, a Cd, Te and a CdTe source was used.

The energy of the electron beam used for RHEED was varied between 8.5 keV and 10.5 keV, and an emission current between 0 μA and 200 μA was used. The RHEED pattern was monitored by a CCD camera and stored by a video recorder. On-line RHEED oscillations were measured by a photodiode coupled *via* an optical fiber to the monitor screen [7]. Growth oscillations of the RHEED intensity were usually monitored after a growth interruption of approximately 10 min. To measure RHEED oscillations during the desorption of CdTe, the RHEED intensity was monitored after a growth stop under UHV conditions.

0921-5107/93/$6.00

© 1993 - Elsevier Sequoia. All rights reserved

Throughout this work, the specular spot was used to measure RHEED intensities. Beam equivalent pressures (BEP) for the different molecular beams were measured with an ionization gauge at the substrate position. To obtain the absolute flux (particles cm^{-2} s^{-1}), such BEPs were calibrated through film thickness measurements by a step profiler. For this purpose, Cd, Te, Mn and CdTe films were grown on top of a partly masked CdTe-covered silicon wafer to produce a step on the substrate, while the substrate was held at 20 °C. At this temperature, the sticking coefficient of the impinging atoms and molecules is assumed to be unity. Flux calibrations carried out at different days were reproducible within a 10% error.

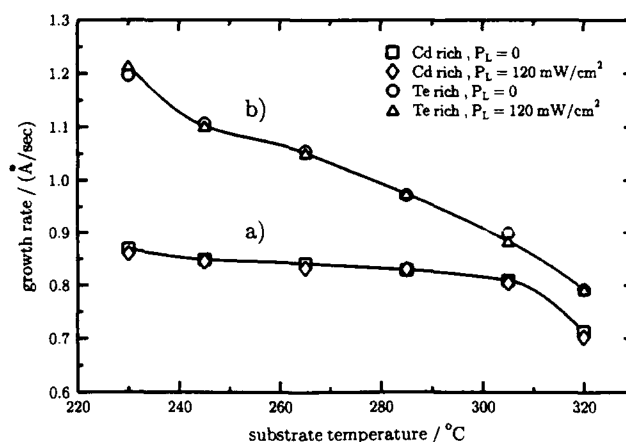

Fig. 1. Growth rate of CdTe as a function of substrate temperature for a Cd–Te ratio $F > 1$ (curve a) and $F < 1$ (curve b). For both curves, experimental points obtained with and without laser illumination are plotted. No change of the growth rate with laser intensity P_L could be detected.

3. Laser and electron irradiation

In the past, both static and dynamic (during MBE growth) RHEED reconstructions of (100)-CdTe surfaces were investigated by various groups [8–10]. It was shown that, under Cd-stabilized conditions, with a Cd–Te flux ratio F much larger than unity, the growing (100)-CdTe surface exhibits a $c(2 \times 2)$ reconstruction. If a single CdTe molecular source is used, producing a flux ratio $F = 1$, Te-stabilized (2×1) reconstruction usually occurs during growth. After a growth stop, this Te-stabilized (2×1) reconstruction changed to a $c(2 \times 2)$ reconstruction, and the corresponding transition times were measured by RHEED [10, 11] and assumed to result from Te desorption.

Recently, this was demonstrated experimentally by comparing surface coverages measured by X-ray photoelectron spectroscopy (XPS) and RHEED measurements [11]. In addition, both laser illumination and high energy electrons (from the RHEED gun itself) were shown to decrease the Te desorption times drastically [9, 12].

This electron and photon stimulated desorption, which was also found for MBE growth of other II–VI materials [13, 14], could possibly influence, and therefore falsify, growth rate and desorption measurements *via* RHEED. For ZnSe for example, it has already been demonstrated that the growth rate is reduced with laser irradiation [15]. Therefore we investigated in detail the influence of electron and photon irradiation on the growth rate as well as desorption of CdTe.

Figure 1 shows the growth rate of CdTe, as determined by RHEED oscillations, as a function of substrate temperature. Separate Cd and Te sources were used for this experiment. The growth rate with and without laser illumination was determined for both Cd and Te rich conditions. With increasing temperature, the growth rate decreases because of the higher desorption and a lower sticking coefficient of Cd and Te. For both Cd and Te rich conditions, experimental results are plotted in Fig. 1 for the illuminated and non-illuminated case. As is clearly seen, no change in the growth rate of CdTe can be detected with laser illumination.

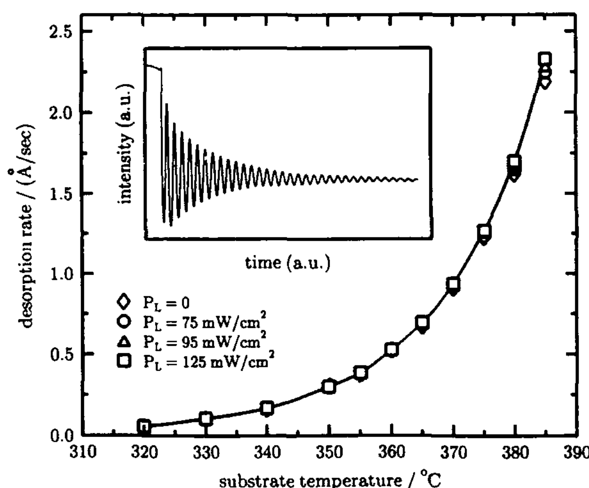

Fig. 2. Desorption rate as a function of temperature for different laser intensities. An example of RHEED desorption oscillations is given in the inset.

The desorption of CdTe was measured *via* RHEED oscillations after a growth stop. Neither Cd nor Te atoms were impinging onto the CdTe substrate surface in this case. Over 30 desorption oscillations could be monitored under good conditions (see inset in Fig. 2). The desorption rate increases exponentially with temperature. In Fig. 2 this desorption rate is plotted for four different laser intensities. Again, no change of the desorption with laser illumination can be detected.

To determine the influence of high energy electron irradiation on the desorption as well as on the growth rate of CdTe, both were measured in the same way as described above for different electron beam intensities. In Fig. 3 the desorption is plotted as a function of the reciprocal temperature for three different RHEED beam intensities. No change with the RHEED intensity can be seen. The same is true for different electron energies between 8.5 keV and 10.4 keV. From the slope of the desorption *vs.* $1/T$ the desorption energy of CdTe can be determined. For the CdTe desorption energy, we obtain 1.93 ± 0.05 eV, independent of electron or laser irradiation. In addition, no change in the growth rate can be detected for the three RHEED intensities studied. We also checked the growth rate without electron irradiation by switching off the electron beam for some time and then comparing the phase of RHEED oscillations before and after this RHEED interruption. Again no influence of the electron beam could be detected. From the experimental results described above, we can conclude that neither electron irradiation nor laser illumination (in the parameter range measured) can influence the growth rate or desorption of CdTe to an extent that could be interesting from a technological point of view. However, we have demonstrated that electron irradiation does not falsify the growth and desorption rates of CdTe obtained by RHEED oscillation measurements.

4. Kinetic model of CdTe MBE growth

To obtain more information on the CdTe growth mechanisms, we determined the growth rate as a function of the impinging Cd–Te flux ratio F and tried to simulate this dependence with a kinetic growth model, which will be described below.

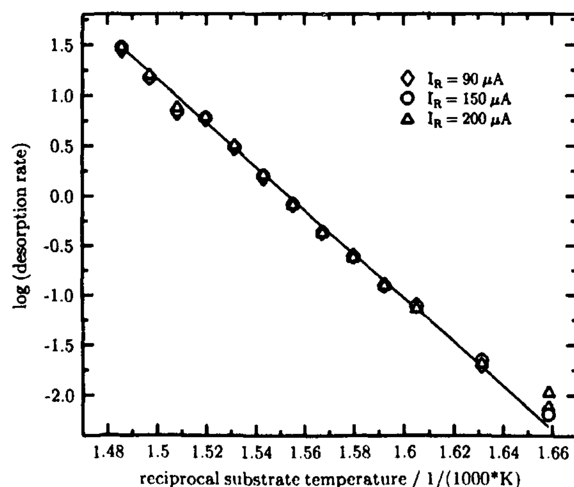

Fig. 3. Desorption as a function of temperature for different electron beam intensities on a semi-logarithmic scale. The slope gives a desorption energy of 1.93 ± 0.5 eV.

In general, the number of Cd and Te atoms chemisorbed in a time interval dt, dN_{Cd} and dN_{Te} respectively, will be given by eqn. (1):

$$dN_{Cd} = S_{Cd} F_{Cd}\, dt \qquad dN_{Te} = S_{Te} F_{Te}\, dt \tag{1}$$

where S_{Cd} and S_{Te} are the corresponding sticking coefficients, and F_{Cd} and F_{Te} are the fluxes of Cd and Te. After the growth start, the sticking coefficients, which usually depend on the surface coverage, will in general change with time until steady-state conditions have been reached after growth of a few monolayers.

In this way, the problem of MBE growth is reduced to two dimensions; no attempt was made to include details of the layer-by-layer growth during MBE. The details of chemisorption, physisorption, surface diffusion etc. are put into the sticking coefficients S_{Cd} and S_{Te} respectively, which can depend on temperature, free Cd and Te sites (surface coverage) and step density at the surface, as well as all other conditions influencing the physisorption and chemisorption of the involved molecules or atoms in general. In the following, we assume the step density and other relevant conditions are constant. Desorption from the chemisorbed state was neglected throughout because the temperatures used were too low for desorption to play an important role.

From the differential equations, eqn. (1) steady-state conditions can be calculated by setting $dN_{Cd} = dN_{Te}$. It is this steady-state growth rate ($dN_{Cd}/dt = dN_{Te}/dt =$ growth rate) which was then compared experimentally. The above assumption for the steady-state is only valid if neither Cd nor Te, but only the binary compound CdTe, can grow. At the temperatures studied, this is the case. The following model was found to describe the experimental results quantitatively.

In our model, we introduce a surface-coverage-dependent sticking coefficient and take into account the influence of a precursor state, in which atoms can be physisorbed. This latter was done by including a constant probability k for an atom to probe another surface site if it could not be chemisorbed at the site where it arrived first. The physical idea is that atoms can diffuse somewhat in the weakly-bound precursor state. Starting from this assumption one can calculate the total probability of an atom finding a free site somewhere. The details are given in refs. 16 and 17. The resulting term for the sticking coefficient is given in eqn. (2).

$$S_{Cd} = \frac{p_{Cd}(1 - B_{Cd})}{1 - k_{Cd} B_{Cd}} \qquad S_{Te} = \frac{p_{Te}(1 - B_{Te})}{1 - k_{Te} B_{Te}} \tag{2}$$

where p is the probability for the particle to be

desorbed from the physisorbed state, B is the surface coverage of Cd and Te, and k reflects the influence of the precursor.

With eqns. (1) and (2) and the relation $B_{Te} + B_{Cd} = 1$, B_{Te} and B_{Cd} can be eliminated and the growth rate calculated as a function of Cd and Te flux.

For $k = 0$, the particle cannot diffuse at all. For $k = 1$, the particle can diffuse until it finds an appropriate site where it can be chemisorbed.

Surface diffusion in the chemisorbed state, and desorption from the chemisorbed state, are neglected here. It should be mentioned that the four parameters (p_{Cd}, p_{Te}, k_{Cd}, k_{Te}) entering the model have to be compatible with a function of two independent parameters: growth rate as a function of Cd flux and Te flux, which is obtained experimentally.

Figures 4(a) and 4(b) compare experimental results from RHEED oscillation measurements with those obtained by applying the growth model described above (upper curve in Fig. 4). Growth rates were measured at a substrate temperature of 290 °C. The parameters used are given in the figure caption. The agreement between theory and experiment is very good. If surface diffusion is neglected ($k = 0$), such a good agreement between theory and experiment cannot be obtained (lower curve in Fig. 4), indicating that, under the assumptions made, the influence of a precursor state for both Cd and Te atoms plays a role during MBE growth of CdTe at 290 °C.

4.1. Growth of CdMnTe

To get a first insight into the growth mechanism of CdMnTe, we measured the growth rate of CdMnTe as a function of Mn flux *via* RHEED oscillations. In this case, a CdTe and a Mn source were used. From the Mn–CdTe flux ratio the Mn content of the CdMnTe layer was determined. This was done by using a calibration curve for the x values determined by photoluminescence measurements for different samples grown with varying Mn–CdTe flux ratio. RHEED oscillations could be observed up to a Mn–CdTe flux ratio of one. For such high Mn fluxes, a very rapid transition to three-dimensional growth could be observed.

The growth rate of CdMnTe increases with Mn flux. In Fig. 5(b) the Mn x value is plotted *vs.* the corresponding relative change of growth rate. A Mn flux corresponding to 10% in the CdMnTe films results in an increase in growth rate of around 4%. This clearly indicates that Mn is not only pushing Cd atoms away from the available II-sites, but increases the sticking coefficient of Te to a certain degree. It should be mentioned that in Fig. 5(b) experimental results are plotted for varying absolute CdTe fluxes. All points are lying on the same curve, which indicates that the x value depends only on the relative Mn–CdTe flux ratio.

The Mn x value is plotted as a function of the impinging Mn flux—this scale is calibrated to the growth rate of Te atoms—in Fig. 5(a). The slope of this curve gives the Mn sticking coefficient. In this way we obtain a sticking coefficient of 0.9 for Mn x values lower than 10%. For higher x values the Mn sticking coefficient is decreasing.

5. Summary

In summary, we have checked the influence of electron and laser irradiation on the growth rate as well as

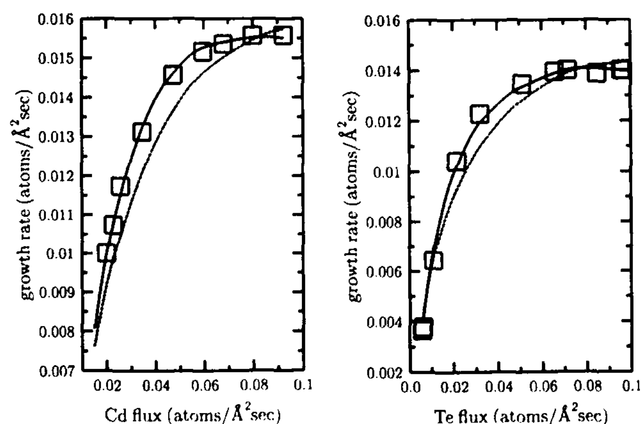

Fig. 4. Growth rate of CdTe (in Te atoms Å^{-2} s^{-1}) as a function of (a) Cd and (b) Te flux. Points: experimental; solid upper line: kinematic model including surface diffusion; lower line: neglecting surface diffusion. The parameters used for the model: (compare with eqn. (2)) $S_{Cd} = 0.65$; $k_{Cd} = 0.58$; $S_{Te} = 0.76$; $k_{Te} = 0.24$. (a) Constant Te flux = 0.025 atoms Å^{-2} s^{-1}; (b) constant Cd flux = 0.024 atoms Å^{-2} s^{-1}.

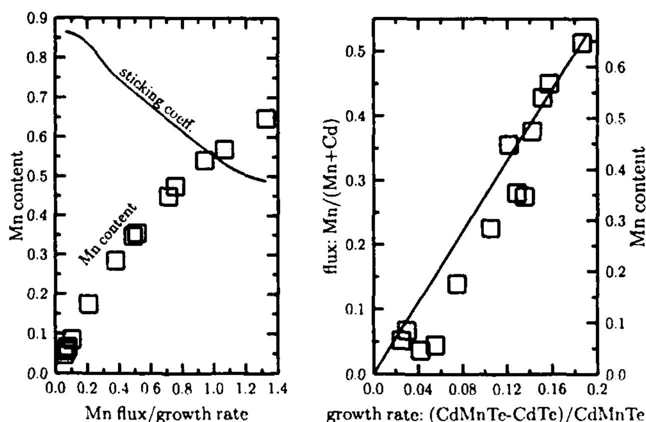

Fig. 5. (a) Experimental points show the Mn x value as a function of the ratio of impinging Mn flux to the growth rate of Te. The slope of this curve gives the Mn sticking coefficient, which is indicated in the figure by a solid line. (b) Mn content as a function of the relative change in growth rate of CdMnTe compared to CdTe.

desorption of MBE grown CdTe. These effects were, in general, found to be negligible for the range of standard growth parameters usually used for CdTe growth. The situation is different in the case of ZnSe, where the growth rate can be decreased by laser illumination.

In the second part of the study, a kinetic growth model was introduced that can quantitatively describe the experimental dependence of growth rates as a function of Cd–Te flux ratio. For this model the influence of a precursor state, in which surface diffusion is allowed, has to be taken into account.

In addition, the growth rate of CdMnTe as a function of Mn flux was measured. From this, the sticking coefficient of Mn can be derived. A value of 0.9 for the Mn sticking coefficient during the growth of CdMnTe with an x value less than 10% was estimated. For higher Mn x values, the sticking coefficient is decreasing. For high Mn flux (Mn–Cd flux ratio > 1) a rapid transition to a three-dimensional growth occurs.

Acknowledgments

The authors would like to thank Miss P. Wolf for assistance in sample preparation. This work was supported by the Bundesministerium für Forschung und Technologie, Bonn.

References

1 R. N. Bhargava, *J. Cryst. Growth*, *117* (1992) 894.
2 D. R. Yakovlev, W. Ossau, G. Landwehr, R. N. Bicknell-Tassius, A. Waag, S. Schmeusser, I. N. Uraltsev, A. Pohlmann and E. O. Göbel, *J. Cryst. Growth*, *117* (1992) 854.
3 G. R. Pozina, A. V. Kavokin, V. P. Kochereshko, I. N. Uraltsev, D. R. Yakovlev, G. Landwehr, R. N. Bicknell-Tassius and A. Waag, *Solid State Commun.*, *81* (1992) 639.
4 J. Cibert, R. Andre, C. Deshayes, Le Si Dang, H. Okumura, S. Tatarenko, G. Feuillet, P. H. Jonneau, R. Mallard and K. Saminadayar, *J. Cryst. Growth*, *117* (1992) 424.
5 R. Hellmann, A. Pohlmann, D. R. Yakovlev, A. Waag, R. N. Bicknell-Tassius and G. Landwehr, *Int. Conf. on the Physics of Semiconducting Compounds, Peking, 1992*, World Press, 1993.
6 R. N. Bicknell-Tassius, A. Waag, Y. S. Wu, T. A. Kuhn and W. Ossau, *J. Cryst. Growth*, *101* (1990) 33.
7 C. J. Sa and H. H. Wieder, *Rev. Sci. Instrum.*, *61* (1990) 917.
8 J. D. Benson, B. K. Wagner, A. Torabi and C. J. Summers, *Appl. Phys. Lett.*, *49* (1986) 1034.
9 Y. S. Wu, C. R. Becker, A. Waag, R. N. Bicknell-Tassius and G. Landwehr, *J. Appl. Phys.*, *69* (1991) 268.
10 Y. S. Wu, A. Waag and R. N. Bicknell-Tassius, *Appl. Phys. Lett.*, 57 (1990) 1754.
11 Y. S. Wu, C. R. Becker, A. Waag, M. M. Kraus, R. N. Bicknell-Tassius and G. Landwehr, *Phys. Rev. B 44* (1991) 8904.
12 J. D. Benson and C. J. Summers, *J. Cryst. Growth*, *86* (1988) 354.
13 H. H. Farrell, J. L. de Miguel and M. C. Tomargo, *J. Appl. Phys.*, *65* (1989) 4084.
14 N. Matsumura, K. Senga, J. Kakuta and J. Saraie, *J. Cryst. Growth*, *117* (1992) 129.
15 J. Simpson, S. J. A. Adams, S. Y. Wang, J. M. Wallace, K. A. Prior and B. C. Cavenett, *J. Cryst. Growth*, *117* (1992) 134.
16 P. Kisliuk, *J. Phys. Chem. Solids*, *3* (1957) 95.
17 P. Kisliuk, *J. Phys. Chem. Solids*, *5* (1958) 95.

Properties of dry-etched CdTe–epitaxial layer surfaces and microstructures

M. Neswal, K. H. Greßlehner and K. Lischka
Forschungsinstitut für Optoelektronik, Universität Linz, Altenberegerstrasse 69, A-4040 Linz (Austria)
P. Bauer and A. Brandstötter
Institut für Experimentralphysik, Universität Linz, A-4040 Linz (Austria)
K. Lübke
Institut für Mikroelektronik, Universität Linz, A-4040 Linz (Austria)

Abstract

In this paper we report the dry etching of epitaxially grown CdTe layers on GaAs using a CH_4–H_2 gas mixture in a barrel reactor. We obtain the etch rate as a function of gas composition and total flow rate for (100)- and (111)-oriented CdTe epitaxial layers (epilayers). We find clear evidence for both isotropic and preferential etching along crystallographic planes depending on the set of etch parameters used. We demonstrate that this effect can be used for the preparation of structures with submicrometre dimensions using conventional lithography with micrometre resolution. The surface of the etched epilayers was analysed by Auger electron spectroscopy. Special attention was paid to the surface composition as a function of the CH_4-to-H_2 gas ratio. We obtained a set of etch parameters for stoichiometric etching.

1. Introduction

In the late 1980s and at the beginning of the 1990s, II–VI semiconductors gained importance as materials for the production of optoelectronic devices [1–3]. This interest initiated the application of various dry-etching processes to II–VI compound semiconductors. Approaches which have been used so far are ion beam milling [4], laser-assisted photochemical etching [5], BCl_3 etching [6], dry etching using a secondary after-glow reactor [7], dry etching using an H_2 plasma [8], and dry etching using a CH_4–H_2 plasma [9].

In this paper we report the dry etching of CdTe epitaxial layers (epilayers) using a CH_4–H_2 plasma in a barrel reactor. The etching process was developed for (100)- and (111)-oriented CdTe epilayers. CdTe is well known as a substrate material for $Hg_{1-x}Cd_xTe$ epitaxy. The effects of various process parameters on the etch rate were studied and the conditions for sample preparation and etching were investigated and optimized. Special interest was paid to the surface stoichiometry. The surface composition was investigated using Auger electron spectroscopy (AES).

We find clear evidence for both isotropic and preferential etching along crystallographic planes, depending on the set of etch parameters used. We demonstrate that this effect can be used for the preparation of structures with submicrometre dimensions using conventional lithography with micrometre resolution.

2. Experimental set-up

All our experiments were performed in a Technics Plasma PP 300/M barrel reactor. An aluminium Faraday cup is used to confine the plasma glow region and to shield the samples from impacting ions. The gases are introduced through the door of the reactor and pumped out at the rear side of the chamber. Methane and hydrogen are used as support gases. An r.f. frequency of 2.45 GHz is applied externally at two electrodes using a matching network. A rotary vane pump with a pumping speed of 35 m^3 h^{-1} maintains a base pressure of about 2 mTorr in the chamber. The samples are mounted on a glass substrate holder and are placed inside the Faraday cup. The typical steady state temperature inside the reactor was about 85 °C at an r.f. power of 300 W. All the samples were grown by hot-wall beam epitaxy [1] on GaAs. Both (100)- and (111)-oriented CdTe epilayers grown on (100)- and (111)-oriented GaAs with a 2° misorientation towards the next (110) direction were used. A typical layer

0921-5107/93/$6.00
© 1993 – Elsevier Sequoia. All rights reserved

thickness was about 15–25 μm. The samples were cut along the (110) cleavage planes with a sample size of 4 mm × 4 mm and patterned with an AZ 1518 photoresist mask.

Etch depth measurements were performed with a Rodenstock RM 600 laser stylus profilometer. Scanning electron micrographs were used for inspection of the etched structures and provided visual assessment of anisotropy and horizontal surface smoothness. A Perkin-Elmer PHI 15-255 GAR double-pass cylindrical mirror analyser was used to measure the integral Auger electron spectra, providing information on the elemental composition of samples in the near-surface region.

3. Results and discussion

3.1. Effects of process parameters on the etch rate

The etch depth in (100)- and (111)-oriented CdTe was measured as a function of the total flow rate and the methane fraction r of the CH_4–H_2 gas mixture, where r is equal to the total ratio of methane flow over the total gas flow. In Fig. 1 the etch depth in (100)- and (111)-oriented CdTe is plotted as a function of total gas flow. The r.f. power was 300 W, the etch time 40 min and the gas composition $r = 0.1$. The etch depth for (100)-oriented samples increases from zero to yield a maximum at about 3.2 μm at a total flow of 22 standard cm^3 min^{-1}. As the gas flow increases further, the etch depth decreases to 0.4 μm at a total flow of 200 standard cm^3 min^{-1}. The increase between 10 and 30 standard cm^3 min^{-1} is most probably due to the increasing density of methane and thus methyl radicals in the reactor. The decrease of the etch depth may be attributed to (a) the decreasing mean free path of radicals [7] and/or (b) a change in reaction kinetics [10]. Between 55 and 65 standard cm^3 min^{-1} a local maximum appears. The double-maximum structure of the etch depth vs. total gas flow curve may be due to the simultaneous action of two different etch processes which exhibit a maximum etch depth at different values of the gas flow. We assume that one affects only (100) planes and one is isotropic. The etch depth for the (111) orientation exhibits only one maximum at a total flow of about 65 standard cm^3 min^{-1}. At a total flow below 50 standard cm^3 min^{-1} the etch depth in (111)-oriented CdTe is significantly smaller than that in (100)-oriented CdTe, indicating the effectiveness of the processes. When the total flow rate exceeds 50 standard cm^3 min^{-1}, no difference between CdTe(100) and CdTe(111) is observed, indicating an isotropic etch process. These results indicate preferential etching along crystallographic planes when $Q_{tot} < 50$ standard cm^3 min^{-1}. It should also be noted that the point where the difference disappears coincides with the second local maximum in the curve for (100) orientation. Further details of microstructures which were produced using the crystallographic etching processes will be given in the Section 3.3.

The dependence of etch depth vs. gas composition was measured using $Q_{tot} = 33$ standard cm^3 min^{-1}, $p = 64$ mTorr, $P = 300$ W and $t = 40$ min and is shown in Fig. 2. The etch depth is found to increase rapidly from a non-zero value, to reach a maximum and to decrease at methane levels above about 10%. The general trend in Fig. 2 is similar to that observed with III–V compound semiconductors [11] and $Hg_{1-x}Cd_xTe$ [8]. Using pure hydrogen the samples exhibit porous surfaces. This is most probably due to preferential etching of tellurium which leads to a cadmium drop-like surface. However, at $r = 0.02$ no effect of surface roughening was observed. Using pure methane,

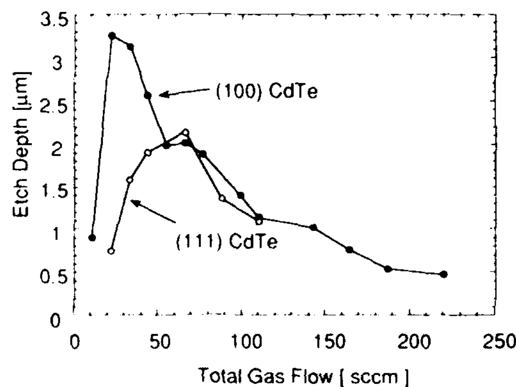

Fig. 1. The etch depth in (100)- and (111)-oriented CdTe as a function of the total gas flow. The etch parameters are $r = 0.09$, $P = 300$ W and an etch time t of 40 min.

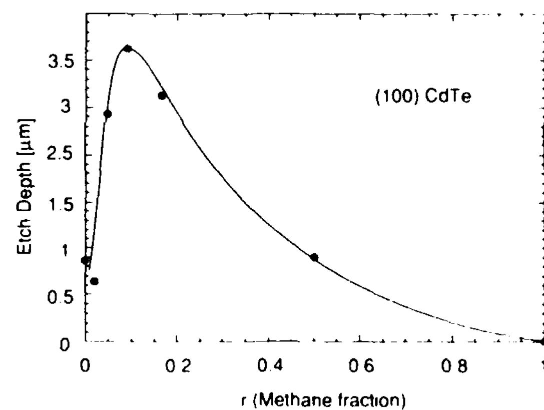

Fig. 2. The etch depth in a (100)-oriented CdTe epilayer as a function of the methane fraction r, which is the ratio of the methane flow to the total gas flow ($Q_{tot} = 33$ standard cm^3 min^{-1}; $p = 64$ mTorr; $P = 300$ W, $t = 40$ min).

the samples are covered with a polymer overlayer that can easily be removed using an oxygen plasma.

3.2. Properties of dry-etched surfaces

We have used AES to measure the elemental composition in the near-surface region [12]. In order to obtain quantitative results it is necessary to determine the concentration of cadmium and tellurium by an absolute method such as Rutherford backscattering spectroscopy (RBS). This allows one to quantify the AES measurements for samples of similar compositions. RBS was measured using a beam of 4.2 MeV ^{4}He ions. From the yields of the ions backscattered by cadmium and by tellurium respectively, the composition of the near-surface region of the sample was determined using standard procedures [13]. Thus, for the sample measured, the composition in the near-surface region was found to be $Cd_{0.472}Te_{0.528}$ with a relative uncertainty of $\pm 2\%$. This deviation from stoichiometry may be attributed to possible outdiffusion and evaporation of cadmium from the CdTe surface region that takes place after the termination of the growth process while the sample is still kept at elevated temperatures. This process has been reported to yield a cadmium deficit of 2–5 at.% by Juza *et al.* [14].

For the AES measurements, 3 keV electrons were used for primary ionization and a double-pass cylindrical mirror analyser was used to measure the integral Auger electron spectra. The Cd MNN transition at 376 eV and the Te MNN transition at 483 eV were used for the quantitative analysis of the spectra. All other elements were considered only in terms of a qualitative analysis but not for quantitative measurements.

Prior to the measurements a beam of 2 keV Ar^+ was used to clean the surface. This process is known to leave the composition of the surface unchanged [15]. In fact, we observed no change in the AES spectra, once the surface impurities were removed.

Figure 3(a) shows a numerically differentiated Auger spectrum of an as grown sample. Taking the peak-to-peak heights as a measure of the line intensities an intensity ratio I_{Te}/I_{Cd} of 0.733 is obtained for the cleaned sample. From the concentrations of cadmium and tellurium determined by RBS the ratio of the relative AES sensitivities is found to be $S_{Cd}/S_{Te} = 1.53$. Using these sensitivity factors we are able to obtain a quantitative concentration for any CdTe surface as long as the material composition is close to stoichiometry. The cadmium concentration c_{Cd} can be found using

$$c_{Cd} = \frac{1}{1 + (I_{Te}/I_{Cd})(S_{Cd}/S_{Te})} \quad (1)$$

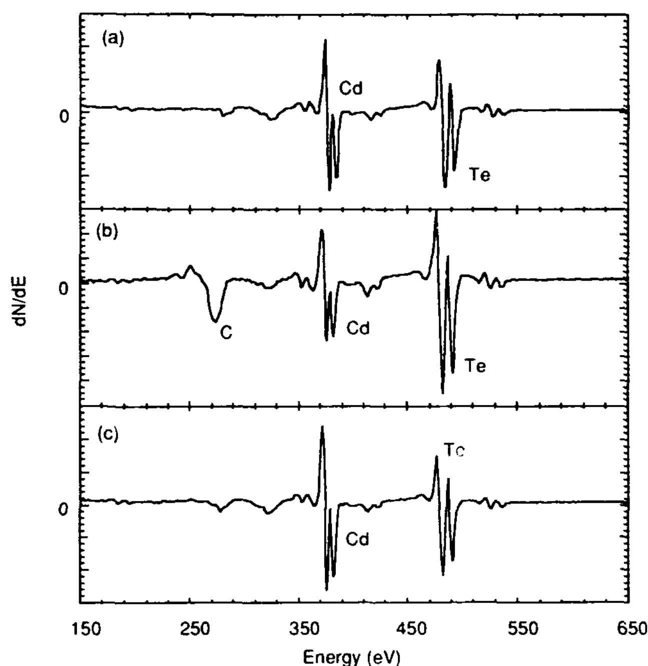

Fig. 3. Numerically differentiated Auger spectra of CdTe samples following different surface treatments: (a) as-grown sample; (b) wet etching using Br_2-methanol; (c) dry etching using $Q_{tot} = 33$ standard cm^3 min^{-1}, $r = 0.09$, $P = 300$ W and an etch time of 40 min.

where I_{Cd} and I_{Te} are the intensities of the Cd MNN and Te MNN Auger transitions respectively.

Figure 3(b) shows the Auger spectrum of CdTe which was etched for 5 s using Br_2–methanol. This process is frequently used for CdTe and $Hg_{1-x}Cd_xTe$ and is known to yield a tellurium-rich surface [16]. The Auger spectra show excess tellurium and carbon contamination. Figure 3(c) shows the Auger spectrum of a dry-etched sample using $Q_{tot} = 33$ standard cm^3 min^{-1}, $P = 300$ W, $t = 40$ min and $r = 0.09$. The surface composition is almost stoichiometric. Using eqn. (1) and the ratio of the numerically differentiated Auger peak-to-peak signal Cd MNN/Te MNN we obtain $Cd_{0.46}Te_{0.54}$.

Figure 4 shows the surface concentration of cadmium as a function of the gas composition used for dry etching. This plot reveals the optimum conditions for stoichiometric etching to be at $r = 0.05$. Nevertheless an experimental error of about 10% should be taken into account. Notwithstanding any quantitative arguments, Fig. 4 indicates that it is possible to control the surface composition in a wide range and even to restore stoichiometric composition.

3.3. Dry-etched microstructures

We produced microstructures in CdTe using electron beam lithography and dry etching. Figure 5(a)

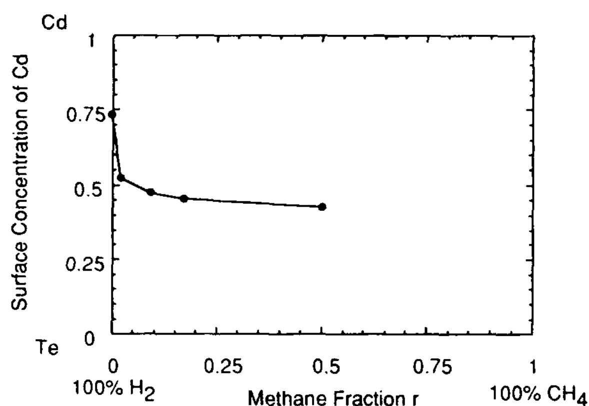

Fig. 4. Surface composition of CdTe as a function of the gas composition used for dry etching.

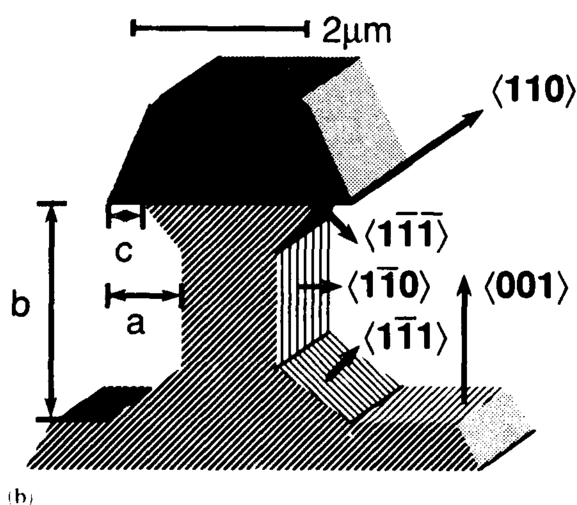

Fig. 5. (a) Scanning electron micrograph of an etched structure in a (001)-oriented CdTe epilayer ($r=0.17$; $Q_{tot}=33$ standard cm^3 min^{-1}; $p=64$ mTorr; $P=300$ W, $t=40$ min) with photoresist stripes 3 μm wide parallel to the (110) direction. (b) Schematic diagram of the structure with crystallographic orientations and lateral dimensions ($a=0.86$ μm; $b=2.90$ μm; $c=0.85$ μm) as indicated.

shows a scanning electron micrograph of an etched structure in a CdTe (001) epilayer. Hereafter, { }, ( ), [ ] and ⟨ ⟩ will refer to families of planes, specific planes, families of crystallographic directions, and specific directions respectively. The structure was etched using $r=0.17$, $Q_{tot}=33$ standard cm^3 min^{-1}, $p=64$ mTorr, $P=300$ W and $t=40$ min. The epilayer was patterned with photoresist stripes 3 μm wide. The photoresist mask was not removed after etching and can be seen in Fig. 5(a) on top of the etched structure. The sample was cleaved along one {110} cleavage plane in order to reveal the lateral dimensions of the feature. Figure 5(b) shows a schematic diagram of the same sample with the crystallographic directions indicated.

The scanning electron micrograph in Fig. 5(a) shows that the mask is undercut by the etch process, and from this figure the anisotropy of the etch rate can be obtained. The etch depths in different directions are $a=0.86$ μm, $b=2.90$ μm and $c=0.85$ μm. With these values we obtain an anisotropy factor of $A=1-a/b=0.66$, where a and b are the horizontal and vertical etch depths respectively. The vertical planes of the etched structure in Fig. 5 are {110} crystal planes, the planes which are inclined by about 54° to the epilayer surface are {111} planes. These planes appear during the etch process owing to different etch rates for crystal planes with different orientations.

The preferential etching along crystallographic planes was used for the production of submicrometre structures using lithography with micrometre resolution as shown in Fig. 6. The structure in Fig. 6 was produced using a photoresist mask 2 μm wide, $r=0.17$, $Q_{tot}=33$ standard cm^3 min^{-1}, $t=40$ min and $P=300$ W. A structure width of 270 nm is obtained.

4. Summary and conclusions

We have applied a dry-etch process using a barrel reactor with CH_4–H_2 feedstock gases to etch (100)- and (111)-oriented CdTe. The etch rate in CdTe(100) was measured as a function of total flow rate and gas composition. A maximum of 800 Å min^{-1} is observed for a total flow of 33 standard cm^3 min^{-1} and a methane concentration of 9%. At a total gas flow above 50 standard cm^3 min^{-1} we found no difference between the etch rates of (100)- and (111)-oriented CdTe epilayers. However, below 50 standard cm^3 min^{-1} a significant dependence of the etch rate on the crystallographic direction was measured. The etch rate in (100)-oriented CdTe exceeds that in (111)-oriented CdTe by a factor of up to 3. This is considered as one of the first observations of crystallographic effects in II–VI semiconductors. We have demonstrated that this effect can be used for the preparation of structures with

Fig. 6. Scanning electron micrograph of a dry-etched structure in (001)-oriented CdTe with a structure width of 270 nm.

submicrometre dimensions using conventional lithography with micrometre resolution. The effects of sample preparation and gas composition on the surface stoichiometry were studied using AES. It is shown that dry etching allows one to control the surface composition and even to restore a stoichiometry composition.

Acknowledgments

This work was supported by the Jubiläumsfond der Österreichischen Nationalbank and by Fonds zur Forderung der wiss. Forschung. We thank J. Humenberger for the preparation of the samples.

References

1 J. Humenberger, H. Sitter, K. Lischka, A. Pesek and H. Pascher, in E. M. Anastassakis and J. D. Joannopoulos (eds.), *Proc. 20th Int. Conf. on the Physics of Semiconductors, Thessaloniki, 1990*, World Scientific, Singapore, 1990, p. 981.
2 M. A. Haase, J. Qui, J. M. DePuydt and H. Cheng, *Appl. Phys. Lett.*, *59*(1991) 1272.
3 H. Jeon, J. Ding, W. Patterson, A. V. Nurmikko, W. Xie, D. C. Grillo, M. Kobayashi and R. L. Gunshor, *Appl. Phys. Lett.*, *59*(1991) 3691.
4 G. Bahir and E. Finkman, *J. Vac. Sci. Technol. A*, 7 (1989) 384.
5 M. Rothschild, C. Arnone and D. J. Ehrlich, *J. Mater. Res.*, *2* (1987) 244.
6 E. M. Clausen, Jr., H. G. Craighead, L. M. Schiavone, M. C. Tamargo and J. L. deMiguel, *J. Vac. Sci. Technol. B*, *6* (6) (1988) 1899.
7 J. E. Spencer, J. H. Dinan, P. R. Boyd, H. Wilson and S. E. Buttril, *J. Vac. Sci. Technol. A*, 7(3)(1989) 676.
8 L. Svob, J. Chevallier, P. Ossart and A. Mircea, *J. Mater. Sci. Lett.*, *5*(1986) 1319.
9 A. Semu, L. Montelius, P. Leech, D. Jamieson and P. Silverberg, *Appl. Phys. Lett.*, *59*(14)(1991) 1752.
10 K. Tachibana, M. Nishida, H. Harima and Y. Urano, *J. Phys. D*, *17*(1989) 1727.
11 T. R. Hayes, M. A. Dreisbach, P. M. Thomas, W. C. Dautremont-Smith and L. A. Heimbrook, *J. Vac. Sci. Technol. B*, *5* (1989) 1130.
12 P. Bauer, O. Benka, A. Brandstötter, M. Geretschläger and E. Steinbauer, in M. Alnot, J. J. Ehrhardt, C. Launoi, B. Mutaftschiev and M. R. Tempère, *Book of Abstracts, Symp. on Surface Science, La Plagne, 1992*, p. 159.
13 W. Doolittle, *Nucl. Instrum. Methods B*, *9*(1985) 344.
14 P. Juza, W. Faschinger, K. Hingerl and H. Sitter, *Semicond. Sci. Technol.*, *5*(1990) 191.
15 U. Solzbach and H. R. Richter, *Surf. Sci.*, 97(1980) 191.
16 R. Tenne, R. Brener and R. Triboulet, *J. Vac. Sci. Technol. A*, 7(4)(1989) 2570.

Qualification of a new defect revealing etch for CdTe using cathodoluminescence microscopy

C. C. R. Watson and K. Durose
Department of Physics, University of Durham, Durham (UK)

A. J. Banister
Department of Chemistry, University of Durham, Durham (UK)

E. O'Keefe and S. K. Bains
Philips Infra-red Defence Components, Southampton (UK)

Abstract

The action of a new defect revealing etch comprising a saturated $FeCl_3$ solution has been investigated. The etch was found suitable for use on (111)A, $(\bar{1}\bar{1}\bar{1})$B and other surface orientations of CdTe, and (111)A and $(\bar{1}\bar{1}\bar{1})$B surfaces of $Cd_{0.96}Zn_{0.04}Te$. Direct correlations with cathodoluminescence and infra-red microscopy have shown the etch to successfully reveal twin boundaries, precipitates and dislocations. A background etch rate of approximately 2 μm min^{-1} has been measured.

1. Introduction

Bulk single crystals of CdTe and (Cd,Zn)Te are well known as substrates for the epitaxial growth of (Cd,Hg)Te. However, they contain a high density of as-grown structural defects and therefore quick and reliable techniques for defect assessment are desirable. Chemical etchants such as Nakagawa's (HF, H_2O_2, H_2O) [1], Inoue's ($AgNO_3$, HNO_3, $K_2Cr_2O_7$, H_2O) [2], Rockwell (HNO_3, HCl, $K_2Cr_2O_7$) [3], Schenk's (HF, CrO_3, HNO_3) [4] and 1/2% bromine and methanol under illumination [5] are in common use. Some of these tend to be unreliable and selective of the crystal faces on which they work. It is of special importance that defects on the $(\bar{1}\bar{1}\bar{1})$B face are revealed, for this is the technologically important growth surface.

Scanning electron microscopy (SEM)/cathodoluminescence microscopy (CL) provides a rapid, contactless and non-destructive technique for defect observation. It provides the capability of depth profiling (on varying the primary beam energy) and also, by temperature dependent CL contrast measurements, the discrimination of qualitatively similar defects [6].

The aim of this paper is to report the action of a saturated $FeCl_3$ solution as a new defect revealing etchant for CdTe and (Cd,Zn)Te. Furthermore by correlating etch features observed using optical microscopes with images obtained by CL and infra-red (IR) microscopy, the success of the etch in revealing and distinguishing between as-grown defects is assessed.

2. Experimental

The etch was prepared by dissolving 35 g of Analar $FeCl_3(H_2O)_6$ in 10 ml of demineralized water to produce a saturated solution. Prior to etching all samples were chemically polished in a 2% bromine in ethylene glycol solution and washed thoroughly in clean methanol. When successive etch steps were used the etching reaction was quenched and the samples cleaned in distilled water.

Excepting a small amount of work involving polycrystalline vapour grown CdTe [7] grown in Durham, all the CdTe and (Cd,Zn)Te samples were Bridgman grown material provided by Philips Infra-red Defence Components of Southampton.

The SEM/CL studies were performed using a Cambridge S180 scanning electron micrograph fitted, with an Oxford Instruments CL302/1 light collector, a Hammamatsu S1 response photomultiplier tube and an Oxford Instruments CF301 cold stage. A "hovcr-probe" was used for specimen thickness measurements, etch features were profiled by use of an α-step 200 stylus profilometer and Nomarski optical, and transmission infra-red, microscopy was also utilized.

0921-5107/93/$6.00 © 1993 – Elsevier Sequoia. All rights reserved

3. Results and discussion

The CdTe crystal orientations examined were the (111)A, $(\bar{1}\bar{1}\bar{1})$B, {511}, {5 7 13} faces and a random polycrystalline boule, all of which developed pits when etched with a $FeCl_3$ solution. The background etch rate was measured, using a hoverprobe, for the (111)A and $(\bar{1}\bar{1}\bar{1})$B faces and found to be linear with time and have a rate of approximately 2 μm min^{-1}.

The chemistry of the dissolution process is thought to proceed as follows. $FeCl_3$ is hydrolysed in aqueous solution and the species below are in equilibrium (all with coordinated water and/or chloride ion) [8]:

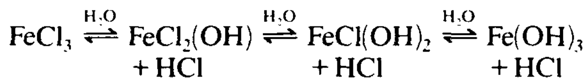

$$FeCl_3 \overset{H_2O}{\rightleftharpoons} FeCl_2(OH) + HCl \overset{H_2O}{\rightleftharpoons} FeCl(OH)_2 + HCl \overset{H_2O}{\rightleftharpoons} Fe(OH)_3 + HCl$$

$2Fe(OH)_3 \equiv Fe_2O_3 + 3H_2O$, the latter being rust.

$FeCl_3$ thus forms a brown acidic "solution" (a colloidal dispersion of $Fe_2O_3 \cdot xH_2O$). The etching of CdTe then proceeds by dissolution of Cd^{+2} as $CdCl_2$ and (with the aid of atmospheric oxygen and in the presence of HCl^{aq}) the oxidation of Te^{-2} to Te^{+4} as $TeCl_4$. In HCl^{aq} $TeCl_4$ is complexed as $TeCl_5H_2O^-$ and $TeCl_6^{2-}$ and these species are in equilibrium with their hydrolysis products, *e.g.*

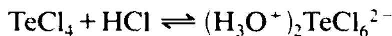

$$TeCl_4 + HCl \rightleftharpoons (H_3O^+)_2TeCl_6^{2-}$$

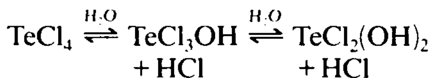

$$TeCl_4 \overset{H_2O}{\rightleftharpoons} TeCl_3OH + HCl \overset{H_2O}{\rightleftharpoons} TeCl_2(OH)_2 + HCl$$

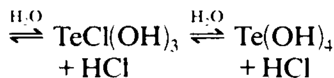

$$\overset{H_2O}{\rightleftharpoons} TeCl(OH)_3 + HCl \overset{H_2O}{\rightleftharpoons} Te(OH)_4 + HCl$$

In the event that the surface of the crystal is oxidized prior to etching or else by dissolved oxygen the stable oxide will be TeO_2. This is soluble in acidic solution:

$$TeO_2 \overset{H_2O}{\rightleftharpoons} TeCl_4 + 2H_2O$$

As HCl is consumed during the reaction Fe_2O_3 is plated out onto the crystal surface giving the characteristic features shown in Fig. 1.

Twin boundaries clearly defined by $FeCl_3$ solutions, were seen to be decorated by circular pits approximately 2 μm in size on etching. A direct 1:1 correlation was observed between these pits and precipitates intersecting the surface as seen by IR microscopy at the same point. These etch pits therefore undoubtedly indicate the presence of precipitates associated with the boundaries. Likewise a correlation was observed between similar pits and areas of very dark CL contrast. Figure 2(a) shows a CL image of a twinned region, on the $(\bar{1}\bar{1}\bar{1})$B surface, and Fig. 2(b) is an SEM image of the same area after etching. It can be seen that the strongest CL contrast corresponds to segments of the twin decorated by precipitates, assumed to be small Te inclusions [9]. Semi-metal elemental Te has an infinite surface recombination velocity producing an efficient quenching, at all specimen temperatures, of the luminescence, hence precipitates are revealed by a CL contrast darker than that associated with other defects such as dislocations. Surface profiles across twin bands on {111} faces indicated a higher etch rate on {511} (twin) than on {111}A and B faces (matrix).

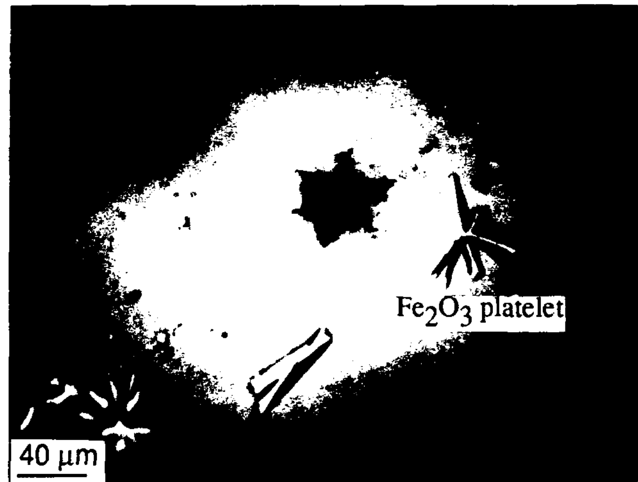

Fig. 1. IR microscope image of a large Te inclusion and platelets of rust.

Larger Te inclusions approximately 40 μm in size identified by IR microscopy as shown in Fig. 1, were also revealed by CL and etching as shown in Figs. 3(a) and 3(b) respectively. All of the micrographs show arms of contrast radiating from the central feature every 60°. The CL and optical micrographs show longer arms than the IR micrographs and are made up of individual etch pits. These features can be explained using a dislocation "punch out" mechanism for stress relief at a stress concentrator (see Hull, for example [10]). The thermal expansion coefficients of CdTe and Cd are 4.5×10^{-6} K^{-1} and 31.8×10^{-6} K^{-1} respectively so rapid cooling from approximately 594 K (Cd freezing point) to room temperature can generate a significant tensile stress on the lattice which is relieved by dislocations on {111} slip planes. These intersect the {111} surface at 60° intervals giving the characteristic rosettes shown here. The observation that the IR micrograph shows contrast at the rosette arms indicates that the dislocations closest to the inclusion have been decorated by Cd, however weaker CL contrast at the outer reaches of the arms indicates that the dislocations furthest from the inclusion are undecorated and that the pits revealed by the etchant are due to dislocations only.

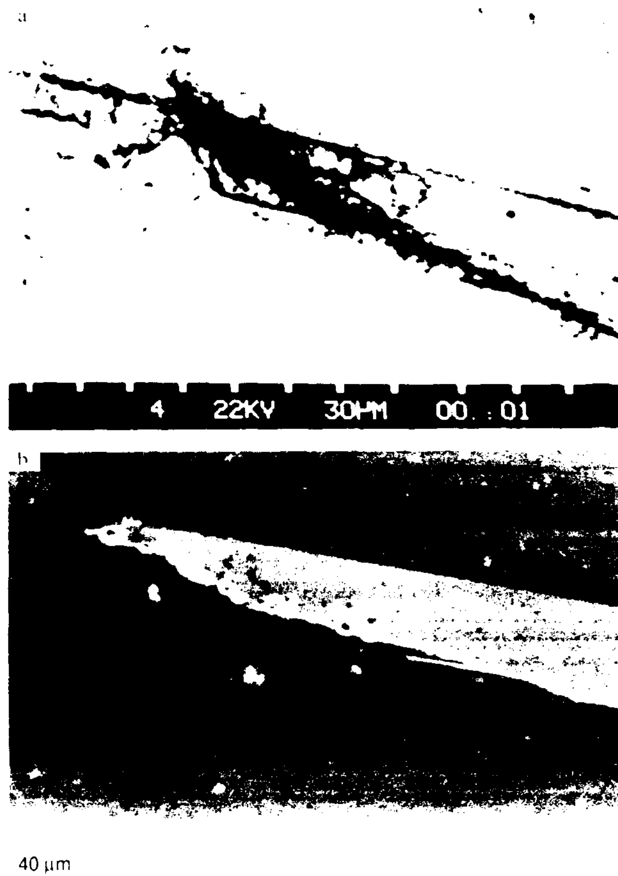

Fig. 2. Twin boundary decorated by precipitates as seen by: (a) CL; (b) SEM, after etching in $FeCl_3$.

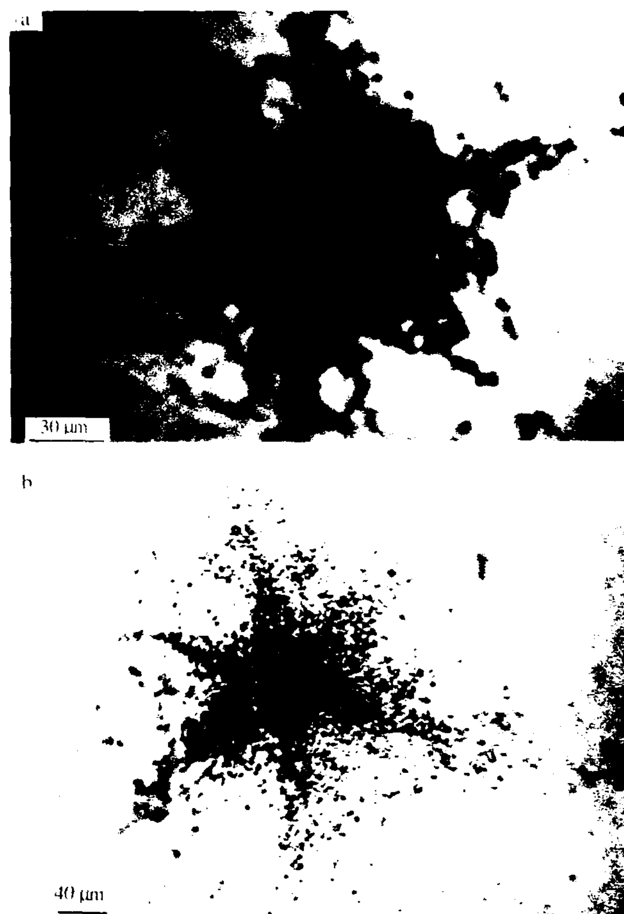

Fig. 3. Large Te inclusions as seen by: (a) CL; (b) optical microscopy, after etching in $FeCl_3$.

Small inclusions approximately 1–2 μm in size were revealed by the etch as circular pits after etch times of approximately 2 min. On continued etching these pits were seen to grow in size before becoming indistinct. A similar sequence was observed at precipitates in (Cd,Zn)Te samples and Fig. 4 shows such an example. The $FeCl_3$ etch thus has the ability of profiling through defects leaving a shadow of the original feature. This depth profiling action of the etch is expected to make it of value in obtaining estimates of the volume densities of defects.

Networks of circular pits consistent with the presence of sub-grain boundaries were observed on all surfaces examined. Figure 5 shows a typical network on the (111)A face of a Bridgman specimen with an average pit density of approximately 10^4–10^5 cm^{-2}. Experiments on identical sample areas has shown CL (Fig. 6(a)) to reveal a higher number of features than that disclosed by etching (Fig. 6(b)), this being due to the penetration of the electron beam. Therefore correlation of all dark spots with etch pits is not expected, however at A, in Figs. 6(a) and 6(b) a correlation between individual etch pits and CL spots is observed.

Fig. 4. Profiling of a precipitate in (Cd,Zn)Te.

$FeCl_3$ etching was seen to produce a higher resolution than the CL technique, for example in the dense cluster of etch pits seen in Fig. 6(b) individual features are resolved but no individual dark CL spots are visible in

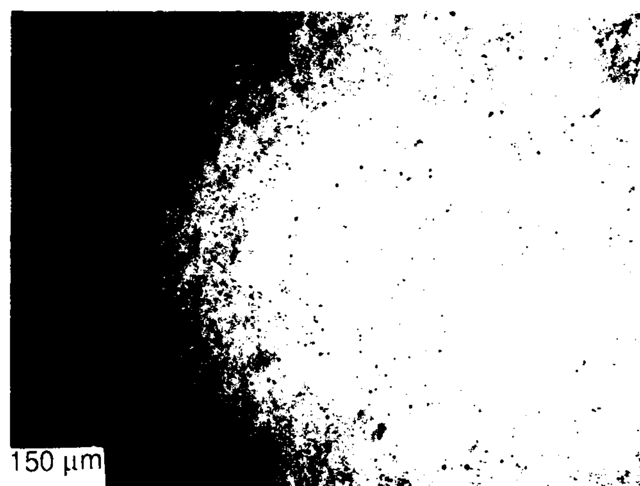

Fig. 5. Sub-grain boundaries in (111)A CdTe as revealed by $FeCl_3$ etching.

Fig. 6. Dislocations in CdTe as seen by: (a) CL; (b) optical microscopy, after etching in $FeCl_3$.

the corresponding area of Fig. 6(a). Correlation of the pits developed by $FeCl_3$ solutions with those revealed by Nakagawa's etch [1] has not been attempted.

The (111)A and $(\bar{1}\bar{1}\bar{1})$B faces of $Cd_{0.96}Zn_{0.04}Te$ were also etched in $FeCl_3$. As for CdTe pits were produced on both faces, at the sites of both precipitates and dislocations. Background etch rate results were identical with CdTe, all close packed faces having a rate of approximately 2 μm min^{-1}.

While it is straightforward to identify those etch pits produced by large precipitates, visible with IR microscopy, it is not so for pits of less than 1 μm which are beyond the resolution of the IR microscope. These small pits may indicate precipitates or dislocations. However, as this work has indicated, precipitates are represented by a CL contrast darker than that which reveals dislocations and therefore utilizing CL temperature dependent contrast analysis, defects of similar appearance may be quantitatively distinguished.

4. Conclusion

Correlations with complementary techniques such as CL and IR microscopy have indicated that a saturated $FeCl_3$ solution is a reliable defect revealing etch for defects in both CdTe and (Cd,Zn)Te. The etch works on a range of crystal orientations including the technologically important $(\bar{1}\bar{1}\bar{1})$B surface. All common crystal defects such as precipitates, dislocations, sub-grain boundaries and twin boundaries are revealed. A linear etch rate of approximately 2 μm min^{-1} has been measured for both the (111)A and $(\bar{1}\bar{1}\bar{1})$B faces of CdTe and $Cd_{0.96}Zn_{0.04}Te$, enabling the use of the etch in profiling experiments.

Comparisons of CL micrographs with optical microscope images of etch pits has indicated that a greater resolution of individual features is obtainable with $FeCl_3$ etching but the CL technique was seen to reveal a large number of defects. However, there is a need to discriminate between etch pits representing fine (less

than 1 μm) precipitates and those indicating dislocations and although qualitative discrimination of the CL contrast representative of dislocations and precipitates has been obtained, further work is required on developing CL temperature dependent contrast theory to provide a quantitative discrimination.

References

1 K. Nakagawa, K. Maeda and S. Takeuchi, *Appl. Phys. Lett.*, *34* (1979) 574.

2 M. Inoue, I. Teramoto and S. Takayangi, *J. Appl. Phys.*, *33* (1962) 2578.

3 United States Patent No. 4 897 152, Etchant for revealing dislocations in II-VI compounds, 1990.

4 I. Hahnert and M. Schenk, *J. Cryst. Growth, 101* (1990) 251.

5 D. J. Williams, unpublished work, 1985.

6 C. C. R. Watson and K. Durose, *J. Cryst. Growth*, in press.

7 K. Durose, G. J. Russell and J. Woods, *J. Cryst. Growth, 72* (1985) 85.

8 J. C. Bailar (ed.), *Comprehensive Inorganic Chemistry*, Vol. 1, Pergamon Press, Oxford, 1973, p. 1046.

9 K. Durose and G. J. Russell, *J. Cryst. Growth, 86* (1988) 471.

10 D. Hull, *Introduction to Dislocations*, Pergamon Press, Oxford, 1975.

Materials Science and Engineering, B16 (1993) 118-122

In situ reflectance anisotropy studies of the growth of CdTe and other compounds by MOCVD

V. Sallet, R. Druilhe, J. E. Bouree and R. Triboulet

Laboratoire de Physique des Solides, CNRS, 92195 Meudon Cedex (France)

O. Acher

CEA-DAM, DETN, 91680 Bruyeres-le-Chatel (France)

V. Yakovlev and B. Drevillon

LPICM, Ecole Polytechnique, 91128 Palaiseau (France)

Abstract

Using reflectance anisotropy (RA), we investigate *in situ* the metal-organic chemical vapor deposition (MOCVD) of CdTe and ZnTe on GaAs (100). RA transient signatures are observed at the beginning of the heteroepitaxy of lattice-mismatched semiconductors: CdTe on ZnTe and ZnTe on GaAs. RA records also exhibit a fast initial variation ($\delta r/r = 10^{-3}$) during the homoepitaxial growth of these II–VI compounds. In order to clearly understand those phenomena, surface coverage is analyzed by alternating the precursor flows. Large RA signals ($\delta r/r = 10^{-2}$) correlated with the 3D growth of ZnTe on GaAs are observed, before the material relaxation. These signals can be interpreted in terms of surface roughness evolution within the framework of the effective medium theories (EMT). Moreover, *ex situ* spectroscopic measurements of CdTe layers are performed and simulated; a good agreement is obtained between EMT models and experiments.

1. Introduction

Organometallic chemical vapor deposition (MOCVD) is one of the most commonly used techniques for the growth of thin layers (semiconductors, superconductors), and for the realization of heterostructures [1]. In comparison with molecular beam epitaxy (MBE), MOCVD suffers not only from higher temperatures of growth, but also from a high pressure in the reactor (atmospheric in our case) that prohibits the use of a surface characterization method such as reflectance high-energy electron diffraction (RHEED). A real-time *in situ* technique, reflectance difference spectroscopy (RDS) or reflectance anisotropy (RA), has been developed [2] to investigate the semiconductor surface during crystal growth by MOCVD. Such a method can allow a better understanding of the reaction mechanisms and optimize the epitaxy of heterostructures [3]. Free-carrier concentration has also been determined by RDS [4].

Reflectance anisotropy has been used up to now to study III–V compounds [5, 6]; we present the first application of RA to the growth of II–VI semiconductors: CdTe and ZnTe. Many efforts are made to grow CdTe either as optoelectronic material or as buffer layers for the HgCdTe epitaxy (infrared detectors). ZnTe is also studied as a buffer layer between GaAs substrate and CdTe (14.6% lattice mismatch). RA is similar to phase modulated ellipsometry [7, 8]; a difference with this latter technique is the normal incidence of the beam onto the sample. But the main feature of RA is selective sensitivity to the surface when used to characterize isotropic materials [9]. Extrinsic contributions arise from physi- and chemisorbed molecules, anisotropic surface films and surface roughness (SR). Relative reflectance difference $\Delta r/r = (r_{011} - r_{01\bar{1}})/r$ is measured where r_{011} and $r_{01\bar{1}}$ are the normal incidence reflectances parallel to [011] and [01$\bar{1}$] directions, and r is the average value.

2. Experimental details

Coupling RA (ISA Jobin-Yvon spectrometer) to MOCVD offers the possibility of following both real ($S_{2\omega} = \mathrm{Re}(\Delta r/r)$) and imaginary ($S_{\omega} = \mathrm{Im}(\Delta r/r)$) components of the anisotropy during the growth [10]. Figure 1 shows the arrangement of the optical components. Using the photoelastic effect, the polarization of a light is modulated, and then reflected on the sample

0921-5107/93/$6.00

© 1993 - Elsevier Sequoia. All rights reserved

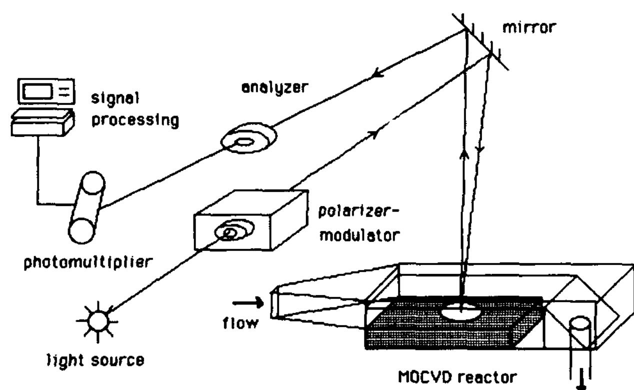

Fig. 1. Schematic diagram of the RA system.

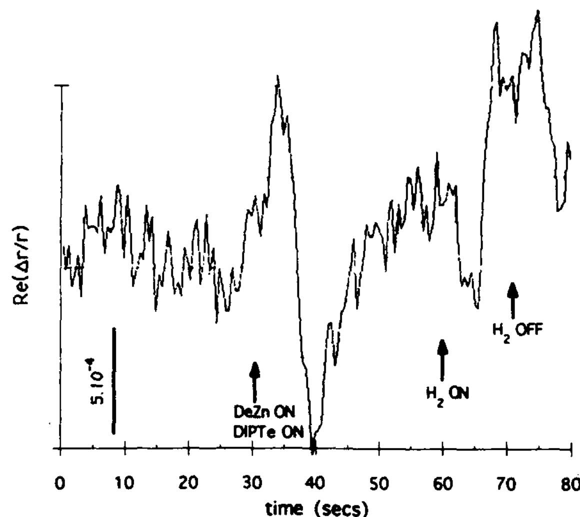

Fig. 2. RA signal for ZnTe growth at 365 °C; precursor (DIPTe: 200 cm^3 min^{-1}, DEZn: 100 cm^3 min^{-1}) and hydrogen (550 cm^3 min^{-1}) flows were switched on and off at the times indicated by the arrows. Total flow is 5000 cm^3 min^{-1}.

surface. The interaction with the material leads to a change in the polarization. After the analyzer, the beam enters a photomultiplier; the parameters characterizing the reflexion are extracted by signal processing. We do not consider mirror effects (a mirror allows normal incidence on the sample) or window birefringence.

In situ we will work at a fixed wavelength, but spectroscopies of CdTe epilayers will be performed *ex situ*. Light sources are, respectively, a low power HeNe laser emitting at 633 nm and a 75 W xenon lamp for *in situ* and *ex situ* experiments. Experiments are conducted using a horizontal commercial reactor including three silica walls (two fixed windows and a liner). ZnTe is grown at 365 °C using diisopropyltelluride (DIPTe) and diethylzinc (DEZn) on GaAs. CdTe is grown at 365 °C on ZnTe(buffer)/GaAs and directly on GaAs using DIPTe and dimethylcadmium (DMCd). The orientation of GaAs substrates is (100) 2° off [110]. In these conditions of epitaxy, we check the (100) orientation of all the layers by pseudo-Kikuchi lines, except for CdTe epilayers on GaAs which present (111) orientation. For RA, relative orientations of all the optical components are essential for the relevance of the data. Modulator and analyzer eigenaxes are chosen parallel to those of the mirror in order to minimize its effects. The polarizer axes are oriented at 45° to the modulator as for those of the sample to provide equal illumination along [011] and [01$\bar{1}$] directions.

Measurements with the substrate position rotated by 90° changes the sign of the RA signal, since $(r_{01\bar{1}}-r_{011})/r$ or $(r_{011}-r_{01\bar{1}})/r$ is recorded; this proves the RA main contribution to the signal. Unfortunately, parasitic sources like an r.f. generator make the measure noisy (about $2-3\times10^{-4}$). Another consideration is the birefringence of the three silica windows. This birefringence adds an offset level to the RA signal; therefore only variations of the optical anisotropy can be measured, rather than absolute values.

3. Results

There may be a variety of structural and chemical contributions to the surface anisotropy. At the onset of ZnTe homoepitaxial growth, the RA signal changes abruptly, exhibiting one large oscillation during 15 s (Fig. 2). The same transient is recorded when a heterojunction of ZnTe on GaAs is grown, whereas the heteroepitaxy of CdTe on ZnTe is quite different. Except for this last experiment, the form of RA signal is reproducible. Oscillation at the beginning of the growth is still observed, even when equilibrating the pressure before and after the commutation of the precursor flows.

We also observe transients of 10–15 s time-scale when adding or subtracting 500 cm^3 min^{-1} hydrogen flow during the growth of ZnTe (Fig. 2). This perturbation (10% of the 5000 cm^3 min^{-1} total flow) seems to involve dilution effects, changing the chemical state of the surface. The fact that any commutation of precursor flows or any perturbation (adding a flow) involves a 10–15 s time-scale transient can emphasize a problem of the epitaxist. Without understanding precisely what happens at the onset of the growth, we clearly see that multilayer processes calling for less than 15 s growth between two precursor commutations seem difficult to perform, thus inducing a limitation in the MOCVD heterostructure growth.

Figure 3 shows RA signatures of alternances of one precursor flow (hydrogen saturated in DIPTe or in DMCd); 30 s of hydrogen flow separate each alternance. Nevertheless this procedure cannot be called

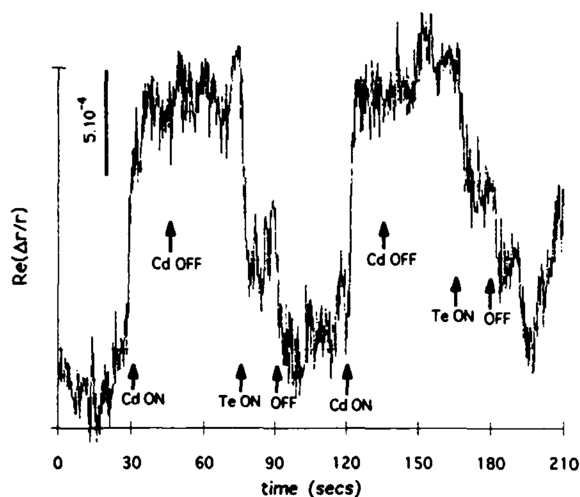

Fig. 3. RA signal for CdTe growth at 365 °C, alternating precursor flows (DIPTe: 200 $cm^3 min^{-1}$, DMCd: 50 $cm^3 min^{-1}$). Total flow is 5000 $cm^3 min^{-1}$.

atomic layer epitaxy of CdTe since the amount of organometallic molecules sent is much more than that needed for a monolayer. However, stable and reproducible states of the surface are performed for each alternance. The time constants associated with the switching on and off are very fast (≈ 1 s). Figure 3 also shows that DMCd switch-off does not involve any change in the signal, whereas DIPTe switch does. At this point, it is clear that these observations are directly correlated to the reaction mechanisms.

4. Optical model

Lattice-mismatched growth induces elastic strain in the epilayer. One can expect a weak contribution of the optical anisotropy related to the strain as this strain is probably isotropic in the plane of reflectance [11, 12]. Therefore, the optical axis is normal to the interface. Nevertheless the induced optical anisotropy of the epilayer is taken into account as we found that the RA signal is sensitive to its contribution. Generally, surface morphology of CdTe (ZnTe)/GaAs epilayers are rough, exhibiting hillocks and pyramids [13]. As a result, both the time and spectral character of the RA signal at the lattice-mismatched growth are determined by an appearance and evolution of anisotropic surface roughness (SR) whereas a contribution of adsorption can be dominated only at the initial stage of deposition [6].

Consider the SR as a single layer that has an effective thickness d and a set of effective dielectric constants ε_j ($j = 1$, 2 and 3) determined by Bruggeman effective medium approximation (BEMA) [14]. BEMA can predict the effective dielectric constant ε_j for the electric field in the jth direction, provided that the corresponding depolarization factor q_j for the effective medium is given. The effective dielectric constants for the anisotropic SR are calculated from:

$$\frac{1-\varepsilon_j}{1+k_j\varepsilon_j} f_v + \frac{\varepsilon-\varepsilon_j}{\varepsilon+k_j\varepsilon_j}(1-f_v) = 0 \quad j = 1,\ldots,3 \text{ or } x,\ldots,z \tag{1}$$

where ε is the dielectric constant of the deposited material, f_v is the volume fraction of voids, and k_j is the screening parameter. This latter quantity accounts for the accumulation of charge at the boundaries of the SR and is related with the depolarization factor q_j, for the direction along the electric field, according to the expression $k_j = (1-q_j)/q_j$. The depolarization factor q_j incorporates the effect of the shape of the individual regions that comprise the surface microstructure.

Let z be the axis normal to the growing surface. The depolarization factors (q_x, q_y, q_z) of the SR overlayer along the three directions must satisfy the conditions that $q_x + q_y + q_z = 1$. If the SR consists of hemispherical isotropic hillocks, the depolarization factors for such a 2D symmetric system $q_x = q_y = (1-q_z)/2$, and the RA signal should equal zero. But if hillocks are triangular or exhibit a more complicated form then $q_x \neq q_y \neq q_z$, and the RA signal is expected to be dependent on the surface morphology.

To compute the relative reflectance anisotropy for the sample, the anisotropic SR is taken into account. The two-layer system is represented as a uniaxial anisotropic film (SR) on the top of an epilayer which is grown on an isotropic substrate. The optical (z-) axis of the uniaxial film is perpendicular to the surface. The relative reflectance anisotropy $\Delta r/r$ is related to the ellipsometric parameters ψ and Δ by the following manner $\Delta r/r = 2\psi' + i\Delta'$, where $\psi' = \psi + \pi/4$ and $\Delta' = \Delta - \pi$ in the case of small anisotropies [10]. The parameters ψ and Δ are defined according to $r_{011}/r_{01\bar{1}} = \tan\psi \exp(i\Delta)$. The reflection coefficients for [011] and [01$\bar{1}$] polarizations are related both to the dielectric constants of substrate, deposited epilayer and effective dielectric constants of the anisotropic SR. They are also related to the thickness of the epilayer and the effective thickness d_{SR} of the rough layer [8]. In order to simulate the kinetics of the deposition we suggest a constant deposition rate V_d and the following law to describe an evolution of the SR:

$$d_{SR} = at^b e^{-ct} \tag{2}$$

This general law can describe both increase and reduction of the SR.

Since RA detects anisotropy changes but does not provide an immediate identification of the origin of the

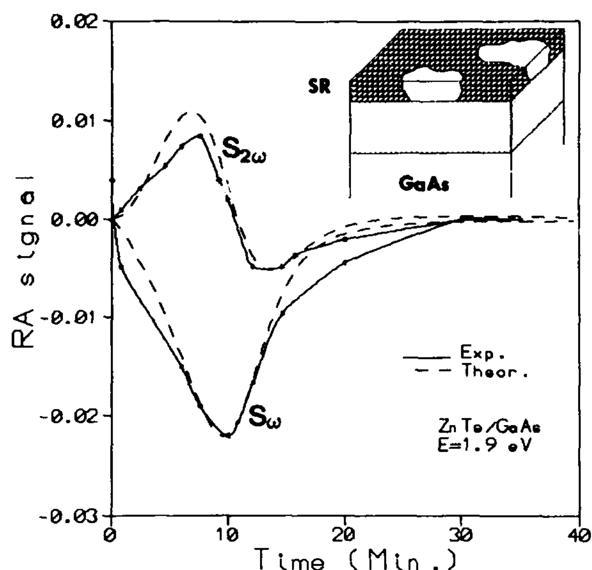

Fig. 4. Comparison between experiment and theory for the RA records (S_{ω} and $S_{2\omega}$ as a function of time) of ZnTe growth at 365 °C.

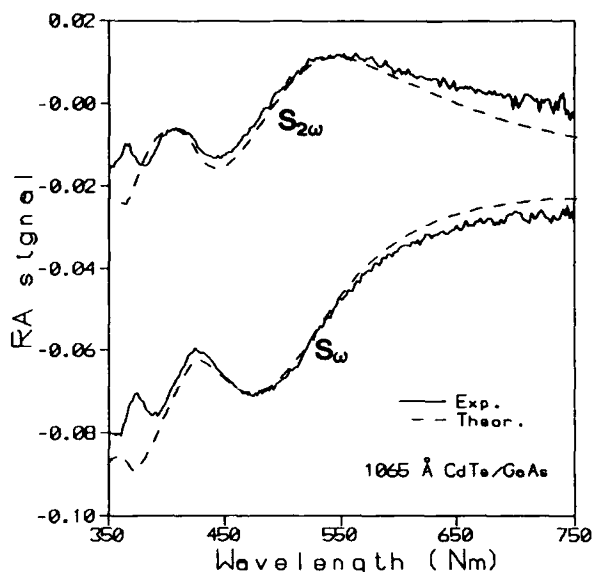

Fig. 5. Comparison between experiment and theory for the RA spectroscopic records (S_{ω} and $S_{2\omega}$ as a function of energy) of 1000 Å CdTe epilayer.

signals, it is important to carry out both kinetic and spectroscopic measurements to characterize unambiguously the process under investigation. Figure 4 shows both the experimental kinetic results of ZnTe deposition on GaAs and simulation of the process with $V_d = 0.8$ Å s^{-1}, $a = 34$ Å, $b = 1.6$ and $c = 0.26$ s^{-1}. Damping oscillations are related with light interferences in the deposited epilayer. The simulation reveals that SR reaches a maximum around 125 Å after about 6 min of deposition and then relaxes to a smooth and/or isotropic morphology.

Figure 5 shows the results of spectroscopic measurements on a 1000 Å thick film of CdTe on GaAs, and the simulation with the effective width of the SR, $d_{SR} = 60$ Å, and volume fraction of voids $f_v = 0.39$. Depolarization factors are $q_x = 0.0$, $q_y = 0.69$ and $q_z = 0.31$ indicating a strip character of the surface morphology. In order to get a best fit to the experimental curves, the induced optical anisotropy of the epilayer is described by $\varepsilon_x^{el} = \varepsilon_{CdTe}(1 + \delta\varepsilon_x^{el})$, where ε_{CdTe} is the dielectric function of CdTe and $\delta\varepsilon_x^{el} = 0.008$. For a 1 μm thick film $d_{SR} = 93$ Å, $f_v = 0.14$ which indicate a reduction of the SR. Depolarization factors are $q_x = 0.0$, $q_y = 0.8$ and $q_z = 0.2$.. An additional anisotropy $\delta\varepsilon_x = 0.3$ of the material of the SR layer (CdTe) has to be introduced in order to get both the relatively high level of the RA signal and an acceptable fitting to the experimental curves. This latter assumption reveals a surface stress in the epilayer. We attribute the observed discrepancy in characters of experimental and calculated curves in the UV range to a fine microstructure of the SR.

5. Summary and conclusion

Using reflectance anisotropy, we investigated *in situ* the growth of II–VI semiconductors (CdTe and ZnTe) by MOCVD. Preliminary results show that signal changes occurring over different time-scales are related to different contributions to the optical anisotropy of the material. Spectral dependence of the anisotropy has been recorded *ex situ* for two different thicknesses of CdTe epilayers. Within the framework of effective medium theories, a model has been developed to describe surface roughness anisotropy. Good agreement between experiments and simulation has been found. The preceding results illustrate the potential of using reflectance anisotropy as an *in situ* technique to study the MOCVD growth mechanisms of II–VI compounds, and to optimize the epitaxy of heterostructures.

Acknowledgments

The authors would like to thank R. Benferhat and Y. Josserand (ISA Jobin Yvon) for technical assistance.

References

1 M. Razeghi, *The MOCVD Challenge*, Adam Hilger, London, 1989.
2 D. E. Aspnes, J. P. Harbison, A. A. Studna and L. T. Florez, *Phys. Rev. Lett.*, *61* (1988) 2782.

3 S. Koch, O. Acher, F. Omnes, M. Defour, B. Drevillon and M. Razeghi, *J. Appl. Phys.*, *69* (1991) 1389.
4 H. Tanaka, E. Colas, I. Kamiya, D. E. Aspnes and R. Bhat, *Appl. Phys. Lett.*, *59* (1991) 3443.
5 O. Acher, F. Omnes, M. Razeghi and B. Drevillon, *Mater. Sci. Eng.*, *B5* (1990) 223.
6 O. Acher, S. Koch, F. Omnes, M. Defour and M. Razeghi, *J. Appl. Phys.*, *68* (1990) 3564.
7 B. Drevillon, J. Parey, M. Stchakovsky, R. Benferhat, Y. Josserand and B. Schlayen, *SPIE Proc.*, *1361* (1990) 1188.
8 R. M. A. Azzam and N. M. Bashara, *Ellipsometry and Polarized Light*, North Holland, Amsterdam, 1977.
9 M. Born and Wolf, *Principles of Optics*, Pergamon Press, Oxford, 1964, p. 619.
10 O. Acher, R. Benferhat, B. Drevillon and M. Razeghi, *SPIE Proc.*, *1361* (1990) 1156.
11 H. Leiderer, G. Jahn, M. Silberbauer, W. Krohn, H. P. Wagner, W. Limmer and W. Gebhardt, *J. Appl. Phys.*, *70* (1991) 398.
12 Le Si Dang, J. Gibert, Y. Gobil, K. Saminadayar and S. Tatarenko, *Appl. Phys. Lett.*, *55* (1989) 235.
13 A. Raizman, M. Oron, G. Cinader and H. Shtrikman, *J. Appl. Phys.*, *67* (1990) 1554.
14 D. A. G. Bruggeman, *Ann. Phys. (Leipzig)*, *24* (1935) 636.

Materials Science and Engineering, B16 (1993) 123-127

Specific behaviour of CdTe ion implantation damage

G. Leo*
Centre de Spectrométrie Nucléaire et Spectrométrie de Masse, IN2P3/CNRS, Bât. 108, 91405 Campus, Orsay (France)

A. V. Drigo
Dipartimento di Fisica, Università di Padova, Unità GNSM-INFM, Via Marzolo, 8. 35100 Padova (Italy)

A. Traverse
Centre de Spectrométrie Nucléaire et Spectrométrie de Masse, IN2P3/CNRS, Bât. 108, 91405 Campus, Orsay (France)

Abstract

In order to study the damage produced as a function of both the chemical nature of the ion and the implantation energy, [111] CdTe single crystals were implanted with 150 keV Mn and 50, 100 and 200 keV P ions. Analysis of the damage was carried out by Rutherford backscattering spectrometry and ion channeling measurements using ^{4}He beams at different energies. These measurements show that the disorder induced by ion implantation in CdTe exhibits specific features: (i) saturation of damage without reaching the amorphous state; (ii) existence of an almost undamaged near-surface region. In fact, whatever the implantation conditions, the normalized channeling yield (which is a measure of the integrated disorder) reaches the value of 0.6–0.7 at saturation and the low damaged layer depth is about 40 nm thick. The channeling measurements are consistent with a previous study in which the residual damage was identified as small-sized dislocation loops mainly located beyond the ion projected range R_P. These results are interpreted as indicating a high mobility of defects in CdTe together with a high efficiency of the surface in their recombination process, and the role played by the dislocation-loop-induced stress.

1. Introduction

Ion implantation as a doping technique has been widely used in recent years in the attempt to obtain p-type CdTe with a high dopant concentration [1-4]. The problem related to this doping technique is the difficulty of recovering the damage produced by the bombarding ions. The main reason for this is the anomalous damaging process which has been observed in ion-implanted CdTe with respect to other semiconductors [2, 5-8].

More recently, because of the great technological interest in HgCdTe (MCT), many studies have been undertaken concerning the implantation damage in this material [9-11]. The main characteristics of the damaged layer produced are similar in both MCT and CdTe, and can be summarized as follows: (i) the implanted layer does not become amorphous at room temperature, even at very high implantation fluences; (ii) a layer of extended defects is created, deeper than the calculated ion projected range R_P.

*Author to whom correspondence should be addressed. Permament address: Dipartimento di Scienza dei Materiali, Unità GNSM-INFM, Via per Arnesano, 73100 Lecce, Italy.

Although in MCT these characteristics have been ascribed to the very high mobility of the mercury interstitials, the general trend of the damage mechanism appears to be the same in both materials, so that the problem of understanding this damage mechanism could be related to specific features of CdTe and, possibly, of other II–VI compounds.

A previous study undertaken by Uzan-Saguy *et al.* [5] on indium-implanted $Hg_xCd_{1-x}Te$ ($x = 0, 0.24, 0.7, 1$) shows the same general trend in the damage evolution as a function of the fluence, independent of the mercury molar fraction. Three different damage regions have been identified as a function of the implanted dose. The fluences at which the changes in the damage behaviour have been observed correspond, for all the compositions, to the same residual damage surface density. A qualitative model where the ionic forces existing in the lattice are responsible for the defect recombination that prevents the amorphization of the implanted layer has been proposed [5]. Moreover, when damage saturation is reached, an in-depth defect redistribution, related to a radiation-assisted diffusion process, has been suggested.

In a previous study performed by ion channeling analysis of phosphorus-implanted CdTe as a function

0921-5107/93/$6.00 © 1993 - Elsevier Sequoia. All rights reserved

of implantation fluence and energy, evidence was found that the damage mechanism involves a defect diffusion both at depths greater than R_P and towards the surface, where a defect annihilation mechanism must be particularly efficient [8]. Moreover, by *in situ* transmission electron microscopy (TEM) observations of plan sections, the residual defects have been identified as small-sized, interstitial-type dislocation loops [12].

Our present results, together with other literature data, allow us to conclude that the main features of the damage process are independent of the implantation parameters and are therefore related to the matrix characteristics.

2. Experimental details

Brome-methanol-etched samples of [111] CdTe, grown from the melt by the Bridgman technique and supplied by COMINCO, were implanted with 50, 100 and 200 keV P, and 150 keV Mn ions at fluences ranging from 1×10^{14} to 1×10^{16} ion cm^{-2}. All the implants were performed at room temperature with a current density below 0.2 μA cm^{-2}, in order to restrict the temperature rise during implantation. Both the ion implantor of the University of Padova and that of the Centre de Spectrométrie Nucléaire et Spectrométrie de Masse (CSNSM) at Orsay were used. The values of the ion projected range R_P calculated using the TRIM program [13] for the different implantation conditions are reported in Table 1 and range from 56 to 186 nm.

The characterization of the damage produced in the implanted samples was performed by RBS and ion channeling measurements at Laboratori Nazionali di Legnaro (Italy) and *in situ* at the CSNSM in Orsay (France) with the ARAMIS accelerator in line with the ion implantor IRMA [14]. Unlike previous works [5–7] performed by low energy hydrogen beams, ^{4}He beams of energies ranging from 400 keV to 4 MeV were used for the analysis, allowing a good depth and mass resolution in the surface region.

TABLE 1. Summary of the implantation conditions: ion, implantation energy E_{imp} and ion projected range R_P. The last column reports the thickness t_{LD} of the low damage layer measured with ^{4}He beams of different energies E_{RBS}

Ion	E_{imp} (keV)	R_P (nm)	E_{RBS} (MeV)	t_{LD} (nm)
P	50	56	1.0	33
			4.0	28
P	100	99	1.0	46
			2.0	37
P	200	186	0.4	35
			2.0	42
Mn	150	92	0.4	50
			2.0	46

3. Results

Figure 1 shows typical RBS spectra taken in channeling conditions along the [111] CdTe direction for the sample implanted with 150 keV Mn ions at several fluences. As observed in previous studies, the implanted layer does not become amorphous even at the highest implantation dose. Nevertheless, the sequence of the spectra in Fig. 1 shows a damage quasi-saturation on increasing the fluence. Moreover, these spectra show a low channeling yield extending from the surface down to a depth at which quite a sharp variation in the dechanneling rate sets in. The high dechanneling rate extends down to a knee, where it becomes nearly equal to that of a virgin sample. This fact leads to the assumption that the knee represents the end-point of the damaged layer produced by ion implantation. The knee depth increases with the implantation fluence, ranging from roughly R_P up to $2R_P$ when damage saturation is reached. This increase of the damaged layer depth is not due to dopant-enhanced diffusion, because secondary ion mass spectrometry (SIMS) measurements show that the dopant profile is centred just around the calculated R_P.

The low channeling yield observed in the surface region for all the implantation fluences indicates the presence of a nearly damage-free surface layer (low

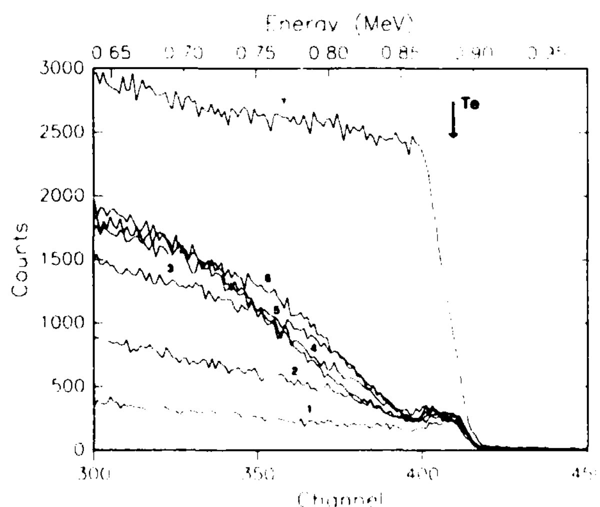

Fig. 1. 1 MeV *in situ* ^{4}He RBS spectra in channeling condition along the [111] axis for a 150 keV Mn implanted sample at several fluences: (1) virgin sample; (2) 2×10^{14} ion cm^{-2}; (3) 5×10^{14} ion cm^{-2}; (4) 1×10^{15} ion cm^{-2}; (5) 3×10^{15} ion cm^{-2}; (6) 5×10^{15} ion cm^{-2}. A random spectrum (7) is also shown for comparison.

damage layer). This fact is also supported by the clearly evident channeling surface peak. It is important to emphasize that this low damage layer is a common feature of all the examined samples, independent of the implantation conditions. Thus the surface region has been systematically analysed for all the samples using ^4He beams of different energies. In fact, the kinematic energy separation between the cadmium and the tellurium signals corresponds to 9 nm and 127 nm at 0.4 MeV and 4 MeV respectively. While the surface minimum yield χ_{min}, which is a measure of the surface disorder, slowly increases from 6% for the virgin sample to 20% at 5×10^{15} ion cm^{-2}, no significant variation of the thickness t_{LD} of the low damage layer is observed. The values of t_{LD}, averaged for the different implantation doses, are reported in Table 1 for the different implanted ions and implantation energies. The table shows that t_{LD} has a mean value of 40 nm with a standard deviation of ± 7 nm, independent of the ion projected range.

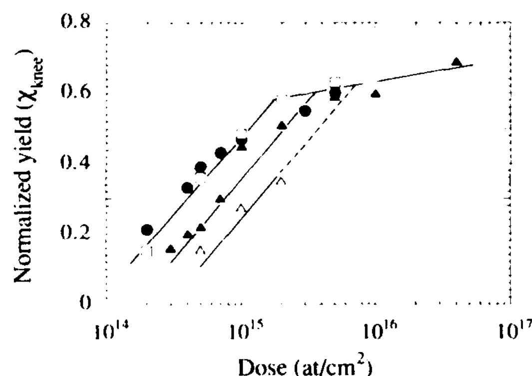

Fig. 2. The channeling normalized yield χ_{knee} calculated at the knee depth as a function of the implantation fluence for 150 keV Mn implantations (●) and phosphorus implantations at 50 keV (△), 100 keV (▲) and 200 keV (□). The lines through the data points are only drawn to guide the eye.

In order to get information on the nature of the residual damage, the normalized channeling yield χ_{knee} at the knee depth was measured at different ^4He beam energies ranging from 0.4 to 4 MeV. No energy dependence was found for any samples, suggesting that the residual defects are mainly small-sized dislocation loops; this is in agreement with the TEM observations [12].

The evolution of the lattice disorder with the implantation fluence is shown in Fig. 2 where χ_{knee} is reported as a function of the fluence. The behaviour is qualitatively the same for all the implantation conditions, showing a rapid increase in disorder up to a quasi-saturation by increasing the fluence. The saturation value of the channeling yield, which depends on the integral disorder, is always about 0.6, whereas the fluence Φ_{sat} at which the damage saturation is reached decreases by increasing the energy $\nu(E)$ lost in nuclear collision, as shown in Table 2. In the case of 50 keV P, the saturation was not reached at the highest implanted dose but Φ_{sat} can be estimated by extrapolating the experimental yield measured at lower fluences and by assuming a χ_{knee} saturation value equal to that found for the other implantation conditions. The values of the saturation dose in each sample are reported in Table 2 together with values deduced from some literature data [5, 15].

4. Discussion

The results presented above clearly show that CdTe never becomes amorphous following room temperature implantation, even after high dose ion implantation (5×10^{15} ion cm^{-2}), which agrees with previous literature data. Nevertheless, the residual damage exhibits a quasi-saturation at a level independent of the implantation parameters. When this damage saturation is reached, residual defects are found at a depth almost

TABLE 2. The energy lost in nuclear collisions in CdTe, $\nu(E)$ and the ratio $\nu(E)/R_p$ as calculated by TRIM-90 program for several implanted ions and implantation energies

Ion	E (keV)	$\nu(E)$ (keV)	$\nu(E)/R_p$ (eV nm^{-1})	Φ_{sat} (ion cm^{-2})	$\nu(E)\Phi_{sat}/R_p$ (eV cm^{-3})	$\nu(E)\Phi_{sat}$ (eV cm^{-2})
P	50	26	464	7×10^{15}	3.2×10^{25}	1.8×10^{20}
P	100	47	475	3.5×10^{15}	1.6×10^{25}	1.6×10^{20}
P	200	80	430	2×10^{15}	0.9×10^{25}	1.6×10^{20}
Mn	150	92	1000	2×10^{15}	2.0×10^{25}	1.8×10^{20}
Hg[a]	350	227	3247	7×10^{14}	2.3×10^{25}	1.6×10^{20}
In[b]	320	211	2184	8×10^{14}	1.7×10^{25}	1.7×10^{20}

The damage saturation fluences Φ_{sat} obtained from Fig. 2 and from literature data are also reported, together with the volume energy density $(\nu(E)/R_p)\Phi_{sat}$ and the surface energy density $\nu(E)\Phi_{sat}$.
[a] After ref. 15.
[b] After ref. 5.

twice the ion projected range, suggesting a very high mobility of the primary defects.

Diffusion data for CdTe [16] indicate a very high mobility of tellurium interstitials, while the vacancy mobility (of both cadmium and tellurium) is nearly three orders of magnitude lower. Because of the high interstitial mobility, the probability of defect recombination and defect clustering is increased. However, as pointed out in ref. 17, following the kinematics of the collision cascade, excess interstitials are mainly found at a depth greater than R_P, leaving an excess of vacancies at depths lower than about $0.8 R_P$. This fact together with the interstitial diffusion explain both the TEM results [12] and our present channeling data. In fact, TEM observations have shown that the residual defects are small-sized interstitial-type dislocation loops (15 nm or less) located far from the surface, which is in agreement with the depth measured by RBS channeling ranging from R_P to $2R_P$. Moreover, the small size of the dislocation loops accounts for the independence of the dechanneling probability from the analysing beam energy. The TEM measured density and size of the dislocation loops show that the number of interstitials clustered in the loops is almost three orders of magnitude lower than the number of primary displacements. This fact indicates a very high interstitial–vacancy recombination probability and this is also supported by the suggested interstitial mobility. The enhanced probability of vacancy–interstitial recombination can also explain the surface low damage region. However, the fact that the thickness of this layer is 40 nm, independent of the ion projected range, indicates that the crystal surface plays a specific role as a defect sink in the damage mechanism during CdTe ion implantation. This thickness thus seems to be connected to an effective recombination range characteristic of the CdTe surface.

The damage saturation mechanism is more difficult to explain because it requires the assumption of some change in the diffusion mechanism of the primary defects as the implanted dose (and hence the residual damage) increases. One possible hypothesis is that the increase in strain between R_P and $2R_P$ caused by the interstitial dislocation loops acts as a diffusion barrier for the newly generated interstitials so they preferentially diffuse toward the surface, where they easily recombine with the vacancies. This hypothesis is supported by the fact that damage saturation always corresponds to the same amount of integral residual disorder as shown by the normalized channeling yield ($\chi_{knee} \approx 0.6$). The critical stress responsible for the damage saturation does appear to be related to a well-defined density of dislocation loops.

For most semiconductors, damage saturation (amorphization) is generally achieved when a given amount of energy per unit volume has been deposited in nuclear collisions. A rough estimate of this parameter can be given by $(\nu(E)/R_P)\Phi$, where $\nu(E)$ is the energy lost by the implanted ion in nuclear collisions and Φ the fluence. In the case of phosphorus implantation, the data in Table 2 show that $\nu(E)/R_P$ is virtually independent of the ion energy (456 ± 19 eV nm^{-1}), while the damage saturation fluence changes by almost a factor of four. It can be concluded that damage saturation in ion-implanted CdTe is not related to a critical volume energy density $\nu(E)\Phi_{sat}/R_P$. Instead, a strong inverse correlation of the saturation fluence is found with $\nu(E)$, *i.e.* a critical surface energy density instead of a volume density (see last column in Table 2). Not only our data but also literature data support this conclusion which is most significant because both the $\nu(E)$ and $\nu(E)/R_P$ values span almost one order of magnitude. Hence, the data in the last column of Table 2 lead to the conclusion that ion implantation damage saturation in CdTe is related to a surface density of energy deposited in nuclear collision, which is of the order of $1.7 \pm 0.1 \times 10^{20}$ eV cm^{-2}, independent of the implantation conditions. The fact that the critical parameter is a surface energy density provides further evidence that the damaging process is completely dominated by diffusion processes, in agreement with the previous discussion.

5. Conclusions

A systematic study of the ion implantation damage in CdTe leads to the following conclusions.

(i) The high interstitial mobility produces both a high defect recombination efficiency and interstitial clustering in dislocation loops at depths greater than R_P, where vacancies are not available. This fact prevents the amorphization.

(ii) A low damage surface layer is always observed. Its thickness is independent of the ion projected range and it appears to be a specific feature of the CdTe surface, which acts as a preferential defect sink.

(iii) Independent of the implantation conditions, damage saturation is reached at a given surface density of residual disorder. This condition, characteristic of CdTe, is believed to steer the interstitial diffusion preferentially towards the surface because of the lattice strain induced by the dislocation loops.

(iv) Damage saturation is reached when 1.7×10^{20} eV cm^{-2} are deposited in nuclear collisions. The fact that the relevant parameter is a surface energy density instead of a volume density again indicates the dominant role played by primary defect diffusion in the disordering process.

References

1 J. P. Donnelly, A. G. Foyt, E. D. Hinkley, W. T. Lindley and J. O. Dimmock, *Appl. Phys. Lett.*, *12* (1968) 303.
2 M. Getting and K. G. Stephens, *Radiat. Eff.*, *22* (1974) 53.
3 M. Chu, A. L. Fahrenbruch, R. H. Bube and J. F. Gibbons, *J. Appl. Phys.*, *49* (1978) 322.
4 C. Y. Sun, Y. J. Hsu and H. L. Hwang, *J. Cryst. Growth, 101* (1990) 420.
5 C. Uzan-Saguy, D. Comedi, V. Richter, R. Kalish and R. Triboulet, *J. Vac. Sci. Technol. A*, *7* (1989) 2575.
6 G. Bahir and R. Kalish, *J. Appl. Phys.*, *54* (1983) 3129.
7 V. Richter, D. Comedi and R. Kalish, *IBMM '90*, Knoxville, TN.
8 G. Leo, A. Traverse, M. O. Ruault and A. V. Drigo, *Nucl. Instrum. Methods B*, *63* (1992) 41.
9 G. L. Destefanis, *J. Cryst. Growth, 86* (1988) 700.
10 L. O. Bubulac, *J. Cryst. Growth, 86* (1988) 723.
11 C. Blanchard, J. F. Barbot, M. Cahoreau, J. C. Desoyer, D. Le Scoul and J. L. Dessus, *Nucl. Instrum. Methods B, 47* (1990) 15.
12 G. Leo, *PhD. Thesis*, Lecce University, Italy, 1991.
13 J. F. Ziegler, J. P. Biersack and G. Cuomo, *TRIM-90 Program*, version 5.1 (Transport of ion in matter).
14 E. Cottereau, J. Camplan, J. Chaumont and R. Meunier, *Mater. Sci. Eng., B, 2* (1989) 217.
H. Bernas, J. Chaumont, E. Cottereau, R. Meunier, A. Traverse, C. Clerc, O. Kaitasov, F. Lalu, D. Le Du, G. Moroy and M. Salomè, *Nucl. Instrum. Methods B, 62* (1992) 416.
15 A. Traverse, personal communication, 1991.
16 F. A. Kröger, *Rev. Phys. Appl.*, *12* (1977) 205.
17 A. M. Mazzone, *Phys. Status Solidi A, 95* (1986) 149.

Materials Science and Engineering, B16 (1993) 128–133

Structural properties of defects in $Cd_{1-x}Zn_xTe$

D. M. Hofmann, W. Stadler, K. Oettinger and B. K. Meyer
Physikdepartment E 16, Technische Universität München, D-8046 Garching (Germany)

P. Omling
Department of Solid State Physics, University of Lund, Box 118, S-22100 Lund (Sweden)

M. Salk and K. W. Benz
Kristallographisches Institut, Universität Freiburg, Hebelstr. 25, D-7800 Freiburg (Germany)

E. Weigel and G. Müller-Vogt
Kristall- und Materiallabor, Universität Karlsruhe, Engesserstr. 7, D-7500 Karlsruhe (Germany)

Abstract

Optically detected and conventional spin resonance investigations have been successful in determining the structure of cation vacancy–donor pairs (A-centers) and anion vacancies (V_{Te}) in CdTe. Investigations in the ternary alloy system $Cd_{1-x}Zn_xTe$ for the complete range of x show that the A-center binding energy is almost independent of the composition. In CdTe the $V_{Te}^{+/0}$ level position is 0.2 eV above the valence band and correlation to a deep luminescence band at 1.15 eV can be drawn. In the alloys this photoluminescence band closely follows the conduction band from CdTe to ZnTe. Studies of the spectroscopic g-values of the shallow donors in $Cd_{1-x}Zn_xTe$ show that they shift linearly from −1.69 in CdTe to −0.4 in ZnTe.

1. Introduction

In the wide gap II–VI compounds the identification and structure determination of intrinsic defects by electron paramagnetic resonance (EPR) and optically detected magnetic resonance (ODMR) has been very helpful for the understanding of the self-compensation mechanism in these materials.

Isolated intrinsic defects such as cation vacancies, acting as acceptors, anion vacancies acting as donors and interstitials have been studied in particle irradiated or additively colored ZnO, ZnS and ZnSe [1, 2].

A-centers, which are complexes of a cation-vacancy and a nearby donor impurity and which act as single acceptors, were shown to be responsible for the high resistivity of ZnS and ZnSe in the as-grown state. ODMR investigations made it possible to directly correlate these defects to so-called "self-activated" luminescence bands [3]. The EPR investigations resolved that the A-centers have trigonal symmetry when a group VII donor is involved (nearest neighbor pairs) but have lower symmetry for a group III donor (next nearest neighbors pair). The g-values of the A-centers were close to the free electron value of ≈ 2.00, reflecting that these centers are deep level defects [4].

In CdTe and ZnTe knowledge of intrinsic defects or complexes of intrinsic defects and impurities is much less definite. No identification of an isolated intrinsic defect has been reported so far in the literature and contradictory results for A-centers exist.

In ZnTe a defect was detected by EPR having similar g-values as A-centers in ZnS and ZnSe [5]. This was taken as evidence for the existence of deep A-centers in ZnTe. But hyperfine interaction with the surrounding tellurium ligands has not been observed, which would confirm that the defect is located on the anion sublattice. A defect with comparable properties has been found in neutron irradiated CeTe again without observation of any hyperfine interaction [6]. In 1985 Cox and co-workers observed by ODMR, a defect in ZnTe:Cl with trigonal symmetry and with lower symmetry in Al-doped material [7]. The observation of the Te ligand hyperfine interaction showed that the defects are located on the Cd sublattice. They presented a conclusive interpretation of their data and identified these defects as being A-centers. The g-values and optical data were significantly different compared to A-centers in ZnS and ZnSe. These properties reflect that A-centers in ZnTe act as shallow defects, not as deep ones.

The outline of the paper is as follows: first, we will

0921-5107/93/$6.00

© 1993 – Elsevier Sequoia. All rights reserved

briefly describe the method used for our investigations, the optical detection of magnetic resonance (ODMR) using the magnetic circular polarization of the emission (MCPE). This technique was very successful when identifying the A-centers in the 1.42 eV luminescence band of CdTe [8]. With a binding energy of 120 meV the A-centers are shallow centers in CdTe as they are in ZnTe. The behavior of the A-center over the complete composition range of x will be discussed. The centers preserve their shallow character, thus having similar optical properties as the residual transition metal impurity Cu.

The second part of the paper deals with the 1.15 eV photoluminescence band in CdTe. The dependence of the emission energy on the alloy composition x in $Cd_{1-x}Zn_xTe$ gives evidence that the responsible defect is located on the tellurium sublattice. With conventional EPR investigations the first isolated intrinsic defect in CdTe, the tellurium vacancy (F-center), could be detected. The defect is a single donor in CdTe with a level at $E_v + 0.2$ eV.

Finally, we describe the determination of the composition dependence of the donor g-values in $Cd_{1-x}Zn_xTe$.

2. Experimental details

The CdTe samples used in the experiments were grown either by the travelling heater method (THM) or by the Bridgman technique. For the purpose of obtaining high resistive material, the growth was performed under Te-rich conditions. Up to 10^{19} cm^{-3} group III or VII donor dopants were added to the melt.

The ternary $Cd_{1-x}Zn_xTe$ crystals were grown by THM from a CdTe seed in a Te zone with a ZnTe reservoir at about 800 °C with a speed of 3 mm per day. With this technique crystals covering almost the complete composition range of x were obtained in one boule. The samples were cut from these crystals and the composition was determined by energy dispersive analysis of X-rays.

For the MCPE and ODMR experiments the samples were placed in an open cylindrical TE_{011} microwave resonator (12 GHz or 24 GHz) situated at the center of a superconducting magnet. The sample and the resonator were directly immersed in superfluid helium ($T \leq 4.2$ K). Photoluminescence was excited by typically 100 mW of the 514 nm line of an Ar-ion laser. The emission spectra were detected using an LN_2-cooled Ge-detector or a photomultiplier. For the MCPE measurements a linear polarizer and a piezoelectric quartz modulator were inserted into the emission beam. To analyze the circular polarization components of the emitted light (σ^+, σ^-) the modulation frequencies were used as reference for lock-in detection. The signal output of the lock-in is proportional to the intensity difference for the left and right-circularly polarized components of the emitted light ($I_{\sigma^+} - I_{\sigma^-}$). The EPR experiments were performed on a commercial Bruker (ESR 300) spectrometer (X-band, 9.5 GHz).

3. Results and discussion

3.1. A-centers

As early as 1959 it was proposed that A-centers are present in CdTe, and give rise to a photoluminescence band centered at 1.42 eV [9]. However, a correct assignment has been possible only recently by ODMR [8]. This was partly due to the fact that not only A-centers contribute to the 1.42 eV PL band in CdTe, but also the residual impurities Cu, Ag and Au show radiative recombination in this spectral range [10]. In addition, a defect of yet unknown structure also emits at 1.475 eV [11] (see Fig. 1). Without going into the details of the ODMR analysis of the A-centers, we briefly summarize the results. A trigonal (111) symmetry was obtained for A-centers in Cl-doped CdTe. The g-values obtained are $g_{\parallel} = 2.2$ and $g_{\perp} = 0.4$ for a description within an effective spin $S' = 1/2$ state.

The hyperfine interactions with the three nearest Te neighbors with nuclear spin $I = 1/2$ have been resolved. The optical excitation spectra of the A-center ODMR

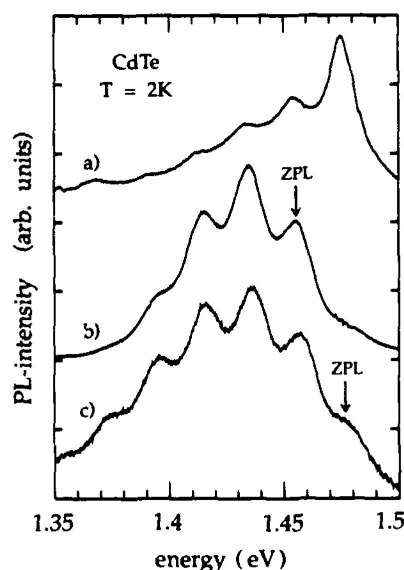

Fig. 1. Photoluminescence spectra of different CdTe samples: (a) spectrum originating from an unidentified defect; (b) donor–acceptor recombination between the Cu acceptor and the Cl donor; (c) excitation spectrum of the A-center ODMR signal.

signals (Fig. 1(c)) show a well-resolved emission band with a zero phonon line (ZPL) located at 1.478 eV and followed by LO-phonon replica. The emission is explained by the recombination of shallow donors with distant acceptors (A-centers), since both shallow donors ($g = 1.69$) and A-center ODMR signals were observed. If we compare these results to the properties of the "classical" A-centers in ZnSe we find striking differences [3, 4]. In ZnSe these centers show a broad deep luminescence band around 1.9 eV ($E_{gap} = 2.7$ eV); the binding energy is estimated to be 0.7 eV. The g-values are close to 2.00. In contrast the recombination energy of A-centers in CdTe is much closer to the bandgap energy of 1.6 eV. The binding energy is calculated from the position of the ZPL to be 125 meV. Therefore the coupling to the lattice is weaker, which explains qualitatively the observed phonon structure of the PL band.

The binding energy of the A-centers is comparable to 145 meV of Cu acceptors in CdTe [10]. The g-value of the copper acceptor ($J = 3/2$ state) with cubic symmetry was determined from Zeeman spectroscopy to be $g = 0.71$ [12]. In the description of a shallow acceptor, the g-value of the A-centers would be $g_{\parallel(1/2)}/3 = g_{(3/2)} = 0.73$ again similar to the value for Cu.

The optical properties of the A-centers differ, however, from those of the "shallow" acceptors Cu, Au and Ag when considering the strength of the phonon coupling as a function of the binding energy (Fig. 2). From Hopfields theory a linear dependence of the phonon coupling, described by the coupling parameter $S\hbar\omega$, on the binding energy is expected (S is the Huang–Rhys factor; $\hbar\omega$ is the phonon energy) [13]. This is indeed found for the transition metal acceptors Ag, Au and Cu [14]. The A-centers do not follow this rule and exhibit stronger phonon coupling. The binding energy is constant, independent of the chemical nature of the donor involved in the A-center complex, but the phonon coupling changes remarkably.

With respect to ZnTe and the alloy $Cd_{1-x}Zn_xTe$, we find that the luminescence band located at 1.42 eV in CdTe follows the band-gap shift and is located in ZnTe at about 2.2 eV (Fig. 3). Cu, Au and Ag as well as the A-center complexes maintain their properties. For the shallow acceptors, only slight changes in the binding energies are found [14].

The same holds for the A-centers: the binding energy shifts from 125 meV in CdTe to 160 meV in ZnTe (Cl–A-center), the phonon coupling S is reduced from 2.2 to 1.6, respectively. This behavior can be understood from the fact that A-centers, as well as Ag, Au and Cu, reside substitutionally in the Cd sublattice. The four nearest Te neighbors do not change in the alloys. This is in line with the resolved Te ligand hyperfine interaction for A-centers in ZnTe and CdTe. It is the dominant interaction of the paramagnetic electron and the spin density of the defects is located to a great extent on the Te neighbors. In the $Zn_{1-x}Se_xS$ alloys in contrast, the nearest neighbor atoms change from 4 Se to 4 S atoms with increasing alloy composition. This causes significant changes in the optical properties of the A-centers in these compounds [15].

3.2. Deep luminescence bands

In our PL studies of various CdTe crystals either doped or undoped, we realized that apart from the 1.42 eV band, additional deeper bands in the spectral region from 1.2 to 0.8 eV are present. As an example

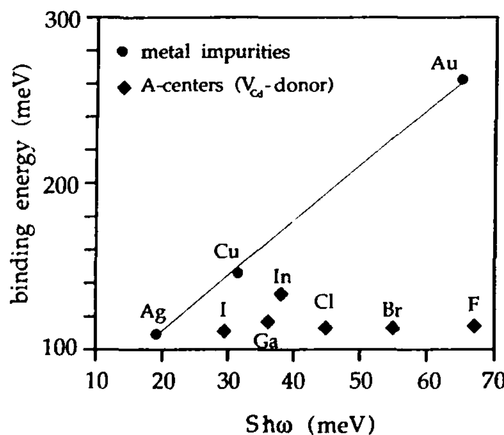

Fig. 2. Binding energy as a function of the phonon coupling ($S\hbar\omega$) for acceptors in CdTe; full circles: Ag, Cu, Au; full squares: cadmium vacancy-donor complexes (A-centers) with different donors involved.

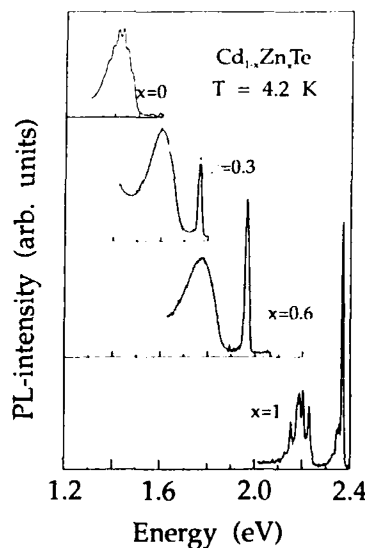

Fig. 3. A-center photoluminescence band in $Cd_{1-x}Zn_xTe$ for crystals of different composition x.

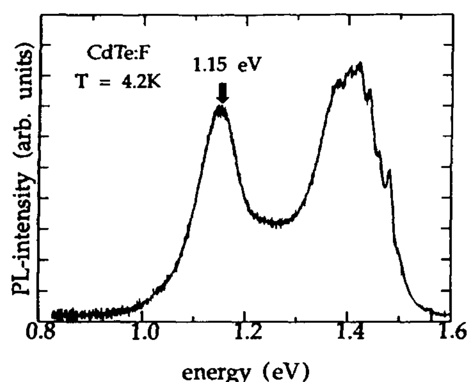

Fig. 4. Photoluminescence spectrum of nominally undoped CdTe. In addition to the 1.42 eV a deep luminescence centered at 1.15 eV is visible.

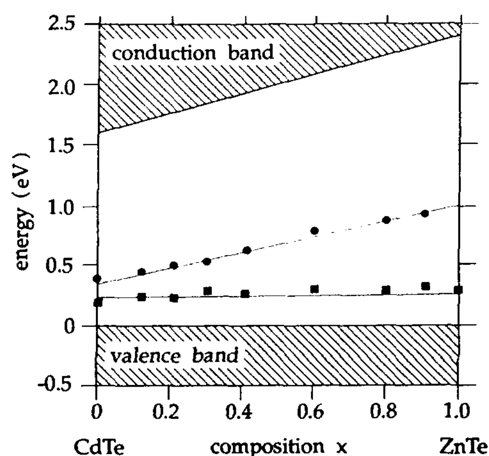

Fig. 5. Peak positions of the A-center photoluminescence band (full squares) and the 1.15 eV band (full circles) in CdTe as a function of the alloy composition x in $Cd_{1-x}Zn_xTe$.

we show a spectrum of a PL band located at 1.15 eV in Fig. 4. The broad gaussian band suggests a strong electron–phonon coupling (*i.e.* $S>6$). $S=17$ and $h\omega=13$ meV was obtained from the temperature dependence of the emission band halfwidth. From the peak position at 1.15 eV and the Stokes shift ($Sh\omega$) we estimate a binding energy of 1.38 eV, which is consistent with the onset of the PL band. Investigating this band as a function of the alloy composition x, we found that its emission energy starting from 1.15 eV in CdTe, remains almost constant up to ZnTe ($x=1$) while the A-center luminescence energy increases as the band gap from CdTe to ZnTe. This behavior is shown in Fig. 5. It should be noted that the values for the energy shift of the valence and conduction band were taken from Langer and Heinrich [16]. According to this work, the valence band, being set up from Te $5p$ bonding states, shifts only about 40 meV from CdTe to ZnTe. The conduction band on the other hand contributes most to the bandgap shift, being set up from Cd $5s$ antibonding states and Zn $4s$ antibonding states. As we have seen from the discussion of the A-centers, these shallow centers located on the Cd sublattice follow the valence band properties in the alloy. The defect responsible for the 1.15 eV band in CdTe shows an opposite behavior: the rather constant emission energy indicates that it is correlated to the conduction band, *i.e.* being located on the Te sublattice. The 1.15 eV band is observed in various crystals independent of doping, this indicates that it may be either due to an omnipresent residual impurity or an intrinsic defect.

In the literature only a few investigations on PL bands at an energy below the 1.42 eV band are reported. Kernöcker *et al.* attributed a PL band at 1.15 eV to Fe in Fe-implanted CdTe [17]. However, substitutional Fe is located on the Cd sublattice. In electron-irradiated CdTe a similar PL band has been observed. From annealing experiments of the irradiation induced defects, it was concluded that this band originates from a Te vacancy defect [18]. EPR experiments described in the next section identified V_{Te} in CdTe. Based on the energy level determination of V_{Te}, it is not unlikely that this intrinsic defect is responsible for the emission band.

3.3. Te vacancy in CdTe

The formation and defect structure of anion vacancies (F-centers) have been studied extensively in ionic crystals of rocksalt structure [19]. Apart from the wide band-gap materials with high ionicity, for instance, BeO and ZnO, ZnS is the only member of a compound semiconductor in which the anion vacancy has been identified by EPR [1].

It was unexpected to observe these defects in CdTe grown under Te-rich conditions favoring the formation of V_{Cd}. Additionally, the samples were annealed in an argon atmosphere for 1 h in a temperature range from 380 °C to 780 °C. Already a 380 °C anneal was sufficient to make the V_{Te}^+ EPR signal observable.

The EPR spectrum (Fig. 6(a)) consists of nine lines due to the hyperfine interaction with the four nearest Cd neighbors (^{111}Cd and ^{113}Cd, nuclear spin $I=1/2$, natural abundances 12.75% and 12.26%, respectively). The outermost of these nine lines are hardly resolved in the experiment. The spectrum is isotropic (isotropic g-value, $g=2.000\pm0.001$) consistent with an F-center groundstate of s-type symmetry.

To study the electrical properties of V_{Te} we have illuminated the sample with sub-band-gap light. The result is shown in Fig. 6(b). For light energies of 1.4 eV and above, a strong increase of the V_{Te}^+ EPR signal is observed. We propose that the vacancy is directly ionized in a transition from the neutral charge state to the singly positive (paramagnetic) state:

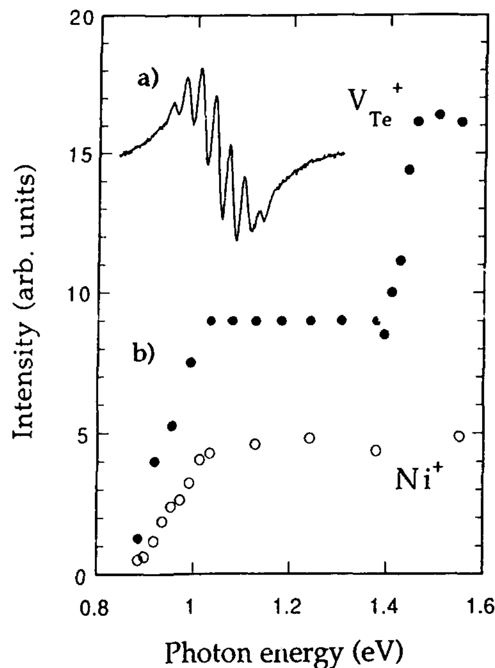

Fig. 6. (a) Electron paramagnetic resonance (EPR) spectrum of the singly ionized tellurium vacancy (V_{Te^+}) in CdTe. (b) Photo-excitation spectrum of the V_{Te^+} EPR spectrum in CdTe.

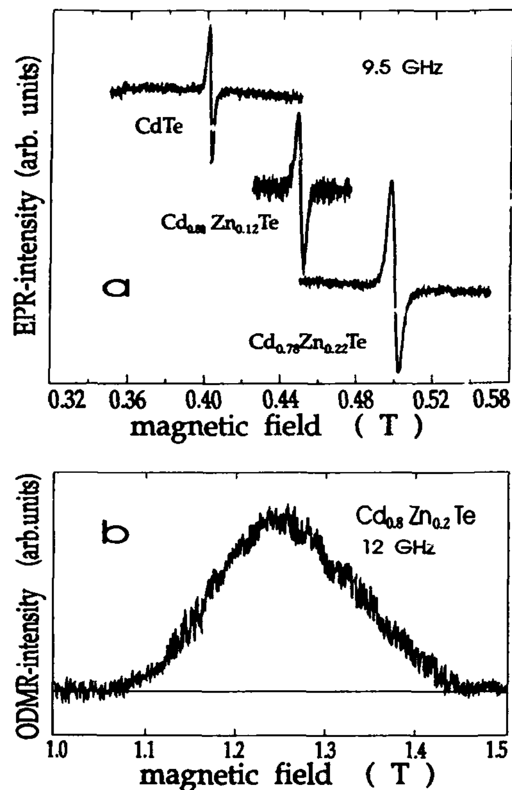

Fig. 7. (a) Electron paramagnetic resonance spectra of the donor resonances in $Cd_{1-x}Zn_xTe$ of different composition x; (b) optically detected magnetic resonance spectrum of the donor resonance in $Cd_{0.18}Zn_{0.82}Te$.

$V_{Te}^0 \rightarrow V_{Te}^+ + e^-$. The corresponding energy level would hence be at $E_v + 0.2$ eV. In the second threshold at 0.92 eV Ni acceptors are involved. The $Ni^{2+/+}$ level is at $E_v + 0.95$ eV [20]. Ni^{2+} is the equilibrium charge state in this high resistive material. The ionization transition $Ni^{2+} \rightarrow Ni^+$ creates free holes, which are trapped by the neutral vacancy and create paramagnetic V_{Te}^+. Since Ni^+ is also paramagnetic this has been confirmed by monitoring the Ni^+ EPR signal.

From these investigations we can conclude that V_{Te} acts as a single donor in CdTe with a level position of 0.2 eV above the valence band. This energy is in reasonable agreement with the onset of the 1.15 eV PL band and the estimate of the corresponding level position described in section 3.2. Furthermore, the behavior of the 1.15 eV PL in the ternary compound supports the involvement of V_{Te}.

3.4. g-values of shallow donors in $Cd_{1-x}Zn_xTe$

The sign of the g-values of shallow donor conduction electrons has been discussed for ZnTe [21]. $g_e = -0.4$ has been measured by Zeeman spectroscopy, whereas $g_e = +0.4$ has been determined from ODMR experiments. In CdTe a negative value of $g_e = -1.7$ was found [22]. For a positive g_e-value in ZnTe, g_e in the alloy $Cd_{1-x}Zn_xTe$ is expected to become zero for a composition of about $x = 0.8$. In a spin resonance experiment this would correspond to a resonance position at infinitely high magnetic field, and is thus unobservable. If g_e is -0.4 in ZnTe we expect for a linear interpolation $g = -0.7$ for $x = 0.8$. Using 12 GHz microwaves, a resonance position would be at 1.25 T. Figure 7 shows our results of EPR and ODMR investigations for the donor resonances in $Cd_{1-x}Zn_xTe$. For the compositions $x = 0.0$, $x = 0.12$ and $x = 22$ we used conventional EPR techniques (9.5 GHz). The resonance shifted from 402.2 mT through 450 mT to 500 mT. This corresponds to $g_e = |1.69|$, $|1.51|$ and $|1.36|$, respectively. For higher compositions of x no donor resonances could be found by conventional EPR, possibly due to the compensation of the material which forces Zn-rich alloys to become p-type. However, for the higher alloy compositions ODMR experiments were successful. The result for the $x = 0.82$ sample is shown in Fig. 7(b): a broad resonance occurs at $g_e = |0.69|$ which was the value estimated above for this alloy composition. Supported by temperature and magnetic field dependent studies of the MCPE of the donor acceptor recombination [23] the dependence of the g_e-values in the $Cd_{1-x}Zn_xTe$ alloy was found to be:

$$g_e(x) = -1.69 + 1.30x \quad (1)$$

A nonlinear dependence of the g_e values as a function

of the alloy composition (observed in $ZnS_{1-x}Se_x$) was not found and nonlinearity is expected to be small [23].

4. Conclusions

To summarize, the ODMR and EPR investigations present a detailed picture of the atomic and optical properties of the A-centers and the tellurium vacancy. A-centers are a single acceptor in CdTe with a level position of 125 meV above the valence band. In $Cd_{1-x}Zn_xTe$ they maintain their properties, following the valence band shift. The V_{Te} defect (F-center) is expected to follow the conduction band shift from CdTe to ZnTe. A luminescence band located at 1.15 eV in CdTe showing such behavior has been observed. Experiments to verify this assignment are currently under way.

References

1 J. Schneider and A. Räuber, *Solid State Commun., 5* (1967) 779.
2 J. M. Smith and W. H. Vehse, *Phys. Lett., A31* (1970) 147.
3 D. J. Dunstan, J. E. Nicholls, B. C. Cavenett and J. J. Davis, *J. Phys. C., 13* (1980) 6409.
4 J. Schneider and A. Räuber, *Solid State Commun., 5* (1967) 779.
5 S. Title, *Phys. Rev., 136* (1964) A300.
6 S. Brunthaler, W. Jantsch, U. Kaufmann and J. Schneider, *J. Phys. Cond. Matter, 1* (1989) 1925.
7 J. Bittebierre and R. T. Cox, *Phys. Rev., B34* (1984) 2360.
8 D. M. Hofmann, P. Omling, H. G. Grimmeiss, B. K. Meyer, K. W. Benz and D. Sinerius, *Phys. Rev., B45* (1992) 6247.
9 D. de Nobel, *Philips Res. Rep., 14* (1959) 361.
10 J. P. Chamonal, E. Molva and J. L. Pautrat, *Solid State Commun., 43* (1982) 801.
11 C. Onodera and T. Taguchi, *J. Cryst. Growth, 101* (1990) 502.
12 E. Molva, J. M. Francou, J. L. Pautrat, K. Saminadayar and L. S. Dangh, *J. Appl. Phys., 56* (1984) 2241.
13 J. J. Hopfield, *J. Phys. Chem. Solids, 10* (1959) 109.
14 E. Molva, J. L. Pautrat, K. Saminadayar, G. Milchberg and N. Magnea, *Phys. Rev., B30* (1984) 3344.
15 R. Mach, P. Flögel, L. G. Sulina, A. G. Arschkin, J. Maege and G. Voigt, *Phys. Status Solidi, (B), 109* (1982) 607.
16 J. M. Langer and H. Heinrich, *Phys. Rev. Lett., 55* (1985) 1414.
17 R. Kernöcker, K. Lischka and L. Palmetshofer, *J. Cryst. Growth, 86* (1988) 625.
18 F. J. Byant and E. Webster, *Phys. Status Solidi, 21* (1967) 315.
19 W. R. Fowler (ed.), *The Physics of Color Centers*, Academic Press, New York, 1968.
20 W. Jantsch, G. Brunthaler and G. Hendorfer, in H. J. v. Bardeleben (ed.), *Defects in Semiconductors*, Materials Science Forum, Trans Tech, Switzerland, Vols. 10-12, 1986, 545.
21 D. J. Robins, P. J. Dean, P. E. Simonds and H. Tews, in S. T. Pantelides (ed.), *Deep Centers in Semiconductors*, Gordon and Breach Science Publishers, New York, 1986, p. 717.
22 A. Nakamura, D. Paget, C. Herman, C. Weisbuch, S. Lampel and B. Cavenett, *Solid State Commun., 30* (1979) 411.
23 D. M. Hofmann, K. Oettinger and B. K. Meyer, submitted to *Phys. Rev.*

Materials Science and Engineering, B16 (1993) 134–138

Positron trapping at native vacancies in CdTe crystals: In doping effect

C. Corbel, L. Baroux, F. M. Kiessling and C. Gély-Sykes*

Laboratoire Positons, Institut National des Sciences et Techniques Nucléaires, Centre d'Etudes Nucléaires Saclay, 91191, Gif-sur-Yvette Cédex (France)

R. Triboulet

Laboratoire de Physique des Solides, CNRS Meudon Bellevue, 1 place A. Briand, 92195 Meudon Cédex (France)

Abstract

Positron lifetime measurements give evidence on vacancies in n-type CdTe crystals. The crystals are either nominally undoped or In doped and grown by the travelling-heater method (THM) or the Bridgman technique. In THM CdTe(In) crystals grown using Te as the solvent, the concentration of vacancies correlates with the concentration of In and electrons. This correlation is in agreement with the model of self-compensation where the In donors are compensated by In–vacancy complexes. In addition to $(V_{Cd}–In)^-$ complexes, it is found that positrons are trapped by negative ions.

1. Introduction

The growth of undoped CdTe crystals leads to materials of various resistivities. CdTe crystals are n or p type depending on the growth conditions as well as the nature and the concentration of residual impurities. Nowadays, highly resistive CdTe is obtained under conditions of p-type growth by doping with an n-type impurity. Native acceptors are thus compensated by the donors introduced, and a semi-insulating material can be obtained by choosing the right donor concentration. Different models, especially in the case of In doping, have been proposed to explain this self-compensation [1–4]. In some of them, vacancies play an important role as the native acceptors [1, 2, 4].

Positrons can be used as a probe of vacancy-type defects in semiconductors by studying their annihilation with electrons or their diffusion properties. We have earlier performed positron lifetime measurements in CdTe(In) crystals [5] to investigate the role of vacancies in the In compensation. We show here that undoped n-type CdTe contain also vacancies and that in addition to V_{Cd}–In complexes CdTe(In) crystals obtained by the travelling-heater method (THM) contain a high concentration of negative ions.

*Permanent address: Laboratoire SRI, Bâtiment de Chimie Physique, Université Pierre et Marie Curie, 11 rue Pierre et Marie Curie, 75231 Paris Cédex 05, France.

2. Experimental details

The CdTe crystals were electrically characterized by Hall effect measurements performed between 5 and 300 K. Pairs of identical samples (4 mm × 4 mm × 1 mm) between which the positron ^{22}Na source is sandwiched were selected to carry out the positron lifetime experiments. Before mounting the samples in the lifetime spectrometer [6], we etched them chemically in a 5% bromine–methanol solutio to remove thin oxidized layers. The lifetime spectra were recorded as a function of temperature from 15 to 300 K by using fast–fast coincidence spectrometers [6] with a full width at half-maximum resolution of 260 or 275 ps associated with a closed-cycle He cryocooler. Each spectrum recorded about 2×10^6 annihilations. After source and background corrections, the lifetime spectra $n(t)$ were analysed as the sum of decaying exponential components $\Sigma_i I_i \exp(-t/\tau_i)$. The intensities I_i ($\Sigma_i I_i = 1$) and the time constants τ_i are determined with a fitting program. The average positron lifetime, *i.e.* the centre of mass of the lifetime spectra, is given by $\tau = \Sigma_i I_i \tau_i$. In our experiments, only one or two components were resolved.

3. Positron lifetime in nominally undoped CdTe

Positron lifetime spectra were measured in p- and n-type CdTe crystals. The CdTe samples were cut from p-type (n-type) ingots grown at CNRS Bellevue by the

0921-5107/93/$6.00

© 1993 – Elsevier Sequoia. All rights reserved

TABLE 1. Calculated values of the cadmium vacancy V_{Cd}^{2-} concentration in undoped and In-doped CdTe crystals

	Growth method	Sample number	Type	n_{300K} ($\times 10^{16}$ cm^{-3})	c_{In} ($\times 10^{16}$ cm^{-3})	τ_{300K} (ps)	k ($\times 10^{8}$ s^{-1})	V_{Cd}^{2-} ($\times 10^{16}$ cm^{-3})
As grown, undoped	Bridgman	CT5.1	p	—	—	289 ± 1	4.5 ± 1.3	0.6 ± ±0.1
As grown, undoped	THM	CTHM4A	p	—	—	285 ± 1	—	—
As grown, undoped	THM	CTHM54	n	0.1 ± 0.01	—	292 ± 1	8.8 ± 1.6	1.1 ± 0.2
As grown, In doped	Bridgman	CT50	n	5 ± 0.5	5	295 ± 1	14.0 ± 2.0	1.8 ± 0.3
As grown, In doped	Bridgman	CT48	n	4.4 ± 0.4	4.4	294 ± 1	12.1 ± 1.9	1.5 ± 0.3
As grown, In doped	Bridgman	CT45	n	20 ± 2	20	293 ± 1	10.4 ± 1.7	1.3 ± 0.2
As grown, In doped	THM	CTHM52	SI	—	3	293 ± 1	10.4 ± 1.7	1.3 ± 0.2
As grown, In doped	THM	CTHM45/27-1	n⁻	0.003	10	304 ± 1	41.7 ± 5.1	5.2 ± 0.6
Annealed, In doped	THM	CTHM45/27-2	n⁺	10 ± 1	10	293 ± 1	10.4 ± 1.7	1.3 ± 0.2

In as-grown THM CdTe(In) the vacancies are associated with In. V_{Cd}^{2-} is calculated from positron lifetime data (see text and eqn. (1)) using a positron trapping coefficient μ of 8×10^{-8} cm^{-3} s^{-1}. In undoped crystals, the charge transitions 2− or − from n- to p-type crystals have been disregarded, which possibly underestimates V_{Cd} in p-type crystals by a factor of 4–10. In the In-doped crystals, c_{In} is taken to be equal to the carrier concentration n_{300K} after decompensation annealing.

THM using Te(Cd) as the solvent and from p-type ingots grown at the Nippon Mining Co. by the Bridgman technique. The electron concentration n_{300K} at 300 is 10^{15} cm^{-3} in the n-type samples.

The average positron lifetime τ remains constant as the temperature decreases from 300 K to 77 K in the p-type crystals as well as in the n-type crystals. We resolve one lifetime in p-type crystals which has the value of 285 ± 1 ps in THM samples and 289 ± 1 ps in Bridgman samples. The average lifetime in n-type CdTe is longer than in p-type CdTe and reaches 292 ± 1 ps (Table 1). Two lifetime components are found in the n-type crystals and the long component τ_2 is 320 ± 5 ps in the temperature range 77–300 K.

The lifetime spectra in CdTe reveal one or two components. This indicates that positrons can annihilate from different states, either delocalized in the bulk or localized in defects. We consider that the two decay constants 285 ± 1 ps and 320 ± 5 ps correspond to positrons annihilating in two well-defined states. The decay constant 320 ± 5 ps appears in several different crystals and over a wide range of temperatures [5]. The decay constant 285 ± 1 ps appears as the limit of decay constants seen at low temperatures in CdTe(In) crystals (Fig. 1). We discuss below the nature of the states which give rise to these two positron lifetimes.

The lifetime of 285 ps is the lowest that we measured in CdTe crystals. We attribute it to positron annihilation either in the bulk or at negative ions. There is increasing evidence that, in semiconductors, positrons annihilate with the same lifetime even if they are delocalized in the bulk or localized at Rydberg states around negatively charged acceptors [7, 8]. The bulk positron lifetime τ_b in CdTe is not yet well established. According to different experiments, its value is 278 ± 2 ps [9] or 283 ± 1 ps [10]. These values are in agreement with theoretical estimates [11]. Using the local-density approximation, Puska [11] found that, at room temperature, τ_b in CdTe varies from 277 to 282 ps depending on whether electron densities are taken from atomic superposition or "self-consistent" linear muffin tin orbital calculations with the atomic spherical approximation.

The lifetime of 320 ps is the longest that we have measured in as-grown CdTe crystals. Lifetimes in the range of 325 ± 5 ps have also been measured in CdTe crystals and after electron irradiation [9]. This lifetime characterizes positron annihilation in vacancy-type defects where the trapped positrons see an electron density lower than in the bulk [6]. The ratio $\tau_2/\tau_b = 320/285 = 1.11$ is comparable with the ratio of vacancy lifetime *vs.* bulk lifetime in other semiconductors. The lifetime of a positron trapped in a Cd vacancy (or in a Te vacancy) has been calculated to be around 293 ps (or 304 ps) whereas the lifetime of a positron trapped at a divacancy is around 384 ps [11]. Our conclusion is that the lifetime of 320 ps is due to a native monovacancy. The monovacancy is either isolated from or associated with another point defect.

We consider the charge state of the vacancy to discuss which isolated vacancy—V_{Cd} or V_{Te}—traps positrons. Positrons are positively charged and consequently positron trapping at positive vacancies is not observed. On the contrary, positron trapping has clearly been observed in neutral or negative vacancies in semiconductors [12]. In CdTe, Te vacancies are believed to be positive and Cd vacancies to be neutral (V_{Cd}^{0}) or negatively charged (V_{Cd}^{-} and V_{Cd}^{2-}) depending on the position of the Fermi level [1]. Several workers have proposed that the ionization level 2− or

– of the V_{Cd} vacancy is located at about $E_c - 0.7$ eV [1] (E_c is the minimum of the conduction band). The expected charge state in n-type CdTe crystals is then V_{Cd}^{2-}. This leads us to conclude that the isolated monovacancies which can give rise to the lifetime of 320 ps is V_{Cd}^{2-}.

The trapping rate k into the vacancies can be calculated in the framework of the trapping model [6] by using the formula

$$k = \frac{\tau - \tau_b}{\tau_b(\tau_2 - \tau)} \quad (1)$$

where τ is the average positron lifetime, τ_b is the bulk lifetime (285 ps) and τ_2 is the vacancy lifetime (320 ps). In n-type crystals, the trapping rate is then 8.8×10^8 s^{-1}. The vacancy concentration is obtained by dividing the trapping rate k by the trapping coefficient μ in a vacancy. This last quantity is difficult to determine since very few techniques give reliable information on the vacancy concentration. In ref. 5, we have estimated for the trapping coefficient in $(V_{Cd}\text{-In})^-$ a value of about 8×10^{-8} $cm^3\,s^{-1}$. It can be reasonably compared with the values estimated by calculations for a negative vacancy [12]. Using this value, we find that the V_{Cd}^{2-} concentration is about 10^{16} cm^{-3} in n-type crystals.

It is noticeable that in p-type CdTe crystals no (Te-saturated THM) or only a few (Bridgman) vacancies are seen by positrons. In such crystals, we could expect V_{Cd} to be present [13]. The situation is different in p-type HgTe or $Hg_{0.8}Cd_{0.2}Te$ grown by THM under Te-saturated conditions where it can be observed that in some crystals the vacancy concentration increases with increasing hole concentration at 77 K [14, 15].

4. Positron lifetime in In-doped crystals

Positron lifetime measurements were performed on as-grown Bridgman as well as on as-grown and annealed Te-saturated THM CdTe(In) samples. The electron concentration increases in THM crystals when they undergo a so-called decompensation annealing at 700 °C under a saturated Cd vapour pressure for 3 h. In contrast, it remains unchanged in the Bridgman crystals. Thereafter, the In concentration is taken to be equal to the carrier concentration.

4.1. Bridgman CdTe(In) crystals

The Bridgman ingots were grown at CNRS Bellevue from melts containing an In concentration of 1.6×10^{17}, 3.25×10^{17} or 1.3×10^{18} cm^{-3}. For the samples cut from the first two ingots, the electron concentrations n_{300K} are 5×10^{16} cm^{-3} and 4.4×10^{16} cm^{-3} respectively. For the samples cut from the third ingot, it is four times higher: 2×10^{17} cm^{-3}. We found that τ at 300 K is the same within 3 ps for the three pairs of samples and is on average 294 ± 1 ps (Table 1). The spectra can be resolved into two components and the long component is 319 ± 4 ps. We concluded that the Bridgman CdTe(In) crystals contain vacancies as Cd-saturated THM n-type CdTe crystals. The vacancy concentration is independent of electron and In concentrations.

4.2. Te-saturated THM CdTe(In) crystals

A weakly n^--type and a semi-insulating (SI) ingot were obtained using In-doped Bridgman ingots which were successively regrown several times by THM [4] using Te as the solvent. In the n^--type samples, n_{300K} varies from 4.0×10^{12} to 1.4×10^{14} cm^{-3} for samples which have been cut from the same wafer. It increases to 2.1×10^{15} cm^{-3} for crystals cut from a wafer located 5 mm from the other. This difference of more than two orders of magnitude in n_{300K} for crystals of the same region in the ingot illustrates the difficulty in obtaining as-grown n-type crystals with well-controlled carrier concentrations. In the SI crystals, the resistivity is 1.2×10^{10} Ω cm at 300 K. After decompensation annealing, the crystals from the weakly n^- type and SI ingots are n^+ type with n_{300K} equal to 1.0×10^{17} cm^{-3} and 3×10^{16} cm^{-3} respectively.

In Fig. 1 the upper curve is characteristic of the positron lifetime behaviour as a function of temperature in the as-grown n^--type THM samples. In three pairs of samples, we observe that the average lifetime is constant below 60 K and above 250 K and increases from 285 ± 1 to 304 ± 1 ps between 60 and 250 K. Two components are satisfactorily resolved in the spectra from 115 to 300 K. The long component τ_2 increases noticeably by 20 ps between 115 and 250 K and then reaches a plateau at 320 ± 5 ps.

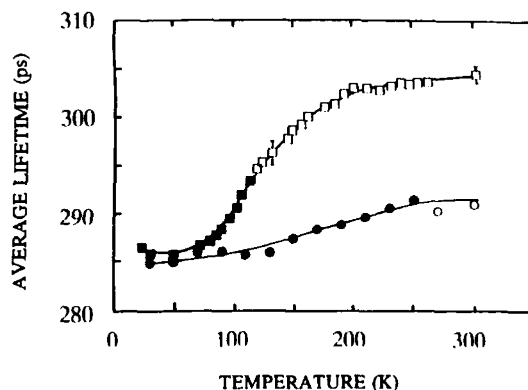

Fig. 1. Average positron lifetime as a function of temperature in as-grown (■) and annealed n-type (●) CdTe(In). The lifetime spectra are resolved into one component (■, ●) or two components (□, ○).

The lower curve in Fig. 1 is obtained after the decompensation annealing. The main feature is the strong decrease in the average lifetime which, above 250 K, is 10 ps lower after annealing than before. There are two components above 250 K but it is difficult to resolve them.

In the as-grown n^--type CdTe(In) crystals, the lifetime of 320 ps is detected between 250 and 350 K. In the annealed n^+-type CdTe(In) crystals, the decomposition in two components is difficult but we can analyse the spectra into two components by fixing the long component at 320 ps. This means that we can assume that there is also a positron annihilation state corresponding to 320 ps in the annealed n^+-type CdTe(In) crystals. The strong decrease in τ in the annealed n^+-type CdTe(In) crystals indicates that the positron trapping rate at the 320 ps vacancy defect is lower after annealing than before. By considering that the trapping coefficient of the 320 ps vacancy defect is the same in the as-grown and annealed crystals, we obtain that the ratio of the concentration c_b of defects before annealing to the concentration c_a of defects after annealing is directly given by the ratio of the trapping rates. The calculations (see eqn. (1)) give a value of 0.21 for the ratio c_a/c_b. This fraction is at least two orders of magnitude greater than that calculated in the self-compensation models involving only V_{Cd} vacancies. It is difficult to imagine that the trapping coefficient in the 320 ps vacancy defect could increase at 300 K by two orders of magnitude after annealing. Also, our conclusion is that the positron behaviour cannot be explained in the models of In compensation involving only V_{Cd} vacancies. In ref. 5, we have shown that the positron behaviour is consistent with the self-compensating models involving V_{Cd}–In complexes in addition to V_{Cd} vacancies. We have proposed that the positrons detect the V_{Cd} vacancies in the annealed crystals and the V_{Cd} vacancies and/or the V_{Cd}–In complexes in the as-grown crystals. In the complexes, although the position of the In atoms with respect to the V_{Cd} vacancy is not well known, it is likely to be a second neighbour. We can then expect that the positron lifetimes in the complex and in the vacancy are very close. The Fermi level at 300 K is above $E_c - 0.3$ eV in all the CdTe(In; n) crystals. The V_{Cd} vacancies and V_{Cd}–In complexes are then believed to be in the charged state V_{Cd}^{2-} and $(V_{Cd}\text{–In})^-$ respectively [1]. Consequently, we attribute the lifetime of 320 ps to $(V_{Cd}\text{–In})^-$ or V_{Cd}^{2-}.

In the SI CdTe(In) crystals, the average lifetime is low: 293 ps. There are two components above 250 K but it is difficult to resolve them. In ref. 5, we have shown that the decrease in τ from as-grown CdTe(In; n) to CdTe(In; SI) crystals matches the decrease in the concentration of $(V_{Cd}\text{–In})^-$ vacancies expected in the self-compensation model [2]. This supports further our identification of the vacancies to the complexes V_{Cd}–In in CdTe(In). Our conclusion that V_{Cd}–In complexes are involved in the compensation of carriers in THM CdTe(In) samples is different from that reached in Bridgman CdTe(In) samples by using time-differential perturbed angular correlation (PAC) studies. PAC studies performed on In-implanted CdTe [16] have previously shown that about 60% of the In atoms were located to a metal site and associated with an intrinsic defect believed to be a Cd vacancy. However, in diffused or quenched Cd-rich Bridgman CdTe(In) samples [17], another defect, the nature of which is not identified, has been observed to be associated to In and most probably plays a role in the carrier compensation.

In the as-grown n^--type CdTe(In) crystals, the transition between the lifetime spectra with one component and the lifetime spectra with the long lifetime at 320 ps occurs over a wide range of temperature between 70 and 250 K. This transition cannot be correlated with the ionization of the donor level since, as seen in Fig. 2, the ionization of the donor level takes place below 100 K in the as-grown n^--type samples. As mentioned above, negative ions are able to trap positrons at Rydberg states with a weak binding energy. We explain the positron behaviour in the as-grown n^--type crystals by the competition between trapping in negative ions and the 320 ps vacancies. Once trapped at the negative ions, positrons annihilate with a lifetime close to the bulk lifetime. As the temperature increases, the fraction of positrons annihilating in these shallow traps decreases owing to thermal detrapping, and more trapping at the vacancy-type defects takes place. The acceptors are either residual impurities or intrinsic defects (interstitials or antisites). By fitting the τ curves in Fig. 1 with a trapping model taking into account the negative ions and the vacancies [18], we can determine the concentration of the negative ions and the positron

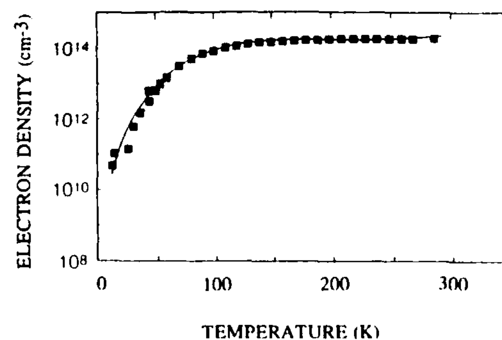

Fig. 2. The carrier concentration as a function of temperature in as-grown n-type CdTe. The increase in the carrier concentration occurs below the increase in the positron lifetime in Fig. 1.

binding energy. The main result is that the amount of negative ions is quite high, about $(3 \pm 2) \times 10^{17}$ cm^{-3}, in as-grown CdTe(In; n) samples and that the binding energy is 33 ± 2 meV. The temperature dependence in the annealed CdTe(In; 2×10^{17}) sample can also be fitted with the same concentration of acceptors and the same binding energy. Our conclusion is that there is a high concentration of negative ions which seems to be rather insensitive to the decompensation annealing.

5. Conclusion

Positron lifetime measurements give direct evidence of monovacancies in n-type CdTe crystals. In Te-saturated THM CdTe(In) crystals their concentration decreases after decompensation annealing. These monovacancies are characterized by a lifetime of 320 ± 5 ps and assumed to be V_{Cd}^{2-} either isolated from or in CdTe(In) crystals associated with the donor In. As the temperature decreases, trapping in negative ions also takes place in CdTe(In) crystals. These acceptors of the ion type are either residual impurities or intrinsic defects.

Acknowledgments

The authors are grateful to Nippon Mining Co. for providing the CdTe crystals. They thank Dr. Yves Marfaing for valuable discussions and Gérard Didier and Abou Katty for their contribution to experimental work.

References

1 S. S. Chern, H. R. Vydyanath and F. A. Kröger, *J. Solid State Chem., 14* (1975) 33.
2 Y. Marfaing, *Prog. Crystal Growth Charact., 4* (1981) 317.
3 J. L. Pautrat, N. Magnea and J. P. Faurie, *J. Appl. Phys., 53* (1982) 8668.
4 T. Ido, A. Heurtel, R. Triboulet and Y. Marfaing, *J. Phys. Chem. Solids, 48* (1987) 781.
5 C. Gély-Sykes, C. Corbel and R. Triboulet, *Solid State Commun., 80* (1991) 79.
6 P. Hautojärvi, *Positrons in Solids, Top. Curr., Phys.*, Vol. 12, Springer, New York, 1979.
7 K. Saarinen, P. Hautojärvi, A. Vehanen, R. Krause and G. Dlubek, *Phys. Rev. B, 39* (1989) 5287.
8 C. Corbel, F. Pierre, P. Hautojärvi, K. Saarinen and P. Moser, *Phys. Rev. B, 41* (1990) 10632.
9 P. Moser, J. L. Pautrat, C. Corbel and P. Hautojärvi, *Proc. 7th Int. Conf. on Positron Annihilation, New Delhi, 1985*, World Scientific, 1985, pp. 753.
A. Sen Gupta, P. Moser and J. L. Pautrat, *Phys. Lett. A, 141* (1989) 429.
10 C. Gély, C. Corbel and R. Triboulet, *C. R. Acad. Sci., Paris, Ser. II, 309* (1989) 179.
11 M. J. Puska, *J. Phys.: Condens. Mater., 3* (1991) 3455; personal communications, 1992.
12 M. Puska, C. Corbel and R. Nieminen, *Phys. Rev. B, 41* (1990) 9980.
13 M. Hage Hali, B. Yaacoub, S. Mergui, M. Samimi, B. Biglari and P. Siffert, *Appl. Surf. Sci., 50* (1991) 377.
14 C. Gély-Sykes, C. Corbel, R. Triboulet, F. Soisson and L. Baroux, *Ann. Chim. Fr., 16* (1991) 541.
15 R. Krause, A. Klimakow, F. M. Kiessling, A. Polity, P. Gille and M. Schenk, *J. Cryst. Growth, 101* (1990) 512.
16 R. Kalish, M. Deicher and G. Schatz, *J. Appl. Phys., 53* (1982) 4793.
17 D. Wegner and E. A. Meyer, *J. Phys. C, 1* (1989) 5403.
18 C. Corbel, F. Pierre, K. Saarinen, P. Hautojärvi and P. Moser, *Phys. Rev. B, 45* (1992) 3386.

New method for the determination of V_{Cd} concentrations in p-CdTe

H. Zimmermann, R. Boyn, P. Rudolph, J. Bollmann and A. Klimakow
Fachbereich Physik der Humboldt-Universität zu Berlin, Invalidenstrasse 110, O-1040 Berlin (Germany)

R. Krause
Fachbereich Physik der Martin-Luther-Universität Halle, Friedmann-Bach-Platz 6, 4020 Halle (Germany)

Abstract

If p-CdTe crystals are dipped in an $AgNO_3$ solution followed by storage of the crystals at 300 K, one can observe a strong decrease in the hole concentration after some days. This is obviously due to fast diffusion of silver, which takes place most probably via interstitial sites (Ag_i), and is consistent with the increase in the degree of compensation detected by photoluminescence (PL) analysis. Deep-level transient spectroscopy investigations have shown the appearance of a new hole trap at 0.47 eV after the silver diffusion procedure, which is tentatively assigned to the Ag_i deep donors.

If the silver treatment is applied to p-CdTe crystals annealed in a tellurium atmosphere, the concentration of Ag_{Cd} impurities grows owing to the defect reaction $V_{Cd} + Ag_i \rightarrow Ag_{Cd}$ as can be seen from the enhancement of the corresponding (A^0, X) line in the PL spectra. Positron annihilation measurements with the same crystals have confirmed this reaction by the observation of a decrease in the average positron lifetime before the silver treatment (about 295 ps) to a value of about 285 ps which occurs after some hundred hours.

By means of a quantitative PL analysis we are able to estimate the concentration of isolated V_{Cd} in p-CdTe from the increased Ag_{Cd} concentration. Other possible defect reactions are discussed on the basis of our PL investigations.

1. Introduction

So far, there has been no definite information about the manifestation of isolated cadmium vacancies (V_{Cd}) in CdTe in spectroscopic data. This is in contrast, for example, with the well-established assignments of many photoluminescence (PL) lines to other types of defect centres (including substitutional impurities and vacancy–donor complexes (see for example refs. 1 and 2)) in that material.

We have developed an indirect method for the detection of V_{Cd} in PL spectra. This method makes use of the extremely fast diffusion of silver at room temperature [3, 4], which leads to the transformation of V_{Cd} into Ag_{Cd} and enables the latter to be detected by means of the corresponding bound-exciton and donor–acceptor pair lines. Since the silver diffusion should occur through interstitial sites, the relevant reaction will be

$$Ag_i + V_{Cd} \longrightarrow Ag_{Cd} \qquad (1)$$

In the following we demonstrate by a combination of experimental techniques (PL, IR absorption, deep-level transient spectroscopy (DLTS) and positron annihilation) that this reaction really takes place and can be used to estimate V_{Cd} concentrations.

2. Experimental details

The p-type CdTe single crystals were grown in pyrolytically coated quartz ampoules by the conventional vertical Bridgman method with a slight tellurium excess (less than 10^{-2} at.%) [5].

The room-temperature diffusion of silver was started by dipping (30 s at 300 K) the samples into a 1% aqueous solution of $AgNO_3$ and subsequent rinsing in distilled water. Our results show that in samples of thickness about 1 mm a uniform distribution of silver is reached after some hundred hours (see Section 3.1 and Fig. 1).

The PL measurements were made (i) on the surfaces exposed to the $AgNO_3$ solution as well as (ii) on surfaces produced by cleaving the samples after a near-homogeneous silver distribution had been established. The PL spectra were measured, with the specimen immersed in liquid helium, using a GDM 1000 double monochromator (Carl Zeiss Jena). The excitation of the PL was performed by means of the 514.5 nm line of an ILA 120 Ar^+ laser or the 647.1 nm line of an ILK 120 Kr^+ laser.

For the DLTS, Schottky diodes were prepared using the same crystals as for the IR absorption measurements and evaporating gold contacts. To make one of

0921-5107/93/$'.00

© 1993 – Elsevier Sequoia. All rights reserved

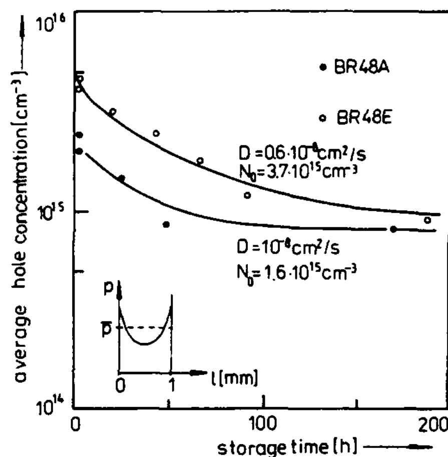

Fig. 1. Dependence of the average hole concentration p in two p-CdTe samples (thickness, 1 mm) on the time after an $AgNO_3$ treatment: ——, calculated (see text).

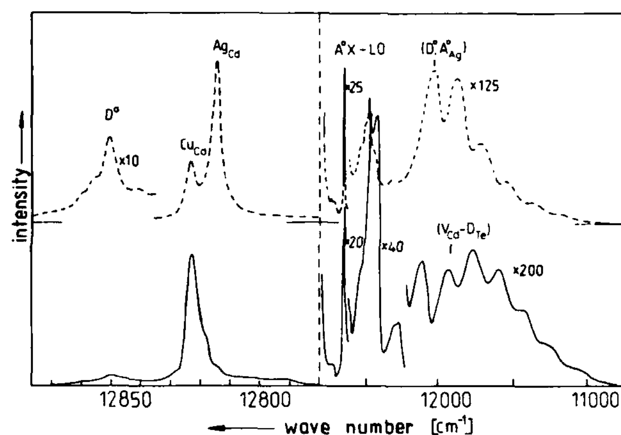

Fig. 2. PL spectra of a tellurium-annealed p-CdTe sample (BR 33III) before (——) and after (- - -) an $AgNO_3$ treatment at 1.8 K under Kr^+ laser excitation, showing the formation of Ag_{Cd} centres (reaction (1)).

the contacts ohmic, a higher density of defects was produced at the corresponding area by mechanical grinding before gold evaporation [6].

The positron annihilation investigations were performed at room temperature by means of a conventional fast–fast lifetime spectrometer with a time resolution of 230 ps (full width at half-maximum). $^{22}NaCl$ (20 μCi) was used as the positron source.

3. Results and discussion

3.1. Hole concentration

The in-diffusion of silver leads to a decrease in hole concentration p. As will be shown later, this is due to partial compensation of the dominant acceptors by the Ag_i deep donors. The average hole concentrations p (average over the diffusion profile; see inset in Fig. 1) were determined by IR transmission measurements at room temperature, in the range of intravalence band transitions [5]. Figure 1 shows the strong decrease in p with increasing storage time after the $AgNO_3$ treatment, for two typical CdTe crystals. This result is in complete agreement with the results in ref. 3. For the diffusion coefficient D for this process, one obtains $D \approx 10^{-8}$ cm^2 s^{-1} (Fig. 1) from the solution of the time-dependent diffusion equation under the assumption of non-depletive silver reservoirs at the surfaces, with a boundary concentration depending on the hole concentration of the crystals.

3.2. Defects in tellurium-annealed crystals

To produce high V_{Cd} concentrations, various p-CdTe crystals were annealed in a tellurium atmosphere under equilibrium conditions at temperatures between 625 and 800 °C for 4 weeks and then quenched to room temperature.

In Fig. 2 we compare the PL spectra of an annealed crystal before and after a silver diffusion procedure. Clearly, the (A^0, X) and the donor–acceptor pair lines due to the Ag_{Cd} acceptor appear after the $AgNO_3$ treatment of the sample. Obviously, this behaviour can be explained by the occurrence of reaction (1).

For a more quantitative discussion we use our method described in ref. 7 to estimate the concentrations of the neutral acceptors and donors from intensity ratios of the corresponding bound-exciton lines to the free-exciton first-longitudinal-optical-phonon satellite. The results (including data for as-grown crystals) are summarized in Table 1 together with the free-carrier concentrations obtained by the IR extinction analysis [5] and Hall measurements. After the silver diffusion we observe a remarkable increase in the Ag_{Cd} concentration in all annealed samples covering the range $(1\text{–}5)\times 10^{14}$ cm^{-3}. In agreement with the discussion in Section 3.1, we find that the silver diffusion leads to a decrease in p for all these samples because of an increasing degree of compensation. Since by our method [7] we see only the neutral fraction of the acceptors, the total Ag_{Cd} concentrations should be higher than the values given in Table 1. From the behaviour of Ag_{Cd} in the as-grown crystals (see Section 3.3) we estimate deviations by factors of between 15 and 20. On this basis we can estimate an upper limit of about $(8\text{–}10)\times 10^{15}$ cm^{-3} for the concentration of the isolated V_{Cd} in our annealed crystals (which corresponds to complete occupation of the vacancies by silver atoms).

Positron annihilation measurements with the same crystals were performed at room temperature to

TABLE 1. Concentrations of neutral (substitutional) acceptors and donors from the photoluminescence analysis [7] including the hole concentrations from the IR extinction analysis [5] and from Hall measurements for tellurium-annealed and as-grown p-CdTe crystals

Sample	Concentration ($\times 10^{15}$ cm^{-3})									
	Before Ag diffusion					After Ag diffusion				
	Ag_{Cd}	Cu_{Cd}	Na_{Cd} or Li_{Cd}	D^0	p	Ag_{Cd}	Cu_{Cd}	Na_{Cd} or Li_{Cd}	D^0	p
Te-annealed										
BR 52T10	—	2.4	—	—	?	0.15	1	—	—	0.033
BR 52T12	—	1	—	—	1.2	0.25	1	—	—	?
BR 33III	—	0.6	—	—	?	0.8	0.16	—	2.3	?
As-grown										
HBM1[a]	—	4.0	—	1	1.7	0.5	1	—	0.8	0.05
BR 39E	0.6	4	—	0.35	10	0.04	2	—	1.5	2.3
BR 41E	1.1	5	1.1	0.8	8	0.05	1.8	—	1.0	—
BR 41A	0.05	1.3	1.5	2.6	0.2	0.05	1.3	0.7	2.6	0.2

—, not detectable; ?, no information.
[a]In this sample a high V_{Cd} concentration was established owing to extraordinarily rapid cooling after crystal growth.

monitor directly the decrease in the V_{Cd} concentration according to (1). This method which has already been applied to CdTe [8, 9] is based on the fact that in the presence of V_{Cd} the average positron lifetime τ is higher than the "bulk" material ($\tau_b = 285$ ps [9]).

Figure 3 shows the dependence of the average positron lifetime τ on the storage time after $AgNO_3$ treatment. Before this treatment, τ for the annealed p-CdTe was found to be 295 ps, which is clearly above τ_b. Already after short times a distinct decrease in τ is observed. After 400 h, τ tends to a stationary value equal to τ_b. The decrease in the average lifetime is a result of the disappearance of the V_{Cd} or their complexes because of filling by silver atoms. To estimate the concentration of V_{Cd} we need the positron-trapping coefficient μ_v. We shall use the value 8.4×10^{-8} cm^3 s^{-1}, which has been determined for the $(V_{Cd}\text{-In})^-$ complex in ref. 9 and is close to the value 6×10^{-8} cm^3 s^{-1} obtained in ref. 10 for negatively charged metal vacancies in $Hg_{1-x}Cd_xTe$. Then the sum of V_{Cd} and the $(V_{Cd}\text{-D})$ concentrations may be calculated using the relation [10]

$$C = \frac{1}{\mu_v \tau_b} \frac{\bar{\tau} - \tau_b}{\tau_2 - \bar{\tau}} \qquad (2)$$

Here τ_2 is a characteristic positron lifetime referring to a given type of vacancy defect. We put $\tau_2 = 330$ ps according to data obtained in ref. 8. With our experimental results we estimate that $C \approx 2 \times 10^{16}$ cm^{-3} for the initial defect concentrations (V_{Cd} and $(V_{Cd}\text{-D})$) in the annealed p-CdTe crystals. The small difference between the V_{Cd} concentrations deduced from PL and

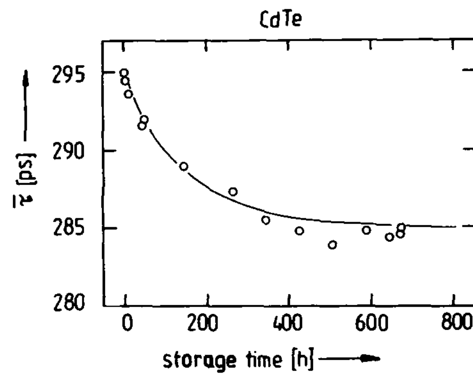

Fig. 3. Plot of the average positron lifetime τ *vs.* time at $T = 300$ K after $AgNO_3$ treatment for a tellurium-annealed CdTe sample (BR 52T11).

positron annihilation measurements can be explained by the additional detection of V_{Cd} complexes in the second case. In Section 3.4, we shall give support for this argument by the observation of new lines in the PL spectra of our annealed and $AgNO_3$-treated crystals which we ascribe to defect reactions between Ag_i and V_{Cd} complexes.

3.3. Defects in as-grown crystals

Figure 4 shows the effect of silver diffusion on the PL spectrum in the bound-exciton and pair transition ranges for an as-grown crystal. Obviously there is a decrease in the Ag_{Cd} (A^0, X) line intensity corresponding to a decrease in the neutral fraction of the Ag_{Cd} concentration (Table 1). We conclude that (i) in the as-grown crystals the V_{Cd} concentration is negligible, so that reaction (1) is not significant and (ii) an additional

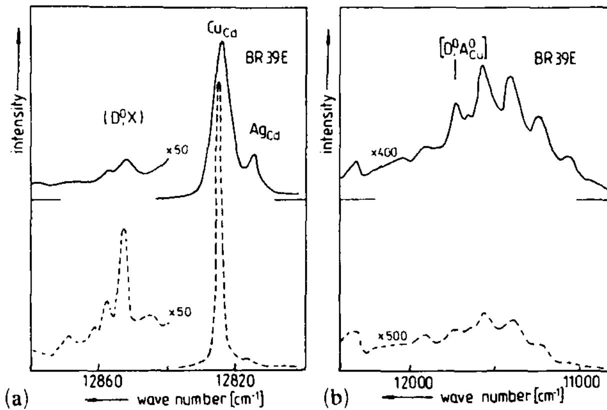

Fig. 4. PL spectra of an as-grown p-CdTe sample (BR 39E) before (——) and after (- - -) $AgNO_3$ treatment in (a) the excitonic and (b) the donor–acceptor pair transition range (Kr^+ laser excitation; $T = 1.8$ K).

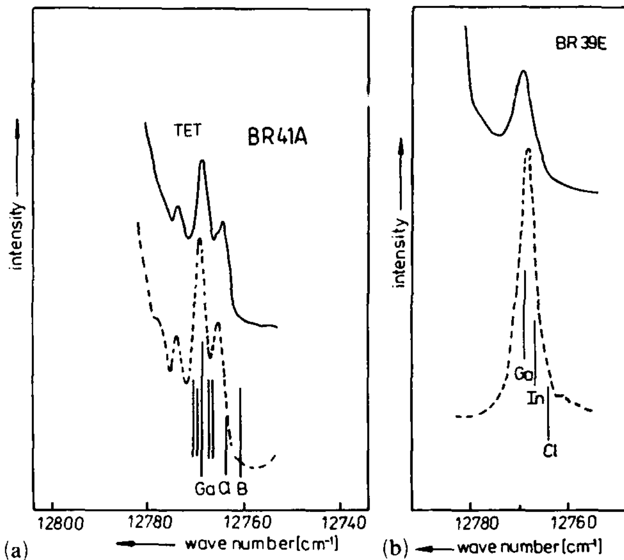

Fig. 5. PL spectra at $T = 1.8$ K of as-grown p-CdTe crystals in the spectral range of TET before and after $AgNO_3$ treatment: (a) under interband excitation (Kr^+ laser) before (——) and after (- - -) $AgNO_3$ treatment; (b) under intradonor (dye laser) excitation at 12852 cm^{-1} before (——) and after (- - -) $AgNO_3$ treatment.

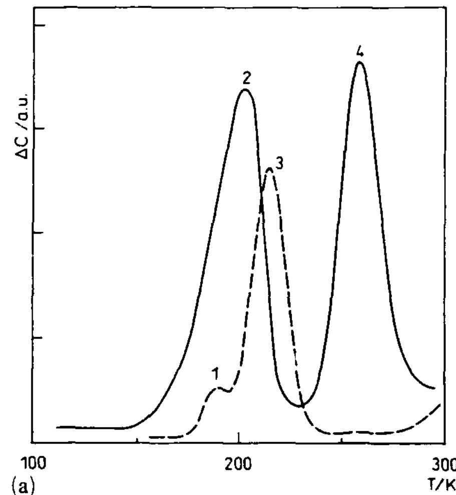

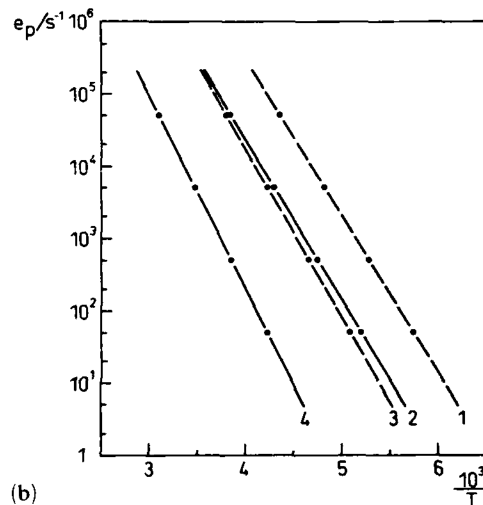

Fig. 6. (a) Deep-level transient spectrum of a p-CdTe sample (BR 41E) before (——) and after (- - -) $AgNO_3$ treatment (rate window at $e_p = 500$ s^{-1}) (arbitrary units). (b) Arrhenius plot of the hole emission rate before (——) and after (- - -) $AgNO_3$ treatment.

amount of the Ag_{Cd} impurities present before the diffusion is compensated by the Ag_i donors. These conclusions are supported (a) by positron annihilation measurements which show that the average lifetime τ agrees with the "bulk" value τ_b in the as-grown state and (b) by the observation that the neutral fractions of other types of acceptors (Cu_{Cd}, Li_{Cd}, Na_{Cd}) also tend to decrease owing to the diffusion process (Table 1).

The observed narrowing of the bound-exciton linewidths after silver diffusion is probably due to decoration and "filling" of crystal defects (*e.g.* dislocations and grain boundaries) by silver atoms, which should give rise to a reduction in the internal strain caused by these defects. Further investigations of this problem are planned by us.

To find out whether Ag_i acts as a shallow donor we looked for possible diffusion-induced changes in the range of two-electron transitions (TETs) in the PL spectrum. In Fig. 5(a) we show, as an example, the emission spectra of sample BR 41A under conventional laser excitation. From the coincidence of the observed TET lines before and after silver diffusion we conclude that the Ag_i impurities do not act as shallow donors. In Fig. 5(b) we present analogous results for a sample with a higher hole concentration (sample BR 39E, Table 1), which have been obtained with intradonor (dye-laser) excitation. Within experimental accuracy (limited by line broadening and background effects) we again do not see the appearance of a new

type of shallow donor. The assignment of the TET lines to the donor species was made on the basis of work in ref. 11.

To obtain information on the appearance of diffusion-induced deep donor levels we performed DLTS measurements before and after the silver treatments (Fig. 6(a)). In this figure, one recognizes two peaks (hole traps) in the initial state of the sample. After the silver diffusion these are absent and two new hole traps are observed. By variation of the rate window and the corresponding Arrhenius plot of the hole emission rate (Fig. 6(b)) the thermal activation energies E_a can be deduced. The energies of the untreated sample are $E_a(2)=0.43$ eV and $E_a(4)=0.54$ eV. The trap labelled 2 in this work can be clearly identified as the corresponding trap H_3 observed in refs. 12 and 13. The additional hole trap labelled 4 is not mentioned in the literature to our knowledge. After the silver diffusion the new traps 3 and 1 with the activation energies $E_a(3)=0.47$ eV and $E_a(1)=0.44$ eV appear. We think that the high concentration level 3 is due to a silver-related defect, probably the Ag_i donor. Thus we identify $E_a(3)$ with the separation between the corresponding donor level and the top of the valence band.

3.4. Formation of complexes

In some samples we found diffusion-induced changes in the low energy part of the bound-exciton spectrum which is usually attributed to complex centres. This shows that the silver treatment occasionally leads to defect reactions additional to (1).

In some cases we observed that after silver diffusion a new band at 1.555 eV (12 550 cm^{-1}) appears. This band could be also detected in as-grown CdTe crystals intentionally doped with silver during the Bridgman growth process (Fig. 7). We believe that this band is associated with a complex centre containing silver. It should also be noted that in many samples we observed a band at 1.541 eV (band A at 12 430 cm^{-1} in Fig. 7); this band was always found to vanish owing to the $AgNO_3$ treatment.

In tellurium-annealed samples we detected two diffusion-induced lines at 1.5837 eV and 1.5809 eV (X_3^{Ag} and X_4^{Ag} in Fig. 8). The X_4^{Ag} line is close to the bound-exciton line X_2^{Ag} at 1.5815 eV reported by Monemar *et al.* [14] for silver-doped CdTe crystals after aging for about 1 year. In ref. 14 the X_2^{Ag} line was tentatively assigned to an (Ag_{Cd}–Ag_i) complex. From the fact that our new lines (with their corresponding phonon replicas) were observed only in annealed crystals, we infer the occurrence of defect reactions between V_{Cd} complexes and Ag_i.

Acknowledgments

The authors are indebted to M. Wienecke and C. Albers from the Humboldt-Universität Berlin for the Hall and the IR transmission measurements. The posi-

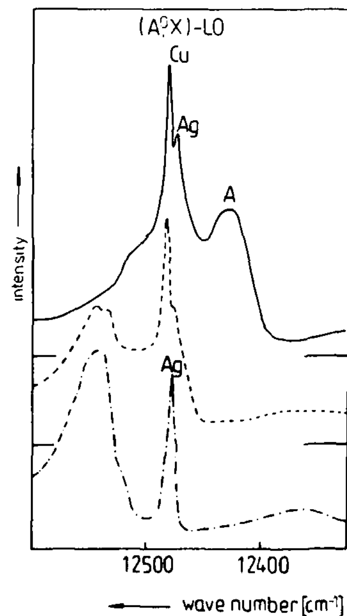

Fig. 7. PL spectra due to complex centres for sample BR 41E before (——) and after (- - -) $AgNO_3$ treatment (Kr^+ laser at $T=1.8$ K); — · —, spectrum of silver-doped sample during crystal growth.

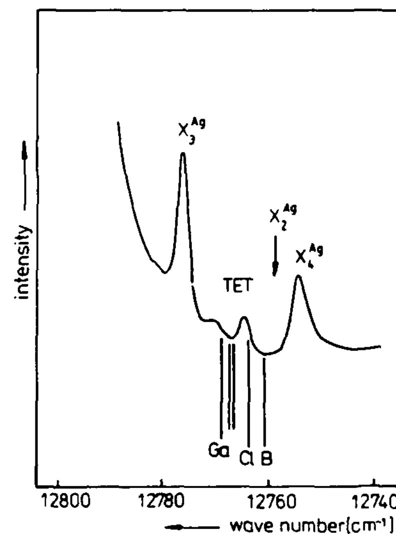

Fig. 8. PL spectrum of sample HBM1 after $AgNO_3$ treatment at 1.8 K under Kr^+ laser excitation, demonstrating the appearance of two new lines (X_3^{Ag} and X_4^{Ag}) due to complex formation. In this sample a high V_{Cd} concentration was established owing to extraordinarily rapid cooling after crystal growth.

tron annihilation investigations were performed by Th. Drost from the Martin-Luther-Universität. This project was supported by the Deutsche Forschungsgemeinschaft (Bonn).

References

1 J. L. Pautrat, J. M. Francou, N. Magnea, E. Molva and K. Saminadayar, *J. Cryst. Growth, 72* (1985) 194.
2 B. K. Meyer, W. Stadler, D. M. Hofmann, P. Omling, D. Sinerius and K. W. Benz, *J. Cryst. Growth, 117* (1992) 656.
3 M. A. Kovalets, N. I. Kuchma, E. S. Nikonjuk, I. P. Chiokan and M. M. Skvydka, *Fiz. Khim. Obrab. Mater., 3* (1987) 125.
4 J. Tregilgas and B. Gnade, *J. Vac. Sci. Technol. A, 3* (1985) 156.
5 U. Becker, P. Rudolph, R. Boyn, M. Wienecke and I. Utke, *Phys. Status Solidi A, 120* (1990) 653.
6 M. Wienecke, personal communication, 1992.
7 H. Zimmermann, R. Boyn, C. Michel and P. Rudolph, *Phys. Status Solidi A, 118* (1990) 225.
8 C. Gély, C. Corbel and R. Triboulet, *C. R. Acad. Sci., Paris, 309* (1989) 179.
9 C. Gély-Sykes, C. Corbel and R. Triboulet, *Solid State Commun., 80* (1991) 79.
10 R. Krause, A. Klimakow, F. M. Kiessling, A. Polity, P. Gille and M. Schenk, *J. Cryst. Growth, 101* (1990) 512.
11 J. M. Francou, K. Saminadayar and J. L. Pautrat, *Phys. Rev., 41* (1990) 12035.
12 R. T. Collins and T. C. McGill, *J. Vac. Sci. Technol. A, 1* (1983) 1633.
13 J. P. Laurenti, G. Bastide, M. Rouzeyre and R. Triboulet, *Solid State Commun., 67* (1988) 1127.
14 B. Monemar, E. Molva and Le Si Dang, *Phys. Rev. B, 33* (1986) 1134.

Materials Science and Engineering, B16 (1993) 145–150

Effect of the $\{h11\}$ orientations and polarities of GaAs substrates on CdTe buffer layer structural properties

A. Tromson-Carli
Laboratoire de Physique des Solides de Bellevue, CNRS, 1 Place A. Briand, F-92195 Meudon Cedex (France)

G. Patriarche
Laboratoire de Physique des Matériaux, CNRS, 1 Place A. Briand, F-92195 Meudon Cedex (France)

R. Druilhe, A. Lusson, Y. Marfaing and R. Triboulet
Laboratoire de Physique des Solides de Bellevue, CNRS, 1 Place A. Briand, F-92195 Meudon Cedex (France)

P. D. Brown and A. W. Brinkman
Department of Physics, Durham University, Durham DH1 3LE (UK)

Abstract

CdTe layers were grown by metallo-organic chemical vapour deposition on GaAs substrates of different $(h11)$ orientations and polarities. The morphology and structural properties of the epilayers were investigated using several techniques, namely scanning electron microscopy, transmission electron microscopy and double crystal X-ray diffraction. The best results were obtained for epitaxy on (211) A and (311) B substrate orientations. The occurrence of twinning in the cases of opposite polarity, i.e. (211) B and (311) A, was attributed to the presence of single dangling bonds on the etched substrate surfaces.

1. Introduction

The high crystalline perfection, relatively low price and its ready availability make GaAs an ideal substrate for (Hg,Cd)Te (MCT) heteroepitaxy. However, the large 14% lattice mismatch between GaAs and MCT makes it necessary to use a buffer layer. The structure and morphology of CdTe buffer layers grown on GaAs are highly dependent on the substrate orientation [1–3]. This is also true for CdTe and GaAs homoepitaxy [4, 5]. CdTe grown on {111}-oriented substrates contains a high density of lamellar twins lying parallel to the interface [6, 7], and sometimes has a high doping level [8–10]. The commonly used {100} GaAs substrate orientation is also far from ideal for the heteroepitaxy of CdTe: slightly misoriented GaAs{100} substrates give rise to surface features and polycrystalline defects, *e.g.* hillocks [8, 10, 11], which severely affect device fabrication [12]. To overcome the problems of defects a number of different solutions have been tried in attempts to grow CdTe buffer layers and to obtain MCT layers of good crystalline quality [5, 8, 13–15].

This paper reports a systematic investigation of the influence of $\{h11\}$ GaAs substrate orientation and polarity on the structural properties and surface morphology of CdTe layers grown by metallo-organic vapour phase epitaxy (MOVPE). Growth on these low index surfaces allows the study of several parameters, such as surface shape, III–V atom ratio and surface polarity. The surface polarity of the $\{h11\}$ GaAs substrates was determined without ambiguity by electron microscopy [16, 17]. The structural quality of the CdTe epitaxial layers was assessed by double crystal X-ray diffraction (DCXRD), electron channelling pattern (ECP) and cross-sectional transmission electron microscopy (TEM). In some instances, complementary information was obtained from photoluminescence.

2. Epitaxial growth

CdTe epitaxial layers 3–4 μm thick were grown on GaAs substrates of different orientations, including 2° off {100}, $\{h11\}$ A and $\{h11\}$ B, with $h = 2$, 3 and 5. The layers were grown at atmospheric pressure in an MR

0921-5107/93/$6.00

© 1993 - Elsevier Sequoia. All rights reserved

Semicon MOVPE reactor under nominally identical conditions at 365 °C. Dimethylcadmium (DMCd) and diisopropyltelluride (DipTe) were used with a II-VI ratio of 0.7 in the vapour phase in a total hydrogen flow of 4000 cm^3 min^{-1}. The alkyl partial pressures were about 10^{-4} atm.

The {*h*11} GaAs substrates were supplied ready polished by Sumitomo, while the {100} GaAs substrates were obtained from Wacker, also ready polished. Before loading into the reactor, the substrates were cleaned using trichloroethylene and methanol, etched in a mixture of $2NH_4OH$, $1H_2O_2$ and $8H_2O$, and then rinsed in high purity water. Immediately prior to growth, the substrates were heated to 365 °C in the reactor in a hydrogen flow. This treatment results in an arsenic-rich surface as shown in a number of works [18–20].

3. Results and discussion

Table 1 shows some results of structural characterization for the different orientations of the GaAs substrates used: {100}, {211} A, {211} B, {311} A, {311} B, {511} A and {511} B. This table includes as a reference a CdTe layer grown on a [100] misoriented 2° off towards (100) GaAs substrate. In this case, the [100] layer orientation was stabilized by interposing a thin (100 nm) ZnTe layer [21]. The surface morphology was determined by SEM observations with magnification in the range 4000–10 000×. The angle between the layer and the {*h*11} substrate plane was deduced from the ECPs and verified by DCXRD which also provided the rocking curve widths. We now consider in more detail the different orientations studied.

3.1. {311} surfaces

On the A face, the surface morphology shows a pyramid-like surface cut by lines which presuppose twinning (Fig. 1(a)). This twinning was apparent on TEM micrographs made on a $(0\bar{1}1)$ plane perpendicular to the interface (Fig. 2(a)). Numerous twins are visible lying in {111} planes. A high magnification permitted us to evaluate a tilt angle of about 5°–5.5° between the layer and the substrate (Fig. 2(b)).

We found two different values of the rocking curve width in two orthogonal directions. The smallest value (175″) occurred when the axis of the rocking curve was parallel to the $(0\bar{1}1)$ cleavage plane. In the orthogonal direction the rocking curves were found to be asymmetric and broader, indicating that the layer was tilted on the substrate by about 5° and more disoriented around this direction.

On the B face, the surface morphology is rough and does not show lines indicative of twinning (Fig. 1(b)). The TEM micrographs are also quite different from those taken on the A face (Fig. 3(a)). Very few twins are visible but numerous dislocations are present at the interface because of the lattice mismatch between the layer and the substrate. On a high magnification micrograph very few stacking faults are encountered (Fig. 3(b)). The layer is tilted with respect to the substrate by about 5°, as on the A face. We also found on this face two different values of the rocking curve width for two orthogonal measurement directions. The tilt occurs around the $[0\bar{1}1]$ direction, with a broad rocking curve indicating misorientation around this direction. Also, the rocking curve width is affected by the high density of dislocations. It should be noted that the layer tilt of 5° found on both A and B surfaces is smaller than the theoretical value of 8° needed to match perfectly the two crystals. This difference is accounted for by the

TABLE 1. Structural characteristics of CdTe epitaxial layers grown on GaAs substrates of various crystallographic orientations

GaAs substrate	CdTe layer thickness (μm)	Asymmetry around [011] (degree)	DCRC width (arc sec)	SEM morphology	TEM cross-section
(211) A	2.85	4	175	No polycrystalline defects, small facets	No twins, dislocations: 10^8–10^9 cm^{-2}
(211) B	3.5	4	280	Irregular, rough surface	Twins, very few dislocations
(311) A	3.75	5.5	175	Lines on top of pyramids	Twins, very few dislocations
(311) B	3.2	5.5	300	Rough surface	Stacking faults, numerous dislocations
(511) A	3.7	8	500	Numerous lines, faceted pyramids	–
(511) B	3.7	0	600	Very rough surface, a few lines	–
(100)	3	0	300	High faceted pyramids, polycrystalline defects	No twins, dislocations: 10^9 cm^{-2}

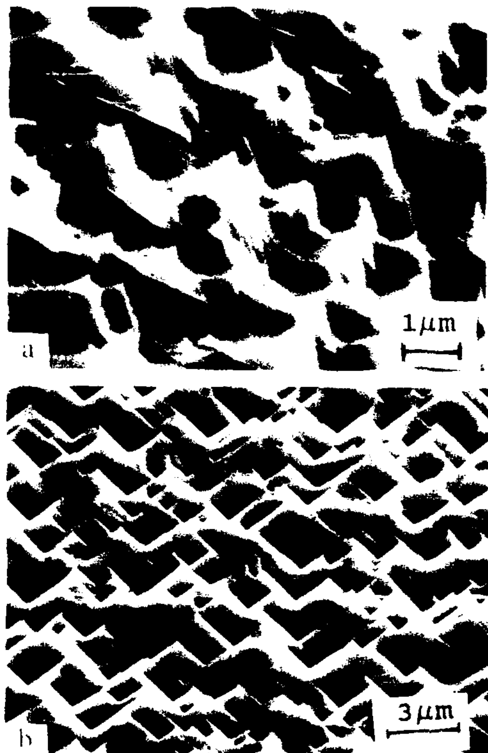

Fig. 1. Surface morphology of CdTe layers grown on (a) (311) A GaAs substrate and (b) (311) B GaAs substrate.

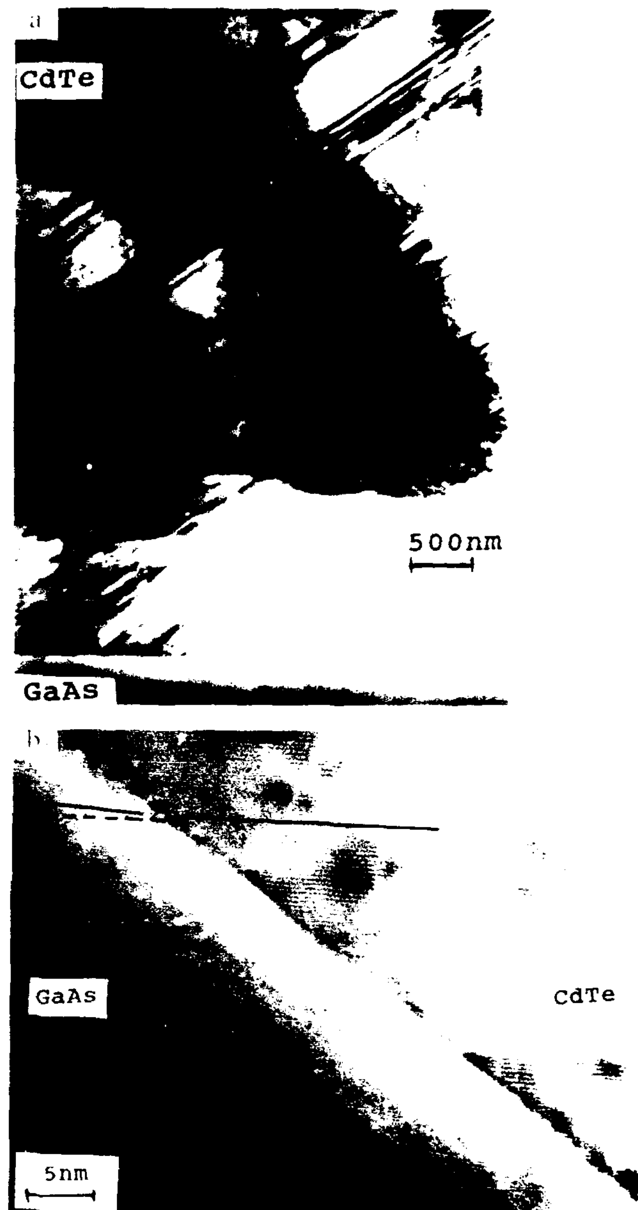

Fig. 2. Cross-sectional TEM micrographs of a CdTe epitaxial layer grown on (311) A GaAs substrate and observed in the (011) plane under (a) low magnification and (b) high magnification.

presence of interface defects: dislocations for the B face and heavy twinning for the A face [22].

The above observations can be understood by considering the type of atoms present at the surface and the bonds—both established and potential—around the surface atoms. The atomic structures of ideal A and B surfaces projected on the (01̄1) plane are presented in Fig. 4. They are composed of terraced or staircase-like structures in which the (100) planes form the terraces or treads, and the (111) planes the risers [23]. Atoms located at the outer edges of the terraces are bonded to the lattice by two bonds and those located at the inner edges are bonded by three bonds. Assuming a tetrahedral configuration they can be considered to bear double dangling bonds and single dangling bonds, respectively, in the (01̄1) plane. This configuration will tend to fix the location of an epitaxial atom on a B face to a position (number 1 in Fig. 4b) between the atom with the single dangling bond and one of the two neighbouring atoms with the double dangling bonds. In this case, twinning is avoided as it is observed experimentally. The (311) A face behaves differently because of its termination by gallium atoms, which are more easily removed by chemical etching (Section 2). Considering the different types of bonding of the surface atoms (Fig. 4 a), it thus appears that the uppermost atoms with only two established bonds are preferentially removed. This leaves at the surface gallium atoms triply bonded to the lattice. Thus an epitaxial atom will be bonded with a single bond. The three other bonds are not fixed and this can induce twinning, in accordance with our observations.

In conclusion, the (311) B face leads to better epitaxy than does the (311) A face.

3.2. (511) surfaces

The morphologies of the layers grown on the A and B faces look like those grown on the (311) A and

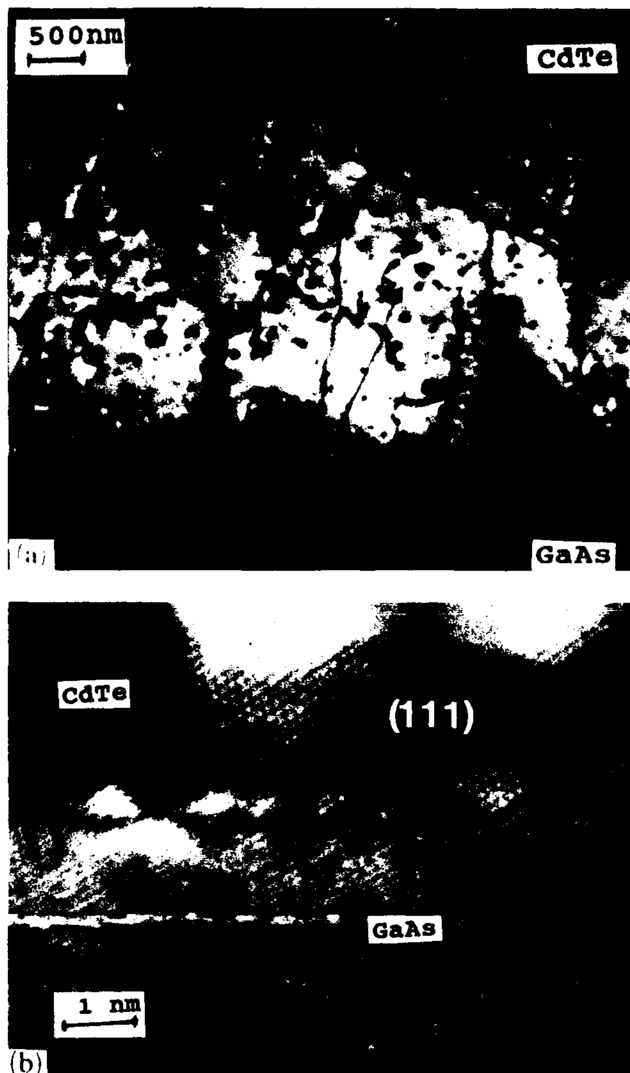

Fig. 3. Cross-sectional TEM micrographs of a CdTe epitaxial layer grown on (311) B GaAs substrate and observed in the $(0\bar{1}1)$ plane under (a) low magnification and (b) high magnification.

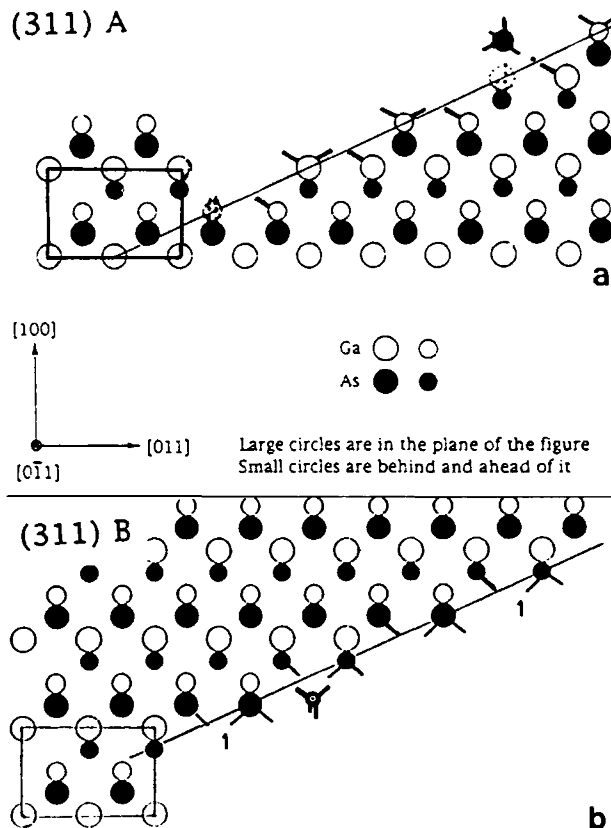

Fig. 4. Atomic structure of (a) an ideal (311) A surface and (b) an ideal (311) B surface projected on the $(0\bar{1}1)$ plane.

(311) B faces respectively. However, the (511) A layer shows more linear features, suggesting a very significant twinning. Furthermore, the layer is tilted by about 8° around the $[0\bar{1}1]$ direction. These two observations seem to indicate that epitaxial atoms bind with the single dangling bond of the gallium atoms lying just below the ideal surface (position 1 in Fig. 5(a)), while many gallium surface atoms have been removed by etching (position 2). The (511) B layer is neither tilted nor twinned. In this case, epitaxy should occur by bonding to two neighbouring arsenic atoms (positions 1 and 2 in Fig. 5(b)). Broad rocking curves were measured in both cases, indicating a high level of misorientation in the epilayers.

In conclusion, both (511) A and (511) B faces are not good substrate orientations for growing high quality CdTe buffer layers.

3.3. {211} surfaces

On the A face, the surface morphology is not smooth but is regularly faceted and does not show polycrystalline defects (Fig. 6). No twinning is observed on cross-sectional TEM micrographs. However, numerous dislocations, about 10^8 cm^{-2}, rise from the interface through the buffer layer. The ECP picture indicates a tilt of 4°. The layer surface orientation is between (211) A and (311) A owing to some rotation around $[0\bar{1}1]$. This asymmetry is verified using DCXRD measurements in two orthogonal directions. The smallest rocking curve width (180″) occurs when the measurement axis is parallel to the cleavage plane.

On the B face, the surface morphology is very rough. The ECP shows poorly defined Kikuchi lines owing to the roughness and a layer misorientation of 4° around $[0\bar{1}1]$ as on the A surface. The rocking curve is also asymmetric around this direction and diffraction widths are larger than those measured on the (211) A layer. The cross-sectional TEM micrograph indicates that twinning occurs at the interface (Fig. 7).

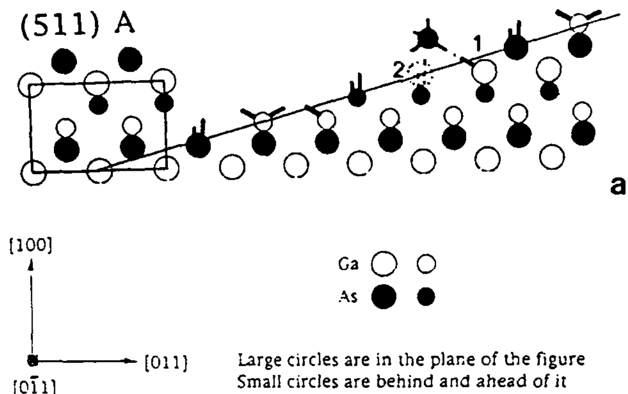

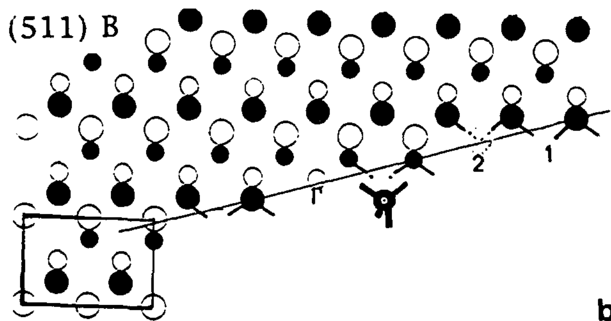

Fig. 5. Atomic structure (a) of an ideal (511) A surface and (b) an ideal (511) B surface projected on the (0$\bar{1}$1) plane.

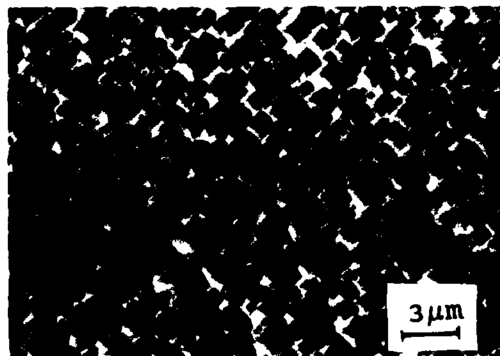

Fig. 6. Surface morphology of a CdTe layer grown on (211) A GaAs substrate.

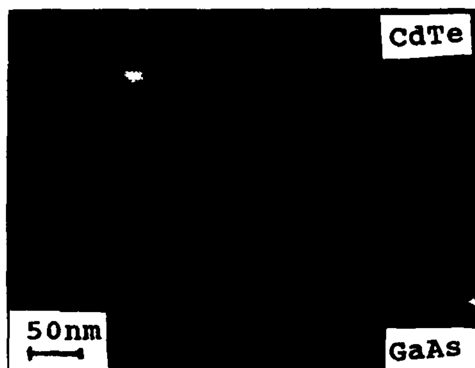

Fig. 7. Cross-sectional TEM micrograph of a CdTe epitaxial layer grown on (211) B GaAs substrate.

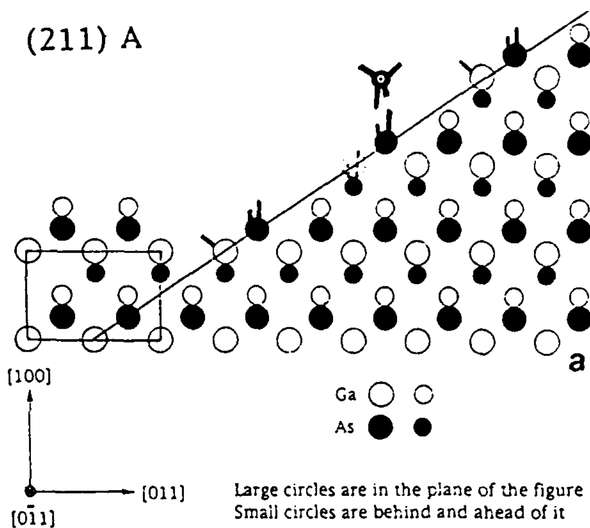

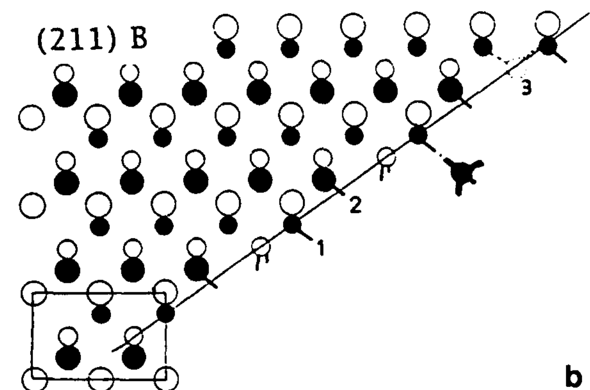

Fig. 8. Atomic structure of (a) an ideal (211) A surface and (b) an ideal (211) B surface projected on the (0$\bar{1}$1) plane.

Considering, in the same spirit as above, the atoms and bonds present on the {211} surface, it is seen that an ideal (211) A or (211) B surface possesses an equal number of gallium and arsenic atoms, but the bonds are not identical (Fig. 8). On the A face, when gallium atoms have been removed by etching, arsenic atoms with double dangling bonds remain on the surface, these being able to induce epitaxy without twinning. On the B face, gallium atoms can be easily removed by etching because of their double dangling bonds. Arsenic atoms then remain with single dangling bonds, as in the position 1 and position 2 in Fig. 8(b). These bonds may induce twins, which are indeed visible on the cross-sectional TEM micrograph (Fig. 7). An epitaxial atom may also be deposited in position 3. Hence, the existence of three possibilities for atom bonding induces lattice distortion and explains the large rocking curve widths (see Table 1).

4. Conclusions

It has been shown that several $\{h11\}$ substrate orientations are suitable for growing epitaxial CdTe layers, with the $\{211\}$ and $\{311\}$ faces especially suitable. For these orientations, the coverage of the surface is different from that of $\{111\}$ planes and is variable, because each $(h11)$ surface is formed with a different number of steps in $\{100\}$ planes. Moreover, the influence of the A and B polarity is great due to the possible formation of single dangling bonds on the surface after preferential etching of gallium atoms in the chemical treatments performed before growth.

We have thus demonstrated that the (211) A and (311) B surfaces have a polarity suitable to avoid twinning. In contrast, twinning is induced on the opposite surfaces (211) B and (311) A where single dangling bonds are present at the surface.

The structural properties associated with the different orientations are also confirmed by photoluminescence measurements. The best resolved excitonic photoluminescence spectrum was obtained on the (211) A layer. In general, additional deep transitions related to structural defects are observed on $\{h11\}$ B surfaces.

References

1 G. N. Pain, C. Sandford, G. K. G. Smith, A. W. Stevenson, D. Gao, L. S. Wielunski, S. P. Russo, G. K. Reeves and R. Elliman, *J. Cryst. Growth, 107*(1991) 610.
2 G. Cinader, A. Raizman and A. Sher, *J. Vac. Sci. Technol. B,* 9(1991) 1634.
3 M. D. Lange, R. Sporken, K. K. Mahavadi, J. P. Faurie, Y. Nakamura and N. Otsuka, *Appl. Phys. Lett., 58* (1991) 1988.
4 P. Gibart, A. Tromson-Carli, Y. Monteil and A. Rudra, *J. Phys. C, 50* (1989) C5-529.
5 F. Desjonqueres, A. Tromson-Carli, P. Cheuvart, R. Druilhe, C. Grattepain, A. Katty, Y. Marfaing and R. Triboulet, *J. Cryst. Growth, 107*(1991) 626.
6 P. D. Brown, J. E. Hails, G. J. Russel and J. Woods, *Appl. Phys. Lett., 50* (1987) 1144.
7 H. Shtrikman, M. Oron, A. Raizman and G. Cinader, *J. Electron. Mater., 17*(1988) 105.
8 R. Druilhe, F. Desjonqueres, A. Katty, A. Tromson-Carli, D. Lorans, L. Svob, A. Heurtel, Y. Marfaing and R. Triboulet, *J. Cryst. Growth, 101* (1990) 73.
9 R. Korenstein, P. Hallock, B. Macleod, W. Hoke and S. Oguz, *J. Vac. Sci. Technol. A, 8* (1990) 1039.
10 P. Capper, C. D. Maxey, P. A. C. Wiffin and B. C. Eaton, *J. Cryst. Growth, 96* (1989) 519.
11 I. B. Bhat and S. K. Ghandhi, *J. Cryst. Growth, 75* (1986) 241.
12 S. M. Johnson, M. H. Kalisher, W. L. Ahlgren, J. B. James and C. A. Cockrum, *Appl. Phys. Lett., 56* (1990) 946.
13 L. M. Smith, C. F. Byrne, D. Patel, P. Knowles, J. Thompson, G. T. Jenkin, T. Nguyen-Duy, A. Durand and M. Bourdillot, in *Proc. MCT US Workshop, 1989, J. Vac. Sci. Technol. A, 8* (1990) 1078.
14 J. B. Mullin, S. J. C. Irvine, J. Giess, J. J. Gough, A. Royle and M. C. L. Ward, in *Future Infrared Detector Materials, SPIE Proc., 1106* (1989) 17.
15 D. W. Snyder, S. Mahajan, M. Brazil, E. I. Ko, P. J. Sides and R. E. Nahory, *Appl. Phys. Lett., 58* (1991) 848.
16 P. Brown, K. Durose, G. J. Russel and J. Woods, *J. Cryst. Growth, 101* (1990) 211.
17 P. D. Brown, A. Tromson-Carli, R. Druilhe, R. Triboulet and Y. Marfaing, *Proc. 10th European Congress on Electron Microscopy, EUREM '92, Granada, Spain, 1992.*
18 T. Oda and T. Sugano, *Jpn. J. Appl. Phys., 15* (1976) 1317.
19 M. J. Johnson, K. J. Kuhn and R. B. Darling, *Appl. Phys. Lett., 58* (1991) 1893.
20 J. Massies and J. P. Contour, *J. Appl. Phys., 58* (1985) 806.
21 G. Cohen-Solal, F. Bailly and M. Barbe, *Appl. Phys. Lett., 49* (1986) 1519.
22 G. Patriarche, *Thesis*, University of Paris VI, 1992, unpublished.
23 R. C. Sangster, in E. K. Willardson and H. L. Goering (eds.), *Compound Semiconductors*, Reinhold, London, 1962, p. 241.

Scanning tunneling microscope investigation of the effects of CdTe substrate preparation on molecular beam epitaxially grown *n*-CdTe layers

M. Ehinger, M. Wenzel, T. Litz and G. Landwehr
Physikalisches Institut der Universität Würzburg, Am Hubland, D-W-8700 Würzburg (Germany)

Abstract

Because of the small lattice mismatch, CdTe is used as a substrate material for the molecular beam epitaxial (MBE) growth of CdTe and $Hg_{1-x}Cd_xTe$. For investigations of its structural surface properties on a nanometer scale, which greatly influence homogeneous growth, a scanning tunneling microscope is well suited. The surface roughness was determined after different surface preparation steps. Mechanically polished samples show a surface roughness of about 1000 Å, caused by the polishing powder. By chemico-mechanical polishing it was possible to reduce roughness to about 60 Å. Typical surface structures with lateral dimensions of up to 200 Å and vertical dimensions of 40 Å remained after etch-polishing. Further, we studied the effect of substrate polishing on the roughness of the MBE grown layers and found a strong correlation between substrate and layer roughness even for thick layers (> 1 μm). The dependence of the growth temperature on the roughness of *n*-type CdTe layers is under investigation and the first results are presented.

1. Introduction

There is a great interest in II–VI materials and their applications, especially in the field of new devices and narrow gap detectors. The possibility of tuning the bandgap by different *x*-values in $Hg_{1-x}Cd_xTe$ turns this material into the technologically most interesting representative of the II–IV semiconductors. For its growth, epitaxial techniques such as molecular beam epitaxy (MBE) [1, 2] or metal-organic chemical vapor deposition (MOCVD) [3, 4] are commonly used. The good lattice matching of CdTe has led to the use of this material as a substrate; however, the quality of the commercially available crystals is not sufficient. Therefore, an often-used procedure is to grow a buffer layer of CdTe on the substrate before growing the layer of $Hg_{1-x}Cd_xTe$ [5, 6].

In the following, we report upon the roughness of commercially acquired substrates and the effect of different polishing procedures measured with a scanning tunneling microscope (STM) described in ref. 7. The measuring parameters for the topographies which were taken in the constant current mode were −4 V bias voltage and 100 pA tunneling current. The (100) nominally undoped *p*-type CdTe substrates were bought from II–VI Inc. and contacted on the back side [8].

2. Experimental details and results

The roughness of the delivered substrates, which are mechanically prepolished by the manufacturer with 0.1 μm alumina powder, was measured as a first step. Typical corrugations in the shape of long scratches [8] with a height of up to 1200 Å (see Fig. 1(a)) were found. These can be explained as the effect of the grains of the polishing powder. Thus, less damaging polishing steps are absolutely necessary for the treatment of CdTe surfaces. For this purpose, bromine-containing etch solutions are widely used [9–11]. Figure 1(b) shows a cross-section of a surface etched for 2 min in an aqueous solution consisting of 25 vol.% HBr and 0.6 vol.% bromine. The deep scratches disappeared and the remaining surface structure is dominated by hillocks with a typical length of 550 Å and a height of 200 Å. This clearly reduced roughness (compared to that of Fig. 1(a)) could only be decreased slightly by heating the substrates for 15 min at 350 °C in an ultra high vacuum, as this is the typical preheating procedure before growth (see Fig. 1(c)). However, this roughness is not suited for MBE growth of epitaxal layers and therefore the etching performance of a bromine–methanol-based solution [9–11] was studied. We used a solution consisting of 61.5 vol.% methanol, 38.5 vol.% ethylene glycol and 2 vol.% bromine in which the

0921-5107/93/$6.00

© 1993 – Elsevier Sequoia. All rights reserved

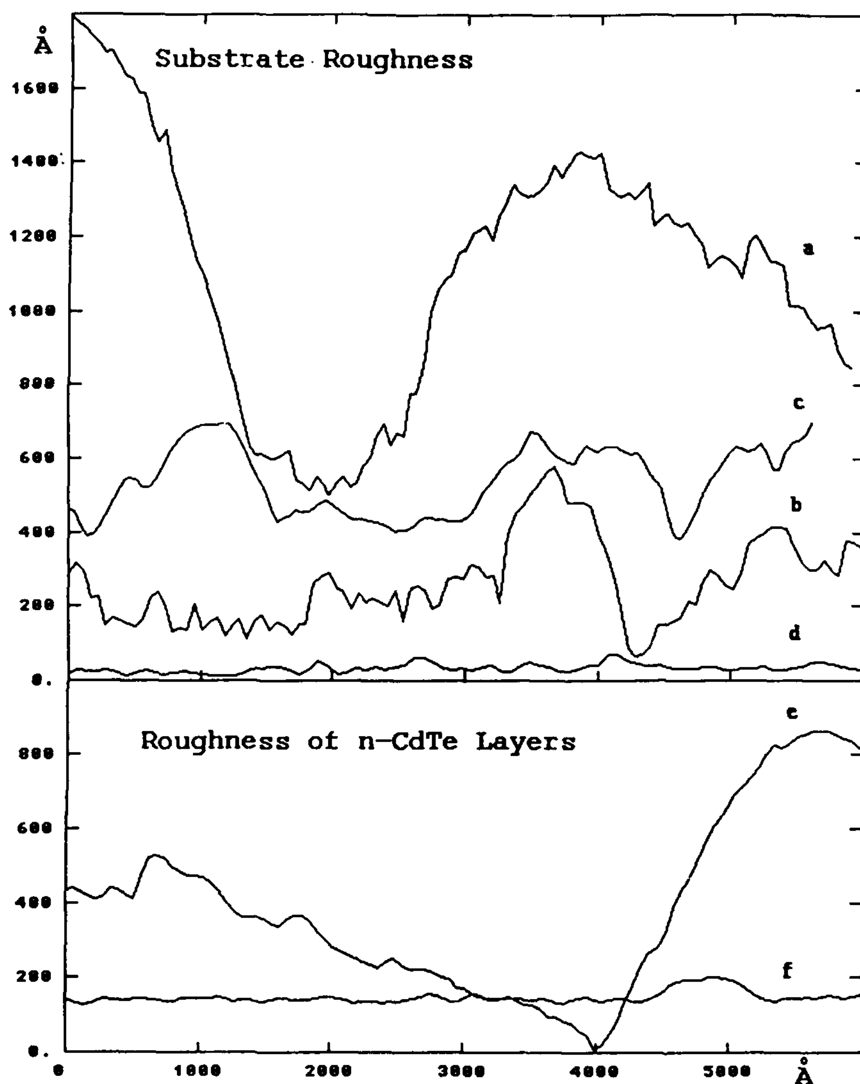

Fig. 1. Cross-sections of a mechanically polished substrate (a), an HBr-etched substrate (b) and an HBr-etched sample after heating (c). Cross-sections (d), (e) and (f) are taken from Figs. 2, 3 and 4, respectively, each going from point A to B. The upper curves correspond to substrates after different treatments, while the lower curves (e) and (f) denote cross-sections of grown layers (see text). The curves are shifted against each other for clarity.

samples were polished for 5 min. This procedure leaves a featureless surface (see Fig. 2) with a roughness of less than 60 Å (see Fig. 1(d)). Again the preheating procedure did not affect the surface structure but the roughness increased to a typical value of 120 Å.

The roughness of CdTe layers grown on mechanically prepolished and bromine-methanol-treated substrates under the same growth conditions were found to show a strong correlation with the roughness of the substrate (see Figs. 3 and 4). This is remarkable as the thickness of the grown layers was about 2 μm and, therefore, much thicker than the observed corrugations on the substrate. The layer grown on the prepolished substrate (see Fig. 3) shows a hillock-like topography with a typical hillock diameter of 700 Å (Fig. 1(e)). Once more, in the upper right part of the figure there is a scratch with a depth of almost 1000 Å very similar to the scratches found on the mechanically prepolished substrates (see Fig. 1). We came to the conclusion that the large scale, substrate surface structure-like scratches dominate the roughness of the grown layers and are not smoothed significantly during the growth process.

On the contrary, the layer grown on the polished substrate shows two-dimensional growth in large areas with a roughness below 25 Å. It is only disturbed by single islands with a height of 70 Å (see Fig. 1(f)). This indicates that a low substrate roughness is extremely important for the growth of epilayers with a high

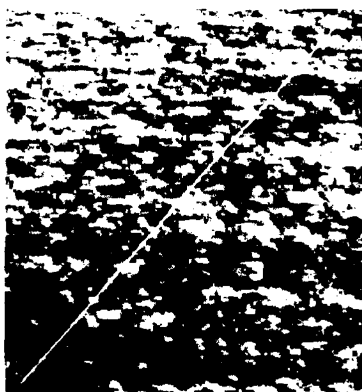

Fig. 2. STM grayscale image of bromine–methanol-etched substrate (6500 Å×6500 Å). The z-scale from the lowest (darkest) to the highest (brightest) point is 120 Å. See also Fig. 1(c) for a cross-section from point A to B.

Fig. 3. STM grayscale image of a 2 μm-thick CdTe layer grown on an unpolished substrate (5300 Å× 5300 Å). The z-scale from the lowest (darkest) to the highest (brightest) point is 1000 Å. See also Fig. 1(e) for a cross-section from point A to B.

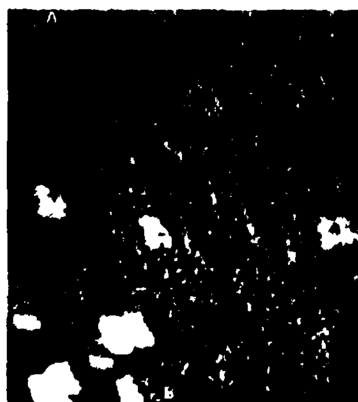

Fig. 4. STM grayscale image of a 2 μm-thick CdTe layer grown on a polished substrate (7000 Å× 7000 Å). The z-scale from the lowest (darkest) to the highest (brightest) point is 180 Å. See also Fig. 1(f) for a cross-section from point A to B.

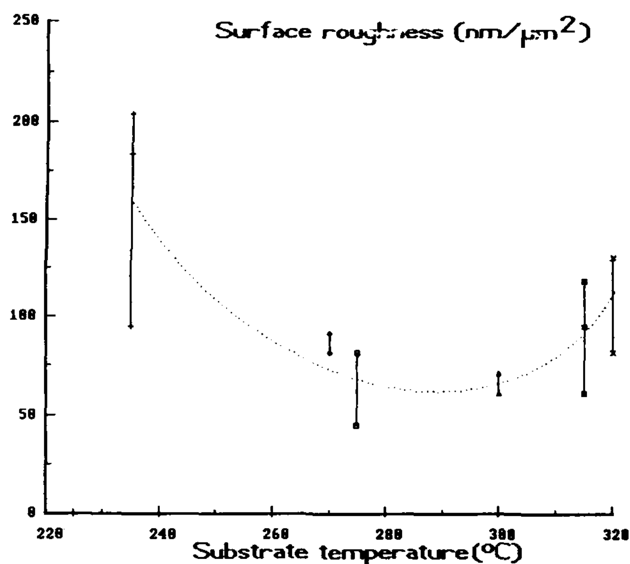

Fig. 5. Influence of the substrate temperature on the roughness of the grown layers. A minimum is clearly visible in the temperature range from 280 °C to 300 °C.

surface quality. Thus, the above-described bromine–methanol polishing procedure gives a reliable base for further investigation of the influence of other growth parameters.

The growth temperature is one parameter for which an optimal value is still under discussion. Several groups use temperatures ranging from 180 °C [12] up to 350 °C [13]. From growth simulations [14] we expect an influence of the temperature on the surface roughness. Therefore, we studied this dependence with an STM and present in the following the first results.

The roughness values are evaluated following DIN 4768. As the total roughness depends on the measured area, these values are normalized to the area size from which they were taken to have the possibility for a direct comparison. The results at temperatures between 230 °C and 320 °C are shown in Fig. 5. The dashed line is drawn as a guide to the eye. A minimum is evident in a temperature range from 280 °C to 300 °C. Each data point in Fig. 5 corresponds to a different location on the same sample. The variation of these data points shows the large scale uniformity of the surface. This variation increases significantly for temperatures besides the optimal range and indicates that the temperature not only affects the absolute roughness but also the homogeneity of the roughness distribution.

3. Conclusion

In conclusion, different CdTe substrate preparation procedures were examined and their effect on the

surface roughness was measured quantitatively by an STM. The commercially acquired samples showed corrugations of more than 1100 Å, which could be reduced to 200 Å by an etch step with HBr. By polishing the substrates in a bromine–methanol solution, the surface roughness could be decreased down to 50 Å. It was shown that the substrate roughness has a strong influence on the quality of the grown layers even for a layer thickness more than 10 times larger than the corrugations. The bromine–methanol polishing was found to be a sufficient preparation procedure to get a two-dimensional layer growth. The first results on the influence of the growth temperature indicate that the layer roughness has a minimum in the range between 280 °C and 300 °C.

Acknowledgments

We thank S. Scholl for helpful discussions, W. Gold, K. v. Schierstedt and Li He for making the contacts, and P. Wolf for preparing the samples.

This project was supported by the Bundesministerium für Forschung und Technologie, Bonn (TK 0369).

References

1 N. Otsuka, L. A. Kolodziejski, R. L. Gunshor, S. Datta, R. N. Bicknell and J. F. Schetzina, *Appl. Phys. Lett.*, *46* (1985) 860.
2 H. A. Mar, K. T. Chee and N. Salansky, *Appl. Phys. Lett.*, *44* (1984) 237.
3 M. Oron, A. Raizman, H. Shrickman and G. Cinader, *Appl. Phys. Lett.*, *52* (1988) 1059.
4 W. E. Hoke, P. J. Lemonias and R. Traczewski, *Appl. Phys. Lett.*, *44* (1984) 1046.
5 R. Bean, K. Zanio and J. Ziegler, *J. Vac. Sci. Technol.*, *A7* (2) (1989) 343.
6 P.-Y. Lu, L. M. Williams and S. N. G. Chu, *J. Vac. Sci. Technol.*, *A4* (4) (1986) 2137.
7 M. Wenzel, M. Ehinger, R. N. Bicknell and G. Landwehr, *Fresenius' J. Anal. Chem.*, *341* (1991) 189.
8 M. Ehinger, M. Wenzel, A. Waag and G. Landwehr, *J. Cryst. Growth*, *123* (1992) 42.
9 S. P. Kowalczyk and J. T. Cheung, *J. Vac. Sci. Technol.*, *18* (3) (1981) 944.
10 B. K. Janousek and R. C. Carscallen, *J. Vac. Sci. Technol.*, *21* (2) (1982) 442.
11 J. S. Ahearn, G. D. Davis and N. E. Byer, *J. Vac. Sci. Technol.*, *20* (3) (1982) 756.
12 R. N. Bicknell, N. C. Giles and J. F. Schetzina, *J. Vac. Sci. Technol.*, *B5* (3) (1987) 701.
13 R. J. Koestner, M. W. Goodwin and H. F. Schaake, *J. Vac. Sci. Technol.*, *B9* (3) (1991) 1731.
14 A. Jakobs, personal communication, 1992.

X-ray photoelectron diffraction from the CdTe(111)A polar surface

G. Granozzi, G. A. Rizzi, A. M. Capobianco, R. Bertoncello, M. Casarin and E. Tondello
Dipartimento di Chimica Inorganica, Metallorganica ed Analitica, Università di Padova, Via Loredan 4, 35131 Padova (Italy)

Abstract

Polar and azimuthal X-ray photoelectron diffraction (XPD) data on a CdTe(111)A (Cd terminated) surface are reported and discussed on the basis of a single scattering cluster (SSC) theory. Significantly distinct patterns are predicted for the two different (111)A and (111)B polar surfaces, suggesting that the XPD technique is a valid tool for the absolute determination of the surface polarity. Moreover, the azimuthal diffraction patterns obtained at grazing polar angles (so that the probed surface region is very shallow) revealed details which can be elucidated assuming either a surface relaxation, where Cd and Te atoms of the outermost double layer are almost coplanar, or a $(2\sqrt{3} \times 2\sqrt{3})$ R30° surface reconstruction.

1. Introduction

II–VI semiconductor crystalline compounds have been the subject of many surface characterization studies, particularly with respect to the (110) cleavage surface [1]. Even if the (111) surface is of particular technological importance for epitaxial growth of II–VI compounds, relatively few studies have appeared in the literature. In contrast, the structural properties of the substrate (111) surface, *i.e.* termination, relaxation and reconstruction, can effect the quality of subsequent epitaxial layers.

X-ray photoelectron diffraction (XPD) has proved to be quite a powerful technique for the determination of surface structures [2]. In such a technique, the core level photoelectron intensities are monitored as a function of the emission direction (azimuthal and polar scans). The rather large (10%–50%) intensity fluctuations are originated by the interference phenomena of the photoelectron waves elastically scattered by the near-surface atomic layers. Therefore, this can be considered as a sort of electron diffraction where the electron source (emitter) is located inside the sample and the resulting diffraction pattern contains information on the structural features of the surface. The peculiarity of this technique is that it allows a simple geometric interpretation of the dominant intensity maxima in terms of emitter–scatterer directions [2, 3]. XPD phenomena can be quantitatively described using a multiple scattering (MS) approach [4], but a simple single scattering (SS) theory has proven to be adequate in most cases [5]. For example, such an SS approach to XPD recently has been adopted to study the (111)A (cation-terminated) and (111)B (anion-terminated) polar surfaces of HgCdTe and CdZnTe [6]. In the case of HgCdTe, the accuracy of the measurements, particularly at grazing emission angles, was somehow limited because a perfectly clean and crystalline surface was unachievable because ultrahigh vacuum (UHV) annealing, after sputter cleaning, causes the loss of Hg from the sample. Information on the surface structure that could have been obtained from the analysis of azimuthal scans taken at grazing emission polar angles, where the contribution to the XPD pattern arises mainly from the outermost layers, therefore has been lost.

In the present work, we analyse a series of new polar and azimuthal scans taken on a CdTe(111)A sample sputter cleaned and annealed in UHV. Very accurate XPD azimuthal curves recorded at several different polar angles are now compared with the results of numerical simulations carried out adopting the single scattering cluster (SSC) model within a spherical wave (SW) formalism.

2. Experimental details

The intensities of Cd $3d_{5/2}$ (KE = 1082 eV; de Broglie wavelength 0.329 Å) and Te $3d_{5/2}$ (KE = 914 eV; de Broglie wavelength 0.406 Å) peaks were measured on a VG ESCALAB MKII using Al Kα radiation. The spectrometer is equipped with a modified manipulator which allows both polar (Θ) and

0921-5107/93/$6.00 © 1993 - Elsevier Sequoia. All rights reserved

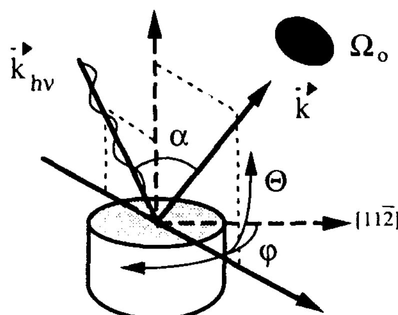

Fig. 1. Experimental set-up of an XPD experiment: α is the angle (fixed) between the incoming photon direction ($k_{h\nu}$) and the analysis direction (k); Ω_0 is the acceptance angle of the analyser; the polar angle (Θ) is referred to with respect to the surface and the azimuthal angle (ϕ) is referred to with respect to the [11$\bar{2}$] direction.

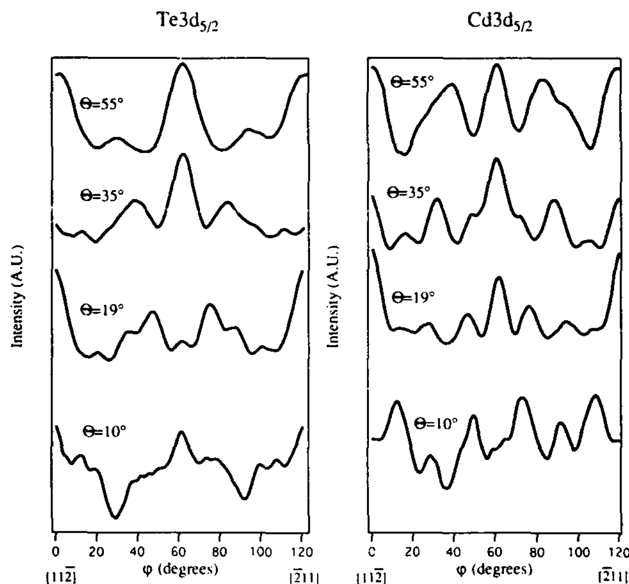

Fig. 2. Azimuthal scans of Te $3d_{5/2}$ and Cd $3d_{5/2}$ XPS peaks of CdTe (111) at several polar angles.

azimuthal (ϕ) rotations with an accuracy better than 0.5° (see Fig. 1 for definitions), a five channeltron detection unit and a shutter in front of the electrostatic lenses to achieve good angular resolution (± 1.5°). Automatic angular scans can be obtained by two computer-controlled stepping motors driving the sample rotations.

All the azimuthal and polar scans were obtained using 2° steps; the full 360° range was scanned for azimuthal scans and the data were then threefold averaged into 120° because of the ternary symmetry of the (111) surface. The CdTe crystals were grown by liquid phase epitaxy (LPE) and mirror polished. *In situ* ion bombardment (1 KeV Ar^+ ions) was applied to remove the oxide overlayer and the sample was then annealed at 300 °C for 10 min. During all the runs, the base pressure was in the 5×10^{-10} mbar range; surface contamination by O and C was checked periodically by XPS.

In analysing our data, we have used spherical wave, single scattering cluster (SW-SSC) calculations according to the model described in detail elsewhere [2, 7]. The theory includes the correct SW nature of the final states' photoelectron waves [7]. In comparing experimental and theoretical curves, we have also used R factors [8] as a quantitative measure of the goodness of the fit. All the calculations were run using an inner potential of 15 eV, inelastic mean free paths (Λ_e) of 14.8 Å for Te $3d_{5/2}$ and 16.8 Å for Cd $3d_{5/2}$, and muffin-tin scattering phase shifts.

3. Results and discussion

3.1. ϕ azimuthal scans

Azimuthal scans were recorded at the following polar angles: $\Theta = 55°$, 45°, 35°, 19°, 16°, 14°, 12° and 10°. Some of the data are reported in Fig. 2 where ϕ varies in a 120° interval.

From a preliminary analysis of the azimuthal scans it clearly appears that the diffraction patterns depend on both the nature of the emitter and its crystallographic site. In fact, the Te $3d_{5/2}$ XPD scans are completely different from the Cd$3d_{5/2}$ scans recorded at the same Θ value. A simplified interpretation of the XPD curves can be attempted, knowing that the recorded intensity is enhanced for those directions where the scattering angles between the emitter and its nearest neighbours are close to 0°. To maximize these "forward-scattering effects" (also for crystal alignment purposes) it is convenient to select a particular set of Θ polar angles so that, when scanning through the range of ϕ, some of these directions coincide with the direction of analysis. In the present case, the polar angles for which nearest-neighbour forward-scatterers can be found are $\Theta = 19°$, 35° and 55°, corresponding to crystal directions [11$\bar{1}$], [010] and [110], which become [11$\bar{2}$], [$\bar{1}$2$\bar{1}$] and [11$\bar{2}$] when projected on the (111) plane.

The reason why an XPD experiment can give directly information about the surface polarity is, as already discussed for HgCdTe [6], the dependence of an azimuthal scan on the emitter type and its crystallographic site. It is easy to understand that a simple azimuthal scan, recorded at a polar angle of $\Theta = 19°$, allows us to distinguish between polarity A and B. Actually, the photoelectron wave emerging from the emitter at this polar angle finds nearest neighbours only when the emitter is located in the bottom atomic layer of each double layer. Therefore, the azimuthal scans recorded at $\Theta = 19°$ must be characterized by the

presence of strong forward-scattering peaks only in the case of the Te $3d_{5/2}$ scan for a (111)A (Cd-terminated) surface or in the case of the Cd $3d_{5/2}$ scan for a (111)B (Te-terminated) surface. In Fig. 3, Cd $3d_{5/2}$ and Te $3d_{5/2}$ azimuthal scans at $\Theta = 19°$ are compared with the results of SSC-SW calculations, assuming model A or B for the surface. It is well evident that model A allows better reproduction of the experimental data. In the same figure, the values of the *R* factor are also reported, indicating significantly lower values for model A than for model B. Good agreement between the experimental data and theoretical simulations carried out with model A is evident also for azimuthal scans at different polar angles.

3.2. Θ polar scans

Polar scans were collected along [11$\bar{2}$] and [$\bar{1}$2$\bar{1}$] for both Te $3d_{5/2}$ and Cd $3d_{5/2}$. Each curve was recorded three times, shifting the azimuth by 120° to verify the (111) surface alignment. On analysing the data, one can infer that the (111) orientation is correct within 1.0°. A higher degree of misalignment with respect to the (111) orientation would cause a shift of the peaks, corresponding to equivalent crystal directions. In Fig. 4, an average of the three symmetry-equivalent curves is compared with SSC-SW calculations. A polar-angle-dependent background, which is a function of $1/\sin\Theta$, was subtracted from the experimental curves. The background was measured experimentally as the intensity coming from inelastically scattered photoelectrons with the same KE as that of the recorded XPS peaks. Residual diffraction effects, visible in these background curves, were smeared out by a simple smoothing procedure. Looking at the polar curves in Fig. 4, it is clear that, in addition to the forward-scattering peaks, other peaks arise from higher order diffraction effects.

The angular position of all these peaks is correctly reproduced by the SSC-SW calculations. However, it is important to notice that the relative intensity of the peaks in the theoretical curves is comparable with the experimental data only in the case of the scan at the [$\bar{1}$2$\bar{1}$] azimuth. In particular, the intense peak along the [110] direction is highly overestimated in the calculation. In fact, the photoelectron waves along this direction are transmitted through rows of atoms belonging to the same sublattice and, as already suggested [4], in such a situation MS events produce a strong defocusing effect. The SSC approximation used in our calculations does not take into account this effect and, therefore, overestimates the intensity of the peak at $\Theta = 55°$ along the [11$\bar{2}$] azimuth. Nevertheless, our calculations demonstrate how a simple SSC theory allows us to

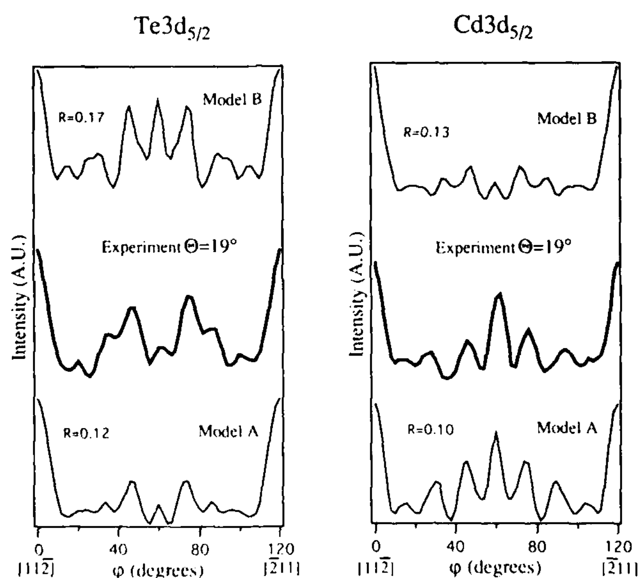

Fig. 3. Comparison between experimental and SSC-SW theoretical azimuthal scans of Te $3d_{5/2}$ and Cd $3d_{5/2}$ XPS peaks of CdTe (111) at $\Theta = 19°$. The two different surface polarities (models A and B, unrelaxed) furnish rather different visual agreement with the experiment and different *R* factors.

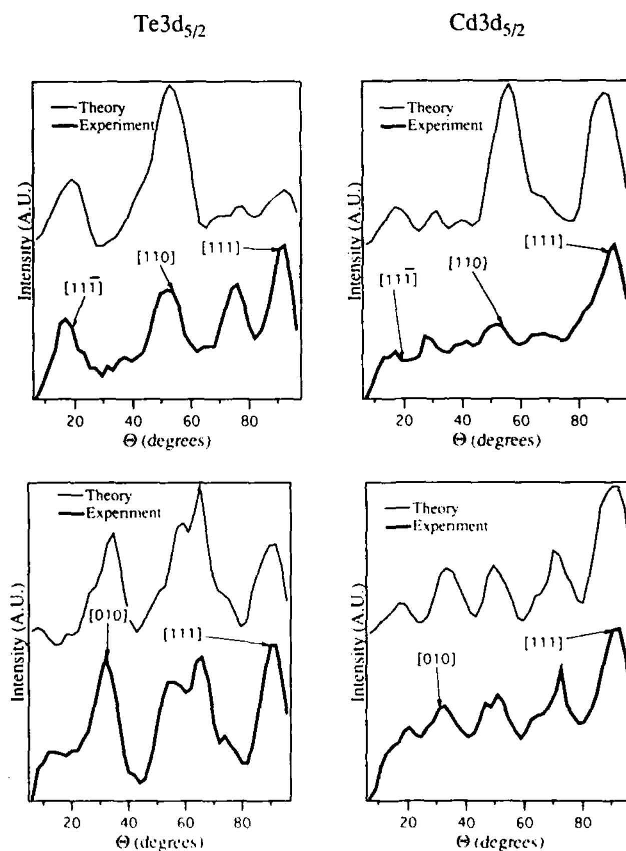

Fig. 4. Experimental and SSC-SW theoretical polar scans of Te $3d_{5/2}$ and Cd $3d_{5/2}$ XPS peaks of CdTe (111) at the two different azimuth [11$\bar{2}$] (top) and [$\bar{1}$2$\bar{1}$] (bottom).

reproduce correctly almost all the diffraction features present in the spectra and, therefore, this theory can safely be used for a detailed determination, by a 'trial and error' procedure, of the surface structure in those cases where MS effects are negligible.

3.3. Surface structure

Taking advantage of the very good surface quality of our sample (very clean, crystalline and well oriented), we decided to collect azimuthal scans at grazing polar angles ($\Theta = 14°$, $12°$ and $10°$—lower values are forbidden by natural surface roughness) to achieve a high surface sensitivity. The data at $\Theta = 10°$ are reported in Fig. 5 for Cd $3d_{5/2}$ and Te $3d_{5/2}$ together with SSC-SW simulations.

It is clear from Fig. 5 that the degree of agreement between the experimental data and the SSC-SW simulation is not satisfactory. It can be easily demonstrated that, at a polar angle of emission of 10°, more than 60% of the XPS signal comes from the first 5 Å below the surface. Then we are confident of the reliability of the SSC calculations since at these low emission angles MS effects are negligible. We therefore decided to optimize the structure of the outermost double layer, moving both the Cd and Te atoms to look for evidence of some surface relaxation. We found the best agreement with the experiment by decreasing the z coordinate of the Cd atom by 1.35 Å and that of the Te atom by 0.2 Å. As a consequence, we have a contraction of the Cd–Te bond of 5%–7%. In this configuration, Cd and Te atoms are almost coplanar, the Cd atom being at a slightly lower z than the Te atom.

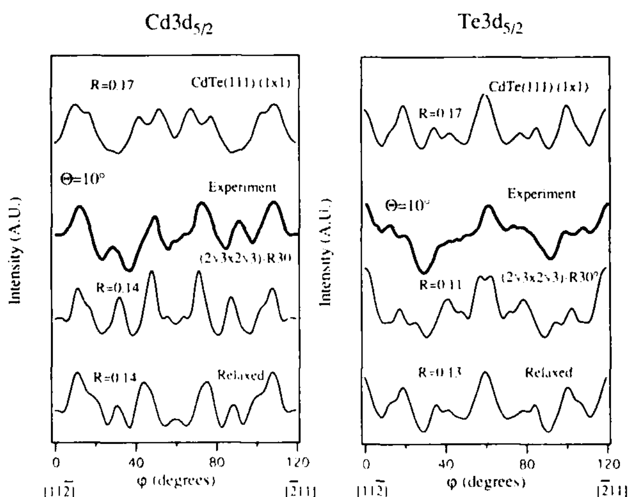

Fig. 5. Comparison between experimental and SSC-SW theoretical azimuthal scan of Te $3d_{5/2}$ and Cd $3d_{5/2}$ XPS peaks of CdTe (111) at $\Theta = 10°$. The cluster adopted for the theoretical simulation (model A) is either bulk like (unrelaxed), relaxed (such that Cd and Te atoms of the outermost double layer become almost coplanar—see text) or reconstructed.

The calculations obtained assuming a relaxed cluster better reproduce the experimental curves of Cd $3d_{5/2}$, as is confirmed by the R factor values reported. The calculation for an unrelaxed bulk structure at $\Theta = 10°$ does not reproduce peaks at $\phi = 30°$, $60°$ and $90°$; however, these are well reproduced in the relaxed calculation. If we now look at the Te $3d_{5/2}$ scan, we see that the differences between the relaxed and unrelaxed models are less important than for Cd. This can be easily understood if we think that the scattering geometry of the Te atom, viewed as an emitter at a polar angle of 10°, is almost insensitive to the above-described surface relaxation. Actually, considering the Te atom as the emitter at the origin, the analysis direction is almost midway between the Te–Cd directions of the unrelaxed and relaxed models, so that the scattering process is very similar in both cases.

It is important to point out that a similar good agreement between theory and experiment can be obtained by assuming a $(2\sqrt{3} \times 2\sqrt{3})$ R30° surface reconstruction as already found for CdTe(111)B [9]. To reproduce the three-fold symmetry found in experiment, we needed to assume a three-domain model where the reconstructed cell has three different orientations rotated by 120° with respect to the bulk lattice. Further measurements are in progress, in our laboratory, in order to settle this matter.

Acknowledgments

This work has been partially funded by Progetto Finalizzato "Materiali Speciali per Tecnologie Avanzate" of the CNR (Rome). Thanks are due to Dr. S. Bernardi for a gift of the LPE-grown CdTe samples.

References

1 C. B. Duke, in J. R. Chelikowsky and A. Franciosi (eds.), *Electronic Materials: a New Era in Materials Science*, Springer, Berlin, 1991, pp. 113–134 and references cited therein; in D. A. King and D. P. Woodruff (eds.), *Surface Properties of Electronic Materials*, Elsevier, Amsterdam, 1988, pp. 69–118.
2 C. S. Fadley, *Phys. Scr.*, *T17* (1987) 39; *Prog. Surf. Sci.*, *16* (1984) 275.
E. L. Bullock and C. S. Fadley, *Phys. Rev. B*,*31* (1985) 1212.
3 W. F. Egelhoff, Jr., *Phys. Rev. B*,*30* (1984) 1052.
4 S. Y. Tong, H. C. Poon and D. R. Snider, *Phys. Rev. B*,*32* (1985) 2096
M. L. Xu, J. J. Barton and M. A. Van Hove, *Phys. Rev. B*,*39* (1989) 8275.
M. L. Xu and M. A. van Hove, *Surf. Sci.*, *207* (1989) 215.
5 M. Sagurton, E. L. Bullock and C. S. Fadley, *Phys. Rev. B*,*30* (1984) 7332; *Surf. Sci.*, *182* (1987) 287.
6 G. Granozzi, G. A. Rizzi, G. S. Herman, D. J. Friedman, C. S. Fadley, J. Osterwalder and S. Bernardi, *Phys. Scr.*, *41* (1990) 413.

G. S. Herman, D. J. Friedman, T. T. Tran, C. S. Fadley, G. Granozzi, G. A. Rizzi, J. Osterwalder and S. Bernardi, *J. Vac. Sci. Technol. B*, *9* (1991) 1870.
M. Seelman-Eggebert and H. J. Richter, *Phys. Rev. B*, *43* (1991) 9578.
7 D. J. Friedman and C. S. Fadley, *J. Electron Spectrosc. Relat. Phenom.*, *51* (1990) 689.
8 M. A. Van Hove, S. Y. Tong and M. H. Elconin, *Surf. Sci.*, *64* (1977) 85.
9 R. Duszak, S. Tatarenko, J. Cibert, K. Saminadayar and C. Deshayes, *J. Vac. Sci. Technol. A9* (1991) 3025.

Materials Science and Engineering, B16 (1993) 160–164

Ion channelling Rutherford backscattering spectrometry structural characterization of CdS/CdTe heterostructures

A. Guerrieri

Centro Nazionale Ricerca e Sviluppo Materiali, CNRSM, SS 7 per Brindisi - km 7, I-72023 Mesagne (Italy)

A. V. Drigo and F. Romanato

Dipartimento di Fisica, Università di Padova e Unità GNSM-INFM di Padova, Via Marzolo 8, I-35100 Padova (Italy)

N. Lovergine* and A. M. Mancini

Dipartimento di Scienza dei Materiali, Università di Lecce e Unità GNSM-INFM di Lecce, Via per Arnesano, I-73100 Lecce (Italy)

Abstract

We report on the structural characterization by ion channelling Rutherford backscattering spectrometry (RBS) of thin (less than 3 μm) CdS epitaxial layers grown on {111}A-oriented CdTe substrates by chemical vapour deposition. The overall crystalline quality of the present epilayers has been studied as a function of their thickness. Also, the occurrence of single crystal growth *vs.* highly textured polycrystalline growth has been checked by studying channelling angular dips at different $^4He^+$ beam energies. The CdS epilayers turned out to be essentially single crystalline, although the present RBS measurements show that extended defects are contained in the layers and at the CdS/CdTe interfaces. The dechannelling beam energy dependence allows us to identify these defects as stacking faults, whose concentration profile in the epilayers is reported.

1. Introduction

The growth and characterization of CdS/CdTe-based heterostructures continue to be the subject of much research effort, because these heterostructures have potential applications in the field of photovoltaic solar cells. Their main advantages are related to the physical characteristics of the constituent materials: in fact, the energy gap value of CdS (*i.e.* 2.42 eV at 300 K) makes it suitable as a semiconducting material for the realization of highly conductive window layers, whereas the corresponding value for CdTe (*i.e.* 1.44 eV) is near optimum for photovoltaic solar energy conversion. Research in this field has initially focused on the study of low-cost, polycrystalline, thin film devices, resulting in photoconversion efficiencies typically below 10%. However, since the early works of Yamaguchi and co-workers [1, 2], the use of solar cells based on the epitaxial CdS/CdTe heterostructure has gained increasing attention in the attempt to improve cell efficiencies. Although the maximum theoretical efficiency of the n-CdS/p-CdTe heterojunction is 19.7% under AM0 (air mass zero) sunlight spectral conditions [2], actual cell performances are limited by problems concerning the conductivity control of, and the realization of low resistance ohmic contacts on, p-type CdTe [3, 4]. Meyers [5] proposed a novel p–i–n solar cells structure of the type p-ZnTe/i-CdTe/n-CdS in which CdTe is used as an intrinsic absorber layer, thereby avoiding the above-mentioned problems. Recently, monocrystalline p-ZnTe/i-CdTe/n-CdS solar cell structures have been realized by sequential metallo-organic vapour phase epitaxy (MOVPE) of ZnTe and CdTe layers on CdS substrates, resulting in device efficiencies of up to 13% under AM1 (air mass one) illumination [6].

Despite their attractive features, the CdS/CdTe-based heterostructures raise the problem of matching the hexagonal (wurtzite) CdS lattice with the cubic (zincblende) lattice of CdTe. As a consequence, several substrate orientations have been investigated to assess the growth of both CdTe/CdS and CdS/CdTe heterostructures. The best epitaxy has been reported recently [7] for CdTe layers deposited by MOVPE on non-metal surfaces of {0001}- and {01$\bar{1}$6}-oriented CdS

*Author to whom correspondence should be addressed.

0921-5107/93/$6.00

© 1993 – Elsevier Sequoia. All rights reserved

substrates, their epitaxial relationships being {111}CdTe‖{0001}B-CdS and {37$\bar{5}$}CdTe‖{01$\bar{1}$6}B-CdS respectively. However, thin lamellar twins were shown to affect CdTe layers deposited on {0001}-oriented CdS substrates, whereas no twinning has been reported for the {01$\bar{1}$6} orientation. Similarly, the growth of CdS epitaxial layers on oriented CdTe substrates has been extensively studied by several authors. Until now, only three CdTe substrate orientations have proved successful in growing CdS epitaxial layers, namely {110} [8], {221} [9] and {111}A [1]. For the first two orientations, no precise epitaxial relationships seem to hold, although for {221}-oriented CdTe substrate a relationship close to {01$\bar{1}$6}CdS‖{221}CdTe has been suggested. However, growth on {111}A-oriented CdTe gives rise to the well-known epitaxial relationship {0001}CdS‖{111}A-CdTe, resulting in a 9.74% mismatch for the in-plane lattice parameters.

Despite such a high value of the lattice mismatch, 10.5% efficiency has been reported for n-CdS/p-CdTe solar cells grown by H_2 transport on {111}-oriented CdTe [1]. To our knowledge, very few structural studies have been reported in the literature about {0001}CdS‖{111}A-CdTe heterostructures. In a previous paper [10], the high crystalline quality of thick (3–30 μm) hexagonal CdS epilayers grown by chemical vapour deposition (CVD) on {111}A-CdTe has been demonstrated by channelling Rutherford backscattering spectrometry (RBS). In this work, we investigate the structural properties of relatively thin (less than 3 μm) CdS epilayers. Their overall crystalline quality has been studied as a function of the epilayer thickness. The occurrence of single crystal growth *vs.* highly textured polycrystalline growth has been checked by studying channelling angular dips at different $^4He^+$ beam energies. Moreover, the presence of extended defects in the layers has been detected and their nature determined by analysing RBS channelling spectra as a function of the ion beam energy. This allowed us to identify these defects as stacking faults and to calculate their concentration profile in the CdS epilayers.

2. Experimental details

{0001}-oriented hexagonal CdS layers have been grown on {111}A-CdTe by CVD using H_2 as the transport agent from the source to the deposition region [11]. Nominally stoichiometric CdS of 99.999% purity from Cerac, Inc. was used as the starting material. The {111}-oriented CdTe substrates, supplied by Cominco, Inc., were lapped and polished with diamond paste to a mirror finish. The {111}A face of the CdTe substrates was identified by selective etching [12] in 1HF:1HNO$_3$:1CH$_3$COOH. A light etch of the substrates using a 1%Br–methanol solution for 1 min immediately before the introduction into the growth chamber was followed by an *in situ* thermal etch at 600°C for 15 min in an H_2–N_2 (2:1) gas flow. The present CdS epitaxial layers were grown in a 300 SCCM total H_2 flow at a deposition temperature of about 600°C, the source temperature being 100°C higher. These conditions resulted in a CdS growth rate of about 0.1 μm min^{-1}. Total CdS epilayer thicknesses ranging from 0.5 to 3.0 μm were considered in the present work.

A high precision goniometer with both repeatability and an overall precision of 0.01° [13] was used for the structural characterization by ion channelling. To minimize the accumulation of damage induced by the analysing beam, care was taken when moving the beam spot on the sample surface, after a given value of the total beam charge was integrated. $^4He^+$ beam energies of 1, 2 and 4 MeV were used for the present measurements.

3. Results and discussion

Figure 1 shows the 2.0 MeV $^4He^+$ RBS spectra in aligned conditions along the CdS *c* axis for three samples with different epilayer thicknesses, *i.e.* 0.5 μm (T60), 0.9 μm (T62) and 3 μm (T61). The random spectrum for sample T60 is also reported in Fig. 1 for comparison. The energy-to-depth conversion for our geometry has been obtained by using the stopping power in ref. 14. The interface width is much larger than the experimental depth resolution. This fact could be due to interface mixing between CdS and CdTe

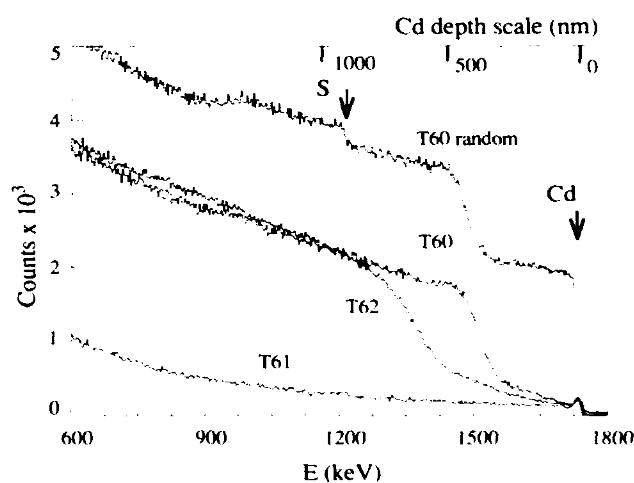

Fig. 1. 2.0 MeV $^4He^+$ RBS spectra in channelling condition along the *c* axis of growth for the three samples investigated with different epilayer thicknesses: (T60) 0.5 µm, (T62) 0.9 μm, (T61) 3 μm. The random spectrum for the sample T60 is reported for comparison.

and/or to thickness inhomogeneities in the epilayers. The spectra show clear Cd surface peaks and relatively low channelling yields. The surface minimum yield χ_{min}, *i.e.* the aligned yield just behind the surface peak normalized to the random yield, is reported in Fig. 2 as a function of the epilayer thickness for the three samples in Fig. 1. The minimum yields for thicker samples are also shown [10]. It appears that the χ_{min} value rapidly decreases with increasing CdS layer thickness up to a few micrometres, and then it reaches a minimum which is slightly higher than the theoretical estimate given by Barrett [14], *i.e.* $\chi^{B}_{min} = 0.0398$.

As reported in a previous work [10], the surface morphology suggests a highly textured grain structure for the present CdS epilayers. Nevertheless, it has been demonstrated that their structure in the near-surface region is single crystalline at least for the higher thickness values. However, a possible textured columnar growth could explain the higher χ_{min} values obtained for the present thin layers. To investigate this point, channelling dips for the conditions aligned with the c axis were recorded at different beam energies. In fact, it has been shown [15] that ion channelling is able to qualify the texture of a polycrystalline material by measuring the experimental critical angle $\Psi_{1/2}$ as a function of the beam energy E, using the expression

$$\Psi_{1/2}^2 = \sigma^2 \ln 2 + \Psi_1^2 = \sigma^2 \ln 2 + \frac{\text{const}}{E}$$

where σ is the standard deviation of the crystallite orientation distribution and Ψ_1 is the channelling critical angle for a perfect single crystal.

Figure 3 reports the square of the experimental critical angle $\Psi_{1/2}$ *vs.* the reciprocal of the beam energy for the same samples as in Fig. 1. The theoretical values [14] are also reported for comparison. It can be seen that our experimental values are systematically slightly lower than the predicted values; moreover, they can be fitted by a straight line whose zero energy intercept coincides with the origin within the experimental uncertainties, thus excluding misalignments higher than a few hundredths of a degree from point to point in the layers. These results lead to the conclusion that even relatively thin CdS epilayers are essentially single crystalline.

From Fig. 1 it appears that the channelling yield for sample T61 is very low, indicating a reduced amount of defects in the layer. It appears that the corresponding yields for the thinner samples smoothly increase up to depth values which roughly correspond to the interfaces, at which point sudden jumps take place. Below the interfaces, the yields of the two samples are equal and the dechannelling rates are nearly the same as that of sample T61. We can thus divide the dechannelling yield profiles into two regions, *i.e.* (i) the surface and (ii) the interface region, where different types of defects seem to be present.

The nature of these defects and their depth distribution can be deduced by comparing the normalized channelling yield as a function of depth with the corresponding yield for the perfect crystal. In fact, the total disorder $N_D(t)$ integrated from the surface to a depth t can be obtained by the equation [16]

$$\ln \frac{1-\chi_V(t)}{1-\chi_D(t)} = N_D(t)\sigma_D = \int_0^t n_D(t')\sigma_D \, dt'$$

where $\chi_V(t)$ and $\chi_D(t)$ are the normalized yields for the reference and the defected crystal, respectively, and σ_D is the dechannelling factor typical of the particular type of defect actually present in the crystal; finally, $n_D(t')$ is the local defect volume density.

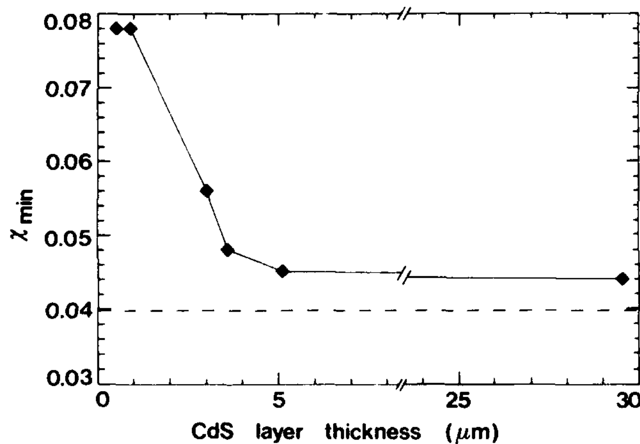

Fig. 2. The surface minimum yield χ_{min} as a function of the CdS epilayer thickness.

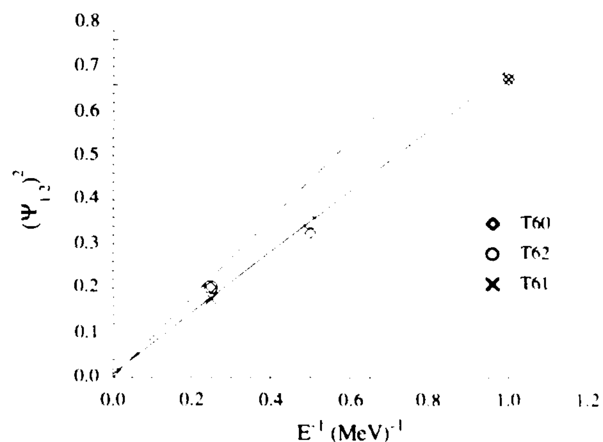

Fig. 3. The square of the experimental critical angle $\Psi_{1/2}^2$ as a function of the reciprocal of the ion beam energies. The solid line represents the linear best fit of the data, whereas the dashed line represents the theoretical estimate.

The $N_D(t)\sigma_D$ values measured at the end of the first (surface) region for different $^4He^+$ beam energies are reported in Table 1 for the two thinnest samples in Fig. 1. In our calculations we assumed the $\chi_V(t)$ values to be coincident with the normalized yield of sample T61. It appears that the defects in the epilayers have a dechannelling probability independent of the beam energy, indicating that these defects are stacking faults. Moreover, as the same holds true for any intermediate depth between the surface and the interface, it also can be concluded that stacking faults are the main defects in the present CdS epilayers.

From the derivative of $N_D(t)\sigma_D$ the defect concentration profile $n_D(t)$ can be obtained. The result is shown in Fig. 4 where the interface has been chosen as the origin of the profile. It appears that the two profiles mimic each other and show a slow decrease in $n_D(t)$ with increasing distance from the CdS/CdTe interface. These data are in agreement with those of Fig. 2, showing that an epilayer thickness of at least 3 μm is necessary to obtain a good surface quality.

As far as the second (interface) region is concerned, the fact that the channelled fraction after the interface yield jump is the same for the spectra of the two thinnest samples of Fig. 1 indicates that the density of these defects is nearly independent of the epilayer thickness. The ion channelling analysis of the interface defects is complicated by the double-layered structure of the overall defect distribution. However, the normalized yield after the interface roughly correlates with the square root of the ion beam energy, suggesting that the interface defects are misfit dislocations formed to accommodate the high lattice mismatch involved with the CdS/CdTe heterostructure.

The presence of stacking faults in CdS epilayers grown on {111}A-CdTe substrates never has been observed before, although similar results have been recently reported by Brown *et al.* [17] for CdS epilayers deposited on {111}B GaAs by MOVPE, for which dense arrays of irregularly spaced stacking faults on close-packed planes parallel to the CdS–GaAs interface have been observed by conventional transmission electron microscopy and attributed to the dimorphism of CdS at the low growth temperatures involved with MOVPE. However, the hexagonal (wurtzite) phase is the stable phase of CdS at the relatively higher growth temperatures (550–750°C) required for the CVD process. In this respect, it should be noted that the characteristic stacking fault concentration profile reported in Fig. 4 strongly indicates that the formation of these defects in the CdS layers is somewhat related to the CdS–CdTe interface. In fact, stacking faults are generally associated with partial dislocations and, therefore, they can contribute to the removal of the high lattice mismatch in the CdS/CdTe heterostructure along with misfit dislocations.

TABLE 1. The integrated disorder $N_D\sigma_D$ values as measured at different $^4He^+$ beam energies for the two thinnest samples

Energy (keV)	$N_D\sigma_D$(T60)	$N_D\sigma_D$(T62)
1000	0.15 ± 0.02	0.19 ± 0.02
2000	0.16 ± 0.02	0.22 ± 0.02
4000	—	0.18 ± 0.02

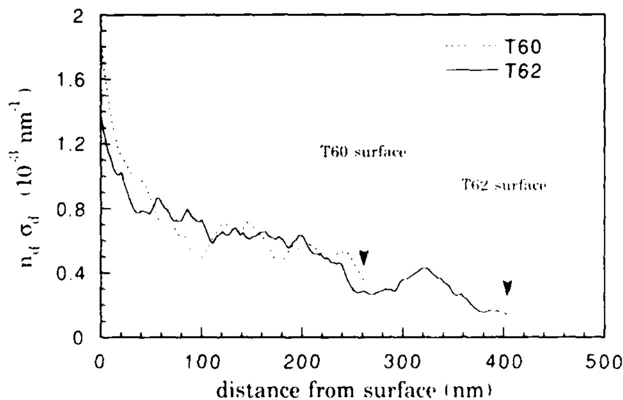

Fig. 4. The stacking fault concentration profile in arbitrary units as a function of the distance from the interface for samples T60 and T62.

4. Conclusions

The epitaxy of CVD-grown CdS epilayers on CdTe substrate has been studied by means of RBS channelling for different epilayer thicknesses, extending a previous work to thinner layers. The main results of the present work can be summarized as follows.

(1) {0001}-oriented hexagonal CdS epilayers on {111}A-CdTe substrates are single crystals independent of their thickness.

(2) In the interface region, a high density of defects is present, which can be reasonably identified with misfit dislocations, as required to accommodate the large lattice misfit between the two structures.

(3) An additional defect distribution spanning from the interface to the surface has been observed, these defects being identified as stacking faults. Their depth concentration profile decreases slowly with increasing CdS–CdTe interface distance, and a good surface crystalline quality can be obtained for CdS epilayer thicknesses above about 3 μm.

Finally, it has been suggested that the higher stacking fault density in regions of the epilayer close to the CdS–CdTe interface is symptomatic of their role in

removing the heterostructure lattice mismatch along with misfit dislocations, although further studies are clearly required on this subject.

References

1 K. Yamaguchi, H. Matsumoto, N. Nakayama and S. Ikegami, *Jpn J. Appl. Phys., 15*(8)(1976) 1575.
2 K. Yamaguchi, N. Nakayama, H. Matsumoto and S. Ikegami, *Jpn J. Appl. Phys., 16*(1977) 1203.
3 C. Ercelebi, A. W. Brinkman, T. S. Furlong and J. Woods, *J. Cryst. Growth, 101* (1990) 162.
4 A. L. Farenbruch, *Solar Cells, 21* (1987) 399.
5 P. V. Meyers, *Solar Cells, 23* (1988) 59.
6 M. Y. Simmons, H. M. Al Allak, A. W. Brinkman and K. Durose, *J. Cryst. Growth, 117*(1992) 959.
7 M. Y. Simmons, P. D. Brown and K. Durose, *J. Cryst. Growth, 107*(1991) 664.
8 O. Igarashi, *J. Appl. Phys., 42* (1971) 4035.
9 G. R. Awan, A. W. Brinkman, G. J. Russell and J. Woods, *J. Cryst. Growth, 85* (1987) 477.
10 G. Leo, A. V. Drigo, N. Lovergine and A. M. Mancini, *J. Appl. Phys., 70*(4)(1991) 2041.
11 A. M. Mancini, M. Lovergine, C. De Blasi and L. Vasanelli, *Nuovo Cimento 10D* (1988) 57.
12 K. Durose, *Ph.D. Thesis*, University of Durham, 1986.
13 A. Carnera and A. V. Drigo, *Nucl. Instrum. Methods B, 44* (1990) 357.
14 J. H. Barrett, *Phys. Rev. B, 3* (1971) 1527.
15 H. Ishiwara, S. Hikosaka and S. Furukawa, *J. Appl. Phys., 50* (1979) 5302.
16 L. C. Feldman, J. W. Mayer and S. T. Picraux, *Materials Analysis by Ion Channeling*, Academic Press, New York, 1982.
17 P. D. Brown, Y. Y. Loginov, K. Durose, J. T. Mullins, T. Taguchi, T. Burbery, S. Lawson-Jack and I. Jones, *J. Cryst. Growth, 117*(1992) 536.

Materials Science and Engineering, *B16* (1993) 165–167

Complete characterization of epitaxial CdTe on GaAs from the lattice geometrical point of view

P. Möck

Humboldt-Universität, Institut für Kristallographie und Materialforschung, Invalidenstrasse 110, O-1040 Berlin (Germany)

Abstract

The complete characterization of two monocrystalline samples of epitaxial CdTe(111) on GaAs(001) rotated 2° around $[1\bar{1}0]$ using a new description tool and X-ray techniques is given. In addition, the structural quality of the deposits was correlated to the angles of epitaxial misorientation.

1. Introduction

In epitaxial CdTe(111) on GaAs(001), double positioning of two kinds, which are caused by different reasons, occurs during the deposition. These two kinds of double positioning are called double positioning of the first and second order [1]. Double positioning of the first order is caused by the face symmetries of the bounded crystal surfaces, in contrast to double positioning of the second order which is related to the growth conditions. The two orders of double positioning are designated commonly as twinning.

Recently, it was found that the problems of double positioning of the first and second order can be overcome in this epitaxial system using GaAs substrates with a vicinal angle of some degrees rotated around the axis $[1\bar{1}0]$ and appropriate growth conditions [1, 2]. Thus, monocrystalline epitaxial samples following the law of overgrowth $(001)_{GaAs} \| (\bar{1}\bar{1}\bar{1})_{CdTe}$, $[110]_{GaAs} \| [11\bar{2}]_{CdTe}$ can be obtained.

It is well known that the laws of overgrowth fail in general because epitaxial misorientations exist (see, for examples, refs. 1–7). Results from other epitaxial systems (see, for example, ref. 5) show that engineering of epitaxial misorientation can lead to a significant improvement of the structural quality of the deposits. Epitaxial misorientations are related in a first approximation to the vicinal angles of the substrate, but up to now this effect has not been fully understood (see, for example, ref. 6). Reviews of the most important literature on epitaxial misorientation are given in refs. 1, 7 and 8.

For complete characterization of epitaxial systems from the lattice geometrical point of view, and also for investigations of epitaxial misorientations, a new description tool using transformation matrices has been developed by this author [1, 8, 9]. To correlate the lattice geometry of monocrystalline CdTe(111) on GaAs(001) rotated 2° around $[1\bar{1}0]$ with the structural quality of the deposits, two epitaxial samples grown by metal-organic chemical vapour deposition under different growth conditions were characterized completely. The crystalline quality of the deposits was determined qualitatively and quantitatively.

2. Experimental details

The transformation matrices of the two epitaxial samples were determined by diffraction goniometry using an X-ray diffractometer equipped with an optical reflection goniometer. The goniometry of reciprocal lattice vectors was performed for 12 reciprocal lattice vectors of the substrate and deposit. The Bragg angles were determined with a precision of about 0.02°. The goniometer adjustments can be described by a spherical coordinate system. The two angles of this spherical coordinate system were determined with a precision of about 0.02°. The cartesian coordinates of the reciprocal lattice vectors under diffraction conditions can be easily derived from the values read on the goniometer circles. The correct signs of the indices of the reciprocal lattice vectors (polarity) were determined in the case of the CdTe deposit by an anomalous X-ray

0921-5107/93/$6.00

© 1993 – Elsevier Sequoia. All rights reserved

scattering method [10] and, in the case of the GaAs substrate, by KOH etching in correlation with polarity determinations using Kossel diffraction [11, 12].

The experimental data for the calculation of the deformation tensors of the deposits were obtained by means of a special X-ray diffractometer using the Soller slit method [13]. The Bragg angles of the nine symmetrically equivalent reciprocal lattice vectors $\{\bar{3}3\bar{7}\}$ of the deposits were determined with a precision of about 0.002°.

The structural quality of the CdTe deposits was determined using double-crystal, rocking-curve halfwidths. In addition to these quantitative measurements, the structural quality of the deposits was determined qualitatively using Kossel diffraction [12]. From one of the epitaxial samples a qualitatively sufficient electron channelling pattern of the CdTe deposit was obtained in a scanning electron microscope (Cambridge Stereoscan S260). The orientations of the GaAs substrate surfaces (including polarities) were checked by optical goniometry in combination with KOH etching [1] as well as by Kossel diffraction [12].

3. Results

From the transformation matrices it can be concluded that the orientation relationships of the two epitaxial samples are different.

The decomposition of the transformation matrices leads to the conclusion that the epitaxial samples differ mostly in the rotation matrices of epitaxial misorientation. The rotation parameters were derived from these matrices and are given in Table 1. This table shows that the samples differ, within the range of the error limits, only in the angles of epitaxial misorientation. The angle of epitaxial misorientation for sample no. 1 agrees with the model of epitaxial misorientation after Pond *et al.* [3]. Therefore, it can be concluded that, in this epitaxial sample, interfacial dislocations exist. Furthermore, according to Pond's theory of line defects in interfaces [14], one can expect that, in the epitaxial sample no. 2, interfacial disclinations and interfacial dispirations exist.

A strong deformation of the deposits was obtained. For example, for the CdTe deposit of sample no. 1, the lattice parameters $a = 0.648185 \pm 0.00007$ nm, $b = 0.648190 \pm 0.00007$ nm, $c = 0.648253 \pm 0.00007$ nm, $\alpha = 89.9880 \pm 0.004°$, $\beta = 89.9890 \pm 0.004°$ and $\gamma = 89.9871 \pm 0.004°$, and the deformation tensor

$$[\mathbf{D}] = \begin{pmatrix} 0.999960 \pm 0.00010 & 0.000112 \pm 0.00002 & 0.000096 \pm 0.00002 \\ 0.000112 \pm 0.00002 & 0.999970 \pm 0.00010 & -0.000105 \pm 0.00002 \\ 0.000096 \pm 0.00002 & 0.000105 \pm 0.00002 & 1.000070 \pm 0.00010 \end{pmatrix}$$

are obtained. Using the arguments given by Haussühl [15], it follows from the components of the deformation tensor that the deformation of the deposit is monoclinic or triclinic. Taking into account the lattice parameters, the deposit belongs to the trigonal or triclinic crystal system. Therefore, it can be concluded from these two statements that the deposit is triclinic.

The calculation of the symmetry group of the deformed deposits using Curie's principle [16] leads to the point symmetry groups m or 1 and, hence, to monoclinic or triclinic symmetry. This is also in agreement with the conclusion that the deformed deposit of sample no. 1 belongs to the triclinic crystal system.

Table 2 gives the results of the investigations of the structural quality of the deposits together with the thickness of the deposits. Comparing Tables 1 and 2, it seems to be true that a high structural quality of a deposit is correlated to the epitaxial misorientation which can be calculated according to the model of Pond *et al.* [3].

Figure 1 shows electron channelling patterns of the deposit and substrate of sample no. 1. In this figure, the (inhomogeneous) deformation of the CdTe deposit and the epitaxial misorientation can be clearly seen. The electron channelling pattern of the CdTe deposit demonstrates also the relatively high structural quality of this crystal.

In conclusion, it must be stated that systematic investigations on monocrystalline CdTe(111) on GaAs(001) rotated by various angles around $[1\bar{1}0]$ are necessary to proceed in engineering of epitaxial misorientation in this epitaxial system.

TABLE 1. Rotation parameters of epitaxial misorientation

Sample no.	Angle of epitaxial misorientation (deg)	Axis of epitaxial misorientation (±0.05°)
1	0.60 ± 0.04	$[\overline{71}\,70\,0]$
2	1.41 ± 0.04	$[\overline{72}\,70\,0]$

TABLE 2. Structural quality and thickness of the deposits

Sample no.	Thickness of deposits (μm)	Half-widths of rocking curves (deg)	Sharpness of Kossel lines
1	1.3 ± 0.2	0.03 ± 0.01	High
2	1.1 ± 0.2	0.10 ± 0.01	Low

Fig. 1. Electron channelling patterns of sample no. 1. The upper right-hand part shows a channelling pattern of the CdTe deposit, and the lower left-hand part shows a channelling pattern of the GaAs substrate. The deposit was removed in the lower left-hand part of the sample by chemical etching before the electron channelling patterns were taken.

Acknowledgments

The author thanks Dr. R. Sukale for the provision of the epitaxial samples, Dr. W. Hoppe for the electron channelling patterns, Dr. G. Nolze for the Kossel experiments, Mr. R. Hedel for the performance of X-ray experiments, and Dr. H. Berger for the critical reading of the manuscript.

References

1 P. Möck, *Thesis*, Humboldt-Universität zu Berlin, 1992.
2 L. Ligeon, C. Chami, R. Danielou, G. Feuillet, J. Fontenille, K. Saminadayar, A. Ponchet, J. Cibert, Y. Gobil and S. Tatarenko, *J. Appl. Phys.*, *67*(1990) 2428.
3 R. C. Pond, M. Aindow, C. Dineen and T. Peters, *Inst. Phys. Conf. Ser.*, *87*(1987) 181.
4 P. Möck, R. Hedel and H. Berger, *Z. Krist. Suppl.*, *3* (1991) 199.
5 A. Ohki, N. Shibata and S. Zembutsu, *J. Appl. Phys.*, *64* (1988) 694.
6 H. Berger, P. Möck and B. Rosner, in K. Bickmann and J. Hauck (eds.), *Proc. Röto '91*, Forschungszentrum Jülich GmbH, Jülich, Germany, 1992, p. 6.
7 M. Aindow and R. C. Pond, *Philos. Mag. A*, *63*(1991) 667.
8 P. Möck, *J. Cryst. Growth*, in press.
9 P. Möck and H. Berger, *Vide Couches Minces Suppl.*, *259* (1991) 23.
10 H. Berger, *Cryst. Res. Technol.*, *22*(1987) 1101.
11 G. Nolze, V. Geist, G. Wagner, P. Paufler and K. Jurkschat, *Z. Krist.*, *193*(1990) 111.
12 G. Nolze, *Thesis*, Universität Leipzig, 1991.
13 H. Berger, *J. Appl. Cryst.*, *17*(1984) 451.
14 R. C. Pond, in F. R. N. Nabarro (ed.), *Dislocations in Solids 8* Elsevier, Amsterdam, 1989, Chap. 38, p. 1.
15 S. Haussühl, *Kristallphysik*, Physik-Verlag, Weinheim, 1983, Chap. 3, p. 133.
16 P. Curie, *J. Phys.*, *3*(1894) 393.

Relation between dislocation density, bulk electrical properties and ohmic contacts of CdTe

I. Hähnert and M. Wienecke

Humboldt-Universität zu Berlin, Fachbereich Physik, Institut für Kristallographie und Materialforschung, Invalidenstr. 110, O-1040 Berlin (Germany)

Abstract

There are large variations in the density and distribution of dislocations in CdTe crystals. The dislocation density was determined by etching. For the electrical measurements (Hall effect and conductivity by the Van der Pauw method), crystal regions were selected which showed extrem ·ly different dislocation densities. The dislocation density did not noticeably affect the bulk electrical properties. For the preparation of ohmic contacts, a thin, strongly disturbed surface region with a high dislocation density appears to be necessary. On crystal disks with low as-grown dislocation densities, dislocations were produced by lapping or other mechanical treatment to prepare ohmic contacts on high-resistivity CdTe for Hall effect measurements.

1. Introduction

The electrical and optical properties of CdTe are important for applications of CdTe. The structural properties and surface phenomena of CdTe also play important roles. CdTe crystals have large variations in dislocation density and distribution, even in neighbouring regions. This leads to the question of whether or not the dislocation density affects the electrical properties important for applications. This question was investigated.

2. Characterization of material and experimental procedure

The crystals investigated were grown by the vertical Bridgman method with an additional auxiliary Cd source. The concentration of native point defects was expected to be uniform. Homogeneity was revealed by the electrical properties measured ˙ : the initial part of the crystal (I), in the middle part (M), and at the end (E):

(I) $p = 7.46 \times 10^{12}$ cm^{-3}, $\mu = 59$ cm^2 V^{-1} s^{-1}
(M) $p = 4.06 \times 10^{12}$ cm^{-3}, $\mu = 87$ cm^2 V^{-1} s^{-1}
(E) $p = 6.10 \times 10^{12}$ cm^{-3}, $\mu = 63$ cm^2 V^{-1} s^{-1}

where p is the carrier concentration and μ the mobility. (Impurities of 1×10^{17} cm^{-3} in the initial part and 4×10^{17} cm^{-3} at the end did not seem to play an important role [1].)

Electrical measurements were made by the Van der Pauw method at room temperature. For this purpose, ohmic contacts have to be produced. For this, the samples were coated with Au by evaporation through an appropriate four-point mask and Au wires were soldered with In. Before that, the surfaces were lapped (7 μm Al_2O_3 powder) and chemically polished (1%Br_2/methanol), removing 15–20 μm of the damaged material (usual procedure). Using this surface preparation, the contacts were ohmic (*i.e.* not acting as barriers) in all cases.

Dislocations were detected by chemical etching. Before etching, each sample was mechanically polished (1 μm Cr_2O_3 powder) and chemically polished (1%Br_2/methanol), dissolving more than 20 μm to remove the damaged layer. The etchant was composed of 60 vol.parts H_2O, 1 vol.part Cr-acid, 1 vol.part conc. HNO_3, 1 vol.part conc. HF [2]. The etch pits produced by the etchant were proved to be due to dislocations by correlating the etch pit patterns with X-ray reflection topographs and by deformation experiments [3]. The examination of a number of crystals has shown that CdTe crystals usually have large variations in their etch pit densities (EPDs) and distributions, even in neighbouring regions of the same crystal disk. To investigate the relation between the dislocation density and electrical properties, such disks with an extreme

0921-5107/93/$6.00 © 1993 – Elsevier Sequoia. All rights reserved

variation were selected. Region (A) (Fig. 1(a)) had a very high but relatively homogeneous dislocation density with very small subgrains (EPD > 5×10^5 cm^{-2}). Region (B) (Fig. 1(b)) had a typical subgrain structure: the EPD in subgrains was about 1×10^4 cm^{-2} and the EPD in the subgrain boundaries was about 3×10^3 cm^{-1}.

After etching, the different regions were separated by cleaving. For the electrical measurements, these samples were chemically polished again to remove an additional 25 μm and then the contacts were made. In these cases, the procedure did not always lead to ohmic contacts.

The surface damage owing to different mechanical preparation was analysed on reference samples by etching and by cathodoluminescence, which is sensitive to dislocations and shows the electrical behaviour of dislocations as luminescence contrast. For cathodoluminescence investigations, the samples were dimpled from the back-side up to the damaged surface by a Br/methanol vapour beam (for the method of sample preparation see Fig. 4(b)).

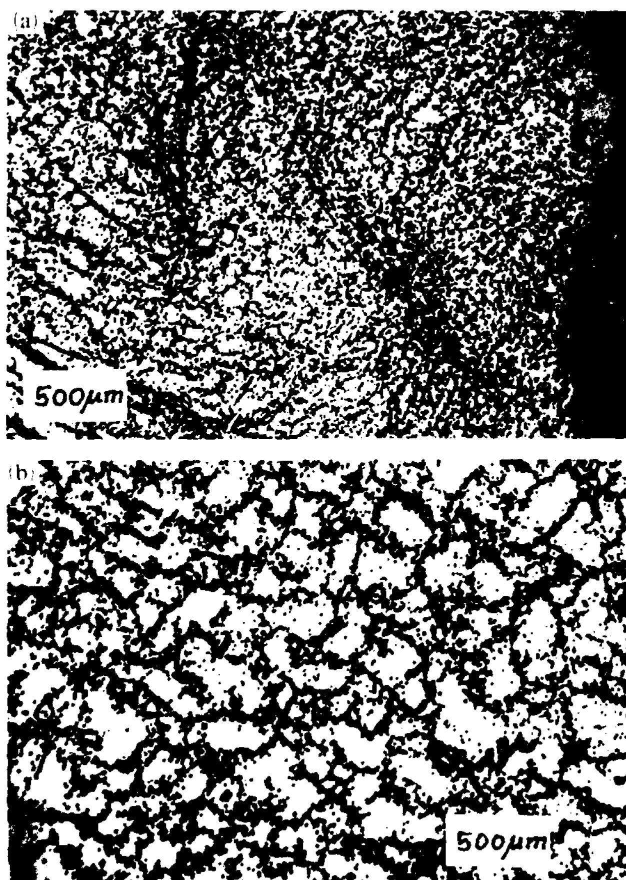

Fig. 1. Etch pattern of regions of the same crystal disk with extreme differences in dislocation density: (a) region (A) and (b) region (B) (see text); orientation of disk (111)A.

3. Results and discussion

On sample (A) with the high dislocation density, a carrier concentration of $p = 1.85 \times 10^{13}$ cm^{-3} and a mobility of 53 cm^2 V^{-1} s^{-1} were measured. Considering the error in Van der Pauw measurements, these data are of the same order of magnitude as measured on the whole crystal (see above). An increased carrier concentration owing to dislocations (in crystals with the zincblende structure, dislocations are probably charged) is not to be expected, because a dislocation density of 10^5 cm^{-2} can only cause a carrier density of less than 10^{13} cm^{-3}.

On sample (B) with large subgrains and a lower dislocation density, the contacts were not ohmic, although they were made in the same way as for sample (A). This leads to the suspicion that the dislocation density affects the contact behaviour.

For that reason, the same samples (A) and (B) were subjected to the usual surface preparation, *i.e.* lapping and short-time chemical polishing. Now, the contacts were ohmic also on sample (B). The electrical measurements yielded the following:

on sample (A) $p = 9.60 \times 10^{12}$ cm^{-3}

$\mu = 86$ cm^2 V^{-1} s^{-1}

on sample (B) $p = 5.78 \times 10^{12}$ cm^{-3}

$\mu = 52$ cm^2 V^{-1} s^{-1}

The carrier densities of both samples were of the same order of magnitude. The different mobilities do not seem to be caused by the surface treatment. In addition, the mechanical surface treatment did not significantly affect the carrier density of sample (A). However, the contacts on sample (B) were ohmic after this processing.

The only difference to the treatment described above was the surface preparation. For that reason, the damage layer owing to different mechanical preparation was systematically investigated. In particular, the dislocation density was analysed for its dependence upon the depth. Figure 2(a) shows the etch pattern of a lapped specimen after chemically dissolving 15–20 μm of the damaged layer. The EPD is over 10^5 cm^{-2}, which corresponds to the as-grown state of sample (A). In Fig. 2(b), the same sample is shown after removing more than 80 μm of the lapped surface. In this case, the EPD is equivalent to that of sample (B) in the as-grown state. It has been found that the surface damaged by lapping has a higher dislocation density to a depth of up to 60 μm. A model of a lapped surface is shown in Fig. 3. In contrast, the surface disturbed by mechanical polishing (1 μm Cr_2O_3 powder) is polycrystalline to a depth of about 3 μm (investigated by reflected high

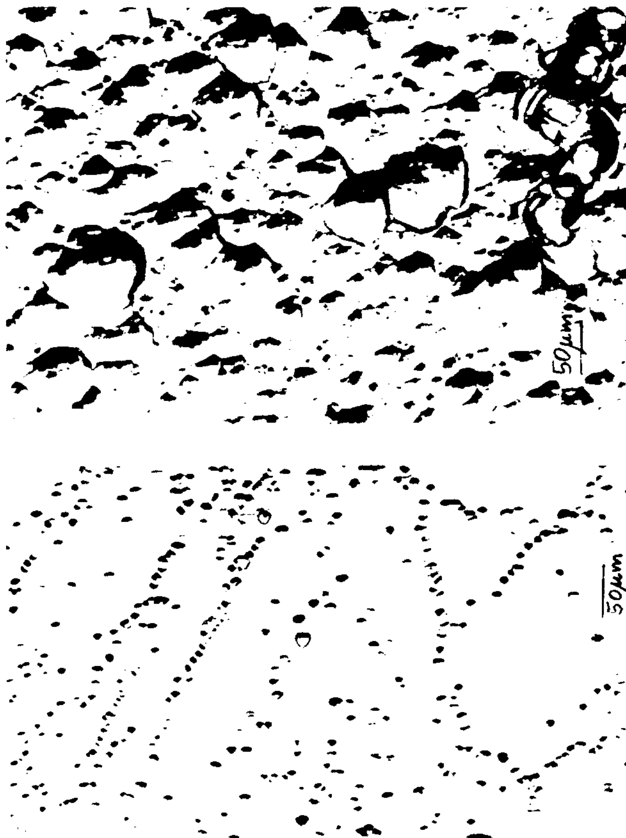

Fig. 2. Etch pattern of the lapped (111) surface: a) 15–20 µm chemically removed, EPD > $10^{?}$ cm^{-2}; b) over 80 µm chemically removed, EPD of as-grown state.

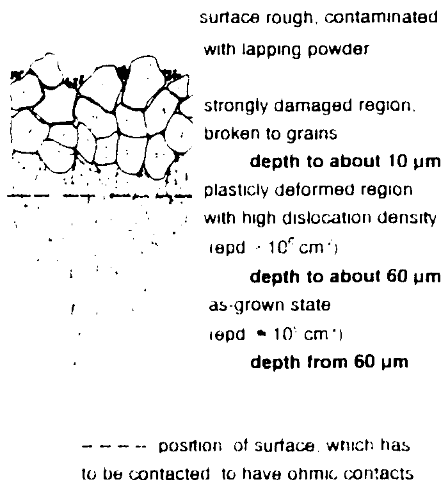

Fig. 3. Model of the surface damaged by lapping

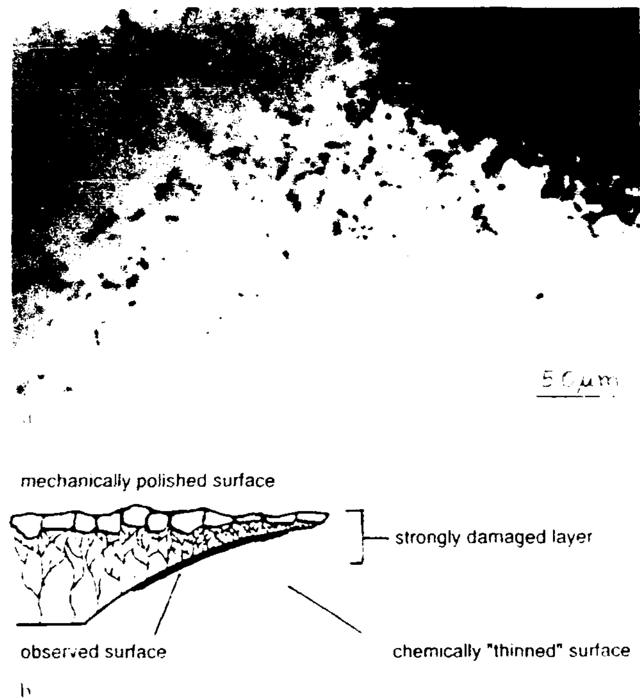

Fig. 4. Cathodoluminescence investigation of a mechanically polished surface: a) dislocation distribution near the treated surface; b) principle of sample preparation

energy electron diffraction) and has a higher dislocation density to a depth of up to 20 µm [4].

As shown in Fig. 3, a thin (40 µm) damaged layer with a higher dislocation density remains after the usual preparation of contacts on a sample surface. Relative to the whole sample thickness (over 1000 µm), this damaged layer does not affect the electrical properties but it does change the contact behaviour of the semiconductor surface, probably because the dislocations are electrically efficient. Therefore, dislocations are visible by cathodoluminescence contrast. Figure 4a shows cathodoluminescence contrast owing to dislocations, and characterizes the increased dislocation density near a mechanically damaged surface [5].

The fact that lapping and short-time chemically polishing lead to ohmic contacts on high resistivity CdTe is confirmed by measurements, e.g. Hall and conductivity measurements [6] and deep level transient spectroscopy measurements [7], which require reproducible ohmic contacts.

4. Conclusions

The carrier concentration of samples with a high dislocation density does not differ from that of samples with large subgrains and a lower dislocation density.

A damaged layer with a high dislocation density to a depth of up to 40 µm remains due to surface treatment

by lapping and short-time chemical polishing. This layer has no significant effect on the bulk carrier concentration.

A high dislocation density near the surface is necessary to prepare ohmic contacts on high resistivity CdTe.

On samples with low as-grown dislocation density, a thin damaged layer can be produced by mechanical treatment—in our case by lapping.

No relation between the dislocation density and mobility was found.

References

1 P. Rudolph, M. Mühlberg, M. Neubert, T. Boeck, L. Parthier, K. Jacobs and E. Kropp, *J. Cryst. Growth, 118* (1992) 204.
2 I. Hähnert and M. Schenk, *J. Cryst. Growth, 101* (1990) 251.
3 I. Hähnert, *Z. Krist.*, to be published.
4 I. Hähnert, to be published.
5 A. Heydenreich, *Diploma*, Humboldt Universität, 1991.
6 U. Becker, P. Rudolph, R. Boyn, M. Wienecke and I. Utke, *Phys. Status Solidi A, 120* (1990) 653.
7 H. Zimmermann, R. Boyn, P. Rudolph, J. Bollmann, A. Klimakow and R. Krause, *Mater. Sci. Eng., B16* (1993) 139–144.

Materials Science and Engineering, B16 (1993) 172–177

Effect of large-scale potential relief on the electronic transport in doped and compensated CdTe: the role of impurity correlations

N. V. Agrinskaya

A. F. Ioffe Physico-Technical Institute, St Petersburg (Russian Federation)

Abstract

We have analysed our experimental data on electronic transport in bulk doped and compensated CdTe crystals. The level of doping has been varied from the weak doping to the high doping limit. It has been shown that the data obtained can be explained by the presence of large-scale potential relief owing to an inhomogeneous impurity distribution. As for the case of heavily doped crystals (including low resistivity samples and semi-insulating samples) the energy and spatial scales of the potential are controlled by the spatial correlation of impurities and defects.

1. Introduction

In any doped semiconductors there is a system of charged impurities and, in general, one cannot expect a long-range ordering of their spatial distribution. On the other hand, it is clear that spatial fluctuations of charge distribution lead to the formation of some potential relief with a spatial scale much larger than the average distance between impurities. This large-scale potential relief (LSPR) does not change either local band structure or the local density of states.

The presence of such LSPR imposes on a semiconductor the features of a disordered system, the degree of the disorder depending on the LSPR energy scale γ and on the temperature. Some specific phenomena occur, such as Anderson localization, variable range hopping and a Coulomb gap near the Fermi level. Despite there being considerable amounts of related literature, the physical picture is not completely clear even for elementary semiconductors. This is even more the case for doped A^2B^6 compounds which were not investigated in such detail. Here, one should take into account these compounds' principal differences from elementary semiconductors which result from larger gaps and a larger degree of compensation available due to the generation of intrinsic defects and the amphoteric behaviour of impurities (self-compensation).

In this article we would like to summarize the results of our studies of electronic transport in doped and compensated CdTe crystals. The level of doping has been varied from the weak doping to the high doping limit, when a condition $Na^3 > 0.02$ has been valid (where N is the impurity concentration and a the localization length). We have also studied the effects of LSPR in semi-insulating crystals of CdTe:Cl. As for theoretical backgrounds, we have used the approach based on percolation theory, as developed by Shklovskii and Efros [1].

2. Weakly doped crystals

Here we shall consider the effects of LSPR on transport properties of weakly doped CdTe with shallow donors ($N_D < 10^{17}$ cm^{-3}). In the case of non-zero compensation $K = N_A/N_D \neq 0$, the presence of localized charges leads to an increase in the dispersion of the impurity levels. This dispersion appears to be greater than one owing to overlapping of wave functions corresponding to different impurities. The model of nonlinear screening for the case of a Poisson distribution of impurities and of large compensation $(1-K \ll 1)$ predicts the following characteristic spatial (R_s) and energy ($\gamma(R_s)$) scales of the LSPR:

$$R_s = \frac{N_t^{1/3}}{n^{2/3}}$$
$$\gamma(R_s) = \frac{e^2 N_t^{2/3}}{\kappa n^{1/3}} \qquad (1)$$

where $N_t = N_D + N_A$, n being the electron concentration, and κ is the dielectric constant.

How does this long-range potential affect the position of the Fermi level and the activation energy ε_1 (Fig. 1)? Attempts have been made to calculate the dependence $\varepsilon_1(N_D, K)$ in the two limiting cases of low temperature [2] (where kT is small compared with the

0921-5107/93/$6.00

© 1993 – Elsevier Sequoia. All rights reserved

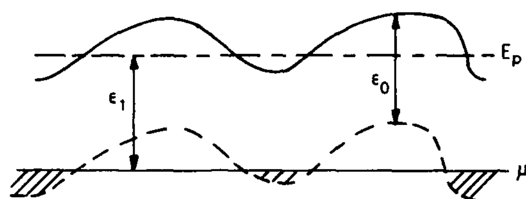

Fig. 1. Energy diagram for a lightly doped and compensated semiconductor with LSPR: μ is the Fermi level and E_p the percolation level.

width of the impurity band $W = e^2 N_t^{1/3}/\kappa$) and of high temperature [3] ($kT \gg W$).

In the first case, the following expression has been obtained:

$$\varepsilon_1 = \varepsilon_0 - \alpha N_D^{1/3} \quad (2)$$

where α is some tabulated function of K and ε_0 is the optical ionization energy.

However, the majority of experiments reported for CdS, CdSe and CdTe [4], have demonstrated that the use of eqn. (2) leads to different values of ε_0 for different values of K for the same type of donor, and that the coefficient α does not agree with the theoretical coefficient. The reason for such a discrepancy is that in real experiments $kT \approx \varepsilon_1 > W$ and the low temperature condition does not hold.

The second regime [3] is closer to the experimental situation. In this case the redistribution of electrons between the states of the impurity band leads to a decrease of ε_1 such that

$$\varepsilon_1 = \varepsilon_0 - f(K) \frac{e^3 N_D^{1/2}}{\kappa^{3/2} (kT)^{1/2}} \quad (3)$$

This equation is valid if $n < N_A$, $N_D \approx N_A$ and $kT > \Delta\varepsilon = \varepsilon_1 - \varepsilon_0$.

In the frameworks of this model we have analysed the results obtained for CdTe in our earlier investigation [6]. We have studied n-type samples which have not been subjected to any deliberate doping but which contained residual impurities. Depending on the type of donor, the optical ionization energy of these samples is 13.5-14.2 meV. The thermal ionization energy ε_1 has been calculated from the temperature dependence of the Hall coefficient in the range 15-100 K. Figure 2 shows the dependence of ε_1 on $N_D^{1/3}$.

It can be seen that it gives two values of ε_0, namely 14 and 17 meV (the first being close to optical ε_0 and the second having been attributed to another sort of donor). However, this discrepancy can be removed by using an alternative approach [3]. We plotted the dependences ε_1 ($N_D^{1/2}$) for samples with different values of K (Fig. 3). The two straight lines shown in Fig. 3 were calculated from eqn. (3) with $K = 0.94$ and

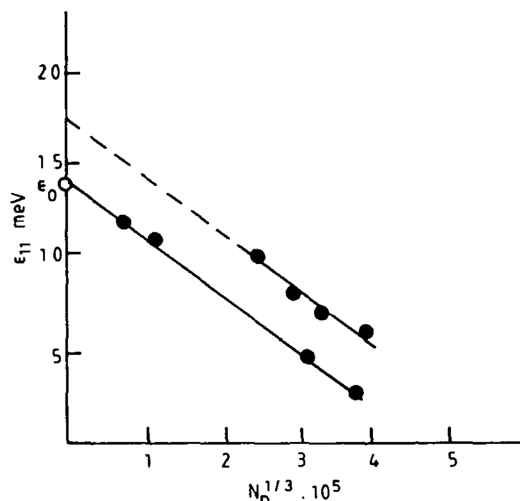

Fig. 2. Effect of the concentration of charged donors ($N_D^+ \approx N_A$) on ε calculated according to eqn. (1).

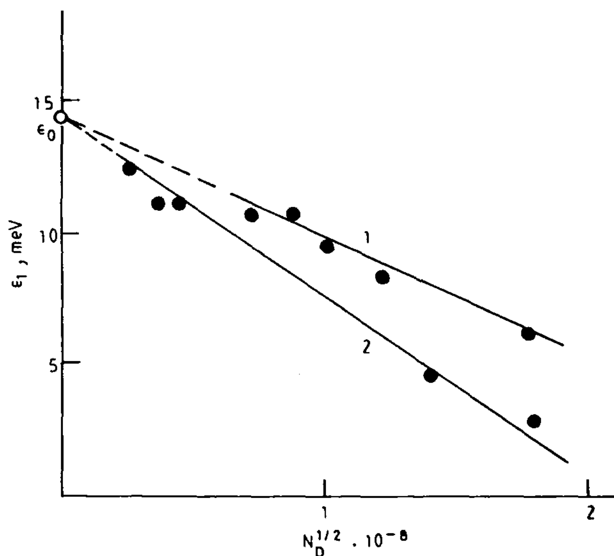

Fig. 3. Effect of the total donor concentration N_D on ε according to eqn. (2): ●, experimental results; ——, theoretical calculation for $T = 50$ K, $K = 0.95$ (1) and $K = 0.8$ (2).

0.8 and $\varepsilon_0 = 13.5$ meV. We found that the points for samples with similar values of K are located on the theoretical lines, whereas the samples with intermediate K values are in the interval between the straight lines.

Figure 4 shows the theoretical and experimental dependences $f(K)$. We can see that at least in the range of large K the theory properly describes the experimental data. It should be noted that this theory does not take into account any correlation in the impurities positions, so the satisfactory agreement with the experiment leads to the conclusion that impurity correlation is of no importance in weakly doped CdTe.

3. Heavily doped and compensated low resistivity crystals

In the case of heavily doped crystals ($Na^3 \gg 0.02$) electron states are delocalized, the impurity band merges with the conduction band and the transition to metallic conduction (the Mott transition) takes place. At a sufficiently high degree of compensation the conduction becomes activated. The density of states in these heavily doped and compensated (HDC) crystals decreases exponentially into the forbidden gap, forming a density of states 'tail' (Fig. 5). It has been shown that the main ideas of non-linear screening theory remain fruitful in the HDC case [1]. Typical values of LSPR scales R_s and $\gamma(R_s)$ are the same as given by eqn. (1). The activation energy ε_1 of d.c. conduction owing to the free carrier band mechanism in the non-metallic phase is $\varepsilon_1 = \lambda\gamma$ where λ is a numerical coefficient.

In HDC CdTe crystals with shallow donor concentration $N_D > 2 \times 10^{17}$ cm^{-3} we have studied the band conduction σ owing to allowed states, its dependences on temperature and on compensation [6], as well as low temperature hopping conductivity [6, 7]. Crystals have been doped with chlorine and indium during the growth process (the donor concentration being $N_D \approx 10^{18}$ cm^{-3}) and have been compensated by prolonged high temperature annealing at $T_a = 900$ °C followed by quenching. By varying the annealing conditions (cadmium vapour pressure) we have been able to obtain low resistivity crystals with different degrees of compensation $K = 0.5$–0.99. Such differences in the degree of compensation have been obtained as a result of different concentrations of intrinsic compensating defects. It is possible to distinguish two regions in the temperature dependence of σ. The first region corresponds to the range 100–300 K and can be characterized by an activation energy ε_1. We have shown that dependence of ε_1 on carrier concentration n cannot be described by a simple theoretical model for the random impurities distribution (eqn. (1)). Figure 6 demonstrates the significant deviation of experimental curves from the theoretical linear dependence of $n^{-1/3}$ in eqn. (1) especially for samples with large values of K. The theory in question is valid if it holds that $R_0 > R_s$ where

$$R_0 = (\kappa T_a / 8\pi N e^2)^{1/2} \tag{4}$$

is the screening radius owing to charged impurities at freezing temperature T_a. In the case of strongly compensated samples one has $R_0 \ll R_s$ and it became necessary to allow for impurity correlations. Since the density of intrinsic carriers at T_a is 10^{16} cm^{-3}, their contribution to the screening is small. The electronic properties of compensated semiconductors with a correlated distribution of impurities have been investigated theoretically in refs. 1 and 8. It has been shown that the energy ε_1 decreases logarithmically with an increase in n such that

$$\varepsilon_1{}^2 = \gamma_0{}^2 \left\{ \ln \left[\frac{(m\gamma_0)^{3/2}}{h^3 n} \right] \right\} \tag{5}$$

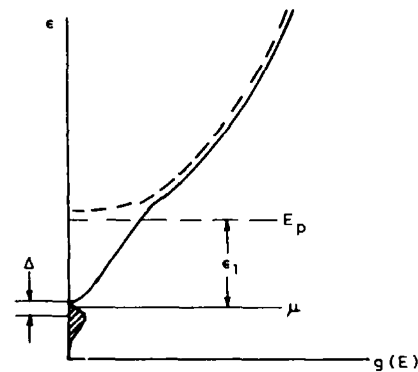

Fig. 5. Density of states of a highly doped and compensated semiconductor in the presence of a Coulomb gap Δ.

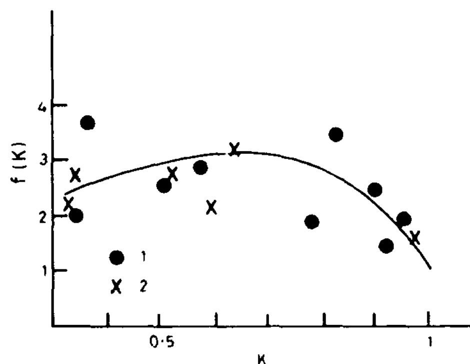

Fig. 4. Dependence $f(K)$ with the curve calculated for $f(K) = \sqrt{\pi}(K+3)\sqrt{\{K(1-K)\}}$. Experimental results are plotted for donors (●) and acceptors (×).

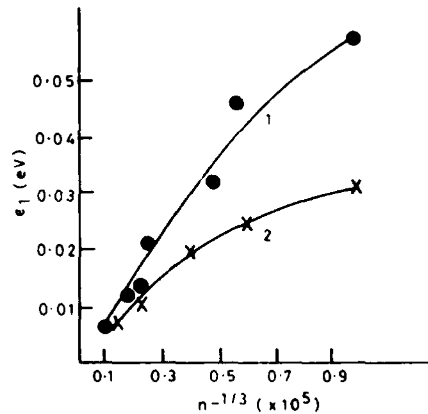

Fig. 6. Dependence of ε_1 on n calculated according to eqn. (1): 1, CdTe:In; 2, CdTe:Cl.

Here the value of γ_0 is controlled by the impurity screening rather than by electron screening such that

$$\gamma_0 = 4\pi^{1/2} e^2 \kappa^{-1} N^{1/2} R_0^{1/2} \qquad (6)$$

We have experimentally observed the dependences $\varepsilon_1(n)$ to be the same as predicted by eqn. (5) (Fig. 7); from the slopes of the curves we have obtained the values $\gamma_0 = 0.026$ and 0.015 eV for CdTe:In and CdTe:Cl respectively. It should be noted that such a correlated impurity distribution can be realized only in wide-gap doped and compensated semiconductors, where the intrinsic carrier concentration at T_a is lower than the charged impurity concentration. Thus, for HDC crystals, the scale of LSPR is independent of n or K but is determined by the concentration of charged impurities and the value of T_a, which should be greater than the freezing temperature of the impurities.

In the temperature range 20–6 K in the Ohmic regime the conductivity of these samples obeys the Mott law which is characteristic for the variable range hopping mechanism.

$$\ln \sigma \approx (-T_0/T)^{1/4} \qquad (7)$$

At the temperatures 8–4 K a transition to a more steep dependence has been observed (Fig. 8); in a low temperature region 1.7–6 K the latter can be approximated by the expression [1]

$$\ln \sigma \approx (-T_1/T)^{1/2} \qquad (8)$$

This type of dependence characterizes hopping conductivity owing to states in the parabolic gap near the Fermi level, which is owing to the Coulomb interaction of localized electrons [1]. Such a transition has been predicted theoretically but, as far as we know, it has not been observed in either crystalline (where the conduction, described by eqn. (8) has been observed) or amorphous semiconductors (where Mott-type hopping conduction has been observed) until our studies. Such a transition has been reported for the compound of the same type, *i.e.* CdSe [9]. It is a specific density of states behaviour in systems with correlated spatial distribution of impurities that, in our opinion, explains the fact that the transition discussed seems to be observable only in a specific class of semiconductors. From the parameters of the $\sigma(T)$ dependence we have obtained the values of the Coulomb gap $\Delta \approx 1 \times 10^{-3}$ eV, density of states near the Fermi level and values of κ and a near the metal–dielectric transition [7].

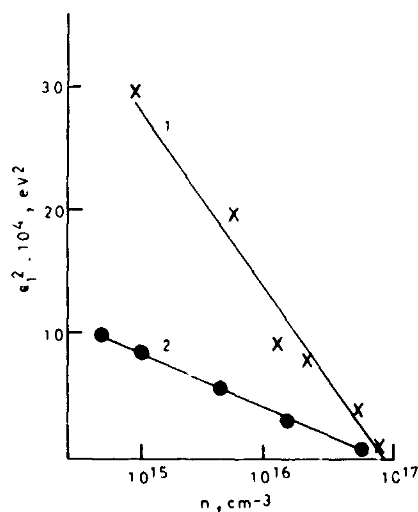

Fig. 7. Dependence of ε_1 on n calculated according to eqn. (5): 1, CdTe:In; 2, CdTe:Cl.

4. Semi-insulating crystals

Semi-insulating semiconductor crystals, such as GaAs and CdTe, are used widely as detectors of radiation but there is no model at present which could account for all electrical and galvanomagnetic phenomena. This makes it difficult to determine the principal parameters of semi-insulating materials, such as density and mobility of carriers. In high resistivity semiconductors the screening of LSPR by free carriers is not effective, therefore the spatial and energy scales of LSPR are expected to be large ($\gamma \approx E_g/2$) [1].

The semi-insulating CdTe crystals have been prepared by shallow donor doping and by a programme of thermal treatments after growth. In the course of such a treatment, intrinsic defects, impurity–defect complexes as well as clusters of impurities and defects are created.

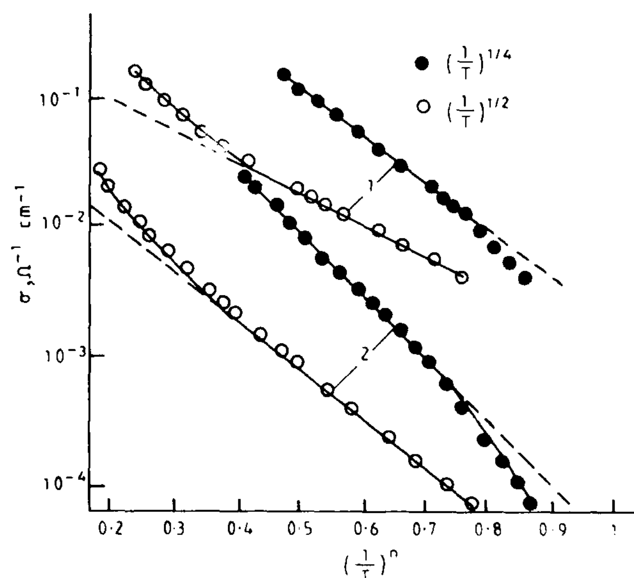

Fig. 8. Low temperature dependence $\sigma(T)$ for two CdTe:Cl samples: 1, $n_{300K} = 1.5 \times 10^{17}$ cm^{-3}; 2, $n_{300K} = 6 \times 10^{16}$ cm^{-3}; ●, $(1/T)^{1/4}$; ○, $(1/T)^{1/2}$.

As is known, electronic transport in these semi-insulating crystals is strongly dependent on the conditions of this treatment. However, we have found some evidence that for semi-insulating CdTe the scales of LSPR are not so large: examples of this evidence include the absence of persistent photoconductivity and the presence of intense, narrow exciton lines and donor–acceptor lines in luminescence spectra.

In the case of p-type crystals the conduction is dominated by holes, and the values of the Hall coefficient R_H and Hall mobility μ_H reflect the actual hole density p and mobility μ_0 (note that at temperatures $T \geqslant 300$ K, μ_0 is determined by optical phonon scattering, with the theoretical estimate being μ_0 ($T = 300$ K) $= 100$ cm^2 V^{-1} s^{-1}). For most p-type crystals $p \approx 10^7$–10^8 cm^{-3} and $\mu_H \approx 50$–80 cm^2 V^{-1} s^{-1}. The dependences $\mu_H(T)$ have appeared to be close to that found theoretically for polar optical scattering. Therefore, it can be concluded that in this case $\gamma \leqslant kT$ while the slight difference between μ_H and μ_0 can be explained by the framework of the effective media model.

The samples with a negative Hall constant exhibit very small values of μ_H, the ratio μ_H/μ_0 being of the order of 10–100 at $T = 300$ K [10]. The value of $\mu_H(T)$ increases with T according to a power law. One could try to explain the low values of μ_H as a result of the presence of mixed n- and p-type conductivities, but the product of experimentally determined electron (n) and hole (p) densities appeared to be $np \approx (10$–$10^3)n_i^2$ (where n_i is the intrinsic carrier density) rather than $np = n_i^2$ which is expected for a homogeneous semiconductor. Therefore, this approach is not self-consistent. Thus we have concluded that the only possible way to explain the behaviour observed is to suggest the presence of LSPR. If the average LSPR amplitude $\gamma > kT$ we can describe electrical properties making use of percolation theories [1]. The behaviour of the Hall effect for such a case has been explained in ref. 11, where it has been shown that the effective carrier density contributing to R_H exceeds the carrier density on a percolation level, such that μ_H is always less than μ_0. It has been predicted also that μ_H obeys a temperature dependence in the form of a power law such that

$$\mu_H \approx \mu_0(kT/\gamma)^m \tag{9}$$

where $m = 2$, 3 or 4.

We have analysed in detail the data for sample 1 (Fig. 9) with the lowest μ_H. We have considered the results obtained using a model of an inhomogeneous semiconductor and assuming that the conduction occurs mainly in an electron cluster because of the negative sign of the Hall effect and the large value of the mobility ratio μ_n/μ_p. Since the application of a magnetic field does not alter the geometry of the flow of the current in an inhomogeneous semiconductor, the relative value of the transverse magnetoresistance $\Delta\rho/\rho$ should represent the true electron mobility μ_0; therefore, the mobility can be estimated experimentally from the values of $\Delta\rho/\rho$ in weak magnetic fields B:

$$\Delta\rho/\rho = \beta(\mu_0 B/c)^2 \tag{10}$$

where β is the magnetoresistance coefficient ($\beta = 0.5$ for inhomogeneous crystals where carriers are scattered by optical phonons).

It is demonstrated in Fig. 9 that the value and temperature dependence of the mobility $\mu(T)$ deduced from the above relation for $\beta = 0.5$ are close to the theoretical results predicted for sample 1. As for the significant discrepancies between the temperature dependences of μ_H and of the mobility deduced from $\Delta\rho/\rho$ measurements, these can be explained only by an inhomogeneity of the current flow in a sample, *i.e.* by the presence of an LSPR.

The dependence $\mu_H(T)$ for samples 1 and 2 is steeper than predicted theoretically for the case with $\gamma = $ constant (eqn. (9)). Such behaviour can occur if the value of γ actually decreases with an increase of T because of the exponential increase of screening carrier density n_0. The value $\gamma \approx 0.088$ eV is then found for sample 1 at 300 K but it decreases to 0.04 eV as T increases.

We have also observed that semi-insulating crystals with low values of μ_H exhibit non-Ohmic behaviour in relatively weak electric fields as well as a strong frequency dependence of σ in a frequency range 10^5–10^7

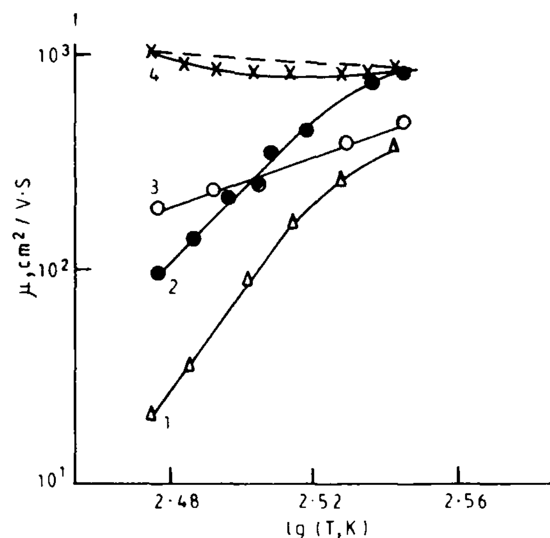

Fig. 9. Dependences $\mu_H(T)$ in semi-insulating CdTe:Cl. Curves 1–3 represent different n-type samples and curve 4 $\mu(T)$ deduced from the measurement of $\Delta\rho/\rho$ for sample 1. The dashed curve is the theoretical dependence $\mu_0(T)$.

Hz [12]. Such behaviour is in qualitative agreement with theoretical results of Pistoulet *et al.* [13].

Thus our investigations of the galvanomagnetic phenomena in semi-insulating CdTe crystals have demonstrated that the low values of μ_H and the great variety of the dependences $\mu_H(T)$ observed for different samples can be explained by the presence of LSPR with different amplitudes. However, the energy scale of the LSPR appears to be much smaller than the value $E_g/2$ expected for semi-insulating crystals. It is the impurity correlation that provides the only possibility to explain this fact.

Here we would like to note that anomalously large degrees of compensation observed for semi-insulating CdTe:Cl can be explained within the frameworks of the low temperature self-compensation model [14]. This model suggests the formation of a compensating defect in the vicinity of the impurity due to some lattice relaxation process driven by the energy gain provided by the compensation. Therefore, in the course of such a process one inevitably obtains some correlation in the positions of impurities and compensating defects, which explains the experimental results discussed.

Therefore, it can be concluded that the peculiar features of the electron transport in weakly doped as well as in heavily doped and compensated CdTe can be explained by the presence of LSPR. As for the case of heavily doped crystals (including low resistivity samples as well as semi-insulating ones), the spatial and energy scales of the potential are controlled by the spatial correlation of impurities and defects.

References

1 B. I. Shklovskii and A. L. Efros, *Electronic Properties of Doped Semiconductors*, Springer, Heidelberg, Berlin, 1984. .
2 N. Van Lien and B. I. Shklovskii, *Sov. Phys. Semicond., 13* (1979) 1025.
3 A. A. Uzakov and A. L. Efros, *Sov. Phys. Semicond., 21* (1987) 562.
4 H. H. Woodbury and M. Aven, *Phys. Rev. B, 9* (1974) 5195.
5 N. V. Agrinskaya, *Sov. Phys. Semicond., 22* (1988) 1062.
6 N. V. Agrinskaya and O. A. Matveev, *Sov. Phys. Semicond., 9* (1975) 1423.
7 N. V. Agrinskaya and A. N. Aleshin, *Sov. Phys. Solid State, 31* (1989) 1996.
8 Yu. S. Galpern and A. L. Efros, *Sov. Phys. Semicond., 6* (1973) 1537.
9 Y. Zhang, P. Dai, M. Levy and M. P. Sarachik, *Phys. Rev. Lett., 64* (1990) 2687.
10 N. V. Agrinskaya, E. N. Arkadeva and A. I. Terentev, *Sov. Phys. Semicond., 23* (1989) 143.
11 V. G. Karpov, A. Ya. Shik and B. I. Shklovskii, *Sov. Phys. Semicond., 16* (1982) 901.
12 N. V. Agrinskaya and O. A. Matveev, *Sov. Phys. Semicond., 14* (1980) 611.
13 B. Pistoulet, P. Girard and G. Hamamdjan, *J. Appl. Phys., 56* (1984) 2275.
14 N. V. Agrinskaya and O. V. Matveev, *Nucl. Instrum. Methods A, 283* (1989) 263.

Efficient n-type doping of CdTe epitaxial layers grown by photo-assisted molecular beam epitaxy with the use of chlorine

D. Hommel, S. Scholl, T. A. Kuhn, W. Ossau, A. Waag and G. Landwehr
Universität Würzburg, Physikalisches Institut, W-8700 Würzburg (Germany)

G. Bilger
Universität Stuttgart, Institut für Physikalische Elektronik, W-7000 Stuttgart 80 (Germany)

Abstract

Chlorine has been used successfully for the first time for n-type doping of CdTe epitaxial layers (epilayers) grown by photo-assisted molecular beam epitaxy. Similar to n-type doping of ZnSe layers, $ZnCl_2$ has been used as source material. The free-carrier concentration can be varied over more than three orders of magnitude by changing the $ZnCl_2$ oven temperature. Peak mobilities are 4700 $cm^2 V^{-1} s^{-1}$ for an electron concentration of 2×10^{16} cm^{-3} and 525 $cm^2 V^{-1} s^{-1}$ for 2×10^{18} cm^{-3}. The electrical transport data obtained by Van der Pauw configuration and Hall structure measurements are consistent with each other, indicating a good uniformity of the epilayers. In photoluminescence the donor-bound-exciton emission dominates for all chlorine concentrations. This contasts significantly with results obtained for indium doping, commonly used for obtaining n-type CdTe epilayers. The superiority of chlorine over indium doping and the influence of growth parameters on the behaviour of CdTe:Cl layers will be discussed on the basis of transport, luminescence, secondary ion mass spectroscopy and X-ray photoelectron spectroscopy data.

1. Introduction

Devices based on II-VI semiconducting compounds are of increasing interest owing to their potential application in optoelectronics. Because of the so-called self-compensation, either n- or p-type doping is hard to obtain for a given II-VI semiconductor. A breakthrough has been achieved in the last year by the 3M Company, demonstrating the first green-blue p-n junction laser based on ZnSe [1]. Also recently a near-IR $Hg_{1-x}Cd_xTe$/CdTe quantum well laser has been reported [2]. For such devices, high carrier concentrations up to 10^{18} cm^{-3} are needed. Substitutional doping of CdTe, grown by molecular beam epitaxy (MBE), can be enhanced by illuminating the growing surface with laser light of an energy larger than the band gap (photo-assisted molecular beam epitaxy (PAMBE)) [3]. Using PAMBE n-type CdTe:In layers with peak mobilities up to 3250 $cm^2 V^{-2} s^{-1}$ for a carrier concentration of 7.7×10^{15} cm^{-3} have been reported [4].

Chlorine, which forms a shallow donor in CdTe, has been widely used in the past to obtain semi-insulating bulk crystals [5]. Bulk CdTe:Cl is also an interesting material for efficient γ-ray detectors [6]. The ionization energy of the shallow donor (chlorine on a tellurium lattice site), is 14.5 meV as determined by photoluminescence (PL) and transport measurements [7, 8]. Although chlorine was found in MBE-grown epitaxial layers (epilayers) as a residual impurity, to our knowledge no attempts have been made so far to use chlorine for intentional doping during MBE growth [9, 10].

2. Sample preparation and experimental details

The CdTe:Cl epilayers were grown on CdTe (100) substrates in a four-chamber Riber 2300 MBE system. Details of the substrate preparation can be found elsewhere [4]. CdTe and $ZnCl_2$ were used as source materials. $ZnCl_2$ was chosen as dopant because elemental halogens, which should give rise to shallow donors on tellurium sites cannot be used in a standard MBE effusion cell. $ZnCl_2$ is used successfully for n-type doping of ZnSe epilayers [11]. The substrate temperature was 200 °C for the growth of the chlorine-doped layers 2 μm thick. Prior to that a 0.2 μm undoped CdTe buffer layer was grown at 300 °C. The growth rate was typically 0.6 $\mu m\ h^{-1}$. The growing surface was illuminated with the 488 nm line of a continuous-wave Ar^+ laser with about 50 mW cm^{-2}. No cap layers were

0921-5107/93/$6.00
© 1993 - Elsevier Sequoia. All rights reserved

deposited onto the CdTe:Cl. The transport properties were measured using samples in the Van der Pauw configuration as well as Hall structures. PL measurements were done at 1.8 K using an excitation well above the band gap. Chlorine and zinc concentrations were determined by secondary ion mass spectroscopy (SIMS). As SIMS investigations are very sensitive to low elemental concentrations but not at all quantitative, X-ray photoelectron spectroscopy (XPS) measurements were performed to qualify the dopant concentrations.

3. Experimental results

3.1. Transport measurements

Free-carrier concentrations between 6×10^{16} and 2×10^{18} cm^{-3} can be obtained reproducibly by changing the temperature of the $ZnCl_2$ effusion cell. This corresponds to resistivities between 8.5×10^{-3} and 2.6 Ω cm. With increasing $ZnCl_2$ source temperature the free-carrier concentration reaches a maximum of about 2×10^{18} cm^{-3} and decreases then to a value between 3×10^{17} and 5×10^{17} cm^{-3} (Fig. 1). As expected for shallow donors, the carriers are frozen out for a low doping level but their concentration remains constant for degenerately doped layers.

The highest peak mobility of 4700 cm^2 V^{-1} s^{-1} at 30 K was found for a free-carrier concentration of n at room temperature of 1.8×10^{16} cm^{-3}, which is the highest reported value for n-type CdTe with this carrier concentration. Peak mobilities for CdTe:Cl layers with $n \geqslant 10^{17}$ cm^{-3} are between 560 and 840 cm^2 V^{-1} s^{-1} depending on the details of the growth conditions. In Fig. 2 the temperature dependences of their mobilities, normalized to their peak value, are given for three characteristic samples. With increasing $ZnCl_2$ flux (dopant incorporation), scattering at ionized impurities, being the limiting factor at low temperatures, becomes more important, resulting in a shift in the peak mobility to higher temperatures.

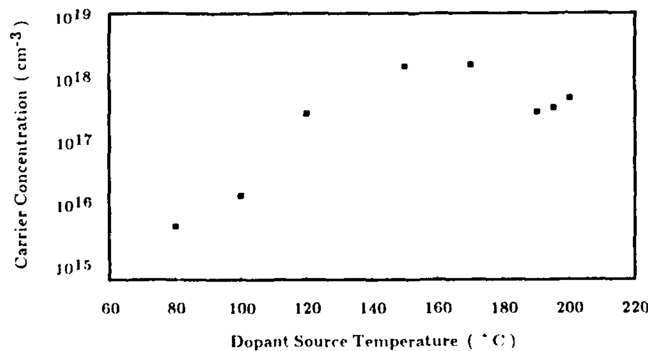

Fig. 1. The free-carrier concentration, measured at 300 K, as a function of the $ZnCl_2$ dopant source temperature.

3.2. Photoluminescence

The PL spectra of different CdTe:Cl layers and an undoped sample are given in Fig. 3. Even for the

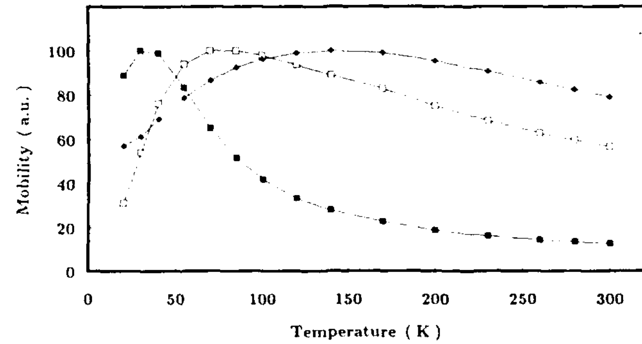

Fig. 2. The temperature dependence of the mobility for CdTe layers with different chlorine content normalized to equal peak values: ■, sample CT523 (T_{Cl} = 100 °C); □, sample CT522 (T_{Cl} = 120 °C); ◆, sample CT512 (T_{Cl} = 200 °C). With increasing dopant concentration the scattering at ionized impurities dominates, resulting in a shift in the mobility maximum to higher temperatures.

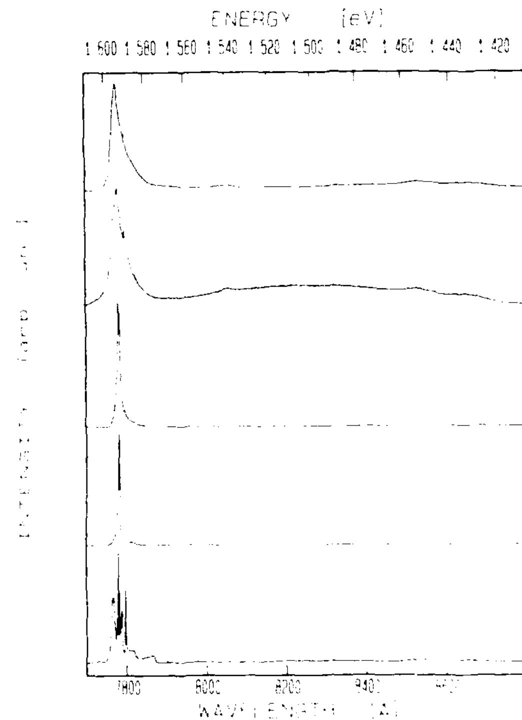

Fig. 3. The 1.8 K PL spectra of, from the bottom to the top, samples CT516 (undoped; high resistance), sample CT523 (T_{Cl} = 100 °C; 1.7×10^{16} cm^{-3}), sample CT522 (T_{Cl} = 120 °C; 3.2×10^{17} cm^{-3}), sample CT511 (T_{Cl} = 170 °C; 1.7×10^{18} cm^{-3}) and sample CT512 (T_{Cl} = 200 °C; 5.5×10^{17} cm^{-3}). Even at the highest dopant incorporation, DAP and DL emissions are negligible.

highest chlorine doping level the donor-bound-exciton (DBE) emission dominates the spectrum. Donor–acceptor pair band (DAP) and deep-level (DL) emission due to the formation of defects are very weak and detectable only for higher doped layers. The acceptor concentration therefore must be lower than 10^{15} cm^{-3}. It has been checked carefully by comparison with undoped layers and substrate luminescence that the observed emission arises from the CdTe:Cl epilayer.

In Fig. 4 the excitonic part of the spectra is seen in detail. The half-width of the DBE line (D^0, X) in the undoped CdTe layer (CT516) is 0.14 meV. The resistivity of this undoped sample was too high to obtain information about the type and net doping from electrical measurements. The half-width is still relatively small (1.55 meV) for sample CT522 with a room-temperature free-carrier concentration of 3.2×10^{17} cm^{-3} and increases with further increase in the $ZnCl_2$ cell temperature because of the interaction of the DBEs. Although at the highest carrier concentrations, screening effects might be expected the observed line shape and the energy position of the peaks discussed here are strong evidence for an excitonic origin of the transitions. For sample CT512, with a free-carrier concentration close to that of CT522, but grown with a higher $ZnCl_2$ flux, this half-width is 6 meV. This is accompanied by a shift in the excitonic peak to a higher energy.

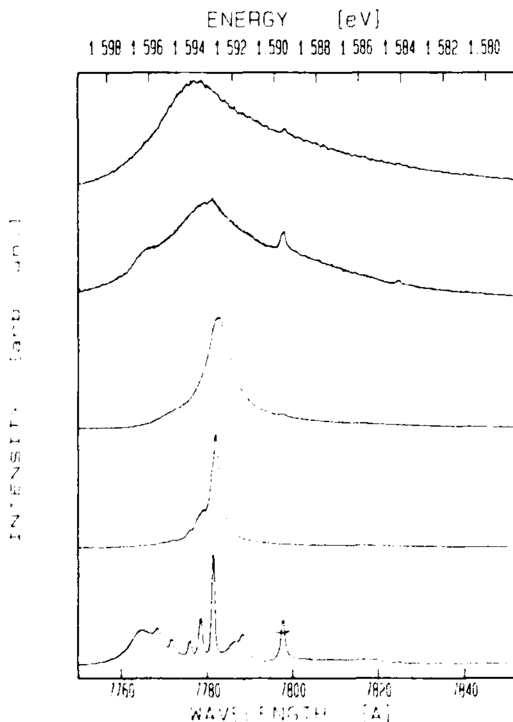

Fig. 4. The excitonic region of the same epilayers as given in Fig. 3. Although samples CT522 and CT512 have similar free-carrier concentrations (see Fig. 1) the (D^0, X) peak is broadened much more for sample CT512 owing to the higher dopant incorporation.

3.3. *Secondary ion mass spectroscopy*

Positive SIMS for the elements zinc, cadmium and tellurium and negative SIMS for the elements chlorine and tellurium were measured subsequent to XPS analysis. The zinc-to-tellurium and chlorine-to-tellurium ratios calibrated to the concentrations specified with XPS for high doped samples (the XPS detection limit is 0.7% for chlorine and 0.07% for zinc). The zinc concentrations obtained by SIMS are half those for chlorine, indicating a nearly stoichiometric incorporation of the $ZnCl_2$ source material into the epilayers.

4. Discussion

In indium-doped CdTe epilayers the strong tendency towards self-compensation limits the achievable free-carrier concentration to the mid-10^{17} cm^{-3}. At such concentrations, DAP and DL emissions are significant in the PL spectra. This is not the case for chlorine-doped CdTe epilayers. Free carrier concentrations up to 2×10^{18} cm^{-3} can be obtained without the formation of deep compensating complexes. Also the influence of laser illumination during growth—a necessary condition for successful indium doping—is not so drastic. Studying a pair of CdTe:Cl samples grown in the same run with only one of them illuminated, the free-carrier concentration in the PAMBE sample is only 40% higher than in the conventionally grown sample. For CdTe:In samples this difference is larger than one order of magnitude and DL emission is much stronger for growth without laser assistance. The mobility of the MBE sample is about 15% lower than that of PAMBE-grown CdTe:Cl epilayers of a similar free-carrier concentration.

As shown in Fig. 1, the carrier concentration as a function of the $ZnCl_2$ cell temperature goes through a maximum and decreases with a further increase in the dopant flux. This is in contrast with results reported for ZnSe:Cl [11, 12]. In CdTe:Cl bulk crystals the formation of deep compensating acceptor complexes has been discussed for higher chlorine concentrations [8]. A molecular complex of a chlorine atom on a tellurium site and a second chlorine atom on one of the nearby interstitial sites (Cl_{Te}–Cl_{int}) has been considered [13], but no significant DAP or DL emission was found in our epilayers. Such compensating defects, which are connected with cadmium vacancies, may not be formed because potential cadmium vacancies could be occupied by zinc atoms.

The observed PL shift of the (D^0, X) peak to a lower wavelength for higher $ZnCl_2$ cell temperatures is due

to the increasing number of zinc atoms in the host lattice, resulting in a larger band gap. To explain the observed shift a zinc concentration not exceeding 0.1 at.% should be assumed. From the nearly stoichiometric incorporation (SIMS or XPS) of zinc and chlorine, it follows that under such growth conditions (CT512) less than 2% of the incorporated chlorine atoms are electrically active (5.5×10^{17} cm^{-3} free electrons at room temperature). According to first SIMS data this ratio might be even worse. The insignificant (D^0, X) shift for sample CT511 with a carrier concentration of 1.7×10^{18} cm^{-3} indicates a much better chlorine activation under optimized growth conditions. Detailed investigations, which allow us to fit SIMS and PL data quantitatively, are in progress.

Shubnikov–de Haas oscillations observed for the first time in high magnetic field measurements indicate the high quality of the CdTe:Cl epilayers too [14].

5. Conclusion

It has been shown that the electron concentration in CdTe:Cl epilayers can be varied easily over three orders of magnitude by changing the temperature of the $ZnCl_2$ dopant source. The emission spectra are dominated by the DBE peak even for heavy doping; thus the tendency towards self-compensation is much lower than in indium-doped CdTe layers grown under optimized conditions. 4700 cm^2 V^{-1} s^{-1} is the highest reported peak mobility for an n-type CdTe epilayer with 10^{16} cm^{-3} grown by PAMBE. The possibility of degenerate doping in the 10^{18} cm^{-3} range is important for device applications. Further studies are needed to understand the underlying physical processes for the observed maximum in the free-carrier concentration.

Acknowledgments

This research is supported by the Bundesministerium für Forschung und Technologie, Bonn and partly (luminescence, T. A. Kuhn) by the Deutsche Forschungsgemeinschaft. The authors would like to thank Miss P. Wolf for assistance with sample preparation.

References

1 M. A. Haase, J. Qiu, J. M. dePuydt and H. Cheng, *Appl. Phys. Lett.*, *59* (1991) 1272.

2 M. Zandian, J. M. Arias, R. Zucca, R. V. Gil and S. H. Shin, *Appl. Phys. Lett.*, *59* (1991) 1022.

3 N. C. Giles, R. N. Bicknell, R. L. Harper, S. Hwang, K. A. Harris and J. F. Schetzina, *J. Cryst. Growth*, *86* (1988) 348.

4 R. N. Bicknell-Tassius, A. Waag, Y. S. Wu, T. A. Kuhn and W. Ossau, *J. Cryst. Growth*, *101* (1990) 33.

5 M. Azoulay and H. Feldstein, in E. M. Anastassakis and J. D. Joannopoulos (eds.), *Proc. 20th Int. Conf. on the Physics of Semiconductors, Thessaloniki, 1990*, World Scientific, Singapore, 1990, p. 2303.

6 P. Siffert, A. Cornet, R. Stuck, R. Triboulet and Y. Marfaing, *IEEE Trans. Nucl. Sci.*, *22* (1975) 211.

7 J. M. Francou, K. Saminadayar and J. L. Pautrat, *Phys. Rev. B*, *41* (1990) 12035.

8 N. V. Agrinskaya, M. V. Alexeenko, E. N. Arkad'eva, O. A. Matveev and S. V. Prokof'ev, *Sov. Phys.—Semicond.*, 9 (1975) 208.

9 J. M. Francou, K. Saminadayar, J. L. Pautrat, J. P. Gaillard, A. Million and C. Fontaine, *J. Cryst. Growth*, *72* (1985) 220.

10 P. Spellward, J. C. C. Day, A. D. Ashford and B. Lunn, in L. M. Brown (ed.), *Electron Microscopy and Analysis Group 1987*, in *Inst. Phys. Conf. Ser.*, *90* (1987) 277.

11 K. Ohkawa, T. Mitsuyu and O. Yamazaki, *J. Appl. Phys.*, *62* (1987) 3216.

12 H. Cheng, J. M. dePuydt, J. E. Potts and M. A. Haase, *J. Cryst. Growth*, *95* (1989) 512.

13 N. V. Agrinskaya and V. V. Shashkova, *Sov. Phys.—Semicond.*, *24* (1990) 437.

14 S. Scholl, A. Waag, D. Hommel, K. Von Schierstedt, W. Ossau and G. Landwehr, *Physica B*, (1992) in press.

Materials Science and Engineering, B16 (1993) 182–185

Effect of thermal annealing on the microstructure of CdTe and $Cd_{1-x}Zn_xTe$ crystals

J. Shen, D. K. Aidun, L. Regel and W. R. Wilcox
Center for Advanced Materials Processing, Clarkson University, Potsdam, NY 13699 (USA)

Abstract

The effect of annealing in cadmium or tellurium vapor on CdTe and $Cd_{0.96}Zn_{0.04}Te$ was investigated using different characterization methods. Tellurium-rich precipitates with a size between 0.5 and 5.0 μm were no longer seen after annealing in tellurium vapor, while precipitates between 5.0 and 15 μm appeared. Annealing in cadmium vapor caused the concentration of the larger precipitates to diminish. The lattice constant was decreased by annealing in cadmium vapor and increased by annealing in tellurium vapor. The etch pit density was decreased by annealing in tellurium vapor and increased by annealing in cadmium vapor.

1. Introduction

The post-growth annealing of CdTe and zinc-doped CdTe has been reported in the literature [1–3]. Lorenz and Segall [4] reported that slow cooling after annealing in the tellurium vapor avoids the formation of finally divided precipitates. In another study [5], the tellurium precipitate density in p-type CdTe was increased by annealing in tellurium vapor and decreased by annealing in cadmium vapor at 650 °C. Triboulet *et al.* [6] reported that cadmium- and tellurium-rich CdTe showed opposite changes in properties by annealing in cadmium vapor. They explained these results by the presence of cadmium-rich or tellurium-rich precipitates in the as-grown crystals.

The goal of the present work was to improve the understanding of the effect of annealing in cadmium and tellurium vapor on the microstructure of CdTe and zinc-doped CdTe crystals. IR microscopy, chemical etching and X-ray powder diffraction were employed to characterize the crystal samples.

2. Experiments

The CdTe ingot used in these experiments was grown in our laboratory by the vertical Bridgman–Stockbarger (VBS) technique. The starting material for CdTe growth was obtained from II–VI, Inc. $Cd_{0.96}Zn_{0.04}Te$ wafers were cut from ingots grown by a modified VBS technique by II–VI, Inc. The original purities of the starting materials were reported to be all 99.9999%. Our growth furnace was a two-zone VBS furnace with the following growth parameters: ampoule translation rate, 2 mm h^{-1}; furnace temperature gradient near the solid–melt interface, about 2.5 °C cm^{-1}; hot-zone and cold-zone temperatures, 1120 °C and 1080 °C respectively; post-growth cooling rate, 10 °C h^{-1} from 1090 to 1000 °C, 20 °C h^{-1} from 1000 to 800 °C, and 50 °C h^{-1} from 800 °C to room temperature. CdTe and $Cd_{0.96}Zn_{0.04}Te$ single-crystal wafers with a thickness of 2.0 mm were mined from the ingots and sectioned into 15 mm × 20 mm samples. Both sides of the samples were mechanically polished and then chemically polished in 2%Br–methanol before annealing. The annealing processes were conducted inside well cleaned and evacuated (less than 10^{-6} Torr) quartz ampoules with excess cadmium and tellurium shot in each ampoule. The experimental parameters for each experiment are listed in Table 1. After annealing, the furnace was cooled at 33 °C h^{-1} from 700 to 500 °C, and then the power was shut off. Both sides of all samples were repolished as before annealing. Finally, samples were cleaned in deionized water and dried in air.

3. Results and discussion

3.1. Precipitates

Based on X-ray energy-dispersive spectroscopy (EDS), the precipitates in the as-grown CdTe crystals were tellurium rich, while the precipitates in the cadmium-annealed sample AE2 were cadmium rich. The

0921-5107/93/$6.00

© 1993 – Elsevier Sequoia. All rights reserved

TABLE 1. Samples and results

Samples			Annealing conditions ($T = 700$ °C)		Results				
Wafer	Plane	Material	Treatment	t (h)	Precipitates			EPD	Lattice constant
					Composition	1–5 μm	>5 μm		
AE2	(111)	CdTe	As grown		Te				
AE2	(111)	CdTe	Cd annealing	25	Cd		↑	↑	↓
AE3	(111)	CdTe	As grown		Te				
AE3	(111)	CdTe	Cd annealing	20	Te	↓	↓	↓	↓
AE3	(111)	CdTe	Te annealing	20	Te	↑	↓	↓	↑
AE4	(111)	$Cd_{0.96}Zn_{0.04}Te$	As grown		Te–Cd				
AE4	(111)	$Cd_{0.96}Zn_{0.04}Te$	Cd annealing	20	Te	↓		↑	↓
AE4	(111)	$Cd_{0.96}Zn_{0.04}Te$	Te annealing	20	Te	↑		↓	↑
AE5	(211)	$Cd_{0.96}Zn_{0.04}Te$	As grown		Te				
AE5	(211)	$Cd_{0.96}Zn_{0.04}Te$	Cd annealing	20	Te	↓			↓
AE5	(211)	$Cd_{0.96}Zn_{0.04}Te$	Te annealing	20	Te	↑			↑

↓, decrease; ↑ increase.

concentration of the precipitates larger than 5.0 μm was increased by annealing in cadmium vapor at 700 °C, as illustrated in Fig. 1(a) and Table 1. No needles or precipitate clusters were observed in these samples. This result may have been caused by the following mechanism. When annealing in cadmium vapor, cadmium atoms diffused into the crystal and combined with tellurium in the precipitates to form CdTe and to eliminate tellurium precipitates. Longer annealing in cadmium vapor put excess cadmium into crystal that precipitated out during the relatively slow cooling process (33 °C h^{-1}).

The precipitates in both cadmium- and tellurium-annealed CdTe samples AE3 were tellurium-rich. The concentrations of both the larger and the smaller precipitates in AE3 were decreased by annealing in cadmium vapor, while these were not changed much by annealing in tellurium vapor, as shown in Fig. 1(a) and Table 1. As seen in Figs. 1(a) and 1(b), the precipitate densities for all as-grown samples were almost the same (about 10^5 cm^{-3}). Thus the difference between the cadmium-annealing results for samples AE2 and AE3 was unlikely to be caused by the difference between the precipitate densities in the as-grown crystals, but rather by the different annealing times.

For $Cd_{0.96}Zn_{0.04}Te$ samples AE4 and AE5, the precipitate density was decreased by annealing in cadmium vapor and increased by annealing in tellurium vapor, as shown in Fig. 1(b) and Table 1. For samples AE4, cluster needle-shaped precipitates were observed in the as-grown and cadmium-annealed samples. The density of the needles in the as-grown $Cd_{0.96}Zn_{0.04}Te$ was approximately 2.3×10^4 cm^{-3}. Their shape was almost unchanged by annealing in cadmium vapor. These needles were all oriented along {111}⟨211⟩. In the corresponding tellurium-annealed AE4 samples, only randomly distributed precipitates with larger sizes were found. Note that {111}⟨211⟩ usually are the directions along which dislocations and stacking faults lie [7–9]. Thus we believe that excess tellurium atoms are deposited along dislocations and/or stacking faults during the post-growth cooling.

The EDS results showed that precipitates in the AE4 and AE5 samples had excess tellurium (except for the as-grown sample AE4, in which both cadmium-rich and tellurium-rich precipitates were observed). We believe that the smaller tellurium precipitates grew during the tellurium annealing.

3.2. Etch pit density

As shown in Fig. 2 and Table 1, the etch pit density (EPD) was either unchanged or increased by annealing in cadmium and was decreased by annealing in tellurium for all experiments (no sample was available for tellurium annealing of sample AE2 and no reliable etchant was available for the (211)-oriented AE5 samples). Schaake and coworkers [9, 10] reported that multiplication of dislocations happened with mercury annealing of $Hg_{1-y}Cd_yTe$ owing to the annihilation of tellurium precipitates. They attributed the increase in EPD during annealing to the formation of larger precipitates and to the annihilation of smaller precipitates along dislocations. The annihilation of smaller precipitates was claimed to have generated dislocation loops owing to dislocation climb. Smaller precipitates (1.0 μm or less) were often found to decorate dislocations or subgrain boundaries in II–VI crystals [11]. According to the transmission electron microscopy (TEM) results of Durose et al. [12], not only the larger precipitates but also the microprecipitates smaller than

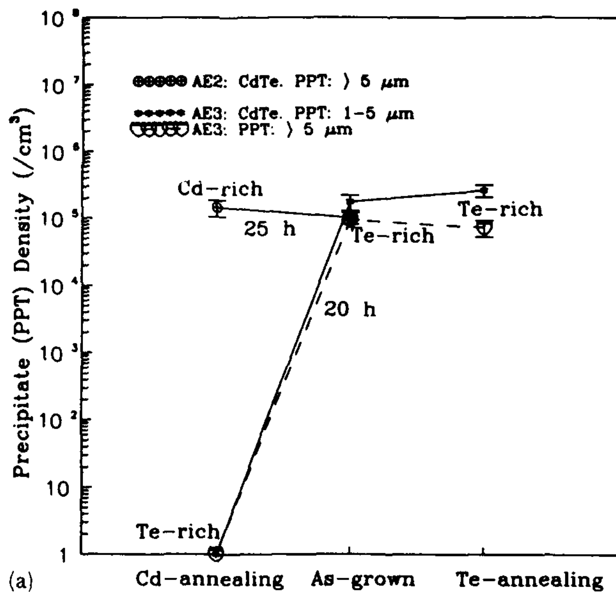

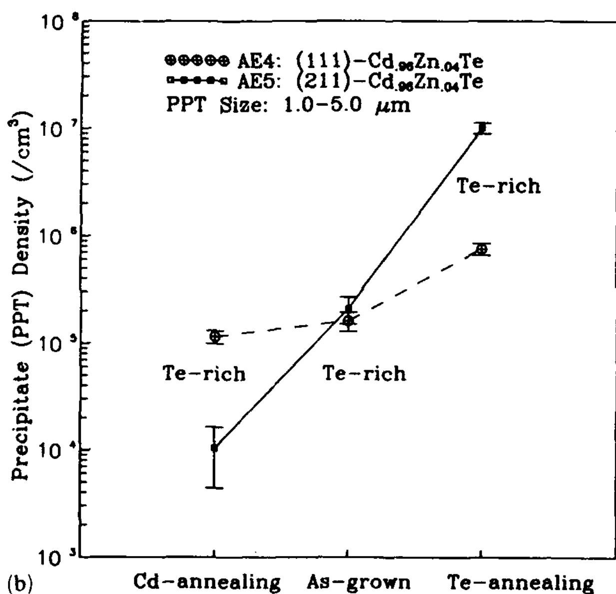

Fig. 1. The variation in precipitate density *vs.* annealing conditions: (a) CdTe samples (700 °C); (b) $Cd_{0.96}Zn_{0.04}Te$ samples (700 °C; 20 h).

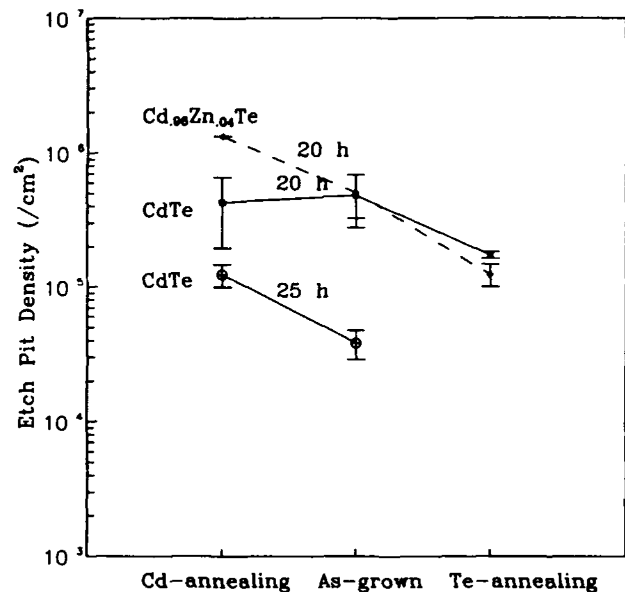

Fig. 2. The effect of annealing on the EPD ($T = 700$ °C; (111) plane).

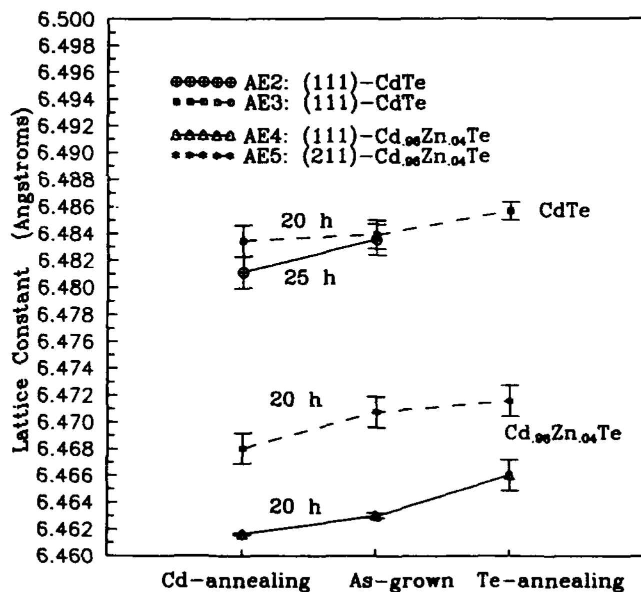

Fig. 3. Variation in lattice constants upon annealing conditions ($T = 700$ °C).

1.0 μm induced significant strain in CdTe. Moreover, it was observed by TEM that cavities and dislocation tangles and small loops developed where precipitates disappeared during cadmium annealing [13]. Subsequently, it is reasonable to attribute the increase in EPD to the disappearance of precipitates.

The decreased EPD caused by annealing in tellurium vapor, as seen in Fig. 2, is puzzling. All observations showed that the density of precipitates larger than 1.0 μm was either unchanged or increased by annealing in tellurium vapor.

3.3. Lattice constant

It was reported [14] that the lattice constant of stoichiometric CdTe at room temperature is 6.482 Å (±0.001 Å), while the lattice constants of crystals grown from cadmium-rich and tellurium-rich solutions are 6.480 Å and 6.488 Å respectively.

As illustrated in Fig. 3 and Table 1, all experiments showed the same tendency, *i.e.* the lattice constant was decreased by cadmium annealing and increased by tellurium annealing. The $Cd_{0.96}Zn_{0.04}Te$ samples changed more sharply than the CdTe samples. The difference between the lattice constants of the two zinc-doped CdTe samples was probably caused by the different

zinc concentrations in the samples. These two samples were taken from two ingots. It was reported [15] that the lattice constant of $Cd_{1-x}Zn_xTe$ decreases with an increase in zinc concentration.

Acknowledgments

This work was supported by the New York Science and Technology Foundation through Clarkson's Center for Advanced Materials Processing. The materials used for the experiments were provided by II–VI, Inc., Saxonburg, PA. We appreciate helpful discussions with Dr. G. Neugebauer at II–VI, Inc. We are grateful to Mr. R. Shetty for his assistance with the annealing experiments and Mr. W. Plunkett for his help with the scanning electron microscopy–EDS analyses.

References

1 Z. Laczik, G. R. Booker, R. Falster and N. Shaw, *Microscopy of Semiconducting Materials, Oxford, April 1989*, in *Inst. Phys. Conf. Ser., 100* (1989) Section 10.
2 H. R. Vydyanath, J. Ellsworth, J. J. Kennedy, B. Dean, C. J. Johnson, G. T. Neugebauer, J. Sepich and P. Liao, *J. Vac. Sci. Technol.*, in press.
3 W. J. Kim, M. J. Park, S. U. Kim, T. S. Lee, J. M. Kim, W. J. Song and S. H. Suh, *J. Cryst. Growth, 104* (1990) 677.
4 M. R. Lorenz and B. Segall, *Phys. Lett.*, 7 (1963) 18.
5 K. Yokota, T. Yoshikawa, S. Katayama, S. Ishhara and I. Kimura, *Jpn. J. Appl. Phys., 24* (1985) 1672.
6 R. Triboulet, R. Legros, A. Heurtel, B. Sieber, G. Didier and D. Imhoff, *J. Cryst. Growth*, 72 (1985) 90.
7 Y.-C. Lu, R. S. Feigelson, R. K. Route and Z. U. Rek, *J. Vac. Sci. Technol. A, 4* (1986) 2190.
8 Y. Y. Loginov, P. D. Brown, N. Thompson, G. L. Russell and J. Woods, *Microscopy of Semiconducting Materials, Oxford, April 1989*, in *Inst. Phys. Conf. Ser., 100* (1989) 433.
9 H. F. Schaake, J. H. Tregilgas, J. D. Beck, M. A. Kinch and B. E. Gnade, *J. Vac. Sci. Technol. A, 3* (1985) 143.
10 H. F. Schaake and J. H. Tregilgas, *J. Electron. Mater., 12* (6) (1983) 931.
11 J. L. Pautrat, N. Magnea and J. P. Faurie, *J. Appl. Phys., 53* (1982) 8668.
12 K. Durose, G. J. Russell and J. Woods, *J. Cryst. Growth*, 72 (1985) 85.
13 A. Nouruzi-Khorasani and P. S. Dobson, *J. Cryst. Growth, 92* (1988) 208.
14 K. Zanio, *Semicond. Semimet., 13* (1978) 54.
15 K. Hirata and O. Oda, *Mater. Lett.*, 5 (1986) 42.

Materials Science and Engineering, B16 (1993) 186-190

Diffusion of gallium in cadmium telluride

G. W. Blackmore
Royal Signals and Radar Establishment, Saint Andrews Road, Malvern, Worcestershire WR14 3PS (UK)

E. D. Jones
Coventry Polytechnic, Priory Street, Coventry CV1 5FB (UK)

J. B. Mullin
Electronics Materials Consultant, "The Hoo", West Malvern, Worcestershire WR14 4DL (UK)

N. M. Stewart
B T Laboratories, Martlesham Heath, Ipswich, Suffolk IP5 7RE (UK)

Abstract

The diffusion of Ga into bulk-grown, single crystal slices of CdTe was studied in the temperature range 350–811 °C where the diffusion anneals were carried out in sealed silica capsules using three different types of diffusion sources. These were: excess Ga used alone, or with either excess Cd or excess Te added to the Ga. Each of the three sets of conditions resulted in different types of concentration profile. At temperatures above 470 °C, a function composed of the sum of two complementary error functions gave the best fit to the profiles, whereas below this temperature a function composed of the sum of one or more exponentials of the form $\exp(-ax)$ gave the best fit. The behaviour of the diffusion of Ga in CdTe is complex, but it can be seen that two diffusion mechanisms are operating. The first is where D appears to decrease with Cd partial pressure, which implies that the diffusion mechanism may involve Cd vacancies, and a second which is independent of Cd partial pressure. The moderate values of D obtained, confirms that CdTe buffer layers may be useful in reducing Ga contamination in $(Hg_xCd_{1-x})Te$ epitaxial devices grown on GaAs substrates.

1. Introduction

The growth of good quality infra-red detectors using epitaxially grown layers of mercury cadmium telluride, $Hg_xCd_{1-x}Te$ (normally referred to as MCT) depends critically on obtaining a suitable substrate. The obvious choice is cadmium telluride, CdTe, but bulk-grown crystals of this material can contain defects, such as twins and subgrain boundaries, which propagate up into the growing epitaxial layer. In addition, tellurium precipitates are quite common in CdTe. Good quality CdTe substrates are in very short supply and are expensive, and attention has changed to using a much cheaper and readily available substrate such as gallium arsenide, GaAs. In these circumstances, an epitaxially grown buffer layer of CdTe is grown on the substrate prior to growing the infra-red detector MCT. The buffer layer is used to reduce the diffusion of constituents such as Hg and Ga from their host lattice because the quality of the device operation will be affected if this occurs [1].

The diffusion of Hg in CdTe has been studied extensively [2, 3] but no work has been reported to date on the diffusion of Ga in CdTe. It is important that the rate of diffusion of Ga in CdTe is known at the temperatures at which these devices are grown because Ga can act as an n-type dopant in MCT. Jones and Mykura [4] have reported on the diffusion of Ga in CdS which possesses a wurtzite crystal structure. They found that the diffusion coefficient was concentration-dependent, with diffusivity proportional to concentration, and the mechanism by which diffusion occurred was a defect complex of the form $(V_{Cd}Ga_{Cd})$.

2. Experimental details

The single crystal slices of CdTe used in this investigation were sawn from bulk-grown material manufactured by Mining and Chemical Products Ltd. (MCP). The surface of each slice that was to be used in the measurement of the diffusion profile was polished using successively finer grades of emery papers followed by successively finer grades of diamond pastes. The last grade that was used was 0.1 μm. This was then followed by etching the slice for a short time.

0921-5107/93/$6.00

© 1993 - Elsevier Sequoia. All rights reserved

The radioactive Ga was produced by the neutron irradiation of high purity metal in the nuclear reactor facility at the Imperial College of Science and Technology, London. Each sample was irradiated in a neutron flux of 10^{12} cm^2 s^{-1} for approximately 7.5 h. In order to reduce the risk of the Ga contaminating the reactor core tube in which the Ga was located, triple encapsulation was used with the inner-most container made of silica and the two outer ones made of polythene. Silica was selected for the inner-most container as liquid Ga metal wetted silica much less than polythene.

The irradiation of naturally occurring Ga, which is composed of two isotopes, produces two radioactive isotopes *via* the reactions $^{71}Ga(n,\gamma)^{72}Ga$ and $^{69}Ga(n,\gamma)^{70}Ga$ with half-lives of 14.1 h and 21.1 min respectively. The half-life of the radioisotope ^{70}Ga is so short that it makes a negligible contribution to the total radioactivity of the Ga when the diffusion profiles were measured. The decay scheme for ^{72}Ga is very complex [5] and it emits several types of radiation including positive and negative beta particles, and gamma rays in the energy range 0.1 MeV to 3.0 MeV.

The experimental procedure used to carry out the diffusion anneals and measure the diffusion profiles were very similar to that reported by the authors in their measurements of the rate of diffusion of Cu in CdTe [6]. The CdTe slices were annealed in evacuated silica capsules that contained sufficient radioactive Ga metal to give a saturated vapour pressure because of the metal over the CdTe slice throughout the diffusion anneal. In addition, an excess of Cd or Te was occasionally added to the capsule in order to define the anneal conditions precisely.

It was originally intended to use anodic oxidation sectioning [7] to measure the diffusion profiles, but work with preliminary experiments showed that the technique was not sensitive enough to measure the small amount of tracer taken up by the CdTe. Consequently, the profiles were measured using a mass difference sectioning technique developed by Jones [8]. The parallel sections were removed from the CdTe slice by lapping the surface on discs of SIA 7×0 emery paper using a lapping jig. The thickness of each section was calculated by weighing the crystal assembly both before and after each lapping step using a microbalance with a resolution of 1 μg. Between 400 μg and 1500 μg of CdTe was removed from the slice at each step in this technique compared with 50 μg removed in each section by anodic oxidation.

The amount of tracer in each section was calculated by measuring the radioactivity in each of the emery discs using low background anti-coincidence geiger counters. The counters were calibrated by measuring the count rate from a small sample of Ga of known mass. As Ga dissolves exceedingly slowly in oxidizing acids, the source was made by heating a small sample of Ga on paper and smearing it to give a thin source. This was done to minimize the effect of self-absorption of the radiation emitted by the radioactive Ga. The purity of the Ga tracer was checked by measuring its half-life using the low background geiger counters and by measuring gamma-ray spectra at periodic intervals using a high purity Ge detector with an 8000 channel analyser. In fact, to within the limits of experimental error, no such impurities were observed.

3. Results and discussion

Diffusion measurements were made over the temperature range 464–811 °C using the mass difference radiotracer sectioning technique and over 350–465 °C using secondary ion mass spectrometry (SIMS). For the measurements carried out at temperatures above 470 °C, each of the three sets of conditions used for the diffusion anneals resulted in different types of profiles which are shown in Fig. 1.

An attempt was made to analyse the experimental curves by fitting them to a function of the form:

$$C = a_1 \mathrm{erfc}(a_2 x) + a_3 \mathrm{erfc}(a_4 x)$$

where a_i are the fitted parameters. A function of this form indicates the existence of two contributions to the diffusion profile but this was not evident in all cases.

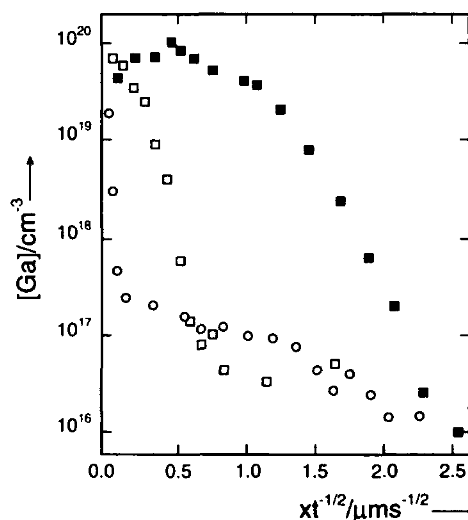

Fig. 1. A plot of the Ga concentration *vs.* $x/t^{1/2}$ for the diffusion of Ga in CdTe for the three different types of diffusion sources used. The graphs illustrate the difference in the shape of the concentration profiles resulting from each type of diffusion source. Key: □ Ga with excess Te: $T=811$ °C, $t=2520$ s; ○ Ga with excess Cd: $T=811$ °C, $t=1800$ s; ■ Ga only: $T=796$ °C, $t=2040$ s.

For the diffusion anneals carried out in Ga with excess Te, two separate contributions could be identified, whereas for the other two diffusion anneal conditions, that is Ga alone and Ga with excess Cd, this was not the case. For diffusion anneals carried out with Ga alone, only one contribution was identifiable, whereas with the diffusion anneals carried out in Ga with excess Cd, the profile dropped away very quickly before levelling out to the main part of the curve giving a much deeper diffusion of lower concentration. It was not possible to measure the diffusion coefficient for this surface layer, as typically this region consisted only of two or three experimental points.

The diffusion coefficients obtained using the computer fitting are shown in Fig. 2, where it can be seen that there appear to be two different distinct diffusion mechanisms operating, possessing similar values of the activation, energy, but widely differing values of the diffusion coefficient. These are: mechanism "A" dominating the profiles under conditions of Ga with excess Te and mechanism "B" dominating under conditions of Ga alone and Ga with excess Cd. The relevant parts of the diffusion profiles shown in Fig. 1 that contributed to each mechanism are shown in the inset to Fig. 2. Fitting the diffusion data for mechanisms "A" and "B" to Arrhenius plots independently gives activation energies of 1.52 ± 0.02 eV and 1.56 ± 0.02 eV and D_0 values of $0.031x/\div 1.3$ $cm^2\ s^{-1}$ and $0.059x/\div 1.3$ $cm^2\ s^{-1}$ respectively.

The fact that the faster diffusing component of the profiles from diffusion anneals performed under conditions of Ga with excess Te shows similar behaviour to the only measurable diffusion component for anneals carried out under conditions of Ga with excess Cd indicates that mechanism "B" is independent of Cd (or Te) partial pressure.

Diffusion anneals carried out under Ga with excess Te indicate clearly the existence of two diffusion mechanisms each possessing widely differing values of the diffusivity. In addition, as the initially high concentration of Ga near the surface for the profiles obtained under Ga with excess Cd covers the same concentration range as the slower diffusion mechanism (mechanism "A") for the diffusion anneals carried out under Ga with excess Te, it is tentatively suggested that the same diffusion mechanism is involved in the two cases. If mechanism "A" involves vacancies on the Cd sublattice then such behaviour would be expected as the excess Cd vapour would suppress vacancy production and thus reduce the diffusion coefficient.

Most of the diffusion measurements carried out at temperatures below 470 °C resulted in profiles of a different shape. This covered most of the experiments using SIMS and one of the experiments using radiotracer sectioning. A typical SIMS profile is shown in Fig. 3 and it was shown that under these conditions the resulting diffusion profiles consisted of a series of

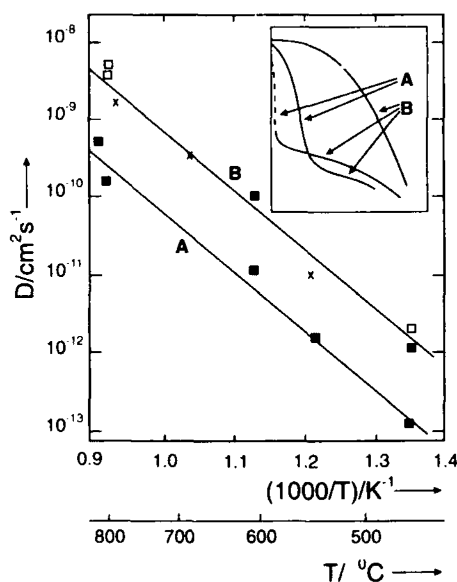

Fig. 2. An Arrhenius plot of the diffusion coefficients obtained for the diffusion of Ga in CdTe. The graph shows how the data appear to be split into two groups referred to as "mechanism A" and "mechanism B" in the text. The symbols ■, □ and × represent diffusions carried out under conditions of Ga with excess Te, Ga with excess Cd and Ga only respectively. An inset of Fig. 1 has been included to show which parts of each profile correspond to the two mechanisms.

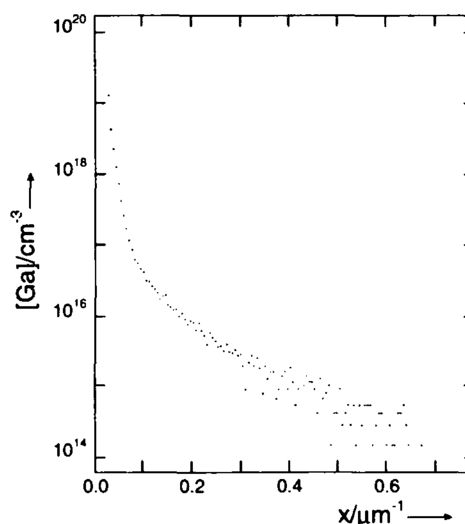

Fig. 3. A typical profile obtained using SIMS for the diffusions of Ga in CdTe. The experimental curve can best be represented by the sum of a series of exponential functions of the form $\exp(-ax)$. The curve shown here was for a diffusion anneal carried out in at atmosphere of Ga with excess Cd. Diffusion details: $T = 320$ °C, $t = 0.328 \times 10^6$ s.

exponential profiles each of the form $\exp(-ax)$. This may be an indication of diffusion with trapping. The penetration of the Ga in all the profiles affected was much shallower than those obtained at temperatures above 470 °C.

A trapping mechanism is one in which atoms diffuse *via* a relatively fast moving defect of low concentration. A typical example of such behaviour is interstitial diffusion which is shown in Fig. 4. At any given moment a fraction $[i]$ of atoms are occupying interstitial sites. An atom that has become an interstitial can move about the lattice with a diffusion coefficient of D_i for a period of time (average of t_i) before becoming a substitutional (trapped) atom again. It can be shown that if the diffusion time is large, then the measured diffusion coefficient is $D_i[i]$ and normal diffusion profiles are measured, but if the diffusion time is less than $t_i/[i]$ then the observed behaviour becomes dominated by the trapping rate, and concentration profiles of the form $\exp(-ax)$ can result [9, 10].

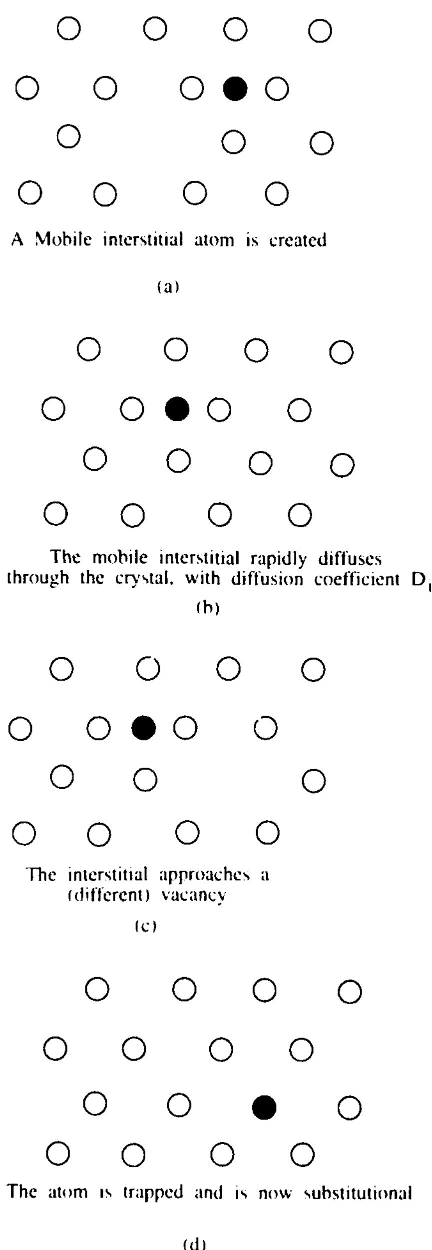

Fig. 4. A diagram showing the sequence of events of interstitial diffusion as an example of a trapping mechanism.

If the diffusion time is long enough for almost all of the atoms to have had an interstitial episode then normal diffusion profiles result, but if only a proportion of the atoms have been mobile *via* this mechanism (less than 10%) then exponential profiles of this form will result. Interstitial diffusion has been used as an example for this in this paper but the same arguments can be used for dislocation diffusion or any other mechanism in which the diffusion atom is part of the mobile defect that is responsible for diffusion.

4. Conclusions

The data given here represents the first investigation on the diffusion of Ga into CdTe so far reported. It is not possible to compare this data with similar measurements made in CdS because the CdS used in the investigation reported above [4] and CdTe used in this investigation possess different crystal structures. To summarize, the behaviour of Ga in CdTe is complex but the following points can be made.

(a) Two diffusion mechanisms are operating, "A" and "B" with activation energies of 1.52 eV and 1.56 eV and D_0 values of 0.0031 cm^2 s^{-1} and 0.059 cm^2 s^{-1} respectively.

(b) The diffusion coefficient resulting from mechanism "A" appears to decrease with increasing Cd partial pressure which implies that the diffusion mechanism may involve Cd vacancies.

(c) Mechanism "B" appears to be independent of Cd partial pressure.

(d) There is evidence that one or more of the mechanisms shows the occurrence of diffusion with trapping in shallow profiles.

(e) The moderate value for the diffusion coefficient of Ga in CdTe (approximately 10 to 100 times the Cd self-diffusion values) confirms that CdTe buffer layers may be useful in reducing Ga contamination in MCT epitaxial devices grown on GaAs substrates.

Acknowledgments

The authors wish to thank Philips Infrared Defence Components, Southampton for providing the CdTe

slices and Dr. R. Hall of Coventry Polytechnic for his technical support.

References

1 G. W. Blackmore, S. J. Courtney, J. Geiss, S. J. Irvine and S. Haq, in A. Benninghoven, A. M. Huber and H. W. Werner (eds.), *Sims VI*, Wiley, Chichester, 1988, p. 311.
2 E. D. Jones, J. B. Mullin and V. Thambipillai, *J. Cryst. Growth, 118* (1992) 1-13.
3 K. Takita, K. Murakami, H. Otaka and K. Masada, *Appl. Phys. Lett., 44* (1984) 906.
4 E. D. Jones and H. Mykura, *J. Phys. Chem. Solids, 41* (1980) 1261-1265.
5 C. M. Lederer, J. M. Hollander and I. Perlman, *Table of Isotopes, 6th edn.*, Wiley, New York, 1968.
6 E. D. Jones, N. M. Stewart and J. B. Mullin, *J. Cryst. Growth, 117* (1992) 249-253.
7 N. M. Stewart, E. D. Jones and J. B Mullin, *J. Mater. Sci. (Materials in Electronics)*, in press.
8 E. D. Jones, *Ph.D. Thesis*, University of Warwick, 1977.
9 N. M. Stewart, *Ph.D. Thesis*, Coventry Polytechnic, 1991.
10 M. D. Sturge, *Proc. Phys. Soc., 73* (1959) 297.

Depth non-uniformities in thin CdTe layers grown by MBE on InSb substrates

D. E. Ashenford, P. Devine, J. H. C. Hogg, B. Lunn and C. G. Scott
Department of Applied Physics, University of Hull, Hull HU6 7RX (UK)

Abstract

Measurements have been made of the carrier concentration as a function of depth through CdTe layers grown by MBE on InSb (001) substrates. Both In-doped and undoped layers are n-type but the free carrier concentration diminishes in the vicinity of the CdTe-InSb interface, possibly due to the presence of an increased density of extended defects in this region resulting from lattice mismatch at the interface. In order to provide more detailed information concerning the origin of these depth non-uniformities, double crystal X-ray diffraction (DCXRD) techniques have been employed to provide information about the crystal quality and lattice strain within the layers. By studying a variety of samples with different structure and quality, it is clearly demonstrated that regions of reduced carrier concentration correspond to those regions where significant strain relaxation has occurred.

1. Introduction

Previous reports have demonstrated that high quality epilayers of CdTe can be grown using (001) InSb substrates provided that appropriate care is taken with the substrate cleaning process [1]. Of course, for device purposes, it is necessary to dope the material in order to achieve a particular conductivity type and to control the free carrier density but, as for other II-VI materials, full activation of the dopant in CdTe is frequently prevented by self compensation effects. For the case of In-doped CdTe the compensation mechanism is thought to be associated with the generation of In-V_{Cd} complexes but for epilayers grown on CdTe single crystal substrates, it has been found that the problem is alleviated by the use of laser radiation during growth [2]. Alternatively, formation of the V_{Cd} complex centres is suppressed by the use of an excess flux of Cd during growth [3]. In this laboratory, using (001) InSb as the substrate material, In-doped CdTe layers with free carrier concentrations up to 10^{18} cm^{-3} have successfully been produced without the use of either an excess Cd flux or illumination during growth. However, we have noted previously [4] that, in the absence of an excess Cd flux, the electrical activity of the dopant is effectively diminished in the region of the epilayer closest to the substrate. This reduction was assumed to be related to the presence of dislocations and other extended defects in the vicinity of the epilayer-substrate interface due to the relief of strain resulting from the lattice mismatch at the interface. In this paper we present new evidence to support this contention.

2. Experimental details

The layers were grown on 0.5 mm thick wafers of (001) InSb using a VG(V80 H) MBE system. Surface preparation within the vacuum chamber involved several argon ion etching and thermal annealing cycles, as described previously [1]. With a substrate temperature in the region 230-240 °C, the growth rate was typically 0.7 μm h^{-1}.

Measurements of the effective shallow donor concentration in the layers were made using capacitance-voltage ($C-V$) techniques and the depth dependence was investigated using a Polaron profiler. Double crystal X-ray diffraction (DCXRD) rocking curves were obtained to provide information about the structural quality of the films.

3. Results and discussion

Figure 1 (curve (a)) shows the depth dependence of the free carrier concentration for a 4 μm thick In doped CdTe layer (sample I) which was grown with a single, stepped reduction in the In flux half way through the growth period. The expected step in the carrier concentration is clearly seen in Fig. 1(a) at a depth of approximately 2 μm but, whereas the upper

0921-5107/93/$6.00 © 1993 - Elsevier Sequoia. All rights reserved

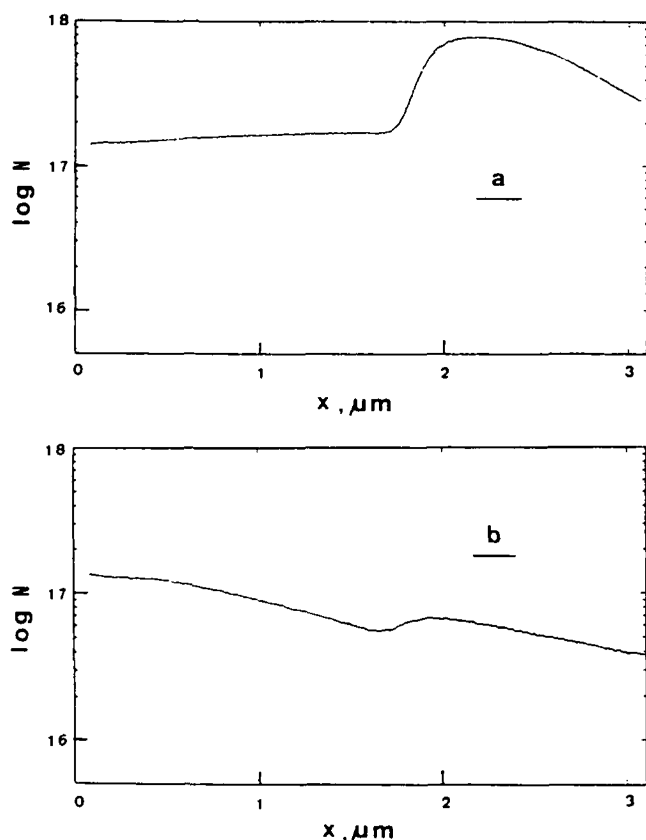

Fig. 1. Carrier concentration as a function of depth for two different samples taken from the same wafer: curve (a) for a high quality sample (sample I); curve (b) for a sample with visible growth defects (sample H).

half of the layer exhibits the expected uniform carrier concentration (approximately 1.4×10^{17} cm^{-3}) the higher concentration (approximately 8×10^{17} cm^{-3}) on the substrate side of the step is found to be maintained for less than 0.25 μm with a subsequent steady reduction towards the substrate interface. Such a reduction is a characteristic feature of both In-doped and undoped n-type layers on InSb and, as previously reported [1], this effect has been attributed to dislocations arising from lattice strain which is relieved over a narrow region of the CdTe layer close to the interface. This association between the presence of extended defects and a reduction in the effective shallow donor density is now supported by the results obtained from several different parts of the wafer from which sample I (in Fig. 1(a)) was taken. Samples taken from areas adjacent to sample I provided depth profiles very similar to that in curve 1(a). However, one small region of this layer exhibited surface defects attributed to some local residual imperfection on the substrate surface prior to CdTe growth. Samples taken from this part of the wafer produced very different depth profiles to that in Fig. 1(a). An example is given in Fig. 1 (curve (b)). This curve (for sample H) shows quite clearly that, for these samples with visible growth irregularities, the region of reduced carrier density extends right through the layer to the surface rather than being confined to a region close to the substrate.

In order to obtain more detailed information concerning the structural differences between the two parts of the wafer yielding the different profiles in Fig. 1, DCXRD measurements were made on samples from these two regions. Corresponding DCXRD rocking curves are shown in Fig. 2. Curve (a) is for sample A which was located adjacent to sample I (giving the "normal" profile in Fig. 1(a)). Curve (b) is for sample G, located adjacent to sample H which produced the profile (b) in Fig. 1. As the CdTe layer had a total thickness of 4 μm, both curves are dominated by a peak due to reflections from the CdTe layer, with a much smaller peak associated with the underlying InSb. However, it is quite clear that the angular separation of the two peaks is greater in curve (a) than in curve (b) indicating a greater strain in the CdTe layer for sample A as compared with sample G. The two peaks are more clearly distinguished in curve (c) which was obtained with the X-ray beam directed into the base of the etch pit resulting from a depth profile measurement of the type shown in Fig. 1. With approximately 3 μm of the CdTe layer removed by the electrochemical etching process, the intensity of the CdTe peak is significantly reduced in comparison with the InSb peak allowing the relative peak positions to be more clearly determined.

While the peak separation provides information about the strain state of the layers, the width of the peaks give a measure of the density of dislocations [5], with the peak width becoming broader as the dislocation density increases. The full width at half maximum (FWHM) values of the rocking curve peaks for the various samples referred to above are summarized in Table 1 together with the peak separation values and the maximum carrier concentrations recorded in the depth profile (the type of which is indicated in the table as type (a) or type (b) according to whether it had the form represented by curve (a) or (b), respectively, in Fig. 1).

It is notable that the smallest FWHM value included in Table 1 is for sample A which had the highest recorded carrier concentration and most uniform depth profile (type (a)). This sample is also seen to provide the largest separation between the CdTe and InSb peaks (104 arc secs) consistent with the least strain relief (approximately 15%) and lowest concentration of extended defects. In contrast, samples G and H (with profiles of type (b)) have the largest peak widths and smallest peak separations consistent with the samples being more relaxed and, correspondingly, containing a

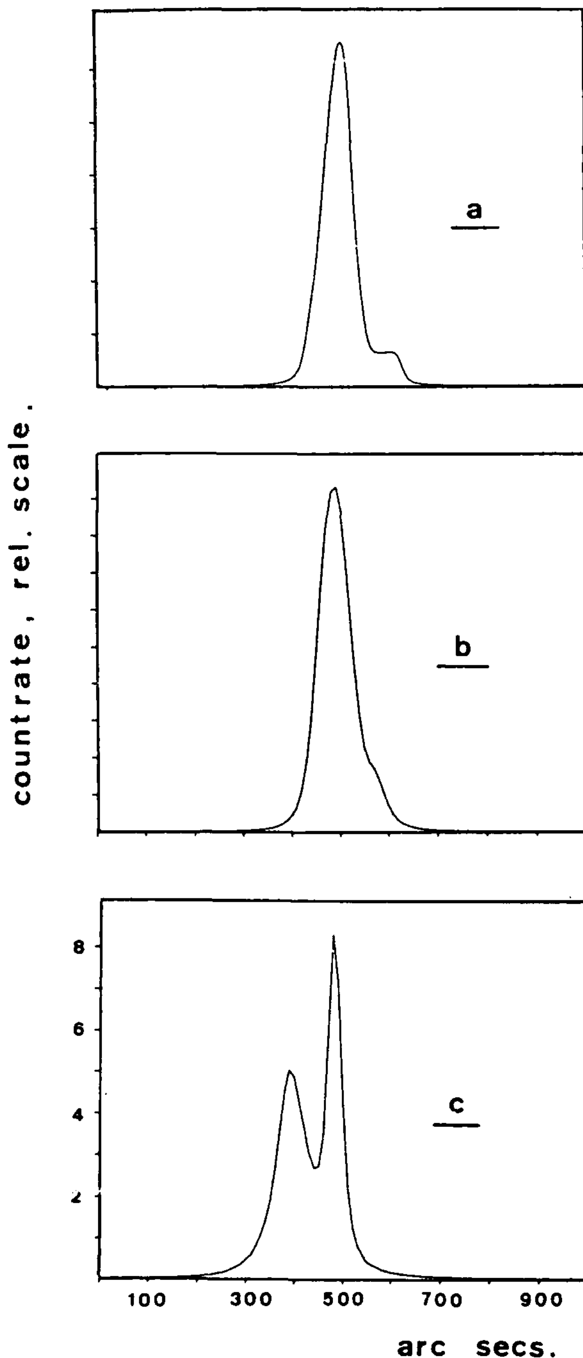

Fig. 2. 004 Cu Kα DCXRD rocking curves for different samples from the same wafer. Curves (a) and (b) are for unetched samples A and G respectively (4 μm thick). Curve (c) is for sample G with 3 μm removed by electrochemical etching.

higher density of dislocations. For these samples (profiles of type (b)), the dislocations appear to be distributed throughout the full thickness of the epilayers but in the higher quality samples (profiles of type (a)) the dislocations appear to be more confined to a region close to the substrate. This is consistent with

TABLE 1. Structural and electrical characteristics for five different samples from the same wafer

Sample	DCXRD		Max. conc., N (cm^{-3})	Profile type
	FWHM (arc secs)	Peak sep. (arc secs)		
A	69	104	8×10^{17}	a
G	81	90	6×10^{16}	b
H	81	80	1×10^{17}	b
I	78	100	8×10^{17}	a
J	76	95	6×10^{17}	a

XRD studies [6] and PL studies [7] of CdTe layers grown on GaAs which provided evidence for a reduction in the density of extended defects with increased CdTe layer thickness. Like XRD rocking curves, PL spectra are very sensitive to crystal quality and the strong, narrow, near band edge exciton lines which characterize the emission from layers grown in this laboratory are indicative of high quality material. However, recent studies of the emission from regions close to the epilayer–substrate interface (exposed by etching as above) have shown that the emission intensity (particularly the exciton emission) is much reduced. This is clearly consistent with increased lattice disorder in this region.

4. Summary

Measurements of the free carrier concentration as a function of depth in CdTe layers grown on (001) InSb have shown a diminution in the carrier concentration in the vicinity of the epilayer–substrate interface. DCXRD techniques have been employed to investigate the relationship between this effect and the strain state of the layers. By examining samples of differing crystal quality, it has been found that the effective carrier density is reduced in regions characterized by significant strain relaxation. In higher quality samples, this relaxation, accompanied by generation of dislocations and other extended defects, is confined to a narrow region of the layer close to the epilayer–substrate interface.

References

1 D. E. Ashenford, D. Johnston, B. Lunn and C. G. Scott, *J. Phys. Condens. Matter, 1* (1989) SB51.
2 R. N. Bicknell-Tassius, *J. Cryst. Growth, 101* (1990) 33.
3 F. Bassani, S. Tatarenko, K. Saminadayar, J. Bleuse, N. Magnea and J. L. Pautrat, *Appl. Phys. Lett., 58* (1991) 2651.

4 D. E. Ashenford, P. Devine, J. H. C. Hogg, B. Lunn and C. G. Scott, *J. Cryst. Growth*, *117* (1992) 233.
5 J. L. Reno, P. L. Gourley, G. Monfroy and J. P. Faurie, *Appl. Phys. Lett.*, *53* (1988) 1747.
6 K. Lischka, E. J. Fantner, T. W. Ryan and H. Sitter, *Appl. Phys. Lett.*, *55* (1989) 1309.
7 H. Sitter, K. Lischka, W. Faschinger, J. Wolfrum, H. Pascher and J. L. Pautrat, *J. Cryst. Growth*, *86* (1988) 377.

Materials Science and Engineering, B16 (1993) 195–198

Chemical diffusion of Hg in CdTe

J. H. C. Hogg, A. Bairstow, G. W. Matthews, D. Shaw and J. D. Stedman
Department of Applied Physics, University of Hull, Hull HU6 7RX (UK)

Abstract

Proton-induced X-ray emission has been used to characterize Hg interdiffusion from the vapour phase into CdTe between 360 °C and 550 °C. The measured interdiffusivities are described by $D = 6.6 \exp(-1.91 \text{ eV}/kT)$ cm^2 s^{-1} for Hg concentrations of 3% or less. The results differ significantly from earlier measurements based on electron microprobe and Rutherford backscattering techniques but are in good agreement with very recent radiotracer experiments. Possible causes for the differences with the earlier measurements are discussed.

1. Introduction

The ternary semiconductor alloy $Hg_{1-x}Cd_xTe$ is an important material for IR opto-electronic applications. An understanding and knowledge of self-diffusion and interdiffusion in the material are clearly necessary for the control and design of annealing procedures used in material and device fabrication. Measurements of the interdiffusivity D have almost all been made using electron microprobe analysis (EMPA) of a bevelled section through the interdiffusion region [1–6]. The results show that D has a strong dependence on both x and temperature (D decreasing with increasing x), with D obtained usually in the range $0.1 \leq x \leq 0.9$. Takita *et al.* [7] measured D for $x = 0.99$ using Rutherford back-scattering (RBS) (40 MeV O^{5+} ions) to determine the Hg concentration profile and found D values substantially greater than extrapolated values from refs. 1–6. Very recently, Jones *et al.* [8] have reported measurements of D ($x < 0.99$) obtained by an Hg radiotracer method. Their results lie between those of ref. 7 and the EMPA data. In this paper, we describe the results obtained for D ($x \approx 0.99$) using proton-induced X-ray emission (PIXE) to obtain the Hg concentration profiles. Our results were obtained over the temperature range 360 °C–550 °C and we find that there is a satisfactory agreement between our data and those of ref. 8 in the temperature range where there is an overlap (360 °C–400 °C). We have previously used PIXE to measure successfully interdiffusion in the $Pb_{1-x}Sn_xTe$/PbTe system [9]. PIXE is even better suited to the $Hg_{1-x}Cd_xTe$ system because the Hg(M) line does not overlap with any of the Cd or Te emission lines.

2. Experimental procedure

Hg was diffused from the vapour phase into undoped, high purity, Bridgman-grown CdTe samples contained within evacuated sealed SiO_2 ampoules. The Hg diffusion source was a droplet of the element located in a small-bore, tubular tip of the ampoule. The overall internal volumes of the ampoules were between 3 and 4 cm^3. The dimensions of the CdTe samples were typically 5 mm × 5 mm × 1 mm and their principal faces were prepared by mechanical lapping followed by chemical polishing using a Br/methanol mixture. Diffusion annealings were performed in a horizontal furnace at temperatures of 360 °C, 400 °C, 450 °C, 500 °C and 550 °C. The Hg tip was between 10 °C and 12 °C cooler than the CdTe sample in all the annealings other than that at 550 °C when the tip was 50 °C cooler in order to reduce the risk of Hg condensing on the CdTe sample. Annealing durations varied between 1 and 168 h.

Following the annealing, a PIXE spectrum was obtained from a principal face of the diffused sample using a 400 keV proton beam (beam diameter about 0.75 mm; beam current about 10 nA; dose 10 μc). The beam was about 10° off normal incidence. Serial sectioning of a single principal face was then carried out using a Br/methanol etching solution. The thickness removed was obtained by mass loss using a microbalance. A PIXE spectrum was collected at each sectioning stage and the Hg concentration profile derived from the Hg(M)/Te(L) ratios and the ratio obtained from a calibration sample of $Hg_{0.80}Cd_{0.20}Te$.

As the surface concentrations of Hg in the diffused samples were 2% or less, we can neglect any variation

0921-5107/93/$6.00
© 1993 - Elsevier Sequoia. All rights reserved

of D with x. From the boundary conditions imposed during the annealing, the Hg diffusion profile should be a complementary error function (erfc) provided the Hg surface concentration is independent of time. This condition should be met in the present experiments because, although chemical diffusion is taking place, we estimate the Hg loss from the source to be about 0.01%, *i.e.* any change in the composition of the external phase is negligible. If $Y(0)$ and $Y(z)$ are the Hg(M) emission yields from the initial diffused surface and at depth z below the initial surface (*i.e.* after a depth z has been etched off) then [9]

$$\mathrm{ierfc}(z/L)/\mathrm{ierfc}(0) \leqslant Y(z)/Y(0) \leqslant \mathrm{erfc}(z/L) \quad (1)$$

where L is the interdiffusion length $2(Dt)^{1/2}$. The lower and upper limits correspond to the proton range being much greater than L and much less than L respectively.

The calculated path length [10] and projected range [11] of 400 keV protons in CdTe are approximately 3.8 μm and 2.6 μm respectively (the presence of Hg at about 1% has little effect on these values). In the present experiments $0.8 \leqslant L \leqslant 5$ μm so that neither of the limits in eqn. (1) is realized. We therefore obtained values of D from probability plots of $Y(z)/Y(0)$ *vs.* z [9] assuming that L was much greater than the proton range (the upper limit in eqn. (1)). This procedure can overestimate the true value by up to 73% depending on the range and values of z/L [9]. The true D value could be determined as described in ref. 9 if the production cross-section *vs.* proton energy was known for the Hg(M) emission. As far as we are aware, no such data are available. If we therefore assume that, to a first approximation, Fig. 2 in ref. 9 is applicable to the present experiments then, as the largest values of z/L varied in our samples between 0.72 and 1.36, we estimate that the method for finding D described above overestimates D by 20% to 43%. Correction for this overestimate only affects the pre-exponential factor in the Arrhenius expressions for D. Following the same analysis and notation in ref. 9 we find that

$$C(0) = \frac{Y(0)}{Y(\mathrm{cal})} C(\mathrm{cal}) \int_0^\infty \Phi(x)\,\mathrm{d}x \bigg/ \int_0^\infty \mathrm{erfc}(x/L)\,\Phi(x)\,\mathrm{d}x \quad (2)$$

where $\Phi(x) = \sigma\{E(x)\}\exp(-\mu x/\cos\Theta)$, $C(0)$ is the Hg surface concentration (*i.e.* $z = 0$), and $Y(\mathrm{cal})$ and $C(\mathrm{cal})$ are the Hg yield from and Hg concentration in a homogeneous sample of (HgCd)Te respectively. σ is the excitation cross-section for protons with energy E at depth x below the surface and μ is the linear absorption coefficient. It is assumed that the $E(x)$ function is the same for both the diffused and calibration samples. As the excitation cross-sections are unknown, the integral ratio in eqn. (2) cannot be evaluated, but it is clear that the ratio is 1 or more so that the term $C^* = Y(0)C(\mathrm{cal})/Y(\mathrm{cal})$ defines a lower limit to the true surface concentration. Although, in the above discussion, the Y terms were defined as the Hg(M) yields, in practice greater precision was obtained with the Hg(M)/Te(L) ratio as noted earlier. Changing Y to represent this ratio does not alter any of the foregoing discussion or statements.

3. Results and discussion

Figure 1 shows one of the Hg profiles obtained using PIXE. The data from all the diffusion anneals are contained in Table 1. The D values listed were obtained by multiplying the values determined from the probability plots by 0.76 in order to correct for the

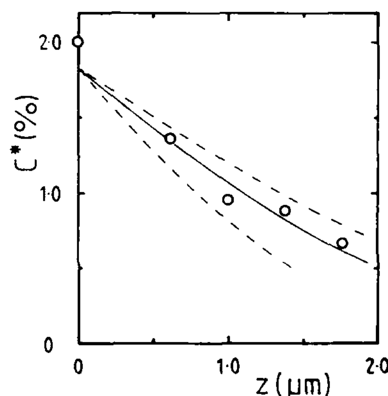

Fig. 1. Hg concentration profile in a CdTe sample after 65 h annealing at 400 °C. The continuous line is an erfc distribution for $D = 7.1 \times 10^{-14}$ cm^2 s^{-1} (*i.e.* uncorrected). The broken lines are erfc distributions for $D = 10.7 \times 10^{-14}$ cm^2 s^{-1} (upper) and $D = 3.6 \times 10^{-14}$ cm^2 s^{-1} (lower) (*i.e.* ±50% variations on 7.1×10^{-14} cm^2 s^{-1}).

TABLE 1. Summary of results for the interdiffusion of Hg into CdTe

Temperature (°C)	Duration (h)	Hg surface concentration C^* (%)	Total thickness removed (μm)	D (cm^2 s^{-1})
360	168	0.46	0.73	$(2.4 \pm 0.1) \times 10^{-15}$
400	65	2.7	2.90	$(4.8 \pm 1.4) \times 10^{-14}$
400	65	2.0	1.70	$(5.4 \pm 0.5) \times 10^{-14}$
450	3	1.0	1.35	$(3.3 \pm 0.3) \times 10^{-13}$
450	24	0.61	3.17	$(1.2 \pm 0.2) \times 10^{-13}$
500	3	0.83	3.80	$(3.9 \pm 0.2) \times 10^{-12}$
500	3	0.61	3.55	$(4.3 \pm 0.1) \times 10^{-12}$
500	1	2.4	1.73	$(1.5 \pm 0.2) \times 10^{-12}$
500	1	0.42	2.30	$(4.2 \pm 0.3) \times 10^{-12}$
550	1	0.45	2.50	$(6.1 \pm 0.6) \times 10^{-12}$

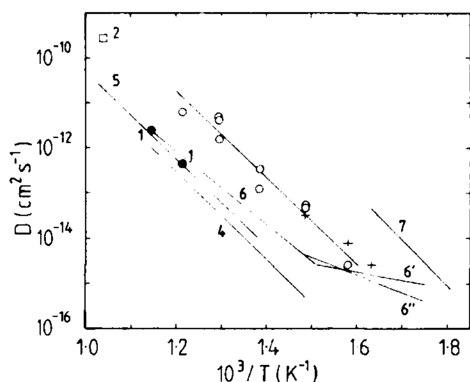

Fig. 2. Arrhenius plots of D from literature data together with the present results taken from Table 1 (o). A plot of eqn. (3) is also shown as the line through the o data points. The results from ref. 3 (500 °C–600 °C) lie between those from refs. 4 and 6, and have been omitted to avoid congestion. The low temperature sections, 6' and 6" of ref. 6 refer to Te- and Hg-rich conditions respectively. The + data points are from ref. 8.

overestimate present in the probability plot value. A least-squares fit of these D measurements to the usual Arrhenius expression gives

$$D = (6.6 \overset{\times}{\div} 14) \exp\{(-1.91 \pm 0.16)\,\mathrm{eV}/kT\}\ \mathrm{cm^2\,s^{-1}} \quad (3)$$

An Arrhenius plot of our D results is shown in Fig. 2 together with eqn. (3). Also shown are Arrhenius plots of the results obtained by other workers for $x = 0.95$ (extrapolated where necessary from a lower x range) together with data points at 360 °C and 400 °C from ref. 8.

The possibility that the proton beam could modify the Hg concentration profile was checked by measuring the Hg(M)/Te(L) ratio, as a function of proton dose in eight stages between 10 and 150 μC on two separate samples diffused for 1 h and 24 h, respectively, at 450 °C. No significant or systematic variations in the yield ratio were found. It is evident from Fig. 2 that the EMPA data above 400 °C lie well below our results and those of refs. 7 and 8. The EMPA plots correspond to $x = 0.95$ and, as $x \to 1$, D will decrease but by no more than a factor of 2 so that the discrepancy still remains. While our results are in reasonable agreement with those for the slow component from [8], where the temperature regions overlap, they lie well below those of [7]. The reasons for these differences are not known, but a dependence on the measurement technique needs to be considered. In the case of $Hg_{1-x}Cd_xTe$ it appears feasible that heating effects owing to the electron beam in EMPA could result in the Hg loss and so distort the Hg profile in a bevelled section [12, 13]. The RBS experiments of Takita *et al.* [7] used 40 MeV O^{5+} ions and a total dose of 8×10^{15} cm^{-2} per profile so that the possibilities of ion beam mixing- and/or radiation-enhanced diffusion occurring during the RBS profiling cannot be automatically excluded. The possibility that a variation of D with Hg partial pressure might be responsible is unlikely as D exhibits little dependence on non-stoichiometry and the same is true for cation self-diffusion in CdTe and in $Hg_{0.8}Cd_{0.2}Te$ [12].

The annealing procedures used by Jones *et al.* [8] and by us only differed in the Hg pressure imposed. In our experiments, the Hg pressure was less than the saturated value whereas in ref. 8 the saturated value was established. The Hg surface concentrations for the slow component of D increased from about 0.07% at 360 °C to about 6.7% (extrapolated) at 550 °C [8]. Takita *et al.* [7] performed their annealings with the CdTe sample immersed in liquid Hg and reported Hg surface concentrations at 310 °C of 2.7%, which is a factor of 80 greater than that obtained in ref. 8 at the same temperature. Our C^* results (Table 1) vary between 0.42% and 2.4% without any obvious variation with temperature: the scatter found at 500 °C may be due to variations in Hg pressure between samples. Owing to the nature of C^* discussed earlier and its possible dependence on Hg pressure, we are limited to concluding that our true Hg surface concentrations are similar in order of magnitude to the results of ref. 8.

4. Conclusions

Agreement has been found between D values in $Hg_{1-x}Cd_xTe$ (at low Hg concentrations) determined by the separate PIXE (present results) and radiotracer [8] techniques. These values are significantly greater than those obtained by the EMPA technique [1–6] and significantly smaller than values determined by RBS [7]. It was established that the 400 keV proton beam did not modify the Hg concentrations in the diffused samples. To account for the differences with the other particle beam techniques, it is suggested that in the EMPA and RBS methods the beams modified the Hg concentrations. In view of the extensive measurements of D that have been made across the composition range of $Hg_{1-x}Cd_xTe$ using EMPA [14], it is important that the cause(s) for these differences be established.

References

1 L. Svob, Y. Marfaing, R. Triboulet, F. Bailly and G. Cohen-Solal, *J. Appl. Phys.*, *46* (1975) 4251.
2 V. I. Ivanov-Omskii, K. E. Mironov and V. K. Ogorodnikov, *Phys. Status Solidi A*, *58* (1980) 543.
3 V. Leute, H. M. Schmidtke, W. Stratman and N. Winking, *Phys. Status Solidi A*, *67* (1981) 183.
4 K. Zanio and T. Massopust, *J. Electron. Mater.*, *15* (1986) 103.

5 J. G. Fleming and D. A. Stevenson, *Phys. Status Solidi A, 105* (1987) 77.
6 M. F. S Tang and D. A. Stevenson, *Appl. Phys. Lett., 50* (1987) 1272.
7 K. Takita, H. Murakami, H. Otake, K. Masuda, S. Seki and H. Kudo, *Appl. Phys. Lett., 44* (1984) 996.
8 E. D. Jones, V. Thambipillai and J. B. Mullin, *J. Cryst. Growth, 118* (1992) 1.
9 M. S. Al-Salhi, D. Shaw, F. J. Bryant and J. H. C. Hogg, *Semicond. Sci. Technol., 3* (1988) 1063.
10 H. H. Anderson and J. F. Ziegler, Hydrogen stopping powers and ranges in all elements. *The Stopping Powers and Ranges of Ions in Matter*, Vol. 3, Pergamon, New York, 1977.
11 H. E. Schiott, *Mat. Fys. Medd. Dan. Selsk., 35* (9) (1966) 3–20.
12 C. K. Shih, D. J. Friedman, K. A. Bertness, I. Lindau, W. E. Spicer and J. A. Wilson, *J. Vac. Sci. Technol. A, 4* (1986) 1997.
13 K. Kanaya and S. Ono, in D. F. Kyser, H. Niedrig, D. E. Newbury and R. Shimizu (eds.), *Electron Beam Interactions with Solids for Microscopy, Microanalysis and Microlithography*, SEM Inc., AMF O'Hare, Chicago, IL, 1984, p. 69.
14 D. A. Stevenson and M. F. S. Tang, *J. Vac. Sci. Technol. B, 9* (1991) 1615.

Effect of interdiffusion on dislocation generation in epitaxial layers on CdTe, (Cd,Zn)Te and Cd(Te,Se) substrates

I. Utke, L. Parthier and M. Schenk
Institute of Crystallography and Materials Science, Humboldt University of Berlin, Invalidenstrasse 110, O-1040 Berlin (Germany)

Abstract

Diffusion modifies the interfacial strain field induced by the composition difference and temperature changes. The strain field is estimated theoretically for liquid-phase epitaxial-grown (Hg,Cd)Te layers on different substrates. The effect on the generation of misfit dislocations is compared with etch pit density profiles.

1. Introduction

The epitaxial growth of (Hg,Cd)Te layers on (111)B CdTe, (Cd,Zn)Te and Cd(Te,Se) substrates is a well-established method used in the fabrication of IR devices. Generally, the epitaxial system is subjected to three temperature ranges [1]: firstly, the range of growth temperature, confined to 450–500 °C for liquid-phase epitaxy (LPE) from a Te-rich solution. The processes of interdiffusion through the hetero-interface and of motion and generation of misfit dislocations take place mainly in this range, *i.e.* during growth. The second range comprises the temperature decrease to room temperature after growth. Diffusion can now be neglected. Stresses are generated owing to the different thermal expansion coefficients of the layer and substrate. The same situation holds true for the third temperature range of device application of about 77 K.

In this paper, the effect of interdiffusion during growth on the change in the lattice parameters and stress near the interface is investigated and compared with its change after growth.

2. Model

2.1. Interfacial compositional profiles

During epitaxial growth of $Hg_{1-x}Cd_xTe$ layers on CdTe, (Cd,Zn)Te and Cd(Te,Se) substrates, the respective solid solutions $Hg_{1-x}Cd_xTe$, $(Hg_{1-x}Cd_x)_{1-v}Zn_vTe$ and $Hg_{1-x}Cd_xTe_{1-w}Se_w$ are formed in the interdiffusion region. The initial substrate composition values of Zn and Se were chosen according to the lattice matching condition with an $Hg_{0.8}Cd_{0.2}Te$ layer. Solving Fick's diffusion equations for the system, and assuming the diffusion coefficients D to be constant and the fluxes independent of each other [2, 3], each compositional profile displays the shape of an erfc distribution, and its width is proportional to $(Dt)^{1/2}$ where t is the time. This approximation serves sufficiently well for the following considerations. Therefore, the composition-dependent interdiffusion coefficient determining the Cd/Hg ratio [4] has been weighted for the calculations to $D = 5 \times 10^{-13}$ cm^2 s^{-1} [2]. The values for the substrate components Zn and Se were found by extrapolation from refs. 5 and 6 to be $D_{Zn} = 3.7 \times 10^{-12}$ cm^2 s^{-1} ($x = 0.0$) and $D_{Se} = 3.2 \times 10^{-11}$ cm^2 s^{-1} ($x = 0.2$) at 460 °C. The computed profiles for the compositions x, v and w are shown in Fig. 1, calculated by means of the expressions given in refs. 2 and 3.

2.2. Interfacial lattice parameter profiles

By means of the compositional profiles in Fig. 1, the lattice parameter profiles $a(z)$ can be calculated [2] such that

$$a_{Hg_{1-x}Cd_xTe} = 6.4614 + 0.0084x + 0.0168x^2 - 0.0057x^3 \quad (1)$$

$$a_{(Hg_{1-x}Cd_x)_{1-v}Zn_vTe} = a_{Hg_{1-x}Cd_xTe} - \{0.381 - 0.02(1-x)\}v \quad (2)$$

$$a_{Hg_{1-x}Cd_xTe_{1-w}Se_w} = a_{Hg_{1-x}Cd_xTe} - 0.3966w \quad (3)$$

It can be seen from these equations that both substrate components (Zn, Se) affect the lattice parameter of CdTe in a stronger manner than does the layer component Hg.

0921-5107/93/$6.00 © 1993 - Elsevier Sequoia. All rights reserved

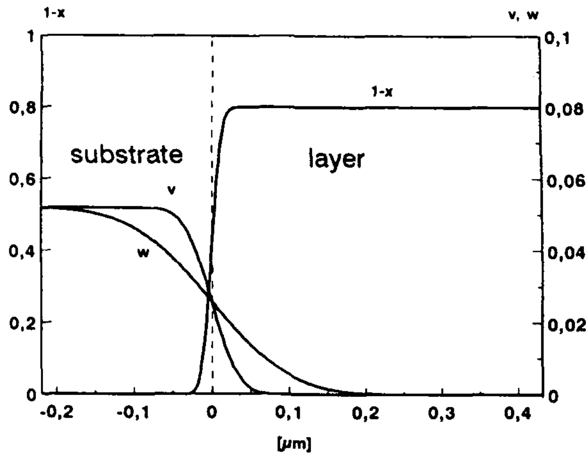

Fig. 1. Calculated interfacial compositional profiles for initial values of substrate $v = w = 0.05$ and layer $x = 0.2$. Position $z = 0$ refers to the interface, $z < 0$ to the substrate and $z > 0$ to the epilayer. See text for values of the diffusion coefficients and growth temperature.

The thermal expansion coefficients α were obtained as $\alpha_{Hg_{1-x}Cd_xTe} = \{4.9-0.9(1-x)\} \times 10^{-6}$ and $\alpha_{Cd_{1-v}Zn_vTe} = (4.9 + 3.4v) \times 10^{-6}$ by linear interpolation of the data in ref. 1. Thus, the temperature dependence was taken into account by multiplying eqns. (1)–(3) by the factor $[1 + \{4.9-0.9(1-x) + 3.4v\}10^{-6}\Delta T]$. Data for $CdTe_{1-w}Se_w$ were not available, and so were assumed to be the same as for (Cd,Zn)Te. We assumed that a constant temperature field exists in the epitaxial system and that no change in the lattice parameter occurs owing to thermal fluctuations. Thermally activated dislocation motion [7] was assumed to be prevented by lattice matching the substrate at the growth temperature T_G, *i.e.* the natural (geometrical) misfit $f_0(T_G) = 0$, where

$$f_0(T) = \frac{a_L(T) - a_S(T)}{a_S(T)} \tag{4}$$

Here a_S and a_L are the stress-free lattice parameters of the substrate and layer, respectively. The abrupt change in the lattice parameter at the interface becomes a continuous distribution as a result of interdiffusion. Consequently, there is defined

$$f(z,T) = \frac{a(z,T) - a_S(T)}{a_S(T)} \tag{5}$$

where $a(z,T)$ is the lattice parameter for a given temperature T at position z from the interface. By inserting the compositional profiles shown in Fig. 1 into eqns. (1)–(3), the lattice parameter profiles $f(z,T)$ in Figs. 2(a)–2(c) were calculated for the three temperature ranges.

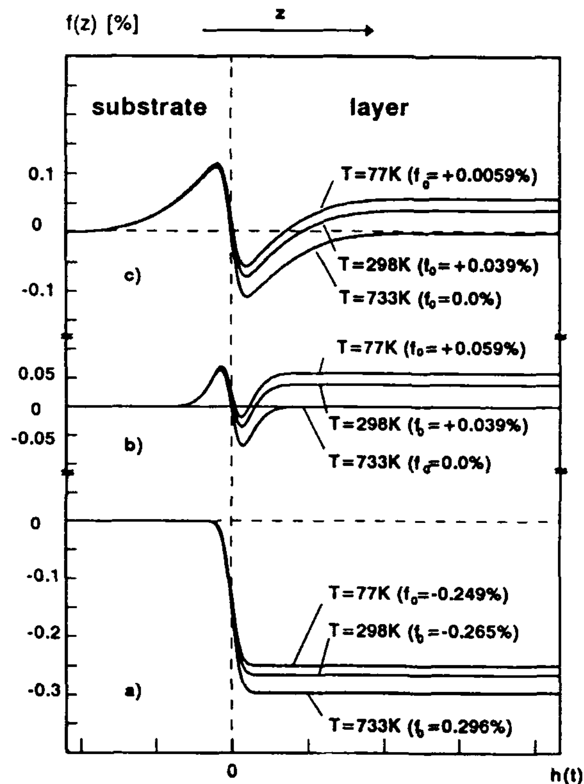

Fig. 2. Computed lattice parameter profiles for (a) CdTe, (b) (Cd,Zn)Te and (c) Cd(Te,Se) substrates at the growth temperature and after rapid cooling to room or device working temperatures. The diffusion-induced misfit is frozen in. Note that in (a) one composition changes and in (b), (c) two compositions change, either x,v or x,w.

The lattice parameter profile for a CdTe substrate (Fig. 2(a)) adapts smoothly to the lattice parameter values of a substrate and layer, and its shape follows mainly the erfc distribution of composition $(1-x)$ in Fig. 1. By using (Cd,Zn)Te or Cd(Te,Se) substrates, the additional wider diffusion regions of v and w account for the "oscillation-like" adaptation behaviour near the interface in Figs. 2(b) and 2(c). While $f_0(T_G)$ equals zero, generally $f(z,T)$ does not equal zero within the diffusion region. In the following, this is termed a diffusion-induced misfit. The effect of the diffusion-induced misfit formed during epilayer growth is of the same order of magnitude as the thermally induced misfit after cooling, as shown in Figs. 2(b) and 2(c). The diffusion-induced misfit is frozen in at lower temperatures.

2.3. *Interfacial stress profiles*

The stress profiles were calculated with a model of the theory of elasticity [8] modified for epitaxial systems in ref. 3, setting the elastic strain equal to $f(z,T)$. This model is valid as long as no relief of stress by plastic deformation occurs, *i.e.* the layer thickness $h(t)$ is less than the critical thickness h_c [1]. The $f(z,T)$

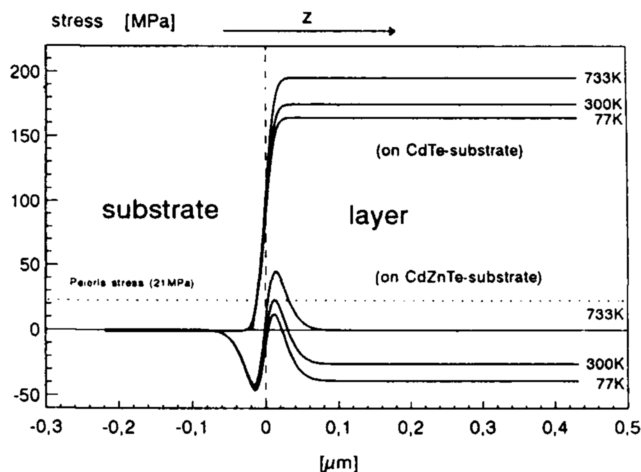

Fig. 3. Calculated stress profiles for $Hg_{0.8}Cd_{0.2}Te$ layers on mismatched CdTe and lattice-matched (Cd,Zn)Te substrates for the same temperatures as in Fig. 2. The current epilayer thickness is less than h_c. The Peierls stress is indicated by the dotted line.

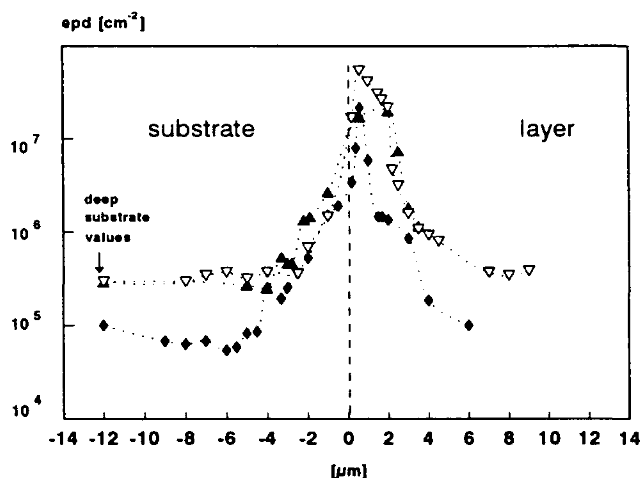

Fig. 4. Etch pit density profiles of LPE-grown (Hg,Cd)Te on (111)B CdTe (▽, $f_0 = -0.28\%$) and (Cd,Zn)Te (▲, $f_0 = -0.12\%$ and ◆, $f_0 = -0.08\%$). The interface $z = 0$ was determined by means of an optical microscope.

profiles in Fig. 2 cause the respective stress profiles presented in Fig. 3. Cd(Te,Se) behaves similarly to (Cd,Zn)Te, and so its stress profile is omitted.

Stresses $\sigma < 0$ are compressive and $\sigma > 0$ tensile. The number and position of the neutral planes ($\sigma = 0$) depend on the substrate material. All the features of the lattice parameter profiles are maintained in the stress profiles. Thus, the stress consists of contributions from diffusion, natural misfit and temperature changes. If h_c is exceeded, the stress profile is partially relieved by the generation of dislocations [9], including a shift of the neutral planes. Half-loops generated on the layer surface can expand only to the first neutral plane where the sign of σ changes. Threading dislocations may be bent already in the substrate owing to the diffusion-induced stresses. Dislocation motion, according to the double-kink mechanism, can occur if the Peierls stress $\sigma_p = 21 \pm 4$ MPa [7] is exceeded.

3. Experimental etch pit density profiles

The etch pit density (EPD) profiles were measured by a method described in ref. 10 and are shown for (Hg,Cd)Te layers on CdTe and (Cd,Zn)Te substrates in Fig. 4. All the EPD maxima are situated in the epilayer near the interface and depend on the absolute value of f_0. EPD values of the substrate and the layer distant from the interface are nearly equal. The depth of increased EPD values is unambiguously independent of f_0 as a result of the diffusion-induced stress.

4. Conclusions

The lattice matching at the heterointerface is determined by the natural misfit, temperature changes and the diffusion-induced misfit. The diffusion-induced misfit leads to the generation of dislocations within the diffusion region of both the substrate and the layer.

References

1 J. H. Basson and H. Booyens, *Phys. Status Solidi A, 80* (1983) 663.
2 T. Teubner, M. Winkler, T. Boeck and L. Parthier, *Cryst. Res. Technol., 26* (1991) 25.
3 I. Utke, L. Parthier and M. Schenk, *J. Cryst. Growth, 123* (1992) 269.
4 K. Zanio and T. Massopust, *J. Electron. Mater., 15* (1986) 103.
5 F. A. Zaitov, V. I. Stafeyev and G. S. Khodakov, *Fiz. Tverd. Tela, 14* (1972) 3072.
6 F. A. Zaitov, L. A. Bovina and V. I. Stafeyev, *Problemy fiziki soedineniij AII-BVI*, Vysschaja schkola, Vilnius, 1972, p. 278.
7 E. Yu. Gutmanas and P. Haasen, *Phys. Status Solidi A, 63* (1981) 193.
8 S. Timoshenko and J. N. Goodier, *Theory of Elasticity*, 2nd edn., McGraw-Hill, New York, 1951, p. 399.
9 S. Prussin, *J. Appl. Phys., 32* (1961) 1876.
10 L. Parthier, T. Boeck, M. Winkler, T. Teubner and W. Frentrup, *Cryst. Prop. Prep., 32–34* (1991) 294.

Materials Science and Engineering, B16 (1993) 202–206

Carbon and silicon in travelling heater method grown semi-insulating CdTe

L. Chibani, M. Hage-Ali, J. P. Stoquert, J. M. Koebel and P. Siffert

Centre de Recherches Nucléaires (CRN), Laboratorie PHASE (UPR du CNRS n° 292), BP 20, 67037 Strasbourg Cedex 2 (France)

Abstract

Carbon- and silicon-doped CdTe have been studied by charged particle activation heavy ion induced X-ray emission and secondary ion mass spectroscopy to determine the impurities present at low concentrations. Electrical characteristics have been investigated by thermally stimulated current and the Van der Pauw resistivity measurements, in order to correlate the impurity concentrations and electrical behaviours.

1. Introduction

High purity CdTe is an optimal material for nuclear gamma-ray detectors working at room temperature and for photovoltaic converters [1]. Several properties of this material depend on the nature and concentration of trace elements present in the crystals. These impurities can originate from the starting products, and may be introduced intentionally as dopants or through contamination during the processing.

As the concentration values are of the order of parts per million (ppm) or less, high sensitivity analytical procedures are needed to identify and control the distribution of dopants and impurities in the crystals. Furthermore, because of the matrix composition, interference effects from cadmium and tellurium have to be avoided or at least limited to a minimal level. This can be achieved by charged particle activation (CPA), by selective heavy ion induced X-ray emission (HIXE), by secondary ion mass spectroscopy (SIMS), by IR spectroscopy or by atomic absorption (AA) analysis. The CPA technique is known to be of great interest for the absolute determination of low concentrations of light impurities or dopants at the ppm level in particular, for the case of carbon in CdTe where this technique is well adapted. The SIMS technique is strongly affected by the presence of impurities: the ion production rate for a given element depends on the presence of foreign atoms in the lattice or at the surface, even at low concentrations. For CdTe, it has been shown [2, 3] that surface layers are formed following the etching of the crystals. These layers influence the ion yields of cadmium and tellurium. The method will therefore yield ambiguous quantitative results despite its high sensitivity, and another analytical technique is useful for the understanding and interpretation of SIMS measurements. HIXE via a quasi-molecular inner shell ionization mechanism, during heavy ion–atom collisions, allows both a high sensitivity for selected elements and the possibility of determining their relative concentrations in several samples [4]. This goal is reached by a convenient choice of the nature and of the energy of the bombarding ion. The choice of argon ions to induce selectively the X-ray emission of elements in the Al–Cl region is justified on the basis of electron promotion diagrams for Ar–Si collisions in the theoretical description of inner shell ionization in heavy ion collisions by Fano and Lichten [5] and Bosat and Lichten [6].

In the case of argon bombardment, a strong excitation of K X-rays of silicon (or of the neighbouring elements) is expected, whereas K X-rays from cadmium or tellurium will be attenuated; only a contribution from Cd L lines due to the Ar 1s–Cd 2p level matching effect is expected.

For electrical measurements we used essentially high resolution thermally stimulated current (TSC) spectra [7] to detect the various trapping levels present in our travelling heater method (THM) grown crystals. The TSC method is well known but improvements have been introduced especially by the "cleaning up procedure" as well as by using adequate computer programs.

The resistivity of each sample was deduced from Van der Pauw measurements using gold contacts deposited on the sample [8].

0921-5107/93/$6.00

© 1993 – Elsevier Sequoia. All rights reserved

2. Crystal growth

Two ingots of CdTe 8 cm in size were grown by THM.

To study the effect of carbon in CdTe and to simulate the carbon layer in the crucible, carbon powder is introduced in one ingot, corresponding to an initial mean concentration of 3.3×10^{19} atoms cm^{-3}. In the second ingot, we have introduced silicon with an initial concentration of the order of 9×10^{18} atoms cm^{-3}. The crystals are grown at a tellurium zone temperature of 850 °C and at a speed of 1 mm per day.

3. Characterization techniques

3.1. The activation method (CPA)

The CPA method has been used at the 4 MV accelerator at CRN in Strasbourg. ${}^{A}X(d,n)^{A+1}Y$ nuclear reactions converting X into positron emitting β^+ radionuclei ${}^{A+1}Y$ with half-time $T_{1/2}$ have been chosen such that

$${}^{A}X(d,n)^{A+1}Y \xrightarrow{\beta^+ T_{1/2}} {}^{A+1}Y$$

where ${}^{A}X$ can be either ${}^{12}C$ or ${}^{29}Si$ and ${}^{A+1}Y$ ${}^{13}N$ or ${}^{30}P$. $T_{1/2}$ for carbon is 10.05 min and 2.5 min for silicon.

Each CdTe wafer is irradiated during one period with an incident deuteron beam of intensity 200 nA and energy 3 or 3.5 MeV. The residual pressure in the target chamber is about 10^{-6} Torr. Unfortunately, at this pressure, the incident beam also deposits carbon atoms on the surface of the sample during the activation [9]. The nuclear activity is determined by β^+ spectrometry. (This method is described in detail in a previous work [6].) The absolute concentration of carbon in CdTe is deduced from the comparison with the activation of a pure carbon target irradiated during 30 s with a beam of 30 nA following the method described by Ishii *et al.* [10].

3.2. Heavy ion induced X-ray emission

The 0.8 MeV Ar^+ ions used in this work are delivered by the 4 MV accelerator. The samples are positioned perpendicular to the beam axis and X-rays are detected in a Si(Li) counter at an angle of 135° with respect to the beam direction [11]. The Si(Li) detector, with an energy resolution ranging from 160 to 250 eV in the region of interest from 1.25 to 15 keV, is applied directly to the vacuum system through a 100 μm beryllium window. In order to avoid pulse pile-up, the counting rate has been kept below 400 pulses s^{-1} by limiting the beam intensity. The goal of these measurements is to study the evolution of the relative concentration of impurities from slice to slice all along the crystals.

3.3. Secondary ion mass spectroscopy

For SIMS analysis, the measurements are performed on the positive ions sputtered from the surface of the samples by a 3 keV O_2 beam. The scanning time of each mass is 3 s. The current density of the oxygen beam is kept low enough to sputter off a negligible thickness of material during the measurements and to avoid contamination. Positive charge accumulation on the semi-insulating sample is avoided by simultaneous low energy electron bombardment. The residual pressure in the analysis chamber is approximately 10^{-9} Torr.

4. Electronic methods

4.1. Thermally stimulated current

In this technique, the traps are filled by illuminating the sample at low temperature with interband light ($\lambda = 0.63$ μm using an He–Ne laser). The discharge current is then measured in the dark and recorded as a function of temperature. The improved TSC procedure involves a precise calculation of the defect levels energy [12] and further uses a microcomputer-based deconvolution procedure of the experimental spectra recorded in a cryostat over a temperature range from 77 to 450 K.

Figure 1 shows the TSC spectrum for a THM grown high resistivity material.

4.2. Van der Pauw technique

This technique is described by Kobayashi *et al.* [13]. We have used this method to determine the resistivity along the two ingots. In nearly all the ingots we have observed a strong decrease in the resistivity—up to 10^8 Ω cm at the first sections of the ingots and down to

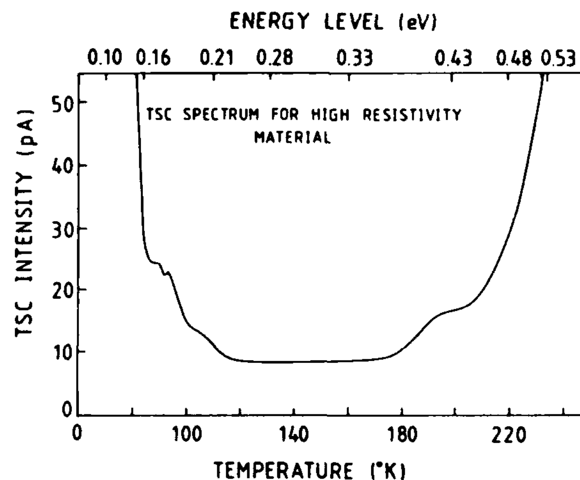

Fig. 1. TSC spectrum for high resistivity THM grown material as a function of the temperature and energy level.

10^4 to 10^6 Ω cm towards the end—which is a normal behaviour in THM crystal growth, corresponding to the gradual saturation of the tellurium zone.

5. Results

5.1. Charged particle activation method

The absolute concentration $C(x)$ in each slice is normalized to the initial concentration C_0. The measurements are compared with Pfann's formula [14]. The value of the apparent segregation coefficient which can be deduced is $K_{eff} = 7\times10^{-3} \pm 1\times10^{-3}$ [9]. We deduce that if some carbon atoms are introduced into CdTe from the graphite protection of the quartz tube during THM treatment, these atoms are carried off to the end of the ingot with the molten tellurium zone.

For the silicon ingot, we relied on the $^{29}Si(d,n)\,^{30}P$ nuclear reaction, which converts the silicon into positron emitting β^+ radionuclei of ^{30}P, with half-life $T_{1/2}$ of the order of 2.5 min.

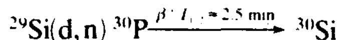

$$^{29}Si(d,n)\,^{30}P \xrightarrow{\beta^+ T_{1/2}=2.5\ min} {}^{30}Si$$

However, the $^{16}O(d,n)\,^{17}F$ nuclear reaction with half-life $T_{1/2}$ of 1.07 min has severely masked the information of the previous reaction.

5.2. Secondary ion mass spectroscopy

A typical mass spectrum obtained by SIMS is shown in Fig. 2. The lines of trace elements originating from different contamination appear mainly at the surface.

The SIMS carbon profile (Fig. 3) is not very significant because the samples are contaminated by hydrocarbon during the measurements. However, this method gives information to compare results of the CPA (Fig. 4) and TSC for the carbon ingot and HIXE (Fig. 5) and TSC (Fig. 6) for the silicon ingot.

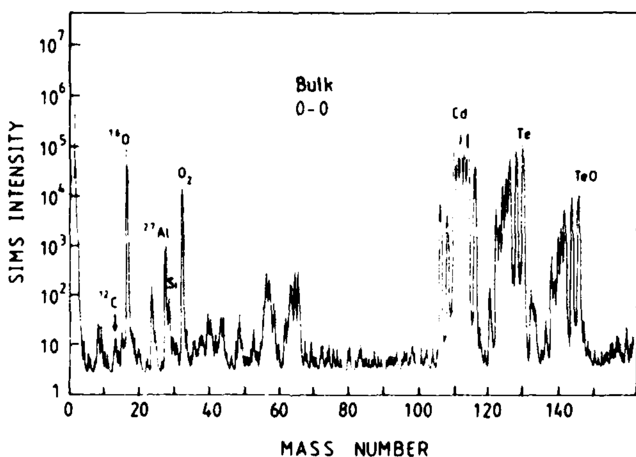

Fig. 2. Typical SIMS spectrum.

5.3. Heavy ion induced X-ray emission

A typical HIXE spectrum obtained by argon ion bombardment is shown in Fig. 5. The detected elements indicated on the spectra are the Cd Lα and Te Lα HIXE rays from the target bulk. For the trace elements, the most important peaks correspond to silicon. The HIXE intensity ratio remains constant along the crystal, revealing a constant mean composition (Fig. 6).

5.4. Discussion

Determination of the concentration of carbon and silicon in CdTe is generally difficult because of the permanent contamination of these two elements during the growing, preparation or measurements by ampoula, skewing, polishing powder (diamond or silicon carbide), vacuum oil, etc. For this reason, results are largely distributed in all cases.

However, we made here an attempt to see if carbon and silicon follow the general behaviour of the other

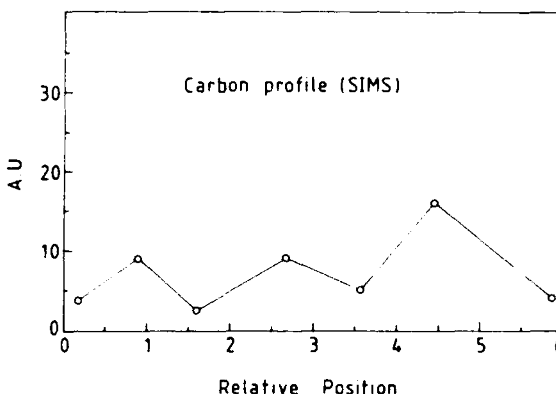

Fig. 3. Carbon SIMS profile as a function of relative position.

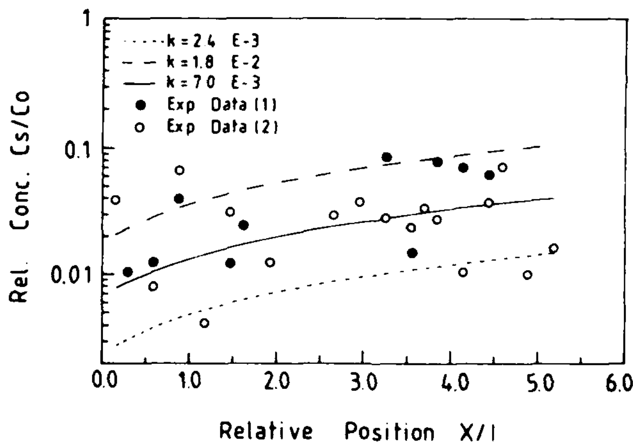

Fig. 4. Pfann's curves for different values of K_{eff} compared with the relative concentration $C(x)/C_0$. A mean value $K_{eff} = 7\times10^{-3} \pm 1\times10^{-3}$ is deduced from the experimental points: (1) $E_d = 3$ MeV; (2) $E_d = 3.5$ MeV.

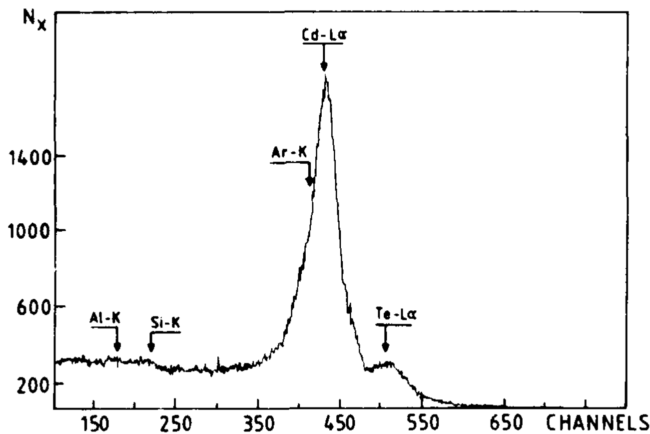

Fig. 5. Typical HIXE spectrum of a CdTe ingot containing silicon.

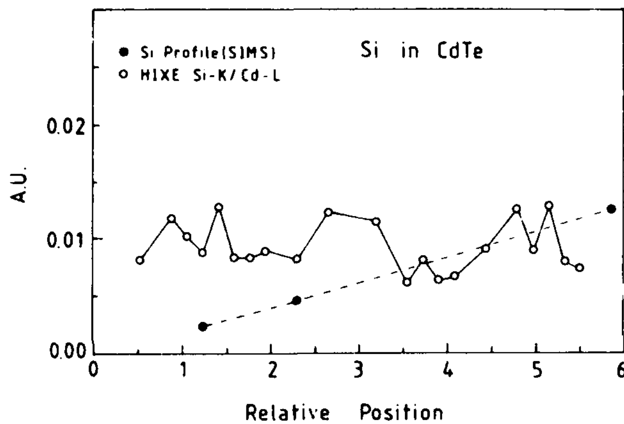

Fig. 6. HIXE intensity ratio from Si K to Cd L lines and silicon SIMS profile as a function of the relative position.

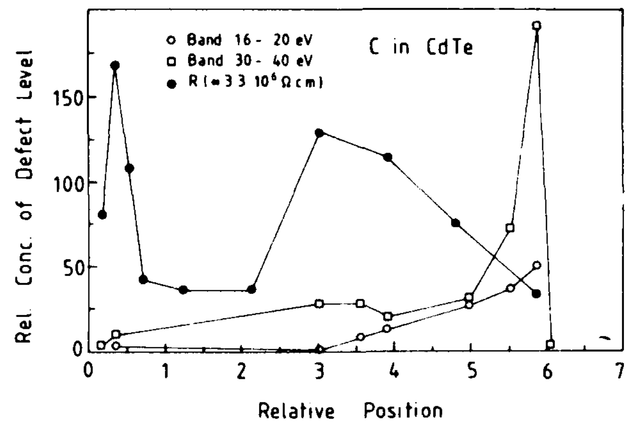

Fig. 7. Relative concentration of defect level and Van der Pauw resistivity in the carbon ingot as a function of the relative position.

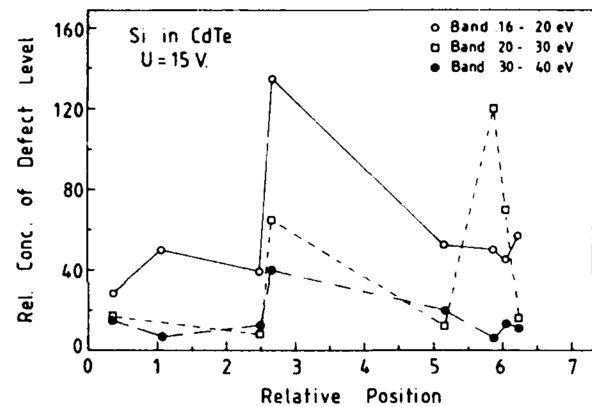

Fig. 8. Relative concentration of defect level in the silicon ingot as a function of the relative position.

elements from group IV—germanium, tin and lead—which relates the electrical activity determined by resistivity and TSC (Fig. 7) to carbon and silicon concentrations measured by CPA (Fig. 4), HIXE and SIMS. The silicon relative concentration of defect level is shown in Fig. 8.

In the case of silicon, AA was used to verify the original concentration because the profile along the ingot is highly distributed in HIXE measurement. We can see either by this method weakly or by SIMS that the silicon concentration increases from the beginning towards the end of the crystal. This is followed by an increase in the 0.3–0.4 eV energy band (TSC) and by a decrease in the 0.16–0.20 eV energy band, corresponding to a decrease in the resistivity towards the end of the ingot; this is the normal trend in THM measurements.

The same trend appears for carbon at the end of the ingot. A slow decrease in carbon either by SIMS or CPA is apparently followed by a sharp increase in the 0.3–0.4 eV energy band (TSC) and a slow increase in the 0.16–0.20 eV energy band, which correspond again to a decrease in the measured resistivity at the end of the crystal.

6. Conclusions

In both cases, weak correlation is found between silicon and carbon concentration below 100 ppm and the electrical characteristics. The possibility of interaction from other dopant action is still present. Electron paramagnetic resonance measurements [15, 16] are in agreement with this behaviour for carbon- or silicon-doped material. TSC or resistivity measurements are sensitive, even if the dispersion is great, but they also do not show large correlation. However, further studies are needed to obtain better statistics and to confirm the donor character of carbon and silicon.

Acknowledgments

The authors are grateful to R. Stuck for SIMS analysis and to C. Rit for valuable technical assistance as well as to M. Brutt for preparing the manuscript.

References

1 P. Siffert, *Nucl. Instrum. Methods, 150* (1978) 1.
2 P. Williams and C. A. Evans, *Surf. Sci., 78* (1978) 324.
3 M. H. Patterson and R. H. Williams, *J. Phys. D, 11* (1978) L83.
4 C. Heitz, M. Kwadow and D. Tenorio, *Nucl. Instrum. Methods, 149* (1978) 483.
5 U. Fano and W. Lichten, *Phys. Rev. Lett., 14* (1965) 627.
6 M. Bosat and W. Lichten, *Phys. Rev. A, 6* (1972) 211.
7 S. G. Elkomoss, M. Samimi, S. Unamuno, M. Hage-Ali and P. Siffert, *J. Appl. Phys., 57* (1985) 12.
8 A. Musa, J. P. Ponpon, J. J. Grob, M. Hage-Ali, R. Stuck and P. Siffert, *J. Appl. Phys., 54* (1983) 3260.
9 L. Chibani, J. P. Stoquert, M. Hage-Ali, J. M. Koebel and P. Siffert, *Appl. Surf. Sci., 50* (1991) 177.
10 K. Ishii, M. Valladon and J. L. Debrun, *Nucl. Instrum. Methods, 150* (1978) 213.
11 A. Al Neami, *Thesis*, University Louis Pasteur, Strasbourg, 1988.
12 M. Samimi, M. Hage-Ali and P. Siffert, *Poly-Micro Crystalline and Amorphous Semiconductors*, Les Editions de Physique, Les Ulis, 1984, p. 273.
13 A. Zaiour, *Thesis*, University Louis Pasteur, Strasbourg, 1988.
14 W. Pfann, *Zone Melting*, Wiley, New York, 1966.
15 W. Jantsch and G. Hendorfer, *J. Cryst. Growth, 101* (1990) 404.
16 R. M. Bilbé, J. E. Nicholls and J. J. Davies, *Phys. Status Solidi B, 121* (1984) 339.

Donor activation efficiency and doping profile quality in In-doped CdTe and CdZnTe quantum structures

F. Bassani* and S. Tatarenko

Laboratoire de Spectrométrie Physique, CNRS-Université Joseph Fourier, BP 87, 38042 Saint Martin d'Hères Cedex (France)

K. Saminadayar*

Laboratoire de Physique des Semiconducteurs SPMM/DRFMC Centre d'Etudes Nucléaires de Grenoble, BP 85X, 38041 Grenoble Cedex (France)

C. Grattepain

CNRS Laboratoire de Physique des Solides de Bellevue, 92195 Meudon Cedex (France)

Abstract

In-doping of CdTe and $Cd_{1-x}Zn_xTe$ ($x<20\%$) layers and quantum structures is performed during molecular beam epitaxy with a Cd overpressure. The In flux is determined as a function of the cell temperature. The role of the Cd overpressure in the activation efficiency is studied. Carrier mobilities of up to 5300 $cm^2\ V^{-1}\ s^{-1}$ are observed at light doping levels. In migration and formation of In-related compounds are studied by X-ray photoelectron spectroscopy. The doping profile quality is studied by secondary ion mass spectroscopy: efficient, well localized doping is achieved for low growth temperatures (200-220 °C) and low sheet densities (about $10^{11}\ cm^{-2}$); otherwise marked migration of the dopant is observed.

1. Introduction

This paper focuses on some aspects of molecular beam epitaxy (MBE) growth of In-doped CdTe and $Cd_{1-x}Zn_xTe$ (CZT) layers and quantum structures. In our previous work, the lowest growth temperature was 280 °C; actually this temperature is not optimum for doping [1] and so the present results are concerned with samples which are grown at two considerably lower temperatures, *i.e.* 200 and 220 °C.

2. Experimental results and discussion

The (001) CdTe epilayers are grown on (001) $Cd_{1-x}Zn_xTe$ ($x=0.03$-0.04) substrates. In concentrations and profiles are deduced from secondary ion mass spectroscopy (SIMS) using a calibrated In-implanted layer. Electrical characterization includes room temperature capacitance-voltage and low temperature Hall effect measurements. In the X-ray photoelectron spectroscopy (XPS) we use the Mg Kα (1253.6 eV) line as source.

2.1. Effect of Cd overpressure

In doping of (001) CdTe can be carried out efficiently by MBE without photoassistance if a Cd overpressure p_{Cd} is maintained during growth [2]. Different samples were grown using identical CdTe and In fluxes ($p_{CdTe}=10^{-6}$ Torr, $T_{In}=325$ °C) but with p_{Cd} varying between 10^{-7} and 6×10^{-7} Torr. For a growth temperature of 220 °C, a constant carrier concentration ($n=2\times10^{16}\ cm^{-3}$) is obtained for p_{Cd} lying in the range from 0.4 to 4×10^{-7} Torr: no critical p_{Cd} value exists within this range. However, for the lowest Cd overpressure, a decrease in the growth rate is observed along with a much lower crystalline quality as determined by luminescence. For p_{Cd} higher than 6×10^{-7} Torr, a "spotty" reflected high energy electron diffraction (RHEED) pattern is rapidly observed; this limit corresponds to a change in the growing CdTe surface's structure from a mixed ($c(2\times2)+(2\times1)$) type to a pure, Cd-rich $c(2\times2)$ type [3]. For higher In fluxes we

*Authors to whom correspondence should be addressed.

0921-5107/93/$6.00 © 1993 - Elsevier Sequoia. All rights reserved

observed a better doping efficiency using the highest tolerable p_{Cd} consistent with good crystallographic quality. For growth at 200 °C, to avoid surface deterioration we have to keep p_{Cd} below 3×10^{-7} Torr; this pressure corresponds also to the surface structure change described above.

2.2. *Control of the In cell flux*

In MBE the only way to control the In flux is by monitoring the In cell temperature T_{In}. In Fig. 1, the straight line (a) is determined from our experiments. It is drawn through the "effective" In flux ϕ_{eff} data points $\phi_{eff} = N_{In} v_g$ where N_{In} is the amount of incorporated In atoms (from SIMS) and v_g is the growth rate (from the RHEED record). Curve (b) is the "theoretical" $\phi_{eff}(T_{In})$ curve calculated using parameters taken from Nesmeyanov's work [4] and geometric parameters of the growth chamber.

The shift between the two lines is attributed to uncertainty in the values of the thermodynamic parameters (which are deduced from experiments at temperatures much higher than ours) and also to uncertainties in the temperature T_{In}. The parallel slopes of the curves demonstrate that In is incorporated into the sample with a constant efficiency over the concentration range studied (up to 3×10^{18} cm^{-3}); line (a) can be used to define the temperature T_{In} necessary to achieve a desired value of the In concentration.

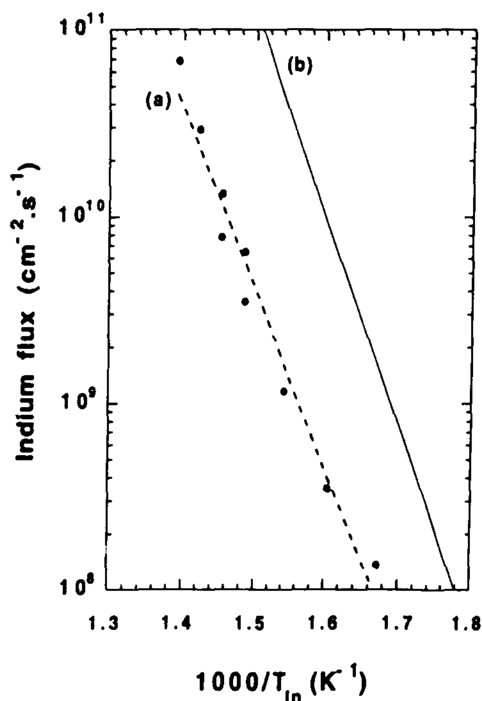

Fig. 1. In flux at the growth surface *vs.* inverse temperature of the In cell. Line (a) is an exponential least-squares fit of experimental results. Line (b) is the theoretical flux deduced from thermodynamic considerations and from the growth chamber geometry.

2.3. *Transport properties of uniform doped layers*

Figure 2 presents the electron mobility *vs.* temperature curves using the Van der Pauw technique. For low doping levels, a classical temperature dependence is observed but for the most highly doped layer the mobility becomes independent of temperature, as already reported by Segall *et al.* for bulk samples [5]. For the layer with the lowest concentration (10^{16} cm^{-3}), the electron mobility is 5300 cm^2 V^{-1} s^{-1} at 40 K; this value demonstrates the lowest degree of compensation of these *n*-CdTe films but it remains an order of magnitude smaller than the mobilities observed for Cd-annealed, undoped bulk CdTe [5].

2.4. *X-ray photoelectron spectroscopy studies of planar In doping limitation*

We have shown that in planar-doped layers the donor concentration limit does not exceed that obtained by the uniform doping method [6]. Two effects can be invoked to explain this result: migration of the In atoms and chemical reactions of In with Te. These phenomena were studied by XPS.

About 5% of a monolayer of In (2×10^{13} In cm^{-2}) was deposited at 200 °C on the (001) CdTe surface and buried by eight monolayers (MLs) of CdTe (1 ML= 3.24 Å). This sample was then annealed and analysed by XPS. At 220 °C, the In XPS intensity begins to increase (electron escape depth is about 15 Å= 4 ML) [7] and it increases again after annealing at 280 °C. In atoms diffuse at a temperature as low as 220 °C. A diffusion coefficient $D_{in} \approx 10^{-17}$ cm^2 s^{-1} at T= 220 °C can be deduced and thus the broadening $(2(2D_{In}t)^{1/2})$

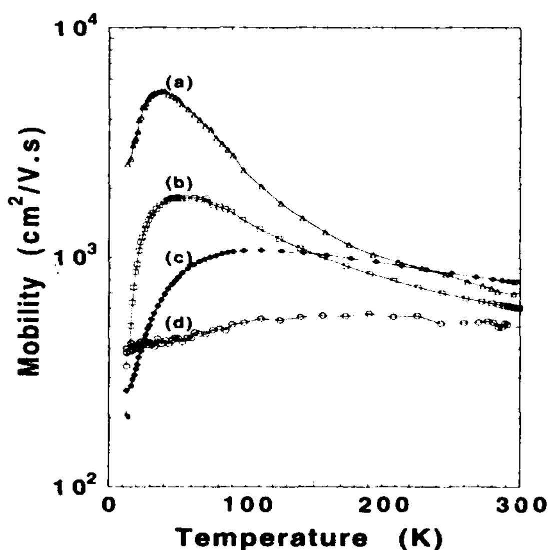

Fig. 2. Electron mobility from Hall measurements for four In-doped CdTe layers grown at 220 °C. The donor concentrations n at room temperature are (a) 8×10^{15} cm^{-3}, (b) 3×10^{16} cm^{-3}, (c) 1×10^{17} cm^{-3} and (d) 1×10^{18} cm^{-3}.

of doping planes could be of order of 10–100 Å during typical growth times (10^2–10^4 s).

To study the chemical reactivity of In with CdTe, about 5% of an In ML is deposited on the (001) CdTe surface at different growth temperatures between 180 and 280 °C and the In $3d_{5/2}$ peaks were studied in detail (Fig. 3). For In adsorption at 180–220 °C (curve a), the XPS peak can be fitted using only one gaussian line (line 1) centred at 444 eV; at 280 °C (curves b) a second gaussian line (line 2) must be added on the high energy side (about 0.3 eV from line 1) to account for the experimental lineshape. We attribute line 1 to In atoms adsorbed on top of the CdTe layer and line 2 to In atoms involved in an In_2Te_3 compound [8].

2.5. Secondary ion mass spectroscopy studies of locally doped CdTe/CZT quantum structures

Discussions on the SIMS resolution will be given elsewhere [6]. In the present work this resolution can be estimated to be $2\sigma \approx 70$ Å. A variety of doped CdTe/$Cd_{1-x}Zn_xTe$ ($x = 0.08$) quantum structures were locally doped either in the CdTe wells or in the CZT alloy barriers [6, 9].

Two examples of doped superlattices (SLs) are presented in Fig. 4. These SLs are made up of 40 CdTe/CZT periods. In Fig. 4(a), each CdTe well is planar doped at the well centre. The In SIMS profile presents one maximum for each CdTe well; these maxima are located in the central part of the wells. The In peaks appear relatively abrupt on the left-hand side (growth direction): for this lightly doped SL there is no large diffusion of In towards the surface during growth. The doping of the SL in Fig. 4(b) consists of two indium planes symmetrically placed inside the CdTe wells 5 ML from the CZT barriers. We clearly resolve two maxima in the In profile for each CdTe well; their separation is in good agreement with the value given by the RHEED oscillations record (30 ML ≈ 97 Å). On closer inspection, we note that the concentration of the lower In plane (the plane grown first, on the right-hand side of Fig. 4(b)) is somewhat higher than that of the upper plane (grown later); we attribute this to the In flux "burst effect".

These results together with other data [6] show that good localization of the In atom sheets can be achieved

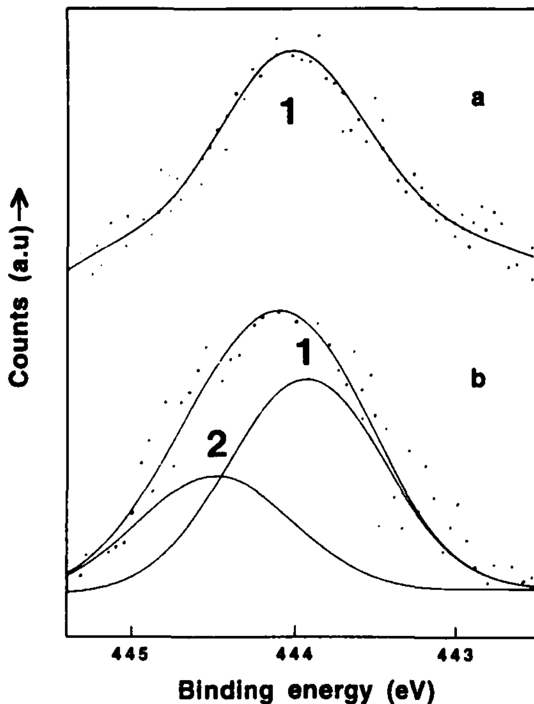

Fig. 3. Variation of the $In_{3d5/2}$ XPS line of samples on which about 5% of a ML of In is deposited on the (001) CdTe surface, the deposition temperatures being (a) 200 °C or (b) 280 °C. Line 1 (centred at 444 eV) is attributed to adsorbed In atoms while line 2 (located about 0.3 eV from line 1) is associated to In atoms involved in In_2Te_3 species.

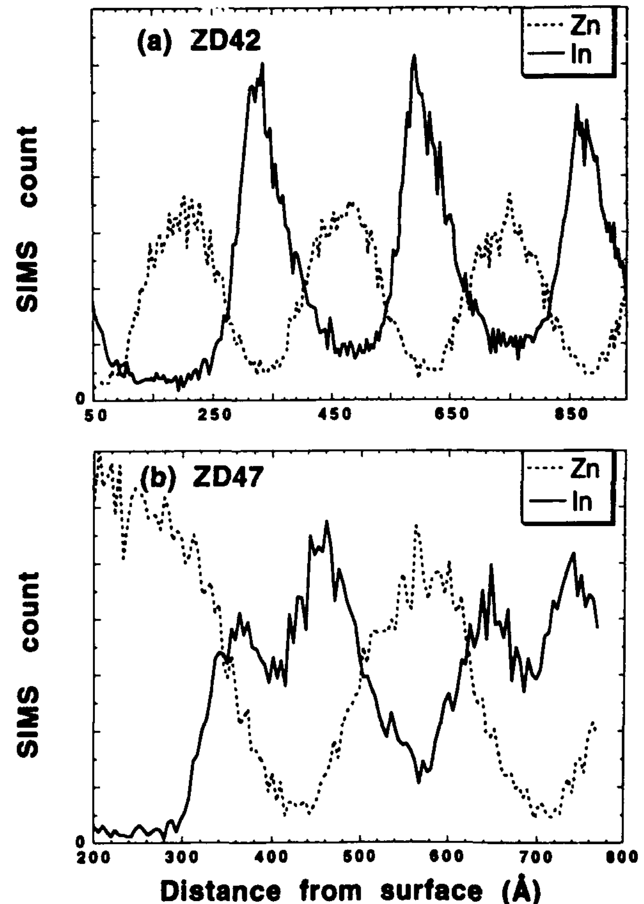

Fig. 4. In and Zn SIMS profiles compared for two CdTe/$Cd_{1-x}Zn_xTe$ ($x = 0.08$) SLs (40 periods of 41MLCdTe/42MLCZT) locally doped with In at a growth temperature of 220 °C: (a) one sheet of In (nominal density $N^{2D} = 1.7 \times 10^{11}$ cm^{-2}) in each CdTe well, at the well centre; (b) two sheets of In ($N^{2D} = 8.5 \times 10^{10}$ cm^{-2}) in each well, symmetrically placed at 5 ML from the CZT barriers.

at low-to-moderate doping levels. Unfortunately, the situation appears very different at high doping levels: a substantial migration of In then occurs, consistent with XPS results [6].

3. Conclusions

Some issues concerning the MBE In doping of CdTe and CdZnTe are presented: the role of the Cd overpressure to achieve high doping efficiency; the control of the In flux; the electron mobility of the doped layers and the doping profile quality. In particular, there is no indication of In migration (at about the 70 Å scale) for low doping levels at a growth temperature of 220 °C. For uniform as well as for planar doping, a practical limit of about 1.5×10^{18} cm^{-3} cannot be exceeded, due partially to the formation of chemical species involving In atoms.

References

1 F. Bassani, K. Saminadayar, S. Tatarenko, K. Kheng, R. T. Cox, N. Magnea and C. Grattepain, *J. Cryst. Growth, 117* (1992) 391.
2 F. Bassani, S. Tatarenko, K. Saminadayar, J. Bleuse, N. Magnea and J. L. Pautrat, *Appl. Phys. Lett., 58* (1991) 2651. D. E. Ashenford, J. H. C. Hogg, D. Johnston, B. Lunn, C. G. Scott and D. Staudte, *J. Cryst. Growth, 101* (1990) 157.
3 Y. S. Wu, A. Waag and R. N. Bicknell-Tassius, *Appl. Phys. Lett., 57* (1990) 1754.
4 A. N. Nesmeyanov, in R. Gary (ed.), *Vapor Pressure of the Chemical Elements*, Elsevier, Amsterdam, 1963, p. 240.
5 B. Segall, M. R. Lorentz and R. E. Halsted, *Phys. Rev. B, 129* (1963) 2471.
6 F. Bassani, S. Tatarenko, K. Saminodayar, N. Magnea, R. T. Cox and A. Tardot, *J. Appl. Phys.*, in press.
7 A. Waag, Y. S. Wu, R. N. Bicknell-Tassius and G. Landwehr, *Appl. Phys. Lett., 54* (1989) 2662.
8 D. R. T. Zahn, K. J. Mackey, R. H. Williams, H. Münder, J. Geurts and W. Richter, *Appl. Phys. Lett., 50* (1987) 742.
9 R. T. Cox, A. Mandray, S. Huant, F. Bassani, K. Saminadayar and S. Tatarenko, *Mater. Sci. Eng., B16* (1993) 83-86.

Materials Science and Engineering, B16 (1993) 211–214

Implantation-enhanced interdiffusion in CdTe/ZnTe quantum wells

A. Hamoudi and E. Ligeon

DRFMC SP2M, Laboratoire de Physique des Interfaces, Centre d'Etudes Nucléaires de Grenoble, BP85X, Grenoble 38041 (France)

J. Cibert and Le Si Dang

Laboratoire de Spectrométrie Physique (CNRS-URA08), Université Joseph Fourier, BP87, Saint Martin d'Hères 38402 (France)

J. L. Pautrat

DRFMC SP2M, Laboratoire de Physique des Semiconducteurs, Centre d'Etudes Nucléaires de Grenoble, BP85X, Grenoble 38041 (France)

Abstract

Implantation-enhanced interdiffusion in CdTe/ZnTe quantum wells (QWs) has been studied using photoluminescence and secondary ion mass spectroscopy. In this system, a strong compositional disorder is produced by implantation alone. This is attributed to defect diffusion during the implantation process. The main effect observed after short-time annealing is the recovery of the QW optical properties.

1. Introduction

Implantation-enhanced interdiffusion (IEI) has attracted increasing interest owing to its potential application for planar confinement and laterally guided laser diodes. It has been extensively studied in III–V semiconductor heterostructures and found to occur via two mechanisms. The first mechanism is induced by implantation defects, as observed in GaAs/GaAlAs after high dose Ar [1] or Si [2], or low dose Ga [3] implantation and rapid thermal annealing. The second mechanism is impurity-induced interdiffusion and appears during long-time annealing [1] when impurities (Zn, Si) have been implanted. This annealing induces long range disordering correlated with impurities diffusion. In II–VI compound heterostructures, IEI has seldom been studied. To our knowledge, the only work found in the literature concerns high dose Si implantation in ZnSe/ZnS [4], where IEI is dominated by the diffusion of implantation defects even after a long annealing time.

2. Experimental details

We report on photoluminescence (PL) and secondary ion mass spectroscopy (SIMS) studies of Zn, Cd and Ar IEI in CdTe/ZnTe quantum wells (QWs). Samples were pieces of a heterostructure grown by molecular beam epitaxy at 320 °C. A ZnTe layer about 1000 Å thick was first deposited on a (001) GaInAs substrate, followed by a $Cd_{0.84}Zn_{0.16}Te$ buffer layer about 2.7 μm thick, prior to the coherent growth of five CdTe (133 Å)/ZnTe (16 Å) QWs. Finally, a $Cd_{0.84}Zn_{0.16}Te$ cap layer 400 Å thick was used. The buffer layer defines the lattice parameter within the growth plane. Thus, a strong expansion is imposed on the ZnTe barriers ($\Delta a/a \approx 5\%$), while the CdTe QWs remain weakly compressed ($\Delta a/a \approx 0.9\%$). We present implantation results at 300 K for doses ranging from 10^{13} to 1.6×10^{14} cm^{-2}. Samples were annealed under an H_2–N_2 flux at 400 °C for times ranging from 5 to 90 min. PL was carried out at 1.8 K using an Ar ion laser with a typical power density of about 50 W cm^{-2}. SIMS experiments were performed at 77 K using a beam of Xe^0 with an energy of 1.8 keV and a flux equivalent to about 10 nA.

3. Results and discussion

Optical spectra are given in Fig. 1. For the as-grown QWs (Fig. 1(a)), the PL exhibits a rather sharp (2 meV or less) e_1h_1 excitonic line (about 1604 meV) with an extrinsic structure on the low energy side. The e_1h_1 line intrinsic character is confirmed by photoreflectance

0921-5107/93/$6.00

© 1993 – Elsevier Sequoia. All rights reserved

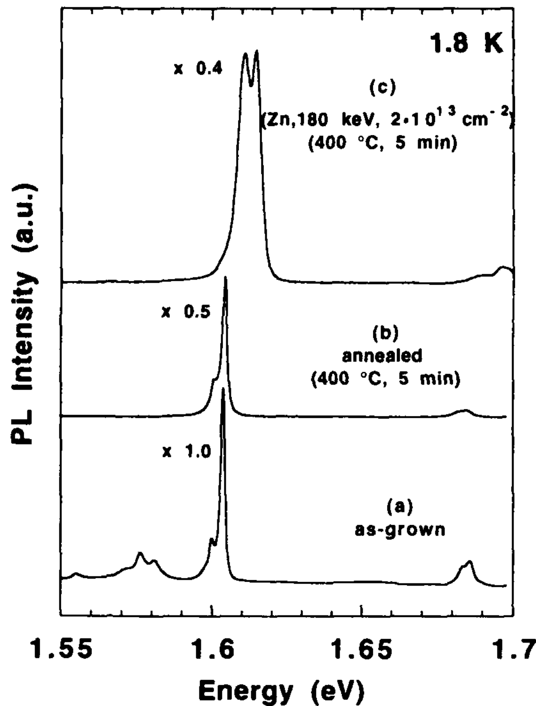

Fig. 1. Photoluminescence spectra from CdTe/ZnTe QWs.

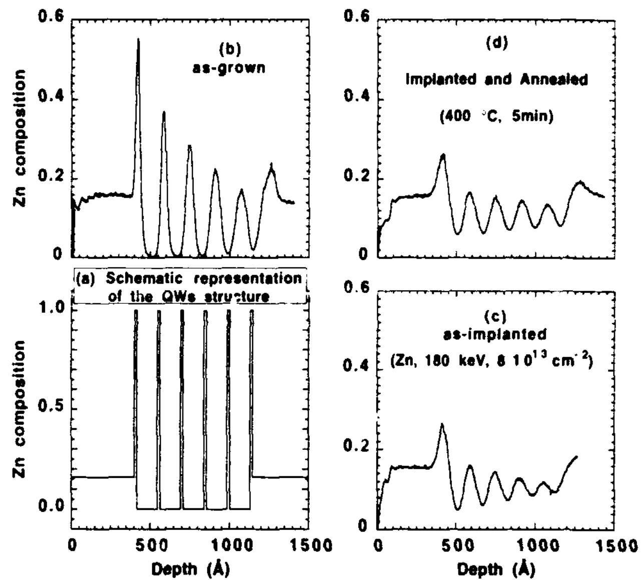

Fig. 2. SIMS profiles obtained for CdTe/ZnTe QWs.

and PL excitation measurements [5]. The position of the e_1h_1 line slightly shifts from sample to sample (3 meV or less), suggesting a fluctuation in the well thickness of plus or minus two monolayers. The peak at higher energy (about 1685 meV) corresponds to the buffer exciton. The origin of the low energy peaks (1550–1590 meV) is not clear at present. After annealing for 5 min (Fig. 1(b)), almost no change is seen either in the position of the e_1h_1 line or in its width. The main effect is the disappearance of the multiple peaks at lower energy, accompanied by an increase in the e_1h_1 intensity (by a factor of two). For longer annealing times (not shown), a small blue energy shift is obtained (for example, 5 meV after annealing for 60 min) while the width of the e_1h_1 line remains below 3 meV and its intensity further increases. Therefore, the QWs structure is weakly affected by the annealing process.

A moderate implantation (180 keV Zn; $R_p \pm \Delta R_p \approx 770 \pm 380$ Å) has a strong effect on the evolution of PL upon annealing (Fig. 1(c)). For the as-implanted QWs, no measurable luminescence could be obtained. However, after annealing of the implanted QWs, the PL yield is more important than for the as-grown QWs; this corresponds to the recovery of the optical quality. The blue shift observed for the implanted and annealed QWs is increased relative to that in the as-grown QW, and the luminescence lines broaden with increasing implanted dose. Also, we note that the extrinsic structure (4 meV below e_1h_1) becomes comparable in intensity with the e_1h_1 intrinsic line. This suggests either a higher defect density, or a better transfer to impurity-bound excitons. The blue shift saturates to 60 meV for a dose of 8×10^{13} cm^{-2} (and annealing for 5 min, not shown); then the splitting between the e_1h_1 line and its extrinsic structure is no longer resolved and the resulting line FWHM ≈ 15 meV. For doses greater than 8×10^{13} cm^{-2} we observe the appearance of an intense, broad band and the increase of the buffer luminescence after annealing. This is probably due to the formation of complex defects.

To clarify the effect of implantation alone and that of thermal annealing on IEI, we performed SIMS measurements to obtain a direct view of the Cd–Zn interdiffusion. In Fig. 2 we present the SIMS Zn signal as a function of depth. The as-grown sample profile (Fig. 2(b)) shows the evolution of the SIMS resolution with increasing depth. The implanted sample (Fig. 2(c)) clearly shows that the dominant contribution to IEI occurs during implantation. This result is similar to that observed for high dose Ar (10^{15} cm^{-2} or more) implantation in GaAs/GaAlAs [1], but contrasts with the case of ZnS/ZnSe [4], where a high Si dose (10^{16} cm^{-2}) does not change the SIMS signal. Upon annealing (Fig. 2(d)), a minor disorder of the composition is induced, *i.e.* no evident enhancement is observed. Thus, the main effect of annealing is the recovery of the PL intensity.

Ar ions (130 keV; $R_p \pm \Delta R_p \approx 820 \pm 415$ Å) exhibit a behaviour similar to Zn after implantation and annealing. Luminescence is more intense and the broadening of the e_1h_1 line remains small (5 meV or

less). However, less disordering occurs, *i.e.* doses two times higher are necessary to produce the same enhanced interdiffusion with these lighter ions. Heavier ions produce a higher defect density and hence a higher disordering efficiency; this is the case for 360 keV Cd ($R_p \pm \Delta R_p \approx 1085 \pm 465$ Å). A dose of 2×10^{13} cm^{-2} produces a continuous energy shift with increasing annealing time, *i.e.* there is no saturation after annealing for 5 min, as observed for Zn and Ar. The blue shift is accompanied by an important broadening and the luminescence line FWHM is about 15 meV.

Figure 3 displays the evolution of the e_1h_1 line FWHM obtained after implantation and annealing for various ions and energies. It appears clear that low dose implantation with Zn and Ar causes a minor broadening (the e_1h_1 linewidth remains smaller than 5 meV), while strong broadening is produced by Cd ions.

Figure 4 displays the interdiffusion length Δ deduced from the PL results for Zn implantation. Calculations were done using an error function profile for the interdiffused interface [6]. For the sake of clarity, the Ar and Cd results have not been reported in this figure. For the annealed (not implanted) sample, a short diffusion is involved (less than 10 Å after annealing for 90 min). The extracted thermal interdiffusion coefficient is then $D \approx 1.6 \times 10^{-18}$ cm^2 s^{-1}. In contrast, for the implanted and annealed sample, Δ is already large after annealing for 5 min (*e.g.* about 8 Å for 2×10^{13} cm^{-2}), and then increases slowly for longer annealing times. Hence the interdiffusion enhancement is related to implantation defects which are annealed out after the 5 min anneal. The strong decay of the PL intensity after implantation is due to the presence of such defects. The interdiffusion length was also extracted from SIMS data for a quantitative comparison. The Zn barrier signal was fitted using a similar profile with a characteristic length Δ_{exp} corrected by taking into account the SIMS resolution Δ_{res}. Δ_{res} is calculated as a function of the depth by fitting the profile of the as-grown sample. It is found to vary between 8 and 28 Å from the first to the last ZnTe barrier. Then, taking $\Delta^2 = \Delta_{exp}^2 - \Delta_{res}^2$, we find $\Delta \approx (27 \pm 2)$ Å, independent of the depth; this is close to the value obtained from PL, *i.e.* $\Delta \approx (35 \pm 8)$ Å. It should be noted that the optical determination of the interdiffusion length Δ is quite precise for small interdiffusion lengths but that, in this last case of strongly interdiffused QWs, SIMS data are more accurate.

Low dose ion implantation creates excess interstitials and vacancies. Their densities increase with ion mass but remain weak owing to the important self-annealing observed during implantation at 300 K in bulk CdTe [7]. These defects obey the following distribution in CdTe: (i) close to the surface, a zone

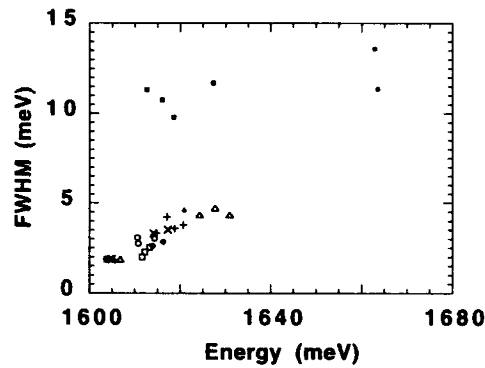

Fig. 3. Exciton line FWHM *vs.* energy. The symbol represents 180 keV Zn for (○) 10^{13} cm^{-2}, (+) 2×10^{13} cm^{-2}, (△) 4×10^{13} cm^{-2}, (●) 8×10^{13} cm^{-2}; 180 keV Ar for (□) 2×10^{13} cm^{-2}, (×) 5×10^{13} cm^{-2}; 130 keV Ar for (◆) 5×10^{13} cm^{-2}, (▲) 8×10^{13} cm^{-2}, and 360 keV Cd for (■) 2×10^{13} cm^{-2}.

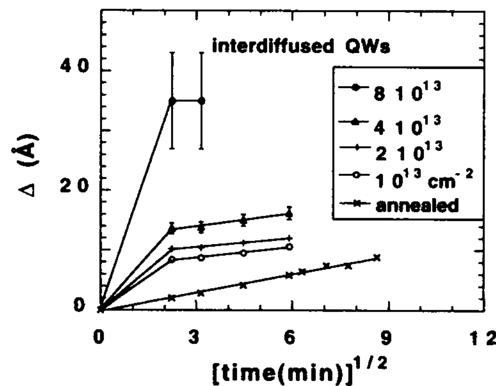

Fig. 4. Dose dependence of the interdiffusion length for Zn implantation. Thermal annealing results are reported for comparison. Doses are indicated on the figure.

approximately R_p thick is free of complex defects, but probably contains isolated points defects with a small density; (ii) deeper in the sample (about $2R_p$), extended defects are observed (by channeling and transmission electron microscopy studies [7]) and identified to be small Frank dislocation loops of the interstitial type. We believe that implantation has similar effects in CdTe/ZnTe QWs. Thus, only isolated points defects are involved for 180 keV Zn, 130 keV Ar and 360 keV Cd which have similar R_p values. From the behaviour of the PL upon annealing, it seems that the residual defects are more abundant and less homogeneous in the case of 360 keV Cd than in the cases of Zn and Ar. For 180 keV Cd ($R_p \pm \Delta R_p \approx 643 \pm 323$ Å), R_p is significantly smaller, so that the QWs are within the zone of complex defects. This assumption, quite natural from electron microscopy observation of bulk CdTe, is confirmed by our PL results (broad bands and poor efficiency of annealing).

Thus, we are led to the following simplified picture. During implantation of CdTe/ZnTe QWs, defects are created (around $0.7R_p \pm \Delta R_p$) and, at the same time, diffuse and are rapidly annealed. They already induce the interdiffusion of the QWs, which is thus almost completed at the end of the implantation process. After implantation, the density of residual defects is low (especially around R_p, *i.e.* the case of Zn and Ar implantation), though it is high enough to kill the PL intensity, with only a weak interdiffusion analogous to the thermal interdiffusion in the as-grown sample. It should be noted that the sharp lines observed after Zn or Ar implantation (in spite of the fact that the calculated distribution of implantation defects is quite inhomogeneous over the five QWs of our structure) support the idea of diffusion (over more than R_p) and annealing of the defects during the implantation stage, which would smooth the actual defect distribution.

To conclude, we would like to stress the fact that a significant blue shift is observed in implanted CdTe/ZnTe QWs with a very weak broadening of the PL line. The binary nature of the QW and barrier materials favours the observation of large shifts, since the ZnTe barrier acts as a localized reservoir of Zn. Broadening seems to be easily less than that in III–V heterostructures [3]: whether this is more favourable to the realization of lateral confinement will depend upon the range of defect diffusion during the implantation stage.

Acknowledgments

This work has been realized within the CEA-CNRS "Microstructure de semiconducteurs II–VI" group. We thank B. Blanchard (LETI) for the SIMS measurements.

References

1 H. Leier, A. Forchel, G. Horcher, J. Hommel, S. Bayer, H. Roth-fritz, G. Weimann and W. Schlapp, *J. Appl. Phys.*, *67* (1990) 1805.
2 S-Tong Lee, G. Braunstein, P. Fellinger, K. B. Kahen and G. Rasjawaran, *Appl. Phys. Lett.*, *53* (1988) 2531.
3 J. Cibert, P. M. Petroff, D. J. Werder, S. J. Pearton, A. C. Gossard and J. H. English, *Appl. Phys. Lett.*, *49* (1986) 223.
4 T. Saitoh, T. Yokogawa and T. Narusawa, *Appl. Phys. Lett.*, *55* (1989) 735.
5 J. Cibert, R. André, C. Deshayes, G. Feuillet, P. H. Jouneau, Le Si Dang, R. Mallard, A. Nahmani, K. Saminadayar and S. Tatarenko, *Superlatt. Microstruct.*, *9* (1983) 271.
6 M. D. Camras, N. Holonyak, Jr., R. D. Burnham, W. Streifer, D. R. Scifres, T. L. Paoli and C. Lindstrom, *J. Appl. Phys.*, *54* (1983) 5637.
7 A. Hamoudi, E. Ligeon and G. Feuillet, unpublished results, 1990.
8 A. Hamoudi, E. Ligeon, K. Saminadayar, J. Cibert, Le Si Dang and S. Tatarenko, *Appl. Phys. Lett.*, *60* (1992) 2797.

Native defect equilibrium in semi-insulating CdTe(Cl)

P. Höschl, R. Grill, J. Franc, P. Moravec and E. Belas
Institute of Physics, Charles University, Ke Karlovu 5, CS-121 16, Prague 2 (Czechoslovakia)

Abstract

CdTe single crystals doped with Cl were grown by normal freezing from a Te-rich solution. The results of charge carrier transport measurements were used to investigate the semi-insulating properties of CdTe(Cl) samples. Using the results of the theoretical calculation of the total energy, it was shown that Cd vacancies V_{Cd} are the dominant defects on the Te-rich side of the phase diagram. The deep acceptor level, probably connected to the second ionized state of divalent V_{Cd}, was determined to be $E_{a2} \approx 0.65$ eV. The probabilities of the occurrence of free vacancies, vacancies bound into acceptor complexes ($V_{Cd}Cl_{Te}$) and neutral complexes ($V_{Cd}2Cl_{Te}$) theoretically determined for various possible distances in the zincblende structure were used to explain the semi-insulating properties.

1. Introduction

The use of wide bandgap II–VI semiconductors in opto-electronic applications is often limited by self-compensation (SC), [1, 2]. Some materials (*e.g.* ZnS and ZnSe) remain n type and some remain p type (*e.g.* ZnTe) independent of doping with foreign acceptors or donors. An exception is CdTe, with which it is possible to prepare both n type and p type materials. In this case, the semi-compensation effect is widely utilized in the preparation of semi-insulating (SI) p-CdTe crystals by doping shallow donors, such as In_{Cd} and Cl_{Te}. The SI properties are important in the preparation of CdTe(In) on the Te-rich side of the phase boundary [3]. Donor impurities In_{Cd} and Cl_{Te} are fully effective as n-type dopants only when the CdTe is equilibrated on the Cd-saturated phase boundary [4, 5].

The basic idea of SI material follows from the three-level model [6]. In material that contains an excess of shallow donors (N_D) over shallow acceptors (N_A) ($N_D > N_A$), the deep acceptor level at about $E_g/2$, to which the Fermi level E_F is pinned, must be present with a concentration $N_t \geqslant (N_D - N_A)$.

In accordance with different estimates in SI p-CdTe(Cl), the total concentration of Cl_{Te} $[Cl_{Te}]_{tot} = 10^{17}$–$10^{18}$ cm^{-3} [7, 8] and the concentration of deep levels does not exceed 10^{13}–10^{15} cm^{-3} [8]. This fact demonstrates very strong compensation, *i.e.* $N_D \approx N_A$.

It is difficult to explain why at different levels of Cl doping foreign residual shallow acceptors (*e.g.* Cu) are present at the same concentration as Cl_{Te}, and why the concentration of deep levels (*e.g.* Ge, Si) is correlated with the residual shallow acceptors. Therefore, the main candidates for shallow and deep acceptors are intrinsic native defects. This paper tries to explain quantitatively the process of SC in close connection to the method of preparation of SI p-CdTe.

2. Experimental details

The vertical Bridgmann method was used to grow CdTe single crystals by normal freezing from a Te-rich solution [7]. CdTe single crystals contain Cl in a total concentration $[Cl_{Te}]_{tot} \approx 10^{17}$ cm^{-3}.

After the completion of growth, the CdTe crystal, which contains some Te precipitates, was equilibrated at 450°C for several days. These conditions are equivalent to annealing on the Te-rich side of the phase boundary where, for a vapour pressure of Cd, we have $p_{Cd} = 2.47 \times 10^7 \exp(-2.45\ \mathrm{eV}\ k_0 T)$ atm. We first shall collect the results of the experimental measurements on our SI p-CdTe samples and combine these with the results of other authors to reach some conclusions, which are a basis for verification of the SC model predicted in the next section.

It was determined by the time-of-flight technique [9] that our samples contain "shallow" acceptors lying 0.10–0.15 eV above the valence band, and shallow donors (Cl_{Te}) in approximately the same concentration, *i.e.* about 5×10^{16} cm^{-3}. We understand "shallow" acceptors to mean acceptors lying below E_F, which is localized in the midgap. The acceptor level is most

0921-5107/93/$6.00 © 1993 – Elsevier Sequoia. All rights reserved

probably created by a complex ($V_{Cd}Cl_{Te}$) whose existence was recently confirmed from photoluminescence measurements [4, 10] and whose position above the valence band was found to be $E_{ac} = 0.120$ eV. The activation energy of the Cl_{Te} shallow donors corresponds to a hydrogenic donor-level depth $E_d = 0.014$ eV [11]. Opinions differ on the position of the first ionized state of a divalent acceptor V_{Cd}. For example, from luminescence measurements it was determined that $E_{a1} = 0.069$ eV [12]. We shall suppose that it is completely ionized. The deep acceptor level $E_{a2} \gtrsim 0.6$ eV above the valence band, which appears in samples equilibrated on the Te-rich side, is often connected with the second ionized state of V_{Cd} [8, 13, 14]. An exact determination of the position of this level is very sensitive to the method of analysis of the experimental data (*e.g.* from $1/eR_H = f(1/T)$).

We have measured the Hall coefficient and conductivity in the temperature range 250–450 K [15]. New simultaneous analyses of $R_H(T)$ and $\sigma(T)$ were performed with the help of theoretically determined mobilities and Hall factors of both electrons and heavy holes. From the electric neutrality condition we obtained the value $E_{a2} = 0.65$ eV above the valence band. The same value for the deep level was determined for our samples by d.c. measurements of space charge limited currents (SCLC) [16]. The Fermi level $E_F = -E_g + E_{a2} + 0.72k_0T$ is pinned to E_{a2}. The electric neutrality condition is

$$(1 + f_2)[V_{Cd}] = [Cl_{Te}] - [V_{Cd}Cl_{Te}] \quad (1)$$

where $f_2 = \{1 + g_{2a} \exp[(-E_g + E_{a2} - E_F)/k_0T]\}^{-1}$ and $g_{2a} = 2/3$. The total concentrations of Cl_{Te} and V_{Cd} are

$$[Cl_{Te}]_{tot} = [Cl_{Te}] + [V_{Cd}Cl_{Te}] + 2[V_{Cd}2Cl_{Te}] \quad (2a)$$

$$[V_{Cd}]_{tot} = [V_{Cd}] + [V_{Cd}Cl_{Te}] + [V_{Cd}2Cl_{Te}] \quad (2b)$$

where

$$[V_{Cd}Cl_{Te}] = \sum_i [(V_{Cd}Cl_{Te})_i]$$

$$[V_{Cd}2Cl_{Te}] = \sum_i [(V_{Cd}2Cl_{Te})_i]$$

and index i is the ord.r of nearest neighbours. The square brackets indicate the concentration. For the binding energy of the complex $(V_{Cd}Cl_{Te})_1$ we have $H_C{}^1 = 2(E_{ac}{}^1 - E_{a2}) = 2(0.12 - 0.65)$ eV $= -1.06$ eV. This value is in a good agreement with the Coulomb binding energy for the first nearest neighbours $H_C{}^1 = -2e^2/(\varepsilon_0 r_1) = -1.08$ eV for $\varepsilon_0 = 9.7$ and $r_1 = a3^{1/2}/4 = 2.8 \times 10^{-8}$ cm, when $a = 6.48 \times 10^{-8}$ cm is the lattice constant.

3. Theory and discussion

3.1. Defect equilibrium

We shall consider the intrinsic defects that can accommodate excess Te: Cd vacancy V_{Cd}, Te anti-site Te_{Cd} and Te interstitial Te_I which can as acceptors affect the process of compensation during Cl doping. The defects, in principle, can be created by thermic generation or as a result of the compensation of shallow donors.

Berding *et al.* [17] have calculated the formation energy of native point defects in CdTe using the full potential linearized muffin tin orbital (FP-LMTO) method. Free atom initial and final states were used as references. It is convenient for the analysis of defects in our case to consider pure solid CdTe(s) and Cd in the vapour Cd(g) as references for the defects. Using the values from Table 1 in ref. 17, we obtain

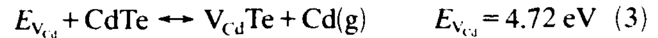

$$E_{V_{Cd}} + CdTe \longleftrightarrow V_{Cd}Te + Cd(g) \qquad E_{V_{Cd}} = 4.72 \text{ eV} \quad (3)$$

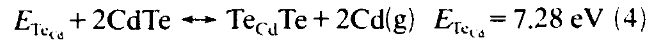

$$E_{Te_{Cd}} + 2CdTe \longleftrightarrow Te_{Cd}Te + 2Cd(g) \qquad E_{Te_{Cd}} = 7.28 \text{ eV} \quad (4)$$

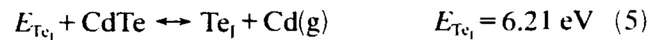

$$E_{Te_I} + CdTe \longleftrightarrow Te_I + Cd(g) \qquad E_{Te_I} = 6.21 \text{ eV} \quad (5)$$

If we calculate the values of the equilibrium constants of reactions (3)–(5), *i.e.* $K_{V_{Cd}} = C_0{}^{-1}[V_{Cd}]p_{Cd}$, $K_{Te_{Cd}} = C_0{}^{-1}[Te_{Cd}]p_{Cd}{}^2$, $K_{Te_I} = C_0{}^{-1}[Te_I]p_{Cd}$, where $C_0 = 1.47 \times 10^{22}$ cm^{-3}, by a method analogous to the method described in ref. 18 for HgTe, for the Te-rich side we obtain $[V_{Cd}] \approx 10^8$ cm^{-3}, $[Te_{Cd}]/[V_{Cd}] \approx 10^{-4}$ and $[Te_I]/[V_{Cd}] \approx 10^{-11}$ at 450°C and $p_{Cd} \approx 2 \times 10^{-10}$ atm, and $[V_{Cd}] \approx 10^{13}$ cm^{-3}, $[Te_{Cd}]/[V_{Cd}] \approx 10^{-4}$ and $[Te_I]/[V_{Cd}] \approx 10^{-8}$ at 700°C and $p_{Cd} \approx 5 \times 10^{-6}$ atm.

We can see that on the Te-rich side the Cd vacancy is the dominant native point defect. The same situation is of course valid for defects generated during the process of SC.

In principle, for the Te-rich side we can take CdTe(s) and Te(s) or Te(l) as references in reactions (3)–(5). Then for the Te-rich side, the energies of creation of V_{Cd} (about 2.15 eV), Te_{Cd} (about 2.14 eV) and Te_I (about 3.44 eV) are directly obvious.

3.2. Self-compensation

To explain the mechanism of SC it is necessary to know which portion of the vacancies created by SC remains free (deep acceptor), and which portion is bound in complexes ($V_{Cd}Cl_{Te}$) separated by various possible distances in the sphalerite structure or in neutral complexes ($V_{Cd}2Cl_{Te}$).

The concentrations $[V_{Cd}2Cl_{Te}]$, $[V_{Cd}Cl_{Te}]$ and $[V_{Cd}]$ are calculated by the partition function formalism

$$Z = \sum_i \exp(-E_i/k_0T) \quad (6)$$

TABLE 1. The configuration parameters, the activation energy of the complexes $(V_{Cd}Cl_{Te})_i$ and the probabilities of different configurations

i	$\frac{r_1}{r_i}$	$E_{ac}{}^i$ (eV)	D_i	$g1_i$	$g2_i$	$\frac{[(V_{Cd}Cl_{Te})_i]}{[V_{Cd}]_{tot}}$	$\frac{[(V_{Cd}2Cl_{Te})_i]}{[V_{Cd}]_{tot}}$
1	1	0.120	1.694	4	6	0.590	0.403
2	0.5222	0.373	1.345	12	12	5.2×10^{-4}	2.1×10^{-3}
3	0.3974	0.439	1.306	12	12	6.2×10^{-5}	1.1×10^{-3}
4	0.3333	0.473	1.244	16	12	2.8×10^{-5}	3.8×10^{-4}
5	0.2928	0.495	1.221	24	24	2.1×10^{-5}	5.1×10^{-4}

$[V_{Cd}{}^{2-}]/[V_{Cd}]_{tot}=8.86\times10^{-4}$.

The energy E_i is here given by the Coulomb interaction of two atoms $Cl_{Te}{}^+$ and a vacancy $V_{Cd}{}^{2-}$ located in the mean volume $1/[V_{Cd}]_{tot}=2/[Cl_{Te}]_{tot}=2\times10^{-17}$ cm^3, corresponding to a fully compensated regime.

By including the most probable events in the calculation, the three dominant configurations are as follows:

(1) Both atoms $Cl_{Te}{}^+$ are distant from $V_{Cd}{}^{2-}$ – the case of a single vacancy $V_{Cd}{}^{2-}$. The partition function contribution is then given by (E_i is neglected here)

$$Z1=\frac{32}{[Cl_{Te}]^2a^6}=Z\frac{[V_{Cd}{}^{2-}]}{[V_{Cd}]_{tot}} \tag{7}$$

(2) One atom $Cl_{Te}{}^+$ is located near $V_{Cd}{}^{2-}$—the case of the complex $(V_{Cd}Cl_{Te})^-$. Here we have

$$Z2=\frac{8}{[Cl_{Te}]a^3}\sum_i g1_i\exp\left[-\frac{H_c{}^1}{k_0T}\left(\frac{r_1}{r_i}\right)\right]$$

$$=Z\sum_i\frac{[(V_{Cd}Cl_{Te})_i]}{[V_{Cd}]_{tot}} \tag{8}$$

(3) Both atoms Cl^+ are near $V_{Cd}{}^{2-}$—the case of the complex $(V_{Cd}2Cl_{Te})$. Here we have

$$Z3=\sum_i g2_i\exp\left[-\frac{H_c{}^1}{k_0T}D_i\right]=Z\sum_i\frac{[(V_{Cd}2Cl_{Te})_i]}{[V_{Cd}]_{tot}} \tag{9}$$

where Z is the total partition function $Z=Z1+Z2+Z3$, $r_i=(a/4)(8i-5)^{1/2}$ is the radius of the nearest neighbour spheres and

$$D_i=\frac{r_1}{r(Cl_1)}+\frac{r_1}{r(Cl_2)}-\frac{r_1}{2r(Cl_1,Cl_2)} \tag{10}$$

describes different configurations of the pair $Cl_{Te}{}^+$ around $V_{Cd}{}^{2-}$. Also, $r(Cl)$ and $r(Cl_1, Cl_2)$ are Cl–V_{Cd} and Cl–Cl distances, respectively, and $g1_i$ and $g2_i$ are the factors of degeneracy. The coefficients used and the activation energies of the complexes $(V_{Cd}Cl_{Te})_i$ given by

$$E_{ac}{}^i=E_{a2}+\frac{1}{2}H_C{}^1\left(\frac{r_1}{r_i}\right)$$

are shown in Table 1. The results for temperature $T=450$ °C are given on the right-hand side of Table 1. As can be seen, the close-packed complexes $(V_{Cd}Cl_{Te})$ and $(V_{Cd}2Cl_{Te})$ are dominant (59% and 40%) in CdTe(Cl), while the single V_{Cd} has a small concentration (0.089%). These theoretical values obtained on the basis of the proposed model of SC are in good agreement with experimental data.

Acknowledgment

The authors thank Dr. Marcy Berding from SRI International for valuable information connected with calculation of total energy of defects in CdTe.

References

1 G. Mandel, *Phys. Rev., 134* (1964) A1070.
2 F. F. Morehead and G. Mandel, *Phys. Rev., 137* (1965) A924.
3 F. W. Wald and R. O. Bell, *Nat. Phys. Sci., 237* (1972) 13.
4 S. Seto, A. Tanaka, Y. Masa and M. Kawaskima, *J. Cryst. Growth, 117* (1992) 271.
5 N. V. Agrinskaya and V. V. Shashkova, *Sov. Phys. Semicond., 24* (1990) 437.
6 A. J. Strauss, *Rev. Phys. Appl., 12* (1977) 167.
7 P. Höschl, P. Polívka, V. Prosser, M. Vaněček, *Rev. Phys. Appl., 12* (1977) 229.
8 N. V. Agrinskaya and O. A. Matveev, *Sov. Phys. Semicond., 21* (1987) 333.
9 P. Höschl, P. Polívka, F. Nava and R. Minder, *Czech. J. Phys. B, 26* (1978) 812.
10 D. M. Hoffmann, P. Omling, H. B. Grimmeiss, B. K. Meyer, K. W. Benz and D. Sinerius, *Phys. Rev. B, 45* (1992) 6247.
11 K. Zanio, Cadmium telluride, in R. K. Willardson and A. C. Beer (eds.), *Semiconductors and Semimetals*, Vol. 13, Academic Press, New York, 1978, p. 129.

12 N. V. Agrinskaya, O. A. Matveev, A. V. Nikitin and V. A. Sladkova, *Fiz. Tekh. Polup.*, *21* (1987) 666.
13 F. A. Kröger, *Rev. Phys. Appl.*, *12* (1977) 205.
14 N. V. Agrinskaya and O. Matveev, *Nucl. Instrum. Methods A*, *283* (1989) 263.
15 P. Höschl, P. Moravec, V. Prosser, R. Kužel, R. Grill, J. Franc, E. Belas and Yu. M. Ivanov, *J. Cryst. Growth*, *101* (1990) 822.
16 A Zoul and E. Klier, *Czech. J. Phys. B*, *27* (1977) 789.
17 M. A. Berding, M. van Schilfgaarde, A. T. Paxton and A. Sher, *J. Vac. Sci. Technol. A*, *8* (1990) 1103.
18 A. Sher, M. A. Berding, M. van Schilfgaarde and A. Chen, *Semicond. Sci. Technol. C*, *59* (1991) 6.

Materials Science and Engineering, B16 (1993) 219-222

Native point defects in CdTe and its stability region

M. Wienecke, H. Berger and M. Schenk
Humboldt Universität zu Berlin, Fachbereich Physik, Institut für Kristallographie und Materialforschung, Invalidenstrasse 110, D-O-1040 Berlin (Germany)

Abstract

The main charged native point defects in CdTe are tellurium vacancies in cadmium-rich CdTe and cadmium vacancies in tellurium-rich CdTe. The stability region seems to be much broader than that measured by methods which are sensitive to electrically charged native defects.

1. Introduction

The compound semiconductor CdTe is of practical interest, for example as a substrate material for IR detectors. Knowledge of the stability region and of the point defects which cause it enables material to be prepared with defined electrical and optical properties.

The native defects and the deviation from stoichiometry of CdTe have been studied in recent years by several authors [1-3]. Their results on the stability region of CdTe differ owing to the diverse methods of analysis used. The types of native point defects in CdTe are also described differently in the literature as vacancies [2], or vacancies and interstitials [4], or antisite defects [5-7]. To investigate the non-stoichiometry in a complex manner, it is desirable to combine several different analytical methods sensitive to certain point defects. In addition, if possible, the measurements should be performed at equilibrium conditions.

This paper is a contribution to describe the limits of stability of CdTe composition and to derive a defect model from the results of high-temperature Hall and conductivity measurements combined with room-temperature investigations of lattice parameters and positron annihilation on annealed and quenched samples (for more details see also ref. 8).

2. Experimental details

CdTe single crystals grown by the unseeded vertical Bridgman technique [9] were used. The excess ratio of tellurium in the starting material, which was highly purified, was less than 10^{-2} at.%. Spark-source mass spectrometry showed total concentrations of impurities of ca. 10^{17} cm^{-3} [10]. As-grown samples had carrier densities $p = 10^{14}$ to 10^{15} cm^{-3}.

n-type CdTe was made by annealing as-grown p-type samples for several days at 800 °C in an isothermal regime with a cadmium-rich additional source, establishing the three-phase equilibrium vapour pressure on the cadmium-rich side of the p–T diagram. Then the samples were quenched to room temperature.

The non-stoichiometry of p- and n-type samples was adjusted by annealing in tellurium- and cadmium-rich CdTe vapour respectively, according to the three-phase equilibrium at the respective temperature. Statistically distributed micro-precipitations play the role of sources and traps of native point defects. The apparatus used for this annealing process [11] was improved for annealing cadmium-rich samples in a closed system to prevent unverifiable evaporation of cadmium due to the high cadmium partial pressure. During the heat treatment, carried out using an isochronic temperature-time procedure, the Hall effect and conductivity were measured by the van der Pauw method at constant temperatures for a defined time to analyse the equilibration process.

After the high-temperature electrical measurements, the ampoules containing the samples were quenched in water. Precise lattice parameters were measured on these samples using the Soller-slit method [12] and corrected for the usual aberrations. Room-temperature lattice-parameter measurements should characterize accurately the real high-temperature defect density, because, owing to rapid quenching, the defect concentration at the annealing temperature should only be

0921-5107/93/$6.00

© 1993 - Elsevier Sequoia. All rights reserved

frozen in near the surface, because the low heat conductivity of CdTe prevents effective quenching of the whole sample.

For the positron annihilation measurements, p-type samples were annealed at different temperatures between 600 and 750 °C in sealed silica ampoules under saturated tellurium conditions and quenched in ice water [13]. The technique of positron lifetime spectroscopy is reported in ref. 14.

3. Results and discussion

The results of high-temperature Hall-effect and conductivity measurements, realized during equilibrium annealing under cadmium-rich and tellurium-rich conditions are shown in Figs. 1(a) and 1(b), respectively. The carrier density for p- and n-type CdTe, calculated from the measured data [8], is a definite exponential function of the reciprocal temperature, at both sides of the stability region, over the whole range of measurement. The additional arrows and crosses in Fig. 1(b) signify changes in concentration of electrically active defects due to annealing at constant temperature (24 h). These changes are caused either by precipitation or by dissolution of precipitations, depending on the direction of the equilibrium process adjusting maximum solubility. The same processes appear at the cadmium-rich side but are not shown in the figure. Time dependence of the measured electrical data was found only up to about 600 °C. Above this temperature, the dissolution or precipitation process takes place so fast that the equilibrium state is reached during the temperature change.

On both sides of the stability region, the limits always appear at the same concentrations as an exponential function of the reciprocal temperature, independent of heating or cooling, *i.e.* the process is reversible. These results were verified by the large number of samples investigated.

In Fig. 1(a), because there were too few of our own results, the data of Smith [15] are drawn in, showing quite good correspondence with our results in the concentration region of about 10^{16} cm^{-3}. The dashed lines on both sides showing the (calculated) intrinsic carrier concentrations confirm the assumption that the high-temperature electrical measurements are not visibly influenced by intrinsic carriers.

The stability region, which is related to the carrier density, extends, at 800 °C, to carrier concentrations of $p = 2.1 \times 10^{17}$ cm^{-3} in tellurium-rich CdTe and $n = 5.9 \times 10^{16}$ cm^{-3} in cadmium-rich CdTe. On both sides of the stability region, the clearly exponential dependence of the carrier concentration on reciprocal temperature leads to the conclusion that one type of electrically active defect is predominant in each case.

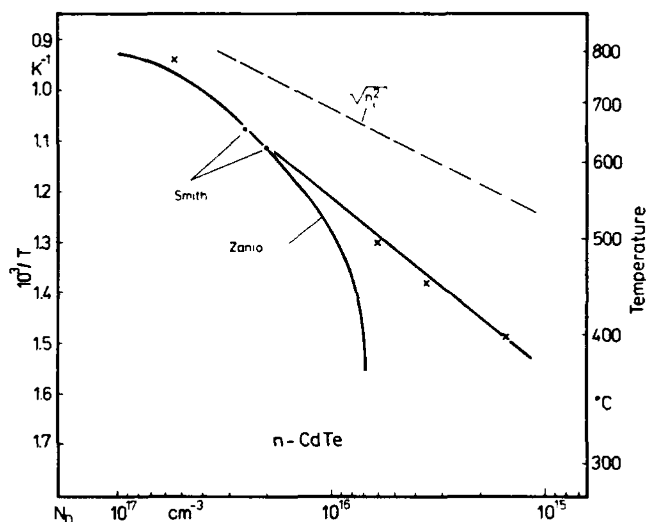

(a)

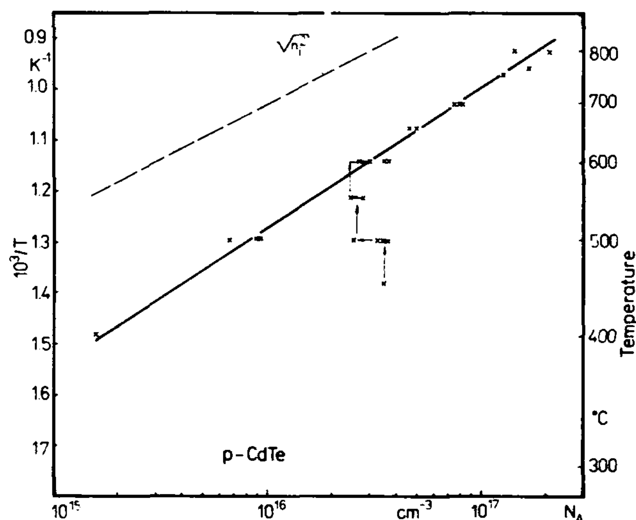

(b)

Fig. 1. Carrier concentration *vs.* reciprocal temperature, measured in three-phase equilibrium for n-CdTe (a) and p-CdTe (b). Arrows in (b) characterize the diffusion process; N_A, N_D, concentrations of electrically active native acceptors ($N_A = p - n$) and donors ($N_D = n - p$) respectively. Data of Zanio [1] and Smith [15] are also shown.

The lattice parameters measured after equilibrium annealing and immediately after quenching from different temperatures are plotted in Figs. 2(a) and 2(b) *vs.* the carrier density measured at the corresponding annealing temperature. On both sides of the stability region, a linear dependence appears between the carrier densities, taken as a measure of non-stoichiometry, and the lattice parameters.

To interpret the results described above, the relation between native point defects and impurities as well as

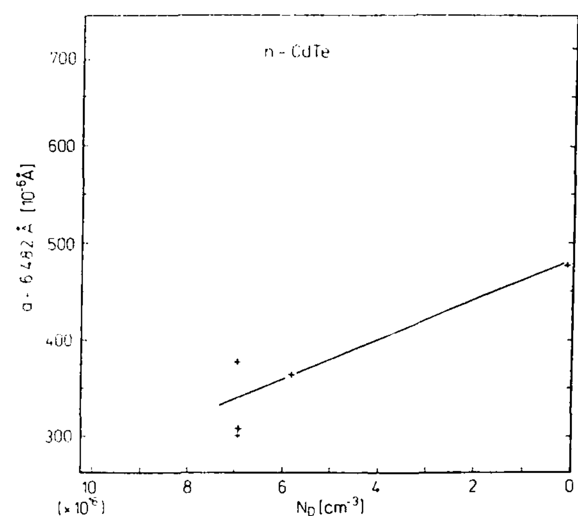

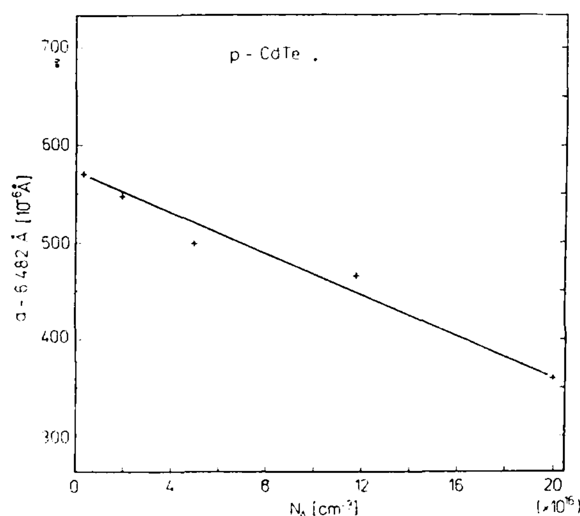

Fig. 2. Lattice parameter immediately after quenching *vs.* carrier density measured in equilibrium at high temperature for n-CdTe (a) and p-CdTe (b) (carrier density on a linear scale according to the continuum model).

other crystal defects, and their influence on the measured properties have to be considered.

As shown above, the impurities exist at an overall concentration of the order of 10^{17} cm^{-3} but the amount of electrically active impurities is unknown. The annealing processes lead to reversible changes in electrical properties; this cannot be explained by such a high concentration of electrically active impurities. The present results imply that the discrepancy between the relatively high overall concentration of impurities and the comparatively low as-grown carrier density, as well as the reversible changes in carrier concentration due to equilibrium annealing, may be explained by compensating effects between point defects and impurities leading to neutral complexes of impurities and native defects. Under thermodynamic conditions, only native point defects determine the electrical properties in the range of carrier concentration from 10^{15} to about 10^{17} cm^{-3}. The curve of Zanio [1] in Fig. 1(a), which deviates from a straight line in the lower concentration range, could be interpreted in this sense by assuming the existence of essentially higher impurity concentrations than in the present studies. The same is valid for his results concerning tellurium-rich CdTe.

The influence of dislocations, probably charged, in the zinc-blende structure, on the measured properties is negligibly small owing to their low concentration [16]. Therefore, only the native point defects remain to explain the present results, giving information about non-stoichiometry.

When discussing the limits of the stability region, one has to consider that the high-temperature Hall-effect and conductivity measurements are only sensitive to electrically active point defects. Assuming one predominant type of defect each for p-CdTe and n-CdTe, one is able to calculate the formation energy of the ionized native point defects as given in ref. 8 as 1.70 eV in both cases. To determine the formation energies of the uncharged defects, the ionization energies have to be known. Using the ionization energy given in the literature [7, 17] for a doubly ionized cadmium vacancy, we obtain the value 0.80–1.00 eV for the formation energy.

The changes in lattice parameters agree qualitatively with the generally accepted vacancy model for non-stoichiometric CdTe, supposing the validity of the simple continuum model [18]. Therefore, it can be concluded that any overcompensation effects caused by repulsion of the equally charged nearest neighbours of the vacancy should not occur, as has been discussed for GaAs [19]. The decrease in lattice parameters with increasing defect concentration for cadmium-rich and tellurium-rich CdTe leads to the conclusion that intrinsic vacancies dominate on both sides of the stability regions of CdTe, *i.e.* V_{Te} and V_{Cd}.

Defect concentrations estimated from the changes in lattice parameter by means of the continuum model are up to two orders of magnitude higher than the density of charged defects measured electrically. Supposing that only vacancies cause the changes in lattice parameter, concentrations of 8×10^{18} and 1×10^{19} cm^{-3} are calculated for p- and n-type CdTe respectively, *i.e.* the real "chemical" stability region should be much larger than is concluded from the electrical measurements.

Positron annihilation measurements only yielded results for p-type CdTe, proving that only negatively charged vacancies like V_{Cd}' or V_{Cd}'' act as lifetime prolonging traps [15]. The investigations provided lifetimes of about 290–300 ps corresponding to a concentration of charged vacancies of about 10^{16} cm^{-3}

[13], in agreement with electrical measurements on quenched samples. These measurements confirm the conclusion that the electrical measurements are determined by charged vacancies and not by impurities.

References

1 K. Zanio, in R. K. Willardson and A. C. Beer (eds.), *Semiconductors and Semimetals*, Vol. 13, Academic Press, New York, 1978.
2 S. A. Medvedev, V. N. Martynov and S. P. Kobol'eva, *Kristallografiya, 28* (1983) 3.
3 S. N. Maksimovskii and S. P. Kobol'eva, *Neorg. Mat., 22* (1984) 922.
4 A. Cornet, *Dr. Sci. Thesis*, University of Strasbourg, 1976.
5 J. A. van Vechten, *J. Electrochem. Soc., 122* (1975) 419.
6 J. T. Schick and C. G. Morgan-Pond, *J. Vac. Sci. Technol. A, 8* (1990) 1108.
7 C. G. Morgan-Pond and R. Raghavan, *Phys. Rev. B, 31* (1985) 10.
8 M. Wienecke, H. Berger and M. Schenk, to be published.
9 M. Mühlberg, P. Rudolph, C. Genzel, B. Wermke and U. Becker, *J. Cryst. Growth, 101* (1990) 275.
10 P. Rudolph, M. Mühlberg, M. Neubert, T. Boeck, P. Möck, L. Parthier, K. Jacobs and E. Kropp, *J. Cryst. Growth, 118* (1992) 204.
11 C. Albers and M. Wienecke, *Cryst. Res. Technol., 22* (1987) K53.
12 H. Berger, *J. Appl. Crystallogr., 17* (1984) 451.
13 H. Zimmermann, R. Boyn, P. Rudolph, J. Bollmann, A. Klimakow and R. Krause, *Mater. Sci. Eng., B16* (1993) 139–144.
14 R. Krause, A. Klimakow, F. M. Kiessling, A. Polity, P. Gille and M. Schenk, *J. Cryst. Growth, 101* (1990) 512.
15 F. T. J. Smith, *Metall. Trans., 1* (1970) 617.
16 G. Dlubek and R. Krause, *Phys. Status Solidi A, 102* (1987) 443.
17 P. Höschl, *Phys. Status Solidi, 13* (1966) K101.
18 P. Paufler and G. E. R. Schulze, in *Physikalische Grundlagen Mechanischer Festkorpereigenschaften I*, Berlin, 1978, p. 65.
19 C. M. H. Driscoll and A. F. W. Willoughby, *Proc. Int. Conf. on Radiation Damage and Defects in Semiconductors*, Conf. Ser. No. 16, Reading, Institute of Physics, London, 1972, p. 377.

Materials Science and Engineering, B16 (1993) 223–227

Deep levels in semi-insulating CdTe

P. Moravec*, M. Hage-Ali, L. Chibani and P. Siffert
Centre de Recherches Nucléaires, Laboratoire PHASE (UPR du CNRS 292) BP20, 67037 Strasbourg Cedex 2 (France)

Abstract

A general review on deep levels in CdTe created by doping of group IV elements and of 3d transition metal impurities is presented. We compare these data with some of our experimental results on Fe- and V-doped CdTe crystals. The problem of compensation is discussed.

1. Introduction

The interest in CdTe crystals arises from the extensive use of this compound in the fabrication of nuclear detectors, epitaxy substrates for HgCdTe and electro-optic devices. The majority of CdTe applications have several severe requirements for the crystals. In particular, a high resistivity ($\rho = 10^8$–10^9 Ω cm) and good charge transport (high $\mu\tau$ product) are needed.

Many of the physical properties of CdTe are controlled to some extent by the relative position of the energy levels within the forbidden gap associated with native defects, impurities and their complexes. The concentrations of defects and dopant atoms are not independent of each other. The introduction of electrically active impurities into a host crystal can induce the formation of electrically active defects and complexes which tend to dope or to compensate the material closely.

The high resistivity usually has been achieved by compensating the native acceptor defect (Cd vacancy) with a shallow donor (halogen) [1]. However, it has been found that, by adding Ge to CdTe, a semi-insulating material can also be obtained [2]. Recently, increased interest has been given to semiconductors in optical data processing and image processing applications. The necessary material criteria are that it must be electro-optic, available in semi-insulating form and must include deep levels which make trapping of photocarriers possible. Study of photorefractive semiconductors has concentrated mainly on GaAs and InP. However, it seems now that V-doped CdTe has better characteristics in the beam coupling experiments [3, 4].

It is seen consequently that further improvement of semi-insulating CdTe, favourable for various devices, cannot be easily realized directly without chemical doping or compensation by appropriate elements for deep level concentration and high resistivity, purification or trace defects apparently being largely insufficient.

Here, we present a general review on the existing data about deep levels in CdTe formed by doping mainly of group IV elements and of 3d transition metal impurities. The goal of this paper is to discuss favourable dopants for applications and verify some of their properties in concrete examples.

2. Deep levels in CdTe

A more general review on investigations of deep levels in CdTe was given recently by Kremer and Leigh [5]. Jantsch and Hendorfer [6] reviewed defect characterization by electron paramagnetic resonance (EPR) in combination with optical methods, such as photo-EPR, optically detected magnetic resonance (ODMR) and photoluminescence (PL), also to obtain information on energy levels.

2.1. Group IV elements

The elements Si, Ge, Sn and Pb have been identified by EPR in their paramagnetic state in cubic II–VI compounds and, except for Si, also in CdTe [7, 8]. The EPR spectra were interpreted as being due to the singly ionized substitutional donor on the cation site. Despite various attempts to incorporate C or Si into CdTe,

*On leave from Institute of Physics, Charles University, Prague, Czechoslovakia.

Elsevier Sequoia

neither EPR nor thermostimulated current (TSC) [9] characteristics of the respective isolated, substitutional donor has been found so far. The presence of a level at $E_v + 0.73$ eV was indicated in Ge-doped crystals by TSC and by the constant photocurrent method (CPM) [10]. The material was semi-insulating but gave weak response when used as a nuclear γ detector. A few deep levels were revealed in both highly resistive and Cd-vapour-annealed, Sn-doped, n-type samples by recording deep level transition spectra (DLTS) [5] and charge transient spectroscopy (QTS) [11] respectively. The only levels which are directly due to the presence of respective dopants of group IV are given in Table 1.

2.2. 3d transition metal impurities

The problem of deep energy levels created by 3d impurities in semiconductors has been studied by several groups, who ascertained universal trends in the binding energies of these impurities in II–VI compounds [12–14]. Langer *et al.* [15] assert that transition metal energy levels are effectively pinned to the average dangling-bond energy level, which serves as the reference level for the heterojunction band alignment. They have shown that an increasingly popular notion on transition metal, energy level pinning to the vacuum level is unjustified and must be abandoned.

The 3d atoms which replace Cd form a centre with the $3d^n4s^2$ configuration, neutral relative to the lattice. Illumination may induce electron transitions from an impurity centre to the conduction band (energy 0/+) or from the valence band to an impurity (energy 0/−). The energies (0/+) and (0/−) are called the donor and acceptor levels of the 3d impurity respectively. These energies for Cr, Fe, Co and Ni identified by photo-EPR and related techniques are presented in Table 2 together with other data referring to the presence of respective dopants of 3d impurities.

Crystals with different Sc and Ti impurity concentrations (10^{16} to 5×10^{19} cm^{-3}) were studied in ref. 16. It was found that $3d^1$ electrons of Sc atoms became free and formed a donor impurity band. A deep level observed in CdTe:Ti crystals was proposed to be formed by the neutral complex $(Ti_{Cd}^{2+}V_{Cd}^{2-})^0$. The initial concentration of V added into the CdTe crystals used in photorefractivity study was 10^{19} cm^{-3} [4]. The sample with the resistivity of 1.3×10^9 Ω cm showed absorption on deep levels, which were probably introduced in the material by V doping. The best fit of the

TABLE 1. Deep energy levels in CdTe doped by group IV elements

Dopant	Energy (eV)	Assignment	Experiment	Reference
Ge	$E_C - 0.95$	D[a]	Photo-EPR	6
	$E_V + 0.73$		TSC, CPM	10
Sn	$E_C - 0.85$	D[a]	Photo-EPR	6
	$E_C - 0.9$		DLTS	5
	$E_C - 0.89$; $E_C - 0.43$		QTS	11
Pb	$E_C - 1.28$	D[a]	Photo-EPR	6

[a]D indicates the substitutional donor.

TABLE 2. Energy levels in CdTe doped by 3d transition metal impurities

Dopant	Energy (eV)	Assignment	Electrical properties (300 K)	Experiment	Reference
Sc	$\approx E_C - 0.01$	Donor band	$\rho \approx 5 \times 10^{-2}$ Ω cm	PL, reflection	16
Ti	$E_c - 0.73(\pm 0.03)$	$(Ti_{Cd}^{2+}V_{Cd}^{2-})^0$	$n \approx 10^7$–10^8 cm^{-3}	PL, reflection Hall effect	16
V	$E_V + 0.74$	0/+		?	12
Cr	$E_V + 1.34$	0/−	Semi-insulating	EPR, ODMR, PL	17
Mn	$E_C - 0.73(\pm 0.02)$		$n \approx 4 \times 10^7$ cm^{-3}	Hall effect	18
	$E_C - 0.05$ to 0.06		$n \approx 7 \times 10^{15}$ cm^{-3}		
Fe	$E_V + 0.35(\pm 0.05)$	0/+	Semi-insulating	EPR, ODMR, PL	19
	1.1, 1.475	Emission lines	Semi-insulating	PL	20
	1.03, 1.13	Emission lines	Semi-insulating	PL	21
	$E_V + 0.15$	0/+		SPS	22
	$E_V + 0.2$	0/+		CPM	23
Co	$E_V + 1.25(\pm 0.05)$	0/−	Semi-insulating	EPR, ODMR, PL	24
Ni	$E_V + 0.92$	0/−	Semi-insulating	EPR, ODMR, PL	19
	$E_C - 0.76$	0/−		CPM	23

beam-coupling gain coefficient was obtained for an effective trap density of 5×10^{15} cm^{-3}. The transport properties of the semi-insulating and Cd-vapour-annealed CdTe:Mn crystals with a high concentration of the dopant (10^{20} cm^{-3}) were studied in ref. 18. The character of the determined levels was not specified in detail.

More knowledge has been obtained for Fe-doped crystals. First investigations of the PL spectra revealed two emission lines, one sharp emission at 1.475 eV and a broad band at about 1.1 eV [20]. In the PL spectrum of Fe^{+}-implanted and annealed CdTe, two lines with the maxima at 1030 and 1130 meV, respectively, appeared [21]. The former may be due to a free-to-bound transition involving Fe impurities and the latter due to an intra-impurity transition or defect complex. The 1.475 eV emission, however, was observed in only a few cases. The surface electronic structure of $Cd_{1-x}Fe_xTe$ crystals with $x=0$ and $x=0.03$ was studied by surface photovoltage spectroscopy (SPS) in ref. 22.

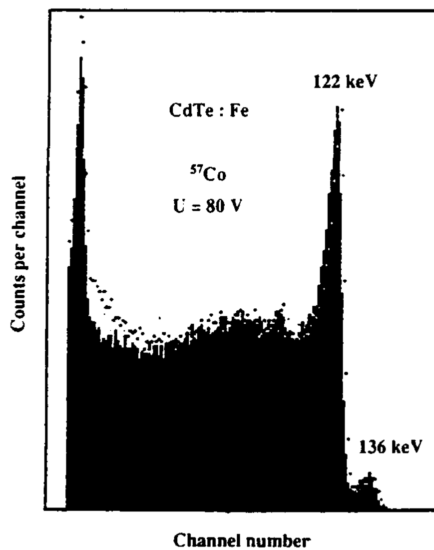

Fig. 1. ^{57}Co γ-ray spectrum of Fe-doped CdTe detector at room temperature.

It is necessary as well to subjoin Cu to this group of transition metals: this is the case for a simple acceptor with the 3d shell filled. A comprehensive study of Cu behaviour in CdTe has been performed by our group [25]. It has been demonstrated that Cu creates complexes with native defects and/or Cl, giving rise to a band of defect levels centred around 0.15 eV. This leads to self-compensation of the material. Secondly, a fraction of the incorporated atoms becomes electrically active by substitution into Cd sites. In this case, Cu acts as an acceptor with an ionization energy of 0.33 eV.

3. Complementary data

Analysing reviewed data and looking at the weak response in our nuclear detectors prepared from Ge-doped crystals [10], we have chosen Fe and V for intentional doping. The crystals grown by the travelling heater method (THM) were prepared starting from Cd and Te of 99.9999% purity. They were grown Cl-compensated with Fe or V addition into the starting material during the synthesis procedure. The Cl concentration of 5–100 ppm was introduced in the Te solvent zone. Large single crystals up to 150 mm in length could be obtained, especially in the case of V doping. The concentration of the residual impurities existing in the THM-grown crystals was determined by high sensitivity atomic absorption spectroscopy. The resistivity of the samples was measured all along the ingots by the van der Pauw technique. The nuclear detectors were prepared in the conventional way [26] and irradiated with ^{57}Co or ^{137}Cs γ-rays (Fig. 1). The basic material characteristics of several crystals are summarized in Table 3. TSC measurements were employed to determine the defect characteristics in high resistivity crystals. The typical spectra are reported in Figs. 2 and 3. In all our crystals a high density band appears below about 0.15 eV. In addition, pronounced peaks are seen in the ranges 0.41–0.46 eV and 0.48–0.55 eV for Fe and V doping respectively.

TABLE 3. Basic properties of Fe- and V-doped crystals

Dopant	Crystal no.	[Dopant] in synthesis	Slice no.	[Dopant] in crystal	Resistivity (Ω cm)	Nuclear detection
Fe	587	1 ppm	13	≤0.1 ppm	1.9×10^{9}	Very good resolution $\mu_p \tau_p \geqslant 10^{-4}$
			45	≤0.1 ppm	1.05×10^{9}	Good resolution
			67	0.15 ppm	4.0×10^{8}	Fair resolution
V	2076	1500 ppm	33	?644 ppm	3.1×10^{9}	Good resolution
	2077	135 ppm	16	0.3 ppm	2.0×10^{9}	Good resolution
	2078	135 ppm	20	0.2 ppm	2.0×10^{9}	Good resolution

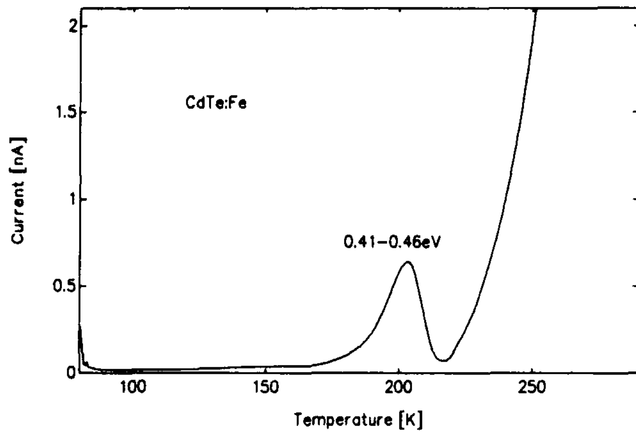

Fig. 2. Typical TSC spectrum of high resistivity Fe-doped CdTe crystal.

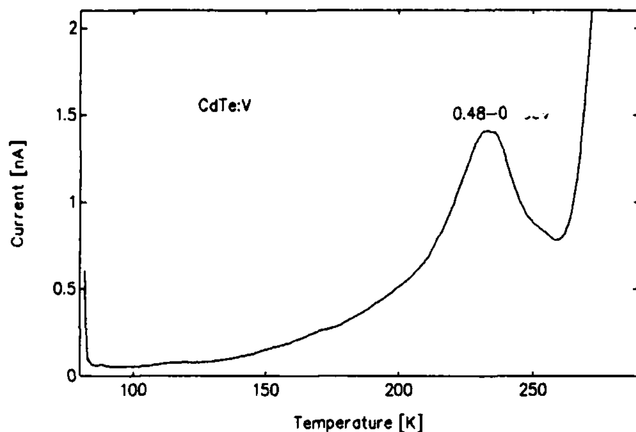

Fig. 3. Typical TSC spectrum of high resistivity V-doped CdTe crystal.

The former is similar to the 1.13 eV emission line observed in ref. 21.

4. Problem of compensation

The growth of Cl-doped CdTe from Te-rich solution yields crystals which are initially Te saturated at the growth temperature to establish the deviation from stoichiometry needed for self-compensation [1, 27, 28]. An existing deep acceptor level plays the essential role in obtaining semi-insulating properties of these crystals. In agreement with a number of compensation models [29–33], it is often connected with the doubly ionized Cd vacancies in the position $E_v + 0.6$ to 0.9 eV. As was shown in a detailed point defect model describing the association of Cd vacancies and Cl atoms [33], the creation of the compensating complex $(V_{Cd}Cl_{Te})$, neutral and singly ionized is the most probable outcome. Regarding the self-consistent model in ref. 34, the complex mentioned above is the dominant ionized one among all the defects comprised in our crystals with the Cl concentration of about 10^{16} cm^{-3}. Recently, the idea of a key role of the V_{Cd}–Cl complex has been supported by PL and electrical measurements [35].

The knowledge about 3d impurities in the compensation behaviour of CdTe is still unsatisfactory. For Fe the presence of the substitutional impurity $Fe^{2+/3+}$ was revealed by EPR. However, another possible candidate could be interstitial Fe^{+} [36]. Our TSC measurements revealed mainly acceptor defect bands at 0.41–0.46 eV and 0.48–0.55 eV for Fe and V doping respectively. Taking into consideration all the foregoing facts, we propose the following microscopic description as a speculative approach, showing the possible role of the Fe and V dopants in Cl-compensated CdTe.

The main compensating process is expected to be realized by the species Cl_{Te}^{+} and $(V_{Cd}Cl_{Te})^{-}$. A fraction of the Fe atoms (concentration of about 10^{15} cm^{-3}) incorporated into the CdTe lattice substitutes the Cd atoms and the remaining part occupies interstitial positions. The former can create a deep donor level $Fe_{Cd}^{2+/3+}$. Part of the Fe_{Cd}^{2+} can be associated with V_{Cd}^{2-}, leading to the formation of a complex $(V_{Cd}Fe_{Cd})^0$. Interstitial Fe_i^{+} may act as a shallow donor and also be associated in the acceptor complex $(V_{Cd}Fe_i)^{-}$ which contributes to the compensation of the material. Finally, we consider that the presence of a complex incorporating Cl_{Te}^{+}, Fe_i^{+} and V_{Cd}^{-} is possible.

We are not able to investigate deep traps over the midgap in our TSC set-up. Consequently, the positions of the deep donors $Fe^{2+/3+}$ and $V^{2+/3+}$ have not yet been revealed in our crystals. However, the deep donor levels occurring below the deep acceptor of V_{Cd}^{2-} could assist in pinning the Fermi level near the midgap. The reason could be a lower value of resistivity (10^6 Ω cm) compared with that in our semi-insulating THM crystals (10^9 Ω cm or more), which is why photo-EPR did not reveal other electrically active levels besides the isolated Fe^{3+} [36].

5. Conclusions

Fe and V have been shown to be promising dopants in photorefractive devices but also in semi-insulating Cl-compensated CdTe favourable for nuclear detection applications. The TSC bands observed in the ranges 0.41–0.46 eV and 0.48–0.55 eV are probably connected with complexes created by the Fe and V doping respectively. To understand the role of 3d impurities in the compensation process, further

detailed investigations have to be obtained for various dopant concentrations in combination with different methods.

References

1 F. V. Wald and R. O. Bell, *Nature Phys. Sci., 237*(1972) 13.
2 V. P. Zayachkivskii, A. V. Savitskii, E. S. Nikonyuk, M. S. Kitsa and V. V. Matlak, *Sov. Phys. Semicond., 8*(1974) 675.
3 R. B. Bylsma, P. M. Bridenbaugh, D. H. Olson and A. M. Glass, *Appl. Phys. Lett., 51*(1987) 889.
4 A. Partovi, J. Millerd, E. M. Garmire, M. Ziari, W. H. Steier, S. B. Trivedi and M. B. Klein, *Appl. Phys. Lett., 57*(1990) 846.
5 R. E. Kremer and W. B. Leigh, *J. Cryst. Growth, 86*(1988) 490.
6 W. Jantsch and G. Hendorfer, *J. Cryst. Growth, 101*(1990) 404.
7 G. Brunthaler, W. Jantsch, U. Kaufmann and J. Schneider, *Phys. Rev. B, 31*(1985) 1239.
8 R. M. Bilbe, J. E. Nicholls and J. J. Davies, *Phys. Status Solidi B, 121*(1984) 339.
9 L. Chibani, M. Hage-Ali, J. P. Stoquert, J. M. Koebel and P. Siffert, *Mater. Sci. Eng. B, 16*(1993) 202–206.
10 C. Scharager, P. Siffert, P. Höschl, P. Moravec and M. Vanecek, *Phys. Status Solidi A, 66*(1981) 87.
11 Ch. Ye and J. H. Chen, *J. Appl. Phys., 67*(1990) 2475.
12 M. J. Caldas, A. Fazzio and A. Zunger, *Appl. Phys. Lett., 45*(1984) 671.
13 V. I. Sokolov, *Sov. Phys. Solid State, 29*(1987) 1061.
14 K. A. Kikoin, I. G. Kurek and S. V. Melnichuk, *Sov. Phys. Semicond., 24*(1990) 371.
15 J. M. Langer, C. Delerue, M. Lannoo and H. Heinrich, *Phys. Rev. B, 38*(1988) 7723.
16 P. I. Babii, V. V. Slynko, Yu. P. Gnatenko, P. N. Bukivskii, M. I. Ilashuchuk and O. A. Parfenyuk, *Sov. Phys. Semicond., 24*(1990) 904.
17 M. Godlewski and J. M. Baranowski, *Phys. Status Solidi B, 97*(1980) 281.
18 V. G. Deybuk *et al., Izv. Vuzov, Fizika, 4* (1982) 24 (in Russian).
19 W. Jantsch, G. Brunthaler and G. Hendorfer, *Mater. Sci. Forum, 10–12*(1986) 515.
20 K. Lischka, G. Brunthaler and W. Jantsch, *J. Cryst. Growth, 72*(1985) 355.
21 R. Kernöcker, K. Lischka and L. Palmetshofer, *J. Cryst. Growth, 86*(1988) 625.
22 A. Sarem, B. A. Orlowski and S. Kuzminski, *Acta Phys. Pol. A, 79*(1991) 183.
23 W. Stadler, F. Wang, R. Schwarz, K. Oettinger, B. K. Meyer, D. M. Hofmann, D. Sinerius and K. W. Benz, *Mater. Res. Soc. Symp. Proc., 25*(1992) 205.
24 G. Hendorfer, G. Brunthaler, W. Jantsch, J. Reisinger and H. Sitter, *J. Cryst. Growth, 86*(1988) 497.
25 B. Biglari, M. Samimi, M. Hage-Ali, J. M. Koebel and P. Siffert, *Nucl. Instrum. Methods A, 283*(1989) 249.
26 P. Siffert, *Nucl. Instrum. Methods, 150*(1978) 1.
27 R. Triboulet, Y. Marfaing, A. Cornet and P. Siffert, *J. Appl. Phys., 45*(1974) 2759.
28 P. Höschl, P. Polivka, V. Prosser, M. Vanecek and M. Skrivankova, *Rev. Phys. Appl., 12*(1977) 229.
29 F. A. Kröger, *Rev. Phys. Appl., 12*(1977) 205.
30 Y. Marfaing, *Rev. Phys. Appl., 12*(1977) 211.
31 N. V. Agrinskaya and E. N. Arkadeva, *Nucl. Instrum. Methods A, 283*(1989) 260.
32 C. Canali, G. Ottaviani, R. O. Bell and F. V. Wald, *J. Phys. Chem. Solids, 35*(1974) 1405.
33 P. Höschl, P. Moravec, J. Franc, E. Belas and R. Grill, *Nucl. Instrum. Methods*, in press.
34 M. Hage-Ali and P. Siffert, *Nucl. Instrum. Methods*, in press.
35 S. Seto, A. Tanaka, Y. Masa and M. Kawashima, *J. Cryst. Growth, 117*(1992) 271.
36 K. W. Benz *et al., Proc. Euro. Conf. on Crystal Growth, Budapest, May 1991*, accepted for publication.

Overview of CdTe-based semimagnetic semiconductors

J. P. Lascaray
Groupe d'Etude des Semiconducteurs, Université Montpellier II, Place Eugene Bataillon, 34095 Montpellier Cedex 5 (France)

Abstract

Semimagnetic semiconductors, also called "diluted magnetic semiconductors", are semiconductor compounds in which some cations are randomly substituted by magnetic ions. The most studied alloys are II-VI semiconductors containing manganese and particularly $Cd_{1-x}Mn_xTe$. During the last 15 years, these compounds have received considerable attention, mainly because they present new and particularly interesting properties arising from the strong exchange interaction between the magnetic ions and the carriers of conduction and valence bands. This paper presents some of these magneto-optic and magnetic properties, such as the giant Faraday rotation and Zeeman effect and the magnetization steeps, which are now quite well explained. Recently, semimagnetic quantum wells and superlattices have been grown. They open new and very attractive fields of research. The last part of the paper will be devoted to these studies.

1. Introduction

Some of the spectacular properties of semimagnetic semiconductors (SMSC), such as the giant negative magnetoresistivity of $Hg_{1-x}Mn_xTe$, have been known since the middle of the 1960s [1]. Nevertheless, real systematic studies of this class of semiconductors started in the late 1970s. A series of works were reported on $Hg_{1-x}Mn_xTe$ [2, 3] as well as on a new wide gap SMSC $Cd_{1-x}Mn_xTe$, which presents very interesting magneto-optical properties [4-6]. Since then, much study has been devoted to SMSC [7]. These compounds are II-VI or IV-VI semiconductors in which some cations are randomly substituted by magnetic ions: Mn (and recently Fe and Co) on II (Cd, Zn) VI (Te, S, Se) and Mn, Fe, Eu, Gd on IV (Pb) VI (Te, S, Se). Nevertheless, $II_{1-x}Mn_xVI$ remains the more studied SMSC. There are several reasons for this choice.

(1) Mn is a transition metal with valence electrons corresponding to the $4s^2$ orbital. It differs from the group II elements by the fact that its 3d orbital is half filled. However, according to Hund's rules, all five spins of the 5d orbital are parallel and it requires a considerable amount of energy to add one electron (with opposite spin) to the atom. In this sense, the $3d^5$ orbital acts as a complete shell and the Mn resembles a group II element. Its $4s^2$ electrons contribute to the s-p^3 bounding.

(2) Mn can be incorporated in place of the group II element in a sizeable amount in the II-VI host matrix without affecting substantially the crystallographic qualities of the resulting material. A diagrammatic overview of the $II_{1-x}Mn_xVI$ alloys and their crystal structure, proposed by Giriat and Furdyna is reported in Fig. 1 [8].

(3) Mn^{2+} possesses the largest magnetic moment of the transition metals ($S=5/2$). A rare earth could be also of great interest as substitute magnetic ions. Unfortunately, they present very low solubility in the II-VI matrix [9].

(4) Mn^{2+} is electrically neutral in the II-VI host.

For reasons related to the obtaining of high quality ingots by the Bridgman method, $Cd_{1-x}Mn_xTe$ is certainly the most studied SMSC. Therefore, it can be considered as a good representative of the typical properties of wide gap $II_{1-x}Mn_xVI$. The first of these properties concerns the classical semiconductor properties of ternary alloys. For example, their ternary nature makes it possible to tune the band parameters and lattice constants by varying the alloy concentration. The second properties are the magnetic properties due to the dilution of the magnetic ions. One spectacular manifestation is the presence of steps in high field magnetization. The third properties are the original magneto-optical effects that arise through the band carrier-Mn^{2+} ion exchange interaction. A new and interesting field of research is now opened by the

0921-5107/93/$6.00

© 1993 - Elsevier Sequoia. All rights reserved

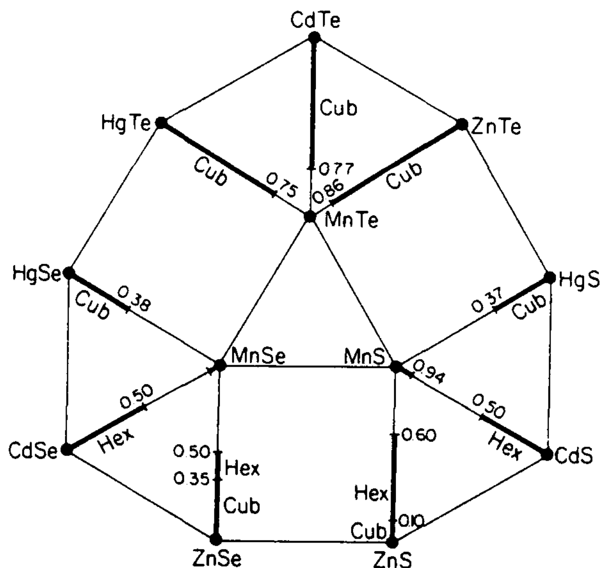

Fig. 1. Diagrammatic overview of the $II_{1-x}Mn_xVI$ alloys and their crystal structure. "Hex" and "Cub" indicate Wurtzite and zincblende respectively [8].

successful elaboration of SMSC thin films, quantum wells and superlattices.

2. Classical semiconductor properties

2.1. Crystal structure

$Cd_{1-x}Mn_xTe$ retains the zincblende structure of its parent CdTe in its whole domain of existence: $0<x<0.77$. X-ray data suggest that the lattice parameter obeys very closely Vegard's law [10]. In reality, the microscopic situation is more complicated and the extended X-ray absorption fine structure show that the CdTe and MnTe bound lengths remain nearly constant throughout the entire composition range [11]. The cation sublattice which is randomly occupied by Cd or Mn ions is, to a first approximation, not distorted. It follows that each Te atom adjusts its position in relation to its neighbouring atom to keep Cd–Te and Mn–Te bound lengths as constant as possible.

2.2. Band structure

$Cd_{1-x}Mn_xTe$ alloys possess a direct band gap with the zone centred band structure characteristic of zincblende crystal. The highest valence band is split by the spin orbit interaction in four subbands Γ_8 and Γ_7. The upper Γ_8 ($J=3/2$) and the lower Γ_7 ($J=1/2$) are, respectively, four-fold and two-fold degenerate. The lowest conduction band Γ_6 ($J=1/2$) is two-fold degenerate. Figure 2 shows the near linear variation of the energy gap with the Mn mole fraction. The position of the occupied Mn $3d^5$ levels and their hybridization with the p valence band states have been studied by

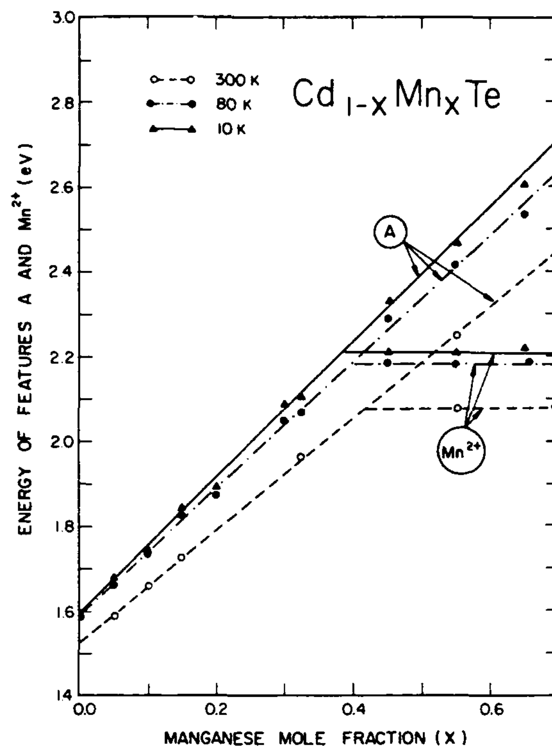

Fig. 2. Variation of the energy gap and Mn transition with Mn concentration in $Cd_{1-x}Mn_xTe$ for 10, 80 and 300 K [12]. A: free exciton; Mn^{2+}: $^6A_1 \rightarrow {}^4T_1$.

photoemission measurements [13]. A sharp peak with a half-width of about 1 eV at 3.4 eV below the valence band edge has been unambiguously attributed to the $3d^5$ ground state. The optical transitions corresponding to intra-Mn transitions (Mn atom in a cubic crystal field) are observed in absorption [14, 15] and luminescence [16, 17] spectra for the Mn concentrated samples.

3. $Cd_{1-x}Mn_xTe$: a diluted magnetic semiconductor

3.1. Magnetism

The remarkable properties of $Cd_{1-x}Mn_xTe$ (and SMSCs more generally) appear mainly at low temperatures and under a magnetic field and they result from Mn-Mn or Mn-carrier exchange coupling. The dilution of magnetic ions allows spin ordering effects to be induced at a reasonable magnetic field. Different magnetic phases are observed [18] depending on the temperature and concentration as reported on Fig. 3. For Mn-rich alloys, an antiferromagnetic (AF) phase appears at low temperatures. With decreasing concentration, the AF phase changes gradually at around $x=0.6$ to a spin glass (SG) phase. It can be explained by a short range antiferromagnetic interaction mechanism, *i.e.* the superexchange. Below the nearest neigh-

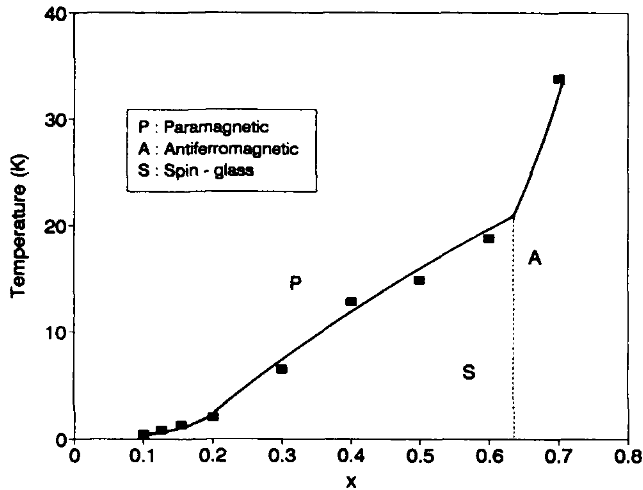

Fig. 3. Magnetic phase diagram for $Cd_{1-x}Mn_xTe$. Insert shows the low x range [19–21].

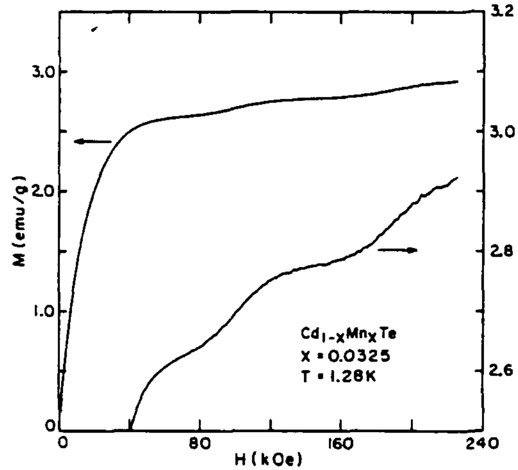

Fig. 4. Magnetization M vs. applied magnetic field for $Cd_{1-x}Mn_xTe$ at 1.8 K [23].

bour percolation concentration limit $x \approx 0.2$ an SG phase persists with extremely low freezing temperature which involves more distant neighbour interactions.

The study of magnetization of very diluted systems is particularly attractive because the short-range exchange interactions allow us to separate the magnetic system into a sum of small clusters (singles, pairs, triplets ...). Step-like behaviour observed in high field magnetization makes possible the direct and easy verification of theories [22]. Figure 4 represents the high field magnetization of $Cd_{1-x}Mn_xTe$. The steps are due to magnetization of nearest neighbour Mn pairs. At low field strengths, due to antiferromagnetic exchange interactions, the effective pair spin S_{eff} is zero. On increasing the field, the effective spin changes from $S_{eff}=0$, 1,... to $S_{eff}=5$ which corresponds to the parallel orientation of spins by step. S_{eff} becomes $S_{eff}=n$ for magnetic field $N_n=n(B_1-b)+b$ where b is an effective field which accounts for the interaction between the pair and the next nearest or more distant neighbours [24].

3.2. Magneto-optics

The origin of the remarkable magneto-optical properties of $Cd_{1-x}Mn_xTe$ (giant Faraday rotation and Zeeman effect, spin-flip Raman scattering, etc. [25] is in the large splitting of conduction and valence bands, in the magnetic field, which arises through the exchange interaction of band carriers with the 3d electrons localized on Mn^{2+} ions. This band splitting is easily accounted for by a simple mean field model, expressing the Mn–carrier exchange interaction in the form of a Heisenberg hamiltonian [26].

$$H_{ex}=-\Sigma J(r-Rn)S_n\sigma$$

where S_n is the spin of the Mn^{2+} localized at the Rn site, σ is the spin of the band carrier and $J(r-Rn)$ is the exchange integral. The magnetic part of the hamiltonian for a band electron in a magnetic field consists of two terms: $H=H_m+H_{ex}$. H_m, which describes the direct influence of the magnetic field on the carriers, can be neglected in wide gap SMSC compared with the effect of H_{ex}. The splitting of the Γ_6, Γ_8 and Γ_7 bands is calculated taking into account the large spin orbit splitting compared with the ion-carrier exchange energy, and attributing to every cation site a fraction $x\langle S_z\rangle$ of the mean spin value (virtual crystal approximation). A schematic representation of the result for Γ_6 and Γ_8 bands is reported in Fig. 5. N_0 denotes the number of unit cells per volume unit, and α and β are the exchange integrals for the conduction and valence bands respectively. Six optical transitions are allowed: four in circular right (σ^+) and left (σ^-) polarization (Faraday configuration) and two in π linear polarization (Voigt configuration).

Typical magnetoreflectance spectra are reported in Fig. 6. It is easy to derive α and β from the equations

$$N_0(\alpha-\beta)=(E_d-E_a)/x\langle S_z\rangle$$

and

$$\beta/\alpha=(E_c-E_b)/(E_d-E_a)$$

where E_a, E_b, E_c and E_d are given by magnetoreflectivity measurements and $x\langle S_z\rangle$ is obtained from magnetization measurements.

The difference in both sign and magnitude of α and β ($N_0\alpha=0.22$ eV; $N_0\beta=-0.88$ eV [27]) were first explained by Bhattacharjee *et al.* [28]. They have noted that the Mn 3d–carrier exchange results in two competing mechanisms. The first, originating from the

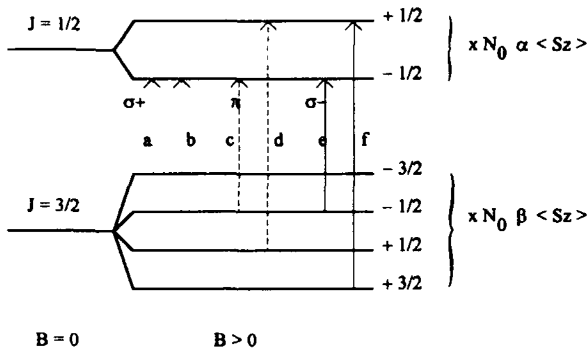

Fig. 5. Schematic illustration of the allowed transitions between the spin split valence (Γ_8) and conduction (Γ_6) bands.

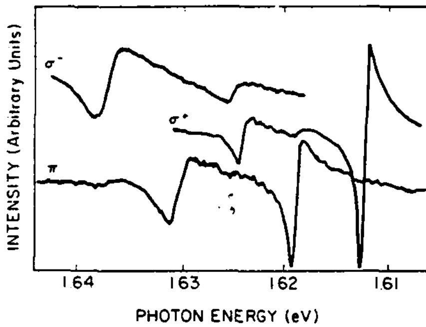

Fig. 6. Magnetoreflectivity spectra of $Cd_{0.98}Mn_{0.02}Te$ at $T = 1.4$ K and $B = 1.1$ T [27].

direct potential exchange interaction between bands and d electrons is relatively weak and ferromagnetic. The second arises from the hybridization between the Mn d orbital and band states. This "kinetic" antiferromagnetic contribution, which is negligible for the conduction band, becomes dominant for the valence band. Recent analysis of α and β values obtained for different transition metals in different host matrices gives a good agreement with this theory [29]. Measurements carried out on concentrated samples have revealed a drastic decrease of the $(E_d - E_a)/x\langle S_z\rangle$ slope when x is increased [30]. A second order correction to the mean field model gives a satisfactory interpretation for this behaviour [31].

The Faraday effect corresponds to the rotation θ of the plane of polarization of linearly polarized light propagating through a sample along the magnetic field in which it is placed. The giant Faraday rotation observed in large gap SMSCs, such as $Cd_{1-x}Mn_xTe$, is of the order of 10^5 deg T^{-1} cm^{-1} [32] and is a direct consequence of the enhancement of the Zeeman splitting of the exciton by Mn ion–band carrier exchange. θ is proportional to $E_d - E_a$ and thus to the magnetization [33]. Many studies have been devoted to this subject as well as to study the Faraday rotation of SMSCs, while fewer studies have made use of its proportionality to magnetization to observe the magnetic properties of SMSCs, *e.g.* the phase transition between the SG phase and the paramagnetic phase of SMSCs [34].

3.3. Effect of exchange interaction in the absence of an applied magnetic field

The absorption edge of classical semiconductors usually exhibits a blue shift when the temperature decreases. In magnetic semiconductors this behaviour is strongly affected by magnetic phase transition, *e.g.* the energy gap of EuO is reduced by about 25%. Below the Curie temperature, an effect on the energy gap of large gap SMSCs *vs.* temperature relation is also observed [35]. An analysis in the case of SMSCs, following the second order calculation used for magnetic semiconductors [36], found a "magnetic" contribution to the variation in the energy gap proportional to the temperature and magnetic susceptibility [37].

We have reported in Fig. 7 the temperature variation of $Zn_{1-x}Mn_xTe$ for different x values. One should notice the "bump" at low temperatures for the highest Mn concentration and the strong variation of the slope of the linear part of the curves with composition.

Another manifestation of the Mn–carrier exchange interaction, which occurs even in the absence of a magnetic field, is the bound magnetic polaron (BMP) formation. The simplest BMP is the donor BMP. The single electron in such a complex moves in a non-degenerate conduction band and has an extended orbit. The alignment of the Mn spins in the donor radius with the electron spin is favoured by Mn–carrier exchange. It results in a local magnetic moment due to the partial alignment of the Mn^{2+} spins inside the donor volume. In this induced magnetization field the donor electron suffers an energy splitting as in the case with an external magnetic field. This electron is both the cause and the method of studying the BMP.

More experimental observations of donor BMPs have been carried out using spin-flip Raman scattering (SFRS) measurements. Figure 8 shows the SFRS of $Cd_{1-x}Mn_xTe$:Ga. The shift of the observed Stokes' line corresponds to the spin-flip energy for the donor electron ΔE_0, which is equal to the conduction band splitting as reported in Fig. 5. Its measurements allows the precise determination of $N_0\alpha = \Delta E_0/x\langle S_z\rangle$. In contrast to the exciton energy splitting, the spin-flip energy does not vanish in the absence of an applied magnetic field. This corresponds to the spin flip of the electron in the BMP field. BMPs bound to an acceptor also exist and exhibit the strongest coupling. Unfortunately, this is not easy to study. The SFRS of a hole has not yet been seen in an SMSC. The first observation of an acceptor BMP has been made through the photo-

luminescence (PL) temperature dependence of acceptor-bound exciton binding energy [40]. More sophisticated measurements were made from analysis of time-resolved measurements of the donor–acceptor PL [41]. Some years ago, problems concerning the dynamics of BMPs were studied using time-resolved techniques [42]. A powerful method was used by Awschalom *et al.* [43] who used a miniature SQUID susceptometer to detect the magnetization of the BMPs induced by optically generated spin-aligned carriers [42].

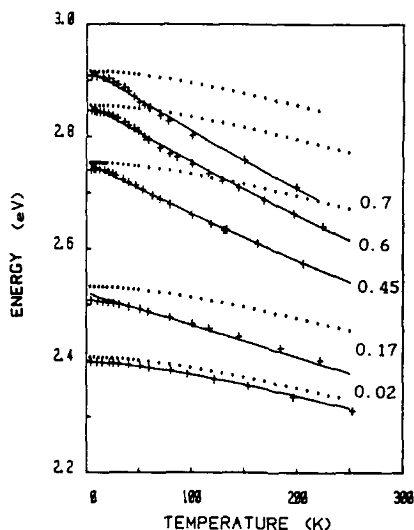

Fig. 7. Fit of the energy gap of $Zn_{1-x}Mn_xTe$ *vs.* temperature (lower lines). The dotted lines were calculated without a magnetic field.

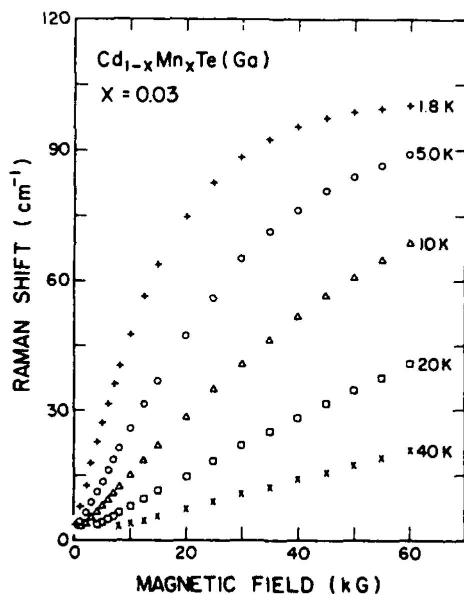

Fig. 8. Magnetic field and temperature dependence of the Raman shift associated with the spin flip of electrons bound to donors in $Cd_{1-x}Mn_xTe$ [39].

4. Quantum wells and superlattices

Bulk SMSC alloys have been extensively studied since 1977 because they present original and attractive physical properties. However, this field of research always remains active with, for example, the possibility to change the magnetic ion and thus to explore the properties of new SMSCs. In 1982, Von Ortenberg [43] pointed out the possibility of inducing new effects in SMSC superlattices, such as the formation of a spin superlattice or the type I→type II magnetic-field-induced transition. Since the first successful preparation of $Cd_{1-x}Mn_xTe$/CdTe superlattices in 1984 [44], many studies have been devoted to these new materials. A unique property of SMSC quantum wells (QWs) and superlattices (SLs) is that the bands' alignment can be tuned by applying a magnetic field. Figure 9 presents a schematic representation of the effect of the external field on a QW. The Zeeman splitting of the SMSC barrier changes the barrier heights V_e and V_h when a magnetic field is applied, which in turn results in changes in both the electron and hole confinement energies. This property has been used to investigate the interesting question of band offset in heterostructures [45]. Deleporte *et al.* [46] have observed a type I→type II magnetic-field-induced transition at a moderate magnetic field (2 T) for a CdTe/$Cd_{1-x}Mn_xTe$ SL. Recently, evidence of the formation of a spin SL has been reported in ZnSe/$Zn_{1-x}Mn_xSe$ [47]. It corresponds to a spatial separation of the spin-up (heavy holes) and spin-down (electrons) states, respectively, in the well and in the barrier when a magnetic field is applied on this SL, which presents small band offset at a zero magnetic field.

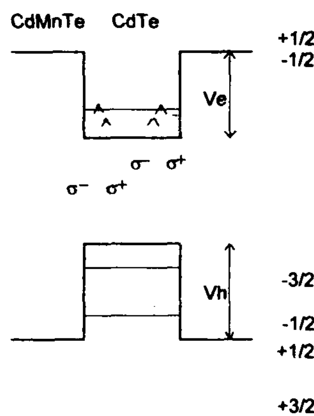

Fig. 9. Schematic representation of the effect of an external magnetic field on a quantum well.

Time-resolved techniques have been used in concert with optical and magnetic probes to study electronic and magnetic spin dynamics in SCSM SLs [48]. Furthermore, crystal growth of ultrathin layered structures by molecular beam epitaxy has made it possible to examine dimensionality effects. A series of experiments have been performed with the aim of exploring the effect of quantum confinement on Mn–carrier and Mn–Mn exchange interactions in SCSM SLs [49]. Recently, a two-dimensional exciton magnetic polaron has been observed for the first time and studied in $CdTe/Cd_{1-x}Mn_xTe$ QWs [50].

References

1 R. T. Delves, *Proc. Phys. Soc.*, *87* (1966) 909, and references therein.

2 G. Bastard, C. Rigaux, Y. Guldner, J. Mycielski and A. Mycielski, *J. Phys.*, *39* (1978) 87, and references therein.

3 M. Jaczynski, J. Kossut and R. R. Galazka, *Phys. Status Solidi B*, *88* (1978) 73.

4 A. V. Komarov, J. M. Ryabchenko, O. V. Terlejskii, I. I. Zheru and R. D. Ivanchuk, *Eksp. Theor. Fiz.*, *73* (1977) 608.

5 J. A. Gaj, R. R. Galazka and M. Nawrocki, *Solid State Commun.*, *25* (1978) 193.

6 J. A. Gaj, J. Ginter and R. R. Galazka, *Phys. Status Solidi B*, *89* (1978) 655.

7 See, for example, the recent reviews, Diluted magnetic semiconductors, in J. K. Furdyna and J. Kossut (eds.), *Semiconductors and Semimetals*, Vol. 25, Academic Press, New York, 1988.
Semimagnetic semiconductors and diluted magnetic semiconductors, in M. Averous and M. Balkanski (eds.), *Ettore Majorana International Science Series*, Vol. 55, Plenum, New York, 1991.
Diluted magnetic semiconductors, in M. Jain (ed.), World Scientific, Singapore, 1991.
O. Goede and W. Heimbrodt, *Phys. Status Solidi B*, *146* (1988) 11.

8 W. Giriat and J. K. Furdyna, in J. K. Furdyna and J. Kossut (eds.), *Semiconductors and Semimetals*, Vol. 25, Academic Press, New York, 1988, p. 1.

9 R. Triboulet, in M. Averous and M. Balkanski (eds.), *Ettore Majorana International Science Series*, Vol. 25, Plenum, New York, 1991, p. 23.

10 J. K. Furdyna, W. Giriat, D. Mitchell and G. Sproule, *J. Solid State Chem.*, *46* (1983) 349.

11 A. Balzarotti, M. Czyzik, A. Kissiel, N. Motta, M. Podgorny and M. Zimmal-Starnawska, *Phys. Rev. B*, *30* (1984) 22995.

12 Y. L. Lee and A. K. Ramdas, *Solid State Commun.*, *51* (1984) 861.

13 See, for example, the references and discussion in A. Fujimori, in M. Jain (ed.), World Scientific, Singapore, 1991, p. 117.
A. Wall, A. Franciosi, Y. Gao, J. H. Weaver, M. H. Tsai, J. D. Don and V. Kasowski, *J. Vac. Sci. Technol. A*, *7* (1989) 656.

14 G. Rebmann, C. Rigaux, C. Bastard, G. Menant, R. Triboulet and W. Giriat, *Physica*, *117–118B* (1983) 452.

15 J. P. Lascaray, J. P. Diouri, M. El Amrani and D. Coquillat, *Solid State Commun.*, *47* (1983) 709.

16 R. Y. Tao, M. M. Moriwaki, W. M. Beker and R. R. Galazka, *J. Appl. Phys.*, *53* (1982) 3772.

17 M. M. Moriwaki, W. M. Becker, W. Gebhardt and R. R. Galazka, *Phys. Rev. B*, *26* (1982) 3165.

18 See, for example, S. Oseroff and P. J. Keesom, in J. K. Furdyna and K. Kossut (eds.), *Semiconductors and Semimetals*, Vol. 25, Plenum, New York, 1991, p. 73.
T. Giebultowicz and T. M. Holden, in J. K. Furdyna and J. Kossut (eds.), *Semiconductors and Semimetals*, Vol. 25, Plenum, New York, 1991, p. 125.

19 J. Furdyna, *J. Appl. Phys.*, *53* (1982) 7637.

20 M. A. Novak, O. E. Symko, D. J. Zheng and S. Oseroff, *Phys. Rev. B*, *33* (1986) 6391.

21 R. R. Galazka, S. Nagata and P. H. Keesom, *Phys. Rev. B*, *22* (1980) 3344.

22 Y. Shapira, in M. Averous and M. Balkanski (eds.), *Ettore Majorana International Science Series*, Vol. 55, Plenum, New York, 1991, p. 121.

23 E. D. Isaacs, D. Heiman, P. Bella, Y. Shapira, R. Kershaw, K. Dwight and A. Wold, *Phys. Rev. B*, *34* (1988) 8412.

24 B. E. Larson, K. C. Hass and L. Aggarwal, *Phys. Rev. B*, *33* (1986) 1789.

25 See, for example, J. A. Gaj, in J. K. Furdyna and J. Kossut (eds.), *Semiconductors and Semimetals*, Vol. 25, Plenum, New York, 1991, p. 276.
J. P. Lascaray, in M. Averous and M. Balkanski (eds.), *Ettore Majorana International Science Series*, Vol. 55, Plenum, New York, 1991, p. 169.
D. Coquillat, in M. Jain (ed.), World Scientific Singapore, 1991; *Phys. Status Solidi B* (1988) 47.

26 K. Kossut, *Phys. Status Solidi B*, *78* (1976) 537.

27 J. A. Gaj, R. Planel, G. Fishman and B. Coqblin, *Solid State Commun.*, *29* (1981) 435.

28 A. K. Bhattacharjee, G. Fishman and B. Coqblin, *Physica*, *117–118B* (1983) 449.

29 J. P. Lascaray, F. Hamdani, D. Coquillat and A. K. Bhattacharjee, *J. Mag. Mag. Mater.*, *104–107* (1992) 995.
F. Hamdani, J. P. Lascaray, D. Coquillat, A. K. Bhattacharjee, M. Nawrocki and Z. Golacki, *Phys. Rev. B*, *45* (1992) 13 298.

30 J. P. Lascaray, D. Coquillat, J. Deportes and A. K. Bhattacharjee, *Phys. Rev. B*, *38* (1988) 7602.

31 A. K. Bhattacharjee, *Solid State Commun.*, *65* (1988) 275.

32 J. A. Gaj, R. R. Galazka and M. Nawrocki, *Solid State Commun.*, *25* (1978) 193.

33 D. U. Bartholomew, J. K. Furdyna and A. K. Ramdas, *Phys. Rev. B*, *34* (1986) 6943.

34 A. Mycielski, C. Rigaux and M. Menant, *Solid State Commun.*, *50* (1984) 257.
E. Kierzek, Pecold, W. Szymanska and R. R. Galazka, *Solid State Commun.*, *50* (1984) 685.

35 J. Diouri, J. P. Lascaray and M. Elamrani, *Phys. Rev. B*, *31* (1985) 7995.

36 F. Rys, J. S. Helman and W. Baltensperger, *Phys. Kondens. Mater.*, *6* (1967) 105.

37 R. B. Bylsma, W. M. Becker, J. Kossut and U. Debska, *Phys. Rev. B*, *33* (1986) 8207.
J. A. Gaj and A. Golnik, *Acta Phys. Sol. A*, *71* (1987) 197.

38 J. A. Gaj, A. Golnick, J. P. Lascaray, D. Coquillat and M. C. Desjardins-Deruelle, *Mater. Res. Soc. Symp. Proc.*, *89* (1987) 59.

39 D. L. Peterson, D. U. Bartholomew, A. K. Ramda and S. Rodriguez, *Phys. Rev. B*, *32* (1985) 323.

40 A. Golnik, J. A. Gaj, M. Nawrocki, R. Planel and C. Benoit a la Guillaume, *J. Phys. Soc. Jpn., Suppl. A*, *49* (1980) 819.

41 Tran Hong Nhung and R. Planel, *Physica, 117-118B* (1983) 488.
Tran Hong Nhung, R. Planel, C. Benoit a la Guillaume and A. Bhattacharjee, *Phys. Rev. B, 31* (1985) 2388.
42 D. D. Awschalom, J. Varnock, J. R. Rozen and B. Ketchen, *J. Appl. Phys., 61* (1987) 3532, and references therein.
43 M. Von Ortenberg, *Phys. Rev. Lett., 49* (1982) 1041.
44 R. N. Bicknell, R. Yanka, N. C. Giles-Taylor, D. K. Banks, E. L. Buckland and J. F. Schetzinn, *Appl. Phys. Lett., 45* (1984) 92.
L. A. Kolodziejski, T. C. Bonset, R. L. Gunshor, S. Datta, R. B. Bylsma, W. M. Becker and N. Otsuka, *Appl. Phys. Lett., 45* (1984) 440.
45 S. K. Chang, A. V. Nurmiko, J. W. Wu, L. A. Kolodziejski and R. L. Gunshor, *Phys. Rev. B, 37* (1988) 1191.
A. Wasiela, Y. Merle d'Aubigne, J. E. Nicholls, D. E. Ashenford and B. Lunn, *Solid State Commun., 76* (1990) 263.
46 E. Deleporte, J. M. Berroir, G. Bastard, C. Delalande, J. M. Hong and L. L. Chang, *Phys. Rev. B, 42* (1990) 5891.
47 N. Dai, H. Luo, F. C. Zhang, N. Sammarth, M. Dobrowolska and J. K. Furdyna, *Phys. Rev. Lett., 67* (1991) 3824.
W. C. Chou, A. Petrou, J. Warnock and B. T. Jonker, *Phys. Rev. Lett., 67* (1991) 3820.
48 D. D. Awschalom and M. R. Freeman, *J. Lumin., 44* (1989) 399.
D. D. Awschalom, M. R. Freeman, N. Samarth, H. Luo and J. K. Furdyna, *Phys. Rev. Lett., 66* (1991) 1212.
49 D. D. Awschalom, J. M. Hong, L. L. Chang and G. Grinstein, *Phys. Rev. Lett., 59* (1987) 1733.
M. Kohl and D. D. Awschalom, *J. Appl. Phys., 70* (1991) 6377.
50 D. R. Yakovlev, I. N. Urltsev, W. Ossav, G. Landwehr and R. N. Bicknel-Tassius, *Surf. Sci., 263* (1992) 485.

Comparative reflectivity study of coupled and uncoupled CdTe/CdMnTe asymmetric double quantum wells

I. Lawrence, G. Feuillet and H. Tuffigo
DRFMC/Physique des Semiconducteurs, CENG, 85X 38041 Grenoble (France)

C. Bodin, J. Cibert, P. Peyla and A. Wasiela
Labo de Spectrométrie Physique, Université J. Fourier, BP 87, 38402 Saint Martin d'Hères Cedex (France)

Abstract

We compare the optical properties of coupled and separated CdTe/CdMnTe asymmetric double quantum wells where one of the two wells of the structure contains some manganese. Photoluminescence at zero field shows very efficient radiative transfer from the wide CdMnTe well to the narrow CdTe well in the case of the coupled sample. Study of reflectivity under a magnetic field allows observation of an anticrossing between the first two heavy hole levels of the coupled sample.

Semimagnetic semiconductors present giant magneto-optical effects due to the strong exchange interaction between the spins of carriers and magnetic ions (for a review, see refs. 1, 2). In a mixed crystal like CdMnTe, an applied magnetic field produces a Zeeman splitting of the valence and conduction bands, two orders of magnitude larger than in a non-magnetic semiconductor (such as CdTe). The incorporation of CdMnTe in a heterostructure offers the possibility of tuning the band structure continuously by applying an external magnetic field. Successful molecular beam epitaxial (MBE) growth of high quality heterostructures involving CdMnTe has allowed studies of the changes in the optical and transport properties due to the modification of the electronic band structure by an external magnetic field [3–5]. Our aim in the present work is to exploit this original feature to modify the coupling between two quantum wells (QW). We will compare the behaviour as a function of a field for two asymmetric double quantum well (ADQW) heterostructures having two different middle barrier thicknesses.

In most of the spectroscopic studies of Mn-based heterostructures the well material is pure CdTe, whereas the CdMnTe alloy corresponds to the barrier material: this offers the advantage of giving an optimal quality for the well (since it is made of pure binary CdTe) but on the other hand, the influence of a magnetic field on such a structure is limited since the carriers are mainly confined in the CdTe wells where there are no magnetic ions. However, it has already been proved [6] that it is possible to obtain high quality $Cd_{1-y}Mn_yTe/Cd_{1-x}Mn_xTe$ heterostructures where the carriers are confined in a ternary CdMnTe alloy. We present here a study of structures where one of the two wells contains magnetic ions so as to increase drastically the influence of the magnetic field on the confined carrier levels.

We have designed ADQW heterostructures where the narrow well (N) is made of pure CdTe whereas the wider (W) one is made of $Cd_{1-y}Mn_yTe$ (see Table 1). The two wells are confined by $Cd_{1-x}Mn_xTe$ barriers; the thickness of the middle barrier is 530 Å for sample ADQW1 and only 10 Å for sample ADQW2. In a magnetic field, the confining potentials (valence and conduction) of the CdMnTe QW move relatively to those of the CdTe QW: this allows us to bring some levels into resonance. Since the heavy hole band is much more field-sensitive (four times more compared to the conduction band and three times more compared to the light hole band [7]) we anticipate heavy hole resonance effects in our samples. The samples were grown at 280 °C by MBE along the {100} orientation on $Cd_{0.96}Zn_{0.04}Te$ substrates. Oscillations of the reflection high energy electron diffraction (RHEED) patterns were used to monitor layer thicknesses. Growth interruptions (of about 4 minutes) were performed at each interface so as to smooth the surface and to allow changing the temperature of the Mn cell in order to vary the composition from x to y. The structures were deposited on a CdMnTe buffer layer (2 μm) of the same composition as the barriers: under such

0921-5107/93/$6.00 © 1993 – Elsevier Sequoia. All rights reserved

conditions, the barriers are strain-free whereas the two wells are under biaxial compression. This splits the hole band and pushes the light hole band to a higher energy: from now on, we will focus on heavy hole-related transitions.

Figure 1 schematizes the change in the band structure under magnetic field B in Faraday configuration, in the case of a *coupled* structure (only the $\sigma+$ configuration is shown, the $\sigma-$ one is of less interest since it does not show the anticrossing effects we are looking for). For clarity, we label the levels in each well independently: $h_{N^1}(h_{W^1})$ means the first hole level in the narrow (wide) well. At zero field the ground state of the structure is $e_{N^1}h_{N^1}$, the $e_{N^1}h_{W^1}$ state being at a higher energy. When $B=B_c$, the two hole levels (h_{N^1} and h_{W^1}) come into resonance, and when $B>B_c$, then ground state of the structure is $e_{N^1}h_{W^1}$.

Figure 2 compares the photoluminescence (PL) and reflectivity spectra (at $B=0$ T and $T=1.8$ K) of the two samples. For the case of ADQW1, we observe very clearly luminescence lines corresponding to direct excitons in the *two* wells (separated by the 530 Å central barrier) that correspond to $e_{N^1}h_{N^1}$ (1s) and $e_{W^1}h_{W^1}$ (1s). This identification was confirmed easily by studying reflectivity under a magnetic field since the $e_{W^1}h_{W^1}$ transition, involving carriers located in the wide CdMnTe well, shifts much more rapidly than $e_{N^1}h_{N^1}$ with the field. Note the small linewidths and small Stokes shifts between PL and reflectivity, which indicate the high sample quality: 4 meV linewidth and 2 meV Stokes shift for the alloy-made QW ($e_{W^1}h_{W^1}$ transition). For the case of ADQW2, the PL spectrum shows only the $e_{N^1}h_{N^1}$ (1s) line corresponding to the recombination in the narrow well at low energy; the $e_{W^1}h_{W^1}$ transition (direct recombination in a wide well)

TABLE 1. Structural parameters of the two samples (the Mn compositions x and y were determined by studying reflectivity under magnetic field, see text)

	L_N (RHEED)	L_B (RHEED)	L_W (RHEED)	y	x
ADQW1	55 Å	530 Å	146 Å	3.9%	12%
ADQW2	55 Å	10 Å	142 Å	4.8%	14.7%

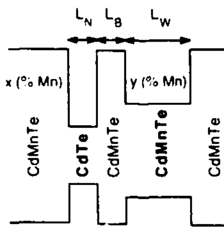

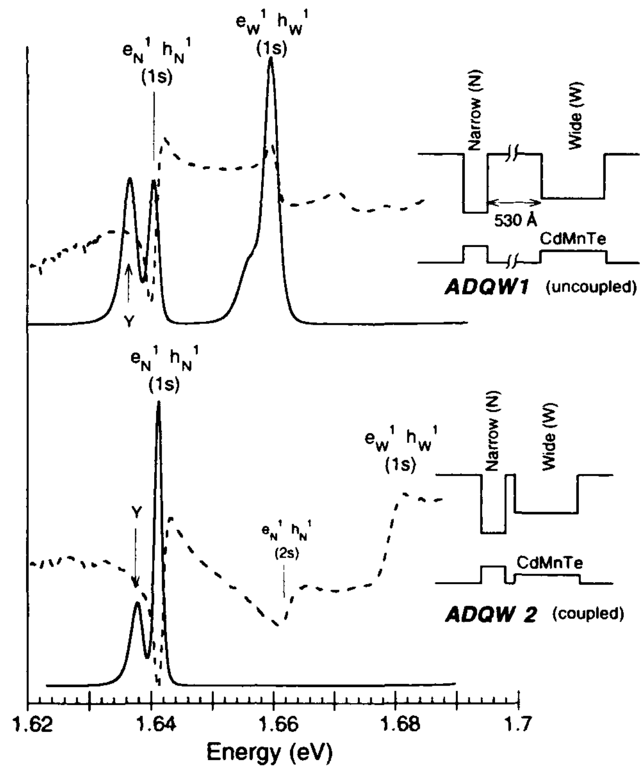

Fig. 2. Photoluminescence (continuous line) and reflectivity (dashed line) spectra obtained at 1.8 K and zero field for the two asymmetric double quantum wells heterostructures. Line Y is a defect exciton line not discussed here.

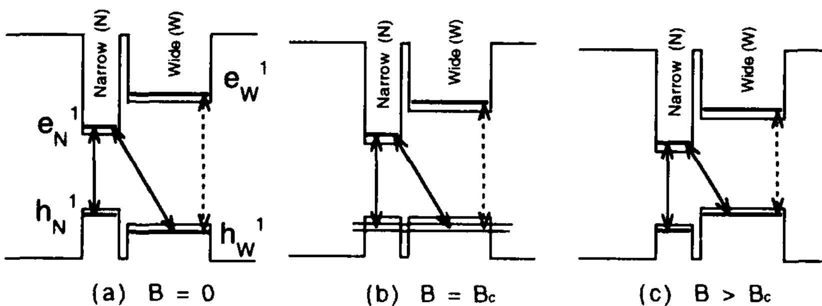

Fig. 1. The change of band structure of a coupled asymmetric double quantum well structure under a magnetic field in the Faraday $\sigma+$ configuration is represented schematically. B_c is the critical field for which the first two heavy hole levels become resonant.

is observed only in the reflectivity spectrum. This shows that there is very efficient transfer from the wide well to the narrow one at lower energy (*i.e.* ADQW2 is indeed a *coupled* sample, whereas ADQW1 is an *uncoupled* sample). The $e_{W^1}h_{W^1}$ transitions appear at slightly different energies for the two heterostructures since the wide wells have slightly different Mn concentrations (see Table 1).

We have studied the reflectivity spectra of both samples under a magnetic field up to 5 T (in the Faraday configuration, in both polarizations $\sigma+$ and $\sigma-$). We fitted the shifts of signal of the barriers and of the $e_{W^1}h_{W^1}$ $\sigma-$ line (of the wide CdMnTe well) with modified Brillouin functions [7, 8] to obtain a more precise knowledge of the Mn concentrations in the barriers and in the wide wells for both samples; for the wide CdMnTe wells, one assumes that the shift of the carrier confinements with the field is negligible compared to the Zeeman shifts of the well bandgap itself (at least for $\sigma-$ polarization), and therefore it is possible to consider the shift of the $e_{W^1}h_{W^1}$ $\sigma-$ line as "bulk-like"; we determined thus the Mn concentrations x and y given in Table 1. We calculated the transition energy for the two polarizations in the following way: at a given magnetic field we determined the form of the confining potentials including composition, strain and Zeeman effects and assuming a chemical valence band offset of 25% of the band gap difference [9]; then we solved the Schrödinger equation (we have used (for CdTe and CdMnTe) the masses given in ref. 10) and obtained the different energy levels and wavefunctions; finally we subtracted from the calculated gaps, the calculated values for the binding energies of the excitons submitted to a magnetic field. (We have worked with the model developed by Leavitt and Little [11] together with the model discussed by Peyla *et al.* [12] and Peter *et al.* [13].)

Figure 3 shows the energy variation of the different lines observed in reflectivity for the *coupled* sample under a magnetic field (we show only the 1*s* transitions for clarity; results concerning the identification of 2*s* excited states—observed in both polarizations—will be published elsewhere). All the transitions observed at zero magnetic field could be followed in both polarizations when increasing the field. However, one notices clearly that the reflectivity spectra look much more complicated in $\sigma+$ polarization (a configuration for which anticrossings are expected to occur) than in $\sigma-$ polarization (a configuration for which no anticrossing should occur); in other words, when increasing the magnetic field, one observes additional lines in $\sigma+$ polarization that correspond to *crossed* exciton transitions that do not have their analogous $\sigma-$ component (in this polarization, the oscillator strengths of these transitions are too small). Let us focus on the transi-

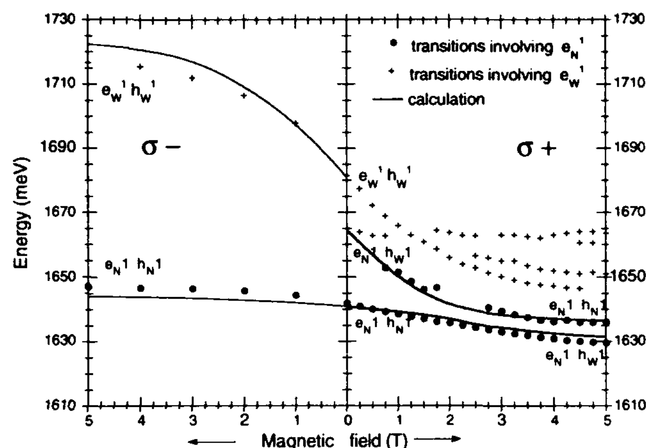

Fig. 3. Change in the energy position of the lines observed in reflectivity for the coupled structure as a function of the magnetic field. For clarity, $\sigma+$ and $\sigma-$ polarizations are plotted on the right and left, respectively. The continuous lines give the result of the calculation; the crosses and full circles correspond to the experimental energy positions of the different transitions observed.

tions associated with e_{N^1} (the conduction band being much less influenced by the magnetic field, this electron level remains in the ground electron state from 0 to 5 T). The comparison between the experimental points and the calculated exciton energies shows that the ground exciton state of the structure changes progressively from $e_{N^1}h_{N^1}$ at zero field to $e_{N^1}h_{W^1}$ at high field; its energy does not saturate rapidly with the field as compared with the $\sigma-$ component. Moreover, the line observed at higher energy is identified as the crossed exciton transition $e_{N^1}h_{W^1}$ at low field; its energy decreases rapidly with increasing B consistent with the fact that it involves the h_{W^1} level (confined in the wide CdMnTe well). In other words, one observes the anticrossing between the hole levels h_{N^1} and h_{W^1}.

Identification of the transitions involving e_W^1 is more problematical. We have noticed in particular a large influence of the value supposed for the valence band offset on the calculated fan diagram of the transitions, and we hope that a careful fit of these experimental data could provide an estimate of this parameter. (We tentatively assign two of the three lines observed at high energy and high field in Fig. 3 to $e_{W^1}h_{W^1}$, $e_{W^1}h_{N^1}$ in order of increasing energy.)

Figure 4 summarizes the results obtained for the e_{N^1}-related transitions for both samples so as to better emphasize the differences between the coupled and uncoupled structures. For $\sigma-$ polarization, the agreement is very good between the energy shifts for both samples—the slight difference (1 meV) between absolute energies observed also at zero field is due to small differences between the two samples (such as in barrier compositions). On the contrary, for $\sigma+$ polari-

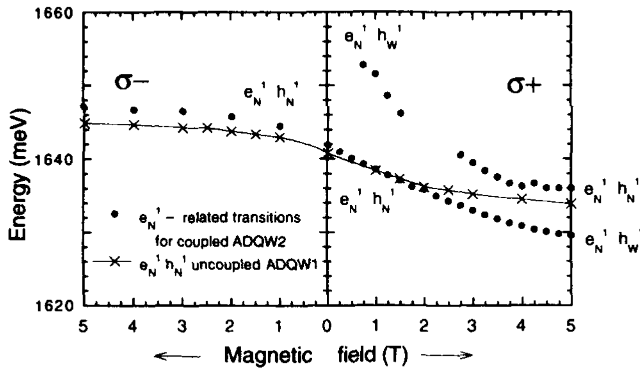

Fig. 4. A comparison between the variation of the *experimental* energy positions of the e_{N^1}-related transitions for the coupled and uncoupled structures as a function of the field; the continuous and dotted lines are only a guide for the eye.

zation clear differences appear: the $e_{N^1}h_{N^1}$ transition of the *coupled* structure moves further and further away in energy from the $e_{N^1}h_{N^1}$ transition of the *uncoupled* structure as the field increases, to finally change into the crossed $e_{N^1}h_{W^1}$ exciton; however, the crossed exciton $e_{N^1}h_{W^1}$ observed at low field (at higher energy) tends towards the energy of the $e_{N^1}h_{N^1}$ transition of the *uncoupled* structure as the field increases.

In conclusion, the preliminary work has shown the interest of studying such structures with Mn incorporated also in wells: the magneto-optical effects are enhanced without loss of the quality of the samples. Future photoluminescence excitation (PLE) studies under magnetic field should provide better resolution in measuring the line positions (which is not very easy in reflectivity) and that should help to assign more confidently the higher energy transitions and therefore to evaluate band offsets.

References

1 J. K. Furdyna, *J. Appl. Phys., 64* (1988) R29.
2 O. Goede and W. Heimbrodt, *Phys. Status. Solidi (b) 146* (1988) 11.
3 A. Wasiela, Y. Merle d'Aubigné, J. E. Nicholls, D. E. Ashenford and B. Lunn, *Solid State Commun., 263* (1990) 263.
4 E. Deleporte, J. M. Berroir, G. Bastard, C. Delalande, J. M. Hong and L. L. Chang, *Phys. Rev., B, 42* (1990) 5891.
5 W. Heimbrodt, O. Goede, Th. Köpp, K. Hiecke, H. E. Gumlich, Th. Pier, B. Lunn and T. Gregory, *J. Cryst. Growth, 117* (1992) 859.
6 L. A. Kolodziejski, T. C. Bonsett, R. L. Gunshor, S. Datta, R. B. Bylsma, W. M. Becker and N. Otsuka, *Appl. Phys. Lett., 45* (1984) 440.
7 J. A. Gaj, R. Planel and G. Fishman, *Solid State Commun., 29* (1979) 435.
8 J. A. Gaj, C. Bodin-Deshayes, P. Peyla, J. Cibert, G. Feuillet, Y. Merle d'Aubigné and A. Wasiela, *Proc. 21st Int. Conf. Phys. Semiconductors, Beijing, 1992.*
9 A. Wasiela, P. Peyla, Y. Merle d'Aubigné, J. E. Nicholls, D. E. Ashenford and B. Lunn, *Semicond. Sci. Technol., 7* (1992) 57.
10 C. Neumann, A. Nöthe and N. O. Lipari, *Phys. Rev., B, 41* (1988) 6082.
11 R. P. Leavitt and J. W. Little, *Phys. Rev., B, 42* (1990) 11774.
12 P. Peyla, Y. Merle d'Aubigné, A. Wasiela, R. Romestain, H. Mariette, M. D. Sturge, N. Magnea and H. Tuffigo, *Phys. Rev. B, 46* (1992) 1557.
13 G. Peter, E. Deleporte, G. Bastard, J.-M. Berrior, C. Delalande, B. Gil, J. M. Hong and L. L. Chang, *J. Lumin., 52* (1992) 147.

Materials Science and Engineering, B16 (1993) 239–242

Time-resolved light-induced Faraday rotation in $Zn_{1-x}Mn_xTe$ and $Cd_{1-x}Mn_xTe$

S. Hugonnard-Bruyere, J. Frey, R. Frey and C. Flytzanis

Laboratoire d'Optique Quantique du Centre National de la Recherche Scientifique, Ecole Polytechnique, 91128 Palaiseau-Cedex (France)

Abstract

The giant Faraday rotation (larger than 90°) photoinduced in ZnMnTe or CdMnTe by picosecond duration pump pulses is analysed by the time-resolved pump and probe technique. Slow thermal and fast photocarrier-induced processes are found to occur depending on the choice of the semimagnetic semiconductor sample.

1. Introduction

Control of the transverse characteristics of a laser beam is of great interest in optical signal processing and other related areas. Non-linear optical processes mediated via magneto-optic interactions can be used for this purpose by judicious choice of the material. Here we analyse how one can exploit the enhanced magneto-optic coupling that leads to giant Faraday rotations in the semimagnetic semiconductors II_{1-x}-Mn_x-VI to also obtain giant photoinduced Faraday rotations under the action of a powerful pulsed laser beam. We first review the physical origin of the linear Faraday effect in these compounds and then outline the mechanisms that underlie the photoinduced effect. Emphasis will be on the dynamics of the different contributions and in particular the thermal one. In this respect we present detailed experimental results and discuss ways of reducing this contribution.

2. Giant Faraday effect in $II_{1-x}Mn_xVI$

2.1. Faraday effect

The Faraday effect in a medium occurs whenever its refractive indices n_+ and n_-, respectively, for right and left circular polarizations of a light beam become different, for instance, by applying a static magnetic field. Then a linearly polarized beam of frequency ω after propagating a distance L inside such a medium, senses a rotation of its polarization state by an angle:

$$\theta_F = \frac{\omega L}{2c}(n_+ - n_-)$$

where c is the velocity of light in vacuum.

This difference of refractive indices for the two circular polarization states can be traced to the Zeeman splitting that the magnetic sublevels undergo in the presence of the static magnetic field. Its strength is expressed by the Lande gyromagnetic factor g, which for most cases has a value of the order of two; this is, for instance, the case for electrons in atomic orbitals but also in such extended states as the valence and conduction band states in binary semiconductors and in particular the II–VI compounds. When the latter are rendered semimagnetic by introducing magnetic impurities, for instance, Mn, this situation changes drastically.

2.2. Exchange interaction in II–VI semimagnetic semiconductors

Usually, in Faraday experiments, the difference of refractive indices between circular polarization states is due to a Zeeman splitting. In the more complex case of semimagnetic semiconductors, three steps are involved in the Faraday effect:

(1) First, there is a Zeeman splitting of the spins of the localized Mn^{2+} $3d$ electrons in the $^6S_{5/2}$ ground state. For a given temperature and a given magnetic field, a Boltzmann equilibrium leads to a magnetization in the material.

(2) Second, the exchange interaction between the spins of the localized Mn^{2+} $3d$ electrons and the delocalized band carriers enhances the usual splitting of the conduction and valence spin sublevels by two orders of magnitude.

(3) Finally, since difference spin projections are involved in right or left circular polarized transitions, these splittings give different refractive indices for the counter-rotating circular polarization states, and this

0921-5107/93/$6.00

© 1993 – Elsevier Sequoia. All rights reserved

leads to a giant Faraday effect (of the order of $10\,000° T^{-1} mm^{-1}$ if the laser frequency is near the band-gap resonance [1]).

2.3. Expected photoinduced Faraday rotation

This enhancement of the coupling of the band electrons with the magnetic field that leads to a giant Faraday effect can also be the origin of giant photoinduced rotations. One can show that for a given wavelength, the refractive index is a function of the position and the population of the levels involved in the optical transitions, and $(n_+ - n_-)$ is almost proportional to the magnetization in the material. Then, the photoinduced effect contains three contributions originated by three distinct mechanisms:

(1) Level displacement caused by an optical Stark effect: such a contribution follows the light pulse which was 30 ps in our experiments (see Section 4).

(2) The population change of the spin sublevels: the excitation of the photocarriers in the bands and their relaxation down to the bottom of the bands take place within 1 ps, so the risetime of this population effect is related to the pulse duration. Besides, the effect lasts as long as the existence of the carriers, *i.e.* 10 ns if there is only spontaneous emission, but less than 1 ns when there is stimulated emission.

(3) The off-equilibrium magnetization change via exchange interaction: on the one hand, because of the spin-exchange interaction, the spin of a carrier changes at the same time as that of an Mn^{2+} ion, keeping constant the sum of the spins. This occurs in less than 1 ps and the ensuing off-equilibrium impurity spin orientation lasts from 100 ns to the μs range, depending on the concentration of the magnetic ions and the sample temperature. In addition, thermal processes can be involved; their risetime is related to the Mn^{2+} spin relaxation (about 100 ns in our experiments), and their lifetime corresponds to the cooling down of the sample, *i.e.* in the μs or ms range in our experiments.

In the next part, we will focus our attention on the "thermal" effects. For a given magnetic field, heating the sample leads to a change in the Mn^{2+} spin distribution in order to obtain the Boltzmann equilibrium at a higher temperature. Then, the Faraday effect changes because of the exchange interaction. When the sample has regained its original temperature, the photoinduced effect vanishes.

3. Thermal contribution

3.1. Expected function $\theta_{NL}(H)$

As shown in Section 2.3 heating the sample can change the Faraday rotation. If we consider only the contribution of magnetization in response to heating, we can theoretically plot the photoinduced rotation as a function of the magnetic field for a given absorbed energy. Indeed, the Faraday rotation angle

$$\theta_F(T,H) = \theta_0 B_{5/2}\left(\frac{5g_{Mn}\mu_B}{2k_B}\frac{H}{T+T_{AF}}\right)$$

is related to the $B_{5/2}$ Brillouin function which monitors the spin statistics of the Mn^{2+} ions. In the argument of this Brillouin function, $g_{Mn} \approx 2$ is the Landé factor, μ_B is the Bohr magnetron, k_B the Boltzmann constant, H the magnetic field amplitude, T the sample temperature, and T_{AF} is an antiferromagnetic temperature which is phenomenologically introduced in order to take into account the exchange interaction existing between Mn^{2+} ions. As a consequence, for a small temperature increase ΔT the photoinduced Faraday rotation angle is:

$$\theta_{NL}(H,T) = \theta_0 \frac{\partial}{\partial T} B_{5/2}\left(\frac{5g_{Mn}\mu_B}{2k_B}\frac{H}{T+T_{AF}}\right)\Delta T \quad (1)$$

If ΔT is consecutive to the linear absorption of the pump pulse, it can be written as:

$$\theta_{NL}(H,T) = \theta_0' I \frac{\partial}{\partial T} B_{5/2}\left(\frac{5g_{Mn}\mu_B}{2k_B}\frac{H}{T+T_{AF}}\right) \quad (2)$$

where I is the pump intensity, and θ_0' another constant taking into account the heat capacity and the absorption coefficient of the pump. Let us note that we checked that the derivative shape was the same as the theoretical difference for two close different temperatures ($\Delta T \leqslant 1$ K).

Figure 1 shows the expected shape of $\theta_{NL}(H,T)$ if a thermal process is involved. So, in order to unambiguously identify such a process, high values of $(H/(T+T_{AF}))$ are needed to show not only the saturation but also the decrease after $H/(T+T_{AF}) = 0.457$. Therefore, for the experiments, we chose the highest possible magnetic field ($H = 5$ T), the lowest temperature (3 K achieved by pumping on a helium bath), and the lowest antiferromagnetic temperature (2 K by taking a small concentration in magnetic ions,

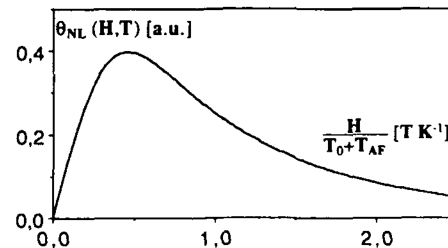

Fig. 1. Expected photoinduced Faraday rotation *vs.* the applied magnetic field in the case of thermal processes.

2.5% and 8%). Besides, as free-carrier contribution had to be avoided, we took ZnMnTe samples where the absorption involved intra-Mn transitions, whose energy is lower than the band-gap, whereas the CdMnTe alloys are the opposite case [2, 3].

3.2. Experimental setup

The experimental setup was based on the usual pump and probe technique. Pump and probe beams were focused on a ZnMnTe sample which was placed in a magnetic cryostat. The pump beam consisted of a 30 ps duration, 0.57 μm wavelength, 100 μJ energy laser, focused onto a 0.7 mm diameter spot. The probe beam was a linearly polarized 10 mW continuous wave HeNe laser focused onto a 0.2 mm diameter spot centred on the pump spot. The polarization direction of the output probe was determined using an analyser and a detector.

3.3. Experimental results

We first measured, as a function of the magnetic field, the linear Faraday rotation of the probe beam with no pump excitation. Fitting the experimental results obtained at $T=2.9$ K with the $B_{5/2}$ Brillouin function provided the value of the antiferromagnetic temperature ($T_{AF}=2.0$ K for the 8% concentration ZnMnTe sample). Taking this value, a good agreement for the theoretical and experimental points for the difference of rotation between 2.9 K and 3.9 K was obtained (see Fig. 2(a)). This very good fit is a supplementary proof of the validity of the fitting function.

Second, in pump and probe experiments, we measured the photoinduced effect of the probe beam rotation as a function of the incident pump energy for different magnetic fields. The curves showed a linear relation as expected for little sample heating. The slopes of these straight lines were plotted as a function of the magnetic field in Fig. 2(b). The experimental results are fitted satisfactorily by eqn. (2), demonstrating the thermal origin of the photoinduced Faraday rotation process.

Considering the analysis of shots in the [10 ns–10 ms] range (using three oscilloscopes), we saw that the effect was created in about 100 ns depending on both the temperature and the concentration of Mn ions. Indeed, this risetime decreases with increasing temperatures and increasing concentrations of Mn ions. Both of these behaviours were expected if the process was attributed to Mn^{2+} spin relaxation [4]; there are more phonons at higher temperatures and Mn^{2+} clusters are more efficient than isolated ions for this spin relaxation. The lifetime (in the 100 μs–1 ms range) could be attributed to thermal diffusion processes, which was confirmed by shifting the pump spot from the probe one.

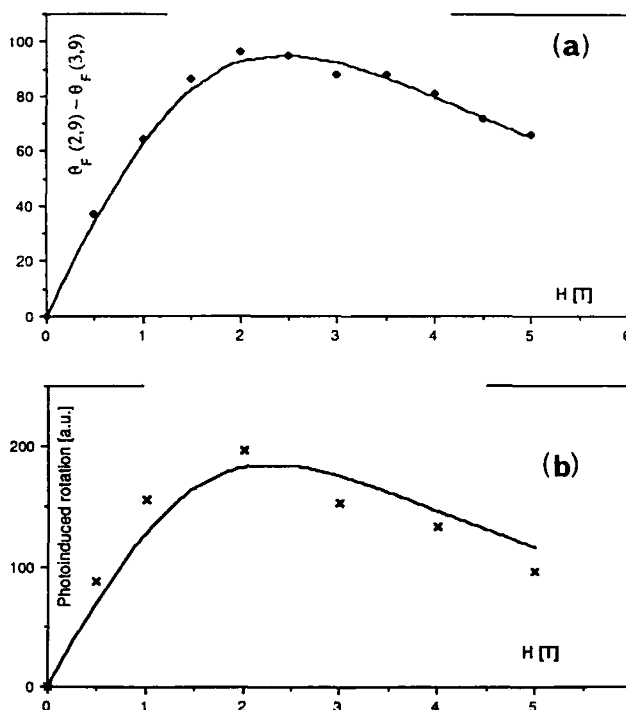

Fig. 2. Faraday rotation as a function of the magnetic field: (a) difference between linear rotations at 2.9 K and 3.9 K and (b) photoinduced rotation. The continuous lines are the theoretical fits obtained using $B_{5/2}$ Brillouin functions (see text).

Experiments were also performed in CdMnTe (25%) in a case where free carriers were created through two-photon absorption. As shown in Fig. 3, which compares the risetime of the photoinduced signal for the ZnMnTe (Fig. 3(a)) and CdMnTe (Fig. 3(b)) experiments, a very fast exponent exists in CdMnTe which is absent in ZnMnTe where the process is only thermal. This fast component, which was attributed to photocarriers, is studied in the next section.

4. Experiments in the non-thermal case

In order to analyse the fast component which is too fast to be thermal, pump and delayed probe experiments were performed in the 30 ps–1 ns range.

As the fast component contains free-carrier-induced contributions (see Section 2.3), the experiment used two-photon absorption of 1.064 μm wavelength pump laser pulses in $Cd_{1-x}Mn_xTe$ ($x=25\%$). The low intensity probe pulses were derived and delayed from the main pump pulse. The polarization direction of the output probe beam, which was measured in exactly the same manner as in the previous experiment, was plotted as a function of the delay between the pump

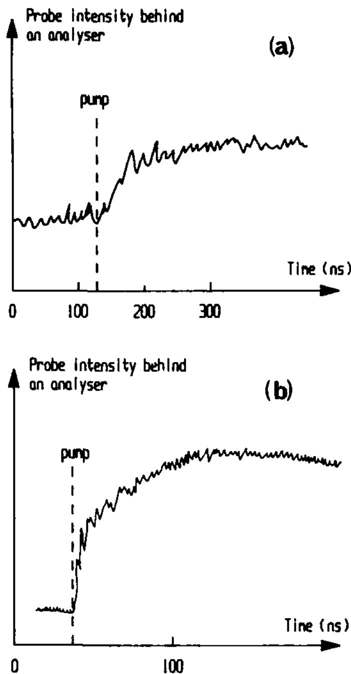

Fig. 3. Risetime of the photoinduced Faraday rotation signal in the case of (a) ZnMnTe and (b) CdMnTe.

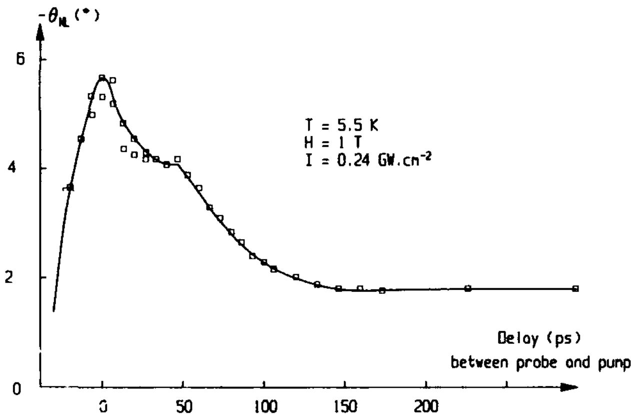

Fig. 4. Photoinduced Faraday rotation in CdMnTe *vs.* the delay between pump and probe pulses.

and the probe pulses. The results are shown in Fig. 4 where three contributions can be easily seen [5].

The long-living pure magnetic contribution is clearly apparent for times longer than 150 ps; the population contribution corresponds to the exponential decrease of θ_{NL} observed between 50 and 150 ps, this decay being related to the stimulated recombination of free carriers which was actually observed experimentally [6]. Finally, the signal occurring around the zero delay is mainly due to the instantaneous Kerr contribution. Indeed, by summing these three contributions with the appropriate constants, one obtains the continuous line in Fig. 4 which, therefore, represents a good qualitative fit with the experimental results.

5. Conclusion

In this work, we saw that II-Mn-VI alloys which provide giant Faraday rotation could also show giant photoinduced effects. Indeed, photoinduced rotations larger than 90° could be obtained, which corresponded to the transition from dark to full light between two crossed polarizers. We saw that thermal effects were very efficient, but only at very low temperatures ($T < 30$ K) because material heating could not be obtained at high temperatures without damage. We also expect the non-thermal phenomena to appear at room temperature, and think that their very fast risetime could be useful for applications in signal processing. Therefore, we have to complete our investigations on this fast component in particular.

Acknowledgment

We thank Dr. R. Triboulet from the Laboratoire de Physique des Solides de Bellevue, in Meudon, for providing the high quality ZnMnTe and CdMnTe samples used in these experiments.

References

1 D. U. Bartholomew, J. K. Furdyna and A. K. Ramdas, *Phys. Rev. B, 34* (1986) 6943.
2 O. Goede and W. Heimbrodt, *Phys. Status Solidi (B), 146* (1988) 11.
3 J. K. Furdyna, *J. Appl. Phys., 64* (1988) R30.
4 D. Scalbert, J. Cernogora and C. Benoit à la Guilhaume, *Solid State Commun., 66* (1988) 571.
5 J. Frey, *Ph.D. Thesis*, University of Orsay, 1991.
6 J. Frey, R. Frey and C. Flytzanis, *Phys. Rev. B, 45* (1992) 4056.

Materials Science and Engineering, B16 (1993) 243-245

Determination of the iron acceptor level in CdTe

B. K. Meyer
Physik-Department E16, Technical University Munich, 8046 Garching (Germany)
H. Linke and P. Omling
Department of Solid State Physics, University of Lund, Box 118, S-221 00 Lund (Sweden)
M. Salk and K.-W. Benz
Kristallographisches Institut, Universität Freiburg, Hebelstr. 27, 7800 Freiburg (Germany)

Abstract

The iron acceptor charge state Fe^{+} in as-grown ZnTe was investigated by electron paramagnetic resonance and photoelectron paramagnetic resonance. The photoelectron paramagnetic resonance results show a threshold energy at 1.75 eV, locating the acceptor level at 0.65 eV below the conduction band. For a valence band offset of 100 meV between ZnTe and CdTe, the acceptor level $Fe^{0/-}$ in CdTe is predicted to be located at about 0.2 eV above the conduction band edge. Our investigations do not confirm that the 1.17 eV emission band in CdTe is related to iron.

1. Introduction

The iron group transition metals (TMs) in semiconductors are important deep level defects, since they can induce donor as well as acceptor states in the forbidden gap [1]. Electron paramagnetic resonance (EPR) and photoelectron paramagnetic resonance (PEPR) served as microscopic means of identification of the isolated TM ions, and in many cases allowed for the charge state and energy level to be determined. In state-of-the-art bulk-grown CdTe, EPR detects nickel, cobalt, iron and manganese as omnipresent impurities. Whereas nickel and cobalt induce acceptor levels (manganese is not electrically active), the role of the isolated iron is not well established. It is interesting to note that EPR investigations in ZnS [2] and ZnTe [3] have shown the presence of an acceptor state Fe^{+} (the donor state of iron is Fe^{3+}); thus iron should induce a donor as well as an acceptor level in the forbidden gap. However, the energy levels in CdTe, ZnTe and ZnS have still to be determined. The isolated TM impurities act as a reference level and allow the determination of the valence band and conduction band offsets in II–VI and III–V semiconductors as demonstrated by Langer and Heinrich [4] (LH). Knowing the band offsets between, for example, CdTe and ZnTe allows the position of acceptor and donor levels to be predicted in one system (CdTe) if they have been determined in the second system (ZnTe).

The deep luminescence bands in CdTe at 1.0–1.2 eV are supposed to involve the iron impurity [5, 6]. Since the iron donor level (3+/2+) is located at about 150 meV above the valence band [7], the recombinations could involve the 3+ and 2+ charge states of iron, or the + charge state, if the acceptor level (2+/+) falls into the gap (in high resistivity material Fe^{2+} is the equilibrium charge state). It was therefore our aim to determine the iron acceptor level in ZnTe and, based on the well accepted and established scheme of LH, to predict the respective level in CdTe. Following the suggestions of refs. 5 and 6, we then discuss the possibility of radiative recombinations involving the iron impurity.

2. Experimental details

EPR and PEPR were performed in a commercial X-band ESP 300 spectrometer while the sample temperature was held at 8 K. Monochromatic illumination was achieved by an *f*/3 25 cm monochromator in connection with a halogen lamp. PEPR transients were measured with the magnetic field held at a resonance position. The photon flux was determined independently and the optical cross-section was correspondingly normalized. The highly resistive samples grown by the Bridgman and travelling heater method con-

0921-5107/93/$6.00

© 1993 – Elsevier Sequoia. All rights reserved

tained nickel, cobalt, manganese and iron as residual impurities ($N_{tot} < 10^{16}$ cm^{-3}).

The Fe^+ EPR signal, which was usually two orders of magnitude stronger if illuminated with light close to the band gap of ZnTe (see inset in Fig. 1), consists of a single line with a g value of 2.28. The isotropic eight-line spectrum with a lower intensity is due to Co^{2+}. The Fe^+ line position is slightly anisotropic according to the higher order terms in the spin hamiltonian [3].

To determine the acceptor level, (0/−) in the charge state notation, PEPR investigations measuring EPR transients were performed. As already mentioned, light illumination close to the band gap increases the intensity by two orders of magnitude. This shows that the dominant charge state of iron is the neutral charge state Fe^{2+}. It is thus possible to determine the optical cross-section for the hole ionization process

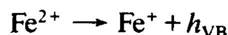

$$Fe^{2+} \longrightarrow Fe^{+} + h_{VB}$$

by employing the initial slope technique. For an exact analysis it is prerequisite that the time dependence of the EPR signal upon illumination with monochromatic photons is the result of only one defect level. Normalizing by the photon flux, the optical cross-section as presented in Fig. 1 has been determined. It shows the shape typical for a TM element in III–V and II–VI semiconductors with one energy level in the gap. From the threshold at 1.75 ± 0.05 eV we estimate the energy level of $Fe^{2+/+}$ in ZnTe at E_V + 1.75 eV. Indeed, our result confirms the strong photosensitivity close to the band gap energy already mentioned [3].

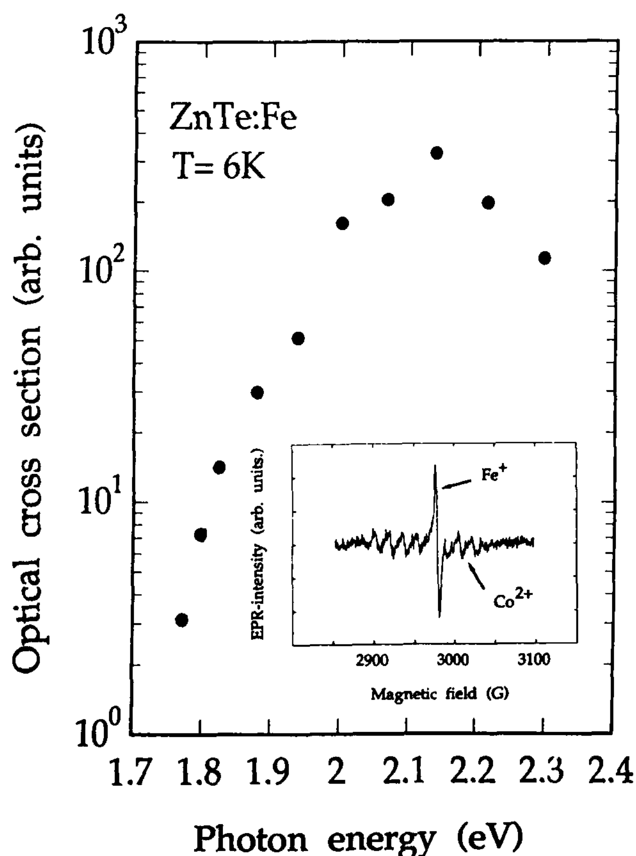

Fig. 1. Optical cross-section for the hole ionization transition $Fe^{2+} \longrightarrow Fe^{+} + h_{VB}$ determined from PEPR investigation. Inset: EPR signal of Fe^+ in ZnTe (T = 8, ν = 9.50 GHz). The partially resolved eight-line spectrum is due to Co^{2+}.

3. Discussion

The isolated TM impurities can act as a reference level to determine the valence band and conduction band offsets in II–VI and III–V semiconductors. This has been clearly demonstrated by Langer and Heinrich [4]. The valence band offset between CdTe and ZnTe is small; values between 40 and 150 meV are discussed [7]. Thus, for a comparison of both systems only the conduction band offset is of relevance. Based on the LH rule [4], the $Fe^{2+/+}$ level in CdTe therefore should be as deep as 0.2 eV in the conduction band (see Fig. 2).

For the deep luminescence bands in CdTe at 1.0–1.2 eV our investigation demonstrates that only the 3+ and 2+ charge states can be involved. For Fe^{2+} ($3d^6$, $S = 2$) the ground state (^5E) and the excited crystal field state $^5T_2$ state, separated by 0.28 eV, can take part in the luminescence process (see Fig. 3). Since the level of 3+/2+ is at E_V + 150 meV, emission close to the band gap at 1.45 eV involving the ^5E state (transition 1 in Fig. 3) as well as at 1.17 eV to the $^5T_2$ state (transition 2 in Fig. 3) could be seen for the Fe^{2+}-related recombinations. In refs 5 and 6 an additional emission band at

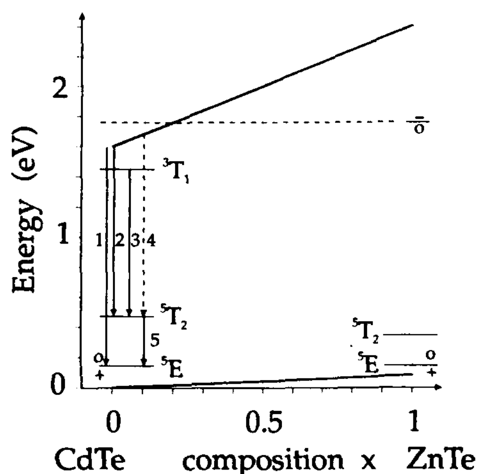

Fig. 2. Energy level diagram showing the position of the donor and acceptor levels of iron in CdZnTe as well as possible radiative and non-radiative transitions involving Fe^{2+}.

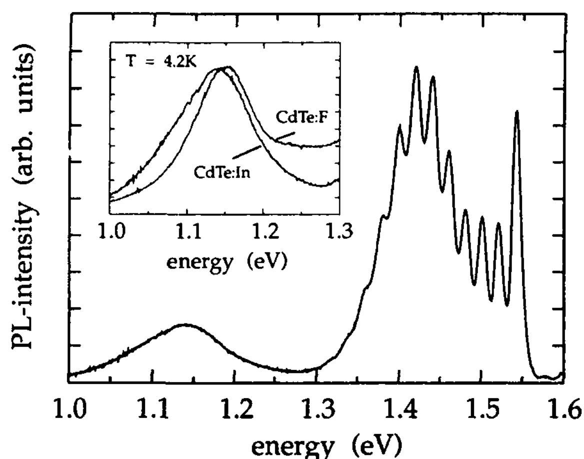

Fig. 3. Photoluminescence spectrum for CdTe:In showing shallow (1.5–1.4 eV) and deep (1.17 eV) recombinations. Inset: the deep luminescence band at 1.17 eV for CdTe:In and CdTe:F (T=4.2 K, Ar^+ excitation 514 nm).

1.07 eV was attributed to an internal $^3T_1 \rightarrow {}^5T_2$ transition within Fe^{2+} (transition 3 in Fig. 3). However, it should be noted that for such a spin-forbidden transition a broad gaussian emission band as found in refs. 5 and 6 is rather unlikely.

In our highly resistive material, Fe^{2+} is the equilibrium charge state. It follows that by above band gap optical excitation electron and hole pairs are generated such that the hole can be trapped at Fe^{2+} leaving the electron in the conduction band. Additionally, Fe^{2+} might also be directly photoionized by the exciting light according to

$$Fe^{2+} + h\nu \rightarrow Fe^{3+} + e_{CB}$$

From comparative studies in III–V semiconductors [8, 9] it is known that the relaxation to the equilibrium charge state Fe^{2+} is via non-radiative electron capture by Fe^{3+} (transition 4 in Fig. 3). The capture is probably more efficient into the $^5T_2$ excited state of Fe^{2+}. Radiative emission then takes place between the $^5T_2$ and ^5E states at 0.28 eV (transition 5 in Fig. 3). The broad gaussian emission band observed in CdTe at 1.17 eV (see Fig. 2) is characteristic of strong electron–phonon coupling. A Franck–Condon shift of 0.22 eV (S= 17, $\hbar\omega$ = 11 meV) is found from the temperature dependence of the emission band halfwidth. Since the $^5T_2$ and ^5E states are further split by the combined effect of spin–orbit and crystal field interactions, multiple, narrow line transitions are expected to be seen in photoluminescence. They are indeed clearly resolved in the absorption and emission spectra between the $^5T_2$ and ^5E states of Fe^{2+} at 0.28 eV [10, 11]. One further objection comes from recent photoconductivity [12] measurements which show that the lattice relaxation energy (Franck–Condon shift) for the iron impurity is at most 22 meV and thus cannot account for the broad emission band at 1.17 eV.

4. Conclusions

In conclusion, we demonstrate that iron in ZnTe acts as a deep donor and deep acceptor. The acceptor level is determined by PEPR at E_V+ 1.75 eV. In CdTe, only the donor level is electrically active. For the deep luminescence bands at 1.17 eV in CdTe we have no direct experimental evidence for an assignment to iron-related transitions.

References

1 For an extensive summary and compilation of data, see A. Zunger, *Solid State Phys.*, *39* (1986) 276.
2 W. C. Holton, I. Schneider and T. L. Estle, *Phys. Rev. A*, *133* (1964) 1638.
3 T. L. Estle and W. C. Holton, *Bull. Am. Phys. Soc.*, *10* (1965) 57; *Phys. Rev.*, *150* (1966) 159.
4 I. M. Langer and H. Heinrich, *Phys. Rev. Lett.*, *55* (1985) 1414.
5 K. Lischka, G. Brunthaler and W. Jantsch, *J. Cryst. Growth*, *72* (1985) 335.
6 R. Kernöcker, K. Lischka and L. Palmetshofer, *J. Cryst. Growth*, *86* (1988) 625.
7 W. Jantsch and G. Hendorfer, *J. Cryst. Growth*, *101* (1990) 404.
8 P. B. Klein, I. E. Furneaux and R. L. Henry, *Phys. Rev. B*, *29* (1984) 1947.
9 S. Bishop, in S. Pantelides (ed.), *Deep Centres in Semiconductors*, Gordon and Breach, London, 1986, Chap. 9.
10 G. L. Slack, S. Roberts and J. T. Vallin, *Phys. Rev.*, *187* (1969) 511.
11 K. Pressel, A. Dörnen and B. K. Meyer, 1992, unpublished.
12 A. J. Szadkowski, *J. Phys. Condens. Matter*, *2* (1990) 9853.

Materials Science and Engineering, B16 (1993) 246–249

Fourier transform IR spectroscopy of CdTe:Fe

M. C. Carmo and M. J. Soares

Departamento de Física, Universidade de Aveiro, 3800 Aveiro (Portugal)

Abstract

We have investigated the optical properties of CdTe doped by Fe diffusion at about 600 °C by means of Fourier transform IR spectroscopy. The results agree with previous results where Fe has been introduced during growth, but a number of IR bands from 300 to 700 cm^{-1} are observed and reported for the first time.

1. Introduction

The optical properties of CdTe in the near and far IR have been reported by a number of workers [1, 2]. With the advances in Fourier transform (FT)IR spectroscopy, the near and far IR are now available with an accuracy and detail never reached before.

It is normally accepted that the Fe impurity diffuses in the charge state Fe^{2+} and substitutes for a Cd atom in the CdTe lattice. The free ion Fe^{2+} has a $^5D(L=2, S=2)$ ground state and, in a tetrahedral site (T_d), the crystal field splits this state into a doublet ^5E and triplet $^5T_2$, the doublet ^5E being lower in energy. The spin–orbit interaction provides additional splitting of these states as follows:

$$^5E \rightarrow A_1 + T_1 + T_2 + A_2$$

$$^5T_2 \rightarrow A_1 + E + 2T_1 + 2T_2$$

Therefore, the ground state of an Fe^{2+} ion in a T_d lattice site is expected to be a non-magnetic A_1 singlet and there will be no localized spin at the impurity site. Any magnetic properties of the CdTe:Fe system will result from mixing between the ground non-magnetic state and the excited magnetic states through the action of a weak perturbation. This will result in standard Van Vleck paramagnetism. The situation expected here is thus theoretically quite different from the better known situation of Mn^{2+}-doped CdTe where the ground state Mn^{2+} is a non-vanishing spin state. The technological interest of these materials in diluted magnetic semiconductors (DMSs) stresses the importance of better qualitative and quantitative knowledge of the behaviour of these 'magnetic' ions in II–VI materials [3, 4].

At low doping concentrations, the optical properties of CdTe:Fe will be dominated by the crystal field and spin–orbit interactions acting on isolated lattice sites. Therefore, we expect optical transitions to occur within the ^5E and $^5E \rightarrow {}^5T_2$ states. According to Slack and co-workers [5, 6], the ^5E transitions occur in the far IR (about 71 cm^{-1}) and the $^5E \rightarrow {}^5T_2$ transitions occur in the near IR (about 2700 cm^{-1}).

From our point of view, it is important to understand clearly the properties of Fe in bulk CdTe in the strongly diluted case. Most of the measurements were made in the late 1960s and since then this and related materials have been the subject of great interest.

2. Experimental details

In this work we used high purity CdTe single crystals grown by a modified Bridgman technique. Fe doping was achieved by diffusion at temperatures in the range 600 to 800 °C for 6–14 h. The samples were sealed in quartz ampoules under vacuum and a Cd overpressure was achieved by means of ultrahigh purity excess Cd.

After diffusion, the samples were mechanically polished and mounted in the cold finger of an APD cryostat with appropriate windows. Control samples were kept at all stages of the diffusion process for comparison. The IR properties were measured with a Bruker 66v FTIR spectrometer.

3. Results

The IR absorption of high purity CdTe is dominated by a number of very weak absorption bands as shown in Fig. 1. We can easily identify the free carrier absorption [1] (from about 0.1 to 0.2 eV) associated with a number of low energy structures attributed to transi-

0921-5107/93/$6.00

© 1993 – Elsevier Sequoia. All rights reserved

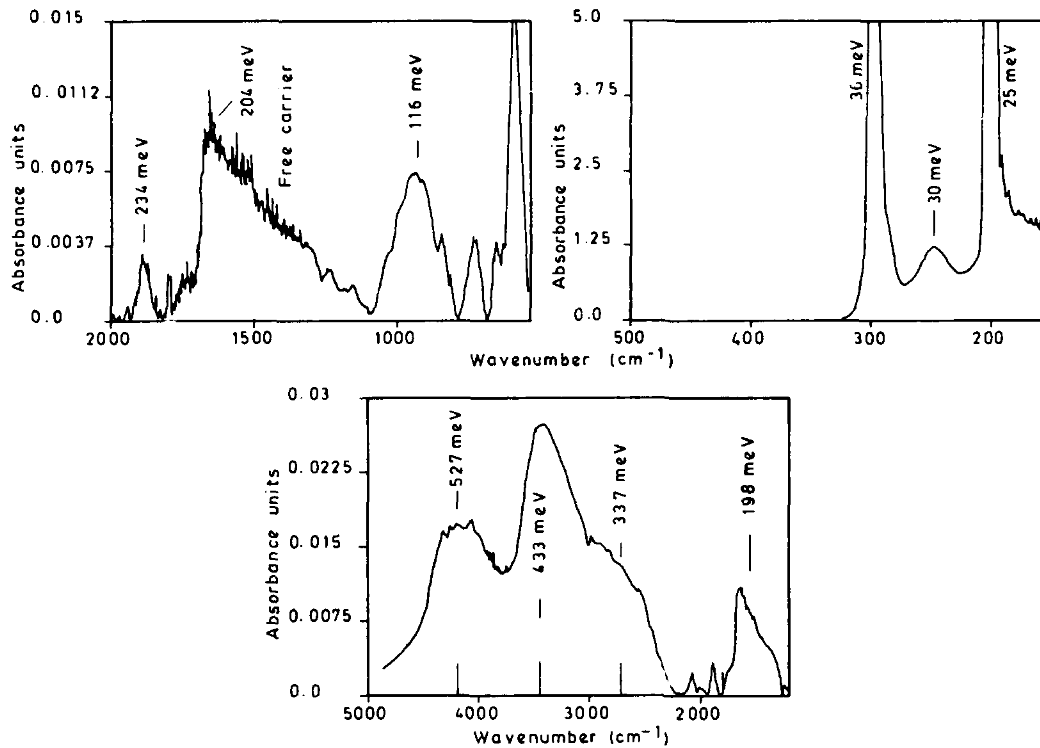

Fig. 1. Typical absorption (taken from the percentage transmittance) of as-grown CdTe.

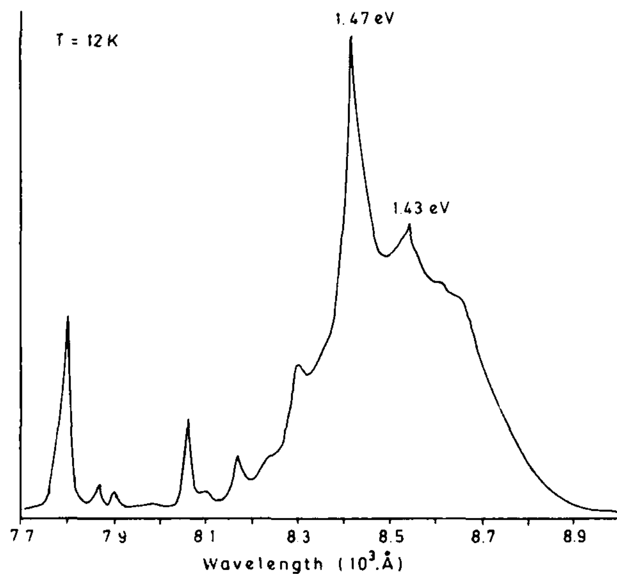

Fig. 2. Near-edge luminescence of pure CdTe showing broad luminescence bands (12 K).

tions from the valence band to localized acceptors. Other broad bands peaking at about 0.4 and 0.5 eV, and typically 50 meV wide, can be identified and attributed to absorption into deep traps. Similar bands at about 0.7 and 1.1 eV have been reported [7]. Broad bands are also present in near-edge photoluminescence of these samples, peaking at 1.47 and 1.43 eV (Fig. 2). These bands are typically 60 meV wide and are persistent at high temperatures. They have been identified by some authors [7, 8] as donor–acceptor pair bands related to intrinsic defect clusters.

Figure 3 shows the IR room temperature absorption (taken from the percentage transmittance of CdTe:Fe). We notice a strong increase in the absorption between about 1000 and 5000 cm^{-1}, peaking at about 2750 cm^{-1}. At low temperatures, the band is resolved and the fine structures already identified as transitions between the ^5E and $^5T_2$ states was observed. Figure 4 shows the logarithmic plot of two room temperature absorption bands from two samples with different Fe concentrations; the more heavily doped sample shows a larger absorption. These results are mainly in accordance with Slack *et al.* [5, 6].

However, in the more heavily doped sample we notice a very strong absorption from 330 to 1000 cm^{-1} which never has been reported before. This region of the spectrum is shown in Fig. 5. These bands are probably related to vibrational bands involving defects (intrinsic or dopants) and defect clusters containing Fe. This indicates that Fe may occupy positions in the CdTe lattice other than the simple substitutional position.

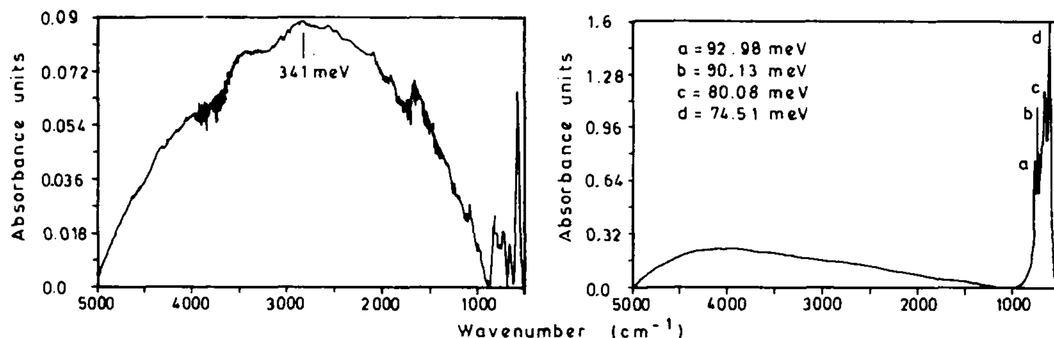

Fig. 3. Room temperature IR absorption of CdTe doped with Fe. Two different samples are shown.

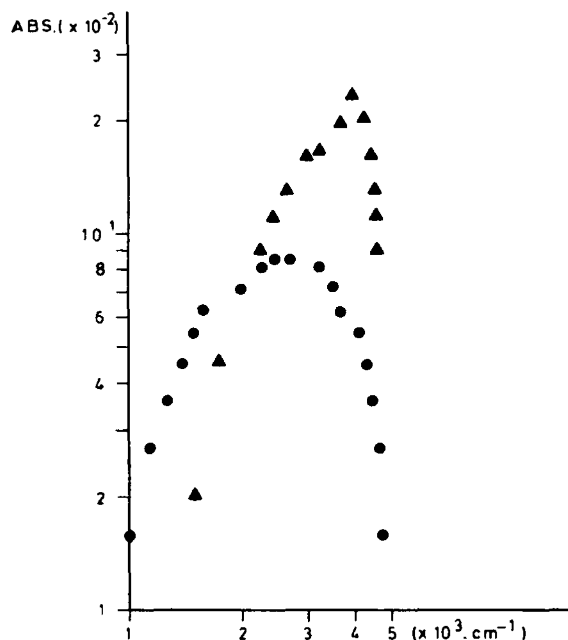

Fig. 4. Logarithmic plot of IR absorption bands shown in Fig. 3.

4. Discussion

We have shown in this paper that absorption from CdTe doped with Fe by diffusion can reproduce previous results obtained for growth doping. Also, we report the presence of new vibrational sidebands in the heavily doped samples. These sidebands are probably related to defect pairs involving Fe and a defect other than the simple substitutional defect. Such defect pairs in CdTe involving Al and Cd vacancies have been reported already [9]. Therefore, we conclude that the present model for Fe diffusion in CdTe, where Fe simply occupies pure substitutional sites, is probably oversimplified and more work in this area is clearly needed to take full advantage of the properties of this dopant in CdTe.

Acknowledgments

This work was performed under JNICT research Contract PMCT/C/MPF/114.90. The authors want to

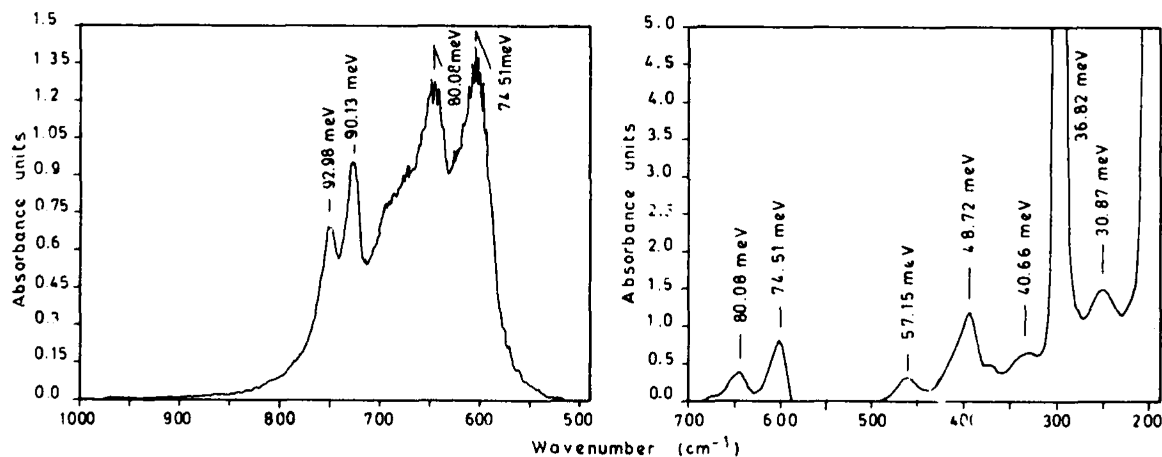

Fig. 5. New absorption bands in CdTe:Fe.

thank Criolab for technical assistance with vacuum and cryogenic equipment. One of us (MJS) is thankful to JNICT for a research grant.

References

1 R. O. Bell, *Rev. Phys. Appl., 12* (1977) 391.
2 O. M. Stafsudd, F. A. Haak, K. Radisavljevic, *J. Opt. Soc. Am., 57* (1967) 1475.
3 Testelin C. Rigaux, A. Mauger, D. Scalbert, C. B. à la Guillaume and A. Mycielski, *J. Appl. Phys., 70* (1991) 6383.
4 A. Mycielski, *J. Appl. Phys., 63* (1988) 3279.
5 G. A. Slack, F. S. Ham and R. M. Chrenko, *Phys. Rev., 152* (1966) 376.
6 G. A. Slack, S. Roberts and J. T. Vallin, *Phys. Rev., 187* (1969) 511.
7 Z. Panosyan, *Sov. Phys. Solid State, 20* (1978) 145.
8 M. C. Carmo and M. J. Soares, *Proc. Materials Research Society Meeting, Boston, MA, 1991*, Vol. 242, p. 287.
9 B. V. Dutt, M. Al-Delaimi and W. G. Spitzer, *J. Appl. Phys. 47* (1976) 565.

Thin films of CdTe produced using stacked elemental layer processing for use in CdTe/CdS solar cells

R. W. Miles, M. T. Bhatti, K. M. Hynes, A. E. Baumann and R. Hill
Department of EEE&P, Newcastle Polytechnic, Newcastle-upon-Tyne NE1 8ST (UK)

Abstract

The stacked elemental layer (SEL) technique has been used to synthesize thin films of CdTe. This technique consists of depositing alternate layers of Cd and Te in the stoichiometric ratio needed to form CdTe and then annealing the stack to react the layers to form the compound. The Cd and Te layers were deposited using thermal evaporation and annealed in N_2, vacuum or air to synthesize the CdTe. Transmittance and reflectance data, X-ray diffraction data and scanning electron microscopy observations of the surface topology are given for the layers produced. Post-synthesis annealing of the layers using $CuCl_2$/$CdCl_2$/methanol was also investigated. Such annealing was found to substantially increase the grain size of the layers produced. The CdS/CdTe solar cells produced using the large grain CdTe have open circuit voltages up to 0.68 V and short circuit currents greater than 11 mA cm^{-2} under AM0 illumination. A preliminary energy analysis has been carried out, and energy payback times and energy ratios are presented in conjunction with a discussion of the environmental costs of using such technology. The SEL technique promises to be a commercially realizable process for manufacturing CdS/CdTe solar cells.

1. Introduction

CdTe is considered to be one of the most promising thin film photovoltaic materials. With a direct band gap of 1.5 eV, near the optimum for solar energy conversion, it also has a high optical absorption coefficient (over 10^4 cm^{-1}) which means that solar radiation with energy in excess of the band gap is absorbed within 1–2 μm of the surface and hence a relatively short minority carrier diffusion length (about 1 μm) in the material can be tolerated. This means that material costs are minimized (because thin layers are used) and that low cost deposition methods can be used to produce the layers (because a long minority carrier diffusion length is not required).

The work presented here is part of a joint European effort (Joule Programme) to develop CdTe solar cells. The techniques used to produce CdTe include electrodeposition (BP Solar International Ltd. [1]), close spaced sublimation (Battelle Institute [2]), screen printing (Gent State University [3]), sputtering and ion-assisted doping (University of Parma [4]), metallo-organic vapour phase deposition (University of Durham [5]) and atomic layer epitaxy (Microchemistry Ltd., Finland [6]). Efficiencies of about 14% have been achieved in refs. 1 and 6 for small area cells and efficiencies of about 9%–10% in ref. 1 for large area (30 cm × 30 cm) modules. The work presented here uses stacked elemental layer (SEL) processing to produce CdTe thin films. This technique was originally developed in our laboratory to produce thin films of copper indium diselenide (CIS) [7]. This technique is simple and it promises to be a low cost method to produce large areas of good quality thin film materials for use in solar cell devices.

To be a viable energy supply option, solar cells should be nett producers of energy and hence an analysis of the energy required to produce these solar cells using SEL processing has been made. The energy payback times and energy ratios have been determined assuming realistic values for the module efficiency and lifetime. A discussion of the environmental issues concerning the use of CdS/CdTe solar cells is also given.

2. Experimental procedure

The evaporations were made in an oil-pumped vacuum system operating in the 10^{-5}–10^{-7} Torr range of vacuum pressures, and the source heaters were of the type described in ref. 8. Two shutters were used, one close to the substrate to prevent deposition onto the substrate and the other, just above the quartz bottles containing the Cd and Te, could be adjusted to cover both sources or just one source to prevent either Cd or Te vapour or both reaching the substrate.

The annealing of the stacks in N_2, air or vacuum to synthesize the layers and the post-synthesis heat treatment using $CdCl_2$/methanol, $CuCl_2$/methanol or

0921-5107/93/$6.00

© 1993 - Elsevier Sequoia. All rights reserved

$CdCl_2/CuCl_2$/methanol solutions, were performed in a separate vacuum chamber which could be evacuated to a pressure of 10^{-2}–10^{-3} Torr. Transmittance and reflectance measurements were made using a Cary 17-D spectrophotometer and the X-ray diffraction data were obtained using an X-ray diffractometer with a Cu Kα X-ray source.

3. Experimental results

It was found to be difficult to evaporate homogeneous, uniform films of Cd directly onto Corning 7059 glass substrates, whereas the deposition of Te films of uniform thickness and without pinholes was found to be straightforward. Good films were obtained using unheated substrates (at a temperature of about 20 °C) for a Te source temperature in the range 220 °C–260 °C. Increasing the substrate temperature was found to produce non-uniform layers with pinholes present so an ambient substrate temperature was used in this work. A Te source temperature of 230 °C (for such a substrate temperature) was adopted so that the quartz crystal monitor in the system could be calibrated to permit controlled deposition of the Te. The deposition rate for these conditions was 10 Å s^{-1}.

Deposition of the Cd onto such Te layers resulted in uniform films free from pinholes for Cd source temperatures in the range 120 °C–150 °C. A standard Cd source temperature of 135 °C was adopted and the quartz crystal monitor calibrated to permit controlled deposition of the Cd. The deposition rate of the Cd for these conditions was 10 Å s^{-1}.

Alternating Te/Cd stacks were deposited using the optimized conditions such that the relative thicknesses of the layers were in the stoichiometric ratio, and these stacks were annealed in N_2, vacuum or air to react the elements to form CdTe. The annealing conditions were optimized by annealing the stacks for 15 min at temperatures in the range 350 °C–600 °C, starting with the lower temperatures and then annealing at 50 °C intervals until good absorption edges were obtained. Annealing at too high a temperature (over 500 °C) was found to degrade the maximum transmittance and the absorption edge, and an annealing temperature of 450 °C (for an annealing time of 15 min) was considered to be optimum for all the different annealing environments.

The results obtained for annealing six-layer stacks (with a total CdTe thickness of 1300 Å) have been reported previously [9]. Good absorption edges were obtained but the grain size was small (typically about 1000–2000 Å). In the work reported here we have increased the number of stacks to produce CdTe films with thicknesses of more than 1 μm.

Transmittance *vs.* wavelength measurements for the stacks annealed in N_2, air and vacuum are given in Fig. 1 and, in conjunction with reflectance measurements, the variation of α with $h\nu$ (Fig. 2) and the variation of $(\alpha h\nu)^2$ with $h\nu$ (Fig. 3) determined. It is apparent that CdTe layers have been successfully synthesized using all three annealing environments. The grain size for annealing in N_2 and vacuum was consistently found to be small (typically about 1000–2000 Å) as shown in Fig. 4(a). Annealing in air produced slightly larger grains with grain sizes typically in the range 1500–3200 Å.

X-ray diffraction data for the samples are given in Fig. 5. For the layers synthesized in N_2, the full width at half-maximum (FWHM) of the (111) peak was 0.42°,

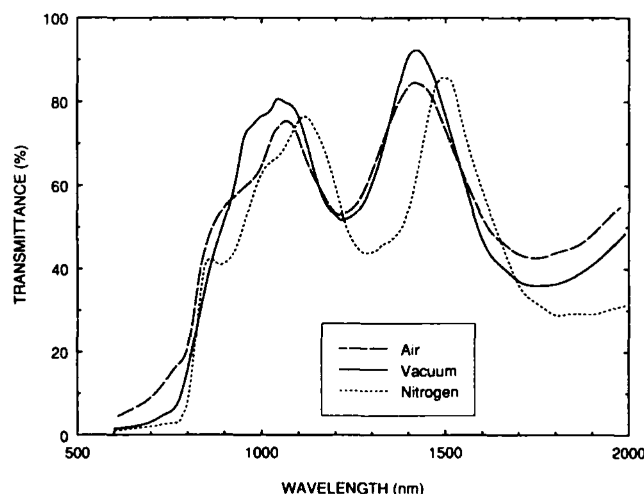

Fig. 1. Transmittance *vs.* wavelength for the CdTe produced by annealing repeated Te/Cd stacks in N_2, in vacuum and in air.

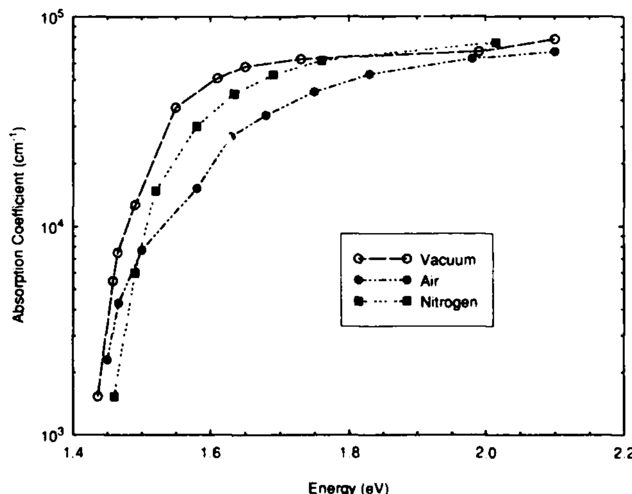

Fig. 2. α *vs.* $h\nu$ for the CdTe produced by annealing repeated Te/Cd stacks in N_2, in vacuum and in air.

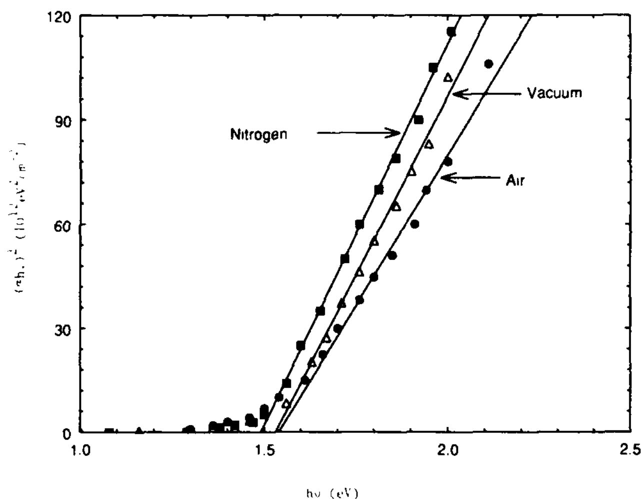

Fig. 3. $(\alpha h\nu)^2$ *vs.* $h\nu$ for the CdTe produced by annealing repeated Te/Cd stacks in N_2, in vacuum and in air.

for the layers synthesized in vacuum it was 0.47° and for the layers synthesized in air it was 0.29°. It is apparent that single-phase, sphalerite structure CdTe was produced for the layers synthesized in the N_2 and vacuum environments, whereas extra peaks caused by the formation of oxides (in particular $CdTeO_3$) are present for the layers synthesized in air.

To increase the grain size, the CdTe samples were dipped into solutions of $CdCl_2$ in methanol or $CdCl_2$ and $CuCl_2$ in methanol and then annealed at 450 °C in air. The grain size was increased to over 1 μm as shown in Fig. 4(b) and the FWHM of the (111) X-ray diffraction peak was reduced to 0.21° (Fig. 5(d)). Such a heat treatment was also found to convert the CdTe samples from n-type to p-type with a nett acceptor concentration up to 10^{16} cm^{-3}.

Solar cells were produced by depositing the Cd/Te stacks onto CdS layers which had been thermally evaporated onto indium-tin-oxide (ITO)-coated glass slides, and the structure annealed in N_2 at 450 °C for 15 min to synthesize the CdTe. The structure was then dipped into the $CdCl_2$/methanol solution or the $CdCl_2/CuCl_2$/ methanol solution, the solution allowed to dry and then colloidal graphite (containing Cu) painted over the layer to form a back contact. The most promising solar cell efficiencies have been obtained by annealing the structure in air at 450 °C for 1 min. Using the $CdCl_2$/ methanol solution, a V_{oc} of 0.68 V, a J_{sc} of 11 mA cm^{-2} and a fill factor of 0.35 have been achieved. The value of V_{oc} obtained indicates that the CdS–CdTe interface is satisfactory, but the fill factor and J_{sc} are both approximately half the best results obtained for CdS/ CdTe solar cells [1, 6]. Detailed studies of the junction [10] indicate that the back contact is rectifying and that the series resistance of the device is too high. More

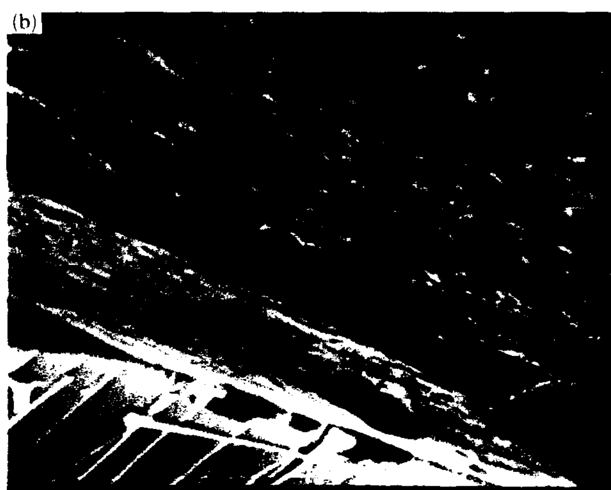

Fig. 4. (a) Scanning electron microscopy (SEM) image of a layer produced by annealing a Te/Cd stack in N_2 at 450 °C for 15 min. (b) SEM image of a layer produced by annealing a Te/Cd stack in N_2 followed by the $CuCl_2/CdCl_2$/methanol heat treatment—plan view. (c) SEM image of a layer produced by annealing a Te/Cd stack in N_2 followed by the $CuCl_2/CdCl_2$/methanol heat treatment—side view.

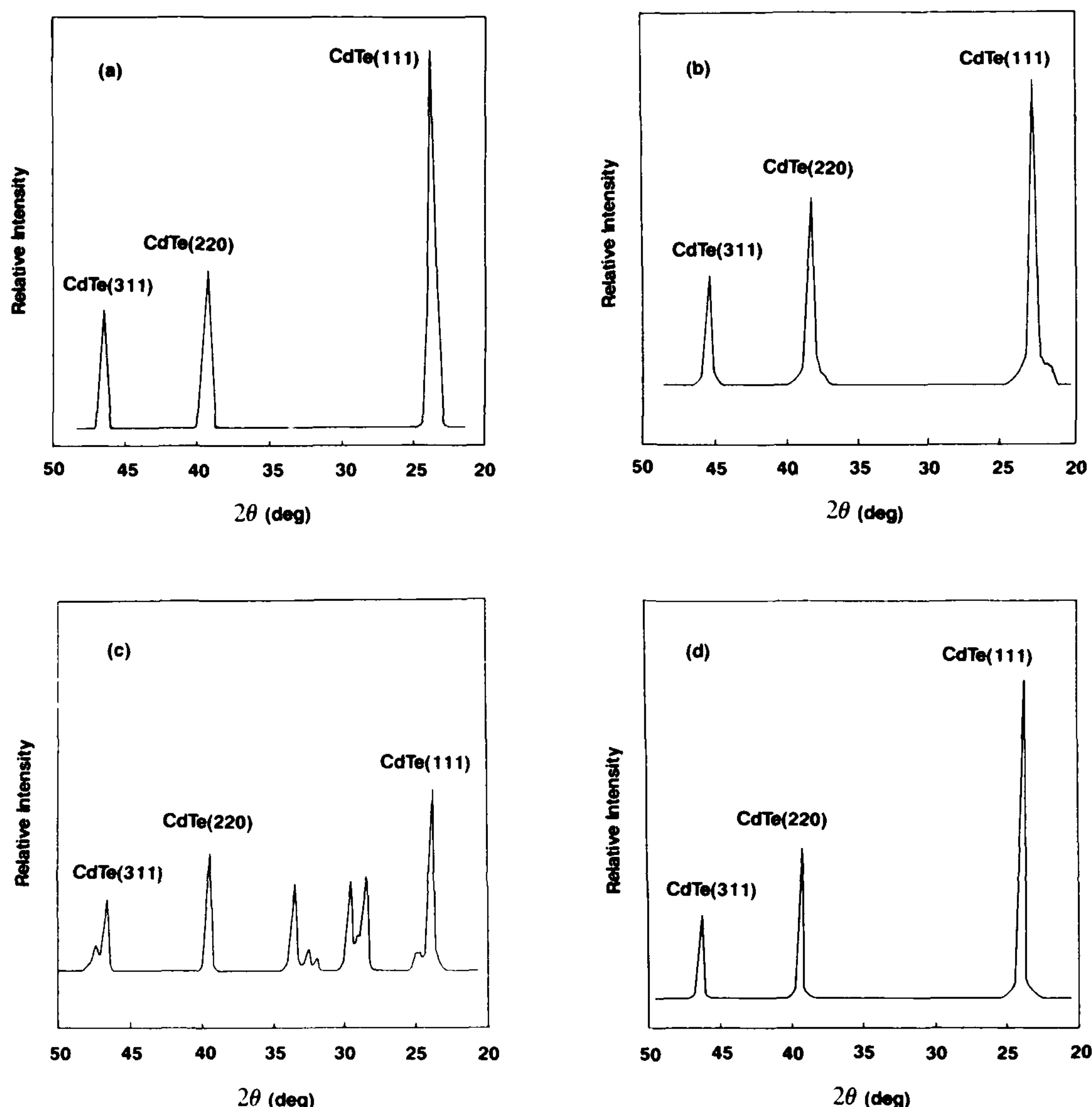

Fig. 5. X-ray diffraction data for the CdTe produced by annealing repeated Te/Cd stacks in (a) N_2, (b) vacuum, (c) air and (d) after synthesis by annealing in N_2 followed by the $CuCl_2/CdCl_2$/methanol heat treatment [FWHM of (111) peak: (a) 0.42°, (b) 0.47°, (c) 0.29° and (d) 0.21°].

extensive experimentation with the back contact and with the doping of the CdS and CdTe deposited will improve further J_{sc} and the fill factor.

4. Energy analysis

Energy analysis is a widely used technique for determining the energy flows in industrial processes, and allows the calculation of the required energy input for unit output of product. In this case unit output is defined in terms of area (*i.e.* 1 m^2 of module area) and a linear production sequence is assumed. This allows the sequence to be broken down into the individual process steps for which the primary energy inputs are determined. The energy input for the whole sequence is obtained by the summation of the inputs for each step. The energy analysis described in this paper conforms to IFIAS Convention Level 3 [11] which includes the inputs from process energy, material input and takes into consideration the energy content of the capital equipment required. These factors are embodied in the three quantities: process, materials and machine energy requirement [12]. The energy used to perform each process step is referred to as the process energy. The materials energy is the amount of energy consumed in manufacturing the materials which appear in the finished product. The machine energy is the energy consumed in the manufacture of the production equipment used in each step.

The production sequence studied in this paper is based on thin film modules produced using SEL CdTe as the absorber material. This preliminary work was done using the following assumptions. Energy values for a particular process step were calculated assuming maximum throughput per machine, based on cycle time, and for continuous three shift operation for 300 days per year. Clearly, in a true production facility, some machines will be operating below maximum capacity to eliminate backlogs in any particular area. Therefore, the energy values were corrected assuming an annual production of 100 000 m^2 of modules meeting the required specification. This involved corrections for reduced throughput for some process machines and for cumulative process yields. Any output not reaching the required standard and, therefore, not proceeding to the next stage of the production sequence, was assumed to be discarded at no energy cost, due to waste disposal, or energy benefit, due to recycling. A conversion factor of 1 kWh(e) = 4 kWh(t) has been used throughout.

Table 1 describes the individual process steps which were considered and also gives the energy requirement for each process step and as a percentage of the total energy requirement. It can be seen that the production steps requiring the greatest energy input are the deposition of the absorber and window materials and the materials requirement of the front and back glass. As the absorber and window materials are both produced by thermal evaporation, the major part of the energy requirement for both steps is due to process energy. If the deposition rates could be improved then this would greatly reduce the process energy and thus the energy requirement of these steps. The machine energy requirement is also slightly higher because vacuum equipment is being used. It should be possible to replace at least one of the sheets of glass with a material which has a lower energy content and this would also reduce the energy requirement of the module.

The energy requirements in Table 1 can be used to give energy payback times and energy ratios for the technology under investigation. These values are shown in Tables 2 and 3, respectively, for a range of isolation levels, cell efficiencies and cell lifetimes. We can see from Table 2 that the energy payback times are very encouraging and, even for modules in operation in Northern Europe with an efficiency of only 10%, the energy payback time is only about 18 months. From the energy ratios for operation in Southern Europe given in Table 3, we can see that the cells are nett producers of energy and that they all have energy ratios greater than 10 which is the standard criterion for the viability of energy sources. These results compare well with similar studies carried out on other thin film technologies [13].

It should be recognized that some of the techniques considered in this analysis have only been proven on a laboratory scale so this does not allow an accurate determination of all the process parameters for large scale production. However, this analysis can be used to compare techniques and steps within various techniques and also to determine the most sensitive process parameters in the production technology in terms of energy requirement. Provided that the accuracy limitations of such analyses are recognized and that the

TABLE 1. Breakdown of process steps and derived energy requirement for thin film CdTe/CdS module production

Process step	Description	Energy requirement ($kWh\ m^{-2}$)	Per cent of total
Front glass	Float glass 3 mm thick	70.61	20.8
Cleaning	Solvent clean	1.38	–
Deposition of front contact	ITO, magnetron sputter	3.32	0.4
Deposition of window layer	CdS, CBD, followed by thermal evaporation	68.01	20.0
Deposition of CdTe	SEL thermal evaporation, annealing, etching	73.86	21.7
Deposition of back contact	Cu/Mo, magnetron sputter	9.4	2.8
Patterning and encapsulation		20	5.9
Back glass	Float glass 3 mm thick	51.31	15.1
Edging	Aluminium	41.74	12.3
Total energy requirement		339.63	100.0

TABLE 2. Energy payback times (in years)

Insolation ($kWh\ m^{-2}$ per day)	Efficiency (%)			
	10	12	15	20
5	0.62	0.52	0.41	0.31
3	1.03	0.86	0.69	0.52
2	1.55	1.29	1.03	0.78

TABLE 3. Energy ratios for operation in southern Europe

Lifetime (years)	Efficiency (%)			
	10	12	15	20
10	9.7	11.6	14.5	19.3
15	14.6	17.4	21.7	29.0
20	19.4	23.1	29.0	38.7

assumptions involved are clearly stated, energy analysis can be used at an early stage of a research programme to identify issues which could restrict competitiveness and therefore require attention. The analysis can be used to feed back information on which materials or processes are energy or cost intensive or have the potential to be so.

5. Environmental issues of CdTe

Energy sources are significant contributors to local and global environmental pollution. The costs for repairing or reversing damages inflicted on the environment and human health are neither represented in the energy industry's calculations nor are they reflected in the consumer's energy price.

To quantify environmental costs associated with photovoltaics/CdTe requires a complete analysis of its life cycle. This means that all stages, from the initial mining of raw materials to waste disposal and/or recycling ("from cradle to grave"), have to be assessed according to the material and energy input as well as the emissions, burdens and multiple environmental impacts. The linkages between a particular energy technology and the associated externalities are shown in Fig. 6.

During operation, CdTe modules can leak Cd into the environment if they are broken or subjected to high temperatures, but they pose little hazard, because broken modules would be replaced quickly in routine maintenance. A fire in a building clad with CdTe modules could pose some hazard, although, for small areas, the hazard would be significant only for those being so close to the fire as to suffer far greater hazards from smoke and flames. A large building clad with CdTe modules, however, could emit Cd vapour—turning to CdO dust—into the smoke plume. According to a study by Moskowitz *et al.* [14], standard fire-safety procedures would protect the population from this Cd hazard.

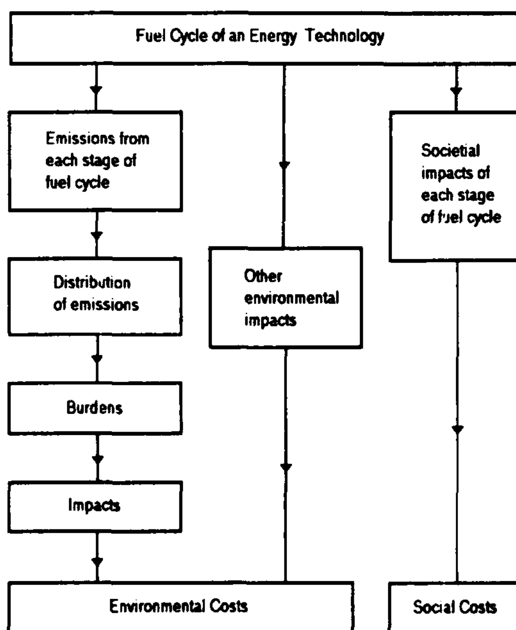

Fig. 6. Linkage between fuel cycle and external cost.

Emissions of CdO dust in the refining stage, emissions of Cd during manufacture and possible leaching of Cd into the ground water from modules discarded at the end of their working life present hazards to personnel and the population close to photovoltaic manufacturing plants. The waste Cd and Te from the manufacturing plant can be economically recycled and emissions reduced to very small levels even for a 100 MW per year production rate. In all these cases, the monitoring and control strategies are well established in existing industries where Cd is used, and no additional problems can be foreseen for photovoltaic manufacture.

Disposal of CdTe modules may need to be controlled more strictly than, for example, CIS, and recycling of materials is important both for environmental reasons and for the value of the Cd and Te. The technological problems associated with this recycling appear to be readily solvable at low cost. Hazardous emissions from CdTe and other various different types of solar cells are summarized in Table 4.

It is interesting to note that the amount of Cd contained in the CdTe modules needed to generate energy of say 1 GWh over their lifetime is about equal to the Cd emitted from the smoke-stack of a typical coal-fired station while generating the same 1 GWh of electrical

TABLE 4. Hazardous emissions from photovoltaics

Material	Production	Operation	Disposal
Silicon	Silica dust Silanes Diborane Phosphene Solvents		
Copper indium diselenide	Hydrogen selenide Cadmium oxide Cadmium dust Selenium Solvents	Cadmium Selenium (In a fire)	Cadmium Selenium (If not recycled)
Cadmium telluride	Cadmium oxide Cadmium dust Tellurium Solvents	Cadmium Tellurium (In a fire)	Cadmium Tellurium (If not recycled)

There is an energy input to all technologies derived from the fuel mix of the nation producing the photovoltaic.

energy. Very little of the Cd would be lost into the environment, so the photovoltaic plant is cleaner, even for Cd emissions, than a coal-fired power station [15].

Photovoltaic/CdTe systems are almost entirely benign in operation, because potential environmental hazards occur at the production and disposal stages.

6. Conclusions

Thin films of CdTe (with thicknesses of more than 1 μm) have been produced by annealing elemental stacks of Cd and Te in N_2, vacuum and air. Annealing in the N_2 and vacuum environments produced single-phase, sphalerite structure CdTe but with small grains, whereas annealing in air produced larger grains but the films were not single phase. Even for the air annealing, the grain size was too small (under 0.5 μm) to make good solar cells.

Post-synthesis heat treatments using $CdCl_2$/methanol and $CdCl_2$/$CuCl_2$/methanol have been developed to improve the grain size and the preliminary measurements of V_{oc}, J_{sc} and the efficiency of the solar cells produced using the CdTe with enhanced grain size are promising. Further optimization of the post-synthesis annealing and further optimization of the CdS window layer and the back contact to the device should further improve the efficiency. This technique has the potential for reproducible, large area in-line production with minimum material usage and is flexible in that, for example, sputtering or electrodeposition could be used as alternative methods for depositing the Cd/Te stacks rather than the thermal evaporation method used here.

Preliminary energy analysis has been used to identify the steps in the production sequence that are the most energy intensive. It has been shown that CdTe thin film modules produced using SEL processing could have very good energy ratios and energy payback times that would be competitive with other thin film technologies.

The major environmental hazard associated with the use of CdTe/CdS cells will be at the production and disposal stages. Controlled disposal of modules will be the key to the acceptance of the wider use of such technology for power generation.

Acknowledgment

This work was supported by the Commission of the European Communities under Contract JOUR-0065-C (MB).

References

1 A. K. Turner, J. M. Woodcock, M. E. Ozsan and J. G. Summers, in A. Luque, G. Saler, W. Palz, G. Don Santos and P. Helm (eds.), *Proc. 10th EC Photovoltaic Solar Energy Conf., Lisbon, 1991*, Kluwer, 1991, p. 791.

2 D. Bonnet and M. Rabenhorst, in W. Palz, G. T. Wrixon and P. Helm (eds.), *Proc. 9th IEEE Photovoltaic Specialists Conf., 1972*, Kluwer, 1989, p. 129.

3 I. Clemminck, M. Burgelman, A. Vervaet and J. De Poorter, in A. Luque, G. Saler, W. Palz, G. Don Santos and P. Helm (eds.), *Proc. 10th EC Photovoltaic Solar Energy Conf., Lisbon, 1991*, Kluwer, 1991, p. 577.

4 N. Romeo and V. Canevari, *Thin Solid Films, 143* (1986) 193.

5 M. Y. Simmons, M. M. Al-Allak, K. Durose and A. W. Brinkman, in A. Luque, G. Saler, W. Palz, G. Don Santos and P. Helm (eds.), *Proc. 10th EC Photovoltaic Solar Energy Conf., Lisbon, 1991*, Kluwer, 1991, p. 570.

6 J. Sharp, Y. Koskinen, S. Lindfors, A. Rautiainen and T. Suntolu, in A. Luque, G. Saler, W. Palz, G. Don Santos and P. Helm (eds.), *Proc. 10th EC Photovoltaic Solar Energy Conf., Lisbon, 1991*, Kluwer, 1991, p. 567.

7 M. J. Carter, I. I'Anson, A. Knowles and R. Hill, *Proc. 19th IEEE Photovoltaics Specialists Conf., New Orleans, LA, 1987*, IEEE, New York, 1987, p. 1275.

8 S. Arshed, *PhD Thesis*, Newcastle Polytechnic, 1989.

9 M. T. Bhatti, E. P. Groarke, R. W. Miles, M. J. Carter and R. Hill, in A. Luque, G. Saler, W. Palz, G. Don Santos and P. Helm (eds.), *Proc. 10th EC Photovoltaic Solar Energy Conf., Lisbon, 1991*, Kluwer, 1991, p. 574.

10 M. T. Bhatti, K. M. Hynes, A. E. Baumann, R. W. Miles, M. J. Carter and R. Hill, in L. Guimares, W. Palz and P. Helm, *Proc. 11th EC Photovoltaic Energy Conf., Montreux, October 1992*, Kluwer, 1992, to be published.

11 I. Boustead and G. F. Hancock, *Handbook of Industrial Energy Analysis*, Ellis Horwood, Chichester, 1979, p. 184.

12 K. M. Hynes, N. M. Pearsall and R. Hill, in A. Luque, G. Saler, W. Palz, G. Don Santos and P. Helm (eds.), *Proc. 10th EC Photovoltaic Solar Energy Conf., Lisbon, 1991*, Kluwer, 1991, p. 461.

13 K. M. Hynes, N. M. Pearsall and R. Hill, *Proc. 22nd IEEE Photovoltaic Specialists Conf., Las Vegas, NV, 1991*, IEEE, New York, 1991, to be published.

14 P. D. Moskowitz, K. Zweibel and V. M. Fthenakis, Health and safety and environmental issues relating to cadmium usage in PV energy systems, *SERI/TR 211-3621*, 1990.

15 A. E. Baumann and R. Hill, in H. Connor-Lajambe (ed.), *Proc. OECD/IEA Workshop on Life-Cycle Analysis: Methods and Experience, Paris, May 1992*, Paris, 1992.

Potentiality of photorefractive CdTe

J. Y. Moisan, P. Gravey, G. Picoli, N. Wolffer and V. Vieux
Département Technologies Appliquées à la Connectique, Centre National d'Etudes des Telecommunications, BP40, 22301 Lannion (France)

Abstract

For optical telecommunication networks, optical switching is now being studied. Different solutions have been proposed (integrated optics, free space switching, etc.), and reconfigurable optical interconnects, based on phase conjugation, should be one interesting method. For example, some results have been obtained with a double-phase conjugated mirror configuration, allowing reconfigurable connection between single-mode optical fibres. These phase-conjugated optics use photorefractive crystals and the first demonstration has been given using $Bi_{12}TiO_{20}$ photorefractive crystals. In a telecommunication network, semiconductive crystals with a good efficiency in the near-IR wavelength are needed. Our first experiments were carried out with InP:Fe crystals at 1.3 μm.

However, it is well known, from published studies, that II-VI materials are, in principle, more interesting for the following reasons. The electro-optic coefficient is higher (and therefore the figure of merit is higher). The solubility of dopants is higher (and therefore the space charge electric field, which modulates the refractive index of the material, may be higher). Next we tested a CdTe:V crystal and, in a two-wave mixing experiment without an external electric field, an amplification gain was observed and a high photosensitivity demonstrated at 1.3 μm.

In this paper, we shall describe the photorefractive effect and explain our choice of the CdTe:V crystal, taking into account the parameters of this photorefractive effect and some other parameters required by the applications in the optical beam steering field. Next the results will be given, and finally an optical configuration using phase conjugation will be presented as an example of application.

1. Introduction

For optical telecommunication networks, optical switching systems are now under study, and some systems using integrated optics have been proposed, but a spatial holographic interconnect is also an attractive solution for the switching of high bit rate channels. Holographic gratings can be used to steer the optical beams, emerging from an input matrix of single-mode optical fibres to an output matrix of single-mode optical fibres. Two characteristics have to be fulfilled in such a system: it must be active at the telecommunication signal wavelength, *i.e.* 1.3 and 1.5 μm, and it must manage as large a number of channels as possible.

Photothermoplastic devices have been proposed [1] and, in such an optical configuration, two recording beams are used in the visible range (their wavelengths depending on the sensitivity of the recording material) and the reading beams, at 1.3 or 1.5 μm, are deflected by the recorded gratings. In this case, the photothermoplastic device is not sensitive to the signal wavelength.

With photorefractive materials, it is possible to imagine an optical system where the signal beam is active itself. Thus, in two-wave mixing (TWM) experiments which are commonly used to estimate the properties of photorefractive crystals, one can consider that the studied material is active to the wavelength used. In an optical switching system used in an optical network, it is essential that the photorefractive crystals are sensitive to the telecommunication wavelengths; this is the first requirement. The second requirement, concerning aberrations in optical configurations, is that the single-mode fibres could be used as an input and output signal source, with little loss.

In this paper, first the photorefractive effect will be presented and the properties discussed. Next we shall explain why the CdTe crystal is an interesting photorefractive material and the first results will be given. Finally an optical configuration will be proposed as an example, which could be considered as a first step of a beam-steering system.

2. Photorefractive effect: properties

The photorefractive effect, which can be described as the combination of two properties, namely photoconductivity and electro-optic effect, is explained in Fig. 1. Two interfering beams are focused on the crystal; so carriers are photogenerated in the

0921-5107/93/$6.00

© 1993 - Elsevier Sequoia. All rights reserved

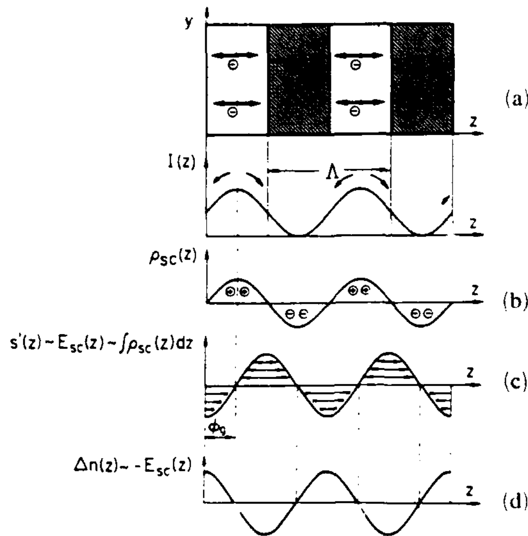

Fig. 1. (a) Illuminating energy, following the interference pattern on the crystal, and generation of carriers. (b) Inside density of carriers. (c) E_{SC}, space charge field built up by the carrier density. (d) Index modulation created in the crystal and phase shifted from the interference pattern.

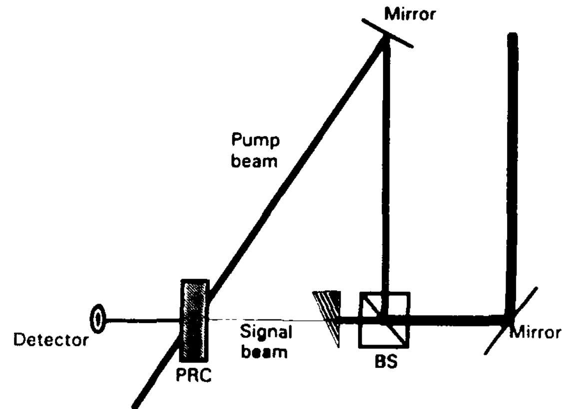

Fig. 2. Two-beam coupling configuration: PRC, photorefractive crystal; BS, beam splitter.

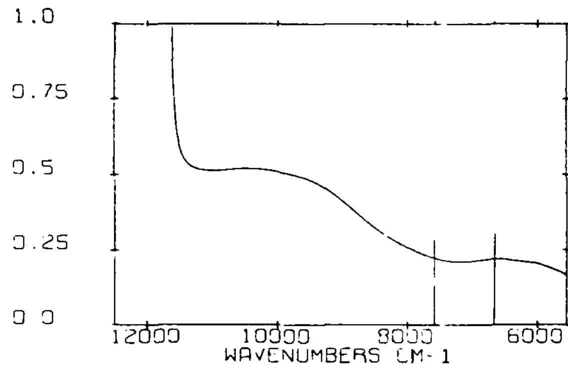

Fig. 3. Absorption spectrum of CdTe:V. The ordinate is absorbance. The thickness was 5 mm. 1.3 and 1.5 μm wavelengths indicated by vertical lines.

illuminated zones of the material. These carriers diffuse into the non-illuminated zones where they are trapped, and then a non-homogeneous density of carriers reproduces the interference pattern. Because of the modulated density of trapped carriers, a space charge field occurs, which is phase shifted by $\pi/2$ from the interference pattern. When the electro-optic coefficient of the crystal is no longer negligible, a modulation of the refractive index can then be observed. So, a phase grating shifted from the recording interference pattern can be read from the recording beams themselves or from a reading beam at a wavelength not active for the material.

The basic equation which describes the index modulation Δn in the crystal is

$$\Delta n = \tfrac{1}{2} n^3 r_{41} E_{SC} \qquad (1)$$

where n is the refractive index, r_{41} the electro-optic coefficient depending on the crystal orientation and E_{SC} the space charge field.

The most commonly used optical experiment for studying the photorefractive behaviour of materials is TWM, and the configuration for this is shown in Fig. 2. Two beams interfere on the crystal: one—the pump beam—with a higher energy than the other—the signal beam. Because of the grating recorded inside the crystal, the pump beam "sees" this index grating and part of its energy is deflected in the signal beam direction; if this deflected energy is higher than the losses due to signal beam absorption and the deflected energy of the signal beam, an amplification gain can be measured with the detector. Note that, in this case, the two beams are active and are used as recording and reading beams. From eqn. (1), it is clear that n and r_{41} are the intrinsic properties of the crystal and depend only on the chosen material and for a given wavelength and that E_{SC} depends on the experimental parameters (and also on the crystal), briefly listed below.

2.1. Carriers photogeneration quantum yield and wavelength sensitivity range

The absorption of a CdTe:V crystal (from R. Triboulet, CNRS, Bellevue) is reported in Fig. 3. It is clear that the semiconductive crystals can be used only at wavelengths corresponding to lower energies than the band gap, where the crystals are sufficiently transparent. In Fig. 3, the 1.3 and 1.5 μm wavelengths are indicated by vertical lines, and a residual absorption, which is said to come from doping agent vanadium, is observed. A similar spectrum has been published [2] for ZnTe:V, and also the photoconductivity studied in this way; the formation time of the holographic grating was measured by following the total intensity of the two beams. It clearly appears that the formation time obeys

the same law as the photocurrent in the material. This means that the photorefractive effect is linearly related to the photogeneration quantum yield. Therefore one can expect from the spectrum in Fig. 3 that CdTe:V will be sensitive to the 1.3 and 1.5 μm wavelengths, which has already been demonstrated [3]. So, two aspects have to be emphasized: the generation quantum yield governs the response time of the material, but the number of trapped carriers will govern the space charge field.

2.2. Trapping level in the photorefractive crystal

Because it comes from the trapped-carrier density, a large space charge field will be observed in two conditions: when the carriers are trapped in deep traps, and when the number of traps is large. For II–VI crystals, it is well known [4] that doping with vanadium, titanium or nickel can induce deep levels, especially in CdTe and ZnTe.

The doping solubilities are larger in II–VI material than in III–V [5]. This means that the photocurrent will be larger and the response time shorter but, above all, that the number of trapped carriers will be larger and, as a consequence, the space charge field larger.

2.3. Space charge field limits

Consider now, in Fig. 1, the diffusion of carriers; when some of them are trapped in the dark zones, the space charge field begins to increase. However, a conduction current in the opposite direction appears, and equilibrium will limit the space charge field when the conduction current becomes equal to the diffusion current. In these conditions, the electric field inside the crystal can be written

$$E_{SC} = \frac{2\pi}{\lambda} \frac{k_B T}{e} \tag{2}$$

where λ is the wavelength used, k_B the Boltzmann constant and T the temperature. Different solutions have been proposed to exceed this limit.

(1) A continuous electric field is applied to the crystal [6], but the phase shift between the interference pattern and the electric field modulation must be preserved. So another limit will now appear

$$E_{SC} = \frac{e\Lambda N_A}{2\pi\varepsilon\varepsilon_0} \tag{3}$$

where Λ is the grating period, N_A the number of effective traps and ε the dielectric constant of the material. Following the grating period, the effective limit can come from the resistivity of the material, limiting the external applied electric field, especially in semiconductive crystals. To avoid too large a dark current, highly resistive materials are needed (10^8–10^9 Ω cm).

(2) Two other solutions have been proposed to exceed the limit in eqn. (3): (a) an applied d.c. field and a moving grating [7]; (b) an applied a.c. electric field, of sinusoidal or square wave nature [8]. However, the same requirement of high resistivity is needed for both these conditions.

(3) Note that resonance mechanisms have also been proposed to increase the gain in the TWM experiment: a Franz–Keldysh effect near the band gap [9], and an intensity-dependent resonant behaviour depending on the temperature of the material [10].

3. Materials and results

In eqn. (1), n and r_{41} are intrinsic parameters of the chosen material. Different photorefractive materials are compared in Table 1. n^3r can be used as a valuable figure of merit, because its value is the effective parameter that one has to take into account. Some points, from Table 1, have to be emphasized.

(1) The largest electro-optic coefficients were measured for the oxide or organic crystals, but unfortunately they are not sensitive enough in the near-IR range.

(2) Because the refractive index occurs as n^3 in the figure of merit, interest in organic materials is reduced; in III–V crystals, n^3 is about twice that in CdTe.

(3) Of the semiconductive crystals, CdTe:V has the largest electro-optic coefficient and therefore the largest figure of merit. Values about the same [3] were measured at 1.06 and 1.5 μm.

Now two comments should be noted.

(a) The comparison between InP:Fe and CdTe:V seems to apply more generally to comparison between III–V and II–VI crystals; for example GaP ($n^3r = 44$ at 0.54 μm) to ZnTe ($n^3r = 133$ at 0.59 μm) have approximately the same n^3r ratio as InP:Fe to CdTe:V.

TABLE 1. Figures of merit of photorefractive materials where the r values are r_{41} for the crystals, except for organic materials

Material	n	r (pm V^{-1})	n^3r (pm V^{-1})	λ (μm)
$LiNbO_3$	2.26	31	360	0.633
$BaTiO_3$	2.36	1640	21500	0.546
$Bi_{12}SiO_{20}$	2.54	5	82	0.633
$Bi_{12}GeO_{20}$	2.55	3.5	58	0.633
GaAs:EL2	3.48	1.43	60	1.06
GaAs:Cr	3.5	1.2	51	1.06
InP:Fe	3.29	1.34	48	1.06
CdTe:V	2.82	5.5	123	1.06
CdTe:V	2.82	5.5	120	1.52
Polymer	1.56	2.5	9.5	0.514
Organic crystal	1.7	24	118	0.676

(b) When an external electric field is applied, n^3r/ε can be taken as a figure of merit. Because ε is slightly smaller in II–VI than in III–V materials, this new figure of merit is more advantageous for II–VI than the previous figure of merit. However, it should be noted that highly resistive crystals are always needed.

Because the figures of merit are well known, II–VI materials have already been tested and the photorefractive properties have been published for CdTe:V [3, 11] and ZnTe:V [12]. The picosecond response of the semiconductive materials shows again [13] that CdTe:V is the most sensitive material in the near-IR range. We carried out some experiments on a CdTe:V crystal, received from R. Triboulet (CNRS, Bellevue) and the results are shown in Figs. 4 and 5. The absorption spectrum of this crystal was reported in Fig. 3. All the measurements were carried out with a 1.32 μm wavelength laser, at room temperature, without an applied electric field. A TWM configuration is used and Γ, the amplification gain, is measured.

In Fig. 4, Γ is plotted against the total incident energy and one can see that the Γ maximum is obtained at about 1 mW cm^{-2} (the grating period was 1.72 μm). The plotted curve is calculated from the equation

$$\Gamma = \frac{\Gamma_0}{1 + I_d/I} \qquad (4)$$

where Γ_0 is the maximum Γ (here 0.105 cm^{-1}), I the irradiance used and I_d the irradiance at which the photoconductivity equals the dark conductivity (here 40 μW cm^{-2}). The same sensitivity was observed at 1.5 μm [3]. In Fig. 5, Γ is plotted against β (I_p/I_s) (where I_p is the pump beam intensity and I_0 the signal beam intensity). The grating period was always 1.72 μm. In the best conditions ($\beta \approx 50$, $I_{total} > 10$ mW cm^{-2} and the grating period is about 2 μm), the largest Γ obtained was about 0.15 cm^{-1}.

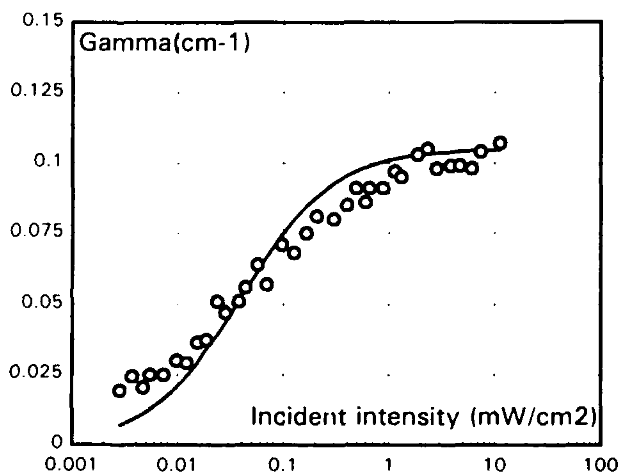

Fig. 4. Amplification gain, for a CdTe:V crystal in TWM experiment, against incident intensity, at 1.32 μm wavelength, without an external electric field, at room temperature. The grating period was 1.72 μm and the ratio of the pump beam intensity to the signal beam intensity was 40.

It seems that, in this first attempt, the vanadium content is low compared with other published results; by improving the physicochemical parameters, 0.6–1 cm^{-1} should be possible. However, it should be noted that the best result with InP:Fe crystals was around 0.15 cm^{-1}, without an external electric field [14].

4. Applications

Photorefractive crystals can be used as signal amplifiers, when high amplifications gains are obtained. Perhaps the most promising applications will use phase conjugation. As an example, an optical configuration, based on a double-phase conjugated mirror (DPCM) will now be discussed. A DPCM is observed when a common grating occurs as a result of two incoherent beams of light, and when the gain Γ measured in the TWM experiment is sufficiently high. Two other beams are now diffracted which are the complex conjugates of the opposite beams. In Fig. 6, the DPCM effect is sketched. This effect has been demonstrated with $Bi_{12}GeO_{20}$ [15] at 633 nm and the condition has been defined as

$$\Gamma L_0 \geqslant 4 \qquad (5)$$

where L_0 is the interaction length in the crystal. A DPCM was also observed with InP:Fe at 1.06 μm [11]. This effect is found when the two interacting beams have the same wavelength. When the wavelengths are slightly different, a double-colour pumped oscillator now results and this effect was also observed [16] with

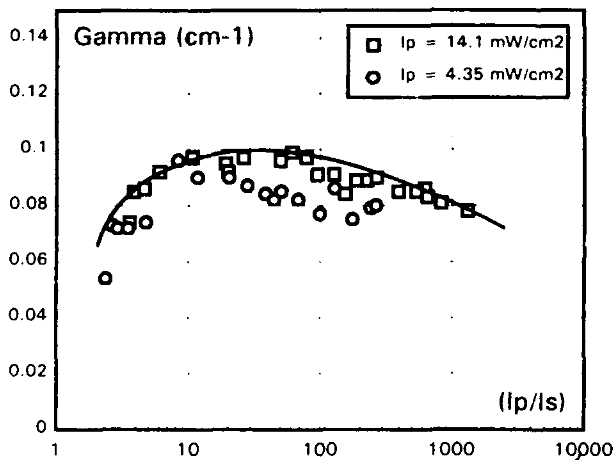

Fig. 5. For the same crystal as in Fig. 4, amplification gain against β, the ratio of the pump beam intensity to the signal beam intensity. The inset indicates the total intensities in the two runs. The other conditions were not changed.

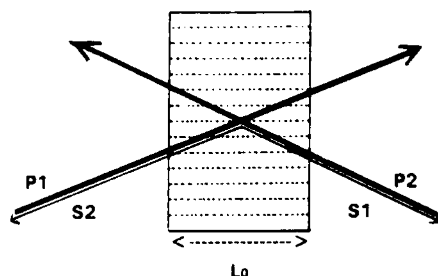

Fig. 6. Optical sketch of a DPCM: two incoherent beams P1 and P2 act as pump beams, and S1 and S2 are diffracted in the opposite direction when the condition (5) is fulfilled.

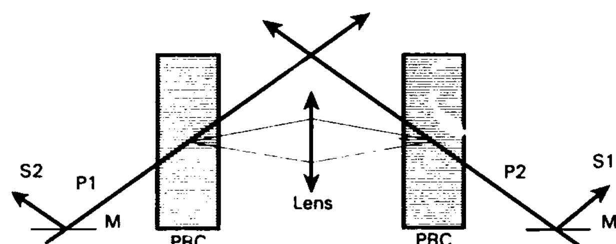

Fig. 7. Optical configuration of a two-face DPCM: PRC, photorefractive crystal; P1, P2, the incoherent beams (from single-mode fibres); M, semitransparent mirrors used to analyse the diffracted beams S1 and S2. When $Bi_{12}GeO_{20}$ is used as the photorefractive crystals and P1 and P2 are beams of wavelength 633 nm, up to 40% of the pump beam intensity can be focused into the output single-mode fibre.

InP:Fe for the pairs of wavelengths 985 and 1047 nm, and 1.06 and 1.32 μm. The law in eqn. (5) is obeyed by $Bi_{12}GeO_{20}$ at 633 nm and by InP:Fe at 1.06 and 1.32 μm. If one considers now the electro-optic coefficients and the figure of merit in Table 1, it is clear that a DPCM would be observed with CdTe:V at 1.32 μm and, above all, at 1.5 μm.

From Fig. 6, one can imagine a spatial interconnect between optical fibres emitting the P1 and P2 beams and receiving the diffracted S2 and S1 beams respectively. In fact, the diffracted beams are not focused on the sources P1 and P2 but are diffracted in conical shape; so a simple interconnect is not allowed in this way. A two-face DPCM has been proposed [17], and the optical configuration is sketched in Fig. 7. The first experiment has been carried out with two $Bi_{12}GeO_{20}$ crystals, with an applied electric field. The two 633 nm pump beams are collimated beams emerging from single-mode optical fibres. The diffracted beams are collimated into the same optical fibres and up to 40% of the incident intensity from pump beams can be focused into the opposite optical fibre. In this way, an optical connection is established between two optical single-mode fibres.

Now, if a third optical fibre is "activated" (with a third He–Ne laser) and another beam, close to P2 for example, is used, a new connection is established between the first and the third optical fibres. The optical interconnect has been reconfigured: such an optical configuration can be considered as the first step of an optical reconfigurable interconnect system. Because the conditions in eqn. (5) are fulfilled here by the crystals, this optical function can be used with $Bi_{12}GeO_{20}$ at 633 nm. Depending on the sensitivity of the material, other wavelengths could be attained when eqn. (5) is obeyed and especially by CdTe:V at 1.5 μm.

5. Conclusion

In an optical telecommunication network, near-IR wavelengths are used as a signal propagation support. To achieve a reconfigurable spatial interconnect as a switching system, phase conjugation could be a suitable solution. We have demonstrated that a DPCM, using phase conjugation in photorefractive crystals, could be an interesting answer.

However, this demonstration was carried out at a 633 nm wavelength with $Bi_{12}GeO_{20}$ crystals, satisfying conditions on gain amplification of optical signal beams into the material. Because of its wavelength range sensitivity, the higher values of figures of merit of II–VI materials compared with other semiconductive crystals, and the possibility of obtaining highly resistive material, one can support the idea that such optical configurations could be achieved with CdTe:V crystals. The first experiments carried out on this material gave us the expected values of gain amplification compared with the other semiconductive crystals.

References

1 P. Gravey and J. Y. Moisan, *Proc. Soc. Photo-Opt. Instrum. Eng., 1507* (1991) 239–246.
2 M. Ziari, *Appl. Phys. Lett., 60* (9) (1992) 1052.
3 A. Partovi, *Appl. Phys. Lett., 57* (9) (1990) 846.
4 J. M. Langer, *Phys. Rev. B, 38* (11) (1988) 7723.
5 W. Giriat and J. K. Furdyna, *Semiconductors and Semimetals*, Academic Press, Vol. 25, 1988.
6 N. V. Kukhtarev, *Ferroelectrics, 22* (1979) 949.
7 G. C. Valley, *J. Opt. Soc. Am. B, 1* (1984) 868.
8 S. I. Stepanov and M. P. Pettov, *Opt. Commun., 53* (1985) 292.
9 A. Partovi and E. Garmire, *J. Appl. Phys., 69* (10) (1991) 6885.
10 G. Picoli, P. Gravey, C. Ozkul and V. Vieux, *J. Appl. Phys., 66* (8) (1989) 3798.
11 R. B. Bylsma, *Appl. Phys. Lett., 51* (12) (1987) 889.
12 M. Ziari, *Appl. Phys. Lett., 60* (9) (1992) 1052.
13 G. C. Valley, *Opt. Lett., 14* (17) (1989) 961.
14 V. Vieux, P. Gravey, N. Wolffer and G. Picoli, *Appl. Phys. Lett., 58* (25) (1991) 2880.
15 N. Wolffer, *Opt. Commun., 73* (5) (1989) 351.
16 N. Wolffer, *Opt. Commun., 89* (1) (1992) 17.
17 N. Wolffer, V. Royer and P. Gravey, *IIème Symp. Franco-Israélien sur l'Optique Non-linéaire, Port-Barcares, May 25–29, 1992.*

Materials Science and Engineering, B16 (1993) 262–267

Deep centres for optical processing in CdTe

E. Rzepka, Y. Marfaing, M. Cuniot and R. Triboulet
Laboratoire de Physique des Solides de Bellevue, 1 Place A. Briand, F92195 Meudon Cedex (France)

Abstract

The characteristics of defect and impurity centres which introduce near-mid-gap localized levels in CdTe are reviewed. Attention is focused on the 0.8–0.9 eV energy depth range corresponding to the wavelength range of optical telecommunications. The most appropriate centres are deep donors of group IV (tin, germanium) and transition metals (either deep donors (titanium, vanadium) or a deep acceptor (nickel)).

1. Introduction

There is increasing interest in the utilization of semiconductors as active media for applications in the field of optical processing. Non-linear optical phenomena near the band edge—preferably within quantum structures—are being extensively studied. In addition, extrinsic excitation from localized deep centres gives rise to particular effects, such as the photorefractive effect. For this, CdTe appears to be a promising material because of the high value of its electro-optic coefficient r_{41} and of a figure of merit which is four times that of InP [1]. The choice of a convenient localized centre for this application must satisfy several criteria: solubility in the range 10^{16}–10^{18} cm^{-3}, the depth of the energy level corresponding to the excitation wavelength domain, and the achievement of a semi-insulating state.

Generally speaking, deep level centres can be searched for in three areas: native defects, impurities with deep valence electrons and impurities with unfilled inner shells (transition metals, rare earths). The purpose of this paper is first to review the properties of these various centres in CdTe from the literature data. We will give particular attention to the energy depth domain corresponding to the wavelength range of optical telecommunications (1.3–1.55 μm or 0.8–0.95 eV), because applications of the photorefractive effect are envisaged in this area. We will then present optical measurements performed on CdTe doped with some transition elements, namely cobalt, vanadium and nickel.

2. Deep levels associated with native defects

Despite the abundant literature devoted to this topic—and specifically to the cadmium vacancy—no definite picture emerges.

The energy levels of the cadmium vacancy, which is assumed to be a double acceptor, appear to be rather deep, because the high temperature electrical measurements performed under a low cadmium vapour pressure give no indication of a native defect [2, 3]. In addition, there are a number of experimental observations showing the presence of a level at $E_c-(0.6–0.7)$ eV in crystals compensated by annealing in vacuum, in tellurium vapour or under a low cadmium vapour pressure [4, 5]. This level may tentatively be associated with the second ionization state of the cadmium vacancy. However, the control of the concentration of this deep centre is quite difficult. If shallow donors are introduced in order to partly fill the deep level by electrons, association between the ionized donors and the negatively charged vacancies occurs, leading to a marked decrease in the deep centre concentration. This has been observed, for instance, in chlorine-doped crystals [6, 7]. For a proper dopant concentration, the crystals become semi-insulating but with a very low density of mid-gap levels. The complex donor–cadmium vacancy is a well-documented centre. It has been studied by thermally stimulated current (TSC) [8], deep level transient spectroscopy (DLTS) [9] and more recently using electron paramagnetic resonance (ESR) [10]. The associated acceptor energy level is rather shallow, being around $E_v+0.13$ eV.

0921-5107/93/$6.00 © 1993 - Elsevier Sequoia. All rights reserved

This rapid survey shows that native defects are not good candidates for optical excitation effects.

3. Deep donor impurity levels

Unlike the group III elements (aluminium, gallium, indium) which introduce shallow donor levels when substituted for cadmium, the group IV elements (germanium, tin, lead) give rise to deep donor levels when incorporated on cadmium sites.

Earlier studies on germanium-doped CdTe using transport measurements [11], TSC and photoconductivity [12] revealed the presence of a level at $E_v + (0.62–0.73)$ eV. More definite conclusions were attained from photoelectron spin resonance performed on CdTe doped with germanium, tin and lead [13]. In the neutral donor state (D^0) the group IV elements have the ionic configurations Ge^{2+}, Sn^{2+} and Pb^{2+}. The singly ionized donors D^+ (Ge^{3+}, Sn^{3+} and Pb^{3+}) have a paramagnetic ground state $^2S_{1/2}$ which gives rise to the observed spin resonance. Light enhancement of the ESR intensity allows the threshold energy of the first ionization step to be estimated

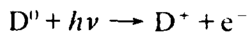

$$D^0 + h\nu \longrightarrow D^+ + e^-$$

These threshold energies are used to locate the upper donor level of the three impurities considered in the CdTe band gap (Fig. 1). It is seen that the level of tin (and perhaps germanium) should allow optical transitions to either the conduction or the valence band in the 0.7–0.8 eV range, while maintaining the semi-insulating state of the material. The maximum solubilities of these impurities are not known.

4. Transition metal impurities

Several experimental results exist concerning the 3d series which have been reviewed recently [14]. These impurities substitute for the cations in II–VI compounds. When incorporated into CdTe the elements from scandium to nickel, in the neutral state (denoted M^0), take the formal oxidation state TM^{2+}. The bonding orbitals are filled and the inner d shell has an open configuration d^n ($n < 10$). The specific optical spectra are characterized by intra-atomic transitions within the d shell. In contrast, charge transfer to the bands of the semiconductor or to other localized levels may occur leading to changes in the d shell configuration and in the charge state. If the transition impurity captures an electron, the configuration and oxidation state become d^{n+1} and TM^{1+} respectively. The impurity acquires a charge -1 with respect to the lattice which characterizes an ionized acceptor centre (M^-). Symmetrically, after capture of a hole the configuration and oxidation state are d^{n-1} and TM^{3+}. The charge state is $+1$ which corresponds to an ionized donor centre (M^+). Depending on the elements the associated energy levels separating two charge states can appear in the band gap of the semiconductor. Figure 2 displays the donor and acceptor energy levels determined for the different 3d elements in CdTe. Such determinations, which are rather inaccurate, mainly rely on two sets of data: first, measurement of the photon energy threshold for quenching or enhancement of the ESR signal of the impurity in a paramagnetic state; secondly, utilization of the fact that the levels of a given transition impurity occur at the same energies within a group of isovalent semiconductors when referred to a common level such

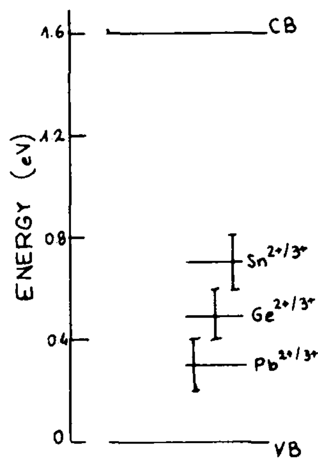

Fig. 1. Positions of energy levels of chemically identified tin, germanium, lead deep impurity centres in CdTe.

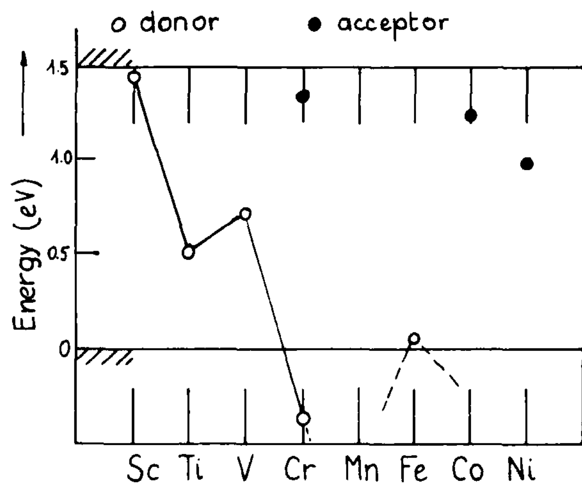

Fig. 2. Energy levels of donors and acceptors of 3d impurities in CdTe.

as the vacuum level [15, 16]. We now consider in more detail each particular impurity.

Scandium

Hall effect measurements indicate that scandium introduces a donor level near the conduction band of CdTe at $E_c - 0.10$ eV [17]. Photoconductivity experiments performed on scandium-doped CdTe and ZnTe show a common absorption band at 1.51 eV [18]. This is interpreted as being the result of transitions from the valence band to the scandium donor level:

$$Sc^{3+} + h\nu \longrightarrow Sc^{2+} + h^+$$

This result confirms the fact that the scandium donor level is shallow in CdTe ($E_c - 0.08$ eV) and is deep in ZnTe ($E_c - 0.8$ eV).

Titanium

Optical absorption spectra have been recorded by several authors and analysed in the frame of crystal field theory as being the results of transitions within the d shell of Ti^{2+} ions [19–21]. A photoionization threshold has been determined from photoconductivity spectra [20] and analysis of the absorption curve [21]. This places the titanium donor level at $E_c - (0.91-1.05)$ eV.

Vanadium

Optical absorption and photoconductivity spectra have also been recorded on vanadium-doped CdTe [19, 20]. The spectra are rather similar to those observed on titanium-doped CdTe. The donor ground state is set at $E_c - 0.78$ eV.

Chromium

An absorption band near 5100 cm^{-1} due to transitions within the d^4 shell of Cr^{2+} ions has been reported in ref. 19. In addition, two charge states were observed by ESR experiments: the ground Cr^{2+} (d^4) state [22] and the excited Cr^+ (d^5) state [23, 24]. The spectral dependence of the light-induced Cr^+ ESR signal [25] is in reasonable agreement with the absorption and photocurrent results near the CdTe absorption edge [24]. Analysis of this dependence makes it possible to locate the chromium-associated acceptor level (Cr^+/Cr^{2+}) at $E_v + 1.34$ eV for thermal excitation and $E_v + 1.5$ eV for optical excitation [25]. The donor level (Cr^{2+}/Cr^{3+}) is resonant with the valence band states.

Manganese

It is well known that the ground state of the Mn^{2+} ion lies below the valence band top in CdTe. The position of the acceptor level (Mn^+/Mn^{2+}) has been estimated from electroreflection, photoconductivity and electroabsorption spectra [26]. These observations correspond to the excitation of a valence band electron to the d shell of Mn^{2+} and to the subsequent binding of the free hold by coulombic attraction. Such bound exciton transitions occur near 1.5 eV at $T = 4.2$ K in CdTe doped with 0.05% Mn. Hence the acceptor level appears to be degenerate with the bottom of the conduction band.

Iron

The optical spectrum within the d^6 shell of Fe^{2+} has been reported and analysed previously [27, 28]. An ESR signal has been observed in p-type crystals and attributed to Fe^{3+} [29]. The spectral dependence of the ESR signal makes it possible to determine the threshold energy corresponding to the transition [30]

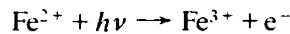

$$Fe^{2+} + h\nu \longrightarrow Fe^{3+} + e^-$$

Thus the donor level (Fe^{2+}/Fe^{3+}) is located at $E_c - 1.45$ eV.

Cobalt

Optical absorption within the d^7 configuration of Co^{2+} has been reported in ref. 28. Light quenching and enhancement of the ESR signal of Co^{2+} makes it possible to locate the acceptor level (Co^+/Co^{2+}) after the two respective transitions [31]

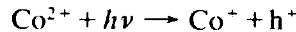

$$Co^{2+} + h\nu \longrightarrow Co^+ + h^+$$

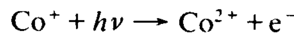

$$Co^+ + h\nu \longrightarrow Co^{2+} + e^-$$

These results lead to the construction of a configurational coordinate diagram for the acceptor state. The zero phonon transition occurs at $E_v + 1.25$ eV. DLTS experiments in n-type crystals yield an energy level at $E_c - 0.47$ eV [31]. The donor state (Co^{2+}/Co^{3+}) is located within the valence band.

Nickel

An ESR spectrum due to Ni^+ ($3d^9$) and associated optical transitions within the d shell have been reported for CdTe in ref. 32. The same state has also been studied in ZnTe [33]. Light quenching of the ESR signal in ZnTe makes it possible to determine the threshold energy for the transition

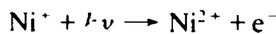

$$Ni^+ + h\nu \longrightarrow Ni^{2+} + e^-$$

Thus the acceptor level (Ni^+/Ni^{2+}) is set at $E_v + 1$ eV. The same value can be taken for the nickel acceptor level in CdTe.

The above results can now be used to select the transition impurities which are most promising for getting useful photorefractivity in the 1.3–1.55 μm wavelength range. The requirements are twofold: the presence of a level in the energy range 0.6–0.8 eV

below the conduction band; compensation by a shallow impurity in order to get a half-filled centre. Vanadium in a p-type sample is an obvious choice and this has been confirmed in specific experiments [1, 34]. A more accurate determination is needed for the titanium donor level which, normally, should also be suitable in acceptor counterdoped crystals.

The nickel acceptor level is also a possible candidate. In that case, the crystal has to be counterdoped with shallow donors.

Finally, let us remark that the scandium donor level and the chromium and cobalt acceptor levels are too shallow in CdTe but could have the correct energy depth in CdZnTe alloys of suitable composition.

5. Optical measurements

We have studied crystals grown by the vertical Bridgman method with the dopant added in the melt. The equipment set up at the laboratory (cold point zone) allows us to control the stoichiometry as well as to eliminate the residual tellurium precipitates by adjusting the partial pressure of cadmium during growth. Different CdTe crystals were grown doped in the melt with 10^{19} cm^{-3} of vanadium or nickel and 1.45 10^{20} cm^{-3} of cobalt.

We have performed optical absorption and photoconductivity measurements for these crystals and these show optical absorption in the near IR. The spectra are described in terms of $3d^n$ metal ions on substitutional cadmium sites in tetrahedral coordinance. In contrast, there is no optical absorption in the middle IR because of the absence of free carriers and this confirms the high resistivity of the samples studied.

5.1. Cobalt-doped CdTe

The energy level diagram for a Co^{2+} (d^7) configuration is shown in Fig. 3 which describes the successive level perturbations of the free ions in a crystal field of T_d symmetry. The fundamental level is ^4F, which is split into $^4A_2$, $^4T_2$ and $^4T_1$ and the lower level is $^4A_2$. The orbital selection rule is $A_2 \rightarrow T_1$ for the electric dipolar transition. The lower transition $^4A_2 \rightarrow {}^4T_2$ is of low intensity because it is not allowed. It gives an evaluation of the Dq parameter such that the energy transition is 10 Dq from which Dq is 300 cm^{-1}; the transition to the second excited state $^4T_1$ is allowed and gives an intense optical absorption band at 5529 cm^{-1}. The transition $^4A_2(^4F) \rightarrow {}^4T_1(^4P)$ appears with a structure at 10928, 11082 and 11453 cm^{-1}. Sharp lines are observable which are caused by spin-orbit interaction (Fig. 4).

5.2. Vanadium-doped CdTe

The energy level diagram for states of the d^3 configuration is similar to that of $Co(d^7)$. The level ^4F is split into $^4T_1$, $^4T_2$ and $^4A_2$, with the lowest state being the level $^4T_1$. The lower transition $^4T_1 \rightarrow {}^4T_2$ is not allowed but appears with a very low intensity at 3793 cm^{-1}. The transition $^4T_1 \rightarrow {}^4A_2$ towards the second excited state is allowed and gives a poorly structured band at 6666 cm^{-1} (Fig. 5). The transition $^4T_1(^4F) \rightarrow {}^4T_1(^4P)$ in the $3d^3$ shell gives a wide and strong band which is partially structured into three bands at 8699, 9313 and 9926 cm^{-1}. Such spectra cannot be due to the spin-orbit splitting alone. It is possible that the broadening of this peak is due to mixing with nearby doublet levels coming from the atomic levels ^2G and ^2H. It has been noted that the peak connected with the transition $^4T_1(^4F) \rightarrow {}^4T_1(^4P)$ observed in ZnSe:V, CdSe:V and CdS:V is always broadened even at low temperature [35].

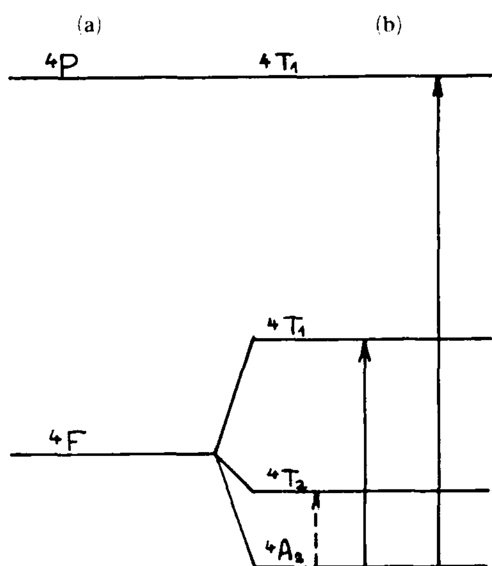

Fig. 3. Energy level diagram for Co^{2+} (d^7) configuration: (a) free ion; (b) substitution of cadmium in CdTe with T_d symmetry.

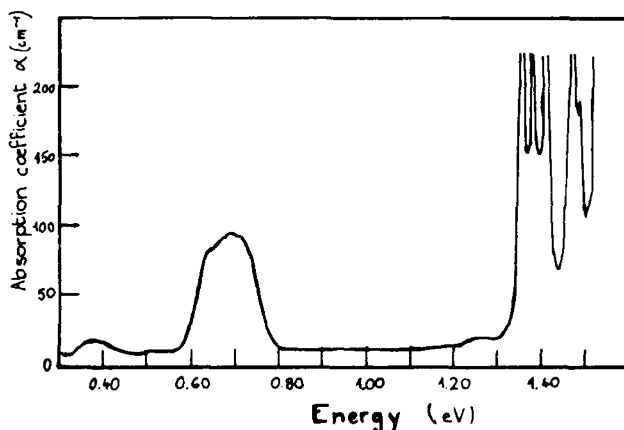

Fig. 4. Optical absorption spectrum at 77 K of cobalt in CdTe.

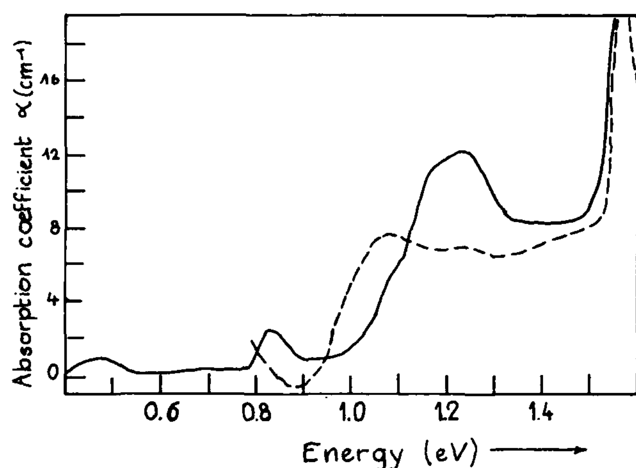

Fig. 5. ——, Optical absorption spectrum at 6 K of vanadium in CdTe; ----, photoconductivity response at 120 K.

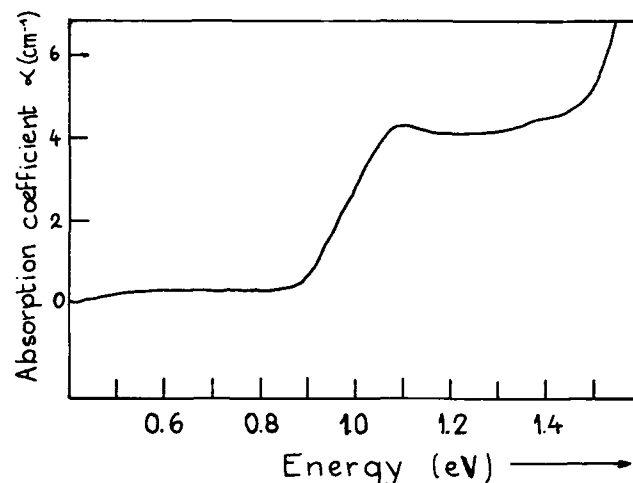

Fig. 6. Optical absorption spectrum at 77 K of nickel in CdTe.

Photoconductivity measurements (Fig. 5) were performed at 123 K. They show that the photoconductivity has the same general spectral shape as the optical absorption. The photoconductivity threshold was not reached in our set-up but it is apparently lower than 0.8 eV. A photoconductivity continuum is observed from 0.9 eV with small peaks at 1.1 and 1.23 eV and a major peak at 1.56 eV which corresponds to the CdTe gap value. Beyond this, intrinsic photoconductivity dominates and its amplitude decreases due to surface recombination.

5.3. Nickel-doped CdTe

The theoretical absorption spectrum for Ni^{2+} (d^8) is quite similar to that of CdTe:V. The level ^3F is split into three levels $^3T_1$, $^3T_2$ and $^3A_2$, with $^3T_1$ being at the lowest energy. However, the spectrum represented in Fig. 6 for CdTe:Ni is quite different from the preceding spectra. There are no structured bands but there is an absorption edge at 1.0 eV. It is possible that the absorption we observe is in fact due to charge transfer transitions from the valence band to the $Ni^{1+/2+}$ acceptor level, in agreement with the expected energy depth of this level (Fig. 2). This should be confirmed with the help of photoconductivity measurements.

6. Conclusions

There exist a number of impurities which introduce near mid-gap levels when incorporated into CdTe. With the additional requirement of an absorption threshold around 0.7–0.8 eV the best candidates are tin, vanadium, titanium and nickel. All these impurities substitute for cadmium. The first three are deep donors and need to be counterdoped with shallow acceptors in order to get the proper semi-insulating state with partially filled deep levels. The reverse applies for nickel. A definitive choice for photorefractive application will also rely on complementary aspects: maximum solubility, absorption oscillator strength or the possibility of optical–thermal resonance [36].

References

1 R. B. Bylsma, P. M. Bridenbaugh, D. M. Olson and A. M. Glass, *Appl. Phys. Lett., 51* (1987) 889.
2 F. T. J. Smith, *Metall. Trans., 1* (1970) 617.
3 Y. Marfaing, *Rev. Phys. Appl., 12* (1977) 211.
4 F. A. Kroger, *Rev. Phys. Appl., 12* (1977) 205.
5 K. Zanio, Cadmium telluride, *Semiconductors and Semimetals*, Vol. 13, Academic Press, New York, 1978.
6 N. V. Agrinskaya and A. O. Matveev, *Rev. Phys. Appl., 12* (1977) 235.
7 B. Biglari, M. Samimi, J. M. Koebel, M. Hage-Ali and P. Siffert, *Phys. Status Solidi A, 100* (1987) 589.
8 M. Samimi, B. Biglari, M. Hage-Ali, J. M. Koebel and P. Siffert, *Phys. Status Solidi A, 100* (1987) 251.
9 T. Ido, A. Heurtel, R. Triboulet and Y. Marfaing, *J. Phys. Chem. Sol., 48* (1987) 239.
10 D. M. Hofmann, B. K. Meyer, U. Probst and K. W. Beng, *J. Cryst. Growth, 101* (1990) 536.
11 V. V. Matlak, E. S. Nikonynk, A. V. Savitskii and K. D. Tovstynk, *Sov. Phys. Semicond., 6* (1973) 1760.
12 C. Scharager, P. Siffert, P. Hösch, P. Moravec and M. Vanecek, *Phys. Status Solidi A, 66* (1981) 87.
13 G. Brunthaler, R. T. Cox, W. Jantsch, U. Kaufmann and J. Schneider, in L. C. Kimerling and J. M. Parsey, Jr (eds.), *Proc. 13th Int. Conf. on Defects in Semiconductors*, The Metallurgical Society of AIME, New York, p. 1199.
14 V. I. Sokolov, *Sov. Phys. Sol. State, 29* (1987) 1061.
15 M. J. Caldas, A. Fazzio and A. Zunger, *Appl. Phys. Lett., 45* (1984) 671.
16 J. M. Langer and H. Keinrich, *Phys. Rev. Lett., 55* (1985) 1414.

17 P. I. Balni, R. B. Gamernik, Yu P. Gnatenko and A. S. Krochuk, *Sov. Phys. Semicond.*, *23* (1989) 485.
18 P. I. Balni, V. V. Sli'nko, Yu P. Gnatenko, P. N. Bukivskii, M. I. Ilashchuk and A. O. Parfenynk, *Sov. Phys. Semicond.*, *24* (1990) 904.
19 P. A. Slodowy and J. M. Baranowski, *Phys. Status Solidi B*, *49* (1972) 499.
20 J. M. Baranowski, J. M. Langer and S. Stefanova, *Proc. Conf. on the Physics of Semiconductors, Warsaw, 1972*, Polish Scientific Publishers, p. 1001.
21 J. Gardavsky, I. Barvik and M. Zvara, *Phys. Status Solidi B*, *84* (1977) 691.
22 J. T. Vallin and G. D. Watkins, *Phys. Rev., B*, 9 (1974) 2051.
23 G. W. Ludwig and M. R. Lorentz, *Phys. Rev.*, *131* (1963) 601.
24 M. Z. Cieplak, M. Godlewski and J. M. Baranowski, *Phys. Status Solidi B*, *70* (1975) 323.
25 M. Godlowski and J. M. Baranowski, *Phys. Status Solidi B*, *97* (1980) 281.
26 V. I. Sokolov and V. V. Chernyaev, *Phys. Status Solidi B*, *122* (1984) 703.
27 G. A. Slack, F. S. Ham and R. M. Chrenko, *Phys. Rev.*, *152* (1966) 376.
28 J. M. Baranowski, J. W. Allen and G. L. Pearson, *Phys. Rev.*, *160* (1967) 627.
29 G. Brunthaler, U. Kaufmann and J. Schneider, *J. Appl. Phys.*, *56* (1984) 2974.
30 K. Lischka, G. Brunthaler and W. Jantsch, *J. Cryst. Growth*, *72* (1985) 355.
31 G. Hendorfer, G. Brunthaler, W. Jantsch, J. Reisinger and H. Sitter, *J. Cryst. Growth*, *86* (1988) 497.
32 U. Kaufmann, J. Windscheif and G. Brunthaler, *J. Phys. C*, *17* (1984) 6169.
33 B. Clerjaud, A. Gelineau, F. Gendron, C. Naud and C. Porte, *J. Cryst. Growth*, *72* (1985) 351.
34 A. Partovi, J. Millerd, E. M. Garmire, M. Ziari, W. H. Steier, S. B. Trivedi and M. B. Klein, *Appl. Phys. Lett.*, *57* (1990) 846.
35 R. Pappalardo and R. E. Dietz, *Phys. Rev.*, *123* (1961) 1183.
36 G. Picoli, P. Gravey, C. Ozkul and V. Vieux, *J. Appl. Phys.*, *66* (1989) 3798.

Materials Science and Engineering, B16 (1993) 268–272

Time-resolved build-up and decay of photorefractive and free-carrier gratings in CdTe:V

Kestutis Jarasiunas*, Philippe Delaye and Gérald Roosen

Institut d'Optique Théorique et Appliquée, Unité de Recherche Associée 14 au Centre National de la Recherche Scientifique, Centre Scientifique d'Orsay, B.P.147, 91403 Orsay Cedex (France)

Jean-Claude Launay

Pôle de Recherche Aquitain pour les matériaux dans l'espace (Prame), B.P.11, 33165 Saint Médard en Jalles Cedex (France)

Abstract

Laser-induced picosecond transient gratings are used to study carrier transport via free carrier and photorefractive nonlinearities. The feedback effect of a light-induced space charge electric field is found responsible for diffracted beam intensity oscillations during the grating recording and its decay.

1. Introduction

Photorefractive semiconductor crystals are of great interest for high speed optical processing in the near infrared. Optical nonlinearities of different origins and various refractive index modulation mechanisms take place in these crystals under excitation by short powerful laser pulses at 1.06 μm [1–7]. We present time-resolved and excitation-energy-dependent analysis of carrier transport and of space charge field mechanisms in photorefractive CdTe:V. These kinds of studies may help to optimize crystal parameters for different applications as well as to improve nonlinear optical techniques for determining electrical parameters of semiconductors.

2. Experimental set-up

Carrier transport studies in vanadium-doped CdTe were performed by using degenerate 4-wave mixing technique at 1.06 μm (Fig. 1). An yttrium aluminium garnet (YAG) laser with pulse duration $\tau_L = 28$ ps full width at half maximum (FWHM) and output energy up to 10 mJ cm^{-2} was used. Two s-polarized beams of equal intensity were used for recording a grating with period $\Lambda = 1.8$ μm. The semi-insulating crystal ($\rho = 5.10^8$ Ω cm) was grown by using the modified Bridgman technique and vanadium-doped to 10^{19} cm^{-3} to produce a deep donor level at $\approx E_c - 0.75$ eV [8]. The absorption coefficient of the $d = 5$ mm thick sample is measured equal to 2 cm^{-1} at $\lambda = 1.06$ μm. The sample was cut with faces along crystallographic directions (110), (−110) and (001). In our experiments, the orientation of the grating vector K_g was along (110) or (001) directions. Probe and diffracted beam polarization states were monitored to separate coexisting refractive index gratings from different origins. The cases when pure photorefractive (PR) grating (*i.e.* p-diffracted component of s-polarized probe beam for K_g along (110)) or pure free-carrier

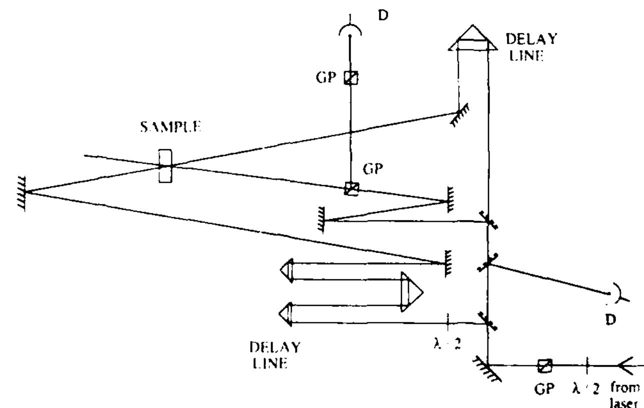

Fig. 1. Experimental set-up: GP Glan-polarizer, $\lambda/2$ half-wavelength plate, D detector.

*Also: Material Research Laboratory INTEST, Semiconductor Physics Department of Vilnius University, Sauletekio 9, bld.3, Vilnius 2054, Lithuania.

0921-5107/93/$6.00

© 1993 - Elsevier Sequoia. All rights reserved

(FC) grating (p-diffracted component of p-polarized probe beam for K_g along (110) or (001)) have been analysed experimentally. A Glan-polarizer oriented to reflect p-polarization was used for separation of a Bragg-diffracted beam counterpropagating to one of the recording beams. The separated beam was directed to a fast silicon photodiode through the next p-transmitting polarizer. Such a set-up allows us to detect diffracted signals as low as 10^{-6}–10^{-7}. Diffracted beam intensity $\langle I_1 \rangle$ or grating efficiency $\eta = \langle I_1 \rangle / \langle I_T \rangle$ (here $\langle I_1 \rangle$ and $\langle I_T \rangle$ are time-integrated values of diffracted and transmitted probe beams) as a function of excitation level E and of probe beam delay time Δt are studied. For qualitative analysis of processes involved in carrier and space charge field dynamics we solved the set of six material equations [1, 5] assuming that carrier generation from and via deep traps dominates.

3. Results and discussion

In Fig. 2 the exposure characteristics (EC) for FC and PR gratings (*i.e.* dependences of the diffracted beam intensity $\langle I_1 \rangle$ versus excitation energy I) are presented. The EC of a semiconductor contains the main information about carrier generation. It usually follows a power-law dependence at low excitation energies, $\langle I_1 \rangle = I^{\gamma}$ with γ-value corresponding to carrier generation rate [9]. Assuming that carrier concentration ΔN increases with excitation by power law as $\Delta N = I^{\beta}$, we have the following relationship between slopes γ and β in the region of linear transmittance T of the sample (*i.e.* low excitations):

$$\langle I_1 \rangle = \langle I_T \rangle (\pi \Delta n d / \lambda)^2 = IT(\pi n_{eh} \Delta N d / \lambda)^2 = AI^{2\beta+1} = AI^{\gamma} \quad (1)$$

Here $\Delta n = n_{eh} \Delta N$ is the refractive index modulation of the grating, with ΔN the spatially modulated free-carrier concentration, and n_{eh} is the refractive index change due to one electron hole pair.

In a general case, band-to-band linear carrier generation will lead to value $\beta = 1$ and corresponding $\gamma = 3$; for two-photon light absorption process $\beta = 2$ and $\gamma = 5$. In our CdTe:V sample, γ-values reveal three excitation regions corresponding to different light absorption mechanisms. For FC gratings, we observe carrier generation from deep levels altered by two-step transitions via impurity states ($\gamma = 4$), two-step and two-photon absorption of light ($\gamma = 5$), and, finally, the saturation of diffracted beam intensity at high excitations. The defocusing of transmitted and diffracted beams at high excitations was observed, and this may be the reason for FC grating profile distortions leading to $\langle I_1 \rangle$ saturation. To avoid this, we mainly carried out our measurements at $E \leqslant 5$ mJ cm^{-2}. Photorefractive nonlinearity, because of its lower sensitivity, reveals two-step and two-photon carrier generation ($\gamma = 5$) at lower excitations with the following decrease of EC slope from value $\gamma = 5$ to $\gamma = 3$ at higher excitations (linear increase with energy). The linear increase of the space charge field with excitation while the carrier concentration increases more rapidly in a nonlinear way, points out that space charge field dynamics is more complicated than FC processes. Indeed, in this regime, both electrons and holes are generated and can compete giving opposite contributions to the space charge field.

Measurements of sample transmittivity *vs.* excitation energy (Fig. 3) have shown a tendency of absorption bleaching at low currents and revealed the increasing role of nonlinear absorption with energy. In this way, transmittivity measurements confirmed the observed processes of carrier generation.

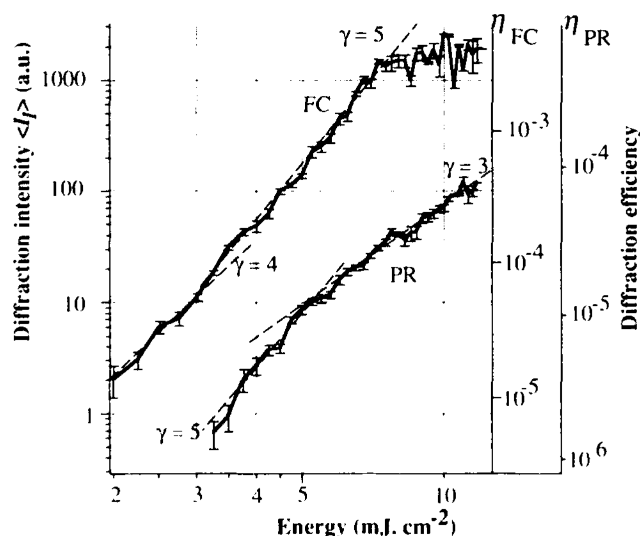

Fig. 2. Dependence of diffracted probe beam intensity $\langle I_1 \rangle$ and efficiency η *vs.* recording energy I for free-carrier (FC) and photorefractive (PR) gratings (probe beam delay time corresponds to the end of the laser pulse; sample orientation K_g along (110)).

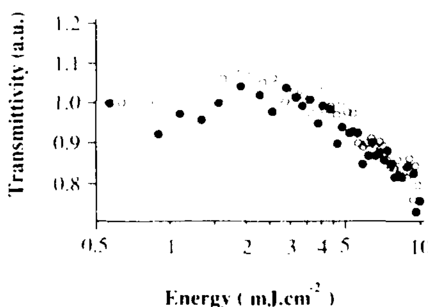

Fig. 3. Transmittivity of the sample at different excitation energies for p-polarized probe beam (filled circles) and for s-polarized one (open circles).

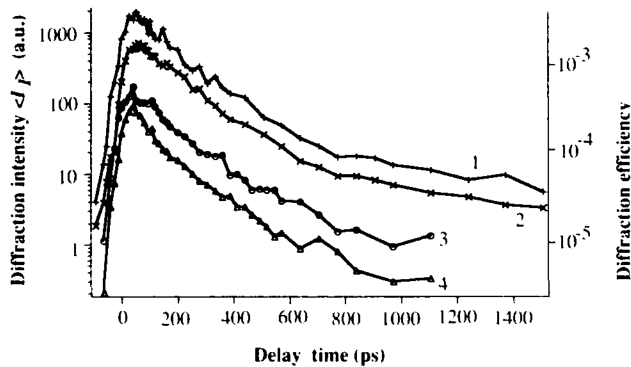

Fig. 4. Free-carrier (FC) grating dynamics at high excitation energies: $E = 8.5 \pm 0.5$ mJ cm^{-2} (1), 6.5 ± 0.3 mJ cm^{-2} (2), 4.5 ± 0.25 mJ cm^{-2} (3) and 3.75 ± 0.25 mJ cm^{-2} (4); sample orientation, K_g along (110).

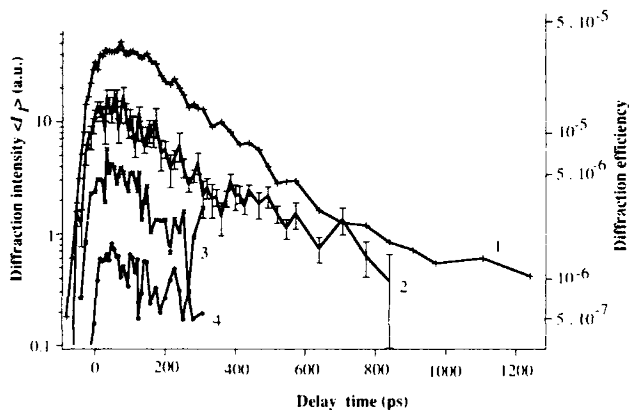

Fig. 5. Photorefractive (PR) grating build-up and decay at different excitation levels: $E = 6.5 \pm 0.5$ mJ cm^{-2} (1), 4.75 ± 0.25 mJ cm^{-2} (2), 2.88 ± 0.12 mJ cm^{-2} (3) and 1.88 ± 0.12 mJ cm^{-2} (4); sample orientation, K_g along (110). Error bars are presented on curve 2 showing the reality of the oscillations.

Carrier transport peculiarities have been observed in the dynamics of both FC and PR gratings (Figs. 4 and 5). We found that the FC grating decay time τ_g varies with excitation energy and with time. The fastest average grating decay time $\tau_{g1} = 80$–100 ps was observed at the lowest excitations used here (≈ 1 mJ cm^{-2}). With increasing incident power, the decay speed was slowing until it reached the value $\tau_{g2} \approx 230$ ps. At high excitation energies the decay rate also slows with time: at $\Delta t \geq 600$ ps we found $\tau_{g3} \approx 365$–410 ps. FC gratings decay finally with a time constant of 1.7 ns, which we attributed to carrier recombination time.

The processes of carrier diffusion and drift in light-induced space charge (SC) field must be taken into account to explain the observed behaviour. One must consider that the value of created electric field E_{SC} is dependent on carrier redistribution and thus varies with time. Electron diffusion during the action of the laser pulse will create an SC field between the mobile charges and ionized deep traps. Then hole-related processes may be observed: (i) the hole drift to grating minima will reduce the negative charge in these positions due to the previous diffusion of electrons and (ii) the build-up of a pure hole grating (that is, π-shifted from its former position) will take place after the holes will reach the minima of the light interference field (here $E_{SC} = 0$). Such behaviour of the free-carrier grating was predicted by computer simulation of carrier dynamics in photorefractive crystals [5]. Thus, the role of the holes increases more and more with time but in addition it increases also with excitation. In a general case, the average speed of FC grating decay will be governed by carrier bipolar diffusion related to electron-hole concentration at the given moment. The values of the bipolar diffusion coefficient D_a are given by eqn. (2):

$$D_a = kT\mu_a/e = (kT/e)(\Delta N + \Delta P)/(\Delta N/\mu_h + \Delta P/\mu_e) \quad (2)$$

with μ_a the bipolar mobility, and $\Delta N(\Delta P)$ the spatially modulated concentration of free electrons (holes).

Thus the grating decay constant at the lowest excitations τ_{g1} corresponds to $\mu = 330$–410 cm^2 V^{-1} s$^{-1} \gg \mu_h$, showing that electron generation is much more efficient than hole generation. At higher excitations decay slows down as the hole concentration approaches the electron one, and value $\tau_{g2} \approx 230$ ps corresponds to carrier ambipolar mobility for the case $\Delta N = \Delta P$ with the value $\mu_a = 135$–140 cm^2 V^{-1} s^{-1}, following from eqn. (2). The value for hole mobility $\mu_h = 80$–90 cm^2 V^{-1} s^{-1}, a typical value for CdTe [10], was obtained from decay time τ_{g3}.

Photorefractive gratings (PR) have shown two decay times at high excitations (Fig. 5), when $\eta \geq 5 \times 10^{-6}$. The fast decay has a time constant $\tau_1 = 220$–230 ps that corresponds to an ambipolar carrier diffusion coefficient equal to 3.56–3.73 cm^2 s^{-1}. Thus the origin of this refractive index modulation mechanism is a transient Dember field between mobile carriers. At longer delays or at lower excitation levels, a slow component of grating decay with $\tau_2 \approx 700$ ps dominates. We attribute this to the relaxation of the ionic grating created in deep traps. Rough estimation of the SC field relaxation time τ_{SC} was made for these conditions by using the formula for the dielectric relaxation time modified by a grating factor [11] and experimental values from FC grating measurements: carrier concentr^'ion $N \approx 3 \times 10^{14}$ cm^{-3}, their lifetime $\tau_R = 1.7$ ns and electron mobility $\mu_e = 520$ cm^2 V^{-1} s^{-1}. A good agreement between the calculated value $\tau_{SC} \approx 600$ ps and the experimental one was found. In fact, the relaxation time is dependent on the ionized donor concentration and will vary in time-scale. What we observed is probably

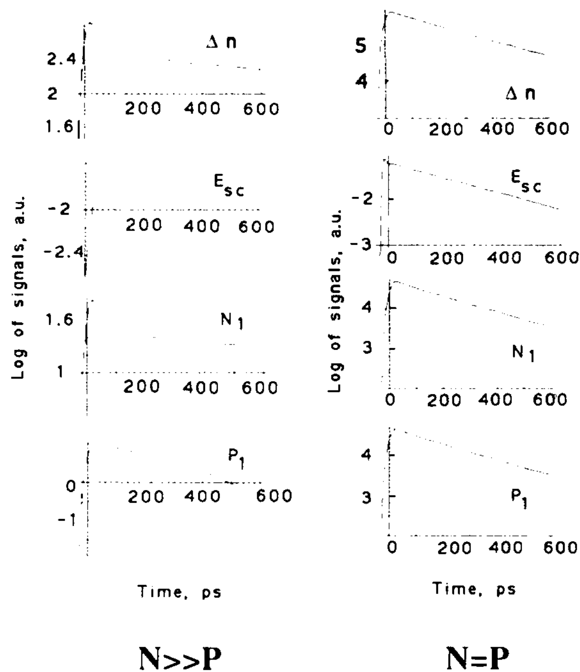

Fig. 6. Computer simulations of carrier and space charge field dynamics for two cases: low excitation case ($N \gg P$, on the left side) and high excitation case ($N = P$, right side). Abbreviations correspond to refractive index modulation (Δn), electric space charge field (E_{SC}), electron and hole grating modulation depths (N_1 and P_1); here $\Delta n = N_1/m_e + P_1/m_h$. We used the following parameters for calculations: deep trap density 4×10^{16} cm^{-3}, ionization cross sections for electrons and holes $S_n = S_p = 5 \times 10^{-17}$ cm^2, carrier recombination coefficients $\gamma_n = 10\gamma_p = 1.2 \times 10^{-7}$ cm^3 s^{-1}, $\mu_e = 520$ cm^2 V^{-1} s^{-1}, $\mu_h = 80$ cm^2 V^{-1} s^{-1}. Note: the delay in E_{SC} build-up at low excitations is an important feature pointing out the diffusive origin of E_{SC}. This was observed experimentally only at low excitations (Fig. 5).

the fastest component of τ_{SC} after the Dember field has decayed.

We performed computer simulations of carrier and E_{SC} dynamics for two cases: high excitation case when $N = P$ and low excitation case when $N \gg P$ (Fig. 6). The fast decay of the grating by electron diffusion creates an SC field which in turn slows the FC grating decay and prevents it from a total decay. At high excitations ambipolar diffusion governs the grating decay and the Dember field dominates over E_{SC} in deep traps. This kind of PR and FC grating behaviour was found experimentally too.

The simultaneous existence of two refractive index modulation mechanisms and their interaction lead to peculiarities observed in time-resolved grating build-up and decay. We have observed a step-like increase of the diffracted beam intensity during the action of laser pulse as well as saw-like oscillations (*i.e.* a fine structure of very fast decay and recovery of the grating on an essentially slower slope of diffusive grating decay) (see Figs. 4 and 5). We attribute this to a feedback effect of the created space charge field on the grating modulation, *i.e.* to the redistribution of the electron concentration due to the SC field. In addition to impeding their diffusion, the field will force carriers to move back to grating peaks from a previous nearly homogeneous distribution. This will lead to electron grating reconstruction and to an increase of the grating efficiency. During the action of a laser pulse, the competition between carrier generation, their diffusion and drift may create a continuing process of variation of τ_g which will lead to a step-like shape of the grating build-up. A similar shape of grating formation was observed in type-II quantum well heterostructures [12] where carrier confinement to the different layers leads to induced electric field.

This fine structure of grating decay and build-up exists on both FC and PR grating decay curves, which shows that grating modulation and E_{SC} temporal values do not equilibrate independently. A time and space varying feedback strength may create trapezoidal carrier distribution with steep edge at position $\bar{l} = \Lambda/4$. As discussed in ref. 1, at low excitations the drift current evolves as the square of the input current while the diffusion current remains linear. The modelling of carrier dynamics in nonhomogeneous electric fields is a very complicated task indeed. The linear model we have given above has shown no evidence of temporal oscillations. However, experiments of light diffraction on FC gratings in external strong microwave fields [13] (with electric vector oriented along the grating vector as in our experiments) have also shown similar peculiarities of diffracted signal: an increase of diffraction efficiency that was dependent on grating period and five-fold stronger in GaAs than in Si, *i.e.* related to electron mobilities.

Further analysis of the obtained data allows us to calculate the electron mobility in CdTe:V. Using the average value of hole mobility $\mu_h = 85$ cm^2 V^{-1} s^{-1} (from FC decay) and the ambipolar one, $\mu_a = 146$ cm^2 V^{-1} s^{-1} (obtained from Dember field decay of PR grating, *i.e.* for the case $\Delta N = \Delta P$), we calculate $\mu_e = 520$ cm^2 V^{-1} s^{-1}. This value is twice as small as in undoped CdTe [10]. The reason is probably a more efficient carrier scattering by neutral and ionized impurities. The mobility-lifetime product $\mu_e \tau_R = 8.8 \times 10^{-7}$ cm^2 V^{-1} follows from our measurements and is in good agreement with the one obtained for electrons by continuous wave (CW) photorefractive gain measurements in this crystal ($\mu_\tau = 8 \times 10^{-7}$ cm^2 V^{-1} [8]). In addition, this transient grating technique permits detailed studies of electron and hole generation rates. Directly measured grating decay times will give values of μ_a and thus the corresponding N/P ratios at different excitation currents will be obtained.

4. Conclusion

We have demonstrated that the simultaneous investigations of coexisting optical nonlinearities in photorefractive media allow direct studies of crystal properties as monopolar carrier mobilities and carrier concentrations. This kind of knowledge is very important for the understanding of deep level behaviour with excitation energy, wavelength, doping, etc. Diffracted beam intensity oscillations during grating build-up and its decay were found and explained qualitatively by light-induced space charge field feedback effect on carrier transport.

Acknowledgment

K. Jarasiunas acknowledges the support by M.R.T., France.

References

1 A. L. Smirl, G. C. Valley, K. M. Bohnert and T. F. Boggess, *IEEE J. Quantum Electron., QE-24* (1988) 289.
2 M. S. Petrovic, A. Suchocki and R. C. Powell, *J. Appl. Phys., 66* (1989) 1359.
3 W. A. Shroeder, T. S. Stark, T. F. Boggess, A. L. Smirl and G. C. Valley, *Opt. Lett., 16* (1991) 799.
4 W. A. Shroeder, T. S. Stark, M. D. Dawson, T. F. Boggess, A. L. Smirl and G. C. Valley, *Opt. Lett., 16* (1991) 159.
5 L. Disdier and G. Roosen, *Opt. Commun., 88* (1992) 559.
6 J. Vaitkus, E. Gaubas, K. Jarasiunas and M. Petrauskas, *Semicond. Sci. Technol.,* 7(1992) A131.
7 K. Jarasiunas, Ph. Delaye, J. C. Launay and G. Roosen, *Opt. Commun., 93* (1992) 59.
8 J. C. Launay, V. Mazoyer, M. Tapiero, J. P. Zielinger, Z. Guellil, Ph. Delaye and G. Roosen, *Appl. Phys. A,* 55 (1992) 33.
9 J. Vaitkus, K. Jarasiunas, E. Gaubas, L. Jonikas, R. Pranaitis and L. Subacius, *IEEE J. Quantum Electron., QE-22* (1986) 1298.
10 A. J. Strauss, *Rev. Phys. Appl., 12* (1977) 167.
11 J. P. Huignard and G. Roosen, in C. Flytzanis and J. L. Oudar (eds.), *Nonlinear Optics: Materials and Devices,* Springer Verlag, Berlin, 1986, p. 128.
12 H. Weinert, K. Jarasiunas and B. Shumann, *Phys. Status Solidi (A), 114* (1989) K183.
13 J. Vaitkus, E. Starikovas, L. Subacius and K. Jarasiunas, *Lietuvos Fiz. Rinkinys, 30* (1990) 336 (in Russian, translated into English in *Soviet Physics – Collections,* Allerton Press Inc., New York.

Materials Science and Engineering, B16 (1993) 273-278

Optical, photoelectrical, deep level and photorefractive characterization of CdTe:V

J. P. Zielinger, M. Tapiero and Z. Guellil

Groupe d'Optique Non-Linéaire et d'Optoélectronique, IPCMS, Unité Mixte 380046 CNRS-ULP-EHICS, 5 rue de l'Université, F-67084 Strasbourg Cedex (France)

G. Roosen and P. Delaye

Institut d'Optique Théorique et Appliquée, Unité associée au CNRS, Centre Scientifique d'Orsay, BP 147, F-91403 Orsay Cedex (France)

J. C. Launay and V. Mazoyer

Laboratoire de Chimie du Solide du CNRS, Université de Bordeaux I, F-33405 Talence Cedex (France)

Abstract

Characterization by different optical techniques, such as photo-induced current transient spectroscopy (PICTS), absorption, photoconductivity spectra and photorefractive wave mixing, of semi-insulating V-doped CdTe crystals prepared by the modified Bridgman method are presented. The aim of this joint research programme is to provide information which can lead to the understanding of the complex processes which determine photorefractive effects and to optimize the key parameters.

1. Introduction

The photorefractive (PR) effect results from non-uniform photogeneration of free charge carriers, followed by their migration by diffusion or drift in an electrical field and their final capture by deep traps. A space-charge field is then created, leading to the formation of a refractive index pattern owing to the electro-optical effect.

A simple two-level band transport model allows us to account for the PR effect [1]. Photocarriers (*e.g.* electrons) are released from an absorption centre (level A) in the illuminated regions of the crystal. Trapping occurs in the non-illuminated zones (level B). Very often levels A and B correspond to the same crystal imperfection X (native defect or chemical impurity), sitting either in the two different valence states X^0 and X^+ (*e.g.* Fe^{2+} and Fe^{3+}) or in different surroundings, and acting, respectively, as photoexcitable centres and traps. To ensure long-term stability of the index pattern, the degree of thermally stimulated emission of electrons from X^0 centres or recombination with free holes must be low.

Recent studies of PR in semi-insulating CdTe have shown that it has a high sensitivity over a large spectral range extending from at least 1.0 μm to beyond 1.5 μm [2, 3]. V was found to be a suitable dopant, producing the appropriate deep levels for PR.

We recently started a joint research programme which focuses simultaneously on PR, physicochemical and physical characterization of Bridgman-grown CdTe:V crystals with the goal of providing information that can lead to the understanding of the complex processes which determine the PR effect and to the optimization of the key parameters. In this context, knowledge of the thermal and optical parameters of the deepest trapping levels (those located more than 0.6 eV away from the bands) which directly affect the PR properties is of prime importance.

Unfortunately, very little is known about V in CdTe. Therefore, a systematic study of the problem of V doping, in particular the evolution of the trap spectrum, absorption and PC spectra, in addition to ESR and PR characterization seems to be indispensable. For a long time it was believed that only the predominant deepest levels are involved in PR. However, since the advent of experiments conducted with pulsed, high energy, nanosecond and picosecond lasers, many new interesting phenomena have been discovered. Clearly, in the pulse regime, shallower

0921-5107/93/$6.00 © 1993 – Elsevier Sequoia. All rights reserved

levels also play an important role [4, 5]. Any defect, provided that its concentration is of the order of 10^{15} cm^{-3}, may be involved. Therefore, a complete knowledge of the identity, thermal and photoionization energies, capture cross-sections and concentrations of the various species present is desirable for optimum control of the material parameters to meet device requirements.

2. Crystal growth and related characterization

Details concerning crystal growth are published elsewhere [6]. V-doped crystals were grown from 6-9 grade CdTe, using the modified Bridgman technique. Directly related studies (X-ray, mechanical properties, microprobe mapping, electron spin resonance) were performed. The goal is to establish growth and doping conditions to satisfy the specific size and crystalline requirements for PR crystals.

The electrical conductivity *vs* T variation has been measured on two samples 1H and 6B (cut from the same ingots as those used for PR analysis) in the temperature range 250–400 K. The resistivities at room temperature are for 1H 3×10^{9} Ω cm and for 6B 8×10^{8} Ω cm. The dark conductivity thermal activation energies for the two specimens are 0.76 (1H) and 0.72 eV (6B).

Figure 1 shows the normalized photoconductivity (PC) spectra. A main extrinsic band which drops sharply for photon energies $h\nu < 1.1$ eV is observed. The peak at roughly 1.5 eV corresponds to band-to-band transitions.

The shapes of the absorption spectra are very similar to that measured in ref. 2; however, smaller values for the absorption coefficient are found. Measuring the PC under laser irradiation at 1.6 μm allowed us to estimate $\mu\tau$ for the majority photo-carriers, which are assumed to be electrons [2], $\mu\tau = 8.10^{-7}$ cm^2 V^{-1}.

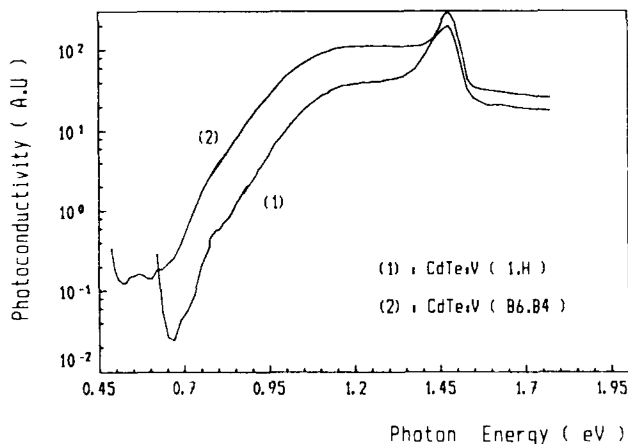

Fig. 1. Normalized PC spectra.

3. Deep level spectroscopy

A number of different trap species have been detected in semi-insulating CdTe (prepared, for example, by the travelling heater method [7]) using thermally stimulated current and photo-induced current transient spectroscopy (PICTS) techniques [7, 8]. However, a complete and precise characterization of deep levels over a wide range of energies so far has not been possible. We have developed an improved PICTS technique which allows significant progress in this direction [9]. The method is applied here for the first time to CdTe.

3.1. Experimental method

PICTS is a transient PC, computer-based measuring technique. The transient current, including both the rise and decay, induced by a square light pulse in a biased sample is recorded every 1 K during a temperature scan from 80 up to 400 K. Three types of numerical processing of the stored data allow us to extract the parameters of the traps, *i.e.* the apparent thermal ionization energy E_t, the capture cross-section S_t and the concentration N_t of the dominant species. We briefly recall the principles of the calculation [9].

For the sake of simplicity, we consider the single-trap model. As usual, retrapping of thermally released carriers is neglected [9]. The trapped charge $n_t(t)$ then decays exponentially according to

$$n_t(t) = N_t \exp(-t/\tau_t) \quad (1)$$

The relaxation time τ_t depends strongly on temperature T and is related to E_t and S_t by

$$\tau_t^{-1} = AS_t T^2 \exp(-E_t/kT) \quad (2)$$

where k is the Boltzmann constant and A a constant factor.

If the decaying charge is measured at two fixed delay times t_1 and t_2, the difference $\Delta n_t(T) = n_t(t_1) - n_t(t_2)$ obviously goes through a maximum at a temperature T_m where τ_t takes a defined value τ_m which can be related mathematically to t_1 and t_2, expressing the condition for the maximum of the function [11]:

$$f(\tau_t) = \exp(-t_1/\tau_t) - \exp(-t_2/\tau_t) \quad (3)$$

The important point is that τ_m can be computed knowing t_1 and t_2, whereas T_m is obtained from the curves $\Delta n_t(t)$ (hereafter called the PICTS spectrum). The spectrum is plotted for several couples (t_1, t_2), so maxima at different temperatures are obtained. The Arrhenius plot $\log(T_m^2\tau_m) = f(1/T_m)$ yields E_t and S_t

according to eqn. (2). The peak height provides a measure of N_t.

In practice, however, $n_t(t)$ is not directly accessible except through the transient current decay which can be expressed as

$$i(t)=(B\mu\tau N_t/\tau_t)\exp(-t/\tau_t) \quad (4)$$

where B is a constant, μ the mobility and τ the recombination lifetime.

If $\mu\tau$ is assumed to be constant [9], the condition for the maximum is deduced from the function

$$g(\tau_t)=\tau_t^{-1}\{\exp(-t_1/\tau_t)-\exp(-t_2/\tau_t)\} \quad (5)$$

Actually, $\mu\tau$ is generally temperature dependent. As a consequence, this simple double-gate (DG) procedure does not yield very reliable values for the trap parameters.

A better alternative is to normalize the DG signal by the photocurrent $i(0)$, which is proportional to $\mu\tau$ (NDG signal). This method is of special interest for the determination of the trap concentrations [9].

A second alternative is to plot the function

$$k(T)=\{i(t_1)-i(t_2)\}/\{i(t_0)-i(t_3)\} \quad (6)$$

where t_0, t_1, t_2 and t_3 are properly chosen delay times. Again, the condition for the maximum can be found mathematically [9]. This four-gate (FG) data processing is a very sensitive method with high spectral resolution, because the pre-exponential factor is eliminated in eqn. (6).

3.2. Results

PICTS measurements were performed on both samples under different excitation conditions (with photons of energy close to the maximum of the photoconductivity spectrum (Fig. 1), in the extrinsic band ($h\nu \simeq 0.9$ eV)) and, in both cases, with different illumination levels. In each case, fairly similar results were obtained. A few representative results will be given here.

It is well known that the spectral response of PC shows a maximum near the absorption edge. This maximum is determined by the relative magnitudes of the surface and volume recombination lifetimes of photocarriers. It usually occurs for that wavelength $\lambda=\lambda_{max}$ corresponding to an absorption coefficient $\alpha_{max} \simeq 1/d$, *i.e.* to $(1-1/e) \simeq 0.63$ of the incident radiation. Exciting the sample during the temperature scan in the PICTS experiment, by turning the monochromator to achieve maximum photoresponse, allows us to perform the measurements at a fairly constant volume photogeneration rate G of photocarriers:

$$G=\alpha_{max}I_0 \simeq I_0/d \quad (7)$$

where I_0 is the photon flux.

The plot of the photocurrent *vs.* T represents th thermal variation of $\mu\tau$ [6]. Curve (1) of Fig. 2 shows a typical NDG spectrum obtained under the described illumination conditions (incident photon flux corrected for reflection). The FG spectrum (curve (2)) clearly provides bett: :pectral resolution. There are 10 peaks observed in the temperature range 80–375 K. Each peak has been analysed separately according to the above-defined procedure which yields an Arrhenius plot from which E_t and S_t are obtained (Fig. 3). Knowing the photogeneration gain G, the concentration of the different traps is determined from the NDG spectra [9]. The parameters of the different traps are listed in Table 1.

4. Photorefractive analysis by two-wave mixing

We have investigated the PR energy transfer between two waves interfering in the crystal at both $\lambda=1.06$ and 1.32 μm [10]. The PR gain as a function of the input intensity has the form

$$\Gamma(I_0)=\Gamma/(1+I_d/I_0) \quad (8)$$

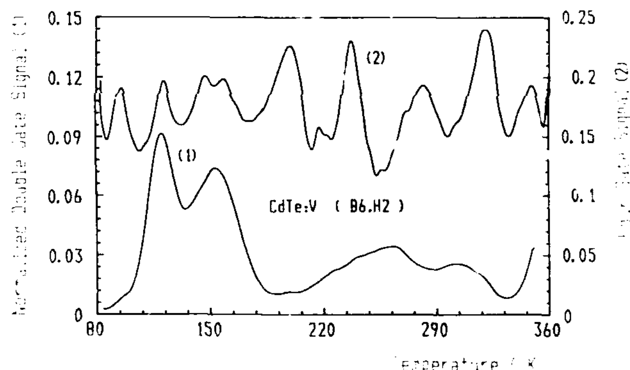

Fig. 2. Typical normalized double gate (curve 1) and four-gate (curve 2) spectra.

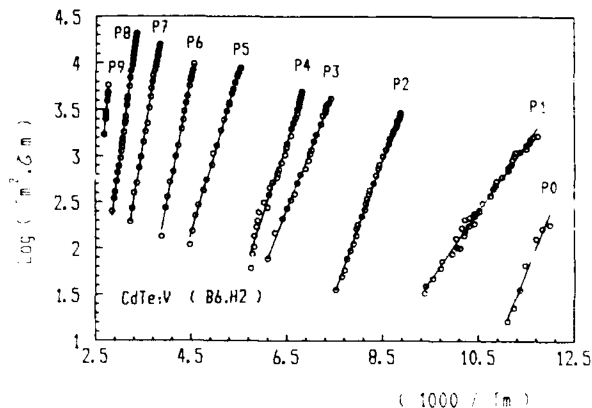

Fig. 3. Arrhenius plots for the 10 peaks detected in the temperature range 80–360 K.

TABLE 1. Thermal ionization energy E_t, capture cross-section S_t and concentration N_t of traps in CdTe:V (sample 6B)

Parameter	Peak number									
	P_0	P_1	P_2	P_3	P_4	P_5	P_6	P_7	P_8	P_9
E_t (eV)	0.25	0.15	0.285	0.26	0.31	0.34	0.53	0.62	0.78	1.1
S_t (cm^2)	$\approx 10^{-9}$	10^{-16}	5×10^{-13}	4×10^{-16}	4×10^{-15}	10^{-16}	4×10^{-14}	2×10^{-14}	2×10^{-13}	$\approx 10^{-10}$
N_t (cm^{-3})		10^{14}	10^{15}	$<10^{14}$	8×10^{14}	$<10^{13}$	4×10^{14}	2×10^{14}		

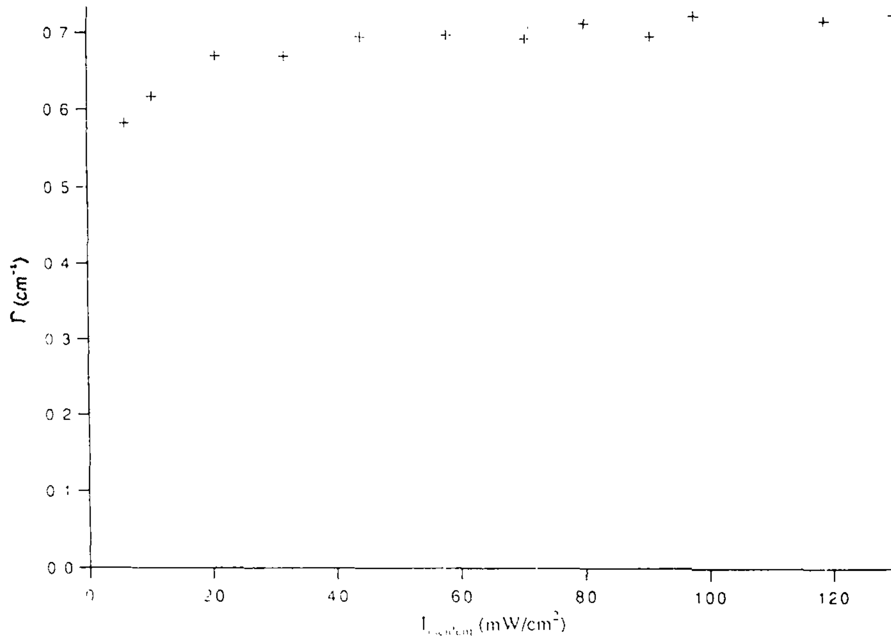

Fig. 4. PR gain of simple 1H vs. incident illumination ($\Lambda = 0.9$ μm), showing a saturation of the gain for incident powers as low as 20 mW cm^{-2}.

where Γ is the saturated gain coefficient and I_d is the illumination at which PC equals dark conductivity. Figure 4 demonstrates that the gain saturates at low illumination values, showing that this material is indeed a good candidate for optical information processing with low power lasers. At a grating spacing $\Lambda = 0.9$ μm, one obtains a PR gain $\Gamma = 0.7$ cm^{-1} that exceeds typical gains in GaAs and InP by more than 50% [10].

Considering a single deep level and two possible charge states, the gain can be expressed as [11]

$$|\Gamma| = \frac{2\pi n_0^3 |r_{41}|}{\lambda \cos\theta} \frac{k_B T}{e} \frac{k|\xi_0 k^2 + b - c|}{(k^2 + k^4/k_0^2 + b + c)} \qquad (9)$$

with

$$k_0^2 = \frac{e^2}{\varepsilon k_B T} N_{eff}$$

$$\xi_0 = \frac{\alpha_n - \alpha_p}{\alpha_n + \alpha_p}$$

$$b = \frac{\alpha_n \kappa_p^2}{\alpha_n + \alpha_p}$$

$$c = \frac{\alpha_p \kappa_n^2}{\alpha_n + \alpha_p} \qquad (10)$$

α_n and α_p are the absorption contributions that come from electron and hole generation respectively, κ_n and κ_p are the inverse of the electron and hole diffusion lengths, k represents the grating wave number and N_{eff} is the effective trap density ($N_{eff} = N^+ N^0/[N^0 + N^+]$) where N^+ and N^0 are the level concentrations in the ionized and neutral states respectively). Note that here we assume that electrons are the majority carriers for the PR effect.

Plotting the experimental data as k/Γ vs. k^2 (Fig. 5) permits the determination of the characteristic PR parameters [12]. For large values of k^2, coefficients b and c are negligible and we get a straight line. Its slope and intercept at the origin give $(r_{41}\xi_0 k_0^2)^{-1}$ and

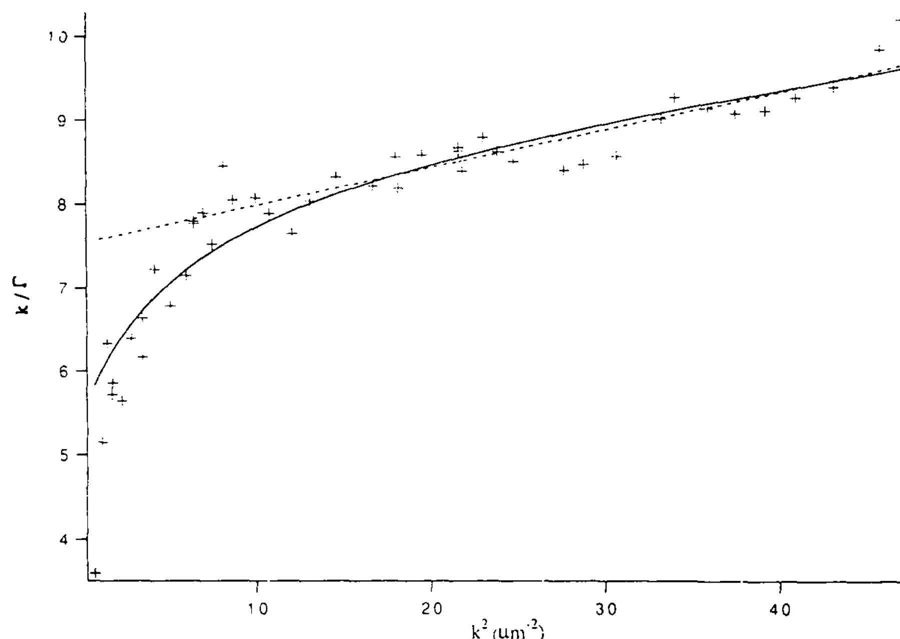

Fig. 5. Experimental k/Γ *vs.* k^2 plot leading to the determination of the PR parameters of crystal 1H. This plot was drawn with Γ in cm^{-1} and k in m^{-1}. The dotted straight line is the fit obtained for large grating wave numbers while the full line curve represents the best fit with the whole gain expression.

$(r_{41}\mathscr{E}_0)^{-1}$. A departure from this straight line is visible at small values of k^2. This indicates the effect of the carrier diffusion lengths. A full fit of the experimental data with the complete gain expression, *i.e.* without neglecting b and c, is now carried out using the previously determined quantities as starting parameters. We obtain $\xi_0 = 0.62 \pm 0.06$, $r_{41} = (5.5 \pm 0.5)$ pm V^{-1}, $k_0^2 = (300 \pm 30)$ μm^{-2}, $b = (3.6 \pm 1.5)$ μm^{-2} and $c \approx 0$. Also known is the measured absorption $\alpha = (2.16 \pm 0.06)\,cm^{-1}$.

These results require the following remarks. First, the $\mathscr{E}_0$ value indicates an electron–hole competition that is larger than previously seen in different samples [15]. Nevertheless, the PR gain has an appreciable value. Secondly, coefficient b permits the estimation of the mobility–lifetime product of the minority carrier for the PR effect. Assuming, as in ref. 3, that electrons are the majority photocarriers for the PR effect, one obtains $\kappa_n^2 \ll \kappa_p^2$ and derives for minority carriers (holes in this case) $\mu\tau = 9.10^{-8}\,cm^2\,V^{-1}$.

From k_0^2 we derive the effective trap density $N_{eff} = 4.3 \times 10^{15}\,cm^{-3}$. The magnitude of the PR gain was very small ($\Gamma = 0.006\,cm^{-1}$ at $\Lambda = 1.5\,\mu m$), impeding any reliable measurement *vs.* fringe spacing. One estimates an electron–hole competition factor of only $\mathscr{E}_0 = 0.1$, that corresponds to nearly balanced absorption coefficients, i.e. $\alpha_n \approx \alpha_p$.

However, an important point we noticed is that the photorefractive gain reverses its sign when changing the wavelength from 1.06 to 1.32 μm. This indicates a change in the nature of the photorefractive majority carrier. This result supports the approach we used to describe the observed PR effect, *i.e.* a single deep level from which both electrons and holes are photoionized. Such a reverse in the sign of the PR gain as the incident wavelength was varied was not noticed for crystals analysed in ref. 3.

5. General discussion

We are here mostly interested in those traps which could be involved in PR effects and in the effect of V doping. Concerning this last point, if one refers to previously published results, our samples can be considered as being moderately doped. According to Babii *et al.* [13], introduction of V at increasing concentrations first results in the filling of Cd vacancies and finally (more than $10^{20}\,cm^{-3}$) in the occupation of interstitial sites, giving rise to a new donor level. However, our absorption and PC spectra agree with those of similarly doped [2] and of undoped [14] CdTe. Finally, at 1.32 μm the PR gain was very small. Therefore, we conclude that, at low and moderate doping rates (lower than about $5 \times 10^{19}\,cm^{-3}$), V is not optically active.

Consequently, both the PR observed at 1.06 μm and the main absorption and PC bands are due to another

imperfection or impurity native to CdTe. We believe that this level, which is located close to the middle of the gap, determines the onset of PC (Fig. 1) and the activation energy of the dark conductivity, and that it is identical to the level responsible for a broad photoluminescence line at 0.75 eV [15], for the E2 line observed in deep-level transient spectroscopy on n-type CdTe at 0.77 eV [16] and finally in PICTS at 0.78 eV (peak P8, Table 1). The low concentration found for this centre (less than about 10^{13} cm^{-3}) in PICTS can be explained either by a nearly 100% compensation rate or by an incorrect estimation if it behaves as a minority carrier trap [9]. In this last case, the concentration could be underestimated by a factor of 10 (see values of $\mu\tau$). The nature of this defect (X) is still unknown. If one makes the plausible assumption that it is sitting in two charge states X^0 and X^+, then the PR process is obvious. However, charge transfer between two charge states of the same species cannot be observed in PICTS, since the crystal is uniformly excited, unless the X^0 and X^+ sites are not completely identical. This also may be an explanation for the low concentration of P8. It must be pointed out that, under special conditions (continuous illumination, pulsed high power excitation), P7 could also be involved in PR effects, although it relaxes within 20–30 ms at 300 K and its concentration is lower than 10^{15} cm^{-3} (an error of the order of a factor 5 is quite possible).

References

1 N. V. Kukhtarev, *Sov. Tech. Phys. Lett.*, *2* (1976) 438.
2 R. B. Bylsma, P. M. Bridenbaugh, D. H. Olson and A. M. Glass, *Appl. Phys. Lett.*, *51* (1987) 889.
3 M. Ziari, W. H. Steier, M. B. Klein and S. Trivedi, *3rd Topical Meeting on Photorefractive Materials, Beverly, Tech. Dig.*, *14* (1991) 159.
4 G. Le Saux and A. Brub, *IEEE J., QE 23* (1987) 1680.
5 G. Pauliat and G. Roosen, *J. Opt. Soc. Am. B*, *7* (1990) 2259.
6 J. C. Launay, V. Mazoyer, M. Tapiero, J. P. Zielinger, Z. Guellil, Ph. Delaye and G. Roosen, *Appl. Phys.*, *A55* (1992) 33.
7 C. Scharager, J. C. Muller, R. Stuck and P. Siffert, *Phys. Status Solidi A*, *31* (1975) 247.
8 M. Samini, B. Biglari, M. Hage-Ali and P. Siffert, *J. Cryst. Growth*, *72* (1985) 213.
9 J. C. Balland, J. P. Zielinger, C. Noguet and M. Tapiero, *J. Phys. D*, *19* (1986) 57.
J. C. Balland, J. P. Zielinger, M. Tapiero, N. Benjelloun, J. G. Gross and C. Noguet, *J. Phys. D*, *19* (1986) 71.
M. Tapiero, N. Benjelloun, J. P. Zielinger, S. El Hamd and C. Noguet, *J. Appl. Phys.*, *64* (1988) 4006.
10 Ph. Delaye, P. U. Halter and G. Roosen, *J. Opt. Soc. Am. B*, *7* (1990) 2268.
11 F. P. Strokhendl, J. M. C. Jonathan and R. W. Hellwarth, *Opt. Lett.*, *11* (1986) 312.
12 M. B. Klein and G. C. Valley, *J. Appl. Phys.*, *57* (1985) 4901.
13 P. I. Babii, N. P. Gavaleshko, Yu. P. Gnatenko, P. A. Skubenko and V. I. Oleinik, *Sov. Phys. Semicond.*, *12* (1979) 1310.
14 N. V. Agrinskaya, O. A. Matveev, A. I. Terent'ev and V. V. Shasshkova, *Sov. Phys. Semicond.*, *23* (1989) 274.
15 He-Xiang Han and B. J. Feldman, *J. Appl. Phys.*, *61* (1987) 2670.
16 R. T. Collins, T. F. Kuech and T. C. McGill, *J. Vac. Sci. Technol*, *21* (1982) 191.

Compact visible microgun-pumped CdTe–$Cd_{1-x}Mn_xTe$ laser

J. Cibert, C. Bodin and Le Si Dang

Laboratoire de Spectrométrie Physique (Unité de Recherche associée au CNRS 08), Université J. Fourier, BP 87, 38402 Saint Martin d'Hères (France)

G. Feuillet and P. H. Jouneau

Laboratoire de Physique des Semiconducteurs, Departement de Recherche Fondamentale sur la Matiere Condensée-Service de Physique des Materiaux et Microstructures, Centre d'Etudes Nucléaires de Grenoble, BP 85X, 38041 Grenoble (France)

E. Molva, R. Accomo and G. Labrunie

Laboratoire d'Etudes et Technologie de l'Informatique (CEA–Technologies Avancées–Département Optronique), Centre d'Etudes Nucléaires de Grenoble, BP 85X, 38041 Grenoble (France)

Abstract

We report on a novel device, the microgun-pumped semiconductor laser (MSL), which has been successfully applied to laser emission from 90 to 300 K using CdTe–$Cd_{1-x}Mn_xTe$ heterostructures. In the MSL, a low threshold quantum well graded-index separate-confinement heterostructure is pumped by a compact microtips electron gun. It is operated at a low voltage and a low current, so that the whole device can be made very compact (a few cubic centimetres). Since there is no need for doping or contacting, it allows one to use the strong potentialities of II–IV compounds in the whole visible range.

Wide applications of laser emission in the blue-green range are expected in several domains including optical recording, reprographics and biotechnology. Commercially available compact lasers, based on III–V heterojunctions, are at present limited to the deep-red–near-IR region. Very recently [1], II–VI blue–green laser diodes have been realized. They use $Cd_{1-x}Zn_xSe$–ZnSe quantum wells (QWs), with ZnS_zSe_{1-z} cladding layers to ensure optical confinement. They were made possible because of significant progresses in the p-type doping of ZnSe grown by molecular beam epitaxy, using a reactive N_2 cell. However, the lifetime of these devices remains short, owing to difficulties in making ohmic contacts to these high band gap materials even at high doping levels and to severe limitations put on the separate confinement heterostructures because of the high lattice mismatch in ZnSe-based epitaxy.

We report on the demonstration of laser emission from CdTe–$Cd_{1-x}Mn_xTe$ structures externally pumped by a microtip electron gun [2]. It allows use of materials for which n- or p-type doping is not satisfactorily controlled. Among them, CdTe–$Cd_{1-x}Mn_xTe$ heterostructures exhibit smaller lattice mismatches than do the selenides and are known as efficient emitters; $Cd_{1-x}Mn_xTe$ QWs were shown to exhibit magnetically tunable laser emission at around 660 nm under optical pumping (with a high threshold, greater than 50 kW cm^{-2} at 2 K) [3]. The luminescence wavelength decreased to the blue–green range when thin CdTe–MnTe QWs are used [4]. However, for the higher band gap tellurides, doping is still under development. Electron beam pumping has been known for many years as an efficient excitation source for semiconductors and as especially promising to obtain laser emission from II–VI compounds [5]. On bulk materials, thresholds are exceedingly high (around 100 kW cm^{-2} or higher), so that rapid degradation occurs; moreover these classical electron-beam-pumped lasers are not compact. Lower thresholds are expected if properly designed heterostructures are used; this is the case for the CdTe–$Cd_{1-x}Mn_xTe$ graded-index separate-confinement heterostructures (GRINSCHs) that we describe here. These structures may thus be pumped at a low current and a low voltage by a microtip electron source, making the whole device very compact, as small as a few cubic centimetres.

The compact electron source is made up of an array of low voltage field-emissive microtip cathodes. A typical 1 mm^2 rectangular array contains 10^4–10^5 micro-

0921-5107/93/$6.00 © 1993 - Elsevier Sequoia. All rights reserved

guns. The cathodes and the gates are evaporated on a single glass substrate. For a typical gate cathode voltage of 80 V the current is around 1 mA mm^{-2}. Such arrangements have been developed for "microtip flat-panel fluorescent displays" [6]. In the microgun-pumped semiconductor laser (MSL) a simplified optics system loosely focuses the electron beam onto the semiconductor platelet. For a compact long-lived device the accelerating voltage must be kept rather low, 5–10 kV, so that electron–hole pairs are created only at approximately $R_p \pm \Delta R_p \approx 2500 \pm 2000$ Å below the surface. Carriers have to be efficiently collected into the QW which acts as the active medium. This function is ensured by a $Cd_{1-x}Mn_xTe$ layer of graded composition inserted between the QW and the semiconductor surface.

The efficiency of the graded layer in carrier collection was checked for the CdTe–ZnTe QW. In this case the graded layers 100 nm thick were made of $Cd_{1-x}Zn_xTe$, with x decreasing from 0.98 to 0.92 towards the QW on both sides. Cathodoluminescence yields were compared with those of a single CdTe–ZnTe QW grown at the same depth (100 nm), under the same growth conditions (GaAs substrate; growth temperature, 320 °C, excess cadmium or zinc flux; thick ZnTe buffer layer). Cathodoluminescence was excited at 10 kV. At 2 K the QW was found to be four times brighter when inserted into the graded layers. At 300 K (Fig. 1) the enhancement was even stronger; moreover the ratio of the QW to alloy luminescence was also significantly increased. Photoluminescence (PL) excited within the barriers using an argon ion laser shows the same enhancement. Since in the case of $CdTe-Cd_{1-x}Zn_xTe$ no optical confinement takes place [7], this better yield is attributed to a better collection of the carriers.

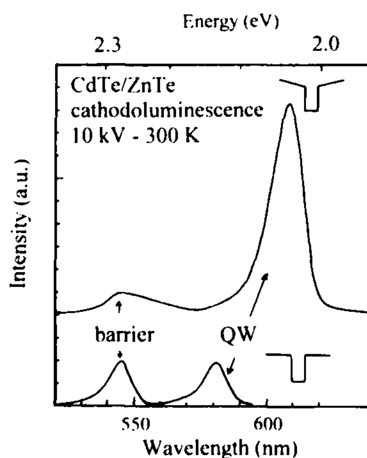

Fig. 1. Room temperature cathodoluminescence spectra, taken under identical conditions on a CdTe–ZnTe QW (bottom), and on a $CdTe-Cd_{0.08}Zn_{0.92}Te$ QW inserted in a graded profile (top).

Another crucial point to obtain a low threshold is optical confinement. This can be realized in separate-confinement heterostructures (SCHs), either through an abrupt change in the optical index, or through a continuous variation (GRINSCHs). In our case the existence of graded-composition layers for carrier collection favours the choice of a GRINSCH configuration; $Cd_{1-x}Mn_xTe$ behaves as $Ga_{1-x}Al_xAs$ regarding the change in optical index [7] and band gap with x, so that the composition gradient which enhances carrier collection also provides optical guiding. Then the coupling between carriers and photons can be optimized by centring the maximum of the guided mode on the QW, so that the overall gain is increased. This optimization is done by computing numerically the profile of the guide mode when varying three free parameters: the width of the graded layers on both sides of the quantum well, and the total change in the manganese content.

This optimization must be done while keeping the whole GRINSCH below the critical thickness t_c for relaxation of misfit strain. The experimental t_c is accurately known for CdTe layers on $Cd_{1-x}Zn_xTe$ [8]. For $Cd_{1-x}Mn_xTe/Cd_{1-y}Mn_yTe$, at least for layers with a low manganese content, we may assume a similar dependence of t_c on the mismatch. This allows us to evaluate the maximum thickness of an abrupt SCH. For $Cd_{0.85}Mn_{0.15}Te/Cd_{0.80}Mn_{0.20}Te$ the lattice mismatch is 1.1×10^{-3} and the corresponding critical thickness $t_c \approx 600$ nm, but the index change is only 0.03 (for $\lambda > 720$ nm). The index change is more than doubled if we use $Cd_{0.85}Mn_{0.15}Te/Cd_{0.75}Mn_{0.25}Te$ but then $t_c \approx 200$ nm, *i.e.* too small for good optical confinement. Clearly the critical thickness limits the optical confinement which can be realized in an abrupt SCH. A larger t_c is expected in a GRINSCH. Detailed models are lacking but we can make a first estimate by following an equilibrium model such as in ref. 9 (equilibrium models are inappropriate for III–V compounds or Si–Ge but are thought to hold better for II–VI compounds). The elastic energy per unit surface of the strained layer is

$$E_s = \tfrac{1}{2} C \int_0^w \varepsilon^2(z)\, dz$$

where C is a combination of elastic coefficients, w the thickness of the layer and $\varepsilon(z)$ the strain at depth z. If a misfit dislocation is formed, the strain is decreased by a quantity $\Delta\varepsilon$, and the elastic energy by $C\Delta\varepsilon \int \varepsilon(z)\, dz$. At t_c, this energy gain exactly balances the energy that it costs to create one dislocation. If we compare two layers with the same thickness w and the same total composition change, one abrupt and one linear (graded), $\int \varepsilon(z)\, dz$ in the graded layer is half that in the abrupt layer, so that t_c in the graded layer should be

twice that in the abrupt layer. One can even hope for a larger increase in t_c; in the equilibrium model [9] indeed t_c is found to vary as the inverse of the lattice mismatch, $t_c \propto (\Delta a/a)^{-1}$, at least for low mismatches where logarithmic corrections are negligible. Experimentally for $CdTe/Cd_{1-x}Zn_xTe$ [8] the dependence is greater, $t_c \propto (\Delta a/a)^{-\eta}$, with $\eta \approx 1.5$. No model at the moment accounts for this dependence, but we can try to use directly the experimental data in the following heuristic criterion; the critical thickness is reached when

$$\int_0^w dz/t_c(x(z)) = 1$$

where $t_c(x(z))$ holds for a layer of uniform composition equal to $x(z)$. This criterion, which is evident for a uniform layer, holds within the equilibrium model for any composition profile since in this model $t_c(x(z))$ is proportional to $1/\varepsilon(z)$. With t_c proportional to $(\Delta a/a)^{-\eta}$, the critical thickness for a linearly graded layer is enhanced by a factor $\eta + 1$. For a complete GRINSCH, the criterion must be applied to the whole structure, QW and graded layers.

Structures designed in the above way have been grown by molecular beam epitaxy, on a (001)-oriented CdTe or $Cd_{0.96}Zn_{0.04}Te$ substrate, at 310 °C, under excess cadmium flux, using three effusion cells: CdTe, cadmium and manganese. Fluxes were measured before growing the actual sample, by recording reflection high energy electron diffraction (RHEED) intensity oscillations for growth of CdTe and MnTe on a (111)-oriented test sample under excess tellurium; this allows us to adjust quite accurately the growth rates and alloy compositions (to within 2 at.%). The temperature ramp to be applied to the manganese cell was checked on the beam equivalent pressure and adjusted to the desired composition profile. RHEED intensity oscillations were also recorded during the growth of the actual sample.

A secondary ion mass spectrometry (SIMS) profile is shown in Fig. 2. It allows us to check the linearity of the graded profile. The QWs (two CdTe QWs, 21 monolayers thick, separated by a 10 nm $Cd_{1-x}Mn_xTe$ layer) are not resolved. The QW characteristics and the maximum manganese content (in the buffer layer) are better controlled by low temperature PL (Fig. 3) and reflectance spectroscopy (not shown). The main PL signal is ascribed to the e_1h_1 QW exciton. As in a simple QW of similar width and barrier composition, it is split into an intrinsic exciton and an extrinsic exciton 3-4 meV lower in energy. Both lines are quite narrow (2 meV full width at half-maximum). The intrinsic or extrinsic nature of the two transitions is checked in the reflectance and PL excitation spectra and through their behaviour under increasing excitation density. In the

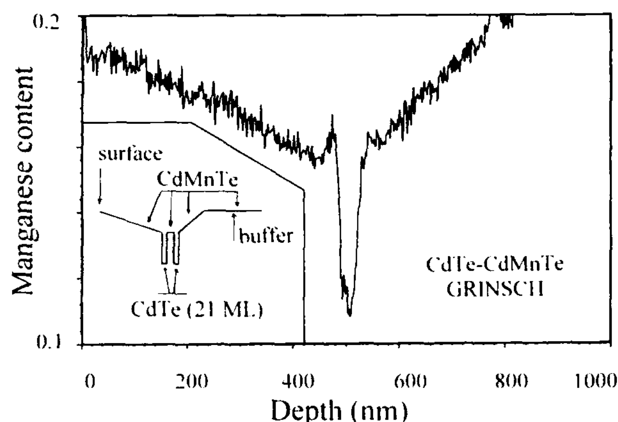

Fig. 2. SIMS profile of a GRINSCH with two QWs 7 nm thick (a.u., arbitrary units).

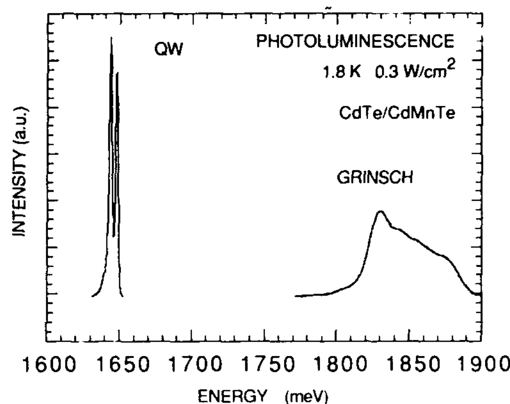

Fig. 3. PL spectrum of the same sample as in Fig. 2 (a.u., arbitrary units).

PL excitation spectra (not shown), one can also identify the e_1l_1 exciton 30 meV above e_1h_1. PL from the alloy appears as a flat trapezoidal line; this is a further indication of the linearity of the graded layer; on poorly linear layers, distinct PL peaks show up owing to composition plateaux. In this sample, no evidence of strain relaxation at the GRINSCH-buffer interface was found by cathodoluminescence and by transmission electron microscopy. This is coherent with the above criterion, since for that profile $\int dz/t_c = 0.6-0.7$.

After mechanical thinning to 120 μm, 200-500 μm cavities were cleaved and indium soldered on a copper block. The temperature of the block was regulated between 90 and 300 K, but no special care was taken for heat sinking. The bare cleavage planes served as cavity mirrors. Laser emission was observed up to room temperature both under optical pumping (double yttrium aluminium garnet laser) in pulsed mode (10 ns pulses, at 10 Hz), and electron pumping (Fig. 4) (microguns at 5-10 kV) in a quasi-continuous mode (5 μs

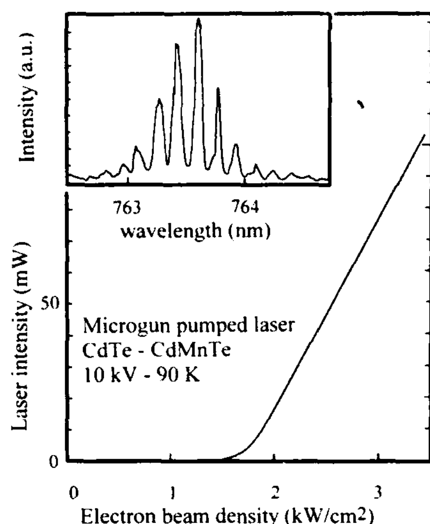

Fig. 4. Laser intensity from a 500 μm $CdTe-Cd_{1-x}Mn_xTe$ cavity. The insert is the spectrum showing the Fabry-Pérot modes of the cavity (a.u., arbitrary units).

pulses; 2% duty cycle). Thresholds are low: under optical pumping, 0.7 kW cm^{-2} at 90 K, and 7 kW cm^{-2} at 300 K. Under electron pumping, they are two to three times higher as expected: 1.5–2 kW cm^{-2} at 90 K, and 15–20 kW cm^{-2} at 300 K (the indicated power densities are incident onto the semiconductor surface). The trace on the sample holder of the red emitted beam was seen by the eye, demonstrating its collimated nature. No degradation occurred over a period of several days.

Further studies are needed to optimize the semiconductor structure; thresholds are already very low but should be even lower with steeper gradients and deeper QWs, while keeping below the critical thickness. A lower threshold and better efficiency have already been obtained at 90 K. In addition to a lower threshold, better heat sinking and lateral confinement should lead to true continuous-wave (CW) emission at room temperature. Most important, lasing at shorter wavelengths should be obtained, *e.g.* from structures with a higher manganese content.

To conclude, room-temperature quasi-CW laser emission has been demonstrated with a MSL. This device can be made compact (a few cubic centimetres), and potentially uses any II–VI material (or others) without doping and without electrical contacts; although the present demonstration is in the red, laser emission at shorter wavelengths is expected very soon.

Acknowledgment

We thank B. Blanchard (Laboratoire d'Etudes et Technologie de l'Informatique) for the SIMS measurements.

References

1 M. A. Haase, J. Qui, J. DePuydt and H. Cheng, *Appl. Phys. Lett.*, *59* (1991) 1272.
2 E. Molva, R. Accomo, G. Labrunie, J. J. Aubert, J. Cibert, Le Si Dang, C. Bodin and G. Feuillet, *Conf. on Laser and Electro-Optics, Anaheim, 1992.*
3 E. D. Isaacs, D. Heiman, J. J. Zayhowski, R. N. Bicknell and J. F. Schetzina, *Appl. Phys. Lett.*, *48* (1986) 275.
4 N. Pelekanos, Q. Fu, J. Ding, W. Walecki, A. V. Nurmikko, S. M. Durbin, J. Han, M. Kobayashi and R. L. Gunshor, *Phys. Rev. B*, *41* (1990) 9966.
5 S. Colak, B. J. Fitzpatrick and R. N. Bhargawa, *J. Cryst. Growth*, *72* (1985) 504.
6 A. Ghis, *IEEE Trans. Electron Devices*, *38* (1991) 2330.
7 E. Molva, to be published.
8 J. Cibert, R. André, C. Deshayes, G. Feuillet, P. H. Jouneau, Le Si Dang, R. Mallard, A. Nahmani, K. Saminadayar and S. Tatarenko, *Superlattices Microstruct.*, *9* (1991) 271.
9 C. Fontaine, J. P. Gaillard, S. Magli, A. Million and J. Piaguet, *Appl. Phys. Lett.*, *50* (1987) 903.

High quality CdTe and its application to radiation detectors

M. Ohmori and Y. Iwase

Special Research Department, Nippon Mining Co. Ltd, 3-17-35 Niizo-Minami, Toda, Saitama 335 (Japan)

R. Ohno

Materials Development Research Laboratories, Nippon Mining Co. Ltd, Niizo-Minami, Toda, Saitama 335 (Japan)

Abstract

CdTe crystal growth by the travelling heater method and the characteristics of its radiation detectors are described. A CdTe polycrystalline ingot is synthesized from purified 99.99999% Cd and Te metals and crystals of 32 mm in diameter are grown at temperatures of 700 °C-900 °C with a growth speed of 2-5 mm per day. A high resistivity of more than 10^9 Ω cm is obtained at a Cl concentration of 1.5 ppm with electron and hole lifetimes of 1.0 and 0.5 μs respectively. The pulse count mode detectors are fabricated using wafers cut from the ingots. For practical application to medical diagnostics, 90-element array detectors with an element size of 1.8 mm × 2 mm × 1.2 mm are developed. The averaged FWHM is 4.0 keV and the count rate variation is less than 4% for a 60 keV γ-ray source. For dosimetry use, detectors as large as 10 mm × 10 mm × 2 mm and 25 mm diameter × 2 mm thickness volumes are fabricated. Environmental and high temperature acceleration tests have been systematically conducted. Mean time to failure is estimated to be 10^9 h at 25 °C.

1. Introduction

Recently, CdTe radiation detectors have begun to be used in practical applications in the field of medical diagnostics and dosimetry [1-4]. The features of CdTe detectors include a large absorption coefficient, compact size and simple assembly compared with those of an Xe gas detector and NaI detector with photomultiplier.

We demonstrated one-element detectors and 90-element one-dimensional array detectors [4, 5], and conducted environmental and high temperature acceleration tests to investigate their reliability for practical use. We also investigated the qualities of CdTe crystals grown by the vertical gradient freezing (VGF) method using In as a dopant [4] and by the travelling heater method (THM) using Cl as a dopant [5]; we obtained superior detector characteristics from the THM-grown crystals.

In the present paper, the most recent work on CeTe crystal growth by THM, the crystal and detector characteristics as well as the device reliability will be described.

2. Crystal growth

2.1. Materials

Figure 1 shows the flow diagram of CdTe crystal growth by the THM for radiation detectors. 99.99% Cd and Te, which are obtained in our company as by-products of Zn and Cu smelting respectively, are used as starting materials. They are separately purified up to 99.99999% by distillation coupled with vaporization in a pure H_2 stream followed by multipass zone refining. Subsequently, the purified Cd and Te are charged with 1:2 weight ratio and vacuum sealed in a quartz ampoule coated with C. The ampoule is heated up to 1000 °C and the Te-rich CdTe polycrystal is synthesized. Thereafter, it is again sealed in a quartz ampoule in pure Ar gas and melted at 1000 °C in a Bridgman furnace. A 1:1 CdTe polycrystal is recrystallized from the bottom of the ampoule, which is used as a starting polycrystal for the THM growth. Because of the low treatment temperature and the gettering effect of Te in this process, detector-grade high quality CdTe polycrystals can be obtained.

2.2. Crystal growth by the travelling heater method

THM growth is performed as follows. Cd-Te-Cl alloy tablets as the starting solution and the refined CdTe polycrystal ingots as the feed are loaded at the bottom and top, respectively, in a C-coated quartz ampoule, and the ampoule is sealed in pure Ar gas. The Cd-Te-Cl alloy tablets are made by melting the 99.99999% Te, the refined CeTe polycrystal and desiccated 99.9999% $CdCl_2$. The THM ampoule is heated up to the growth temperature of 700 °C-900 °C. The growth speed ranges from 2 to 5 mm per day. The temperature gradient at the growth interface is

0921-5107/93/$6.00

© 1993 - Elsevier Sequoia. All rights reserved

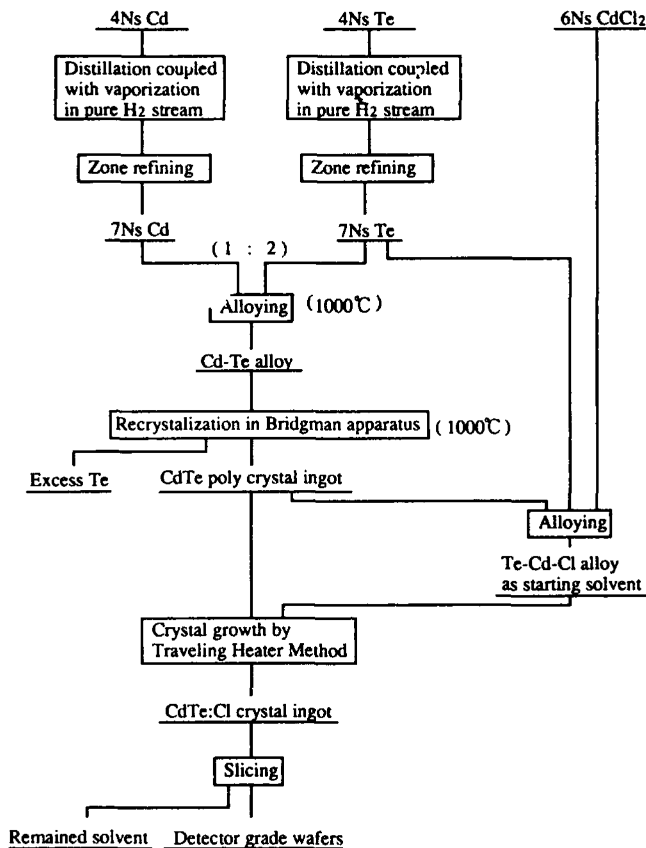

Fig. 1. Flow diagram of CdTe:Cl crystal growth for radiation detectors.

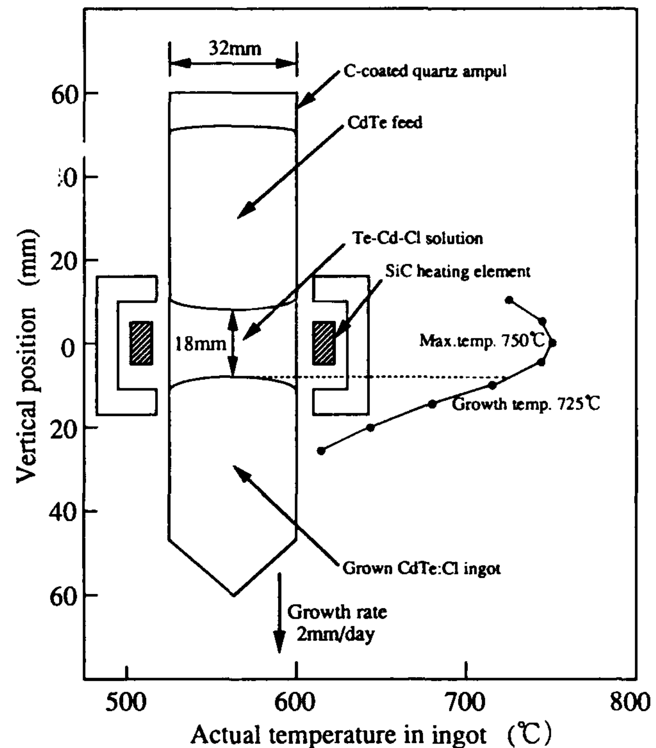

Fig. 2. Typical condition of the THM.

20 °C–60 °C cm^{-1}. The typical condition is that the maximum temperature of the solvent is 750 °C, the growth temperature is 725 °C, as shown in the temperature distribution along the crystal in Fig. 2, and the growth speed is 2 mm per day. After crystal growth, the furnace is cooled down to room temperature at a rate of 10 °C–20 °C h^{-1}. Then the grown crystal ingot is removed from the ampoule and sliced perpendicularly to the growth axis.

2.3. Characterization

The photograph of the THM CdTe ingot grown at 725 °C, the typical grain structures of as-sliced wafers and some detector elements are shown in Fig. 3. The CdTe ingot is 32 mm in diameter and 80 mm long. It is noticed that, while part of the ingot grown earlier contains some grains, the portion grown subsequently is of almost a single grain.

Typical analysis results for the impurities of the THM-grown ingot are shown in Table 1. Cl is examined by ion exchange chromatography of AgCl and other impurities by atomic absorption spectrophotometry. It is found that Cl is distributed through the ingot with 1.3–1.6 ppm and other impurities are below the detection limit; namely, under 0.05 ppm for Al, 0.02 ppm for Cu, Fe, Ni and Si, and 0.01 ppm for Ag.

The resistivity of the ingot is measured by the two-terminal method with contacts formed by In solderings and the carrier lifetime is measured from the current pulse shape on the time-of-flight measurement. The resistivity and the carrier lifetimes of the THM-grown ingot as a function of the Cl dopant concentration, ranging from 0.5 to 30 ppm, are shown in Fig. 4. The resistivity increases with the Cl concentration and a high resistivity of more than 10^8 Ω cm, which is needed for radiation detector applications, is obtained above a Cl concentration of 1.5 ppm. The resistivity saturates above a Cl concentration of 5 ppm, indicating the creation of compensating acceptors doped with the Cl. The lifetimes of electrons and holes increase with the Cl concentration in the region below 1.5 ppm; however, above that, both decrease. The highest lifetimes of 1.0 and 0.5 μs for electrons and holes, respectively, are achieved in a Cl concentration region from 1 to 2 ppm.

3. Detector fabrication

The CdTe wafers cut from the ingot are lapped using the lapping machine with Al abrasive powder and

Fig. 3. Photograph of (from left to right) THM-grown CdTe:Cl ingot, sliced wafers and detector elements.

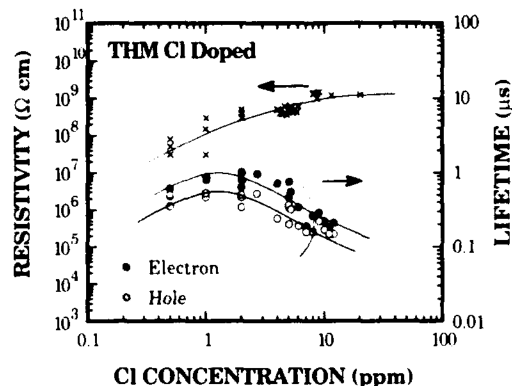

Fig. 4. Resistivity and carrier lifetime as a function of Cl concentration.

TABLE 1. Analysis of impurities through THM-grown ingot

Sampling position	Weight in ppm						
	Cl	Cu	Ag	Fe	Ni	Al	Si
9[a]	410	0.02	–	–	–	–	–
8[b]	1.3	–	–	–	–	–	–
7[b]	1.4	–	–	–	–	–	–
6[b]	1.4	–	–	–	–	–	–
5[b]	1.5	–	–	–	–	–	–
4[b]	1.5	–	–	–	–	–	–
3[b]	1.5	–	–	–	–	–	–
2[b]	1.5	–	–	–	–	–	–
1[b]	1.6	–	–	–	–	–	–
Detection limit	0.1	0.02	0.01	0.02	0.02	0.05	0.02

[a]Amount remained solvent.
[b]Grown crystal (ingot).

controlled mechanical pressure on the wafer surfaces. The wafer surfaces are then polished by mechano-chemical lapping to the device thickness of 1.2 or 2.0 mm and are etched by the Br–methanol solution to a depth of 7 μm. To form the electrodes, electroless Pt deposition using $H_2PtCl_6H_2O$ solution is carried out on both surfaces [6]. In our previous work [5], the Pt–CdTe–Pt system was found to indicate the least time-dependent drift on the radiation detection count rate and the spectrum pulse height. Then, according to the application of the detectors, the Pt-deposited wafer is cut into small pieces of square chips by a circular steel blade.

The detector is tested using Am^{241}(60 keV), Co^{57}-(122 keV) and Cs^{137}(662 keV) γ radiation sources and X-ray sources. The signal detected is amplified by an EG&G ORTEC model 142A preamplifier.

4. Uniformity of the travelling heater method wafer

In Fig. 5 the distribution of the full width at half-maximums (FWHM) for an Am^{241} 60 keV γ source in the 32 mm diameter wafer is shown. Each detector size had dimensions 2 mm × 2 mm × 2 mm.

In Fig. 6 a histogram of the FWHMs for several wafers along the growth direction is shown.

These results demonstrate that excellent uniformity in the wafers as well as along the ingot is achieved. FWHMs as low as 4 keV (6.7%) are obtained in more than 80% of the wafer area. The slight variation of the FWHM characteristics along the growth direction is considered to be mainly caused by the difference of thermal history in the ingot.

5. Radiation detectors

5.1. One-element detectors

Radiation detectors for dosimetry use are usually composed of one CdTe chip of differing dimensions, such as 1.8 mm wide, 2.0 mm deep and 1.2 mm thick, 3.5 mm × 3.5 mm × 2.0 mm, 10 mm × 10 mm × 2 mm, 2.0 mm × 1.2 mm × 10 mm, 25 mm in diameter × 2 mm in thickness, etc., according to the applications. They are packaged in a TO-18 or a TO-5 with or without a cap window, or a specially made Al housing for larger chips.

The measured energy spectrum at an applied voltage of 24 V and the FWHM of the photopeak as a function of the applied voltage for the 60 keV γ-ray for

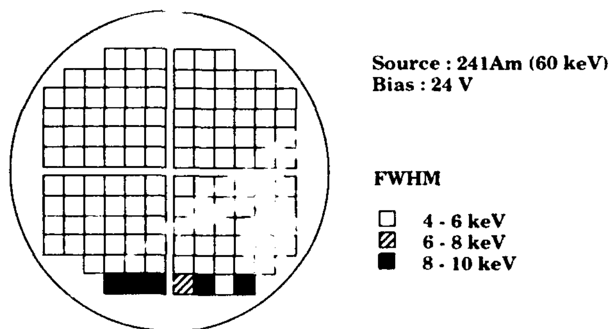

Fig. 5. FWHM homogeneity in a wafer 32 mm in diameter.

the chip dimensions 1.8 mm × 2.0 mm × 1.2 mm are shown in Figs. 7 and 8 respectively. In Fig. 8 the calculated results of the FWHM, using the Hecht relation [7] with $\mu\tau$ products of electrons and holes obtained from the time-of-flight measurement, are also shown. Their agreement with the experimental results is not so good in the low applied voltage region, which is considered to be caused by the non-uniformity in electric field in the experimental diode; however, the agreement becomes quite good in the high voltage region. The FWHM is improved to 4 keV on increasing the applied voltage because of the increase in the drift length of both carriers.

Figure 9 shows the FWHM as a function of the area of the CdTe detector with various dimensions mentioned above for the 60 keV γ-ray. The FWHM increases linearly with the detector area up to 3.67 cm^2, because of the increase in capacitance of the detector. The count rate and the FWHM for the chip with the largest area of 25 mm in diameter are 11 kcps and 13.9 keV, respectively, for the 60 keV γ-ray (Am^{241}, 0.34 MBq; distance, 1.5 cm). For the 122 keV γ-ray source, a peak-to-valley ratio of 5 is obtained (Fig. 10). Its dark current at a bias voltage of 30 V is 200 nA.

The time-dependent stability is one of the key issues of the CeTe radiation detectors. The count rate of the 1.8 mm × 2 mm × 1.2 mm detector with a threshold energy of 15 keV *vs.* time after biasing is shown in Fig. 11. The count rate drift is less than 1% for 1 h after the bias supply, which is not a serious problem for practical applications.

5.2. *Array detector*

The array detector is developed for an application in medical diagnostics. It is composed of 90 elements which are arranged in one line. The dimensions of each element are 1.8 mm × 2.0 mm × 1.2 mm. The element pitch is 2.0 mm and the total detective length is 180 mm. Each chip is mounted on a circuit board made of an Al_2O_3 substrate with Ag epoxy. On the other surface, Au wire is attached also using Ag epoxy. The arrayed detectors are packaged in a specially designed Al box (Fig. 12), or in a Kobar cap box for hermetic sealing.

Figure 13 shows typical data of the FWHM and the count rate for 90 elements operating at an applied voltage of 24 V for the 60 keV γ-ray. The averaged FWHM is 4.0 keV with a maximum and minimum of 4.4 and 3.7 keV respectively. A count rate variation of 4% is obtained. The difference of the depletion layer depth among the elements may cause this variation.

The charge collection efficiency is calculated to be 60% at a 24 V bias, which increases to 90% at 200 V with the increase of the $\mu\tau E$ product.

5.3. *Monolithic detector*

To detect Compton scattered X-rays in real time with a much reduced S/N ratio, a monolithic-type detector is investigated. It has a position-sensitive structure as shown schematically in Fig. 14, and 20-element detectors are monolithically integrated. Each element has a width of 0.35 mm, a length of 10 mm, a thickness of 1.2 mm and a pitch of 0.5 mm.

Measured FWHMs and count rates with the threshold of 15 keV against the 60 keV γ-ray for each arrayed number are shown in Fig. 15. The averaged FWHM and count rate are 8.9 keV and 1.6 kcps respectively. As cross-talk is reduced by half in both the end detectors, the count rate values of these are lower than those of the other detectors located in the middle. These performances seem to be satisfactory at the initial stage of the development.

6. Reliability

The reliability tests using one-element CdTe detectors are systematically conducted following the Japanese industrial standard (JIS) C7021. The detectors are hermetically sealed in TO-5 packages whose leak rate is examined to be less than 5×10^{-8} atm cm^3 s^{-1} by a fine leakage test using He gas. The failure criterion is set at the FWHM level of 12 keV for the 60 keV γ-ray.

6.1. *Environmental tests*

Table 2 shows the test items, their conditions and the results of the environmental tests. 90 samples were subjected to thermal shock, temperature cycling, humidity cycling, vibration fatigue and then low temperature storage tests and no failures were found in any of the tests. Next, 30 of the above 90 samples were examined by the mechanical shock test with no failures found.

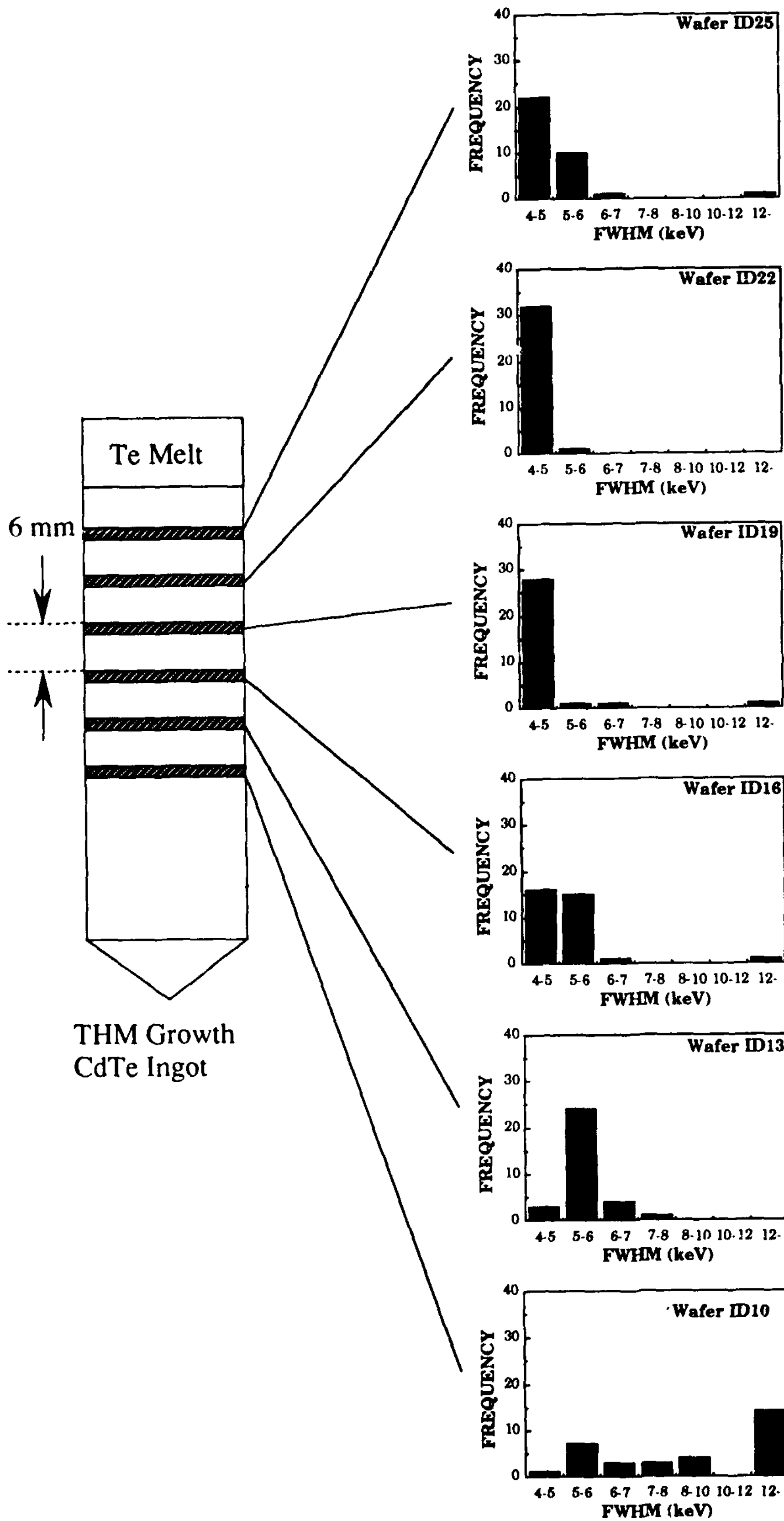

Fig. 6. FWHM distribution in wafers along the crystal growth direction.

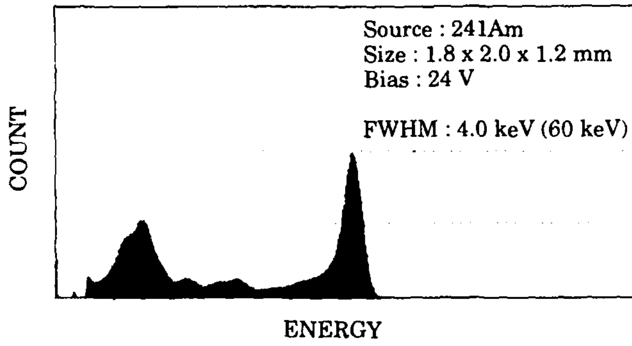

Fig. 7. Measu.ed energy spectrum for a 60 keV γ-ray source.

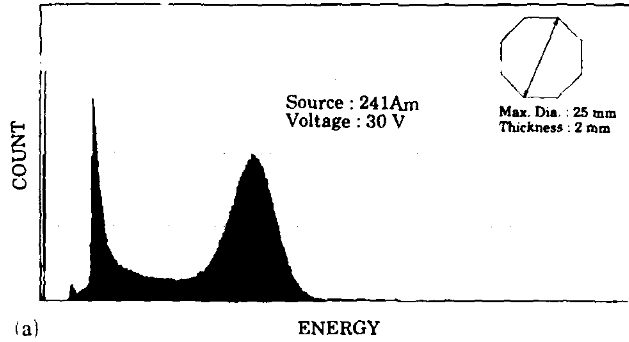

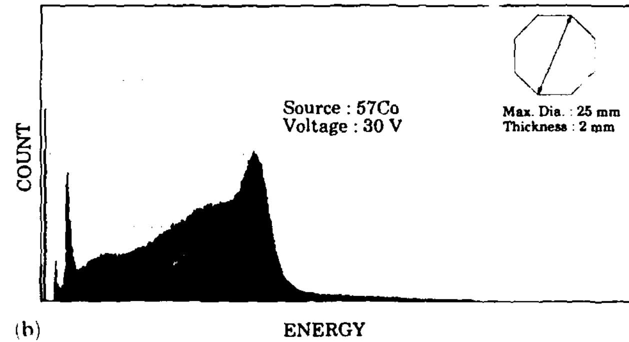

Fig. 10. Energy spectra of a detector 25 mm in diameter for (a) 60 and (b) 122 keV γ-ray sources.

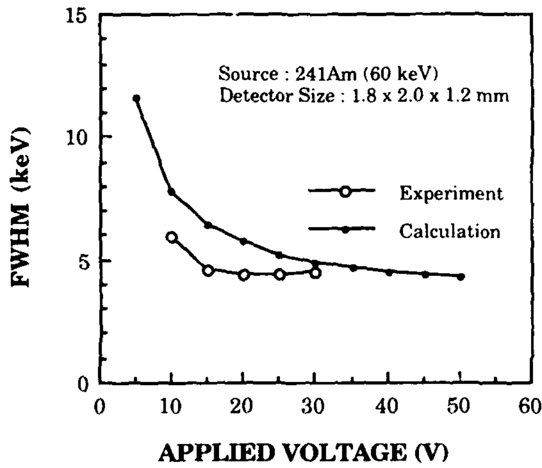

Fig. 8. FWHM as a function of applied voltage.

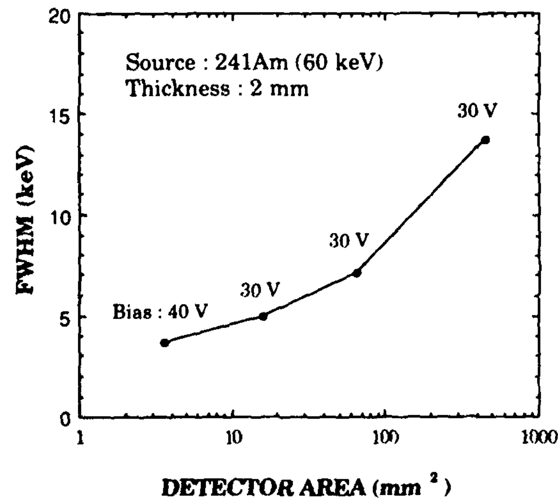

Fig. 9. FWHM as a function of detector area for a 60 keV γ-ray source.

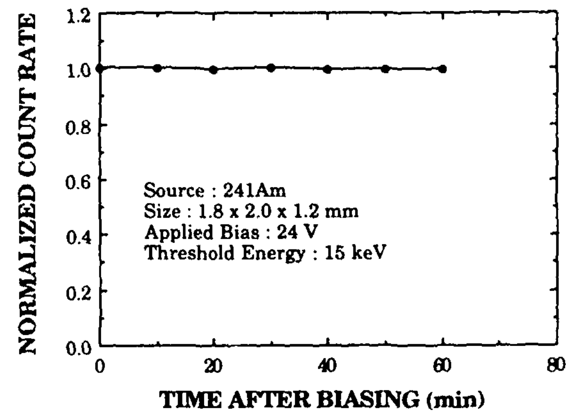

Fig. 11. Count rate as a function of time after biasing. The integration time of each point is 5 s.

6.2. *Reliability life tests*

To estimate the operating life of the developed detectors, accelerated life tests of high temperature storage with and without d.c. biasing were conducted. To avoid the Cd evaporation from the crystal, four stress levels—115 °C, 100 °C, 85 °C and 70 °C—were selected with 18 test samples for each level.

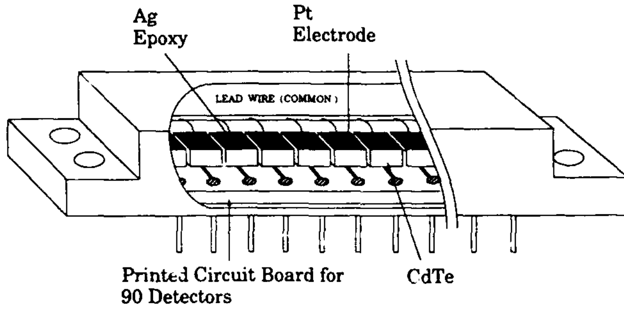

Fig. 12. Schematic view of a one-dimensional arrayed detector. Each element is mounted on a printed circuit board.

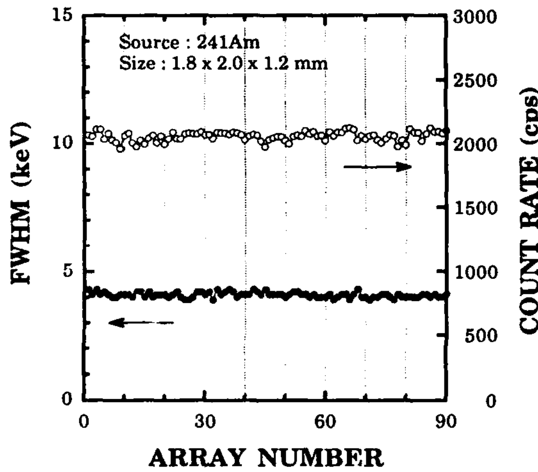

Fig. 13. FWHM and count rate for 90-element cell detectors.

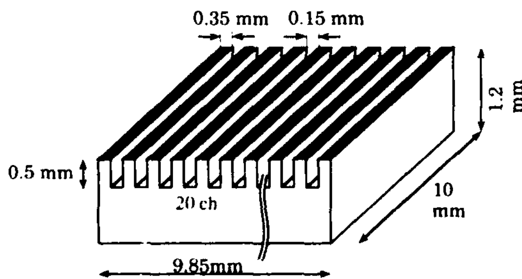

Fig. 14. Schematic view of a monolithic radiation detector.

Figure 16 shows the results of the mean time to failure (MTTF) *vs.* temperature. The MTTF is defined to be the time when the failure rate equals $1 - 1/e$ [8]. The relationship of log(MTTF) *vs.* the reciprocal of the absolute temperature can be represented by a straight line with an activation energy of 1.77 eV. By extrapolating the line to lower temperatures, the MTTF is

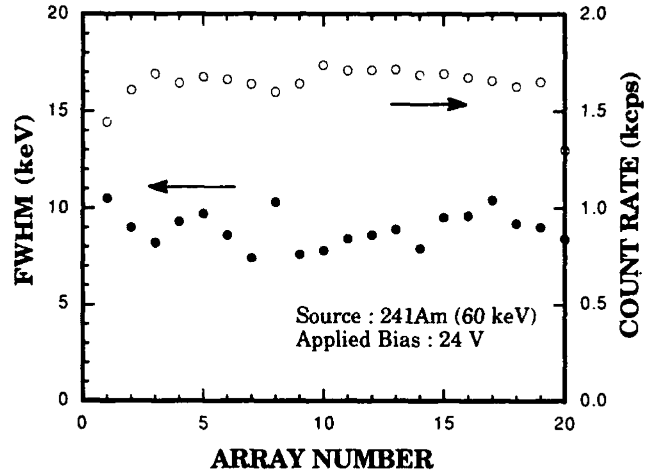

Fig. 15. FWHM and count rate for 20-element cells in the monolithic detector.

TABLE 2. Result of environmental tests

Test item	Condition	No. of samples	Judgement
Thermal shock	0 °C–100 °C; 100 cycles	90	Passed
Temp. cycling	−40 °C–70 °C; 5 cycles	90	Passed
Humidity cycling	95%; −10 °C–65 °C; 10 cycles	90	Passed
Mechanical shock	500 G; 1 ms; *x*, *y*, *z*; 3 times	30	Passed
Vibration fatigue	20 G; 2000 Hz; 48 min	90	Passed
Low temp. storage	−40 °C; 1000 h	90	Passed

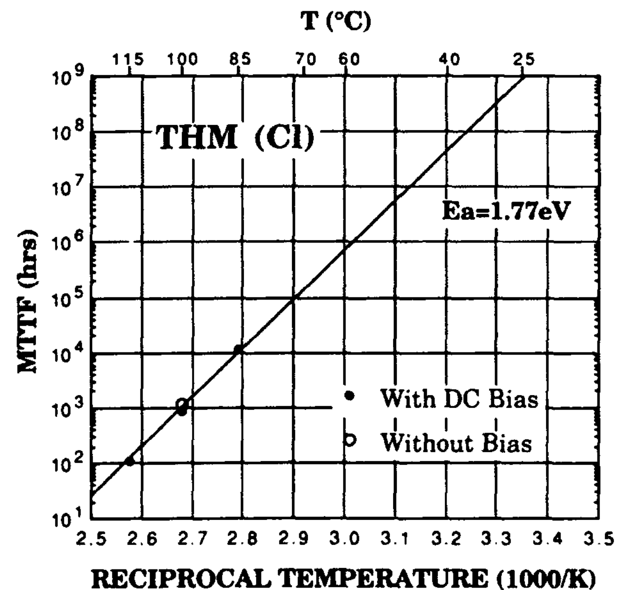

Fig. 16. MTTF as a function of temperature.

estimated to be 1×10^9 h at 25 °C, which is much longer than the measure 2×10^6 h obtained in the previous work [4]. Though the failure mechanism is under investigation, the migration of Ag from the epoxy resin into the CdTe crystal through the Pt electrode may be the main cause.

7. Conclusions

CdTe radiation detectors using THM-grown, Cl-doped crystals have been developed and are demonstrated to be applicable to practical use in medical diagnostics and dosimetry.

THM crystal growth is carried out with the typical growth temperature of 725 °C, growth speed of 2 mm per day, temperature gradient of 25 °C cm^{-1} and a Cl concentration of 1–2 ppm. A resistivity of more than 1×10^8 Ω cm and lifetimes of 1.0 μs and 0.5 μs for electrons and holes, respectively, have been achieved.

The characteristics of an averaged energy resolution of 4 keV and the count rate variation of less than 4% for a 60 keV γ-ray source for a 90-element array detector are achieved. For one-element detectors, a detector area as large as 25 mm in diameter is fabricated with a count rate of 11 kcps and an FWHM of 13.8 keV for a 60 keV γ-ray.

The environmental tests following the evaluation conditions for ordinally electronic devices have been conducted and no failures have been found. High temperature acceleration tests have also been conducted and the MTTF is estimated to be 1×10^9 h at 25 °C.

References

[1] H. B. Barber, J. M. Woolfenden, D. J. Donahue and W. S. Nevin, *IEEE Trans. Nucl. Sci.*, *NS-27* (1980) 496.

[2] G. Entine, P. Waer, T. Tiernan and M. R. Squillante, *Nucl. Instrum. Methods A*, *283* (1989) 282.

[3] T. Ohtsuchi, H. Tsutsui, K. Ohmori and S. Baba, *Proc. Tech. Digest 10th Sensor Symp.*, Inst. Elect. Eng., Tokyo, 1991, p. 97.

[4] Y. Iwase, H. Takamura, K. Urata and M. Ohmori, *Proc. Tech. Digest 6th Int. Conf. on Solid State Sensors and Actuators*, IEEE, San Francisco, CA, 1991, p. 840.

[5] Y. Iwase, M. Funaki, A. Onozuka and M. Ohmori, *Nucl. Instrum. Methods*, in press.

[6] P. Siffert, J. Berger, C. Scharager, A. Cornet, R. Stuck, R. O. Bell, H. B. Serreze and F. V. Wald, *IEEE Trans. Nucl. Sci.*, *NS-23* (1976) 159.

[7] W. Akutagawa and K. Zanio, *J. Appl. Phys.*, *40* (1969) 3838.

[8] Japanese Industrial Standard *JIS Z8115 S18*.

Gamma- and X-ray detectors manufactured from $Cd_{1-x}Zn_xTe$ grown by a high pressure Bridgman method

Jack F. Butler, F. Patrick Doty and Boris Apotovsky
Aurora Technologies Corporation, 7408 Trade Street, San Diego, CA 92067 (USA)
Jean Lajzerowicz and Loick Verger
LETI - (CEA-Technologies Avancees) CENG, BP85X, 38041 Grenoble Cedex (France)

Abstract

Results of recent efforts in the growth of $Cd_{1-x}Zn_xTe$ crystals by a high pressure Bridgman (HPB) method and their use in gamma- and X-ray detector applications are presented. Evidence for crystals of relatively low defect content include etch pit densities of $\leq 10^4$ cm^{-2}, double crystal rocking curve linewidths of 10–15″ and sharp, bright emission lines with excitonic features in low temperature photoluminescence measurements. Resistivities in excess of 10^{11} ohm cm are achieved without impurity doping. The resulting low leakage currents lead to good energy resolution, <6% at 59.5 keV for example. The dependence of leakage current on temperature from 233 K to 373 K implies a Fermi level at mid-gap for $x = 0.2$. The results of flash X-ray experiments indicate that the high current sensitivity, low leakage current and good temporal response of $Cd_{1-x}Zn_xTe$ detectors make them attractive candidates for applications involving short pulses at high dose rates.

1. Introduction

CdTe has long been an attractive material for gamma- and X-ray detection, reflecting its high atomic weight and a relatively wide bandgap which makes room temperature operation possible. Alloying ZnTe with CdTe to form the ternary alloy $Cd_{1-x}Zn_xTe$ results in a wider bandgap, with consequent lower detector leakage currents, and a lower defect density due to alloy strengthening of the lattice. A high pressure Bridgman (HPB) growth method which accommodates the higher melting temperatures of the alloy and allows growths to be carried out at stoichiometric compositions has been perfected; high resistivity is achieved without the introduction of problematic dopants such as Cl. The following sections discuss the application of HPB growth to $Cd_{1-x}Zn_xTe$ and recent detector characterization results for $x \leq 0.20$.

2. Preparation and properties of $Cd_{1-x}Zn_xTe$ crystals

The growth of $Cd_{1-x}Zn_xTe$ crystals from the melt is generally complicated by relatively high melting temperatures and vapor pressures, and the fact that the melting temperatures are comparable to or exceed the softening temperature of quartz. While crystals with $x \leq 0.04$ are often grown in sealed quartz ampoules, the incorporation of oxygen and other impurities from quartz near its softening point can cause significant contamination, even when carbon coatings are applied. It is thus advantageous to grow $Cd_{1-x}Zn_xTe$ crystals in a high pressure chamber in which an inert gas reduces diffusion and consequent evaporation of charge; the high pressure eliminates the need for sealed ampoules and permits a choice of crucible materials.

The HPB furnace design employed by Aurora Technologies Corporation (ATC) has been described in previous publications [1, 2]. All parts exposed to high temperatures are made of high purity graphite. A specially designed graphite heater provides a temperature profile optimized for the Bridgman growth. High purity graphite crucibles are fitted with tight fitting caps to reduce evaporative loss. Crucible travel is effected by a high pressure mechanical feedthrough. The furnaces can accommodate crucibles with internal diameters up to 10 cm and growth charges up to 10 kg. All graphite parts are enclosed in a large steel shell designed to withstand pressures in excess of 100 atm. The furnaces can be operated to temperatures above 1600 °C. Figure 1 shows a photograph of an HPB furnace used by ATC for the production of $Cd_{1-x}Zn_xTe$ and other II–VI compounds.

The starting elements for crystal growth are multiply purified elements weighed out to a stoichiometric composition. No impurity dopants such as Cl are added to

0921-5107/93/$6.00 © 1993 – Elsevier Sequoia. All rights reserved

Fig. 1. Photograph of an Aurora Technologies Corporation high pressure Bridgman furnace used for the growth of $Cd_{1-x}Zn_xTe$ crystals up to 10 cm in diameter and 10 kg. For dimensional reference, the photograph spans 3.5 m from top to bottom.

the charges. The complete crystal growth cycle requires about one month.

$Cd_{1-x}Zn_xTe$ crystals have been grown for the entire range of $0 \leq x \leq 1$ by the HPB method [2]. Table 1 summarizes characterization data for crystals with $x \leq 0.2$, the limit for which useful radiation detectors have as yet been produced. The data in Table 1 are representative averages, generally of a large number of samples.

Resistivities are found to be remarkably uniform throughout a boule, varying approximately ± 20% over a wafer cut transverse to the growth direction and ± 50% over a longitudinal slice. The fact that near-

TABLE 1. Properties of HPB grown $Cd_{1-x}Zn_xTe$ crystals

Property	Zn fraction, x		
	0	0.04	0.20
Resistivity (ohm cm)	3.0×10^9	2.5×10^{10}	1.5×10^{11}
Etch pit density (cm^{-2})	1.8×10^5	1.0×10^4	0.5×10^4
DCRC linewidth (FWHM, arc seconds)	NM	14	12
PL linewidth (FWHM, meV)	0.3	1.0	2.2

intrinsic resistivities are achieved without the introduction of impurities may be related to growth at the metal–tellurium stoichiometric composition.

The etch pit density (EPD) values were quite uniform, varying less than 50% in about 100 samples from 10 boules. The values in Table 1 are significantly lower than those typically reported for crystals grown in sealed quartz ampoules and used in the infrared detector industry as substrate material.

Double crystal rocking curves (DCRCs) were generated with a 2 mm × 8 mm X-ray exposure surface on (111) oriented samples from nine boules with $x = 0.04$ and one boule with $x = 0.20$. The narrowest width observed was 10″, on a sample of 4.0 at.% material, an indication of low defect content.

The low temperature photoluminescence (PL) spectra exhibited bright, sharp emission lines in which free and bound excitons were clearly visible; evidence was found for a two-hole transition (THT) in a ZnTe sample. All of the major lines were accompanied by sharp LO phonons. The sharpness of the phonon lines and existence of the THT line are indicators of high structural quality and low impurity concentrations. It is noteworthy that in PL experiments with ZnTe, the commonly observed emission from an isoelectronic oxygen trap at 1.6 eV was absent. The increase in linewidth with x apparent in Table 1 is attributable to alloy broadening.

3. $Cd_{1-x}Zn_xTe$ gamma-ray detectors

The very high resistivities and evidence for low impurity concentrations and high crystalline quality shown in the data of Table 1 make $Cd_{1-x}Zn_xTe$ an attractive candidate for gamma-ray detector applications. Furthermore, the ability to produce large, homogeneous boules of this material raises interesting new prospects, such as: (1) large quantity, low cost detector manufacturing methods and (2) fabrication of large area detector arrays for a variety of gamma-and X-ray imaging applications in medicine and industry. In earlier experiments, it was found that the established fabrication technology for CdTe detectors was generally applicable to $Cd_{1-x}Zn_xTe$ for x up to at least 0.20, and acceptable gamma-ray detector performance up to this composition was demonstrated [3]. The remainder of this section describes the results of recent experiments designed to characterize and increase our understanding of these devices.

Data presented in Butler *et al.* [3] shows that a $Cd_{0.8}Zn_{0.2}Te$ detector under constant bias for seven days exhibited no change in counting rate (*i.e.* no polarization). A test has since been concluded in which a detector fabricated from HPB-grown CdTe was maintained under a constant bias of 50 V from March 1989 until April 1992, on-line in a factory environment; there was no measurable change in its counting efficiency over the three-year period. Polarization, which has in the past caused difficulties in practical applications of CdTe detectors, has been related to the presence of Cl as a dopant [4].

Current–voltage curves for $Cd_{0.8}Zn_{0.2}Te$ detectors with two commonly employed contacting metals are shown in Fig. 2; detector dimensions are 8 mm × 8 mm × 1.6 mm, the third dimension being the gap thickness. The slopes of the linear regions of both curves indicate a resistivity of approximately 1×10^{11} ohm cm.

Leakage currents at 100 V were measured as functions of temperature from −40 °C to 100 °C. Results are summarized on a semilogarithmic scale in Fig. 3. The excess currents evident in the deviations from linearity at low temperatures, especially for the Pt-metallized sample, are believed to be due to surface conductivity at the edges, and illustrate the importance of proper attention to this factor in the fabrication of detectors. The activation energy derived from Fig. 3 is 0.8 eV, indicating that the Fermi level is at the midpoint of the bandgap.

Figure 4 shows an energy spectrum of the gamma-ray emission from an Am-241 source obtained from a $Cd_{0.8}Zn_{0.2}Te$ detector. The detector was biased at 300 V and its dimensions were 5 mm × 5 mm × 1.2 mm. The linewidth (FWHM) of the 59.5 keV photopeak is less than 6% and includes approximately equal electronic noise contributions from the preamplifier input and a 3 nA leakage current. A low energy tail related to incomplete charge collection is evident.

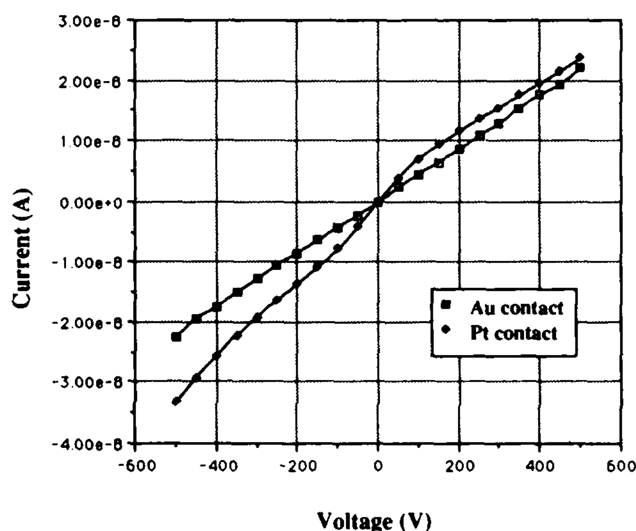

Fig. 2. Current–voltage characteristics for $Cd_{0.8}Zn_{0.2}Te$ detectors. Detector dimensions are 8 mm × 8 mm × 1.6 mm.

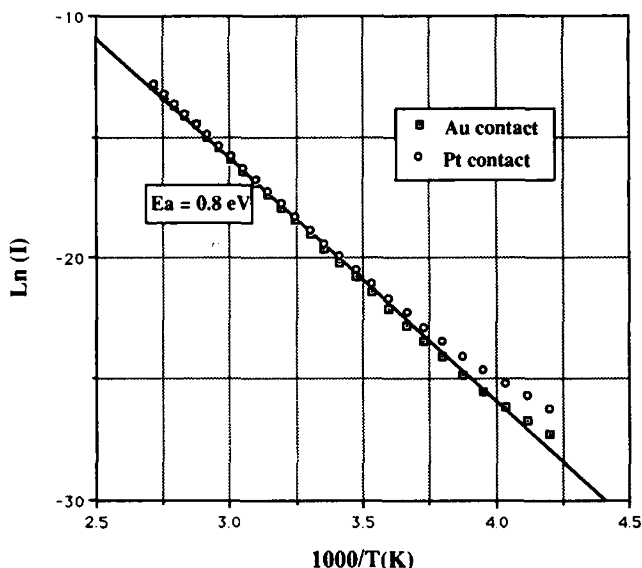

Fig. 3. Leakage current as a function of temperature from −40 °C to 100 °C for $Cd_{0.8}Zn_{0.2}Te$ detectors metallized with Au and Pt. Detector dimensions are 8 mm × 8 mm × 1.6 mm.

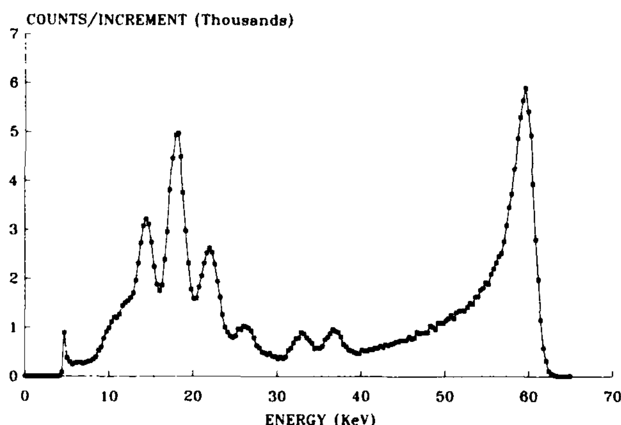

Fig. 4. Energy spectrum of Am-241 gamma-ray emission measured with a $Cd_{0.8}Zn_{0.2}Te$ detector biased at 300 V. Detector dimensions are 5 mm × 5 mm × 1.2 mm.

In order to estimate mobility–lifetime products, $Cd_{1-x}Zn_xTe$ detectors are exposed to the alpha-particle emission from a 1 μCi Am-241 source at a distance of 1 cm. Well-defined peaks are observed and the relative peak position can be measured as a function of applied voltage. When the polarity of the detector surface facing the source is negative, the peak position can be expressed as:

$$q = \frac{\mu_e \tau_e V}{L^2} Q(1 - e^{-L^2/\mu_e \tau_e V}) \quad (1)$$

where q is the charge pulse magnitude at the peak, Q the initial charge generated by the alpha-particle, L the detector thickness, V the bias voltage, and μ_e and τ_e

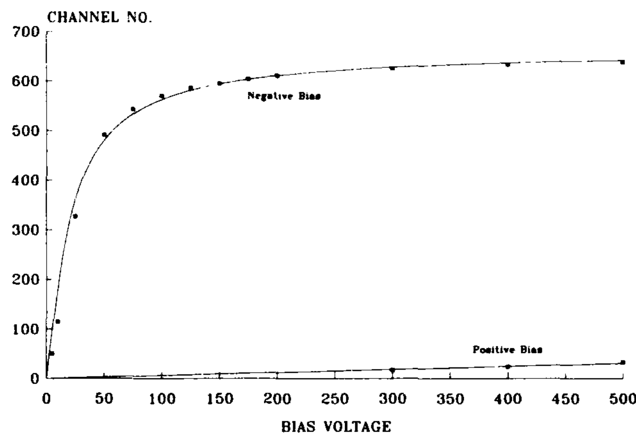

Fig. 5. Energy spectral peak position as a function of bias voltage for a $Cd_{0.8}Zn_{0.2}Te$ detector irradiated with Am-241 alpha-particles. The solid points are experimental data and the smooth curves were fitted from theory by adjusting parameters.

the electron mobility and lifetime, respectively. A similar equation can be written for a positive bias with μ_e and τ_e replaced by the hole parameters μ_h and τ_h.

In Fig. 5, experimental results for a $Cd_{0.8}Zn_{0.2}Te$ detector are shown as points; the theoretical curves were fitted to the points by adjusting the parameters $\mu_e\tau_e$, $\mu_h\tau_h$ and Q. The mobility–lifetime products derived by this method were $\mu_e\tau_e = 8 \times 10^{-4}$ cm^2 V^{-1} and $\mu_h\tau_h = 3 \times 10^{-6}$ cm^2 V^{-1}. Similar results have been obtained for HPB grown CdTe and $Cd_{0.96}Zn_{0.04}Te$. The derived value for electrons is comparable to values typically reported in the literature for electrons in CdTe grown by travelling heater method (THM); the value for holes is lower. As will be shown below, this lower value of $\mu_h\tau_h$ can be related to a correspondingly low value of τ_h.

4. Flash X-ray experiments

In view of recent interest in the use of CdTe and other detectors for flash X-ray radiography and other applications involving short pulses at high exposure rates, flash X-ray experiments were carried out with $Cd_{0.8}Zn_{0.2}Te$ detectors. The temporal behavior of the current output of detectors exposed to 250 kV, 20 ns X-rays was examined, with bias voltage varied from 50 V to 400 V. Typical results are shown in Fig. 6.

The response curves in Fig. 6 do not exhibit the long tails observed with CdTe detectors under similar conditions [5]. The fall times in the present case are consistent with temporal behavior dominated by sweepout of electrons, assuming an electron mobility approximately equal to that of CdTe (about 1000 cm^2 V^{-1} s^{-1}). The long tails reported by Malm and Martini [4] presumably reflect the sweepout time of holes, with

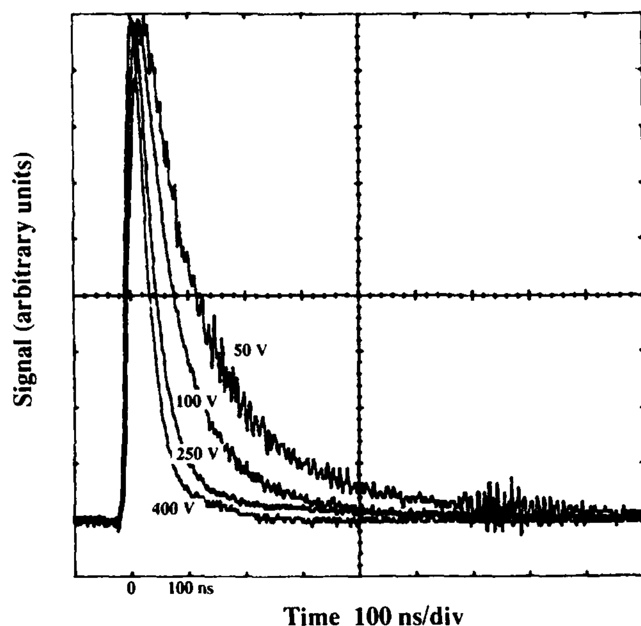

Fig. 6. Normalized flash X-ray response curves for a $Cd_{0.8}Zn_{0.2}Te$ detector at biases from 50 V to 400 V. The 250 kV X-ray source provided 20 ns pulses.

their much lower mobility. The absence of such tails in the $Cd_{0.8}Zn_{0.2}Te$ detector results can be explained by a shorter hole lifetime in this material. If it is assumed that the hole mobility of $Cd_{0.8}Zn_{0.2}Te$ is approximately equal to that of CdTe (about 100 cm^2 V^{-1} s^{-1}), the value for $\mu_h \tau_h$ deduced above implies a hole lifetime of 30 ns.

$Cd_{0.8}Zn_{0.2}Te$ appears to offer a number of advantages for short pulse, high rate detection: the current response is high, comparable to that of CdTe; the very high resistivity and consequent low leakage currents extend the dynamic range at low exposure levels; and the absence of a fall-time tail results in a good temporal resolution, at least for pulse widths greater than a few tens of nanoseconds.

Acknowledgment

The authors wish to acknowledge the valuable technical assistance of Mr. J. Rustique of LETI—(CEA-Technologies Avancees).

References

1 E. Raiskin and J. F. Butler, *IEEE Trans. Nucl. Sci.*, *35* (1988) 88.

2 F. P. Doty, J. F. Butler, J. F. Schetzina and K. A. Bowers, *J. Vac. Sci. Technol.*, *B10* (1992) 1418.

3 J. F. Butler, C. L. Lingren and F. P. Doty, *IEEE Trans. Nucl. Sci.*, *39* (1992) 605.

4 H. L. Malm and M. Martini, *IEEE Trans. Nucl. Sci.*, *21* (1974) 322.

5 L. Verger, M. Cuzin, G. Gaude, F. Glasser, F. Mathy, J. Rustique and B. Schaub, *Nucl. Instrum. Methods*, *A322* (1992) 357.

Materials Science and Engineering, B16 (1993) 296-301

Compensation of trapping losses in CdTe detectors

M. Richter, P. Siffert and M. Hage-Ali

Centre de Recherches Nucleaires (IN2P3)—Laboratoire PHASE (UPR du CNRS No. 292), BP 20, F-67037 Strasbourg Cedex (France)

Abstract

Energy resolution and photopeak efficiency of planar CdTe nuclear radiation spectrometers are degraded by charge trapping effects in the bulk of the detector. Charge loss compensation methods result in an enhancement of energy resolution and photopeak efficiency, but these techniques operate only with certain detectors. In this article we present data from dual-parameter gamma-ray spectrometry and time-of-flight experiments to characterize these devices. A computer model of the charge collection inside the detector will be discussed.

1. Introduction

Cadmium telluride (CdTe) is a material of interest as a highly sensitive, room temperature-operating gamma-ray spectrometer. Modern detectors offer good stability and energy resolution. The best energy resolution up to now of about 0.5% at 662 keV has been achieved by using a slightly cooled detector with a p-*i*-n structure [1]. However, owing to the small electron and hole mobilities in the p-type material generally used, the sensitive region of these detectors is only 0.1-0.3 mm thick. Thus, detection efficiency is rather limited.

In CdTe detectors having a metal-semiconductor-metal (m-s-m) structure the depletion layer can be quite thick (about 1-2 mm). Therefore these devices are much more sensitive; however, the energy resolution and photopeak efficiency of such a thick planar CdTe detector are degraded owing to poor hole transport properties. Consequently, the field of application is still limited. Different approaches to detector geometry and pulse processing techniques have been tested to overcome these shortcomings [2, 3]. However, mostly they did not result in much better resolution or they caused severe problems with detector stability and efficiency loss.

Charge loss correction methods are the most promising [4]. They are based on the assumption that poor energy resolution is mainly related to trapped holes, while the electrons are collected almost without any losses. Because of the much higher mobility of the electrons, the overall charge collection time is determined by the collection time of the holes. The relation between the energy loss fraction and the charge collection time has been measured experimentally and based on these data we could establish a correction function. This results in a tremendous improvement in energy resolution and photopeak efficiency. However, this correction method still demands devices made from materials with sufficiently high hole mobility. In this paper, we present some recent results performed on some of these "good" detectors.

2. Dual-parameter spectrometry

The goal of the experiment was to investigate the variation of the spectrum shape as a function of the charge collection time. Using the Charge Loss Corrector of the firm EURORAD [5], which provides for an optional second output of the risetime information in coincidence with the pulse height at the energy output, we measured dual-parameter spectra of different radiation sources with gamma-ray energies from 60 keV (^{241}Am) up to 662 keV (^{137}Cs).

The spectra show clearly that the initial result can be regarded as a summation of subspectra with shifted photopeaks. The subspectrum near the shortest risetimes offers the best energy resolution and peak-to-Compton ratio (Fig. 1). This matches the experience gained with resolution enhancement using risetime selection systems [3, 4]. Spectra measured with longer risetimes have worse resolution and spectrum shape. Unfortunately, this limits the performance of charge loss correction methods and demands a pulse preselection to suppress pulses with collection times that are too long. The application determines a compromise between efficiency and energy resolution [5].

The photopeak intensity of these subspectra decreases nearly exponentially with increasing charge

0921-5107/93/$6.00

© 1993 - Elsevier Sequoia. All rights reserved

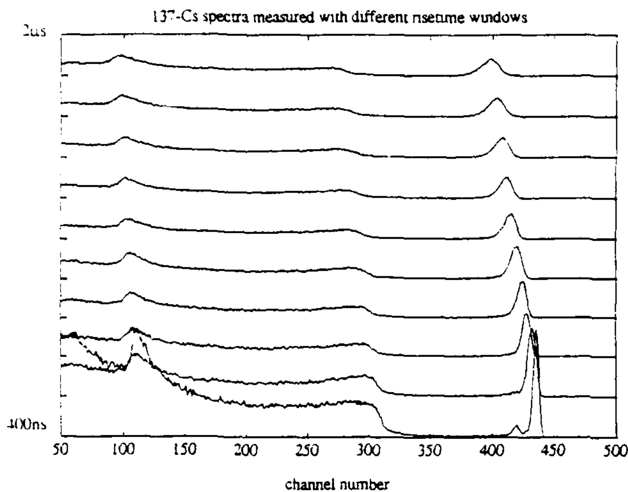

Fig. 1. This dual parameter spectrum of a ^{137}Cs source demonstrates that the untreated energy spectrum measured with a CdTe detector can be regarded as a superposition of shifted subspectra resulting in the low energy tailing of the photopeaks. Each subspectrum is generated in a different layer of the detector.

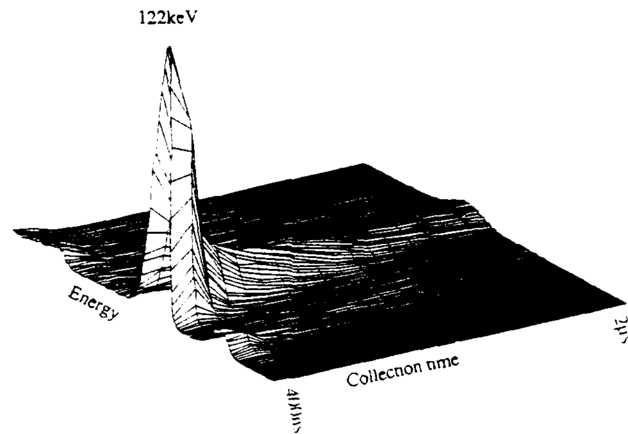

Fig. 3. Dual parameter spectrum of a ^{57}Co source. Compared with the corresponding ^{137}Cs spectrum of Fig. 2, the intensity of the photopeak decays faster. The constant of this exponential function corresponds well with the absorption coefficient.

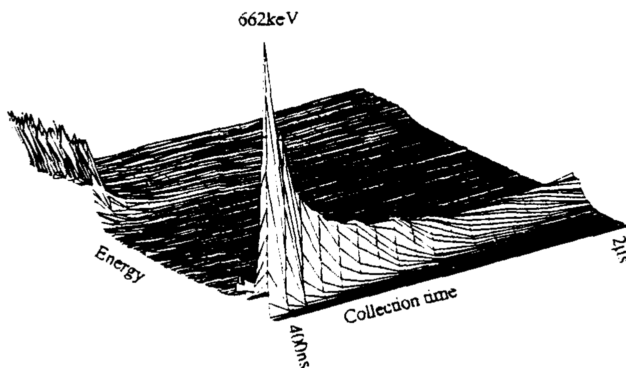

Fig. 2. Dual parameter spectrum of a ^{137}Cs source. The intensity of the 662 keV photopeak decays following the absorption curve.

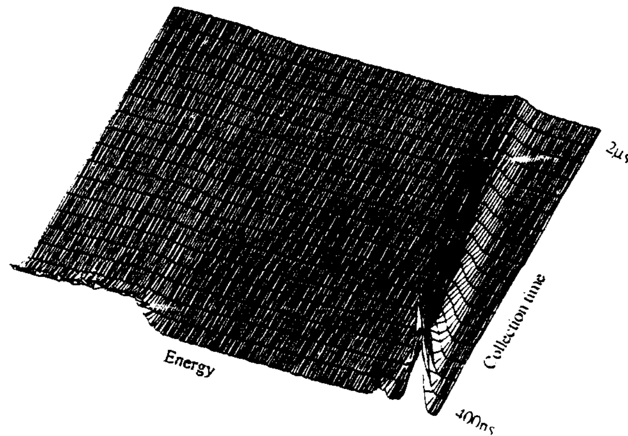

Fig. 4. Dual parameter spectrum of a ^{137}Cs source. This point of view shows clearly the linearity between photopeak shift and charge collection time.

collection time (Figs. 2 and 3). The constant of this exponential function is approximately equal to the absorption coefficient of CdTe for this energy. The error can be explained by the influence of the inhomogenous electrical field inside the detector (see below). This indicates that the phonon energy is absorbed at one point. The relative charge loss depends only on the depth of the carrier generation and not on its initial number.

The low energy tail of the photopeaks appears as a superposition of shifted subspectra with decaying intensity. As already mentioned formerly, the photopeak shift, *i.e.* the relative charge loss, is linearly proportional to the risetime and does not depend on radiation energy (Figs. 4 and 5). Of course the question of why it is linear still remains.

3. Current pulse measurements

To get some more information about the shape of the electrical field inside the detector we must follow the path of the carriers from the point of generation to the contacts. One way to do this is to measure the current pulse. The current is proportional to the number of carriers and their speed. The speed is the product of mobility and electrical field. This means that for a constant number and mobility of carriers the current pulse $I(t)$ gives directly the function $E(t)$. If we arrange a way for the charge to be transported through the whole detector by exclusively one carrier type, then the current pulse $I(t)$ is proportional to $E(x)$.

We can fulfil these conditions if we irradiate the negative-biased surface of a detector with alpha-parti-

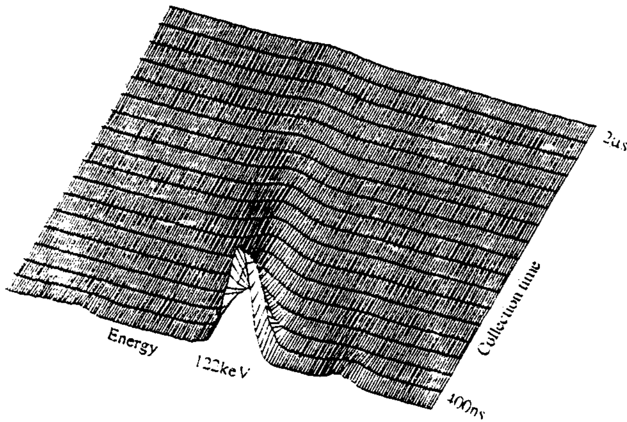

Fig. 5. Dual parameter spectrum of a ^{57}Co source. It is shown that the linear peak shift does not depend on gamma-ray energy.

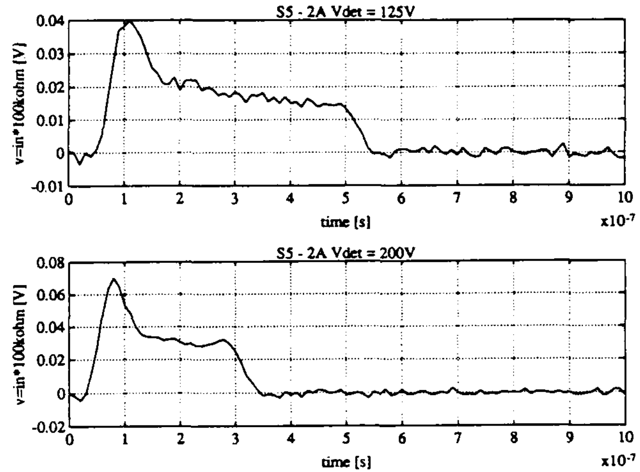

Fig. 6. Current response from alpha-particle irradiation of the negative detector contact. The electron current pulse decays much faster as we would expect from the carrier lifetime. Even for a shorter collection time (see lower curve) the pulse shape does not change substantially. This phenomenon can be explained by a non-homogenous electrical field inside the detector.

cles or soft X-rays. The charge will be transported by electrons to the positive contact. For a sufficiently high bias voltage the carrier transit time is small in comparison with its lifetime. Thus the shape of the electron current pulse is mainly influenced by the shape of the electrical field.

In our experiments we used 2 mm thick CdTe detectors with platinum contacts. The bias voltage varied from 100 V to 300 V. The electron lifetime was measured to be at least 1 μs. A fast current-sensitive preamplifier in a closed loop configuration has been used for the measurements. A high open loop gain ensures short risetimes and accuracy.

The results were rather unusual (Fig. 6). The electrical field has its maximum near the negative contact of the detector and decays more or less exponentially in the direction of the positive side. This is completely contradictory to former investigations of detector polarization [6, 7]. We repeated these experiments with many "good" detectors, that is, with devices which work well with the EURORAD Charge Loss Corrector. The results were always similar.

Further, we observed also the hole current pulses (Fig. 7). Although the collection time of the generated charge is much longer, the current decays only slightly. For higher detector bias voltages the hole current is rising with time. Thus, the higher speed of the holes near the negative contact can obviously compensate for the number of carriers lost by trapping. This also means that the speed of the holes in all layers of the detector is still proportional to the electrical field.

Another unexpected observation was the ratio of the currents of electrons to that of holes. A voltage pulse at the output of a commonly used charge-sensitive preamplifier represents the integral over the detector current pulse. If we compare the slopes of the fast and slow fractions of such a pulse we get a ratio of about 6 to 12. For the penetrating 662 keV radiation of a ^{137}Cs source we got similar results using the current amplifier (Fig. 8).

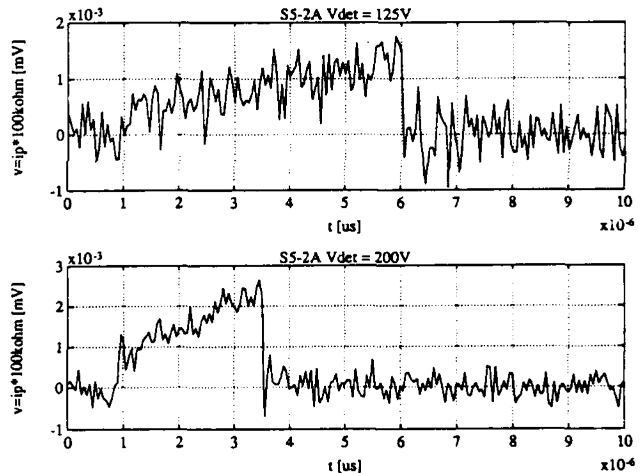

Fig. 7. Hole current pulse after charge generation at the positive detector contact. Although the holes move much slower than the electrons we do not observe a current decay. The electrical field obviously accelerates the holes in the direction of the negative contact and compensates in such a way for the number of carriers lost by trapping. This does not mean that the hole collection efficiency becomes better, as it depends only on the final collection time, but it proves that the electrical field increases against the negative contact.

In experiments with alpha particles we measured an electron current 50 times higher than that of holes. This indicates the existence of a dead layer near the positive contact. Thus, only a small fraction of the

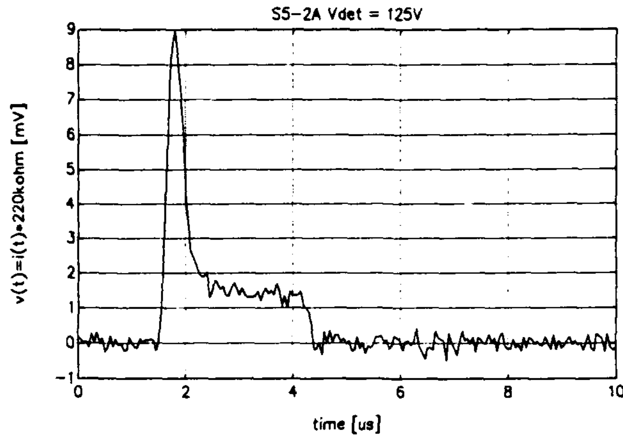

Fig. 8. The detector was irradiated with a ^{137}Cs source. The current pulse demonstrates the ratio of electron and hole current at a point in the middle of the detector.

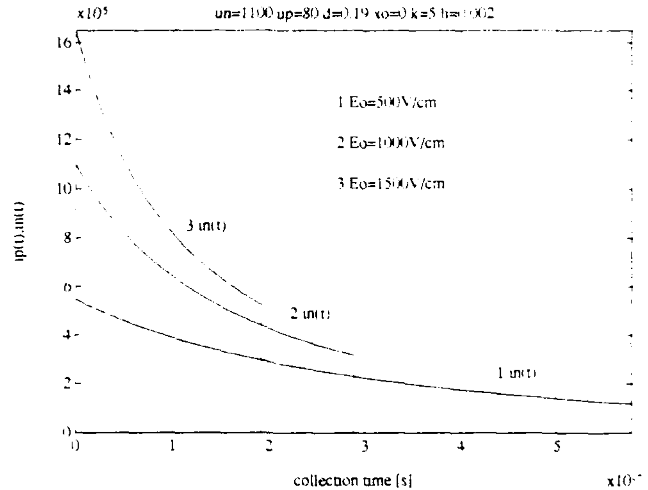

Fig. 9. Electron current pulses $in(t)$ of the model detector calculated for different values of the electrical field at the negative contact. These correspond to detector voltages of 100 V, 200 V and 300 V, for $i = 1$, 2 and 3 respectively. The resulting curve is the superposition of trapping loss and the decay of carrier speed.

generated carriers reaches the internal collection field and the hole current is much smaller. The main result of the current measurements was the discovery of the fast polarization of the used detectors. The electrical field has its maximum at the negative contact and is decaying exponentially. This results in faster hole collection and in some unusual current pulse shapes.

4. Modelling

As a result of these calculations we expected a better understanding of the influence of the different detector parameters on the charge collection efficiency. The basis of our detector model comes from the observation of the current pulses. By varying the model carrier properties, such as mobility and lifetime, and also the field distribution, we fitted the calculated curves to the actual measured pulses. The final model matches well our experiences of real detectors, in which we have:

Electrons: $u_n = 1100\ \text{cm}^2\ \text{V}^{-1}\ \text{s}^{-1} = \text{constant}$

$\tau_n = 1\ \mu\text{s}$

Holes: $up_0 = 80\ \text{cm}^2\ \text{V}^{-1}\ \text{s}^{-1}$

$up(x) = f(E) = up_0 + h^*E(x)$

$\tau p = 1\ \mu\text{s}$

Field: $E = E_0{}^*\exp(-k^*x)$

Detector: thickness $d = 1.9$ mm

negative contact: $x = 0$

With constant hole mobility and a realistic lifetime it was not possible to reconstruct the observed pulse shapes. Oltaviani *et al.* [6] found a relation between the electrical field and the hole mobility (Poole–Frenkel effect). In the case of a high electrical field inside a biased detector this relation can be linearized.

To display the current pulse we have to calculate the speed and number of carriers in the time period t_{coll} between the generation of charge at the point x_0 and its recombination at the contacts. The fraction of the carriers reaching the contacts is determined only by the collection time.

$$n = n_0{}^*\exp(-t_{coll}/\tau) \tag{1}$$

Assuming the proportionality of speed and electrical field we can write for the electrons:

$$v(t, x_0) = -\frac{1}{t^*k + 1/v(x_0)} \tag{2}$$

For the holes the integrals are more complicated owing to the non-constant mobility. We solved the equations numerically.

Figures 9–11 present current pulses for different values of the electrical field generated at different positions inside the detector. The current pulses for $x = 0$ and $x = d$ corresponds to the experiments with alpha particles. The electron current is a good match to the real data. The main difference is the presence of noise and the limited bandwidth of the current amplifier used for the measurements.

The important discrepancy for the holes can be explained by the existence of a thin dead layer under the positive contact which has been neglected in the calculation. We were more interested in the principal pulse shape. For charge generation in the middle of the detector (Figs. 8 and 11) the model is in agreement with the experimental data.

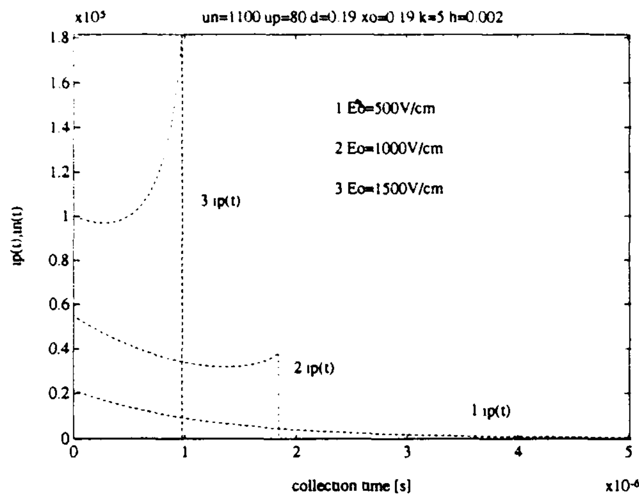

Fig. 10. Calculated hole current pulses $ip(t)$. Near the negative contact the holes are moving faster. The number of carriers lost by trapping can be compensated. For higher electrical fields this effect is more impressive.

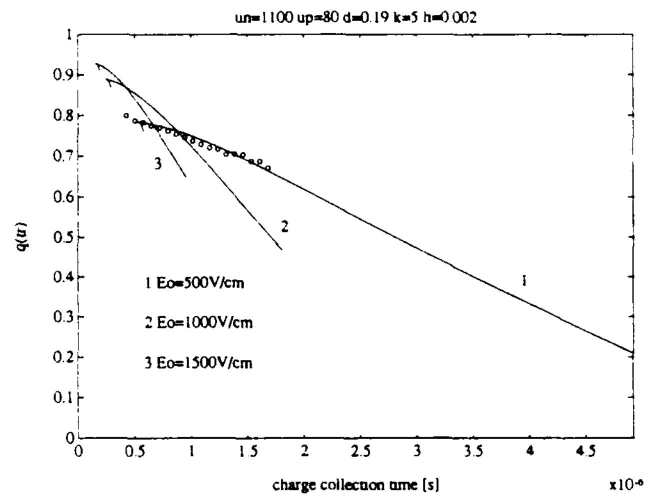

Fig. 12. The function of the collected charge *vs.* collection time of the modelled detector tends to be linear.

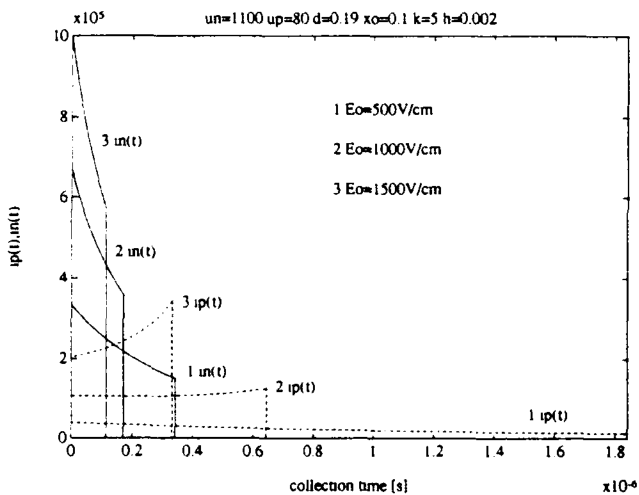

Fig. 11. For this calculation a charge generation in the middle of the detector has been assumed. Both carrier types take part in the charge collection (electron current: solid line; hole current: dashed line).

The resulting curves of collected charge *vs.* collection time of the adapted detector model are presented in Fig. 12. They tend to be linear. The value of the applied electrical field changes only the gradients of the curves, but not their fundamental shape.

5. Discussion

The investigated detectors have followed the evolution of technology since 1983. They are made from highly resistive material which has been grown in a travelling heater method (THM) process under Te pressure. As contact material platinum or gold is used. The sensitive surface area is between 25 mm and 56 mm^2. The devices are mostly 2 mm thick. The best energy resolution can be achieved if the negative side of the detectors is irradiated.

With current pulse measurements it was found that the electrical field inside the detectors has its maximum at the negative contact. Because we still obtained a signal from alpha-particle irradiation of the positive side we think that the "dead layer" there is very thin. This is totally contradictory to former investigations [7]. Only for an old detector made from n-type material with Al contacts did we observe the same direction of polarization. The THM material is normally suspected to be p-type but experimental confirmation is rather difficult owing to its high resistivity.

The influence of contact material is not so clear yet. For detectors from one CdTe ingot the orientation of polarization changes if we contact them with gold instead of platinum; for another ingot the detectors polarize independently of the contact material in the "wrong" direction. Analysis methods such as thermal scanning calorimetry or secondary ion mass spectrometry did not offer suspicious differences. Furthermore, we could not measure a change in the detection efficiency *vs.* time. So we assume that the polarization is a very fast process. Up to now we are unable to explain these phenomena.

Although nearly all newer detectors show this inverted polarization, only a small number of them provide good results with the linear charge loss correction method. As also proved by the model, only detectors with a sufficiently high mobility-lifetime product for holes work well.

To select detectors for the correction, we irradiated them with the deeply penetrating 662 keV gamma rays of a ^{137}Cs source. We observed the output pulses of a normal charge-sensitive preamplifier. If they are composed of slow and fast rising fractions it is probable that this detector works well with our charge loss correction circuit.

6. Conclusion

By means of dual-parameter spectroscopy the function of relative charge loss *vs.* collection time was measured. The experiments demonstrated once more the linearity, and independence of photon energy, of relative charge loss.

With time-of-flight measurements it has been discovered that the electrical field inside some "good" detectors is exponentially shaped. By means of a computer model the influence of this field distribution on the charge collection efficiency has been investigated. The function of relative charge loss *vs.* charge collection time of this model detector is nearly linear and correlates well with experimental data. The observation of fast polarization in CdTe detectors made from highly resistive p-type material is still incomprehensible.

References

[1] A. Kh. Khusainov, *Nucl. Instrum. Methods*, in press.
[2] K. Zanio, *Rev. Phys. Appl.*, *12* (1977) 343.
[3] U. Hagemann, R. Berndt and R. Arlt, *Kernenergie*, *31* (1988) 54.
[4] M. Richter and P. Siffert, *Nucl. Instrum. Methods*, in press.
[5] *EURORAD Charge Loss Detector*, User Manual, Strasbourg, 1992.
[6] G. Ottaviani, C. Canali, C. Jakobini, A. Alberigi Quaranta and K. Zanio, *J. Appl. Phys.*, *44* (1973) 360.
[7] D. Vartsky and P. Siffert, *Nucl. Instrum. Methods*, *A263* (1988) 457.

Materials Science and Engineering, B16 (1993) 302–303

The electronic bistability in doped semiconductors with polar optical scattering: the reversible switching effect in CdTe:Cl at room temperature

N. V. Agrinskaya and V. I. Kozub

A. F. Ioffe Physical Technical Institute, St. Petersburg (Russian Federation)

The behaviour of CdTe in strong electric fields E has been studied in a number of papers. It has been shown that, while in pure materials the Gunn effect is observed at fields $E \geqslant 10^4$ V cm^{-1}, the doped samples exhibit a breakdown behaviour [1]. A reversible switching effect with S-shaped current–voltage curve has been observed and studied in detail in CdTe:Cl at 300 K [2] (Fig. 1). The concentration N_{Cl} of shallow donors was of the order of 10^{18} cm^{-3} but the number of electrons appeared to be $n_0 = 10^{15}$ owing to the presence of compensating defects (with a level $\varepsilon_X = E_c - 0.6$ eV). The origin of such a behaviour (especially in the factor supporting the low resistivity state at weak fields) is, however, unclear. Here we *suggest the mechanism combining the effects of run-away*, impact ionization and electron–electron scattering which we believe explains the phenomenon discussed.

The sharp increase in the conductivity observed in ref. 2 is obviously connected with ionization of the deep compensating level (the shallow donor is already ionized at 300 K). The necessary concentration of electrons with energies $\varepsilon > 0.6$ eV can be provided by the run-away effect characteristic of polar optical scattering ($l \propto \varepsilon$, l being the electron mean free path). Because of this effect the electron distribution function ceases to decrease at energies $\varepsilon > \varepsilon_r$, $\varepsilon_r \approx \hbar\omega_0 T^2/(eEl_0)^2$, $l_0 = l(T)$. Such a run-away is limited in the energy region by the processes involving lateral valleys at $\varepsilon = \varepsilon_l = 1.6$ eV. Thus the distribution function appears to be almost constant in the energy region $\varepsilon_r \leqslant \varepsilon \leqslant \varepsilon_l$. Such a distribution has been modelled for CdTe in Monte Carlo simulations [3].

However, the impact ionization equation

$$\frac{\partial n}{\partial t} = A_t(N - n) - B_t n^2 + A_I n_>(N - n) \qquad (n > n_0)$$

($n_>$ is the number of electrons with $\varepsilon > \varepsilon_X$, and A_t, A_I and B_t are the coefficients of thermal ionization of impact ionization and of thermal recombination respectively) leads in the case $n_> \propto n$, $n_>/n = f(E)$ to a single-valued relation between n and E which cannot explain the S-shaped current–voltage curve.

The necessary multiple-valued behaviour of the electron distribution can be provided by the electron–electron processes. From $\tau_{ee} \to 0$ (τ_{ee} being the characteristic time of electron–electron scattering) they form the electron temperature T_e. From the balance equation, one can find three roots corresponding (at fixed n) to three branches in the current–voltage curve [4]: $T_{e1} \approx T$, $T_{e2} \cong \varepsilon_r/2$ (the branch unstable for fixed E) and $T_{e3} \cong \varepsilon_l$. The state with T_{e3} can exist in relatively weak fields owing to the increase in mobility and therefore in the energy gained in the electric field accompanying the transfer of electrons to the high energy region $\varepsilon \approx \varepsilon_l$. However, the initial concentration $n \approx n_0$ is small, *i.e.* τ_{ee} is large, and the electron temperature cannot be established. Thus a special analysis of electron–electron processes appears to be necessary.

We have shown [4] that a special role is played by the processes in which an electron from the run-away region $\varepsilon \approx \varepsilon_l$ promote an electron from the low energy

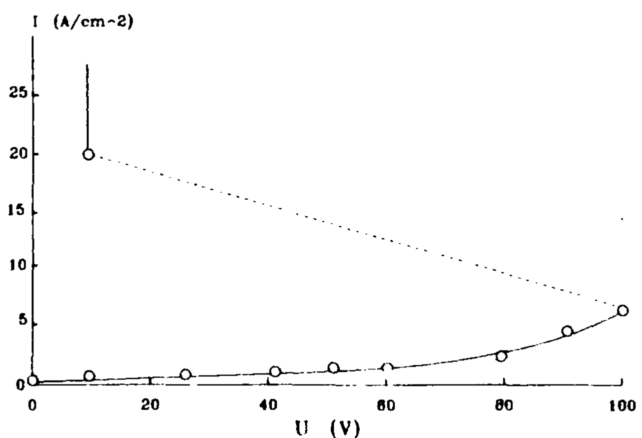

Fig. 1. Typical current-voltage curve of CdTe:Cl crystals, recorded at 300 K using voltage pulses of 2 μs duration; the thickness of the sample was 100 μm.

0921-5107/93/$6.00

© 1993 – Elsevier Sequoia. All rights reserved

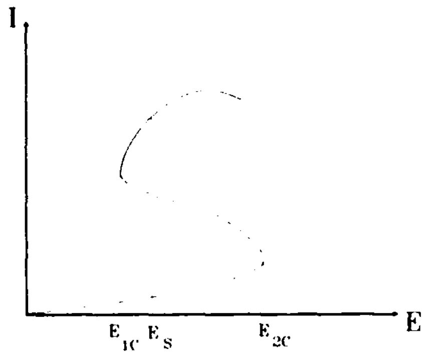

Fig. 2. Schematic representation of the current–voltage curve using the adopted model for the case of a homogeneous distribution of the current in a sample: $E_S \approx E_{1c}$ is the field corresponding to the formation of a filament.

region $\varepsilon \approx T$ to the region $\varepsilon > \varepsilon_r$ corresponding to a small but finite energy transfer $\varepsilon_r < \varepsilon_1$. The probability of these processes is given not by the approximate momentum relaxation time τ_{ee} but rather by the lifetime (which is not a characteristic time between the scattering events) $\tau_1 \approx \tau_{ee}\varepsilon_r L/\varepsilon_1$ (L being the Coulomb logarithm). The spectral flow connected with these processes, about $n_2\varepsilon_1/\tau_1$ ($\tau_1^{-1} \propto n_1$, n_1 and n_2 being the concentrations in the regions $\varepsilon \cong T$ and $\varepsilon \approx \varepsilon_1$) at some critical value $n_1 = n_c \propto (\varepsilon_1/\varepsilon_1 - 1)^{-1}$ exceeds the removal of electrons from the run-away region by electron–electron (about $n_2\varepsilon_1/\tau_{ee}$) and electron–phonon processes. In this case, n_2 sharply increases up to values $n_2 = n - n_c$. Inserting $n_{.}/n = n_2/n$ in eqn. (1), one obtains two roots: $n \approx A_1 N/B_1$ and $n \approx n_c$. Thus, in the lower branch, n increases with an increase in E (owing to ionization) only up to the value $n = n_c$; then a transition to the unstable falling branch takes place where $n = n_c \propto E^{-2}$ (at $\varepsilon_r < \varepsilon_1$). In the vicinity of the point $E = E_{c1}$ corresponding to $\varepsilon_r L \approx \varepsilon_1$, one has $n \to \infty$ which corresponds to a transition to the upper branch where $n \approx A_1 N/B_1$. In this branch the electron temperature is established: $T_e = T_{e3}$. Note that a further increase in E along this branch leads to a region where the Gunn effect occurs, the complete form of the current–voltage curve having an S–N character (Fig. 2). However, at the current values accessible for actual experiment a current filament formation should take place at $E \approx E_{c1}$. The estimates for the mechanism considered are the same order of magnitude as the experimental results [2].

So we believe that the proposed mechanism of electronic bistability controlled by purely electronic time scales (10^{-11} s) explains the S-shaped current–voltage curve in CdTe.

References

1 M. R. Oliver, A. McWhorter and A. C. Fout, *Appl. Phys. Lett.*, *11* (1967) 111.
2 N. V. Agrinskaya, M. V. Alekseenko and O. A. Matveev, *Sov. Phys.–Semicond.*, *9* (1975) 341.
3 G. Ottaviani, *Rev. Phys. Appl.*, *12* (1977) 249.
4 N. V. Agrinskaya and V. I. Kozub, *Sov. Phys.–JETP*, *72* (1991), 515.

Materials Science and Engineering, B16 (1993) 304–308

Power switching with CdTe:Cl

J. Lajzerowicz, L. Verger, F. Mathy and M. Cuzin

LETI (CEA, Technologies Avancées), CENG, BP 85X, 38041 Grenoble (France)

Abstract

CdTe material with its high molecular weight (240) is today widely used for radiation detection. The band-gap energy of CdTe is 1.45 eV. When doped with chlorine, which compensates the acceptor level introduced by cadmium vacancies, CdTe is intrinsic and gives a very high resistivity (more than $10^8\,\Omega$ cm). The contacts were made by electroless metal deposition and further annealing; they were characterized with d.c. and pulsed voltages. For the first time, this paper presents power switching experiments with CdTe material. We investigated different types of crystals and contact geometries with gap sizes varying from less than 1 mm to a few millimetres. The switches were activated by a YAG laser with 10 ns FWHM pulses (1.06 μm) or with 160 kV X-rays with 30 ns FWHM pulses. The time constant of recovery was found to be more than 10 ns. In some cases, for high voltages, corresponding to fields higher than a few kilovolts per centimetre, large recovery times of more than 100 ns were measured. This apparently longer carrier lifetime, combined with the high resistivity, make CdTe an alternative material to silicon and GaAs for some switching applications.

1. Introduction—main properties of CdTe

Semiconductor photoconductive switches have become increasingly useful for pulsed-power applications where high voltages must be switched on a short time-scale. Photoconductive switches can switch tens of kilovolts with picosecond rise times [1]. Most of the research has been concentrated initially on silicon and more recently on GaAs as the switch materials. Different materials, such as diamond and ZnSe, have also been evaluated for this application. To enlarge the group of potential semiconductor for the application, we decided to evaluate CdTe.

CdTe has been recognized for several years as being the most promising detector material for a room temperature operating portable X-ray and gamma-ray detection system. It is also used as a substrate for epitaxial growth of $Hg_{1-x}Cd_xTe$ to produce IR detectors. Semi-insulating CdTe is usually obtained by impurity compensation with chlorine or indium. Different techniques, such as the Bridgman technique or travelling heater method (THM), are used to grow the crystals. Of course, the availability and purity of the crystals grown today cannot be compared with those of silicon and GaAs. *Table 1 gives the main characteristics* of CdTe compared with silicon, GaAs and diamond.

Different properties of CdTe must be pointed out as follows.

CdTe has a direct band gap (Gunn effect is reported [2]). The mobility curve of CdTe presents a maximum in velocity for a feld of the order of 15 kV cm^{-1} [3]. Compared with GaAs and InP, and following some of the given interpretations of the lock-on phenomenon [4], it should present the lock-on property above 15 kV cm^{-1}. (The lock-on property is a non-linear effect: when the field applied is sufficiently high, instead of following the excitation pulse shape, the switch turns on and stays on until the energy is completely discharged from the generator.)

CdTe recovery time is in the range right between the recovery times of silicon and GaAs.

TABLE 1. Comparison of main parameters for CdTe and the three main semiconductor materials

	Si	AsGa	Diamond	CdTe
Band gap (eV)	1.12 (indirect)	1.43 (direct)	5.47 (indirect)	1.47 (direct)
Resistivity (Ω cm)	10^4	10^8	10^{16}	10^9
Mobility ($cm^2\,V^{-1}\,s^{-1}$)	1000	5000	1000	1000
Breakdown field (kV cm^{-1})	10^5	10^5	10^7	10^5
Recovery time (μs)	10–100	0.001–0.01	<0.001	0.01–1

0921-5107/93/$6.00

© 1993 – Elsevier Sequoia. All rights reserved

It seems very interesting to evaluate this material for power switching applications. We will briefly report how we developed ohmic contacts for our CdTe material. We will present the hold-off characteristics for impulsed voltages and, finally, we will show some results obtained when switching with laser or X-ray pulses.

2. Device preparation and characterization

The monocrystalline and large volume CdTe crystals have been grown by the vertical Bridgman method by normal freezing of a tellurium-rich solution at a temperature lower than the melting point of stoichiometric CdTe [5]. Semi-insulating CdTe is obtained by impurity compensation: in the accepted scheme, a shallow donor, *i.e.* chlorine, is introduced into the material to compensate acceptor native defects which are generally thought to be cadmium vacancies. By the self-compensation phenomena, the balance between the chlorine donor and acceptor concentration leads to Fermi level pinning within the gap that makes the material semi-insulating and thus greatly reduces photoconductor dark current [6].

Hall effect measurements exhibit a p-type conduction for the high resistivity chlorine-doped crystals. At room temperature, crystals have a resistivity $\rho = 10^9$ Ω cm, a hole concentration of 10^8 cm^{-3} and a Hall mobility $\mu_H = 50$ cm^2 V^{-1} s^{-1}. (The Hall mobility is not the electron mobility and is much closer to the hole mobility.)

We used two types of samples: one was 10 mm × 15 mm × 1 mm with the two contacts on the same large side separated by a gap of 3 mm and the other 10 mm × 10 mm × t mm (t is from 600 μm to 2 mm) with circular contacts on the opposite large sides.

As with most highly intrinsic semiconductors, it is difficult to produce ohmic contacts on CdTe:Cl. Our philosophy of experimentation was to carry out reliable, stable and reproducible ohmic contacts in order to obtain the lowest current for the highest electrical field applied when doing $I(V)$ characteristics: 1 kV. This was obtained with electroless deposited platinum on mechanically lapped surfaces. (The surfaces are mechanically lapped to reduce the leakage current.) The solution was prepared by dissolving H_2PtCl_6 in deionized water. The approximate thickness is 100 nm. Figure 1 shows the $I(V)$ characteristics obtained for a 10 mm × 10 mm × 1 mm sample (contacts on opposite sides) before subsequent annealing. For applied voltages in the range from −1 kV to 1 kV, the characteristic is linear and symmetric, *i.e.* ohmic behaviour. The sample impedance is found to be between 1 and 2 GΩ, which corresponds to a resistivity of a few gegaohm centimetres.

Unfortunately, under d.c. voltages corresponding to 15 kV cm^{-1} most of our samples fractured. This corresponds to a rapid increase in the dark current at constant voltage. This is probably due to an increasing space charge limited conduction because of trapping on deep levels.

Two different experiments were performed to test the samples under pulsed voltages.

(1) Polarization by a 50 ns, 0–10 kV pulse from a line discharge (sample placed in a SF6 pressure chamber). For the 10 mm × 10 mm × 1 mm sample (contacts on opposite faces), appreciable conduction appears at 3.5 kV while at 10 kV the sample presents a 100 Ω resistance. This corresponds to 20 mJ dissipated in the sample during 50 ns. For the 10 mm × 15 mm × 1 mm sample (contacts on the same side), conduction appears at 5.5 kV and the apparent resistance of the sample at 10 kV is 150 Ω. After this test the $I(V)$ characteristic of the 10 mm × 10 mm × 1 mm sample was degraded.

(2) Polarization by the 0.5 μF capacity discharge in 25 Ω with 0–3 kV. The samples tested are those with contacts on opposite faces. With two contacts of the same dimensions, breakdown appears at about 22 kV

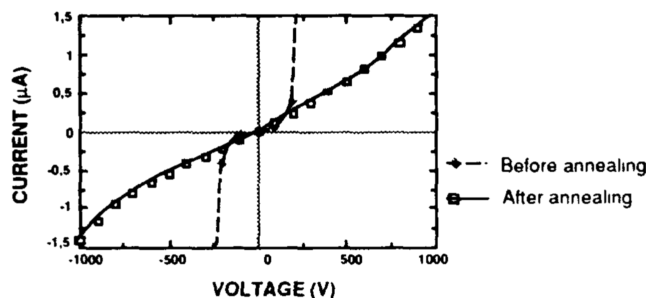

Fig. 1. $I(V)$ characteristics of a 10 mm × 10 mm × 1 mm sample.

Fig. 2. Sample top view with two breakdown paths.

cm^{-1} (1.5 kV for the 680 μm gap and 1.9 kV for the 850 μm gap). The paths are situated right along the contacts as it is shown on Fig. 2. They are holes in which the material melted. The sample shown presents two paths because, after several breakdowns in one path, the metal proceeds to sublimate and there is no more metallic continuity to the first path. The apparent breakdown resistance observed at the first breakdown at 1.5 kV (gap 680 μm) is about 80 Ω, which corresponds to 14 J dissipated in 10 μs, *i.e.* enough to melt CdTe.

The paths go exactly from one contact frontier to the other contact frontier on the opposite side (see Fig. 3). The simplest solution to overcome such behaviour was to use a small contact on one face and a big contact on the opposite face (typically diameters of 2 and 7 mm on the 1 mm × 1 mm faces). Indeed, in this case, the breakdown field doubled to reach 40 kV cm^{-1} (2.5 kV for the 620 μm gap and 3 kV for the 750 μm gap). The paths in this case go from the small contact frontier straight to the middle of the other contact (see Fig. 3).

Fig. 3. Breakdown paths and values for different contact geometries.

3. Results with laser or X-ray activation

We used a YAG YG 480 laser from Quantel. The energy delivered at 1.06 μm during the 12 ns pulse is 320 J. We used only d.c. polarization for laser switching tests. Different behaviours were observed in the recombination time which seems to depend on the geometry of the switch and on the field. Figure 4 gives an example of recorded switch signals at different fields. For 2.5 kV cm^{-1} and above, the apparent recombination times reach nearly 1 μs.

Figure 5 gives the variation of the switch resistance *vs.* the beam attenuation at different voltages. The limit resistance seems to be lower at low fields. When the attenuation is high enough, the variation of the resistance is quasi-linear with the attenuation, with the same linearity whatever the field is. Assuming a mobility of 1000 cm^2 V^{-1} s^{-1}, we can calculate the equivalent energy deposited in the switch for each attenuation. We can then determine roughly the absorption of the beam to find between 0.5% and 1%.

The X-ray generator is an HP 43733A flash generator. The maximum X-ray energy is 300 keV, the mean energy is 140 keV, the pulse width is 30 ns and the dose at 1 m is 0.7 mrad. Figure 6 shows a diagram of the experimental set-up for X-ray switching under 0–3 kV pulsed voltages. The voltage pulse triggers the 300 kV high voltage X-ray tube supply; the delay is less than 1 μs with a jitter of less than 200 ns. The time constant of the V_0 pulsed voltage is 12.5 μs; therefore, during the X-ray pulse, the voltage across the switch is about 95% of V_0. We only performed tests with samples with contacts on opposite faces.

Switched signals give recombination times of the order of 20 ns for irradiation perpendicular to the contact and, in some conditions of irradiation from the

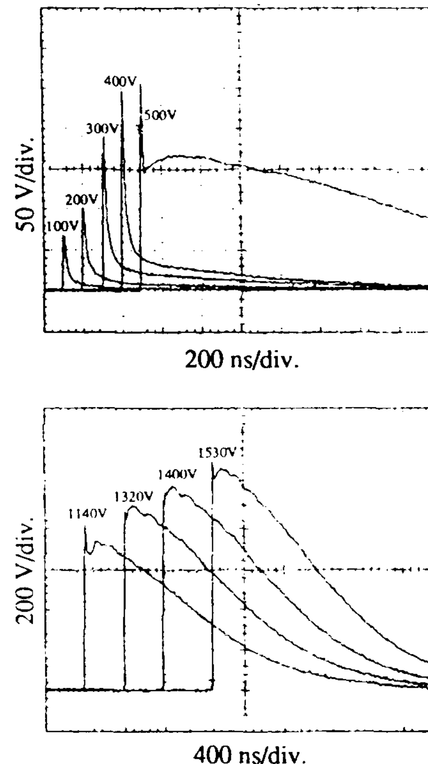

Fig. 4. Signals from laser switching at the same attenuation but at different voltages (contacts on the same face (2 mm gap) and laser beam on the opposite face) (recorded on Tektronix TDS 500).

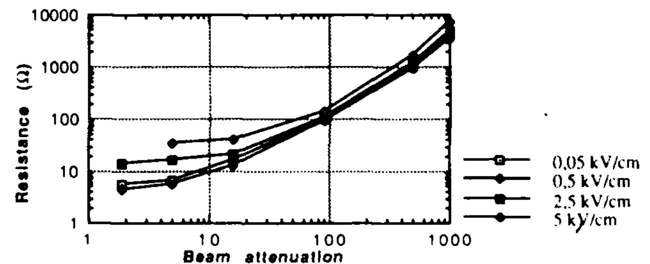

Fig. 5. Switch resistance *vs.* laser beam attenuation (contacts on the same face and laser beam on the opposite face).

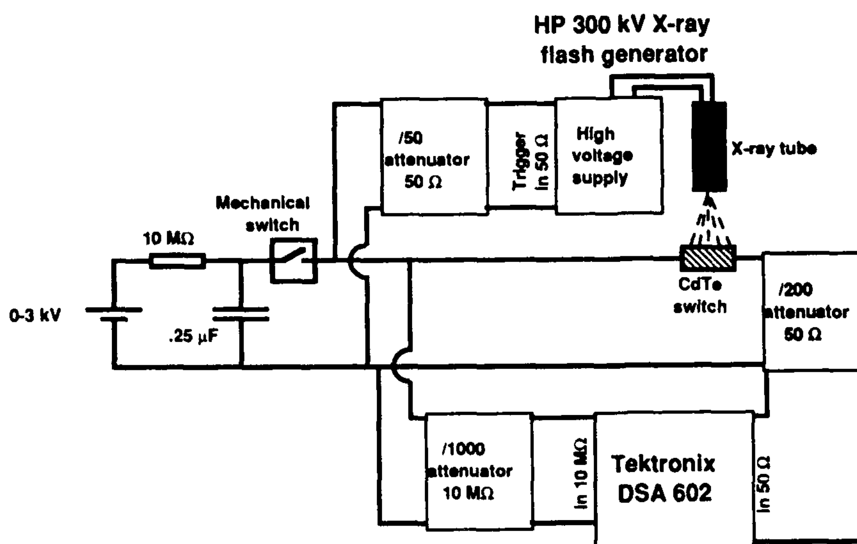

Fig. 6. Experimental setting for switching tests with X-rays.

sides of the sample, the recombination times reach 400 ns. On Fig. 7 is plotted the evolution of the switch resistance with the inverse of the irradiation dose at different fields. The irradiation dose is proportional to $1/d^2$ with d the distance to the source. Computation gives a carrier generation rate of 7×10^{11} cm^{-3} s^{-1} at 1 m and, therefore, a dose of 1 corresponds to 3×10^{13} cm^{-3} s^{-1}. From this value and from the slope of the linear variation of the resistance, we can estimate the mobility, and we find 1150 cm^2 V^{-1} s^{-1} which is in agreement with our theory.

We were able to switch at a field of 38 kV cm^{-1} without observing any lock-on phenomenon.

4. Conclusions

The aim of this work was to evaluate CdTe for power switching applications. We did not obtain answers to all the questions but what we are able to say is that CdTe can withstand 40 kV cm^{-1} and does not present any lock-on at 38 kV cm^{-1}. This breakdown voltage must be associated with the contact technology we used and should be improved when optimizing the technology and adapting the geometries. We were surprised not to see the lock-on and this result must be taken into account by scientists who want to interpret the lock-on phenomenon.

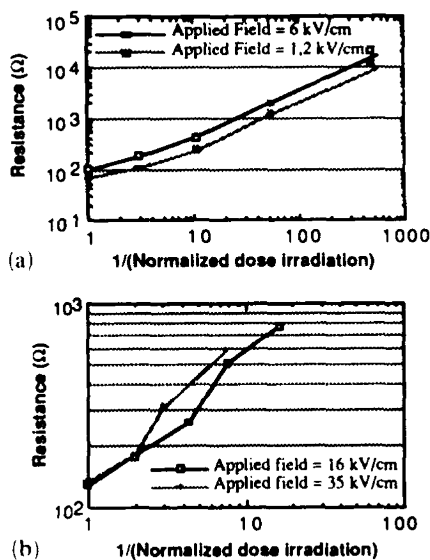

Fig. 7. Switch resistance *vs.* 1/(X-ray dose irradiation). (a) D.c. voltages on 1 mm × 1 mm × 0.8 mm sample. (b) Impulse voltages on 1 mm × 1 mm × 0.6 mm sample (contacts on opposite faces for both samples; contact sizes are different for the second sample).

Acknowledgments

The authors want to thank B. Schaub and G. Gaude for help with crystal growth and sample cutting, and M. C. Gentet, O. Maurice and J. Rustique for technical assistance.

References

1 W. C. Nunnally and R. B. Hammond, Optoelectronic switch for pulsed power, in C. H. Lee (ed.), *Picosecond Optoelectronic Devices*, Orlando, FL, 1984, pp. 374–398.
2 F. V. Vald, *Rev. Phys. Appl.*, *12* (1977) 277.

3 C. Canali, M. Martini, G. Ottaviani and K. R. Zanio, *Phys. Rev. B, 4* (1971) 422.
4 F. J. Zutavern, G. Loubriel, M. W. O'Malley, L. P. Shanwald, W. D. Helgeson, D. L. McLaughlin and B. B. McKenzie, *IEEE Trans. Electron. Dev., 37* (1990) 2472.
5 B. Schaub, J. Gallet, A. Bruno-Jailly and Pelliciari, *Rev. Phys., 12* (1977) 147.
6 N. V. Agrinskaya and O. A. Matveev, *Nucl. Instrum. Methods A, 283* (1989) 263.

Picosecond diffraction kinetics of transient gratings in CdTe and CdZnTe

N. Gouaichault-Brugel, L. Nardo, M. Pugnet* and J. Collet
Laboratoire de Physique des Solides, UPS et INSA, Avenue de Rangueil, 31077 Toulouse Cedex (France)

Abstract

Laser-induced transient gratings generated by picosecond pulses at 1.06 μm in CdTe and CdZnTe samples were used at room temperature to diffract a picosecond probe pulse in the degenerate-four-wave-mixing geometry. Pump and probe experiments performed using the same experimental set-up allowed us to measure the carrier lifetime. The ambipolar diffusion coefficient D was then determined using only one laser material geometrical configuration. In semi-insulating CdTe:W, gratings persisted over more than 1 ns and could be instantaneously half-erased using a homogeneous picosecond pulse, the energy of which was a quarter of the writing energy. We present a model which explains these results.

1. Experimental set-up

1.1. Degenerate-four-wave-mixing

The experimental set-up is shown in Fig. 1. Pulses were generated directly at the wavelength 1.064 μm by an actively mode-locked Nd:YAG laser and their duration was approximately 30 ps. Two equal energy pump pulses (P1 and P2) interacted inside the sample to produce transient gratings. The external angle between these two pump beams was $2\theta = 18.6°$, corresponding to a grating period Λ of 3.3 μm. The grating was then read by a probe pulse (T) which travelled in the opposite direction to P2 and was delayed with respect to the pump pulses P1 and P2. A third pump pulse (P3) with a time delay of 720 ps with respect to the others, was used to erase the grating. The energies of all the pump beams was $E = 8$ mJ cm^{-2}, in the standard experiment. The pump and probe pulse polarizations were vertical and horizontal respectively. Indeed, this was required to eliminate any direct interaction between the two beams. It also made it easier to separate the diffracted probe pulse from the reflected P2 pump pulse. The pump signal reflected along the direction of the probe beam was eliminated using a Glan-Thompson polarizer. We then measured the probe diffraction efficiency (defined as the intensity ratio of the diffracted probe beam to the transmitted beam without excitation) as a function of probe time delay, with a maximum time delay of 1.5 ns. The pump and probe beam sections were limited by a circular diaphragm stuck on the sample. The diameter of the hole was 1 mm.

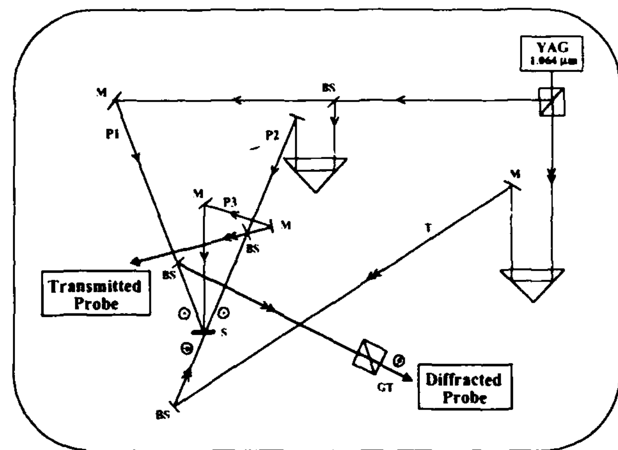

Fig. 1. Experimental set-up for both picosecond degenerate-four-wave-mixing and transmission modulation experiments at room temperature: M, mirror; GT, Glan-Thompson polarizer; BS, beam splitter; P1, P2 and P3, pump beams; T, probe beam (test); S, sample.

1.2. Transmission modulation measurements

The pump-and-probe transmission experiment was performed for excitation pulses P2 and P3, respectively, in the same configuration as the degenerate-four-wave-mixing (DFWM) experiment (the pump

*Author to whom correspondence should be addressed.

0921-5107/93/$6.00
© 1993 - Elsevier Sequoia. All rights reserved

beam P1 was then blocked; see Fig. 1). The pump beam and the cross-polarized probe beam were colinearly incident on the sample and were counterpropagating. The relative timing between them was controlled by the probe variable optical delay line (with a maximum time delay of 1.5 ns). The excitation energy on the sample was of the order of 16 mJ cm^{-2}. This was twice the energy of each pump pulse in the DFWM experiment. However, the probe energy was weaker, being approximately 0.3 mJ cm^{-2}. We measured the probe transmission with the pump switched on (T) normalized by the probe transmission with the pump switched off (T_0) as a function of the probe time delay.

2. Method for fast measurement of the ambipolar diffusion coefficient and experimental results

2.1. Method

We propose here a method for fast characterization of semiconductors by ambipolar diffusion coefficient measurements. It is well known that pulse–probe DFWM recording of grating dynamics on subnanosecond time-scales can be used to measure the ambipolar diffusion coefficient D of free carriers in semiconductors [1]. However, the experiments are complex because of the necessity of phase matching adjustments for different angles between the pump beams. We propose here a new method based on independent measurements of the free carrier lifetime and decay time of the diffraction efficiency. This method allows us to measure the ambipolar diffusion coefficient D with only one laser material geometrical configuration (see Fig. 1). The grating decay time τ_d is given by

$$\frac{1}{\tau_d}=\frac{4\pi^2 D}{\Lambda^2}+\frac{1}{\tau_r}$$

where τ_r is the free carrier lifetime and Λ the grating spacing. The grating diffraction efficiency η can be expressed by [2]

$$\eta=\sin^2\left(\frac{\pi d\,\delta n_{fc}}{\lambda\cos\theta}\right)$$

where d is the interaction length, θ is the half-angle between the two pump beams, λ is the wavelength, and δn_{fc} is the free carrier contribution to the optical index modulation which is proportional to the free carrier density. At a low diffraction efficiency, τ_d is twice the diffracted signal decay time. Fast measurement of the free carrier lifetime τ_r can be performed using the same experimental set-up. The pump beam P1 is now occulted (see Section 2.2). The energy of the pump pulse P2 can be slightly adjusted to get a marked probe modulation.

2.2. Results for CdTe:Cl

The sample thickness was 1 mm and the linear absorption coefficient, determined using transmission measurement at low optical excitation, was found to be $\alpha = 1$ cm^{-1} at the wavelength $\lambda = 1.06$ μm. The pump pulses energies for P1, P2 and P3 were 8 mJ cm^{-2}, and the probe pulse energy was 0.3 mJ cm^{-2}. The diffraction efficiency kinetics are shown in Fig. 2(a). The fast

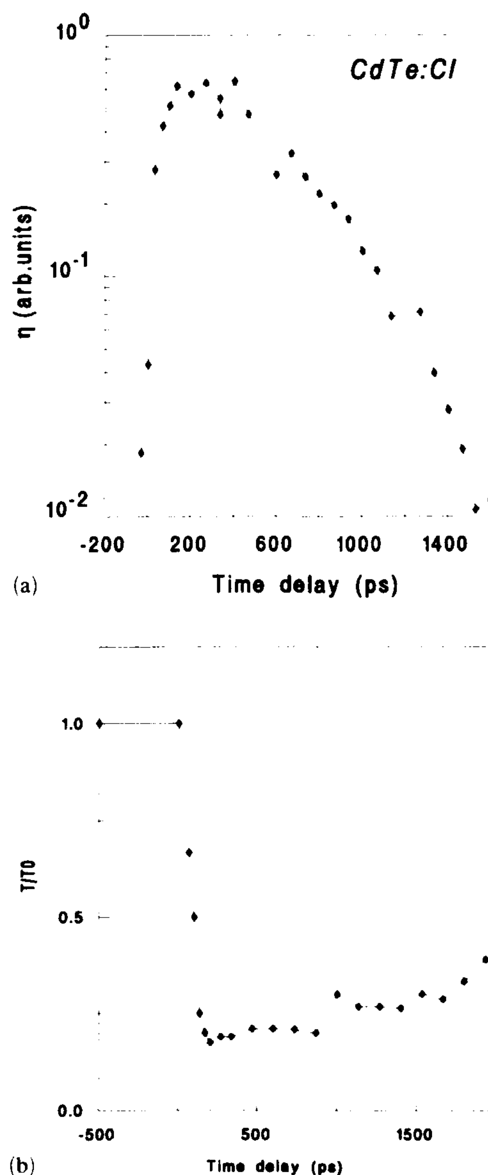

Fig. 2. (a) Diffraction efficiency kinetics following picosecond photogeneration of the grating at $t=0$ in CdTe:Cl. The decay time is 330 ps at $T=300$ K. (b) Normalized probe transmission following the photoexcitation at $t=0$. The free carrier lifetime deduced from the fit equals 2.5 ns at $T=300$ K.

decay time is of the order of 330 ps, corresponding to a grating decay time of 660 ps. The pump and probe results are shown in Fig. 2(b). The strong excitation pulses generate electron–hole pairs by a two-photon absorption process. In CdTe, the two-photon absorption coefficient β equals 15 cm GW^{-1} [3]. The density generated by this process is $\rho \cong 4 \times 10^{17}$ cm^{-3}. Assuming that the free carrier absorption is the dominant process for the probe pulse, we deduce that the carrier lifetime $\tau_r = 2.5$ ns. With $\tau_d = 660$ ps and $\Lambda = 3.3$ μm, we obtain $D = 3$ cm^2 s^{-1}. This result is in good agreement with previous measurements [1].

2.3. Results for CdZnTe

The samples were platelets of $Cd_{0.96}Zn_{0.04}Te$ 0.6 mm thick polished on both sides. The linear absorption at $\lambda = 1.06$ μm was negligible. All the parameters of the previous experiment were kept constant. The diffraction efficiency kinetics are reported in Fig. 3. The measured decay time is 175 ps. Using the previous pump-and-probe method we obtain the carrier lifetime $\tau_r = 550$ ps. We deduce the ambipolar diffusion coefficient $D = 3$ cm^2 s^{-1}. We conclude that our samples of CdTe and CdZnTe exhibit roughly the same carrier mobility, and that the carrier lifetime is lower in CdZnTe than in CdTe material.

3. Picosecond writing and erasure in CdTe:W

3.1. Sample characterization

Tungsten was incorporated into the melt during the growth process. The sample resistivity was greater than 10^8 Ω cm. The low excitation optical absorption was negligible for photons lower than the band gap. The sample thickness was 8 mm.

3.2. Experimental results

The diffraction efficiency of the probe beam was also measured in the DFWM geometry shown in Fig. 1 as a function of time delay. The grating decay kinetics of such an experiment are represented in Fig. 4 for equal writing optical energies and a pump-to-probe ratio equal to 40:1. The squares correspond to data acquired with the usual DFWM configuration, while the diamonds correspond to an experiment where sampling starts at a probe time delay of approximately 500 ps and in the presence of the retarded pump beam (P3) which illuminated the sample homogeneously. When the pump pulse P3 was switched on, a rapid decay was observed at a probe delay of 720 ps, corresponding to the delay of this third pump beam with respect to the others. We interpret this rapid decay as the erasure of the optical index grating.

3.3. Model

During the optical excitation, the sample is inhomogeneously illuminated because of the interference of the two pump pulses. Let us now consider the illuminated areas (IAs). We assume the presence of a deep

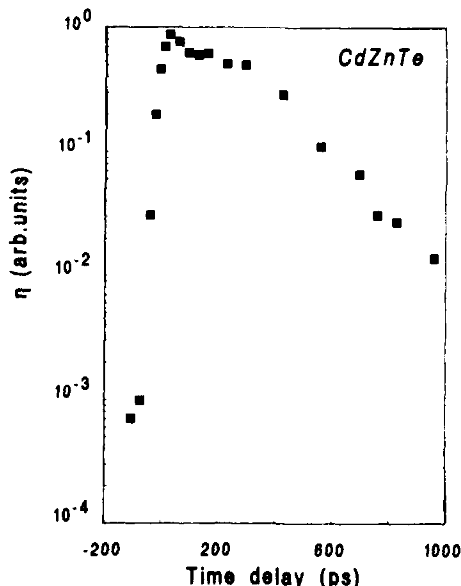

Fig. 3. Diffraction efficiency kinetics following the picosecond photogeneration of the grating at $t = 0$ in CdZnTe. The decay time is 175 ps at $T = 300$ K.

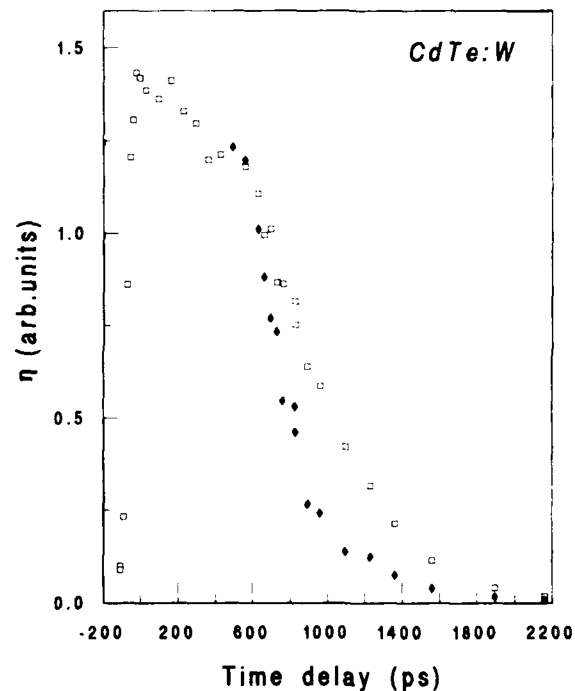

Fig. 4. Diffraction efficiency of the probe pulse vs. time delay with respect to the writing pulses P1 and P2. Squares and diamonds represent the data with the erasure pump P3 switched off and switched on respectively. Each pump energy equals 8 mJ cm^{-2} and the probe energy equals 0.3 mJ cm^{-2}.

level in the upper half of the band gap, associated with a high electron capture coefficient. The photonic capture cross-section σ_n for trapped electrons is high, while this parameter is negligible for trapped holes. Before illumination, or in the dark areas (DAs), the level is entirely populated by trapped holes, because of its energetic position above the Fermi level (semi-insulating material). The strong excitation pulses generate electron–hole pairs by a two-photon absorption process. A portion of the free electrons are "instantaneously" captured in the IAs, while in the DAs the level is still populated by trapped holes (we neglect here the diffusion process which is avoided by the fast trapping). The periodic distribution of charges stored in the deep levels induces a periodic distribution of free electrons and holes via the static screening mechanism. We assume that the trapped charge density is given by

$$\Delta N(x) = \Delta N_0\{1 + \cos(2\pi x/\Lambda)\}$$

The resulting electric field in the presence of the free carrier in excess is

$$\mathscr{E} = \frac{(e/\varepsilon)\,\Delta N(\Lambda/2\pi)\sin(2\pi x/\Lambda)}{1 + q_F^2/q^2}$$

where ΔN is the charge density modulation, $\Lambda = \lambda/2 \sin\theta$ is the fringe spacing, ε is the static dielectric constant, T is the temperature, $q_F = \{e^2(n+p)/\varepsilon k_B T\}^{1/2}$ is the screening vector and $q = 2\pi/\Lambda$ is the wave vector of the grating. The free carrier contribution δn_{fc} to the optical index modulation is given by [4]

$$\delta n_{fc} = -\frac{e^2\,\Delta\rho}{2n_b\varepsilon m_0\omega^2}\left(\frac{1}{m_n^*} + \frac{1}{m_p^*}\right)\frac{\omega_g^2}{\omega_g^2 - \omega^2}$$

where $\Delta\rho = \Delta n = \Delta p$ is the free carrier density modulation, ω_g is the band gap pulsation, ω is the photon pulsation, and m_n^* and m_p^* are the effective masses of electrons and holes respectively. It should be noted that the free electron contribution is dominant ($1/m_n \gg 1/m_p$). Using $\Delta N = 10^{16}$ cm^{-3}, $\Lambda = 3.3$ μm, $k_B T = 26$ meV, $\varepsilon = 11\varepsilon_0$, $n_b = 2.75$, $m_n^* = 0.096$, $m_p^* = 0.5$, $\hbar\omega = 1.17$ eV, and $\hbar\omega_g = 1.50$ eV, we obtain $\mathscr{E}_{max} = 5-10$ V cm^{-1} and $\delta n_{fc} = 2\times 10^{-5}$. The photorefractive optical index modulation δn_{pr} resulting from the actual electric field is $\delta n_{pr} = (2-3)\times 10^{-8}$. The photorefractive contribution to δn is then negligible.

3.4. Erasure

After the homogeneous illumination by the pulse P3, a stationary deep level population is reached in the whole crystal. This mechanism is responsible for the erasure process. In fact, the space charge field is annihilated and free carriers can diffuse again throughout the crystal, leading to the suppression of any free carrier density modulation. A 50% erasure is obtained (see Fig. 4) with an erasing pulse energy of only the quarter of the writing energy.

Acknowledgments

We wish to thank Dr. M. Hage-Ali (Laboratoire PHASE, Strasbourg) for useful discussions and for providing the CdTe samples. We also acknowledge Dr. A. Million (LETI, Grenoble) for providing the CdZnTe samples.

References

1 M. S. Petrovic, A. Suchocki, R. C. Powell, G. Cantwell and J. Aldridge, *J. Appl. Phys.*, *66* (1989) 1359.
2 H. Kogelnik, *Bell Syst. Tech. J.*, *48* (1969) 2909.
3 E. Van Stryland and H. Vanherzeele, M. A. Woodall, M. J. Soileau, A. L. Smirl, S. Guha and T. F. Boggess, *Opt. Eng.*, *24* (1985) 613.
4 D. H. Auston, S. McAfee, C. V. Shank, E. P. Ippen and O. Teschke, *Solid State Electron.*, *21* (1978) 147.

Author Index of Volume 16

Accomo, R., 279
Acher, O., 118
Agrinskaya, N. V., 172, 302
Aidun, D. K., 182
Ali, S., 60
Allègre, J., 87
Apotovsky, B., 291
Ard, C. K., 29
Ashenford, D. E., 60, 191
Azema, A., 64

Bains, S. K., 113
Bairstow, A., 195
Balasubramanian, R., 1
Banister, A. J., 113
Baroux, L., 134
Bassani, F., 83, 207
Bauer, P., 108
Baumann, A. E., 250
Behr, Th., 103
Belas, E., 215
Benz, K. W., 128, 243
Berger, H., 219
Bertoncello, R., 155
Bhatti, M. T., 250
Bicknell-Tassius, R. N., 92
Bilger, G., 178
Blackmore, G. W., 186
Bodin, C., 235, 279
Bollmann, J., 139
Bouree, J. E., 118
Boyn, R., 139
Brandstötter, A., 108
Brinkman, A. W., 145
Brown, P., 96, 145
Bruder, M., 40
Brunet, P., 44
Butler, J. F., 291

Calatayud, J., 87
Capobianco, A. M., 155
Capper, P., 29
Carmo, M. C., 246
Casarin, M., 155
Chang, W. M., 23
Chen, Y. P., 51
Chibani, L., 202, 223
Cibert, J., 211, 235, 279
Collet, J., 309
Corbel, C., 134
Coutal, C., 64
Cox, R. T., 83
Cuniot, M., 262
Cuzin, M., 304

Dang, L. S., 211, 279
Delaye, P., 268, 273
Devine, P., 191
Doty, F. P., 291
Drevillon, B., 118
Drigo, A. V., 123, 160
Druilhe, R., 118, 145
Durose, K., 96, 113
Dutton, D., 29

Ebe, H., 57
Ehinger, M., 151

Faschinger, W., 79
Faurie, J. P., 51
Feuillet, G., 235, 279
Figgemeier, H., 40
Flytzanis, C., 239
Franc, J., 215
Frey, J., 239
Frey, R., 239

Gaucherel, P., 64
Gely-Sykes, C., 134
Gilabert, A., 64
Gołacki, Z., 68
Gouaichault-Brugel, N., 309
Granozzi, G., 155
Grattepain, C., 207
Gravey, P., 257
Gresslehner, K. H., 108
Grill, R., 215
Guellil, Z., 273
Guerrieri, A., 160

Hage-Ali, M., 48, 202, 223, 296
Hagston, W. E., 60
Hähnert, I., 168
Hamoudi, A., 211
Harris, J. E., 29
Hauzenberger, F., 79
Hill, R., 250
Hofmann, D. M., 17, 128
Hogg, J. H. C., 60, 191, 195
Hommel, D., 92, 103, 178
Höschl, P., 215
Huant, S., 83
Hugonnard-Bruyere, S., 239
Hynes, K. M., 250

Iwase, Y., 283

Jackson, S. R., 60
Jarasiunas, K., 268
Jones, C. L., 29
Jones, E. D., 186
Jouneau, P. H., 279
Juza, P., 79

Katty, A., 44
Kiessling, F. M., 134
Klimakow, A., 139
Koebel, J. M., 48, 202
Kozub, V. I., 302
Krause, R., 139
Kuhn, T. A., 178
Kuhn-Heinrich, B., 103
Kurtz, E., 92

Labrunie, G., 279
Lajzerowicz, J., 291, 304
Landwehr, G., 92, 103, 151, 178
Lange, M. D., 51
Lascaray, J. P., 228
Launay, J. C., 268, 273
Lawrence, I., 235
Lefebvre, P., 87
Leo, G., 123
Ligeon, E., 211
Linke, H., 243
Lischka, K., 79, 108
Litz, T., 103, 151
Lovergine, N., 160
Lubke, K., 108
Lunn, B., 60, 191
Lusson, A., 145

Mackett, P., 29
Magnea, N., 71
Maier, H., 40
Mancini, A. M., 160
Mandray, A., 83
Marfaing, Y., 145, 262
Mariette, H., 71
Mathieu, H., 87
Mathy, F., 304
Matthews, G. W., 195
Mazoyer, V., 273
Meyer, B. K., 17, 128, 243
Miles, R. W., 250
Möck, P., 165
Moisan, J. Y., 257
Molva, E., 279
Moravec, P., 215, 223
Mühlberg, M., 8
Müller-Vogt, G., 17, 128
Mullin, J. B., 186

Nardo, L., 309
Neswal, M., 108
Nicholls, J. E., 60

Oettinger, K., 128
Ohmori, M., 283
Ohno, R., 283
Omling, P., 128, 243
Ossau, W., 178
O'Keefe, E., 29, 113

© Elsevier Sequoia/Printed in The Netherlands

Parthier, L., 199
Patriarche, G., 145
Pautrat, J. L., 211
Pelekanos, N., 71
Pesek, A., 79
Peyla, P., 235
Picoli, G., 257
Pugnet, M., 309

Regel, L., 23, 182
Richter, M., 296
Rizzi, G. A., 155
Romanato, F., 160
Roosen, G., 268, 273
Roustan, J. C., 64
Rudolph, P., 8, 139
Rzepka, E., 262

Salk, M., 128, 243
Sallet, V., 118
Saminadayar, K., 83, 207
Schenk, M., 199, 219
Schmitt, R., 40, 92
Schneider, D., 44
Scholl, S., 178
Scott, C. G., 191
Shaw, D., 195
Shen, J., 182
Siffert, P., 48, 202, 223, 296
Sitter, H., 79
Sivananthan, S., 51
Soares, M. J., 246
Sporken, R., 51
Stadler, W., 17, 128
Stedman, J. D., 195
Steer, Ch., 48
Steinbach, B., 17
Stewart, N. M., 186
Stoquert, J. P., 202
Szczerbakow, A., 68

Takigawa, H., 57
Tapiero, M., 273
Tardot, A., 71
Tatarenko, S., 83, 207
Tondello, E., 155
Traverse, A., 123
Triboulet, R., 44, 64, 118, 134, 145, 262
Tromson-Carli, A., 44, 145
Tuffigo, H., 235
Turnbull, A., 96

Utke, I., 199

Verger, L., 291, 304
Vieux, V., 257

Waag, A., 92, 103, 178
Wasiela, A., 235
Watson, C. C. R., 113
Weigel, E., 17, 128
Wendl, W., 17
Wenzel, M., 151
Wienecke, M., 168, 219
Wilcox, W. R., 1, 23, 182
Wolffer, N., 257

Yakovlev, V., 118

Zajicek, H., 79
Zielinger, J. P., 273
Zimmermann, H., 139

Subject Index of Volume 16

Absorption
  Fourier transform IR spectroscopy of CdTe:Fe, 246
Alloys
  short period CdTe–ZnTe and CdTe–MnTe superlattices, 79
  structural properties of defects in $Cd_{1-x}Zn_xTe$, 128
  time-resolved light-induced Faraday rotation in $Zn_{1-x}Mn_xTe$ and $Cd_{1-x}Mn_xTe$, 239
Annealing
  $Cd_{1-x}Zn_xTe$ substrates for $Hg_{1-x}Cd_xTe$ liquid-phase epitaxy, 40
  native point defects in CdTe and its stability region, 219
  power switching with CdTe:Cl, 304
  thin films of CdTe produced using stacked elemental layer processing for use in CdTe/CdS solar cells, 250
Auger electron spectroscopy
  properties of dry-etched CdTe–epitaxial layer surfaces and microstructures, 108

Cadmium
  defects and electrical properties of doped and undoped CdTe single crystals from tellurium-rich solutions, 17
  effect of large-scale potential relief on the electronic transport in doped and compensated CdTe: the role of impurity correlations, 172
Cadmium sulphide
  ion channelling Rutherford backscattering spectrometry structural characterization of CdS/CdTe heterostructures, 160
Cadmium telluride
  basic problems of vertical Bridgman growth of CdTe, 8
  Bridgman growth and assessment of CdTe and CdZnTe using the accelerated crucible rotation technique, 29
  carbon and silicon in travelling heater method grown semi-insulating CdTe, 202
  CdTe rotation growth on silicon substrates by metallo-organic chemical vapour deposition, 57
  chemical diffusion of Hg in CdTe, 195
  comparative reflectivity study of coupled and uncoupled CdTe/CdMnTe asymmetric double quantum wells, 235
  compensation of trapping losses in CdTe detectors, 296
  complete characterization of epitaxial CdTe on GaAs from the lattice geometrical point of view, 165
  computer simulation of CdTe crystal growth and application, 48
  deep centres for optical processing in CdTe, 262
  deep levels in semi-insulating CdTe, 223
  depth non-uniformities in thin CdTe layers grown by MBE on InSb substrates, 191
  determination of the iron acceptor level in CdTe, 243
  diffusion of gallium in cadmium telluride, 186
  donor activation efficiency and doping profile quality in In-doped CdTe and CdZnTe quantum structures, 207
  effect of interdiffusion on dislocation generation in epitaxial layers on CdTe, (Cd,Zn)Te and Cd(Te,Se) substrates, 199
  effect of the {h11} orientations and polarities of GaAs substrates on CdTe buffer layer structural properties, 145
  effect of thermal annealing on the microstructure of CdTe and $Cd_{1-x}Zn_xTe$ crystals, 182
  efficient n-type doping of CdTe epitaxial layers grown by photo-assisted molecular beam epitaxy with the use of chlorine, 178
  floating-zone melting of CdTe, 23
  Fourier transform IR spectroscopy of CdTe:Fe, 246
  gamma- and X-ray detectors manufactured from $Cd_{1-x}Zn_xTe$ grown by a high pressure Bridgman method, 291
  growth and structure of $CdTe/Cd_{1-x}Mn_xTe$ multiple quantum wells showing excitonic 2S states, 60
  growth of CdTe single crystals by vapour condensation on the surface of polycrystalline source material, 68
  heteroepitaxy of CdTe on GaAs and silicon substrates, 51
  high quality CdTe and its application to radiation detectors, 283
  horizontal Bridgman growth of large high quality $Cd_{1-x}Zn_xTe$ crystals, 44
  implantation-enhanced interdiffusion in CdTe/ZnTe quantum wells, 211
  in situ reflectance anisotropy studies of the growth of CdTe and other compounds by MOCVD, 118
  ion channelling Rutherford backscattering spectrometry structural characterization of CdS/CdTe heterostructures, 160
  laser growth of CdTe epitaxial film on CdTe substrate, 64
  mechanical properties of CdTe, 1
  native defect equilibrium in semi-insulating CdTe(Cl), 215
  native point defects in CdTe and its stability region, 219
  new method for the determination of V_{Cd} concentrations in p-CdTe, 139
  optical, photoelectrical, deep level and photorefractive characterization of CdTe:V, 273
  overview of CdTe-based semimagnetic semiconductors, 228
  picosecond diffraction of transient gratings in CdTe and CdZnTe, 309
  piezomodulated reflectivity on CdMnTe/CdTe quantum well structures as a new standard characterization method, 92
  piezoreflectivity investigation of CdTe/(Cd,Zn)Te heterostructures, 87
  positron trapping at native vacancies in CdTe crystals: In doping effect, 134
  potentiality of photorefractive CdTe, 257
  power switching with CdTe:Cl, 304
  properties of dry-etched CdTe–epitaxial layer surfaces and microstructures, 108
  qualification of a new defect revealing etch for CdTe using cathodoluminescence microscopy, 113
  relation between dislocation density, bulk electrical properties and ohmic contacts of CdTe, 168
  RHEED studies of MBE growth mechanisms of CdTe and CdMnTe, 103
  scanning tunneling microscope investigation of the effects of CdTe substrate preparation on molecular beam epitaxially grown n-CdTe layers, 151
  specific behaviour of CdTe ion implantation damage, 123
  spectroscopy of donors and donor-bound excitons in $CdTe/Cd_{1-x}Zn_xTe$ multiple quantum wells, 83
  structural and electronic properties of CdTe-based heterostructures, 71

structural defects in bulk and epitaxial CdTe, 96
structural properties of defects in $Cd_{1-x}Zn_xTe$, 128
the electronic bistability in doped semiconductors with polar optical scattering: the reversible switching effect in CdTe:Cl at room temperature, 302
thin films of CdTe produced using stacked elemental layer processing for use in CdTe/CdS solar cells, 250
time-resolved build-up and decay of photorefractive and free-carrier gratings in CdTe:V, 268
X-ray photoelectron diffraction from the CdTe(111)A polar surface, 155

Carbon
carbon and silicon in travelling heater method grown semi-insulating CdTe, 202
horizontal Bridgman growth of large high quality $Cd_{1-x}Zn_xTe$ crystals, 44

CdTe doping
defects and electrical properties of doped and undoped CdTe single crystals from tellurium-rich solutions, 17
effect of large-scale potential relief on the electronic transport in doped and compensated CdTe: the role of impurity correlations, 172

Chemical vapour deposition
ion channelling Rutherford backscattering spectrometry structural characterization of CdS/CdTe heterostructures, 160

Chlorine
efficient n-type doping of CdTe epitaxial layers grown by photo-assisted molecular beam epitaxy with the use of chlorine, 178
native defect equilibrium in semi-insulating CdTe(Cl), 215
power switching with CdTe:Cl, 304
the electronic bistability in doped semiconductors with polar optical scattering: the reversible switching effect in CdTe:Cl at room temperature, 302

Compound semiconductors
short period CdTe–ZnTe and CdTe–MnTe superlattices, 79
time-resolved light-induced Faraday rotation in $Zn_{1-x}Mn_xTe$ and $Cd_{1-x}Mn_xTe$, 239

Contact resistance
power switching with CdTe:Cl, 304
relation between dislocation density, bulk electrical properties and ohmic contacts of CdTe, 168

Crystal growth
basic problems of vertical Bridgman growth of CdTe, 8
Bridgman growth and assessment of CdTe and CdZnTe using the accelerated crucible rotation technique, 29
$Cd_{1-x}Zn_xTe$ substrates for $Hg_{1-x}Cd_xTe$ liquid-phase epitaxy, 40
computer simulation of CdTe crystal growth and application, 48
floating-zone melting of CdTe, 23
growth of CdTe single crystals by vapour condensation on the surface of polycrystalline source material, 68
high quality CdTe and its application to radiation detectors, 283
horizontal Bridgman growth of large high quality $Cd_{1-x}Zn_xTe$ crystals, 44
positron trapping at native vacancies in CdTe crystals: In doping effect, 134
structural defects in bulk and epitaxial CdTe, 96

Crystallization
computer simulation of CdTe crystal growth and application, 48
growth of CdTe single crystals by vapour condensation on the surface of polycrystalline source material, 68

Defect formation
structural defects in bulk and epitaxial CdTe, 96

Defectors
basic problems of vertical Bridgman growth of CdTe, 8
high quality CdTe and its application to radiation detectors, 283

Defects
basic problem of vertical Bridgman growth of CdTe, 8
Bridgman growth and assessment of CdTe and CdZnTe using the accelerated crucible rotation technique, 29
$Cd_{1-x}Zn_xTe$ substrates for $Hg_{1-x}Cd_xTe$ liquid-phase epitaxy, 40
deep centres for optical processing in CdTe, 262
defects and electrical properties of doped and undoped CdTe single crystals from tellurium-rich solutions, 17
determination of the iron acceptor level in CdTe, 243
effect of large-scale potential relief on the electronic transport in doped and compensated CdTe: the role of impurity correlations, 172
mechanical properties of CdTe, 1
native defect equilibrium in semi-insulating CdTe(Cl), 215
native point defects in CdTe and its stability region, 219
qualification of a new defect revealing etch for CdTe using cathodoluminescence microscopy, 113
relation between dislocation density, bulk electrical properties and ohmic contacts of CdTe, 168
structural defects in bulk and epitaxial CdTe, 96

Detectors
carbon and silicon in travelling heater method grown semi-insulating CdTe, 202
compensation of trapping losses in CdTe detectors, 296
deep levels in semi-insulating CdTe, 223
gamma- and X-ray detectors manufactured from $Cd_{1-x}Zn_xTe$ grown by a high pressure Bridgman method, 291
horizontal Bridgman growth of large high quality $Cd_{1-x}Zn_xTe$ crystals, 44
scanning tunneling microscope investigation of the effects of CdTe substrate preparation on molecular beam epitaxially grown *n*-CdTe layers, 151

Diffraction
growth and structure of $CdTe/Cd_{1-x}Mn_xTe$ multiple quantum wells showing excitonic 2S states, 60
picosecond diffraction kinetics of transient gratings in CdTe and CdZnTe, 309
X-ray photoelectron diffraction from the CdTe(111)A polar surface, 155

Diffusion
diffusion of gallium in cadmium telluride, 186
Fourier transform IR spectroscopy of CdTe:Fe, 246
new method for the determination of V_{Cd} concentrations in p-CdTe, 139
picosecond diffraction kinetics of transient gratings in CdTe and CdZnTe, 309

Doping
defects and electrical properties of doped and undoped CdTe single crystals from tellurium-rich solutions, 17

Doping effects
carbon and silicon in travelling heater method grown semi-insulating CdTe, 202
deep levels in semi-insulating CdTe, 223
donor activation efficiency and doping profile quality in In-doped CdTe and CdZnTe quantum structures, 207
effect of large-scale potential relief on the electronic transport in doped and compensated CdTe: the role of impurity correlations, 172

optical, photoelectrical, deep level and photorefractive characterization of CdTe:V, 273
positron trapping at native vacancies in CdTe crystals: In doping effect, 134
power switching with CdTe:Cl, 304
specific behaviour of CdTe ion implantation damage, 123
spectroscopy of donors and donor-bound excitons in CdTe/$Cd_{1-x}Zn_xTe$ multiple quantum wells, 83

Electric field effect
time-resolved build-up and decay of photorefractive and free-carrier gratings in CdTe:V, 268
Electrical measurements
the electronic bistability in doped semiconductors with polar optical scattering: the reversible switching effect in CdTe:Cl at room temperature, 302
Electrical properties
defects and electrical properties of doped and undoped CdTe single crystals from tellurium-rich solutions, 17
relation between dislocation density, bulk electrical properties and ohmic contacts of CdTe, 168
Electron states
deep levels in semi-insulating CdTe, 223
Electronic properties
donor activation efficiency and doping profile quality in In-doped CdTe and CdZnTe quantum structures, 207
structural and electronic properties of CdTe-based heterostructures, 71
Epilayers
Bridgman growth and assessment of CdTe and CdZnTe using the accelerated crucible rotation technique, 29
$Cd_{1-x}Zn_xTe$ substrates for $Hg_{1-x}Cd_xTe$ liquid-phase epitaxy, 40
CdTe rotation growth on silicon substrates by metallo-organic chemical vapour deposition, 57
complete characterization of epitaxial CdTe on GaAs from the lattice geometrical point of view, 165
depth non-uniformities in thin CdTe layers grown by MBE on InSb substrates, 191
effect of interdiffusion on dislocation generation in epitaxial layers on CdTe, (Cd,Zn)Te and Cd(Te,Se) substrates, 199
efficient n-type doping of CdTe epitaxial layers grown by photo-assisted molecular beam epitaxy with the use of chlorine, 178
heteroepitaxy of CdTe on GaAs and silicon substrates, 51
in situ reflectance anisotropy studies of the growth of CdTe and other compounds by MOCVD, 118
ion channelling Rutherford backscattering spectrometry structural characterization of CdS/CdTe heterostructures, 160
piezoreflectivity investigation of CdTe/(Cd,Zn)Te heterostructures, 87
properties of dry-etched CdTe–epitaxial layer surfaces and microstructures, 108
RHEED studies of MBE growth mechanisms of CdTe and CdMnTe, 103
scanning tunneling microscope investigation of the effects of CdTe substrate preparation on molecular beam epitaxially grown *n*-CdTe layers, 151
structural defects in bulk and epitaxial CdTe, 96
Epitaxy of thin films
laser growth of CdTe epitaxial film on CdTe substrate, 64
short period CdTe–ZnTe and CdTe–MnTe superlattices, 79
Etching
effect of interdiffusion on dislocation generation in epitaxial layers on CdTe, (Cd,Zn)Te and Cd(Te,Se) substrates, 199
effect of thermal annealing on the microstructure of CdTe and $Cd_{1-x}Zn_xTe$ crystals, 182
qualification of a new defect revealing etch for CdTe using cathodoluminescence microscopy, 113
relation between dislocation density, bulk electrical properties and ohmic contacts of CdTe, 168
Evaporation
floating-zone melting of CdTe, 23
Excitons
spectroscopy of donors and donor-bound excitons in CdTe/$Cd_{1-x}Zn_xTe$ multiple quantum wells, 83

Film growth
depth non-uniformities in thin CdTe layers grown by MBE on InSb substrates, 191
effect of the {*h*11} orientations and polarities of GaAs substrates on CdTe buffer layer structural properties, 145
laser growth of CdTe epitaxial film on CdTe substrate, 64
thin films of CdTe produced using stacked elemental layer processing for use in CdTe/CdS solar cells, 250

Gallium
diffusion of gallium in cadmium telluride, 186
Gallium arsenide
complete characterization of epitaxial CdTe on GaAs from the lattice geometrical point of view, 165
effect of the {*h*11} orientations and polarities of GaAs substrates on CdTe buffer layer structural properties, 145
heteroepitaxy of CdTe on GaAs and silicon substrates, 51
mechanical properties of CdTe, 1
properties of dry-etched CdTe–epitaxial layer surfaces and microstructures, 108
short period CdTe–ZnTe and CdTe–MnTe superlattices, 79
structural defects in bulk and epitaxial CdTe, 96
Glass
horizontal Bridgman growth of large high quality $Cd_{1-x}Zn_xTe$ crystals, 44

Heat treatment
thin films of CdTe produced using stacked elemental layer processing for use in CdTe/CdS solar cells, 250
Heterostructures
compact visible microgun-pumped CdTe–$Cd_{1-x}Mn_xTe$ laser, 279
effect of interdiffusion on dislocation generation in epitaxial layers on CdTe, (Cd,Zn)Te and Cd(Te,Se) substrates, 199
ion channelling Rutherford backscattering spectrometry structural characterization of CdS/CdTe heterostructures, 160
piezoreflectivity investigation of CdTe/(Cd,Zn)Te heterostructures, 87
structural and electronic properties of CdTe-based heterostructures, 71

Impurities
basic problems of vertical Bridgman growth of CdTe, 8
carbon and silicon in travelling heater method grown semi-insulating CdTe, 202
deep centres for optical processing in CdTe, 262
deep levels in semi-insulating CdTe, 223
determination of the iron acceptor level in CdTe, 243
native defect equilibrium in semi-insulating CdTe(Cl), 215
native point defects in CdTe and its stability region, 219
new method for the determination of V_{Cd} concentrations in p-CdTe, 139

Impurity correlations
effect of large-scale potential relief on the electronic transport in doped and compensated CdTe: the role of impurity correlations, 172
Indium
defects and electrical properties of doped and undoped CdTe single crystals from tellurium-rich solutions, 17
donor activation efficiency and doping profile quality in In-doped CdTe and CdZnTe quantum structures, 207
positron trapping at native vacancies in CdTe crystals: In doping effect, 134
spectroscopy of donors and donor-bound excitons in CdTe/$Cd_{1-x}Zn_xTe$ multiple quantum wells, 83
Indium antimonide
depth non-uniformities in thin CdTe layers grown by MBE on InSb substrates, 191
growth and structure of CdTe/$Cd_{1-x}Mn_xTe$ multiple quantum wells showing excitonic 2S states, 60
Indium phosphide
potentiality of photorefractive CdTe, 257
Infrared detectors
$Cd_{1-x}Zn_xTe$ substrates for $Hg_{1-x}Cd_xTe$ liquid-phase epitaxy, 40
diffusion of gallium in cadmium telluride, 186
Infrared spectroscopy
Fourier transform IR spectroscopy of CdTe:Fe, 246
qualification of a new defect revealing etch for CdTe using cathodoluminescence microscopy, 113
Interdiffusion
chemical diffusion of Hg in CdTe, 195
effect of interdiffusion on dislocation generation in epitaxial layers on CdTe, (Cd,Zn)Te and Cd(Te,Se) substrates, 199
implantation-enhanced interdiffusion in CdTe/ZnTe quantum wells, 211
Interfaces
CdTe rotation growth on silicon substrates by metallo-organic chemical vapour deposition, 57
horizontal Bridgman growth of large high quality $Cd_{1-x}Zn_xTe$ crystals, 44
short period CdTe–ZnTe and CdTe–MnTe superlattices, 79
Interfacial strain
effect of interdiffusion on dislocation generation in epitaxial layers on CdTe, (Cd,Zn)Te and Cd(Te,Se) substrates, 199
Ion implantation
implantation-enhanced interdiffusion in CdTe/ZnTe quantum wells, 211
specific behaviour of CdTe ion implantation damage, 123
Ionic conduction
the electronic bistability in doped semiconductors with polar optical scattering: the reversible switching effect in CdTe:Cl at room temperature, 302
Ionization
the electronic bistability in doped semiconductors with polar optical scattering: the reversible switching effect in CdTe:Cl at room temperature, 302
Iron
determination of the iron acceptor level in CdTe, 243
Fourier transform IR spectroscopy of CdTe:Fe, 246
specific behaviour of CdTe ion implantation damage, 123

Laser processing
laser growth of CdTe epitaxial film on CdTe substrate, 64
picosecond diffraction kinetics of transient gratings in CdTe and CdZnTe, 309
RHEED studies of MBE growth mechanisms of CdTe and CdMnTe, 103
time-resolved build-up and decay of photorefractive and free carrier gratings in CdTe:V, 268
time-resolved light-induced Faraday rotation in $Zn_{1-x}Mn_xTe$ and $Cd_{1-x}Mn_xTe$, 239
Lasers
compact visible microgun-pumped C lTe–$Cd_{1-x}Mn_xTe$ laser, 279
Liquid phase epitaxy
$Cd_{1-x}Zn_xTe$ substrates for $Hg_{1-x}Cd_xTe$ liquid-phase epitaxy, 40
Luminescence
determination of the iron acceptor level in CdTe, 243
qualification of a new defect revealing etch for CdTe using cathodoluminescence microscopy, 113

Magnetic materials
growth and structure of CdTe/$Cd_{1-x}Mn_xTe$ multiple quantum wells showing excitonic 2S states, 60
overview of CdTe-based semimagnetic semiconductors, 228
Magnetic properties
overview of CdTe-based semimagnetic semiconductors, 228
Manganese
comparative reflectivity study of coupled and uncoupled CdTe/CdMnTe asymmetric double quantum wells, 235
RHEED studies of MBE growth mechanisms of CdTe and CdMnTe, 103
Mechanical properties
mechanical properties of CdTe, 1
Melting
floating-zone melting of CdTe, 23
Mercury
chemical diffusion of Hg in CdTe, 195
Metal-organic chemical vapour deposition
CdTe rotation growth on silicon substrates by metallo-organic chemical vapour deposition, 57
effect of the {*h*11} orientations and polarities of GaAs substrates on CdTe buffer layer structural properties, 145
in situ reflectance anisotropy studies of the growth of CdTe and other compounds by MOCVD, 118
Microstructural development
effect of thermal annealing on the microstructure of CdTe and $Cd_{1-x}Zn_xTe$ crystals, 182
Molecular beam epitaxy
depth non-uniformities in thin CdTe layers grown by MBE on InSb substrates, 191
donor activation efficiency and doping profile quality in In-doped CdTe and CdZnTe quantum structures, 207
efficient n-type doping of CdTe epitaxial layers grown by photo-assisted molecular beam epitaxy with the use of chlorine, 178
growth and structure of CdTe/$Cd_{1-x}Mn_xTe$ multiple quantum wells showing excitonic 2S states, 60
heteroepitaxy of CdTe on GaAs and silicon substrates, 51
piezomodulated reflectivity on CdMnTe/CdTe quantum well structures as a new standard characterization method, 92
RHEED studies of MBE growth mechanisms of CdTe and CdMnTe, 103
scanning tunneling microscope investigation of the effects of CdTe substrate preparation on molecular beam epitaxially grown *n*-CdTe layers, 151
structural and electronic properties of CdTe-based heterostructures, 71

Non-destructive measurements
piezomodulated reflectivity on CdMnTe/CdTe quantum well structures as a new standard characterization method, 92

Nonlinear effects
time-resolved build-up and decay of photorefractive and free-carrier gratings in CdTe:V, 268

Optical absorption
potentiality of photorefractive CdTe, 257
Optical measurements
comparative reflectivity study of coupled and uncoupled CdTe/CdMnTe asymmetric double quantum wells, 235
deep centres for optical processing in CdTe, 262
optical, photoelectrical, deep level and photorefractive characterization of CdTe:V, 273
piezomodulated reflectivity on CdMnTe/CdTe quantum well structures as a new standard characterization method, 92
spectroscopy of donors and donor-bound excitons in CdTe/$Cd_{1-x}Zn_xTe$ multiple quantum wells, 83
structural properties of defects in $Cd_{1-x}Zn_xTe$, 128
Optical properties
compact visible microgun-pumped CdTe–$Cd_{1-x}Mn_xTe$ laser, 279
comparative reflectivity study of coupled and uncoupled CdTe/CdMnTe asymmetric double quantum wells, 235
deep centres for optical processing in CdTe, 262
Fourier transform IR spectroscopy of CdTe:Fe, 246
potentiality of photorefractive CdTe, 257
structural and electronic properties of CdTe-based heterostructures, 71
time-resolved build-up and decay of photorefractive and free-carrier gratings in CdTe:V, 268
time-resolved light-induced Faraday rotation in $Zn_{1-x}Mn_xTe$ and $Cd_{1-x}Mn_xTe$, 239
Oxidation
diffusion of gallium in cadmium telluride, 186

Photocurrent
compensation of trapping losses in CdTe detectors, 296
Photoelectron spectroscopy
optical, photoelectrical, deep level and photorefractive characterization of CdTe:V, 273
X-ray photoelectron diffraction from the CdTe(111)A polar surface, 155
Photoluminescence
comparative reflectivity study of coupled and uncoupled CdTe/CdMnTe asymmetric double quantum wells, 235
defects and electrical properties of doped and undoped CdTe single crystals from tellurium-rich solutions, 17
efficient n-type doping of CdTe epitaxial layers grown by photo-assisted molecular beam epitaxy with the use of chlorine, 178
gamma- and X-ray detectors manufactured from $Cd_{1-x}Zn_xTe$ grown by a high pressure Bridgman method, 291
implantation-enhanced interdiffusion in CdTe/ZnTe quantum wells, 211
new method for the determination of V_{Cd} concentrations in p-CdTe, 139
piezomodulated reflectivity on CdMnTe/CdTe quantum well structures as a new standard characterization method, 92
structural properties of defects in $Cd_{1-x}Zn_xTe$, 128
Photons
compensation of trapping losses in CdTe detectors, 296
Piezoeffect
piezoreflectivity investigation of CdTe/(Cd,Zn)Te heterostructures, 87
Plasma processing
properties of dry-etched CdTe-epitaxial layer surfaces and microstructures, 108

Polarization
compensation of trapping losses in CdTe detectors, 296
time-resolved light-induced Faraday rotation in $Zn_{1-x}Mn_xTe$ and $Cd_{1-x}Mn_xTe$, 239
Positrons
positron trapping at native vacancies in CdTe crystals: In doping effect, 134
Process and device modelling
Bridgman growth and assessment of CdTe and CdZnTe using the accelerated crucible rotation technique, 29
compensation of trapping losses in CdTe detectors, 296
computer simulation of CdTe crystal growth and application, 48
Protons
chemical diffusion of Hg in CdTe, 195

Quantum structures
donor activation efficiency and doping profile quality in In-doped CdTe and CdZnTe quantum structures, 207
Quantum wells
compact visible microgun-pumped CdTe–$Cd_{1-x}Mn_xTe$ laser, 279
comparative reflectivity study of coupled and uncoupled CdTe/CdMnTe asymmetric double quantum wells, 235
growth and structure of CdTe/$Cd_{1-x}Mn_xTe$ multiple quantum wells showing excitonic 2S states, 60
implantation-enhanced interdiffusion in CdTe/ZnTe quantum wells, 211
overview of CdTe-based semimagnetic semiconductors, 228
piezomodulated reflectivity on CdMnTe/CdTe quantum well structures as a new standard characterization method, 92
spectroscopy of donors and donor-bound excitons in CdTe/$Cd_{1-x}Zn_xTe$ multiple quantum wells, 83

Radiation effects
high quality CdTe and its application to radiation detectors, 283
power switching with CdTe:Cl, 304
Reflectance difference spectrometry
in situ reflectance anisotropy studies of the growth of CdTe and other compounds by MOCVD, 118
Reflectance high-energy electron diffraction
RHEED studies of MBE growth mechanisms of CdTe and CdMnTe, 103
Reflection
piezoreflectivity investigation of CdTe/(Cd,Zn)Te heterostructures, 87
Rutherford backscattering
ion channelling Rutherford backscattering spectrometry structural characterization of CdS/CdTe heterostructures, 160

Scanning tunnelling microscopy
scanning tunneling microscope investigation of the effects of CdTe substrate preparation on molecualr beam epitaxially grown *n*-CdTe layers, 151
Secondary ion mass spectrometry
efficient n-type doping of CdTe epitaxial layers grown by photo-assisted molecular beam epitaxy with the use of chlorine, 178
Semiconductors
effect of large-scale potential relief on the electronic transport in doped and compensated CdTe: the role of impurity correlations, 172
overview of CdTe-based semimagnetic semiconductors, 228

Silicon
- carbon and silicon in travelling heater method grown semi-insulating CdTe, 202
- CdTe rotation growth on silicon substrates by metallo-organic chemical vapour deposition, 57
- heteroepitaxy of CdTe on GaAs and silicon substrates, 51
- mechanical properties of CdTe, 1

Silver
- new method for the determination of V_{Cd} concentrations in p-CdTe, 139

Single crystals
- defects and electrical properties of doped and undoped CdTe single crystals from tellurium-rich solutions, 17

Solar cells
- thin films of CdTe produced using stacked elemental layer processing for use in CdTe/CdS solar cells, 250

Solid–solid interfaces
- depth non-uniformities in thin CdTe layers grown by MBE on InSb substrates, 191
- growth of CdTe single crystals by vapour condensation on the surface of polycrystalline source material, 68

Space charge effects
- potentiality of photorefractive CdTe, 257
- time-resolved build-up and decay of photorefractive and free-carrier gratings in CdTe:V, 268

Stoichiometry and homogeneity
- basic problems of vertical Bridgman growth of CdTe, 8
- thin films of CdTe produced using stacked elemental layer processing for use in CdTe/CdS solar cells, 250

Stress
- mechanical properties of CdTe, 1

Structural properties
- effect of the {*h*11} orientations and polarities of GaAs substrates on CdTe buffer layer structural properties, 145
- growth of CdTe single crystals by vapour condensation on the surface of polycrystalline source material, 68
- structural and electronic properties of CdTe-based heterostructures, 71
- structural properties of defects in $Cd_{1-x}Zn_xTe$, 128

Superlattices
- short period CdTe–ZnTe and CdTe–MnTe superlattices, 79

Surface morphology
- effect of the {*h*11} orientations and polarities of GaAs substrates on CdTe buffer layer structural properties, 145

Surface roughness
- *in situ* reflectance anisotropy studies of the growth of CdTe and other compounds by MOCVD, 118
- scanning tunneling microscope investigation of the effects of CdTe substrate preparation on molecular beam epitaxially grown *n*-CdTe layers, 151
- X-ray photoelectron diffraction from the CdTe(111)A polar surface, 155

Surface structure
- properties of dry-etched CdTe–epitaxial layer surfaces and microstructures, 108
- X-ray photoelectron diffraction from the CdTe(111)A polar surface, 155

Tellurium
- defects and electrical properties of doped and undoped CdTe single crystals from tellurium-rich solutions, 17
- effect of large-scale potential relief on the electronic transport in doped and compensated CdTe: the role of impurity correlations, 172
- new method for the determination of V_{Cd} concentrations in p-CdTe, 139

Ternary compounds
- overview of CdTe-based semimagnetic semiconductors, 228

Thermal annealing
- effect of thermal annealing on the microstructure of CdTe and $Cd_{1-x}Zn_xTe$ crystals, 182

Thermal processing
- native point defects in CdTe and its stability region, 219

Thermal properties
- computer simulation of CdTe crystal growth and application, 48

Transport properties
- effect of large-scale potential relief on the electronic transport in doped and compensated CdTe: the role of impurity correlations, 172

Twin boundaries
- qualification of a new defect revealing etch for CdTe using cathodoluminescence microscopy, 113

Vanadium
- optical, photoelectrical, deep level and photorefractive characterization of CdTe:V, 273

Vapour phase epitaxy
- growth of CdTe single crystals by vapour condensation on the surface of polycrystalline source material, 68

X-ray spectroscopy
- chemical diffusion of Hg in CdTe, 195
- complete characterization of epitaxial CdTe on GaAs from the lattice geometrical point of view, 165
- X-ray photoelectron diffraction from the CdTe(111)A polar surface, 155

Zinc
- piezoreflectivity investigation of CdTe/(Cd,Zn)Te heterostructures, 87

Zinc telluride
- gamma- and X-ray detectors manufactured from $Cd_{1-x}Zn_xTe$ grown by a high pressure Bridgman method, 291
- implantation-enhanced interdiffusion in CdTe/ZnTe quantum wells, 211
- *in situ* reflectance anisotropy studies of the growth of CdTe and other compounds by MOCVD, 118
- structural properties of defects in $Cd_{1-x}Zn_xTe$, 128